The Combined Finite/Discrete Element Method in Transient Dynamics of Reinforced Concrete Structures under Blast Loading

Bangash, Tehmiryar

The Combined Finite/Discrete Element Method in Transient Dynamics of Reinforced Concrete Structures under Blast Loading

PhD Thesis
Queen Mary, University of London
2004

Submitted for the degree of Doctor of Philosophy by

Tehmiryar Bangash

Supervisor Dr Ante Munjiza

Declaration

I hereby declare that no portion of the work referred to in this thesis has been submitted in support of an application for another degree or qualification in this or any other University or Institute of Learning.

T Bangash

Abstract

The research here presented has employed the newly evolved finite-discrete element method in the development of novel numerical solutions for the analysis of failure and collapse of reinforced concrete structures under hazardous blast loads. The first step to achieving this was to study the structural response, failure and collapse of individual structural elements. Thus the research in this area is taken further by using numerical solutions to study the behaviour of reinforced concrete beams to the point of failure. The results are implemented into the combined finite-discrete element method through a novel computationally efficient two noded beam element. Numerical integration across the cross section of the beam element is applied to facilitate the application of non-linear constitutive laws for both steel and concrete for the case of multi-axial bending coupled with axial force. The accuracy of this new element is tested and validated under both static and dynamic loading situations using analytical solutions together with experiments undertaken at the University of Alberta and The Swiss Federal Institute of Technology. The proposed element has the advantage of reducing the size of the problem by fifty percent through the elimination of the rotational degrees of freedom using static condensation. The new element, when coupled with NBS contact detection, enables the same finite element mesh to be used for the discretised contact solutions, thus further reducing the CPU time required. When implemented into the finite-discrete element method, the proposed numerical solution also takes into account contact-impact and inertia effects. It is therefore both an accurate and CPU efficient solution to the combined finite-discrete element analysis of structural response, failure and collapse of real life structures when subjected to hazardous loads as demonstrated in the thesis.

T Bangash

Acknowledgements

The candidate wishes to express his appreciation and gratitude to his supervisor, Dr Ante Munjiza for his tireless efforts at various developmental stages of this research. His helpful suggestions were valuable in the completion of this thesis.

The candidate also wishes to extend a very special thank you to his colleagues in the Department of Engineering at Queen Mary College, University of London, in particular special thanks to Mrs Jean Hefford, Professor Aliabadi, Professor Stark, Mr Ken Andrews, Mrs Rebecca Chew, Mr Allem Million, Dr Ranjan Vepa, Dr F Motallebi, Dr Eldad Avital, Mr A W Turner, Mr Mike Collins, Mr M Etheridge, Mrs M Langsbridge, Miss Jun Ma, Dr Sylvia Heubbe-Walker, Mr Esteban Rougier, Mr George Phantos and Dr Graham Dorrington. The most gracious assistance provided by Mr Raymond Lam is enormously appreciated.

The author is indebted to the following for their tremendous help in providing advice and materials in the form of experimental results, data, drawings and background design during this research period: -

Dr W G Corley of CTL Laboratories, Skokie 60077,Illinois, USA

Dr J Bardwell of CTL Laboratories, Skokie 60077,Illinois, USA

Edward R Sturm President of Sturm Engineering Company, Oklahoma, USA

Alan Kirkpatrick of Kirkpatrick Engineering Company,Oklahoma, USA

Mr Mike Chrimes, Chief Librarian, The Institution of Civil Engineers, London, UK

The American Society of Civil Engineers, Reston Virginia

FEMA, 500 C Street, S W Washington D.C., USA

Professor Bachman formerly of the Swiss Federal Institute of Technology, Zurich, Switzerland

Mrs Natalie Amman of the Swiss Federal Institute of Technology, Zurich, Switzerland

Dr Walter Amaann of ,Eidg.Institutfür Schnee-und-Lawinenforschung, SLF

Davos, Switzerland

The candidate is also appreciative of the efforts of those authors and researchers mentioned in the references.

The candidate would also like to take this opportunity to thank the unwavering support provided by his family during this research period.

T Bangash

Contents

Conversion Table

Imperial Units	SI Units
1 in	25.4 mm
1 ft	30.48 cm
10 ga	3.57 mm
1 lb	0.454 kg
1 ton	9.964 kN
1 sq ft	929 cm^2
1 cubic ft	16.4 cm^3
1 psi	6.89 kPa
20 T/ft^2	1915.2 kN/m^2
1 lb/sq ft	992.16 kPa
1 lb/ft^3	16.02 kg/m^3
1 ft/lb	1.356 Nm
1 ft/sec	0.3048 M/s
1 slug	14.59 kg
1 in lb	0.1129848 Nm
1 kip/in^2	175.1268 kN/m^2
1 bar	100 kN/m^2
1 kip	1000 lb
1 short ton (2000 lb)	0.9027 Mg
MKS Units	**SI Units**
I Pascal (Pa)	1 N/m^2
1 kgm	9.807 Nm
1 kgf	9.807 N

List of Photographs

List of Tables

Chapter 1

A literature survey on existing damage scenarios of constructed facilities

1.1 Introduction

Explosive bombs have claimed many casualties in many different parts of the World. Their effects can be quite catastrophic with destruction on an indescribable scale. Blast loading is loosely categorised as follows:-

- *Internal Blast* – occurs due to gas/vapour explosion, solid suspension and air mixtures
- *External Blast* – occurs due to high explosives situated in or on the ground or in the air
- *Impact Loading* – occurring from falling objects or missiles generated by the bomb loading

Impact loading is a direct result of either internal or external explosions and can cause flying debris, smoke and fire.

The threats of bombings are ever increasing as a result of the activities of a myriad of terrorist organisations. Consequently questions are now being asked as to how best to protect buildings and their incumbents from such a danger. A multitude of research organisations are now reviewing design and construction techniques in order to increase the structural resistance to threats posed by commonly used devices such as vehicle bombs.

Such abnormal loading is transient dynamic in nature, thus having short duration time histories ranging from a few milliseconds to a few seconds. Resulting bomb damage depends on the size and type of the bomb as well as the makeup and layout of the target structure.

Steel structures exhibit very little resistance to anything other than the lighter bombs. Concrete structures have greater mass, increased damping and a higher energy absorbing capacity. It is these reasons, why concrete structures resist blast loading with greater effectiveness. The U.S. State department will only allow use of concrete buildings in areas where the threat of explosion is considered high.

The current research is related to bomb explosions in and around buildings. It covers important case studies, a review of existing knowledge for blast effects and protective design techniques.

This chapter is devoted to a review of bomb affected buildings. Lessons from these case studies will pave the way for the development of new analytical, computational and protective techniques for future constructed facilities. Numerous compilations of explosions and damage data exist. Walley, F [1] reviews data from World War Two covering countries in Europe and Asia. Tables 1.1, 1.2 and 1.3 present various explosion data gathered from incidents spanning the last four decades.

1.2 Case studies

1.2.1 Alfred P Murrah building, Oklahoma USA

At two minutes past nine on the morning of the 19th of April 1995 an 1814 kg (TNT equivalent 1905 kg) fertiliser based bomb placed in a parked truck, exploded 3 to 5 metres away from the front of the Alfred P. Murrah building in Oklahoma [3]. Approximately seventy five surrounding buildings were damaged.

The force of the blast was felt mostly on the north side of the building extending for a distance of 2.6 km. The south side remained mostly unaffected as the building itself provided shelter from the blast. Considerable structural damage was evident in many of the nearby buildings. Windows in the range of about 3.2 km were completely shattered. A total of three hundred buildings were damaged with twenty three of them seriously. The total damage amounted to $652million [3].The lives of 167 people were lost and 782 were injured [3].

The Murrah building was designed in 1974, as a nine-storey reinforced concrete structure with a slab/column design. Construction was completed in 1976. Glass cladding was used to cover most of the north side facade, whilst precast concrete shades protruded from the south side. The shades functioned to protect the building occupants from direct sunlight. The staircase and elevator walls situated on the south side were known to have provided most of the resistance against the blast, even though seismic and blast resistance was not considered in the design of the building. Another architectural feature of the building were the four cylindrical towers at each corner of the building. The building had single storey structures on either side, one of which was above an underground car park.

The building on the ground floor measured 61 m x 23 m and was divided into twenty bays. The width of the buildings covered two bays. An atrium at the front of the building was created using four north-facing columns unsupported for two storeys. A spandrel beam on the third floor was used to transfer the load from the floors above. The bomb destroyed three of these columns and in addition destroyed an interior column. The upper floors simply fell down in a progressive manner as the floor slabs broke off from the centre line of columns.

Column G20 (Figure 1.1), closest to the blast failed due to the shattering of the concrete known as brisance [4] (multiple reflection of the shock waves within the material). It was thought that the other columns, which failed, did so between the second and third floors due to the inward movement of the transfer girder. All failures were observed to be brittle. However the east annexe, which was not directly hit by the shock waves did show some flexural behaviour.

Damage to the nearby YMCA building included buckling of the roof system shown in Figure 1.6. One block further down the Regency Tower's building was for the most part undamaged, except for the plasterboard covering some walls. Damage did result, however to the air supply/exhaust systems. This showed that blast waves could propagate through the mechanical ducting system of a building.

Forensic investigations carried out by Corley W.G *et al.* [5] confirmed the design of the building to be well executed and conforming to requirements of the day. Failure was deemed to have occurred within three minutes by progressive collapse after the loss of strategic columns [5]. Figure 1.1 shows the building prior to being subjected to the explosion. Figure 1.2 shows the cluster of buildings around the Murrah Building.

Figure 1.1 Alfred P Murrah building [5]

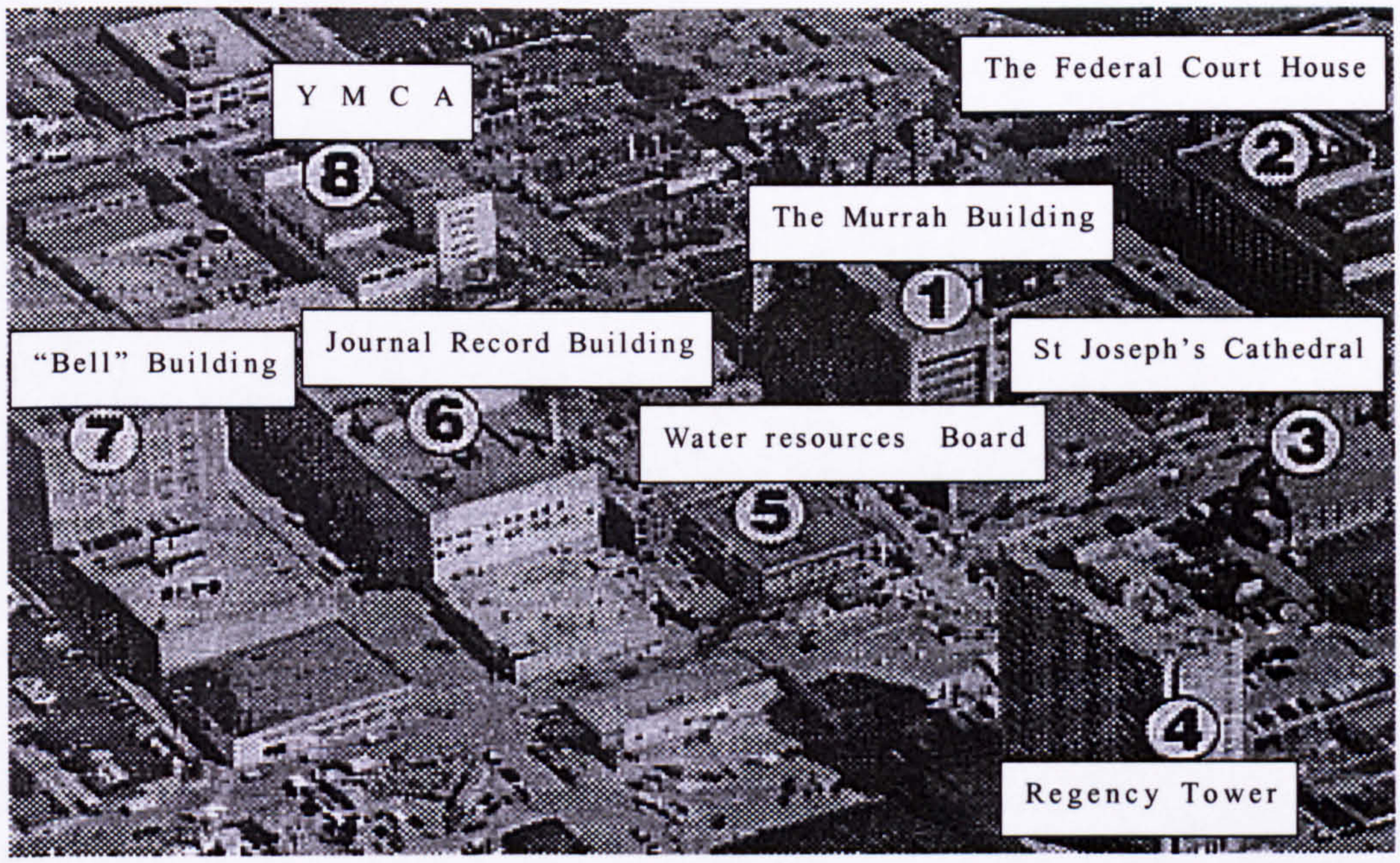

Figure 1.2 Aerial view surrounding the Alfred P Murrah building, Oklahoma [6]

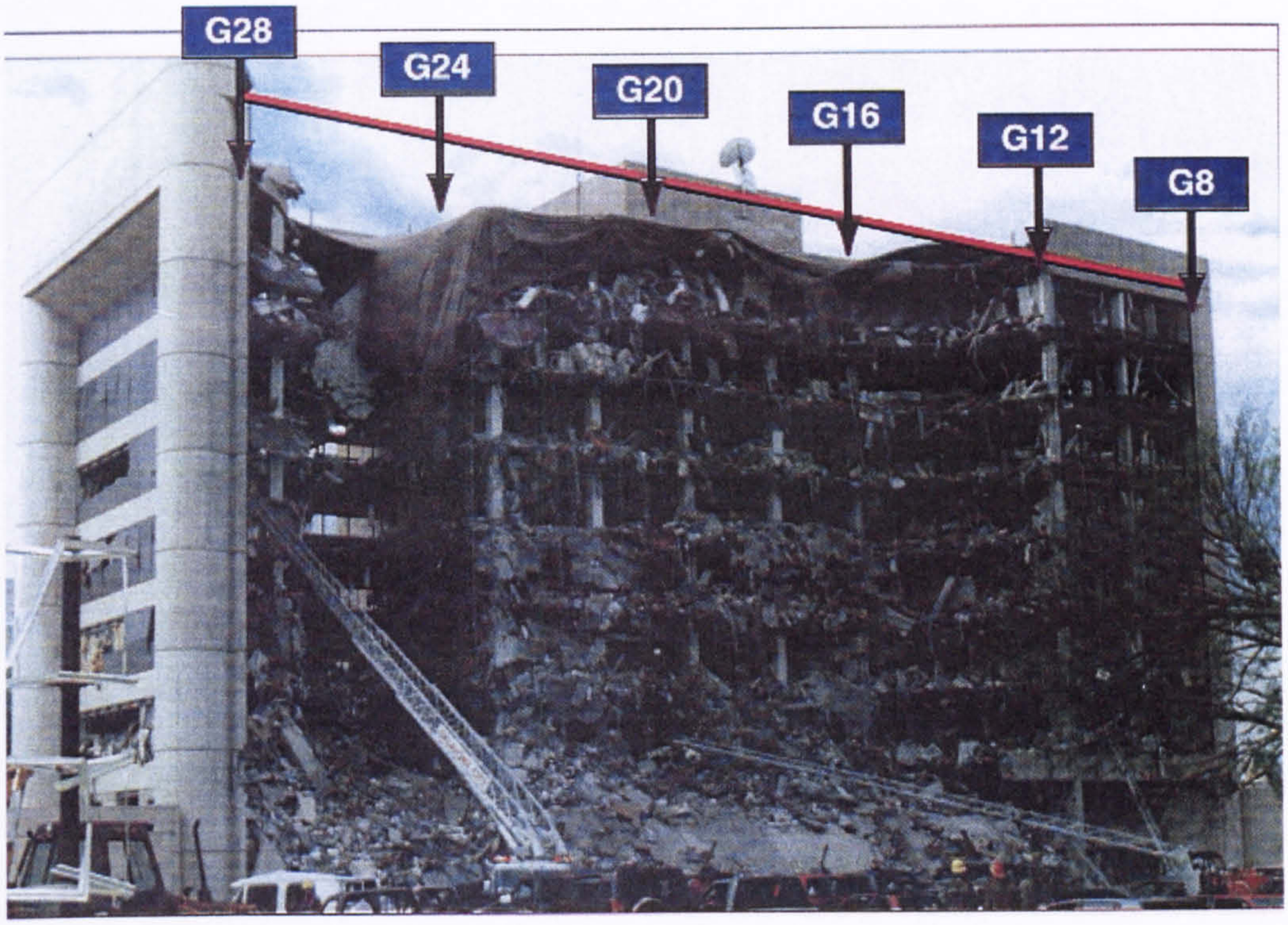

Figure 1.3 North face columns positions of the Alfred P Murrah building [3]

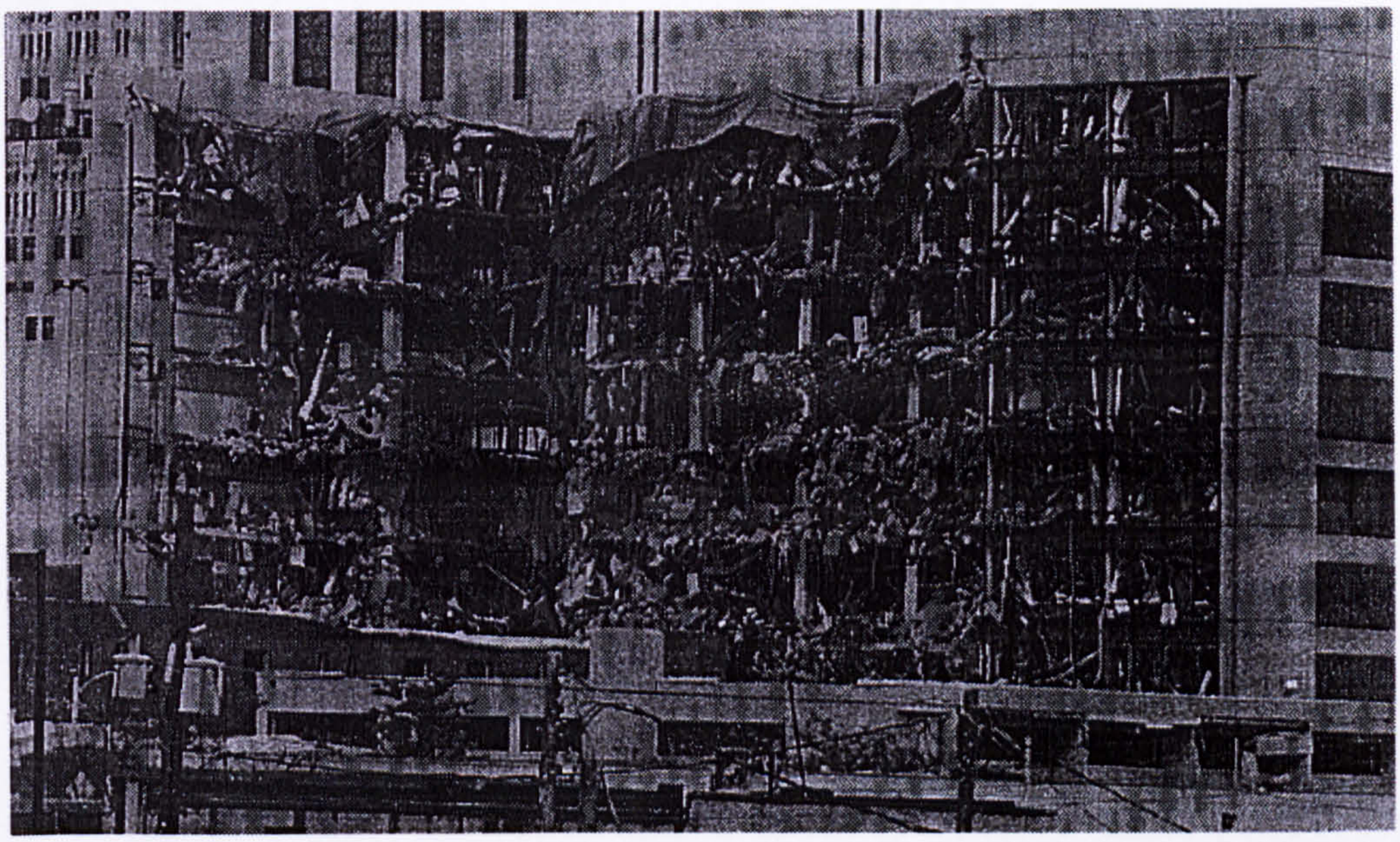

Figure 1.4 Damage resulting from the explosion to the Alfred P Murrah building [3]

Figure 1.5 Damage to a steel structure with steel sheet cladding near the Murrah building [3]

Figure 1.6 Buckled roof in the nearby YMCA building [3]

1.2.2 St Mary Axe, London UK

This explosion took place in 1992, using a 350 kgTNT bomb. In this case the building was shielded from a direct blast load by adjacent buildings. Even so considerable damage was observed, especially to the surrounding buildings which included The European Development Bank [10]. The building was a concrete slab column design with some non-load bearing masonry for the lower three levels. The windows in general were 2.5 m x 2.5 m in size and were made of toughened 10 mm thick double glazing.

1.2.3 The Jewish Community Centre, Buenos Aires, Argentina

This explosion caused progressive collapse of the floor slabs, which were connected, to the exterior walls [10]. The 275 kg vehicle bomb was positioned between 3 to 5 metres from the building, which was a five storey structure of brick and masonry construction.

1.2.4 Bishopsgate, London UK

This 350 kgTNT bomb blast damaged many buildings in the Bishopsgate area of London in 1994. Frames were heavily distorted and considerable internal damage was observed in many buildings [10]. "Sof-Shock" glass was recommended to replace the original laminated glass, as this has the ability to stretch under blast loading, thus minimising load transfer to the adjacent structural components.

1.2.5 Staples Corner, London UK

This bomb produced an explosion equivalent to 300 kg TNT [10]. A nearby steel structure suffered major damage to the sheet steel cladding. The range from the blast was 17 m. As a result severe damage also occurred to sheetings, purlins, blockwork lining the wall and various fittings.

1.2.6 Ronan Point Towers, London UK

The towers at Ronan Point in the Canning Town area of London were built using the Danish Larsen-Nielson construction system popular in the 1960's. A gas explosion, in the second of nine towers at the site, on Thursday the 16th of May 1968 destroyed the load bearing flank wall on the nineteenth floor, thus destroying the support for the floor slabs on that corner of the floor. As a result the nineteenth floor collapsed. The weight of the flank wall and floor slabs caused a progressive collapse of the south east corner of the tower. The damage is shown in Figure 1.7.

Figure 1.7 Ronan Point tower collapse, 1968 [9]

1.2.7 Docklands, London UK

This 500 kg TNT bomb was detonated on the 9th of February 1996 [10]. The vehicle bomb in question was placed in between various buildings and caused over £100 million pounds worth of damage. The resulting pattern of reflection and refraction produced different responses from each of the structures concerned. Those structures with a greater height to base ratio responded more robustly to the loading.

The multi-storey steel buildings on the South Quay Waterside were protected from damage by the Docklands light railway and consequently suffered in the most part damage only to the windows and cladding.

The South Quay Plaza contained three reinforced concrete structures with pitched roofs and a shopping centre. Due to the damage caused by the shock wave, the shopping centre had to demolished. The other buildings were relatively unscathed.

Buildings in the Thames Quay suffered minor damage to cladding. Steel-framed structures of the Great Enterprise had suffered complete damage to their facade but otherwise performed well.

Cracks in the bridge deck of the Docklands light Railway required major reconstruction. Bridge Bearings and circular reinforced concrete piers were not damaged by the blast. The layout of the buildings in this area is shown in Figure 1.8.

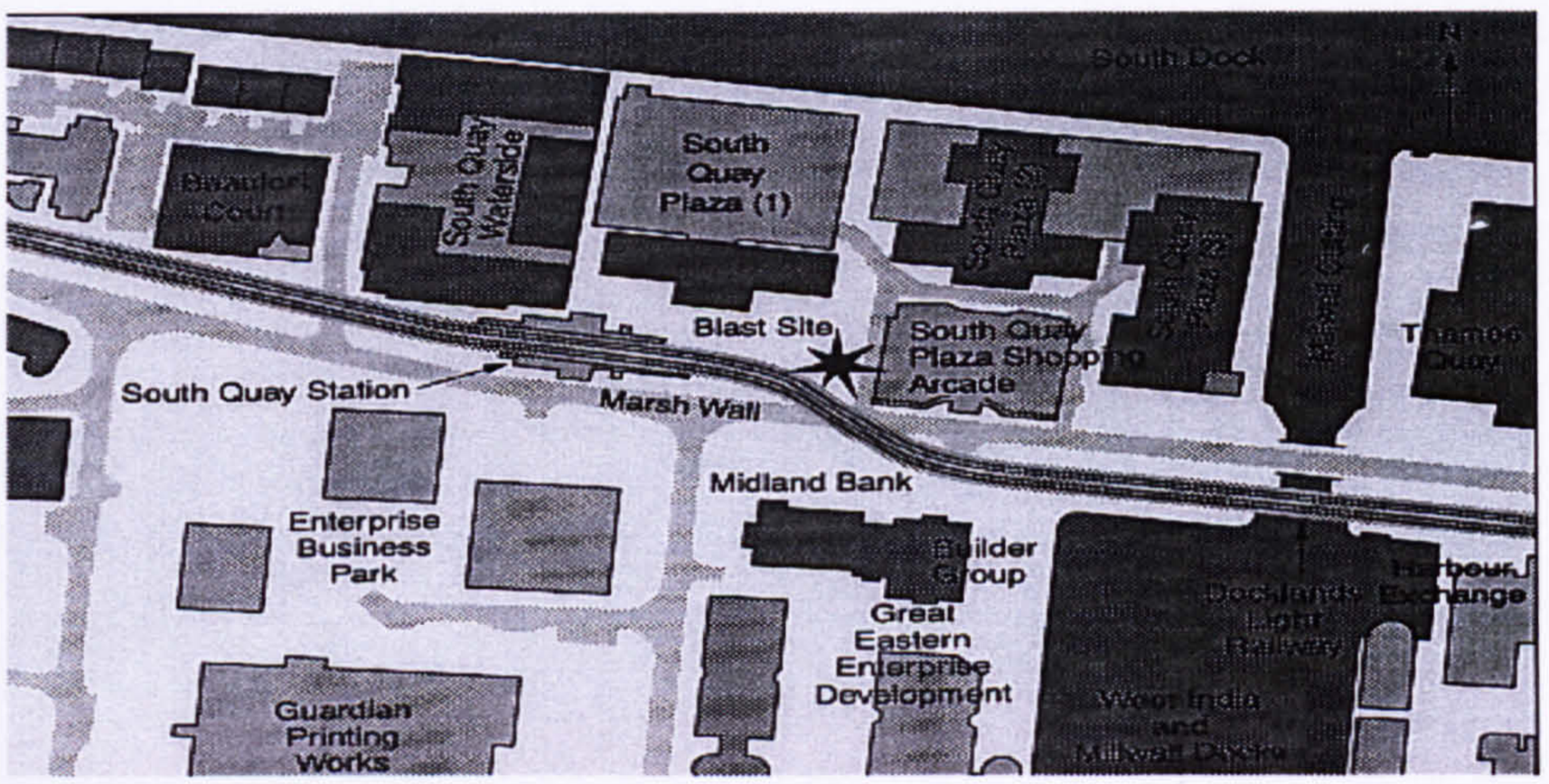

Figure 1.8 Docklands area of London exposed to bomb loading in 1996 [7]

1.2.8 Manchester bomb blast, UK

Manchester City centre suffered intense damage from a 1500 kg (1.5 ton) bomb that exploded on the 15th June 1996 [10]. Figures 1.9 and 1.10 show the destruction of the 280 m^2 Arndale shopping centre and the 30 m high pedestrian footbridge. The shopping centre was a concrete and steel framed structure supporting a concrete plank-flooring and large external cladding panels. Along Corporation Street the frame structure was observed to have buckled and damage in other buildings was seen to rise to as much as twenty metres above ground level. The blast was powerful enough to completely lift a 200000 kg structure from its bearings, thus rendering the structure unsafe. Nearby the steel framed 10 storey Longridge House collapsed. The Royal Exchange building suffered shattered windows and some structural damage. Marks & Spencer's across the road also suffered severe damage to its glazed shopfront and heavy concrete coping. Similar scenes were found streets away. One interesting point of note is that a 26 storey structure 500 m away had no damage to its lower windows, but windows higher up were completely destroyed. For technical reasons the authorities did not reveal the nature of the blast and standoff distances.

Figure 1.9 Damage to the Arndale shopping centre [10]

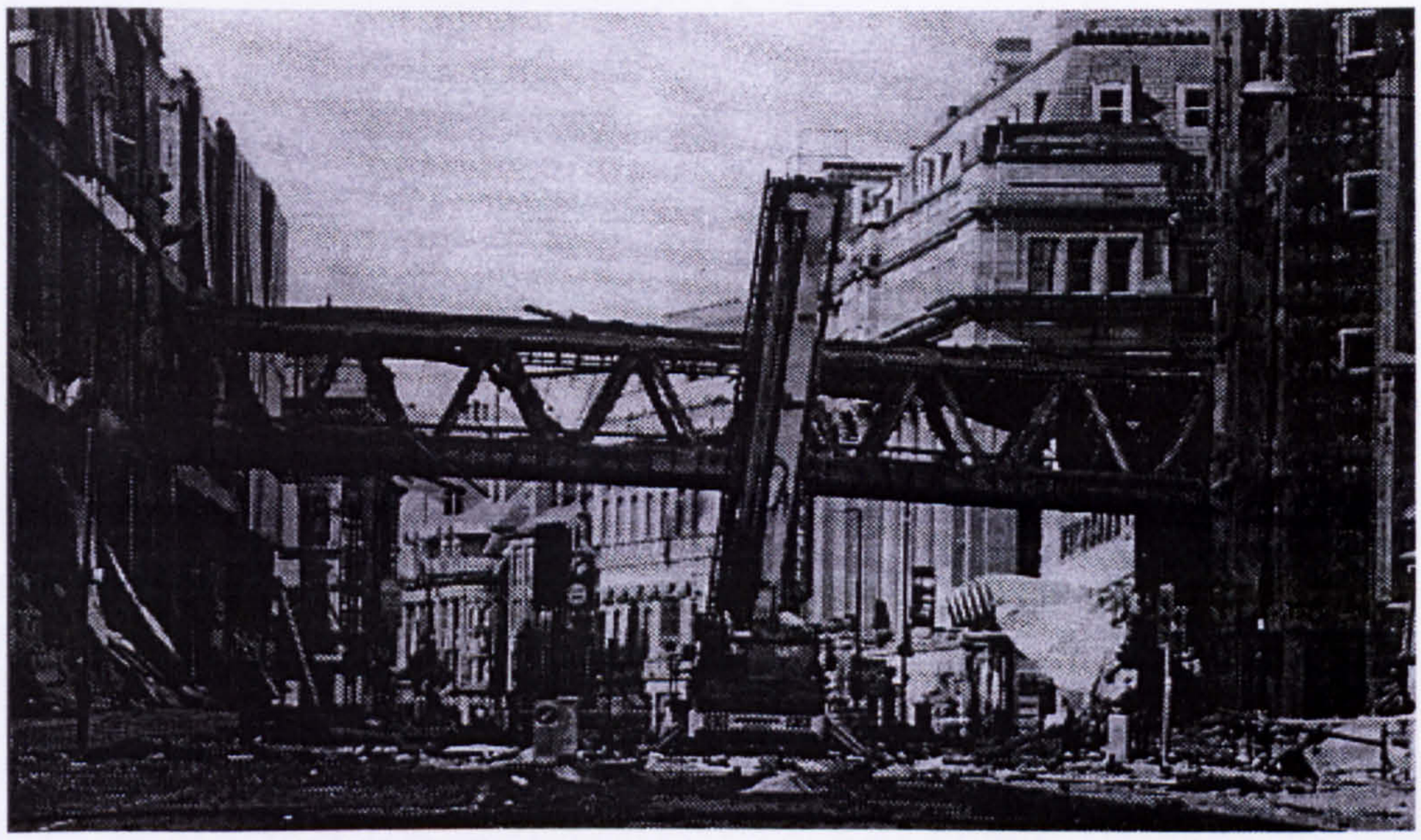

Figure 1.10 Damage to the 30 m pedestrian footbridge in Manchester [10]

1.2.9 Lisburn bombing, Northern Ireland UK

These bombs exploded in the British Army barracks south of Belfast in 1996 causing serious damage. A crater was formed as a result of this bombing, which is shown in Figure 1.11. The damage scenario is shown in Figure 1.12.

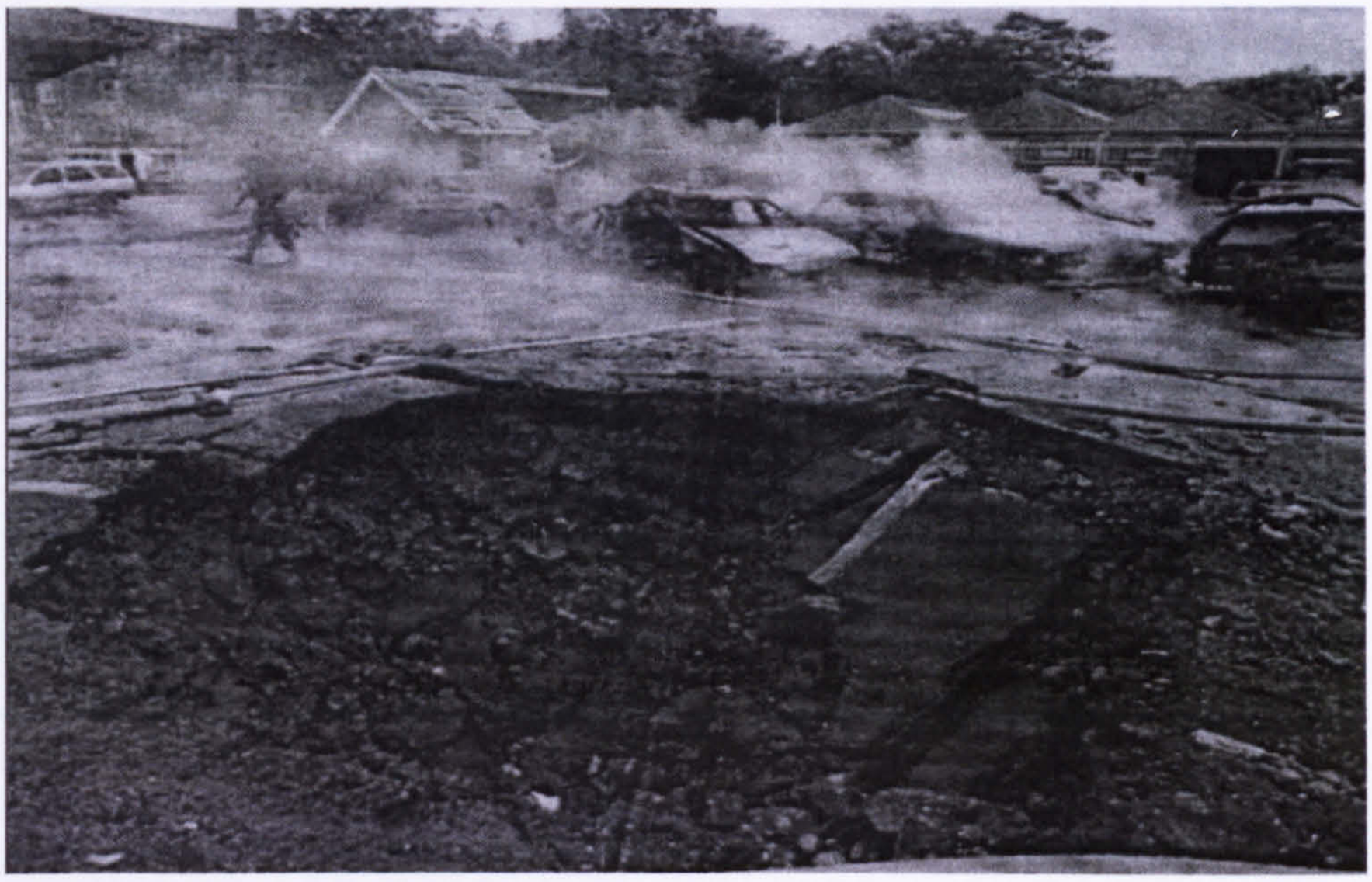

Figure 1.11 The crater formed as a result of the Lisburn bombing [10]

Figure 1.12 Bomb blast scenario at Lisburn, Northern Ireland [10]

1.2.10 Al-Khobar, Saudi Arabia

This explosion took place in the city of Dhahran in June 1996. A 13.7 m long and 10.7 m deep crater was formed by the 2268 kgTNT bomb, which caused extensive damage to the Al-Khobar building as shown in Figure 1.13.

Figure 1.13 Al-Khobar building, Saudi Arabia [10]

1.2.11 Terrorist bomb blasts in Pakistan

Pakistan has suffered countless terrorist bomb attacks in its short history, many of which exploded at bus stands and busy shopping markets. One is known to have exploded in the Shaukat Khanum charity cancer hospital in the city of Lahore.

1.2.12 The Pentagon, Washington USA

A hijacked Boeing 757-200 aeroplane was flown into the US Military headquarters at 9:40 am on the morning of the 11th of September 2001. A total of eight hundred people were known to have died. Figure 1.16 shows the scene at the Pentagon building that morning.

1.2.13 The World Trade Centre, New York USA

This 110-storey plaza suffered comprehensive damage in 1993 as a result of a 571.6 kg TNT high explosive fertiliser-based bomb [10]. The explosion occurred in the underground garage, two levels below the ground floor in front of the north tower's south wall. A crater spanning up to 36 m was created and where the floor slabs had been

destroyed. Other important details were the blowing out of the two-storey 280 mm thick R.C. slabs, along with segments of the North and South masonry walls.

Unfortunately this was not the only attack upon the World Trade Centre. At two minutes past eight o'clock on the morning of the 11th of September 2001, a hijacked Boeing 767-200 airliner was flown into the North tower of the World Trade Centre. This was followed by a second Boeing 767-200 which was flown into the South Tower eighteen minutes later. One of the buildings collapsed approximately one hour after the impact and the other followed forty five minutes later resulting in the tragic loss of thousands of lives.

The impacts were thought to have destroyed some strategic columns connecting the floor slabs on different levels of the buildings [16]. The aviation fuel subsequently poured out igniting and burning at 800 degrees Celsius. The combined effects of the plane impact and the high temperatures resulting from the burning aviation fuel acutely damaged the structure's ability to support itself below the point of impact. Thus the weight of the upper floors induced a progressive collapse [15] as shown in Figure 1.15. The structural components from the upper floors impacted with structural component from the lower floors.

The cost of this disaster could be as much as ten billion pounds [18] as claims may be made for the planes as well as the buildings and their contents.

Figure 1.14 Sequence of events for the WTC south tower [11,12,13,14,17,19]

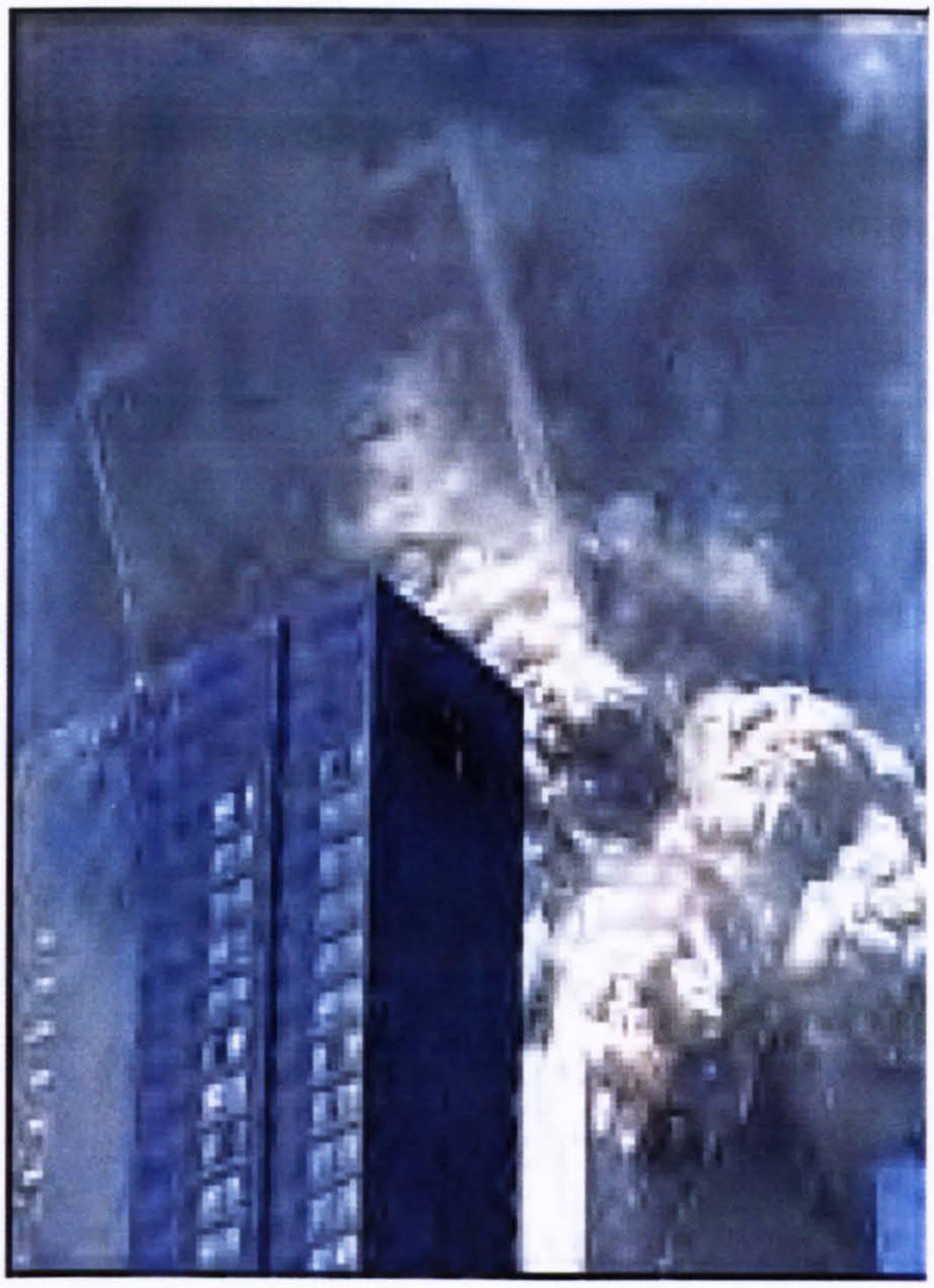

Figure 1.15 Progressive collapse WTC south tower [19]

Figure 1.16 Pentagon fire resulting from crashed aeroplane [19]

1.2.14 Bali bombing, Indonesia 2003

Two night clubs, the Sari club and Paddy's Irish bar were bombed on the Island of Bali. The bombing also had a devastating effect on the local tourism industry, resulting in hardship for the many local people linked with the industry. The destruction is shown in Figure 1.17

Figure 1.17 Bali night club bombing [20]

1.2.15 ParadiseHotel Bombing, Mombassa Kenya 2003

The hotel was subjected to a vehicle bomb hidden in a four wheel drive vehicle. Thirteen people were known to have lost their lives. The hotel scene after the bombing is shown in Figure 1.18. Here too serious concern was raised as to the future of the Kenyan tourist industry.

Figure 1.18 Paradise hotel after the bombing [20]

1.2.16 J W Marriot Hotel, Jakarta, Indonesia

This thirty three storey modern hotel built in the commercial business centre of Jakarta was subjected to a vehicle bombing on the fifth of August 2003 at 12:30 pm local time. Thirteen people were known to have died and one hundred and twenty were injured. Five storeys of the structure were severely damaged. The vehicle was parked at a taxi stand in front of the hotel restaurant. The roof and walls of the adjacent lobby collapsed as a result of the bombing. Staff in the hotel described the bombing as being "like an enormous earthquake"[19,20]. The scenes after the blast are shown in Figure 1.19 to Figure 1.20 and show shattered glass and charred debris.

Figure 1.19 Marriot hotel, Jakarta after the bombing [19,20]

Figure 1.20 Marriot hotel, Jakarta after the bombing [19,20]

1.2.17 Statistical data on bomb blasts (up to 1999)

In this section of this chapter Tables 1.1, 1.2 and 1.3 provide some statistical data for other blast scenarios. The comparative study will assist other researchers wishing to analyse specific explosion scenarios

Table 1.1 Well-known explosions over the last four decades [2]

Whereabouts	*Year*	*Fatalities*
Indianapolis, USA	*1963*	*73*
Gas Pipeline Louisiana, USA	*1965*	*17*
Tila Bund Bridge, Pakistan	*1965*	*80*
Chemical Plant, Quebec Canada	*1966*	*11*
Chemical Plant, NJ, USA	*1967*	*11*
Block of Flats, Moscow	*1967*	*20*
Subway, Osaka Japan	*1970*	*73*
Glasgow Shopping Centre, Scotland	*1971*	*20*
Liquefied Gas Tank NJ , USA	*1973*	*40*
Chasnala Mine, India	*1975*	*431*
Munitions Works, Lupua, Finland	*1976*	*45*
Grain Elevator, Louisiana,USA	*1977*	*35*
Propylene tank truck, Spanish Coast	*1978*	*150*
School Ortuella Spain	*1980*	*64*
Antiques Exhibition, Todi Italy	*1982*	*33*
Salaang Tunnel, Afghanistan	*1982*	*1000-3000*
Oil Pipeline, Brazil	*1984*	*508*
Gas Storage Area, Mexico City	*1984*	*334*
North Sea Oil Rig	*1986*	*166*
World Trade Centre NJ USA	*1992*	*-*
Bishopsgate, London UK	*1993*	*-*
Jewish Community Centre, Buenos Aires	*1994*	*-*
Oklahoma, USA	*1995*	*168*
Docklands, London UK	*1996*	*-*

Table 1.2 Data relating to various types of bomb targets 1989-1998 [2]

Target Classification	*USA*	*UK*	*Pakistan*	*India*	*Israel*	*S.America*
Residential	*2553*	*150*	*15*	*25*	*110*	*200*
Vehicles	*1698*	*200*		*3*	*80*	*50*
Open Areas	*568*	*30*				
Utilities	*143*	*40*	*10*	*2*	*20*	*13*
State and Local Government	*155*	*15*	*20*	*11*	*10*	*80*
Federal Government	*48*	*40*	*21*		*130*	*150*

Table 1.2 Data relating to various types of bomb targets 1989-1998 (contd.) [2]

Target Classification	*USA*	*UK*	*Pakistan*	*India*	*Israel*	*S.America*
Banks	***72***	***10***	***5***	***20***		***20***
Military	***27***	***16***			***10***	***1110***
Airports& Aircraft	***10***		***8***	***100***	***20***	***13***
Energy Facilities	***11***			***8***		***10***
Parks	***89***					
Medical Facilities	***26***		***2***			
Apartments	***244***			***2***	***16***	***10***
Educational	***573***	***16***				***10***
Mail Boxes	***2712***	***25***			***10***	***20***
Commercial	***1468***		***5***		***210***	***300***
Law Enforcement	***108***	***25***	***10***	***19***	***150***	***150***
Religious Facilities	***30***	***10***	***70***		***40***	***5***

Table 1.3 Data on Bomb Affected Facilities in Various Countries [2,10]

Type of Facility	*USA*	*UK*	*India*	*Pakistan*	*Israel*	*Europe*
Residential	***2553***	***150***	***25***	***15***	***110***	***210***
Commercial	***1468***	***315***	***200***	***5***	***210***	***115***
Vehicle	***1698***	***200***	***3***	***-***	***80***	***3***
Educational	***573***	***16***	***-***	***-***	***-***	***-***
Mail Boxes	***2712***	***25***	***-***	***-***	***10***	***5***
Open Areas	***568***	***30***	***-***	***-***	***-***	***-***
Utilities	***143***	***40***	***2***	***10***	***20***	***-***
Law Enforcement	***108***	***25***	***19***	***50***	***150***	***-***
State & Local Govt.	***155***	***15***	***11***	***20***	***10***	***-***
Federal Govt.	***480***	***10***	***-***	***21***	***130***	***-***
Banks	***72***	***10***	***20***	***5***	***-***	***-***
Military	***27***	***16***	***-***	***-***	***10***	***13***
Airports & Aircraft	***10***	***-***	***100***	***28***	***20***	***-***
Religious facilities	***30***	***10***	***-***	***70***	***40***	***10***
Energy Facilities	***11***	***-***	***-***	***-***	***8***	***-***
Parks	***89***	***-***	***-***	***-***	***-***	***-***
Medical Facilities	***26***			***2***	***-***	***-***
Other	***481***	***-***	***-***	***-***	***-***	***-***

1.3 Scope of research

At the turn of the last century structural engineers were faced with the need to develop analytical and numerical tools for the structural response to earthquakes. Today engineers stand at the dawn of a new era and once again the structural engineering profession has been called upon to look into the safety of building structures in the wake of increasing exposure to explosions from bombs and missile/aircraft impact.

The events described in this chapter are but a few of the many occurrences of bomb blasts around the World. It therefore serves to highlight the considerable need for research, which can better prepare building structures to resist explosive shock loading.

The events described and similar such events have added to the need to develop accurate computational tools to analyse the failure modes of structures under these hazardous loads. Such analysis is an invaluable tool during the design stage.

Numerical tools are developed within the confines of this research using the finite-discrete method. Implementing a special element with the NBS contact detection algorithm into the finite-discrete element method has derived novel solutions. The new element reduces the size of the problem by eliminating the rotational degrees of freedom though static condensation. This has the advantage of reducing the CPU time and thus providing the capability of providing solutions to problems with many millions of elements more efficiently.

An accurate understanding of concrete failure is required in order to fully model the response of concrete structures to blast loading. Hence an investigation into the size effect upon rotational capacity of concrete members is undertaken. The investigation is validated against experiments carried out by other researchers. A full understanding of concrete ductility, confinement and strain rates will pave the way to validate the FEM/DEM analysis under both static and dynamic conditions.

The FEM/DEM code developed is then used to provide a global damage scenario of the Alfred P Murrah building in Oklahoma under simulated blast loading conditions.

1.4 References

1. F Walley, "The Effect of Explosions on Structures" *Proc Inst. Civ. Engrs. Structs & Bldgs 104 pp325-334* (1994)
2. MYH Bangash, "Impact and Explosions", *Blackwell* (1993)

3. E Hinmann, "Lessons from the Oklahoma City Bombing-Defensive Design Techniques" *ASCE Press* (1997)
4. PF Mlakar *et al.*, "Blast Loading and Response of the Murrah Building" *Jour. Perf. Constr. Fac. 12 No3 pp 100-112 ASCE Press* (1995)
5. WG Corley *et al.*, "Using Forensic Engineering Techniques To Obtain data from the Oklahoma City Bombing" *Proc 1st Forensic Engineering Congress Reston VA ASCE Press* (1997)
6. Construction News "Oklahoma Blast Forces Unsettling Design Questions" (1-5-1995)
7. New Civil Engineer, Various Editions
8. WG Corley *et al.*, "The Oklahoma City Bombing, Improving Building Performance through Multi-Hazard mitigation" *FEMA Bull 277*
9. A Pugsley, "Collapse of Flats at Ronan Point, Canning Town" *HMSO,* (1968)
10. Times International Index, *Westminster Research Library, London Volumes from* 1961-1997
11. BK Partin, "Bomb Damage analysis of Alfred P Murrah Building, Oklahoma City, Oklahoma" *Alexandria, Virginia* July 13 (1995)
12. TL Holzer *et al.*, "Interpretation of Seismographs of April 19 1995 Oklahoma City Bombing" *US Geological Survey Menlo Pk CA.* (1995)
13. RN Harvey "The Port Authority of New York and New Jersey's Organisational Strategy for recovering The World Trade Centre after February 26 1993 terrorist bombing" *Cost Eng.* (1995)
14. HS Norville *et al.*, "Glass Related Injuries in the Oklahoma City Bombing" *Jour. Perf. Constr. Fac. 13 No 3 pp 100-112 ASCE Press* (1995)
15. WG Corley *et al.*, "World Trade Centre Building Performance Study: Data Collection, Preliminary Observations and Recommendations" *FEMA Report 403,* (2002)
16. http://www.asce.org
17. http://www.ice.org
18. http://www.itn.co.uk
19. http://www.bbc.com/news
20. http://www.cnn.com

Chapter 2
Blast load phenomena and codified methods for the design of structural elements

2.1 Explosions and explosives

All explosions result in hot gases, which expand, thus producing shock waves in solid materials and blast waves in air. This phenomenon is commonly known as blast loading. Explosions are divided into three groups. These are physical, chemical and nuclear [1]. The first group includes volcanic eruption, volatile liquid mixtures and similar physical events. The second requires oxidation of fuel elements in an explosive compound. The third group is based on nuclear reactions producing energy from the interaction of various protons and neutrons (fusion and fission).

Chemical explosions propagate through heat transfer (deflagration) or through shock waves (detonation). Commercial explosives, volatile gases or liquid mixtures such as domestic gas and coal dust usually produce such explosions. High explosives are generally those which have a greater velocity of detonation.

Commercial explosives, which are easily detonated by heat, compression or impact are classed as primary explosives. Nitro-glycerine is an example of such an explosive. Explosives can also be classed as secondary, an example of which is TNT. These require an intense shock wave to induce detonation.

The Observed Damages to Structures (ODS) database amassed by the Israelis over the passed thirty years contains information on vehicle bomb explosions. Explosions are classified according to Table 2.1.

Table 2.1 Classification of explosives

Small Explosives	Medium Explosives	Large Explosives	Very Large Explosives
≤ 5 kgTNT	≤ 20 kgTNT	≤ 100 kgTNT	≤ 2000 kgTNT

Buildings subjected to abnormal loading, caused by bombs and explosives, usually exhibit the following characteristics:

- Stationary Randomness
- Transient Nature
- Short Duration Time Histories

Table 2.2 gives the data for major recent explosions.

The concept of TNT equivalence is also used to classify various explosives. This concept uses the charge factor (C_F) parameter to obtain the equivalent energy of an explosive as compared with an equivalent mass of TNT. The charge factor is given in equation (2.1).

$$C_f = \frac{\text{Actual Mass of Charge}}{\text{Mass of TNT Equivalent}} \tag{2.1}$$

Therefore using C_F as 1.185, 100Kg of RDX is converted to 84.4 kg of TNT using the above formula. Table 2.3 lists major explosives and Table 2.4 Compares various C_F values.

Explosions result in the propagation of shock waves and heat. This heat will result in increasing the pressure of the surrounding medium, for example air.

Equations of a complex nature have been derived to predict blast pressure loadings, using numerical and experimental data from various references [1, 2, 3]. Special hollow and shaped charges can be employed in which the geometry of the detonation wave is altered to produce greater directionality in the way the explosion is delivered. This is known as the *Munroe Effect*.

Table 2.2 Recent terrorist attacks with explosives

Date	***Location***	***Explosion Load***
Oct 1996	***Lisburn, Northern Ireland,UK***	***250 kg of TNT***
Feb 1996	***Docklands, London, UK***	***500 kg of TNT***
April 1995	***Oklahoma City USA***	***1905 kg of TNT***
July 1994	***Manchester City Centre,Manchester, UK***	***1500 kg of TNT***
April 1993	***Bishposgate, London, UK***	***350 kg of TNT***
February 1993	***The World Trade Centre New York USA***	***572 kg of TNT***
April 1992	***St Mary Axe , London, UK***	***350 kg of TNT***
April 1992	***Staples Corner , London UK***	***300 kg of TNT***

Table 2.3 Major explosives

Explosive Name	*Chemical Makeup*	*Temperature °C*	*Use/Origin*
Abbeite	*Ammonium Nitrate, Nitroglycerine, Sodium Chloride, Woodmeal, Dinitrotoluene*		*Coal Mining Explosive*
Amatol	*Ammonium Nitrate & TNT*		*Bursting Charge for High Explosive Shells & Bombs*
Ammonite	*Pottasium Nitrate, Ammonium Nitrate, Solid Hydrocarbon, Napthalene,Gelatinized Nitroglycerine*	*2500*	*Main Explosive in Russia*
Belgian Permite	*Ammonium Nitrate, Calcium Silicide*		*Used to Set off Service Detonators*
Black Powder	*Potassium Nitrate, Sulphur & Charcoal*	*2600*	*Used In US Bombs*
DD60/40 (LE)	*Picric Acid & Dintrophenol*		*French Bursting Charge for Shells*
MDPC (HE)	*Picric Acid , Dintrophenol & Trinitrocresol*		*French Bursting Charge for Shells*
PETN	*PETN & TNT*	*4010*	*High Explosive Charge: Drop Bombs &Torpedo's*
Wetter-astralit	*Gelatinized Nitrogycerine, Ammonium Nitrate, Woodmeal, Coal Powder & Sodium Chloride*		*German Explosive*

Table 2.4 C_F values for some explosives

Explosive Name	C_F
Compound B	*1.148*
Dinitrotoluene	*0.70*
Dynamite	*1.30*
Ethylendinitramine	*1.25*
GDN	*1.6*
HMX	*1.256*
Pentrinite	*1.48*
RDX	*1.185*
Schneiderite	*0.7*
Semtex	*1.25*
TNT	*1.0*

2.2 Blast loads on buildings

After a bomb explosion the resulting energy release can take the form of thermal radiation, air blast or ground shock. The second is the most damaging to buildings. The surrounding air molecules are compressed to create the ambient overpressure, which hits the building with supersonic speeds. This will result in pressure entering the building through apertures such as damaged windows and doors. In turn structural members such as floor slabs and columns can be subjected to 'upwards' loading. Diffraction at various surfaces can serve to increase or decrease this pressure.

The pressure decay is exponential with time. Suction forces can occur and are usually referred to as the negative loading phase. This process is described in more detail in the following sub-section. Figures 2.1 -2.3 gives a typical bomb blast scenario using the example of the Alfred P. Murrah Building in Oklahoma. Figures 2.1 to 2.3 show crater dimensions, peak overpressure and a typical column location relative to the bomb respectively

2.2.1 The sequence of events after blast loading

The detonation of an explosive charge in air or water results in blast waves. These blast waves create the loading on surrounding objects. For instance, in explosions from condensed high explosives, almost all the energy released is turned into blast energy. A typical blast pressure profile is shown in Figure 2.4 and is explained as follows:

1. Detonation gases are generated at 3000 to 4000 °C with pressures of 10 - 30 GN/m^2
2. The detonation gases expand, pushing out the surrounding air
3. At the front of these detonation gases is a layer of compressed air, which contains most of the blast energy
4. The pressure of these detonation gases eventually falls to atmospheric as they continue to expand and cool down. Whilst the static pressure will eventually become atmospheric, the molecules themselves are still moving and so take slightly more time to diminish in momentum.
5. The gases are still moving when the pressure returns to atmospheric and therefore a negative pressure arises to create a balance in the system. This phase is known as the negative pressure phase.
6. Now the gases have "overexpanded" and a flow reversal occurs because of the pressure difference between atmospheric and the gas pressure.

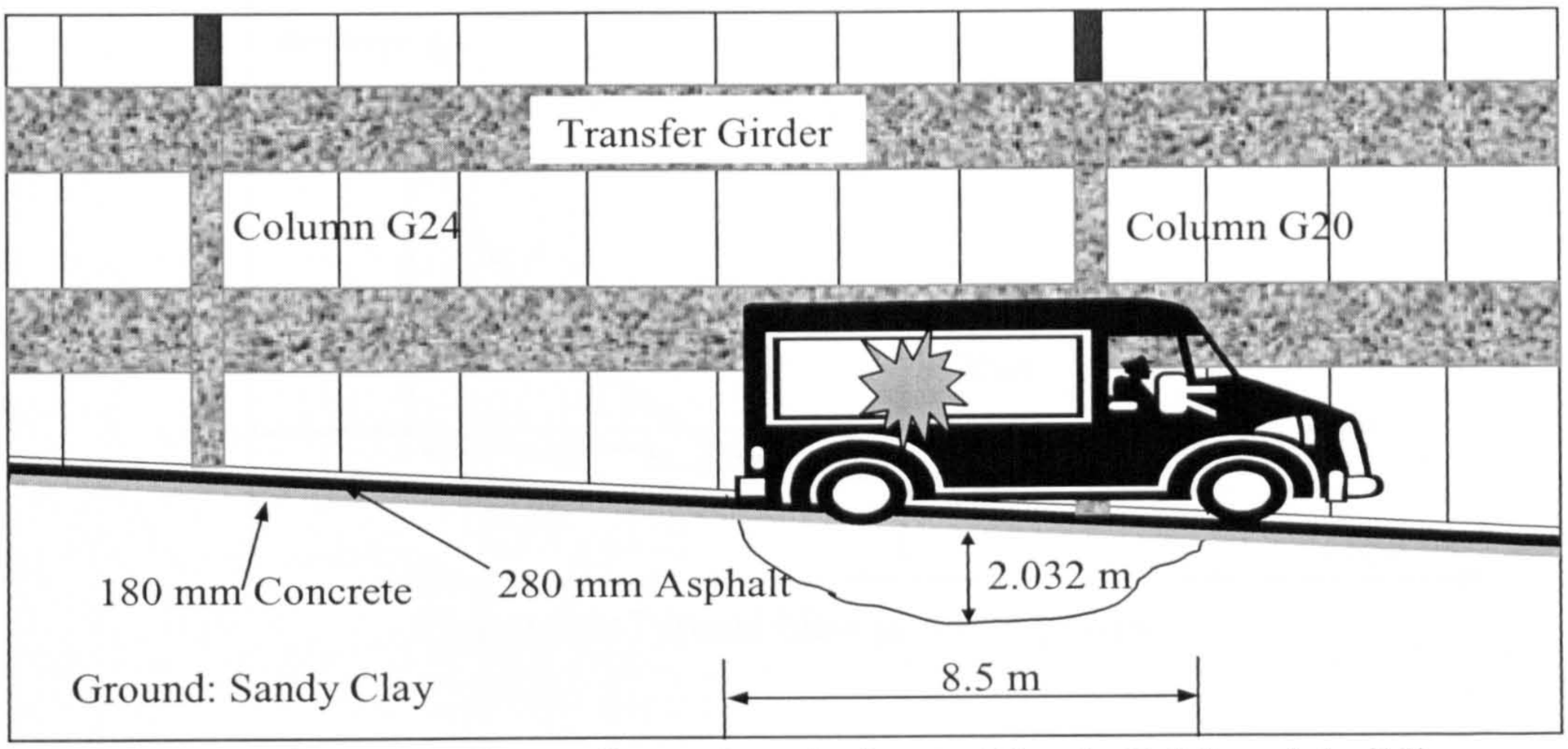

Figure 2.1 Crater dimensions in front of the A. P. Murrah building

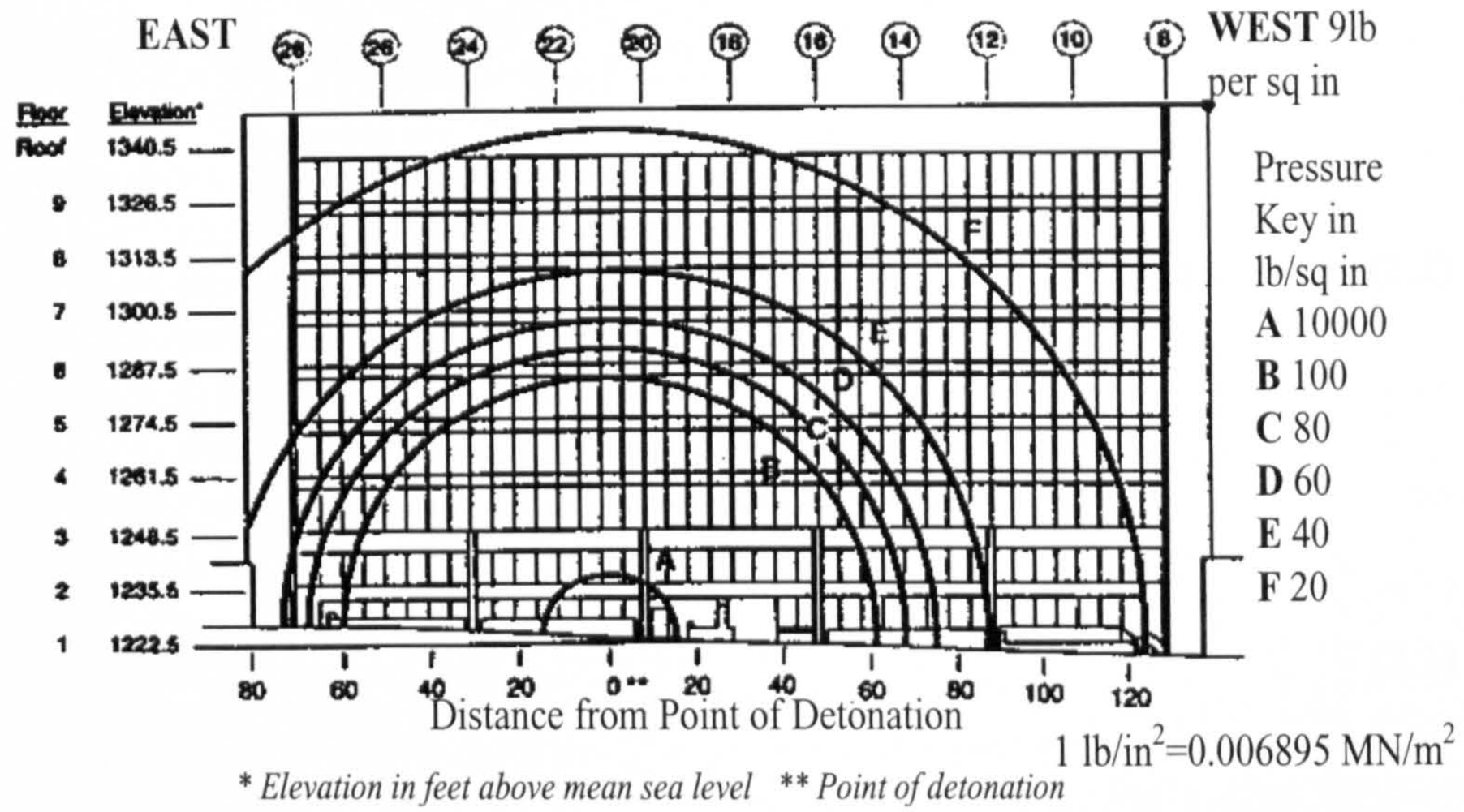

Figure 2.2 Peak overpressures on the North elevation of the Murrah Building

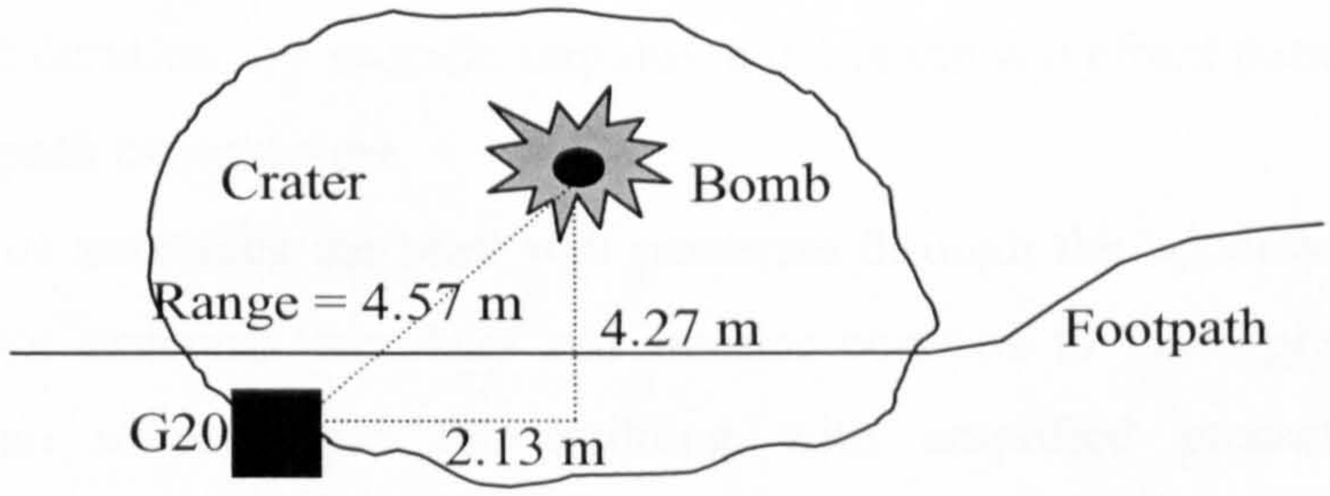

Figure 2.3 Column G20 location relative to the bomb

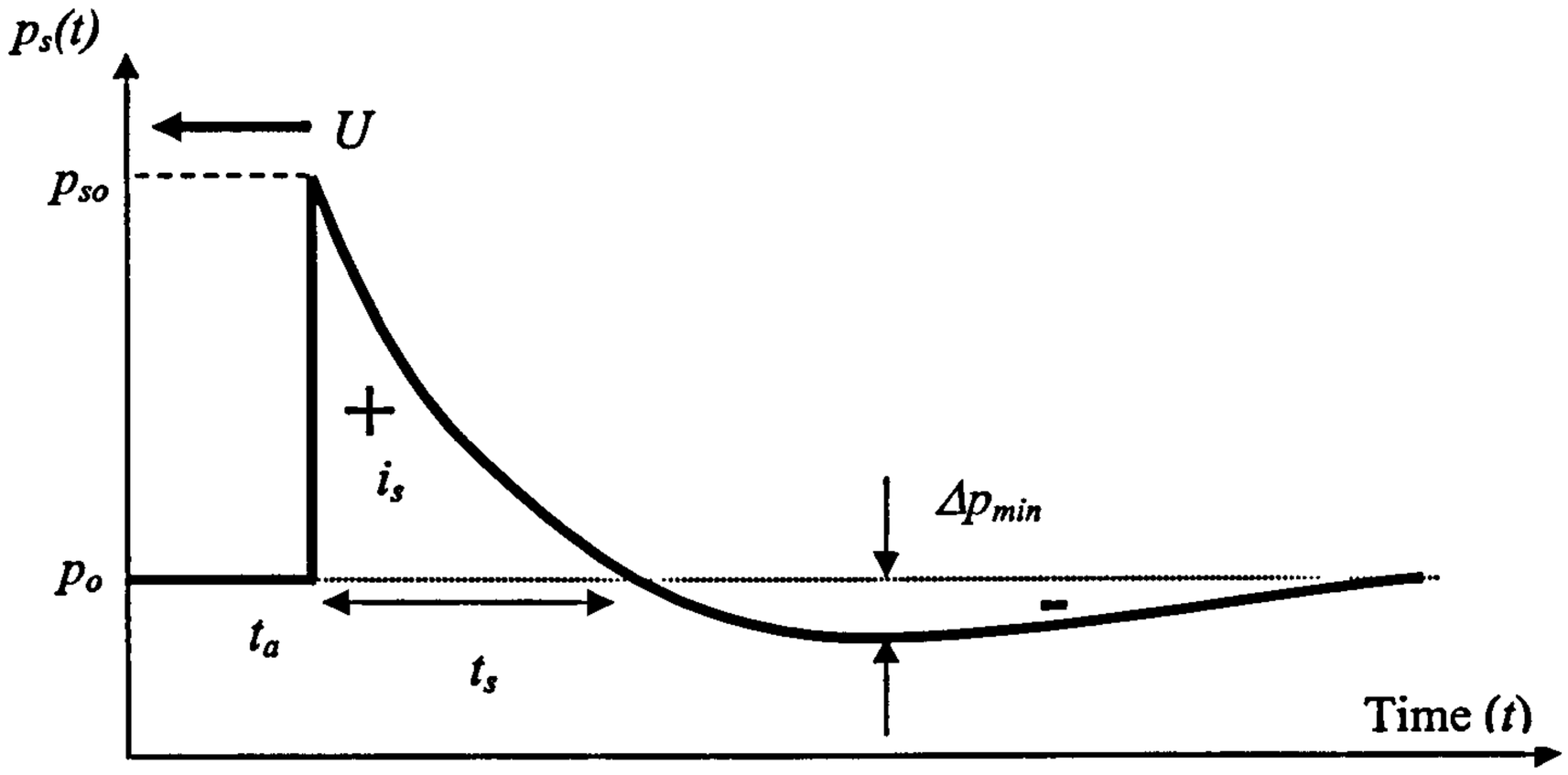

Figure 2.4 Typical blast pressure profile

The Friedlander equation is typically used to represent a blast pressure profile [4] and is given by equation (2.2).

$$p_s(t) = p_{so}\left[1-\frac{t}{t_s}\right]\exp\left\{-\frac{kt}{t_s}\right\} \tag{2.2}$$

$$i_s = \int_{t_a}^{t_a+t_s} p_s(t)\,dt \tag{2.3}$$

where, p_{so} = peak overpressure, p_o = atmospheric pressure, t = time, t_a =arrival time, t_s = positive phase duration, i_s= specific impulse and k is the wavefront parameter, which is a function of peak overpressure

In the case of structures the blast will penetrate through the windows and subject floor slabs, other structural members and interior contents to these pressures. Blast waves will also reflect from the building with amplified pressures. Incident overpressures depend on the stand-off distance of the explosion. Larger stand-off distances will result in a longer positive phase and a lower overpressure. The variation is shown in Figure 2.5.

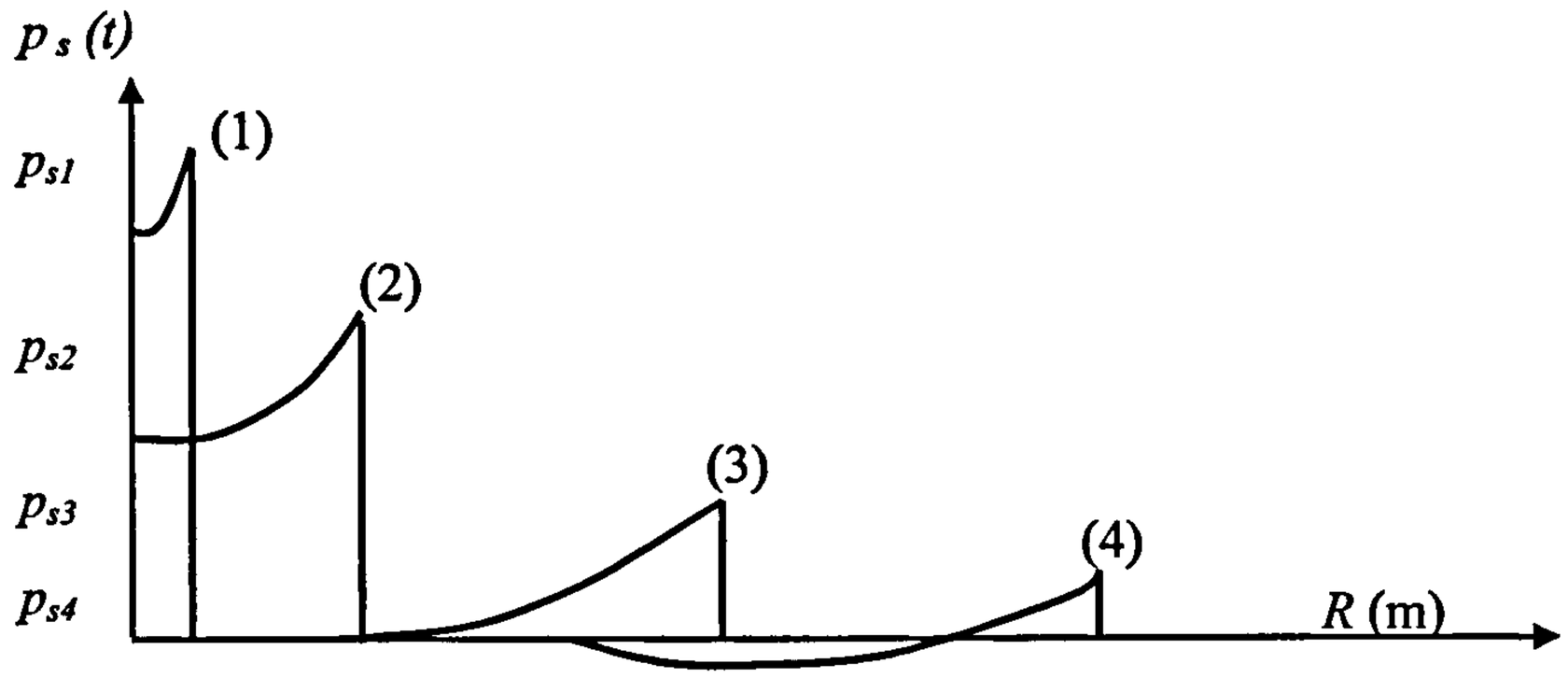

Figure 2.5 Variation in overpressure, p_s and stand-off distance, R

A secondary effect of blast loading is drag loading, which can carry projectiles in its path. The size of this drag pressure, P_D, is related to the range or stand-off distance, R as shown in equation (2.4).

$$P_D \propto \frac{W_{yb}}{R^3} \tag{2.4}$$

where, W_{yb} is the Yield of the bomb.

Blast pressure profiles are usually exponential as is seen from the Friedlander equation (2.2), however sometimes it is more convenient to represent them linearly as shown in Figure 2.6. This is usually done to simplify design. The conservative approach as given by Line 1 represents a linearly equivalent line. However another approach would involve Line 2 where the area beneath is exactly equal to the area underneath the curve, hence retaining the same specific impulse.

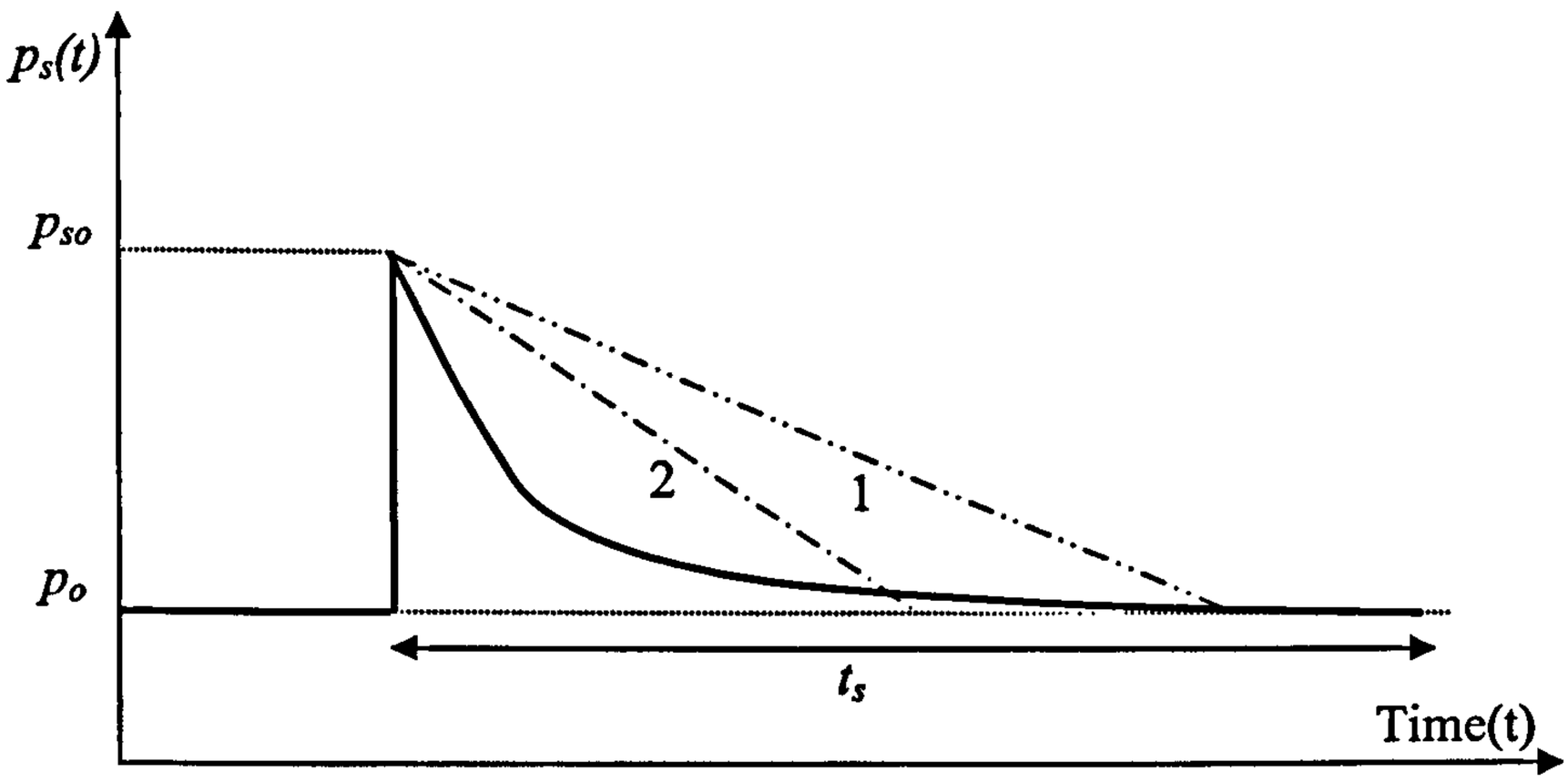

Figure 2.6 Equivalent blast pressure profile

Table 2.5 describes various blast parameters such as wavefront velocity, specific impulse, reflected pressure, dynamic reflection and their duration. They are derived using the principles of momentum conservation and energy conservation. It is also assumed that air behaves as a real gas. These parameters can be used to find the load-time function such as described by Figure 2.4 for any particular case in question. This function can then serve as input for any suitable computer program, such as the code developed during the course of this research which is based on the finite-discrete element method.

Table 2.5 Blast Wavefront Parameters [1]

Blast Parameter	***Mathematical Representation***	
Blast Wavefront Velocity	$u_s = \sqrt{\frac{6\,p_{so} + 7\,p_o}{7\,p_o}}.a_o$	(2.5)
Velocity of the Shock Front	$U = a_o\sqrt{\left(1+\frac{6\,p_{so}}{103}\right)}$	(2.6)
Air Density Behind the Wavefront	$\rho_s = \frac{6\,p_{so} + 7\,p_o}{p_{so} + 7\,p_o}.\rho_o$	(2.7)
Maximum Dynamic Pressure	$q_s = \frac{5\,p_{so}^{\,2}}{2(p_{so} + 7\,p_o)}$	(2.8)
Reflected Pressure	$p_r = 2p_{so}\left(\frac{7_{po} + 4p_{so}}{7_{po} + p_{so}}\right)$	(2.9)
Duration of the Positive Phase	$t_s = t_d$	(2.10)
Associated Specific Impulse	$i^- \approx i_s\left[1-\frac{1}{2Z}\right]$	(2.11)
Specific Impulse of the Wave	$i_s = \int_{t_a}^{t_a+t_s} p_s(t)\,dt$	(2.12)
Highest Value of Underpressure	$\Delta p_{\min} = \frac{-0.35}{Z}$	(2.13)
Negative Phase Duration	$t_d^{\,-} = 1.25W^{1/3}$	(2.14)

where a_o = velocity of sound at ambient and Z = scaled distance

2.2.2 Blast wave scaling laws for bombs

The range, R in metres of a bomb is determined from equation (2.15)

$$R = \frac{KW^{0.333}}{\left\{1+(3.75/W)^2\right\}^{0.1667}} \tag{2.15}$$

Where, W is the mass of the explosive in kgTNT and K is a constant of the value of 5.6 [6].

Scaling Laws are often used to represent blast waves. The scaled distance, Z is represented in equation (2.16).

$$Z = \frac{R}{W^{1/3}} \tag{2.16}$$

The most common scaling law used is known as cube root scaling law, otherwise referred to as Hopkinson-Cranz scaling. This states that the ratio of two diameters and weights of two different size bombs made of the same material are proportional. Hence

$$W_1 \propto d_1^{\,3} \quad \text{and} \; W_2 \propto d_2^{\,3} \tag{2.17}$$

Thus

$$\frac{W_1}{W_2} = \left(\frac{d_1}{d_2}\right)^3 \tag{2.18}$$

The law is expressed by equation (2.19).

$$\frac{d_1}{d_2} = \left(\frac{W_1}{W_2}\right)^{1/3} \tag{2.19}$$

If both bombs produce the same overpressure then the RHS of the equation (2.19) becomes constant and therefore equation (2.19) can also be expressed in terms of the respective bomb ranges. Hence

$$R_1 = ZW_1^{1/3} \quad \text{and} \; R_2 = ZW_2^{1/3} \tag{2.20}$$

Therefore equation (2.19) becomes

$$\frac{R_1}{R_2} = \left(\frac{W_1}{W_2}\right)^{1/3} = \lambda \tag{2.21}$$

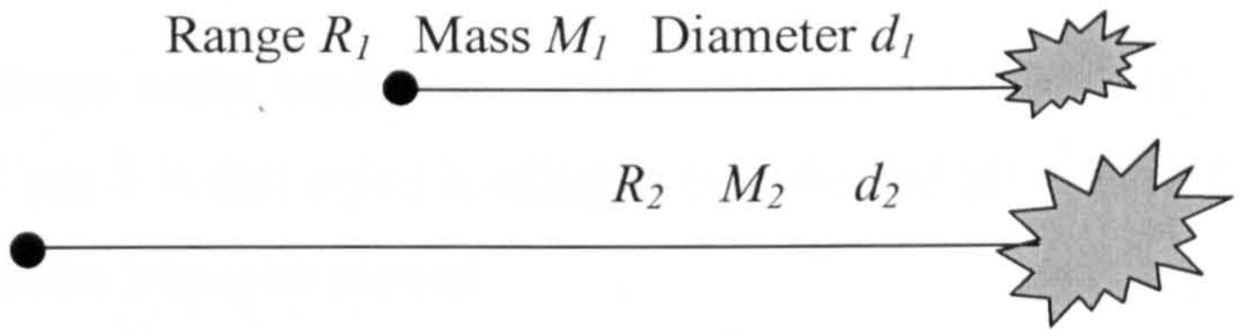

Figure 2.7 Cube root scaling law

The value of Z is given by various graphs from Baker W.E *et al.* [2], presented later in this thesis.

2.2.3 External blast loading

If the blast wave angle of incidence, α_i, for a blast wave is greater than zero, then regular reflection occurs as shown in Figure 2.8.

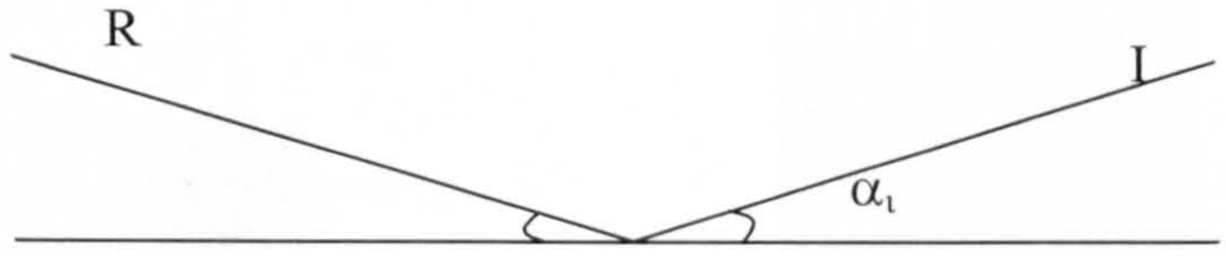

Figure 2.8 Regular reflection

Regular reflection occurs up to a critical value of α_i . Beyond this value Mach reflection is said to occur. This is normally a feature of internal explosions and is described in the next section.

With regard to the overall size of the structure the following cases can be identified:

CASE 1. A large scale blast on a large structure (Figure 2.9). Here the blast loading engulfs the structure and creates a drag force on the structure, which tries to move it. The structure is called a diffraction target and the loading is known as diffraction loading.

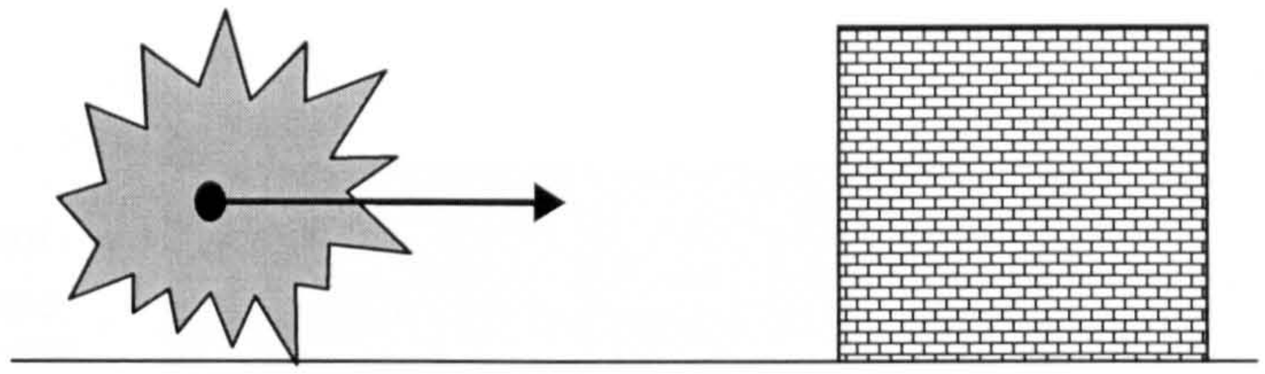

Figure 2.9 A large scale blast on large scale structure

CASE 2. A large scale blast on a small structure (Figure 2.10). Here the only differences with Case 1 is that equal loading is experienced all around the structure and the structure will most likely be moved.

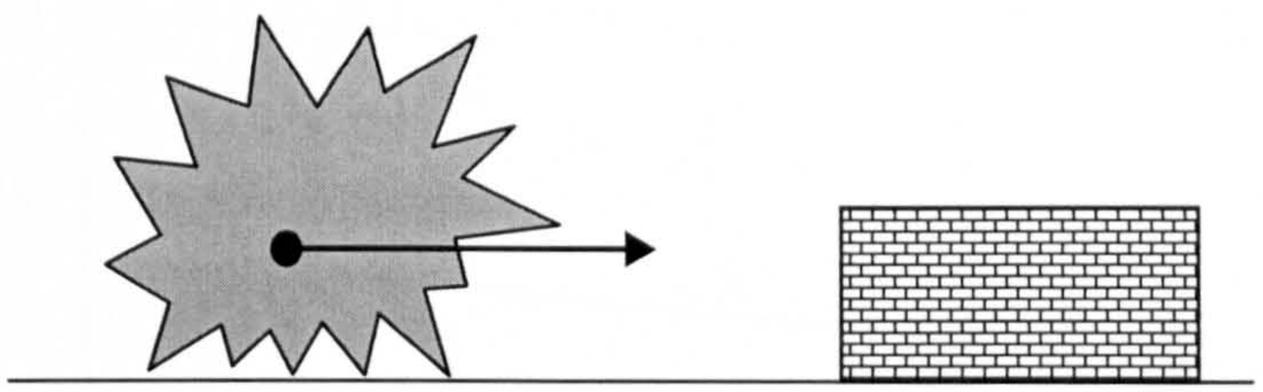

Figure 2.10 A large scale blast on a small structure

CASE 3. A small scale blast on a large structure (Figure 2.11). Here each structural element is analysed separately, as it is most likely that they will be loaded sequentially.

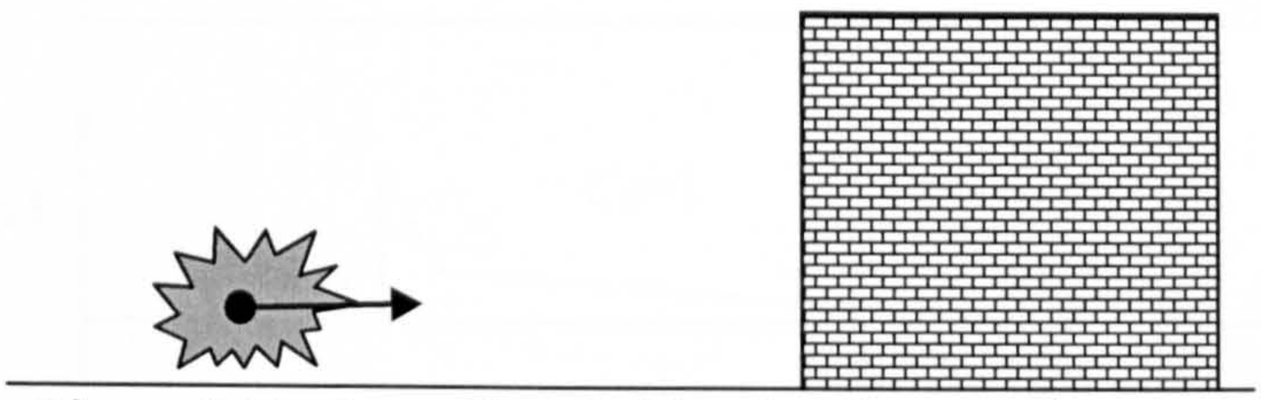

Figure 2.11 A small scale blast loading on a large

In the first two cases the structure experiences a "squashing force" over all exposed surfaces as it is engulfed by the blast wave. Here the structure is pushed forward in the direction of the blast wave, which is followed by a slight "push back" force when the diffraction is completed.

Diffraction effects at each time step

The peak pressure experienced by the front face of a structure at a certain time t, will be a peak overpressure p_r such that this pressure will decay in time t'-t_2.

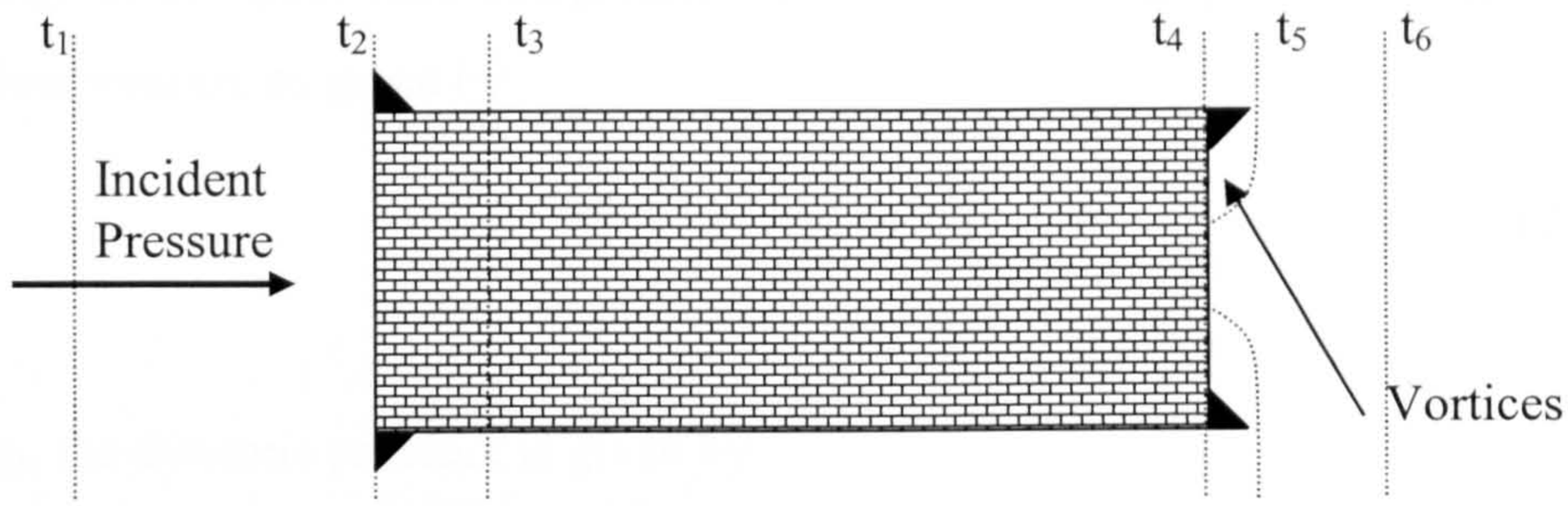

Figure 2.12 Blast loading on a simple structure

The blast wave passing over the top of this structure and around the sides is less than p_r. The peak top and side pressure will be p_{so}. The following gives a clear picture of the decay phenomenon:-

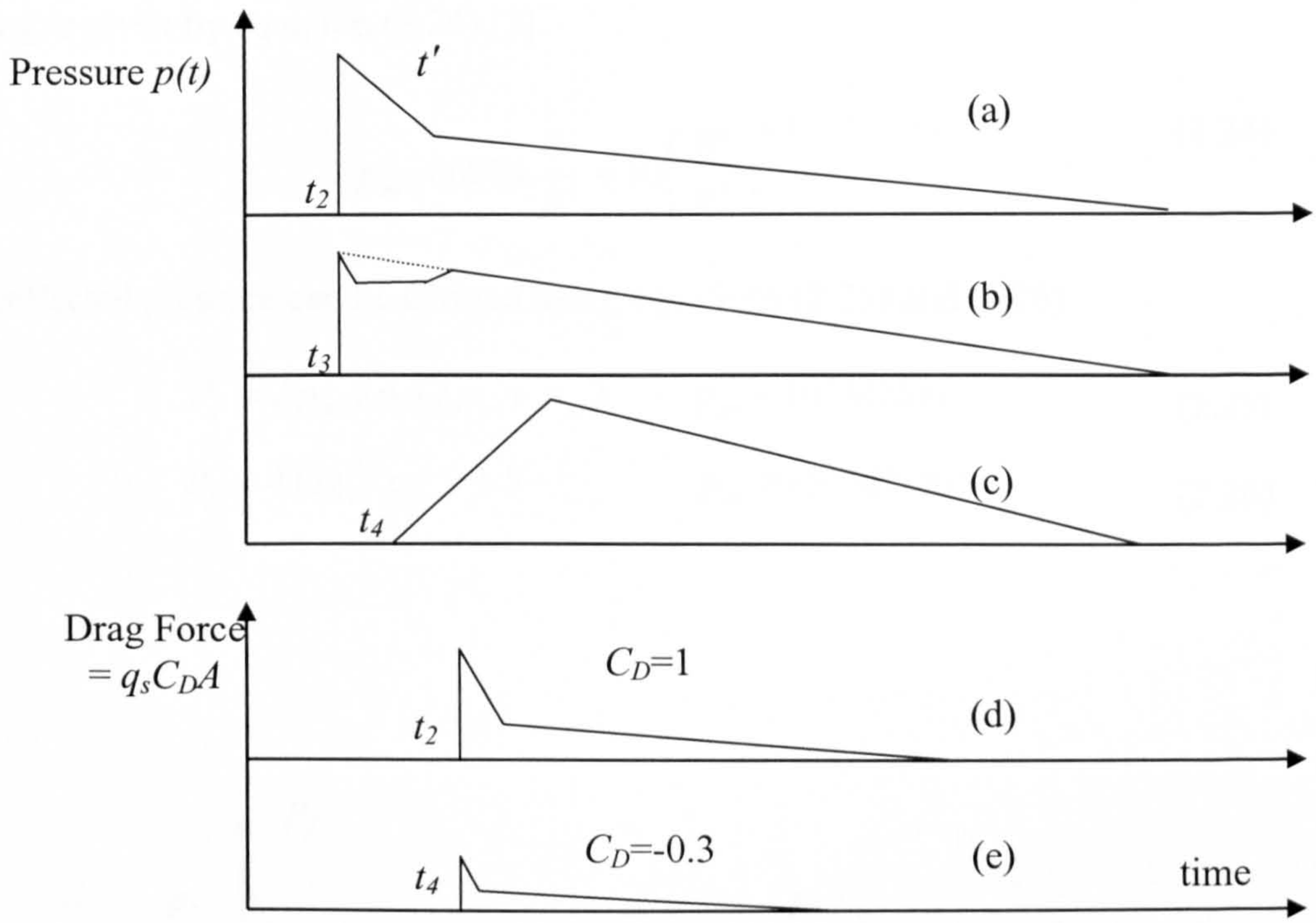

Figure 2.13 Diffraction effects at each time step

(a) The peak reflected overpressure experienced by the front face occurs at time t_2. The pressure decays in time, t'-t_2. because the pressure on the structure is less than p_r.

(b) At time t_3 complex vortices have formed at the corners of the structure, hence the non - linearity in the decay occurs.

(c) The rear face blast profile has a finite rise time and this is because of the time required by the blast wave to finish the propagation process.

(d + e) These diagrams represent the drag force on the front and rear of the structure. The decay in the front face overpressure continues until the pressure is equal to the stagnation pressure as given by

$$p_{stag}(t) = p_{so}(t) + q_s(t) \tag{2.22}$$

where q_s, the dynamic pressure is given by

$$q_s(t) = 0.5\rho_s u_s^{\,2} \tag{2.23}$$

where ρ_s= density of air and u_s = partial velocity behind the wave front

The peak overpressure p_{so} acting dynamically on the walls or front faces of a building is given by equation (2.24) [3].

$$p_{so} = 6874\frac{W}{R^3} + 93\left(\frac{W}{R^3}\right)^{1/2} \tag{2.24}$$

Peak reflected pressure can be derived using equations (2.25) and (2.26).

$$P_f = 2p_o + 6/(7p_o + p_{so}) \qquad p_{so} < 10^6 \text{MN/m}^2 \tag{2.25}$$

$$P_f = 4\log_{10} p_{so} + 1.5 \qquad p_{so} \geq 10^6 \text{MN/m}^2 \tag{2.26}$$

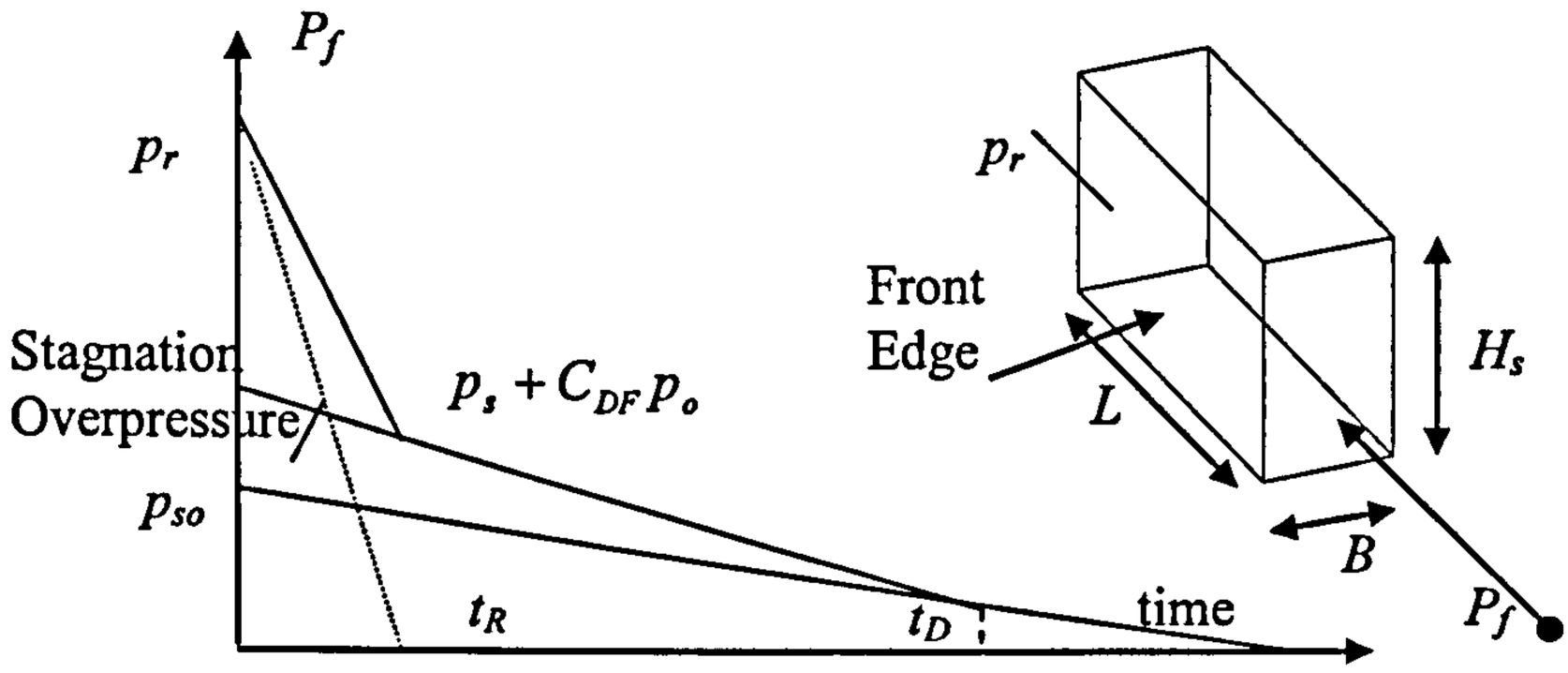

Figure 2.14 Front face pressure - time relationship

$$t_c = \frac{3S_c}{U} \tag{2.27}$$

where

$$S_c = H_S \leq 0.5B \tag{2.28}$$

or

$$S_c = H_S \geq H \tag{2.29}$$

C_{DR}= drag coefficient: front face = 0.8 to 1.6 and rear face = 0.25 to 0.5

The shock pulse duration, t_b is found from equation (2.30) or equation (2.31).

$$t_b = 10.23\frac{W^{1/3}}{\sqrt{p_{so}}} \qquad p_{so} < 7\times10^6 \text{ MN/m}^2 \tag{2.30}$$

or

$$t_b = 20.77\frac{W^{1/3}}{p_{so}^{2/3}} \qquad p_{so} \geq 7\times10^6 \text{ MN/m}^2 \tag{2.31}$$

The time of the drag is found from equation (2.32) or (2.33).

$$t_d = 9.04\left(\frac{W}{p_{so}}\right)^{1/3} \qquad p_{so} < 2\times10^5 \text{ MN/m}^2 \tag{2.32}$$

or

$$t_d = 14.35\left(\frac{W^{1/3}}{p_{so}}\right) \qquad p_{so} \geq 2\times10^5 \text{ MN/m}^2 \tag{2.33}$$

where C_{DF} =Drag coefficient on the front face, C_{DR} =Drag coefficient on the rear face, H_s =Building height, p_r =Peak reflected pressure, t_c =Reflected pulse time or the clearing time, p_o =Ambient atmospheric pressure =1 bar =1 N/m^2 and t_d= Time duration of the drag

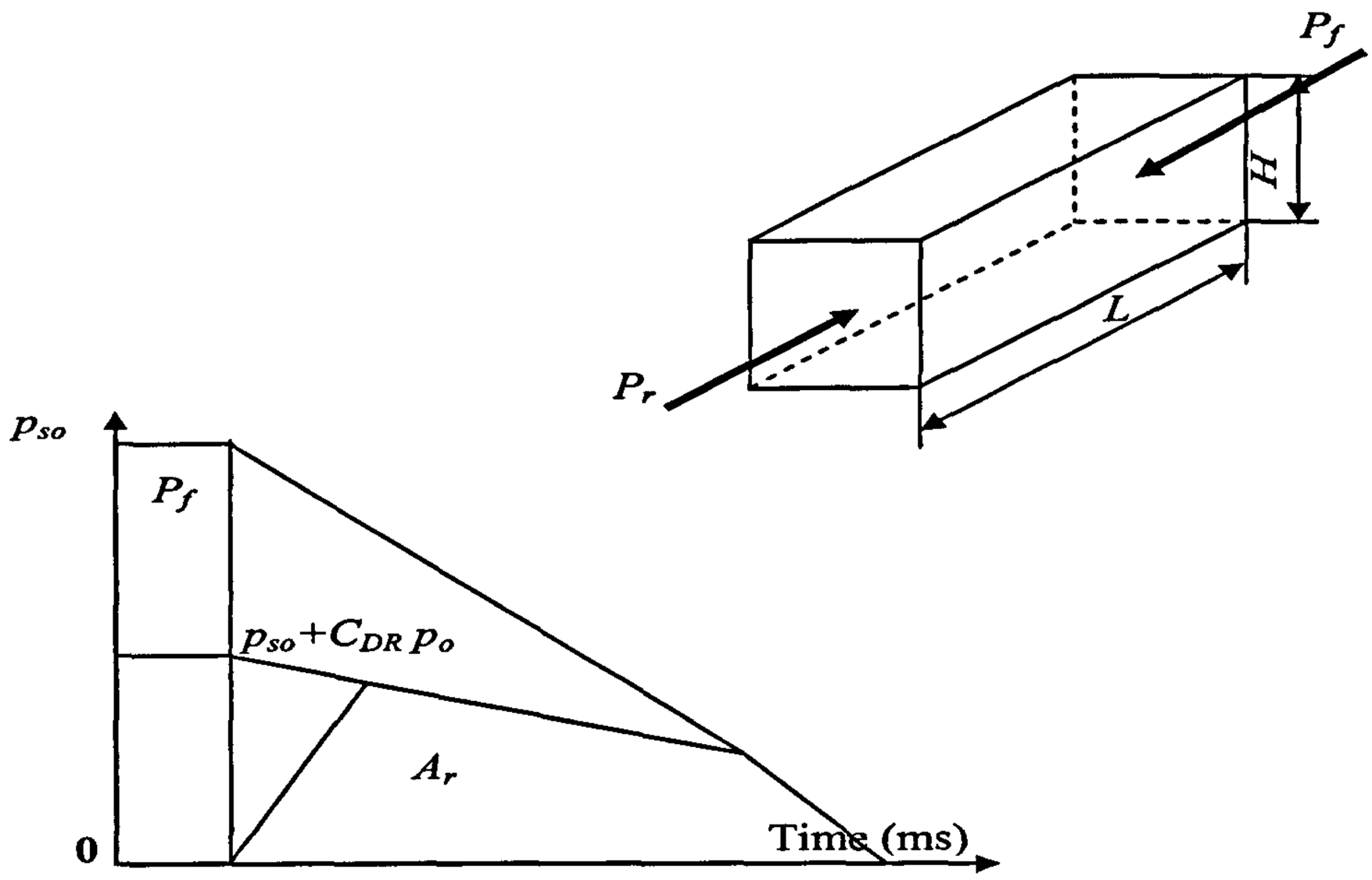

Figure 2.15 Rear face pressure vs time

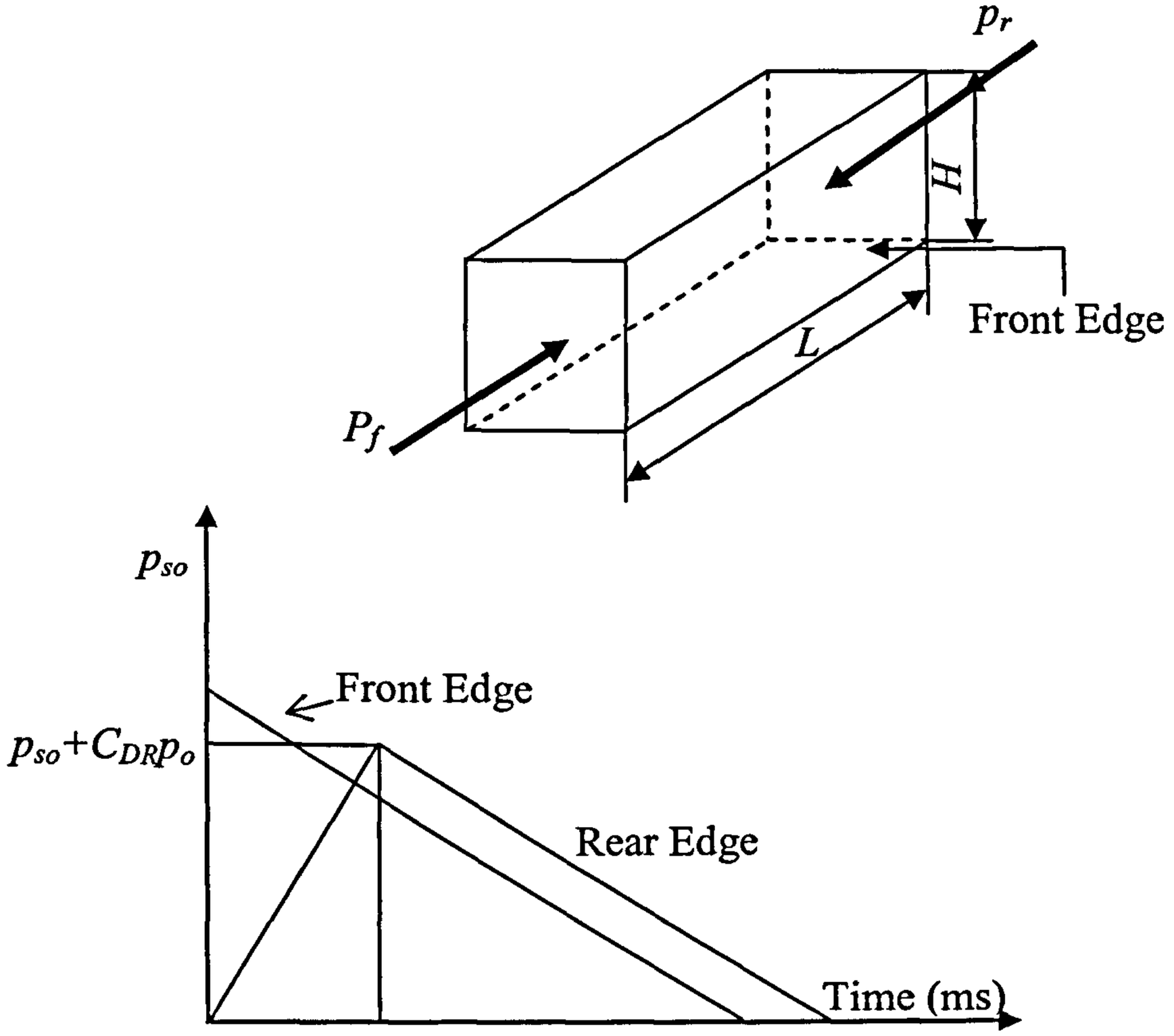

Figure 2.16 Side pressure vs time

Dharaneepathy *et al.* [5] have reported the need to establish a critical distance criterion in order to best analyse structural response to blast load. Critical distance is the term given to the distance at which the cumulative effect of the blast wave is at a maximum. On the basis of this and the methods given above Figure 2.17 and Figure 2.18 show the overpressure duration and the stand-off distances for 816.5 kgTNT bomb and 500 lb (2.5 ton TNT) bomb respectively.

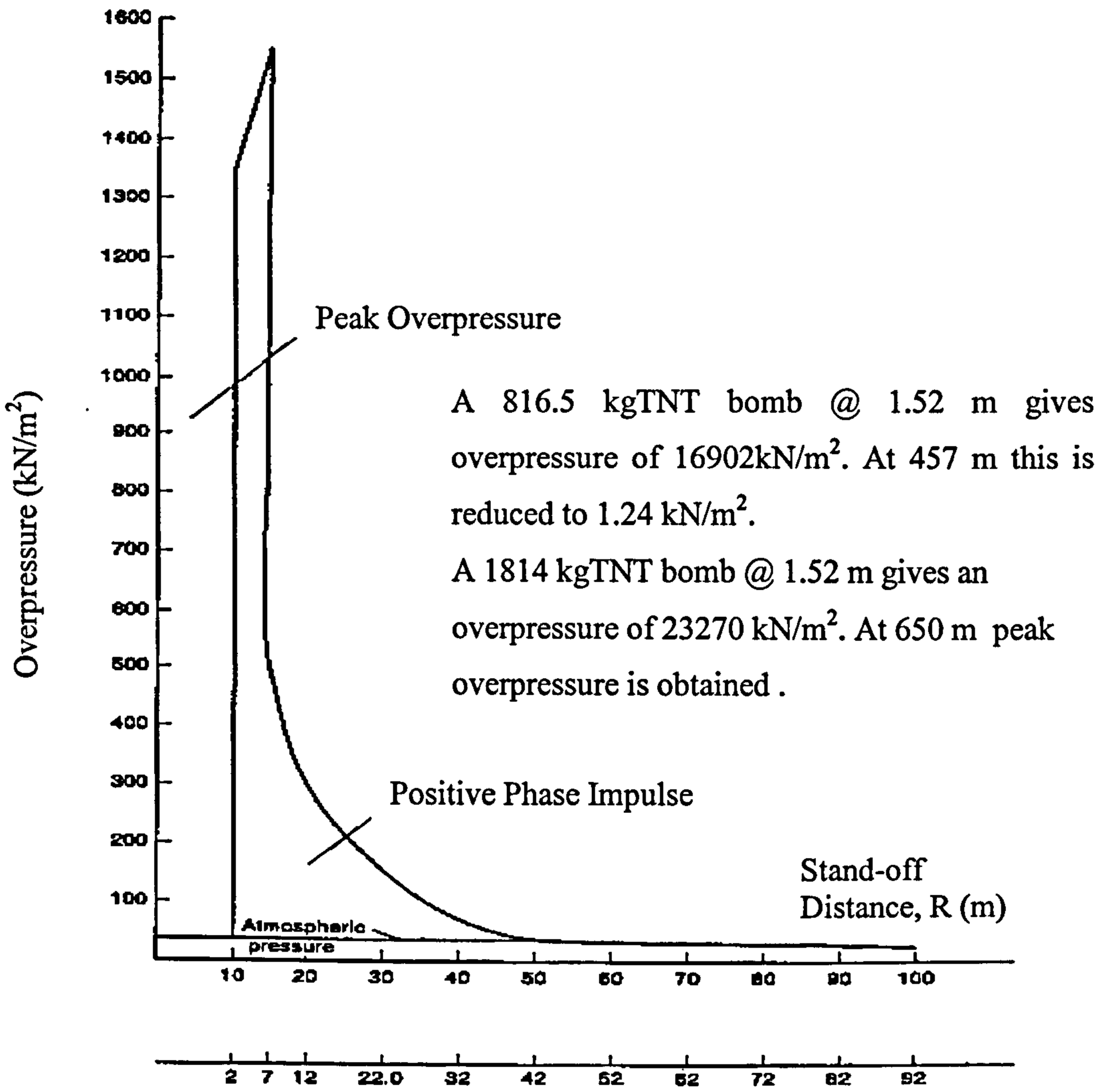

Figure 2.17 Overpressure duration v stand-off distance for a 816.5 kg Bomb [5]

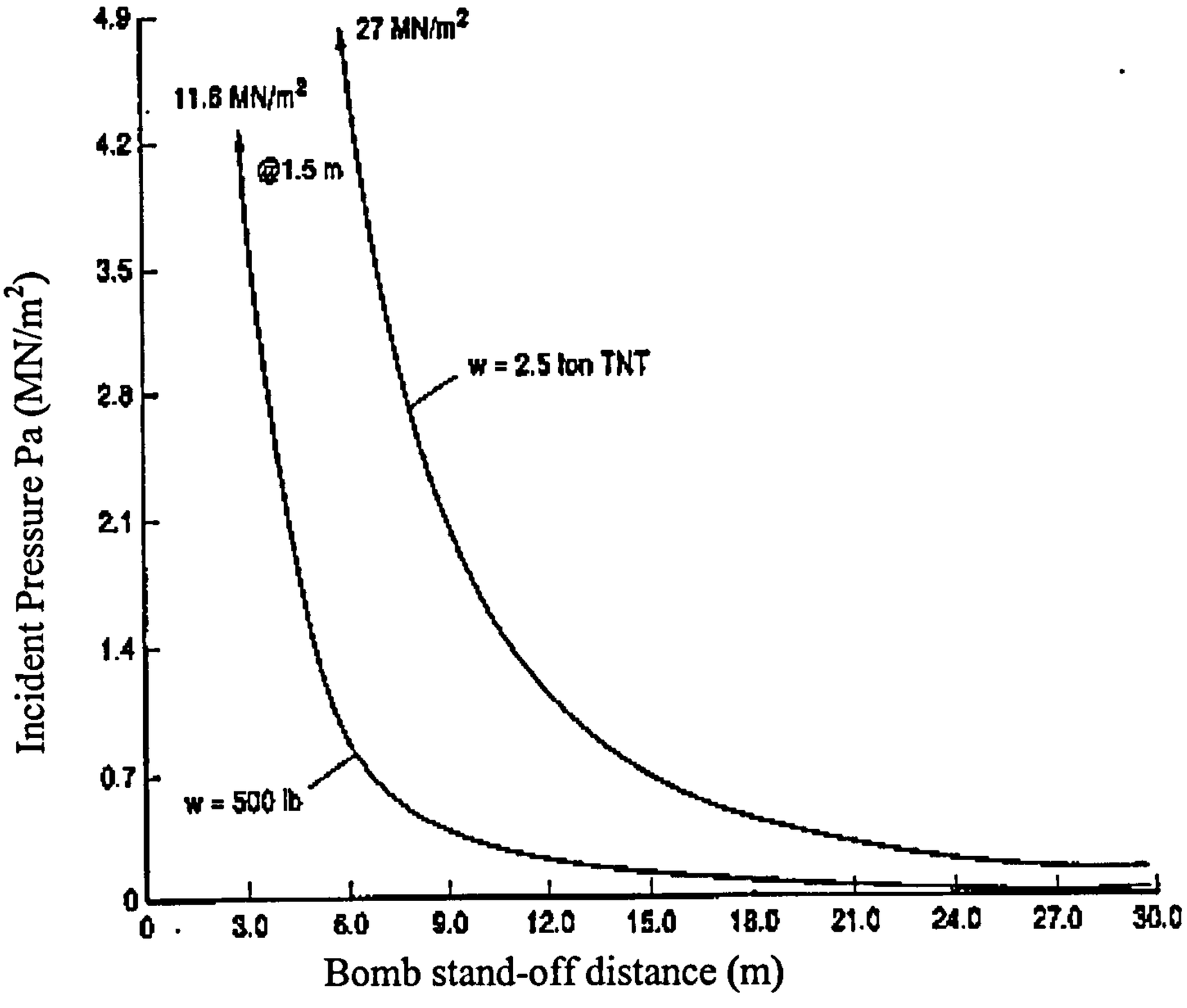

Figure 2.18 Overpressure duration vs stand-off distance for a 816.5 kg bomb [5]

2.2.4 Internal blast loading

In the case of an internal explosion the design requirements are slightly different. Structures are classified as either vented or unvented. A vented structure will include members that are designed to break during an explosion in order to provide pressure relief. Such a structure will need to be much stronger in order to resist an explosion. The practical reality is, however, that venting offers very little advantage in protecting the contents and occupants of a building.

As mentioned in the preceding section, after the critical value of α_{cr}, Mach reflection occurs. Here the behaviour is quite complex. The incident wave skims of the surface. The reflected wave will catch up with the incident waves and in so doing produce a third wavefront, known as a Mach stem. Where all these three meet is known as a Triple point (Figure 2.19). Mach stems are usually observed in internal explosions, which can result from gas air mixtures.

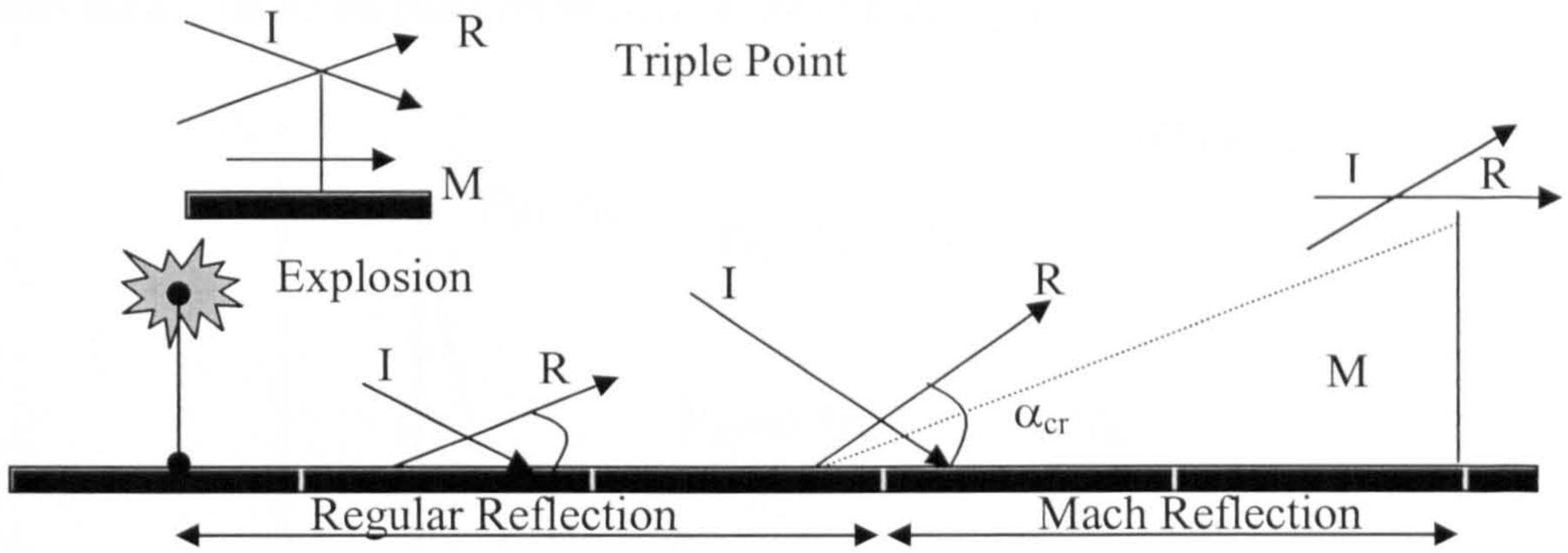

Figure 2.19 Regular and Mach reflection

The pressure-time-history during internal explosions is defined by equations (2.34) and (2.35).

$$p_r(t) = p_r\left(1 - \frac{t}{T_R}\right) \tag{2.34}$$

$$T_R = \frac{2i_R}{p_r} \tag{2.35}$$

where, T_R = positive duration of the reflected overpressure, p_r = peak reflected overpressure and, i_R = specific reflected overpressure impulse

Internal blast waves are very difficult to analyse as they rebound off surfaces creating Mach stems along with a build up of gas pressure, known as Quasi - Static pressure. Reflected blast wave parameters are easily obtained from scaled distance curves. However the prediction of re-reflected waves is more difficult, especially in the case of complex non-symmetrical structures. Approximate analysis assumes triangular pressure pulses for incident and reflected waves (Figure 2.20).

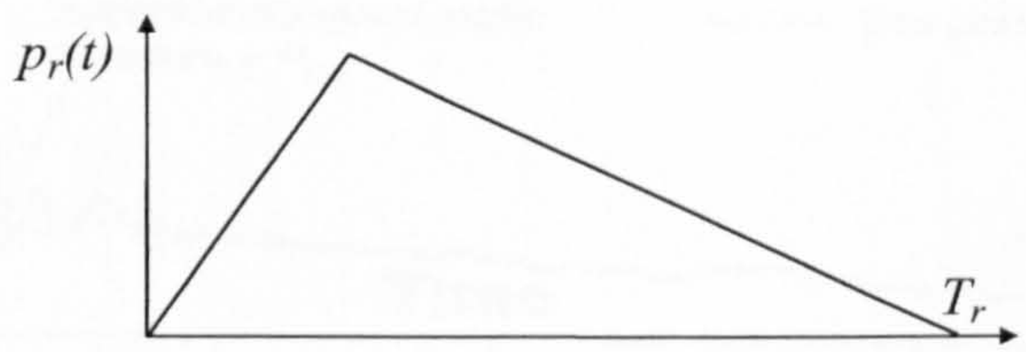

Figure 2.20 Pressure time profile for a reflected blast

Analysis by Baker, WE *et al.* [2] suggests that the pressure and therefore the specific impulse should halve on each reflection, as shown in Figure 2.21.

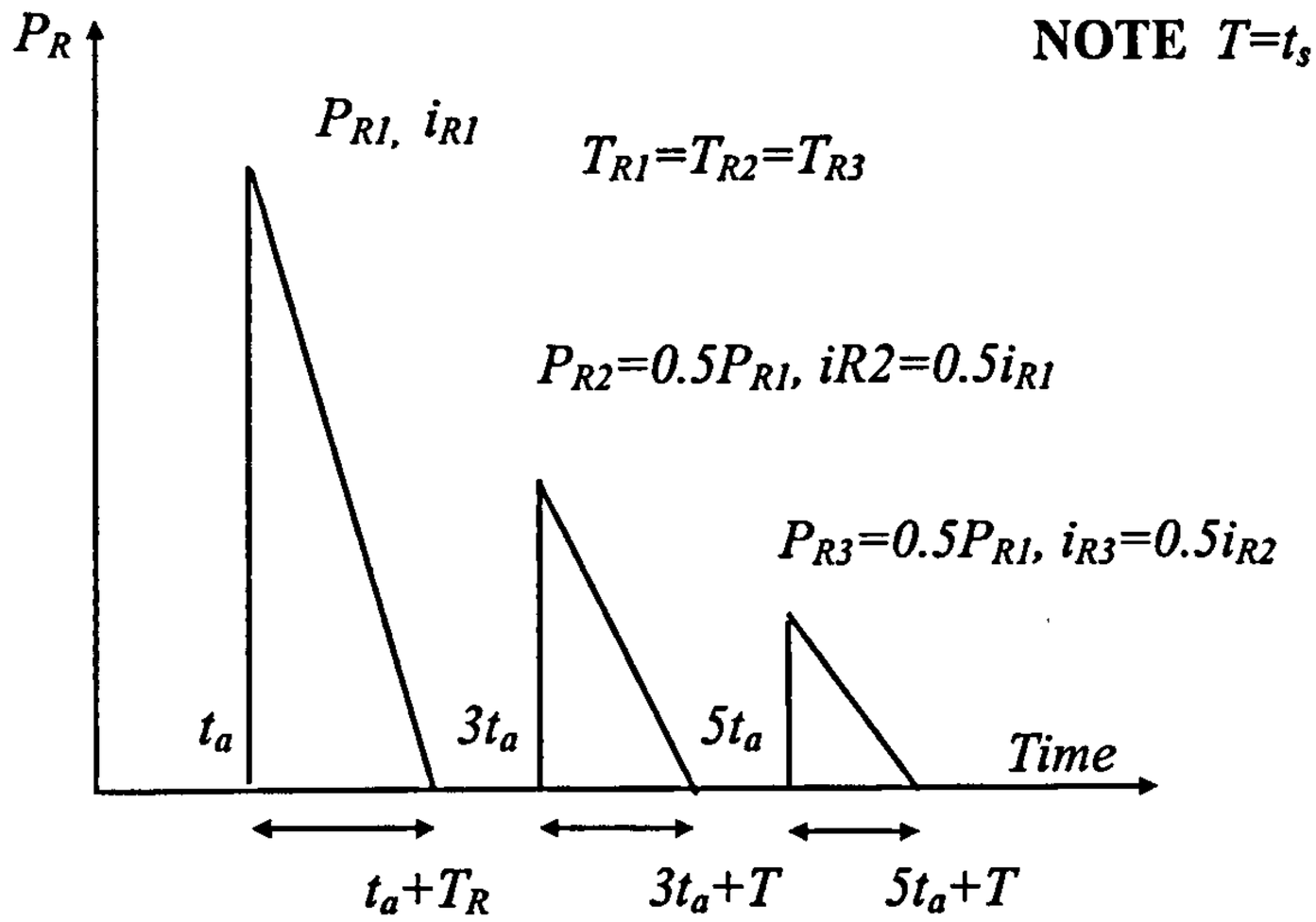

Figure 2.21 Baker's pressure time assumption

In this analysis the time between each reflection of the blast wave on to an internal surface is assumed constant. In real terms this assumption is incorrect as each reflected shock will be weaker and travel with less velocity than the last However, this assumption is justified, in that it yields overestimated results which, consequently produces a safer design. If the response time is much greater than the load duration then the three pulses can be combined as a single pulse with total peak pressure, p_{RT} and specific impulse i_{RT}.

For a partially vented structure the U.S. Corp of Engineers give the pulse time relation shown in Figure 2.22.

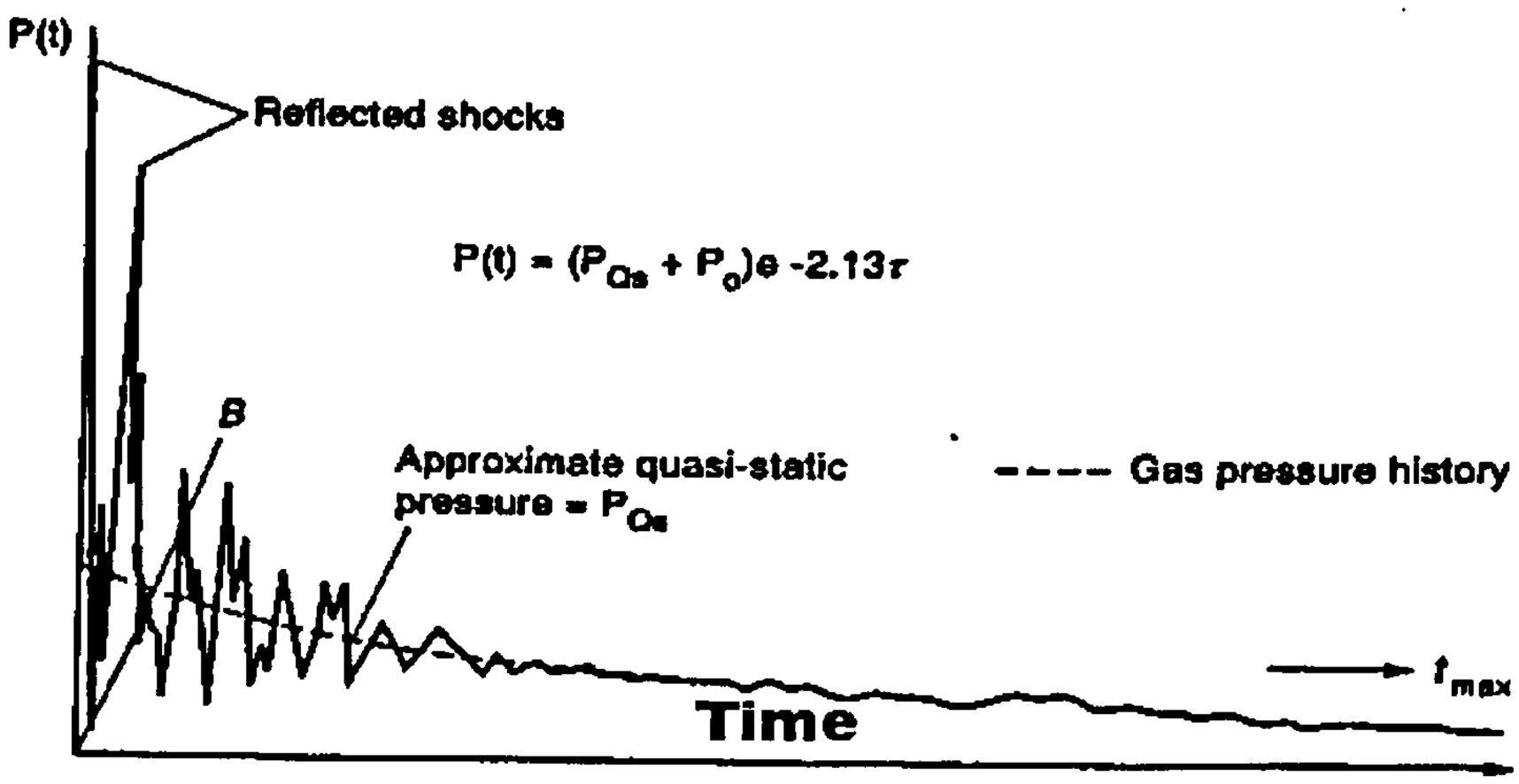

Figure 2.22 Typical internal blast pressure loading for a partially vented structure [7]

The basis of assessing vented and unvented structures is given in the flow chart in Table 2.6 and Figure 2.23.

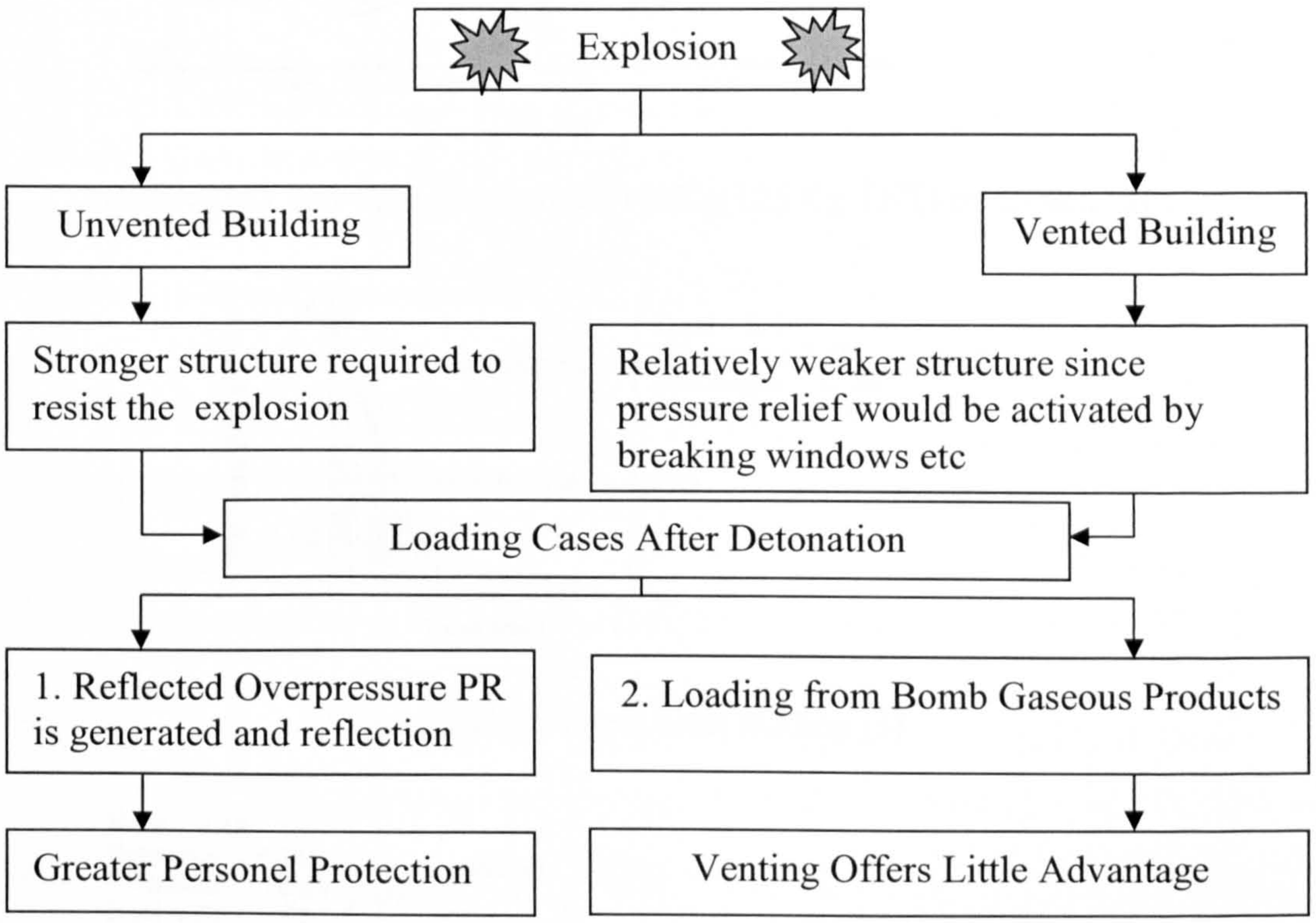

Figure 2.23 Vented and unvented structures under blast loading

Figure 2.24 to Figure 2.26 shows the shock-overpressure relation for 100Kg of semtex. The impulse, peak pressure and duration on the roof and walls are also shown.

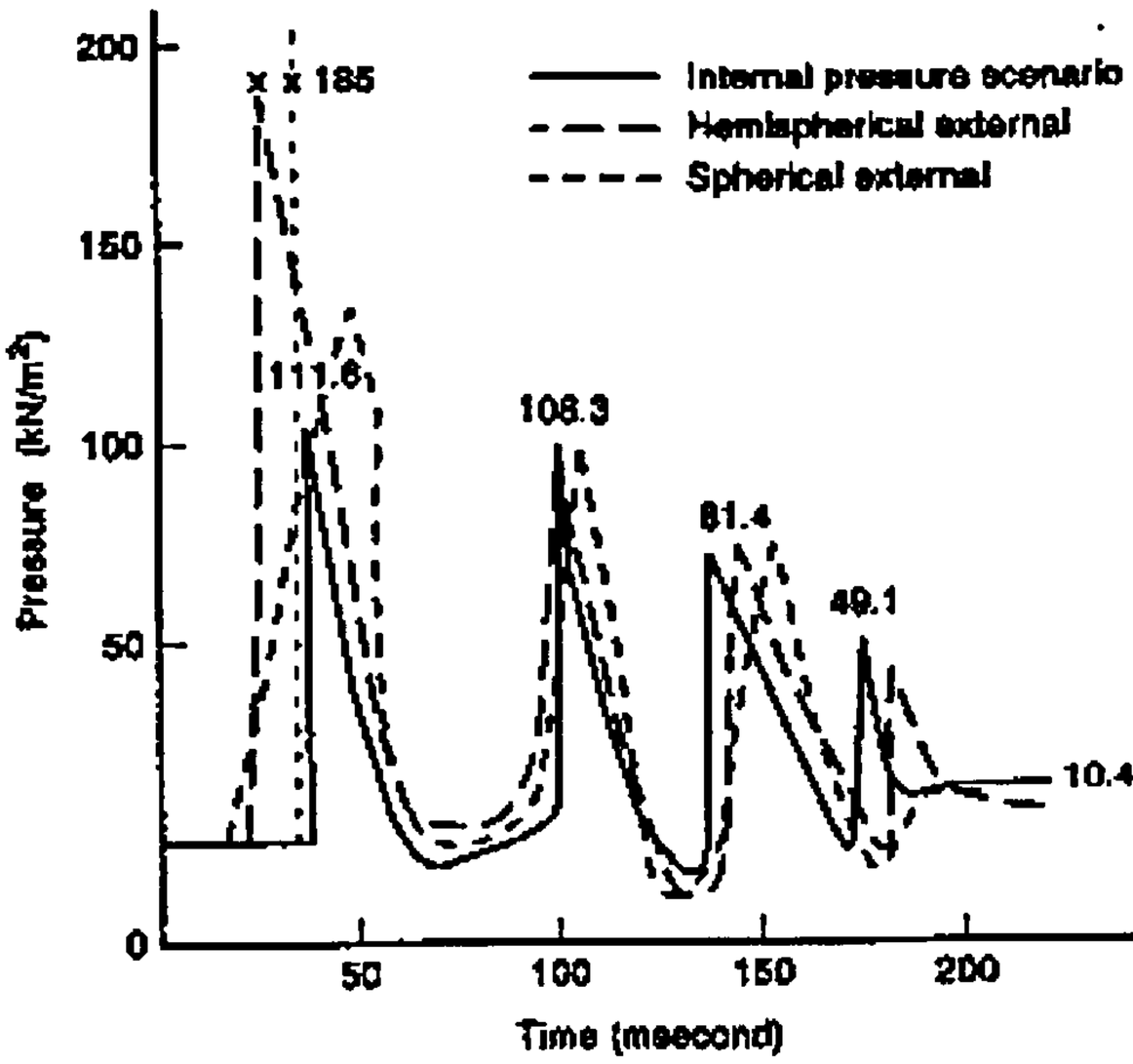

Figure 2.24 Load-time function for 100Kg(125 Kg TNT) of semtex [3]

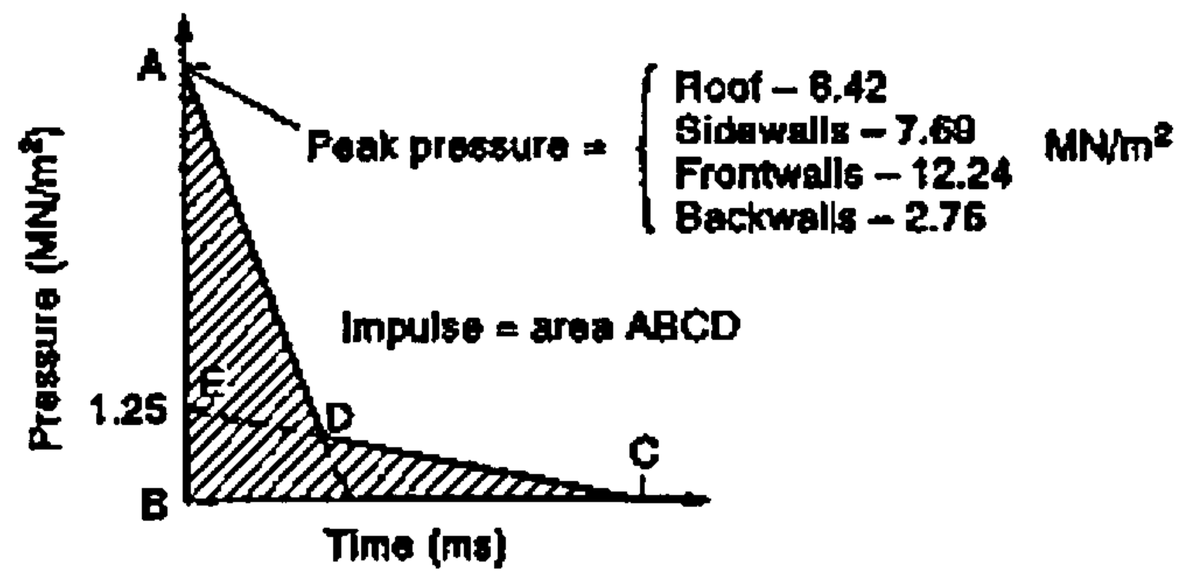

Figure 2.25 Bi-linear blast loading [3]

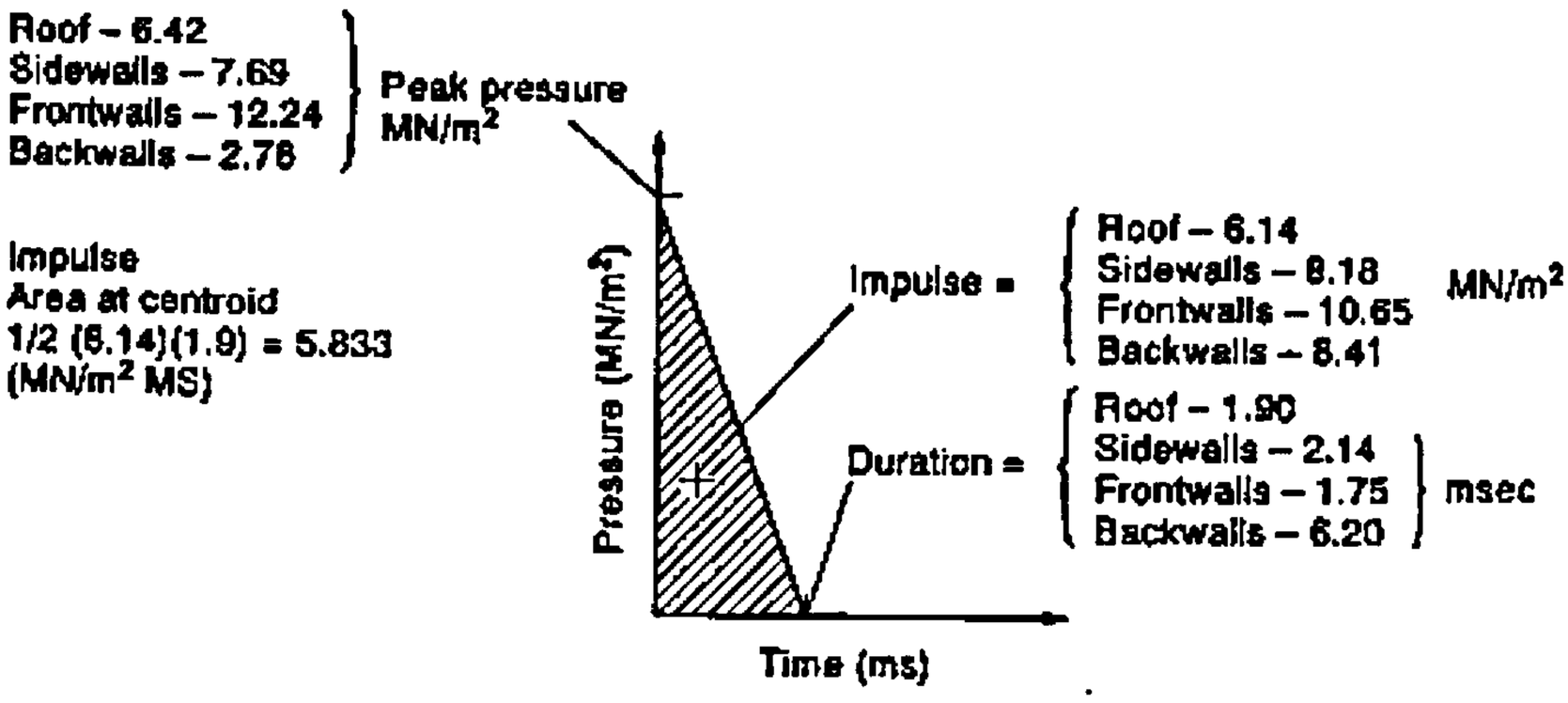

Figure 2.26 Shock overpressure [3]

Table 2.6 Detailed analysis for impulse due to explosion

$P_{R1}+P_{R2}+P_{R3}=1.75P_{R1}=P_{RT}$ **(a)** and $i_{R1}+i_{R2}+i_{R3}=1.75i_{R1}=i_{RT}$ **(b)**

where, the subscript RT represents the Reverberation Time i.e. the time delay between each blast wave arriving at the face of inner wall. This is constant when $t_R=2t_a$, where t_a is the arrival time of the first blast wave on the inner face

$$\text{Reverberation Phase} = (\text{St}_a + T_R) \quad \textbf{(c)}$$

The Pressure-Time-History for the internal blast loading of the bomb gaseous pressure decay in Fig 2.22 is given by

$$p(t) = (P_{QS}+p_o)e^{-2.13\tau} \quad \textbf{(d)}$$

where $$\tau = \frac{\alpha_e A_{St} a_o}{V} \quad \textbf{(e)} \quad \text{and} \quad \alpha_e = \frac{Vent\ Area}{Wall\ Area} \quad \textbf{(f)}$$

$$i_g = \text{Bomb Gas Impulse} = \int_0^{t_{max}} [p(t) - p_o]dt \quad \textbf{(g)}$$

Notation

A_S = total internal surface area, V = volume of the structural part subjected to the blast wave, a_o = speed of sound at ambient condition, t = time, P_{QS} =quasi-static Pressure, p_o = atmospheric pressure, P_a = pressure at ambient temperature, p_i = $P_{QS}+p_o$, t_{max} = blow down time

2.3 General procedures for blast loading design

Bomb blasts can be categorised as either free air or hemispherical surface blast. The latter assumes that the path of the blast is free from any reflective surface. For free air blasts the blast yield is enhanced by 1.8 [7]. For example if the assumed blast yield of 100 kg TNT was a free air burst, it would be necessary to use 180 kg TNT, as the bomb yield, before proceeding with analysis.

Every structure designed to resist blast loading will be assigned a protection category according to the needs of the structure. There are four protection categories as defined by TM5-1300. Protection category one applies to the protection of personnel. It specifies protection from fragments which, are induced by the blast, the blast pressures themselves and any excessive structural motions. In order to maintain this level of protection the support rotation, θ, is recommended to be no greater than 2°. Hence for a simply supported beam, the value of θ will be less than or equal to the maximum deflection of the structure y_m, which occurs at the maximum response time, t_m (Figure 2.24).

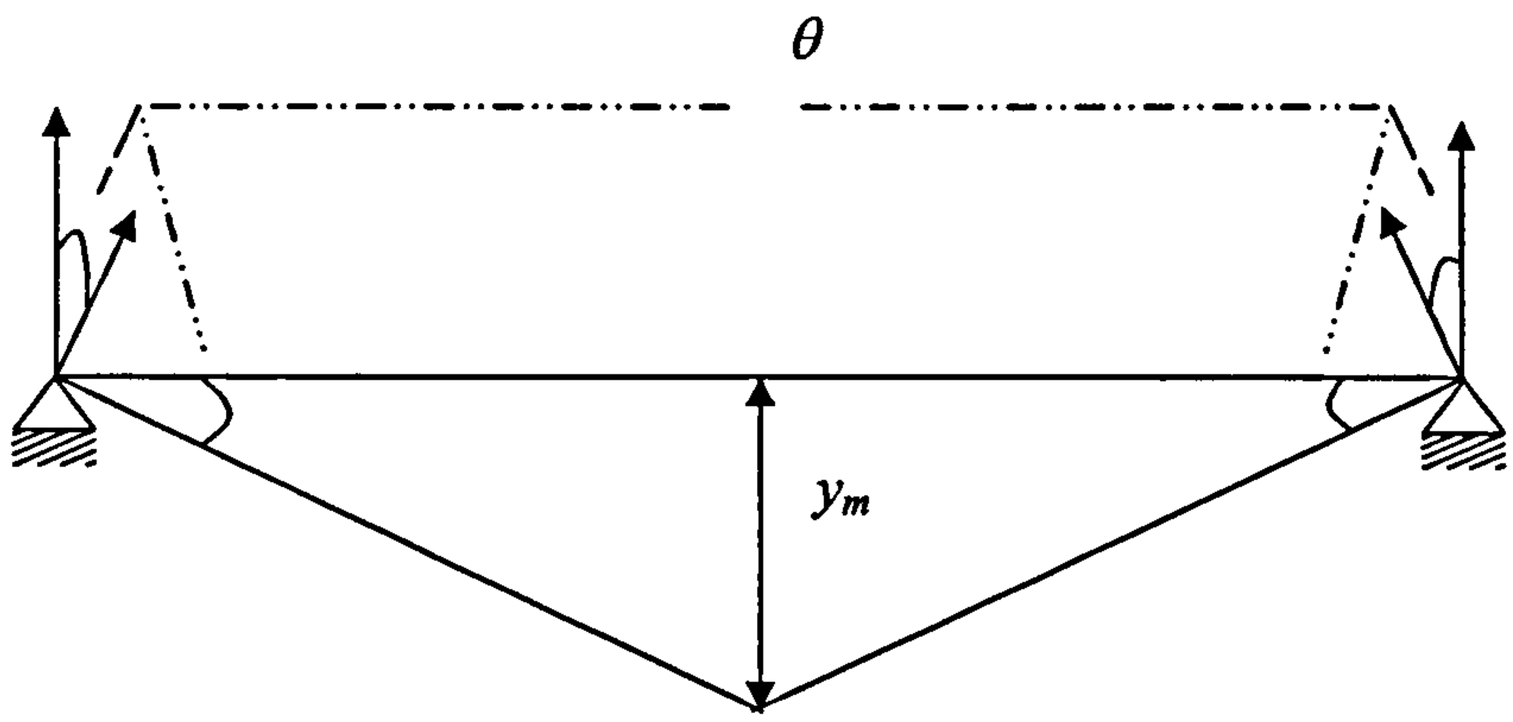

Figure 2.24 Support rotation θ at maximum deflection y_m

Protection category two specifies similar protection as category one except that it applies specifically to equipment within the structure. Hence the rotation allowed is slightly higher at 4°. In both cases the protection provided should prevent structural collapse. Protection category three applies to surrounding walls where controlled failure will prevent the contained structure from receiving the full force of the blast. Here the maximum allowable support rotation is 12°. Category four is similar to category three but restricts the blast force to structures or structural elements adjacent to the surrounding wall, but no further than that. Structural element cross sections to resist each protection category (i.e. each pressure range) are referred to as Type I, Type II or Type III respectively. The degree of protection defines the maximum allowable deflection.

For cases where the structure will require re-use, the ductility ratio, μ will have to be less than or equal to one. The ductility ratio is defined as the ratio of the maximum deflection to the deflection at the elastic limit, y_e. The deflection at the elastic limit occurs at time t_d.

$$\mu = \frac{y_m}{y_e} \tag{1.36}$$

The material strengths are enhanced by the respective Dynamic Increase Factor (DIF) The dynamic increase factor is used to account for the increase in dynamic stresses involved in blast loading. The following dynamic parameters are defined by TM5-1300 [7].

Table 2.7 Dynamic parameters as defined by TM5-1300 [7]

Type of Stress	**Protection Category**	**Concrete**		**Reinforcing Steel**		
		DIF f_{dcu}/f_{cu} =	Dynamic Design Stress f_{dc} =	DIF f_{dy}/f_y =	DIF f_{du}/f_u =	Dynamic Design Stress f_{ds} =
Bending	1	1.25	f_{dcu}	1.2	1.05	f_{dy}
	2		f_{dcu}			$f_{dy}+(f_{du}-f_{dy})/4$
Shear	1	1.00	f_{dcu}	1.10	1.00	f_{dy}
	2		f_{dcu}			f_{dy}

where, f_{dc} = Dynamic design stress for concrete, f_{dcu} = Dynamic ultimate compressive strength of concrete at twenty eight days, f_{cu} = Static ultimate compressive strength of concrete at twenty eight days, f_{ds} = Dynamic design stress for steel, f_{dy} = Dynamic yield stress of the reinforcement, f_y = Static yield stress of the reinforcement, f_{du} = Dynamic ultimate stress of reinforcement, f_u = Dynamic ultimate stress of reinforcement.

The next step in the analysis is to calculate the ultimate dynamic resistance r_u.

Consider a beam idealised as a single degree of freedom, mass-spring system as shown in Figure 2.25.

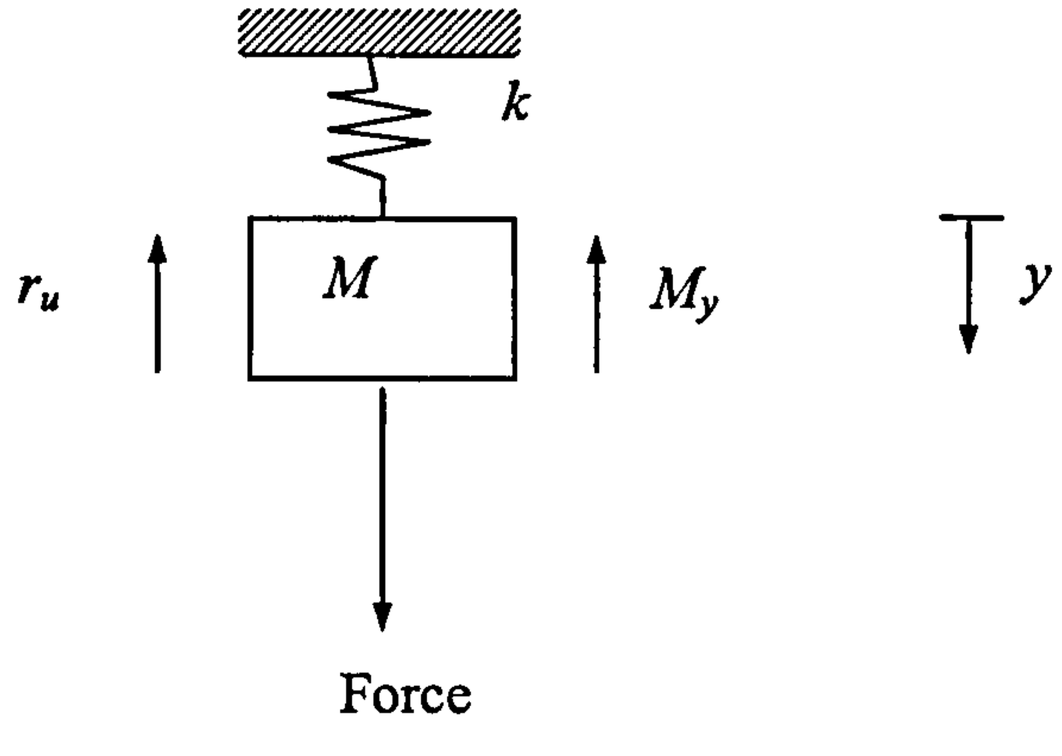

Figure 2.25 One degree of freedom elasto-plasto system

As the displacement increases the spring will offer some resistance r_u. The relationship with the displacement is shown in Figure 2.26

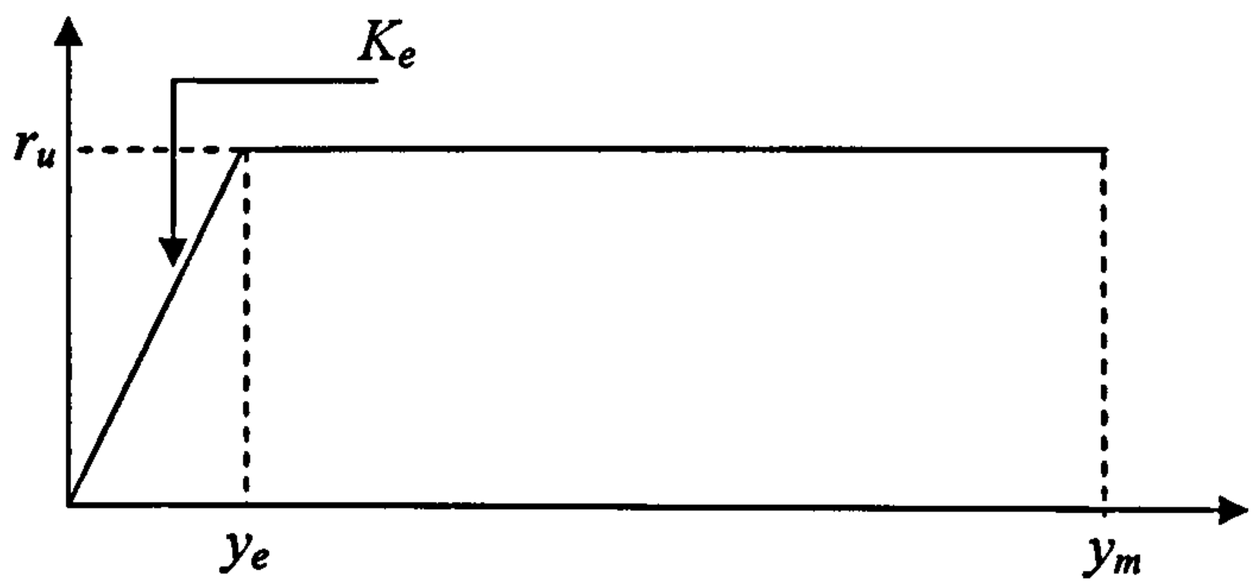

Figure 2.26 Resistance- displacement relationship

It can be seen that the displacement continues linearly until the elastic limit is reached, where the maximum elastic deflection occurs, y_e. Beyond this point the resistance function will be constant until the ductility limit of the structure is reached. At this point the structure will experience maximum deflection, y_m.

The resistance function is the internal force that will tend to restore the structural element to its original static unloaded state. In terms of load distribution, r_u is the total load having the given distribution, which the element could support statically.

Thus for a simply supported beam the plastic moment, m_p is as given in equation (2.37).

$$m_p = \frac{wL^2}{8} \tag{2.37}$$

By the definition of the resistance function $r_u = w$ thus rearranging equation (2.37) gives.

$$r_u = \frac{8m_p}{L^2} \tag{2.38}$$

Thus r_u will be measured as the load per metre square of the element under consideration. r_u will initially increase by the stiffness of the spring k. This can be represented by the elastic unit stiffness, K_E .

The elastic deflection is calculated from Figure 2.26 as

$$y_e = \frac{r_u}{K_E} \tag{2.39}$$

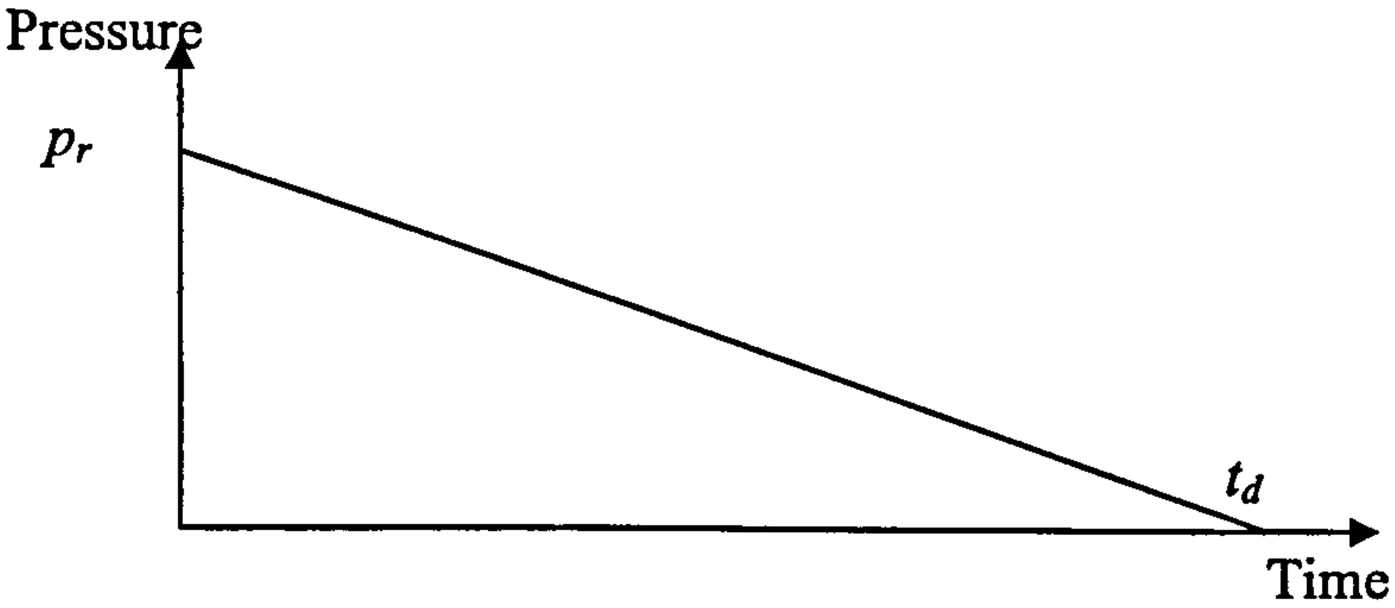

Figure 2.27 Idealised load time function

The total response time, t_m is derived as follows

Using the basic formula for impulse, i

$$i = force \times time \tag{2.40}$$

Taking the resistance function for force and replacing impulse with change in momentum gives

$$r_u = \frac{mv - 0}{t} = \frac{mv}{t} = \frac{i}{t} \tag{2.41}$$

Since the loading occurs over the response time, t_m the following formula is derived.

$$r_u = \frac{i}{t_m} = \frac{\int_0^{t_d} P(t)}{t_m} \tag{2.42}$$

As the above equation shows impulse is the area under the load time graph.

Design Criteria For a structure to resist blast loading the structure must have the flexural rigidity and strength such that the kinetic energy delivered by the impulsive loading may be resisted by the strain energy developed in the member in deflecting by t_m. This is given by the following equation from TM5-1300

$$\frac{i^2}{2K_{LM}m} = r_u\left(y_m - \frac{y_e}{2}\right) \tag{2.43}$$

where m is the unit mass of the element and K_{LM} is the load mass factor, which will be explained later. The m parameter represents an effective mass M. The left side of the above equation represents the kinetic energy and the right side represents the strain energy. The strain energy is calculated as the area under the resistance function as illustrated in Figure 2.26. The term defining kinetic energy is now derived.

Since kinetic energy is

$$KE = 0.5mv^2 \tag{2.44}$$

And impulse is

$$i = mv \tag{2.45}$$

By combining these two equations the expression for kinetic energy is arrived at

$$KE = \frac{1}{2}M\left(\frac{i}{M}\right)^2 = \frac{i^2}{2M} \tag{2.46}$$

For the impulsive loading to be valid TM5-1300 states that the time to reach maximum dynamic displacement, t_m must be at least three times the load duration t_d. If this is not the case then quasi static or dynamic loading apply (Figure 2.28).

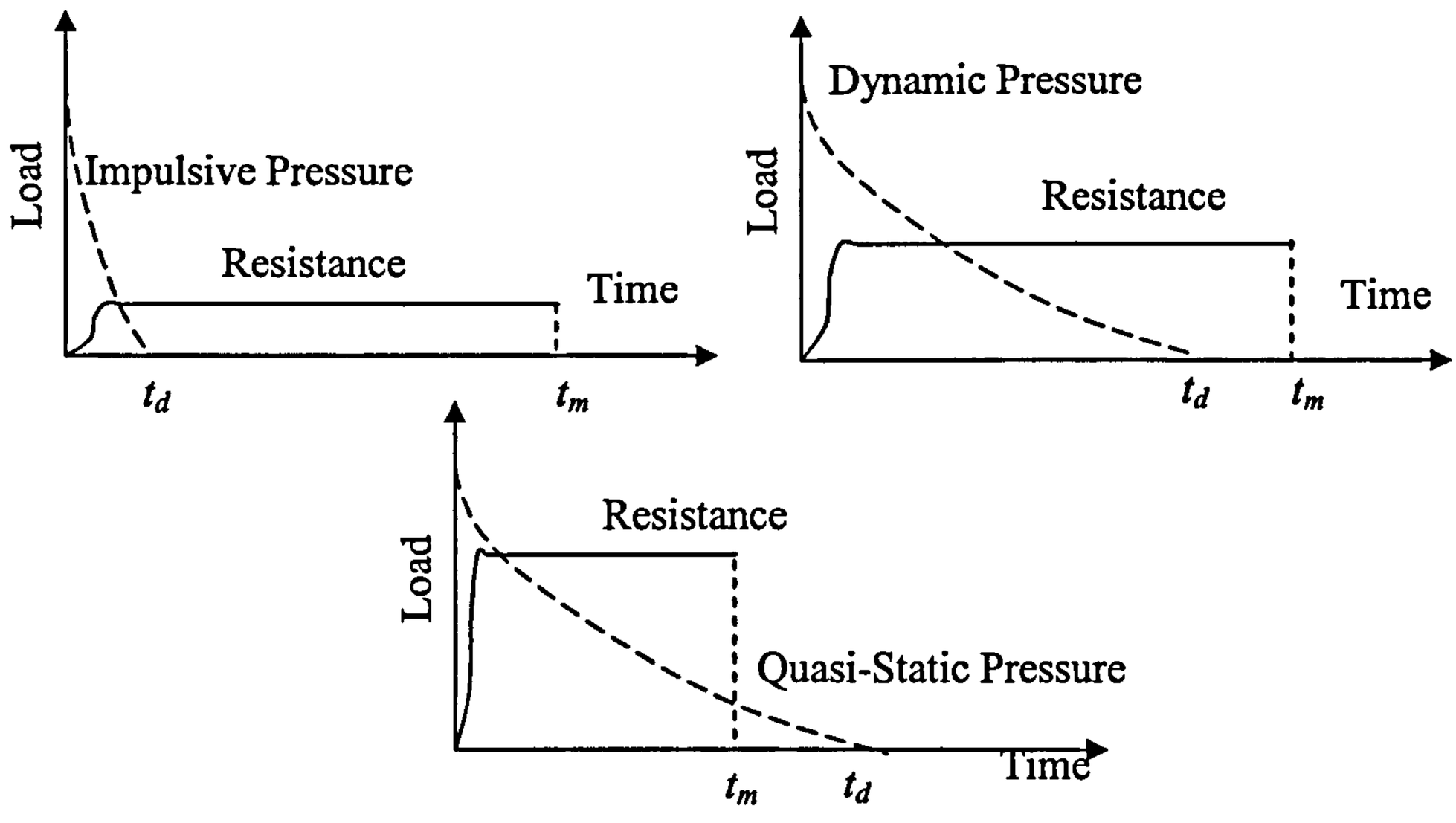

Figure 2.28 Pressure/resistance time function

The load mass factor K_{LM} is a combination of the load factor, K_L and the mass factor, K_M. The load factor is the factor by which the external work done on a structure is multiplied in order to obtain the concentrated dynamic loading on an equivalent system. The mass factor is the factor by which the mass of a real structure is multiplied in order to obtain the mass of an equivalent system.

2.3.1 Typical concrete element detailing

Despite the active and passive measures that can be employed to protect a building against blast loading, it is impossible to isolate precisely the path of travel of the shock wave. This can be due to objects in the path of the wave or the positioning of the explosive device. Hence it is more prudent to provide reinforcement which enables the structure to resist loading from any direction. Hence the provision of reinforcement with lacing, as shown in Figure 2.29, for blasts where the support rotation is greater than 2o is recommended by TM5-1300. Such a layout is more able to resist blast loading from any direction.

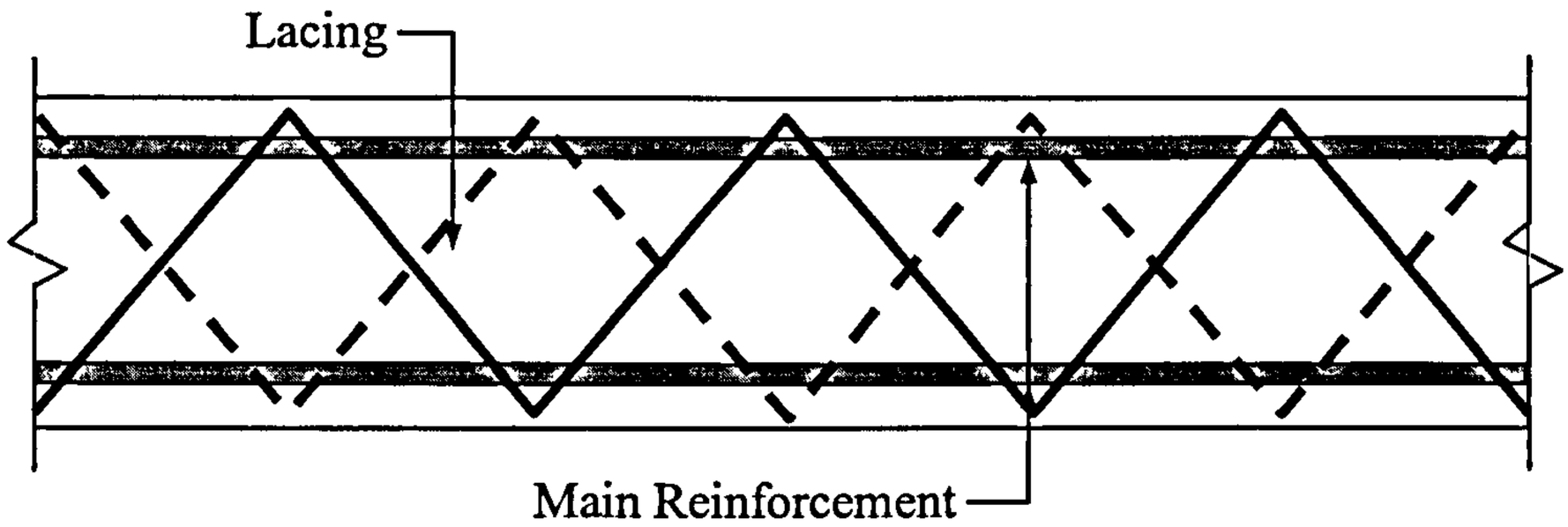

Figure 2.29 Reinforced concrete beam with reinforcement layout

The bent up bars act in tension and compression thus creating a truss system. The angle of inclination of the bars is never taken as less than 45°.

2.4 Case studies

In this section certain structural elements, designed according to various codes, are analysed for blast resistance using current methods [1,8].

2.4.1 Analysis for a simply supported reinforced concrete beam using British Practice

A simply supported beam is exposed to a blast load as shown in Figure 2.30. The beam is designed, initially for the static case, using the procedures as presented by the British Code of Practice, BS8110. Checks are carried out for bending, deflection and shear. Following the initial design, a separate analysis is performed to check the resistance of the beam to a 100 kgTNT bomb. The beam geometry, loading and material characteristics required for the initial design are now described.

Beam Dimensions

L = effective span = 7.0 m

h = beam depth = 500 mm

b = beam width = 250 mm

Loading

Characteristic imposed load = Q_K = 9 kN/m

Characteristic dead load = G_K = 11 kN/m

Characteristic own weight = S_W = 0.5 x 0.25 x 24 kN/m^3 = 3 kN/m

Loading factors γ_F =1.6, γ_G = 1.4, γ_{FSW} = 1.4

Material Properties

Concrete Grade = C30

Cover = 25 mm

$D_C = \gamma_C$ = density of concrete = 24 kg/m^3

f_y = steel stress at yield = 460 N/mm^2

E_c = Young's modulus of concrete

E_s = Young's modulus of steel

ρ_s = percentage of steel reinforcement = 0.012

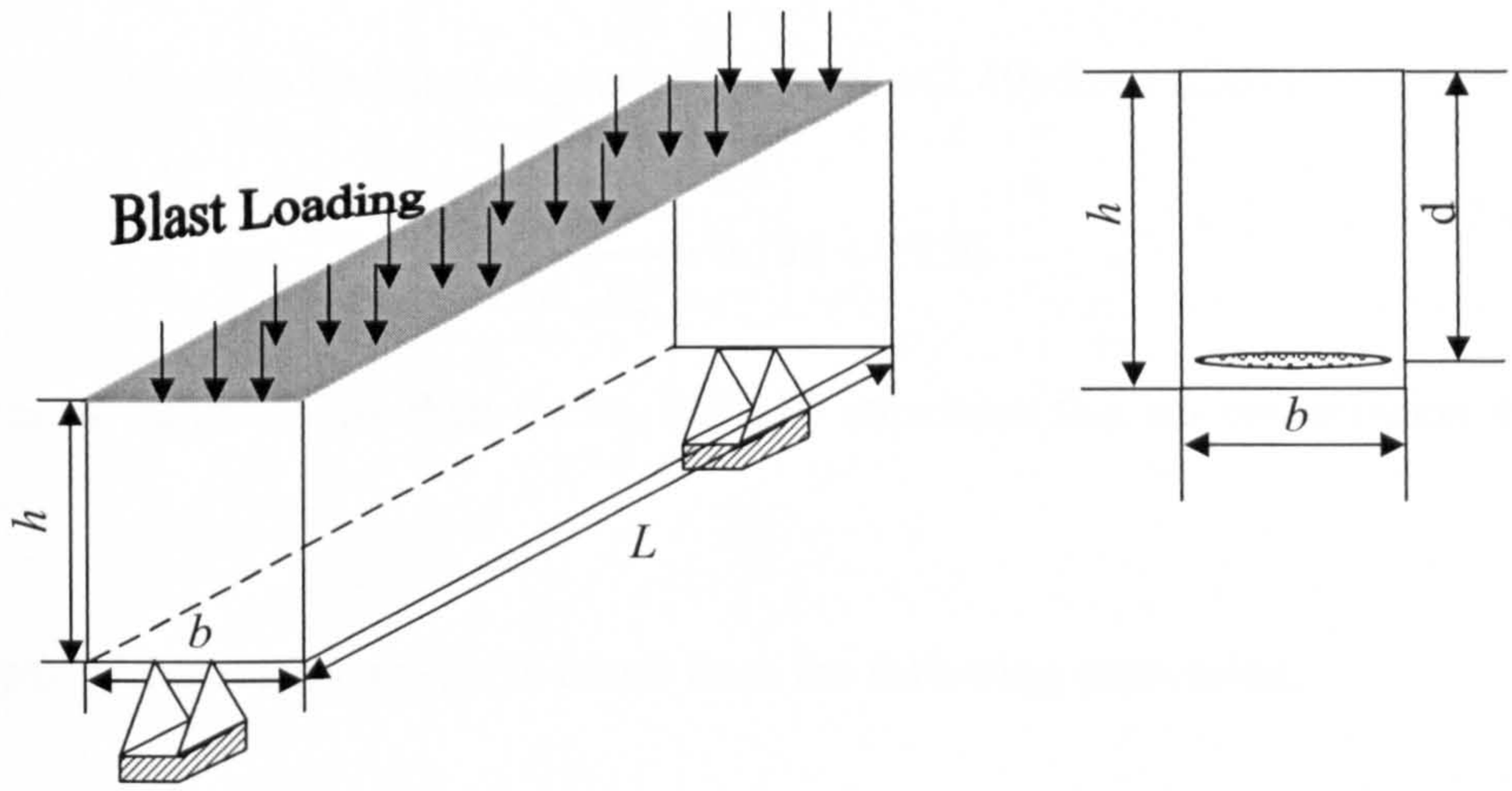

Figure 2.30 Reinforced concrete beam with cross section

Initial Structural Design to BS8110

Check on Bending

The Ultimate Limit State Loading is calculated as follows. Each of the loading components is multiplied by it's load factor, as given by BS8110 and summed to give the total loading.

$$w = (\gamma_f \times Q_K) + (\gamma_f \times G_K) + (\gamma_{fsw} \times Q_K) = (1.6 \times 9) + (1.4 \times 11) + (1.4 \times 3) = 34.14 \text{ kN/m}$$

Substituting this value into equation (2.47), gives the maximum bending moment, M_{max}.

$$M_{\max} = \frac{wL^2}{8} = \frac{34.14 \times 7^2}{8} = 209.1 \text{ kN/m} \qquad (2.47)$$

The maximum Shear Force, V_{max} is found to be

$$V_{\max} = \frac{wL}{2} = \frac{34.14 \times 7}{2} = 119.6\,\text{kN} \tag{2.48}$$

The assumed effective depth d is calculated as follows, using an assumed bar size and cover.

$$d = h - 0.5 \times \text{bar} - \text{link} - \text{cover}$$

Where, h is the overall height of the beam. Therefore

$$d = 500 - 12.5 - 10 - 25 = 452.5\,\text{mm}$$

The factor K can then be found as given by equation (2.49) from BS8110.

$$K = \frac{M}{bd^2 f_{cu}} = 0.136 < 0.156 \tag{2.49}$$

Since the K value is less then 0.156, BS8110 stipulates that no compression steel is required.

The depth of the neutral axis, z, is found from the following expression.

$$z = d\left[0.5 + 0.25 - \frac{K}{0.9}\right] = 0.814d$$

The required area of steel is then

$$A_s = \frac{M}{0.87 f_y z} = \frac{209.1 \times 10^6}{0.87 \times 460 \times 0.814 \times 452.5} \approx 1419\,\text{mm}^2$$

Hence using the relevant tables from BS8110, it is recommended that T25 bars with $A_{sprov} = 1474\ \text{mm}^2$ are adopted.

The percentage of steel content then becomes

$$\rho_s = \frac{1474}{250 \times 500} \times 100 = 1.18 > 0.13 < 4\% \tag{2.50}$$

The beam is satisfactory in deflection, as the criterion specified in equation (2.50) has been satisfied.

Check on Deflection

The deflection is checked using the ratio of span to effective depth. This is then modified for the amount of tension steel provided.

$$\frac{M}{bd^2} = \frac{209.1\times10^6}{250\times452.5^2} = 4.08$$

$$f_s = \frac{5}{8} f_y \frac{A_{srequireed}}{A_{sprov}} = \frac{5}{8}\times460\times\frac{1419}{474} = 276.8$$

The modification factor is then computed as

$$M.F. = 0.55 + \frac{477 - f_s}{120\left(0.9 + \frac{M}{bd^2}\right)} = 0.55 + \frac{477 - 276.8}{120(0.9 + 4.08)} = 0.885 \le 2 \text{ O.K}$$

The modified span to depth ratio is then calculated as

$$\text{Modified span to depth ratio} = 20\times0.885 = 17.7$$

The actual span to depth ratio is

$$\text{Actual span to depth ratio} = \frac{7000}{452.2} = 15.47 < 17.7 \text{ O.K.} \qquad (2.51)$$

The criterion according to BS8110 as set out in equation (2.51) is satisfied and hence the beam can be taken as adequate in deflection.

Check on Shear

The shear stress on the section being considered, v is calculated from equation (2.52).

$$v = \frac{V}{b_v d} \qquad (2.52)$$

where, V = *shear* force due to ultimate loads, b_v = breadth of the section

The following condition holds or the section size would need to be increased

$$v \le 0.8\sqrt{f_{cu}} \text{ or } 5 \text{ N/mm}^2 \text{ which ever is lesser} \qquad (2.53)$$

We have already calculated from (2.48)

$$V = 119.6\,\text{kN}$$

Therefore, from equation (2.52).

$$v = \frac{119.6 \times 10^3}{250 \times 500} = 1.06\,\text{N/mm}^2$$

And so the following criterion is satisfied

$$v = 1.06 < 0.8\sqrt{f_{cu}} = 0.8\sqrt{30} = 4.38\,\text{N/mm}^2 < 5\,\text{N/mm}^2$$

Hence the beam size is therefore satisfactory.

The design shear stress capacity, v_c is now calculated as follows

$$100 \times \frac{A_s}{b_v d} = \frac{100 \times 1474}{250 \times 500} = 1.1792$$

By using BS8110 Part1:1985 Table 1.9 we find for grade 25 concrete and a depth of 452.5 mm.

$$v_c = 0.63\,\text{mm}^2$$

For grade 30 concrete the above value is multiplied with the coefficient calculated using equation (2.54)

$$\left(\frac{f_{cu}}{25}\right)^{1/3} = \left(\frac{30}{25}\right)^{1/3} = 1.062 \qquad (2.54)$$

Therefore

$$v_c = 0.63 \times 1.062 = 0.669\,\text{N/mm}^2$$

Using BS8110:1985 Table 1.8 we find that

$$0.5v_c < v < v_c + 0.4$$

And so shear reinforcement in the form of minimum links is required provided following conditions apply.

- No main tensile reinforcing bar should be more than 150 mm from the vertical leg of a link
- The horizontal spacing of the link legs should not be more than the effective depth d
- The horizontal spacing across the span must never be greater than $0.75d$

The area of the links can be computed as from equation (2.55)

$$A_{sv} = \frac{0.4 b_v s_v}{0.87 f_{yv}} \tag{2.55}$$

Using $0.75d$ as the first trial for the link spacing, s_v, we obtain

$$A_{sv} = \frac{0.4 \times 250 \times 0.75 \times 500}{0.87 \times 460} = 93.7\,\text{mm}^2$$

Hence adopt T8-375 links.

Plastic Moment

The plastic moment, M_p using BS 8110 is calculated as given by the equation

$$M_p = A_s f_y (d - 0.45x) \tag{2.56}$$

Where x is the depth of the neutral axis and is given by the equation

$$x = \frac{A_s f_y}{0.6 b f_c} = \frac{1474 \times 460}{0.6 \times 250 \times 30} = 151\,\text{mm} = 0.151\,\text{m} \tag{2.57}$$

Therefore the plastic moment per beam width, m_p, is

$$m_p = \frac{M_p}{b} = \frac{1474 \times 460}{250}(452.5 - 0.45 \times 151) \times 10^{-3} = 1043\,\text{Nm/m}$$

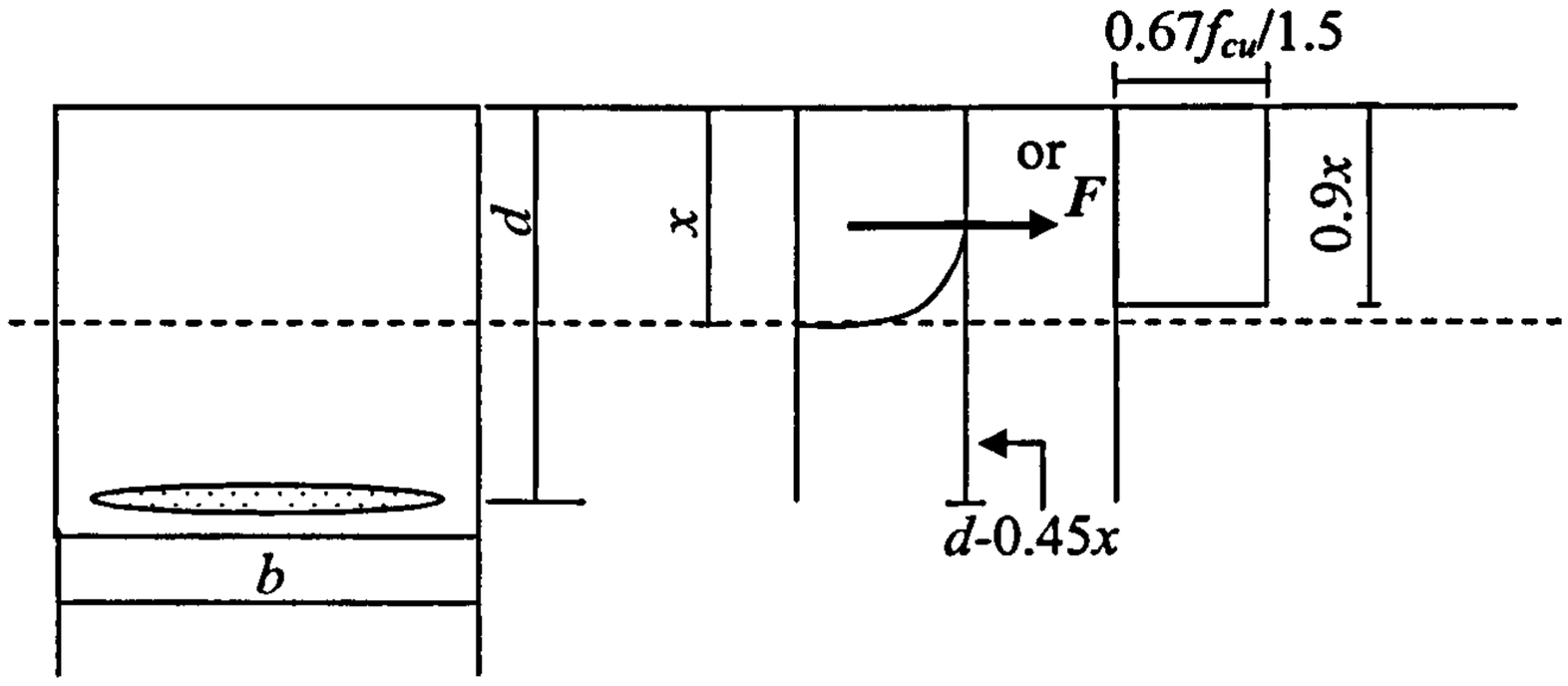

Figure 2.31 Reinforced concrete beam stress block (Fig. 3.3 BS8110)

The initial design using BS8110 is now complete. The beam is now subjected to a blast load and the subsequent analysis is hence presented.

Blast Loading Analysis

The load time function given in Figure 2.27 is found from Figure 2.33 with the scaled distance, Z=0.86 m/kg$^{1/3}$.

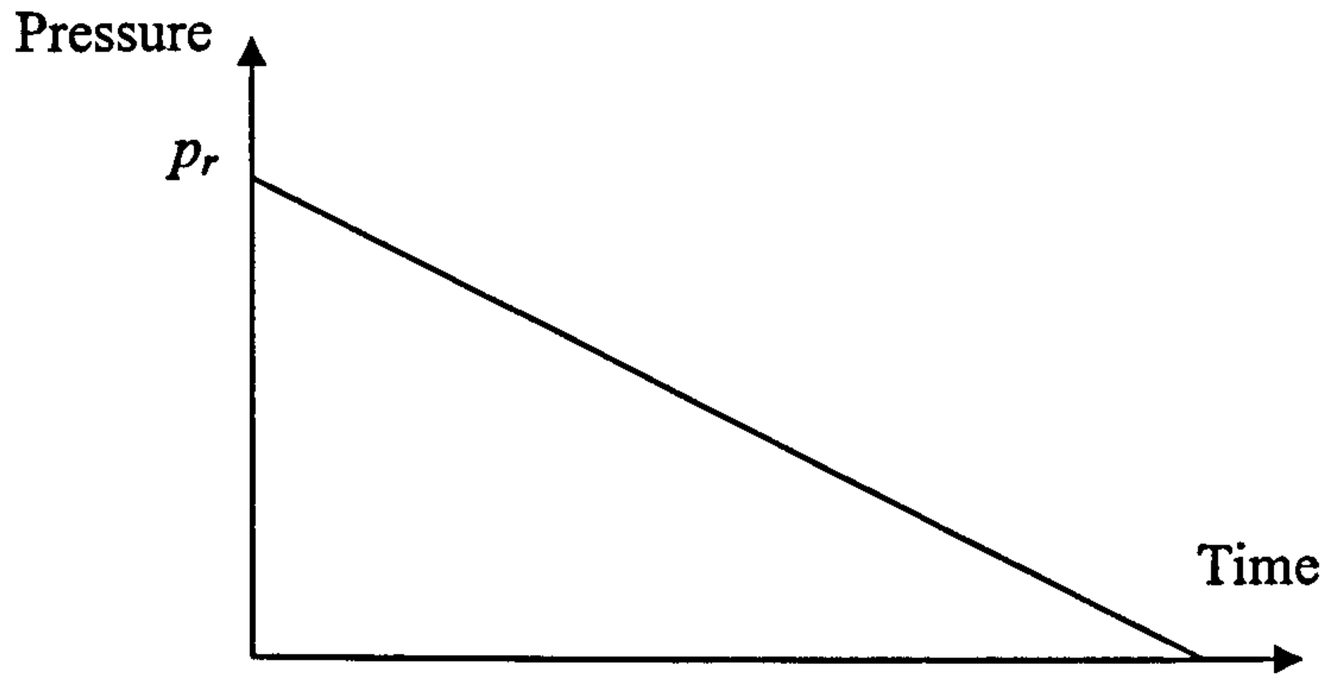

Figure 2.32 Blast wave parameters for spherical charges in free air

The overpressure p_r is 36.5 x 10^6 Pa and the time t_d is 4.83 ms.

Therefore we can obtain

t_d = 4.83 ms

i_r = reflected impulse = 5030 kPa-ms

The material strengths are now computed from Table 1.7, assuming category II protection.

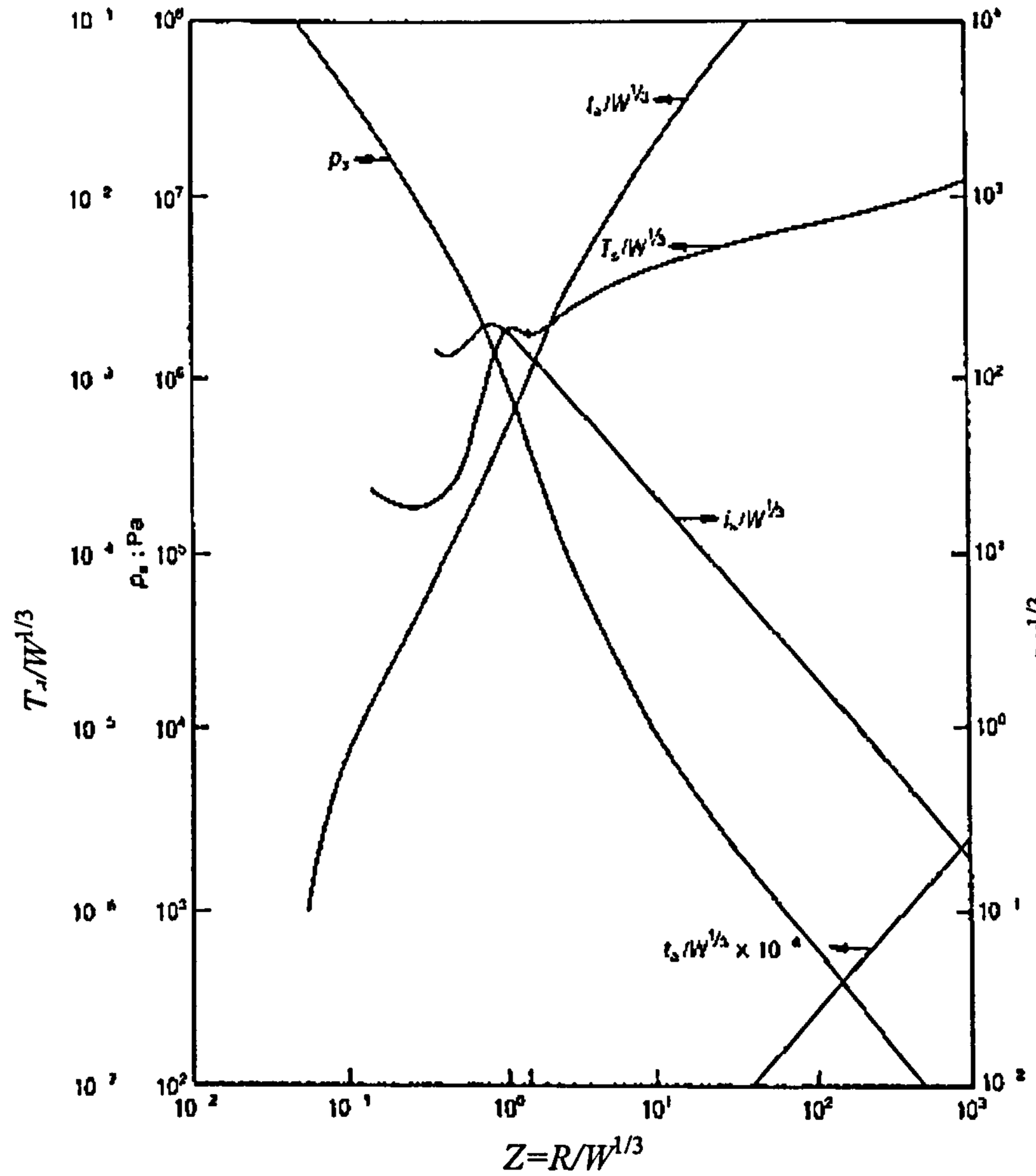

Figure 2.33 Blast wave parameters for spherical charges in free air [2]

The dynamic yield stress for reinforcement f_{dy} is defined as

$$f_{dy} = 1.2 f_y = 1.2 \times 460 = 552 \text{MPa} \tag{2.58}$$

where, f_y is the static yield stress for the reinforcement

The ultimate stress for the reinforcement f_{du} is defined as

$$f_{du} = 1.05 \times f_{dy} = 1.05 \times 550 = 578 \text{ MPa} \tag{2.59}$$

Therefore

$$f_{ds} = f_{dy} + \frac{(f_{du} - f_{dy})}{4} = 552 + \frac{578 - 552}{4} = 558.5\,\text{MPa} \tag{2.60}$$

The dynamic design stress for the concrete, f_{dc} is defined as

$$f_{dc} = f_{dcu} = 1.25 f_{cu} = 1.25 \times 30 = 37.5\,\text{MPa} \tag{2.61}$$

Equations (2.56) and (2.57) are therefore changed as given by equations (2.62) and (2.63) to account for the increase by their respective DIF.

$$x = \frac{A_s f_{ds}}{0.6 b f_{dc}} = \frac{1474 \times 558.5}{0.6 \times 250 \times 37.5} = 146.35\,\text{mm} = 0.146\,\text{m} \tag{2.62}$$

$$M_p = \frac{1474 \times 10^{-6} \times 552 \times 10^6}{0.25}[0.4525 - 0.45 \times 0.146] = 1273181.3 Nm \tag{2.63}$$

The ultimate resistance is calculated as

$$r_u = \frac{8M_p}{L^2} = \frac{8 \times 1273181.3}{49} = 207866.3\,N/m^2 \tag{2.64}$$

The maximum deflection, taking $\theta = 4^o$ is calculated as

$$y_m = 3.5 \tan 4^o = 0.244\,\text{m} \tag{2.65}$$

Taking $\rho_s = 0.012 = A/bd$, the value of the second moment of inertia, I is given by the equation from TM5-1300

$$I = 0.0525 b d_c^{\,3} \tag{2.66}$$

Where $F = 0.0525$ as read from Figure 2.34 where $n = E_c/E_s$ and is approximately 7.

The elastic unit stiffness as given by the equation

$$K_E = \frac{385EI}{5L^4} = \frac{385 \times 28 \times 10^9 \times 0.0525 \times 0.25 \times 0.4525^3}{5 \times 7^4} = 1091972.4\,\text{N/m}^2/\text{m}$$

Hence the elastic deflection is calculated

$$y_e = \frac{r_u}{K_E} = \frac{207886.3}{1091972.4} = 0.19\,\text{m} \tag{2.67}$$

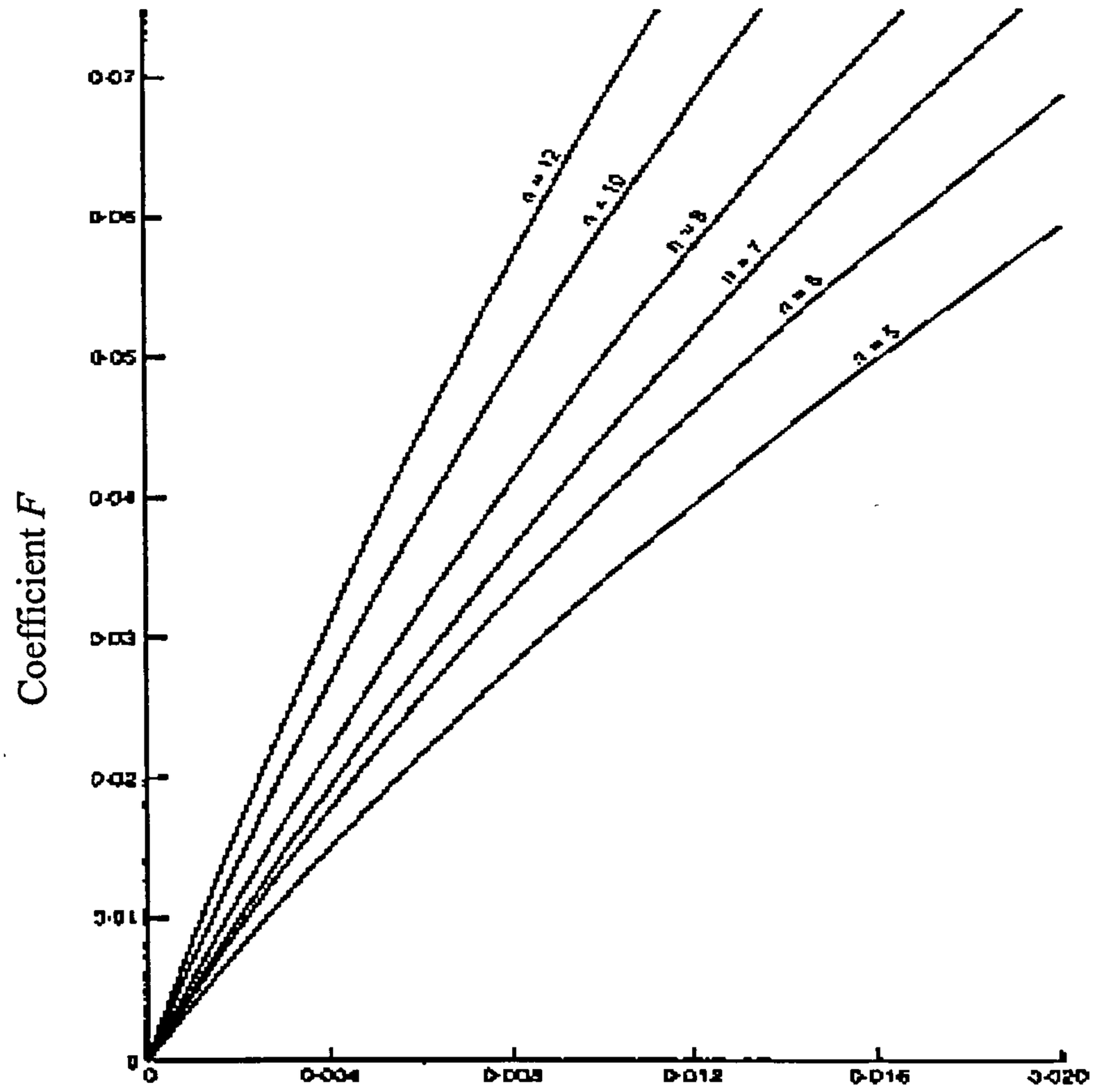

Figure 2.34 Coefficient for moment of inertia for cracked section with equal reinforcement on both faces [2]

The total response time t_m is computed as

$$t_{\text{m}} = \frac{i}{r_u} = \frac{5030}{207866.3} = 0.0242\,\text{s} \tag{2.68}$$

And so the ratio of t_m to t_d is

$$\frac{t_{\text{m}}}{t_{\text{d}}} = \frac{0.0242}{0.00483} = 5 > 3 \tag{2.69}$$

Hence the impulsive loading is valid.

The ultimate shear support, V_s

$$V_s = r_u L = 1441 \times 7 = 10087\ \text{N} \approx 10\ \text{kN} \tag{2.70}$$

This is less than the 119 kN already calculated according to BS8110.

The ultimate shear is found

$$v_u = v_c = \frac{1441(3.5 - 0.4525)}{0.4525} = 9704.8\ \text{N/m}^2 \approx 0.98\ \text{N/mm}^2 \tag{2.71}$$

Therefore the shear reinforcement recommended according to BS8110 is SAFE under this blast load.

Assuming the angle of inclination for the reinforcement to be 45° the shear stress resistance is calculated as follows using BS8110.

$$v_b = \frac{A_{sb} \times 0.87 \times f_y \times \sin 45}{b_v d} = \frac{93.7 \times 0.87 \times 460 \times \sin 45}{250 \times 500} = 0.212\ \text{N/mm}^2 \tag{2.72}$$

Therefore we see that $v_b < v_c$. Hence this section is still O.K.

The values obtained earlier in the analysis will be inserted into the following equation to check if the beam can resist this loading.

The unit mass m_d is

$$m_d = \frac{m}{b} = \rho d \tag{2.73}$$

The load mass factor is $K_{LM} = 0.66$.

$$\frac{\mathrm{i}^2}{2K_{LM}m} = r_u\left(y_m - \frac{y_e}{2}\right) \tag{2.74}$$

$$\frac{5030^2}{2 \times 0.66 \times 2400 \times 0.5} = 207866.3\left(0.244 - \frac{0.19}{2}\right) \tag{2.75}$$

The right hand side calculates to 30972.08 and the left hand side is computed as 17649.5. Since the strain energy is larger than the applied kinetic energy the beam is able to withstand the blast loading.

NOTE As given in Figure 2.29, the reinforcement can be kept on both sides since in practice it is impossible to tell which side will be exposed to blast loading.

2.4.2 Analysis for a wall slab using British practice

This case study will consider a cantilever wall slab, initially designed according to the British Code of Practice for Concrete Design, BS8110. Following this a blast analysis is carried out for the wall. The load time function is obtained using Figure 2.17.

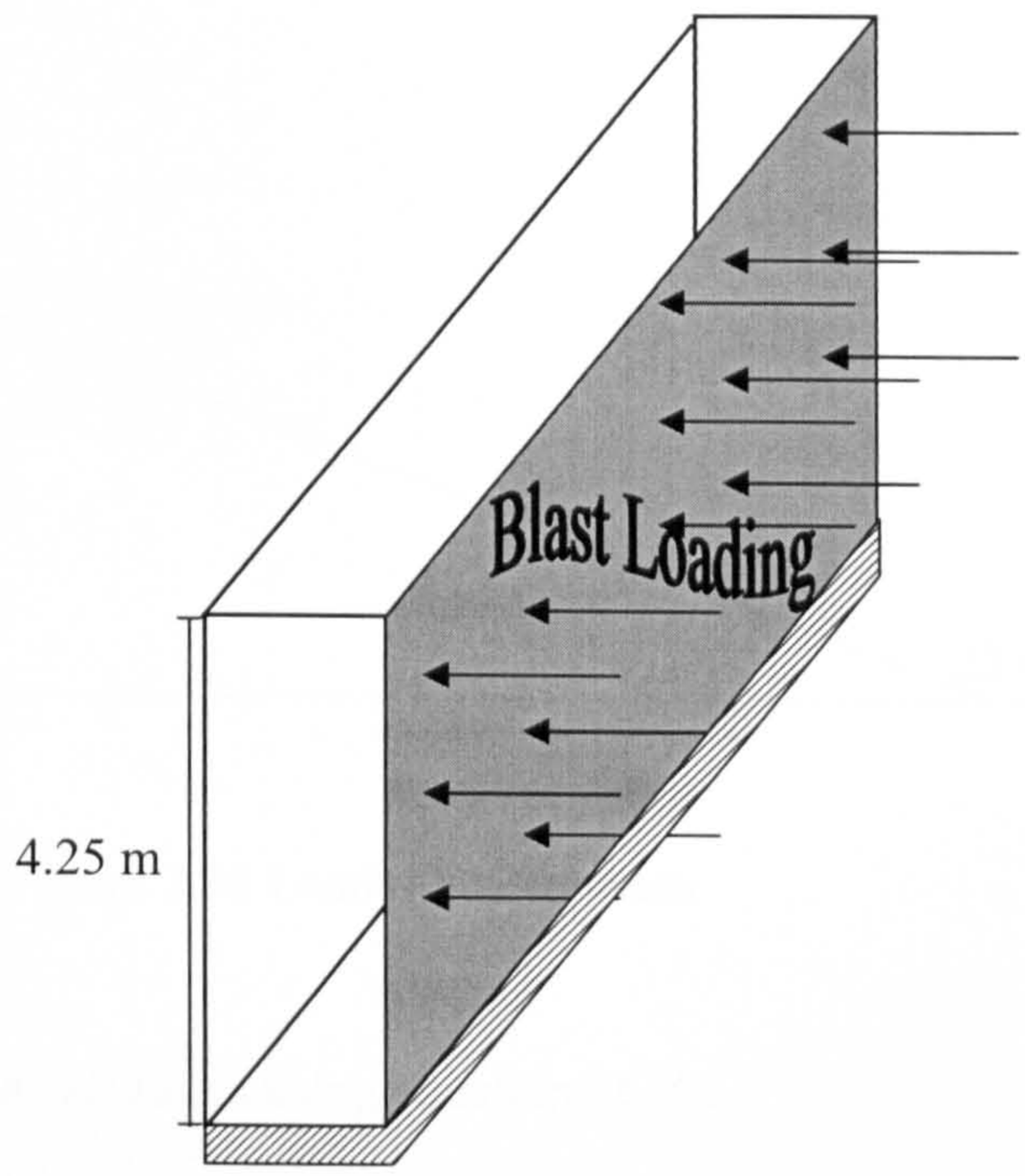

Figure 2.35 Fixed base cantilever wall

Slab Dimensions

H = wall slab height = 4.25 m

Material Properties:
Concrete Grade = C40

$D_C = \gamma_C$ =the density of concrete = 24 kg/m^3

f_y = steel stress at yield = 460 N/mm^2

E_c = Young's modulus of concrete

E_s = Young's modulus of steel

ρ_s = the percentage of steel reinforcement 0.5%

f_{dy} = The dynamic yield stress = $1.2f_y$

Blast Loading

Bomb Yield = 816.5 kgTNT

Range R=30 m

Category II Type Blast with $\theta = 4^o$

K_{LM} = the load mass factor = 0.66

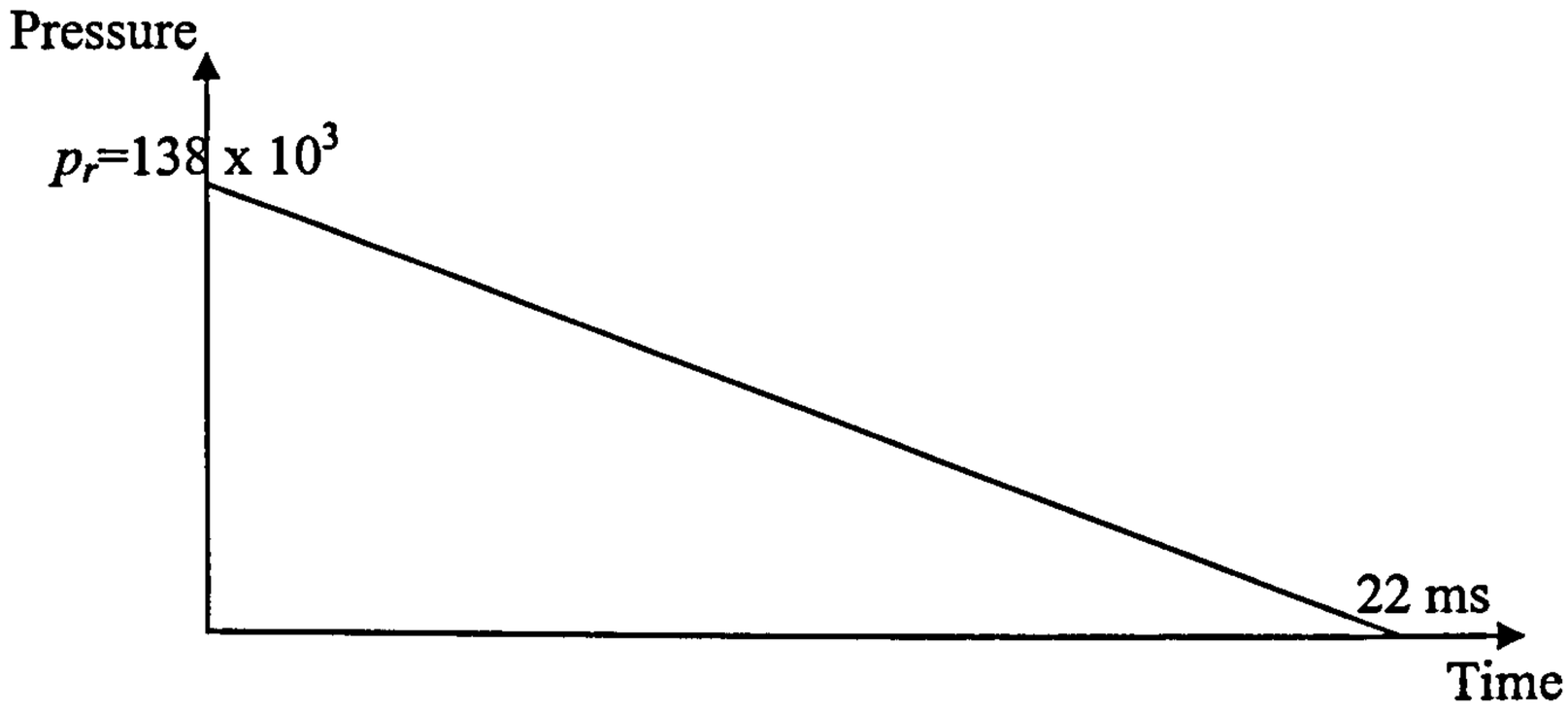

Figure 2.36 Load –time function

Firstly the Scaled distance is calculated using equation (2.16).

$$Z = \frac{30}{816.5^{1/3}} = 3.209 \text{ m/kg}^{1/3} \tag{2.76}$$

The reflected pressure or impulse i_r is found using the chart displayed in Figure 2.34

Hence from the chart

$$\frac{i_r}{W^{1/3}} \times 10^6 = 384210526.3 \tag{2.77}$$

Therefore

$$i_r = 3591.048 \approx 3591\,\text{kPa - ms} \tag{2.78}$$

Using Table 1.7 the following parameters are found

$$f_{dy} = 1.2 f_y = 1.2 \times 460 = 552\,\text{MPa} \tag{2.79}$$

$$f_{du} = 1.05 f_{dy} = 1.05 \times 550 = 578\,\text{MPa} \tag{2.80}$$

$$f_{ds} = f_{dy} + \frac{\left(f_{du} - f_{dy}\right)}{4} = 552 + \frac{578 - 552}{4} = 559\,\text{MPa} \tag{2.81}$$

The maximum deflection, y_m is found as

$$y_m = 4.25 \tan 4^\circ \approx 0.3\,\text{m} \tag{2.82}$$

The moment for a cantilever beam is shown in Figure 2.37

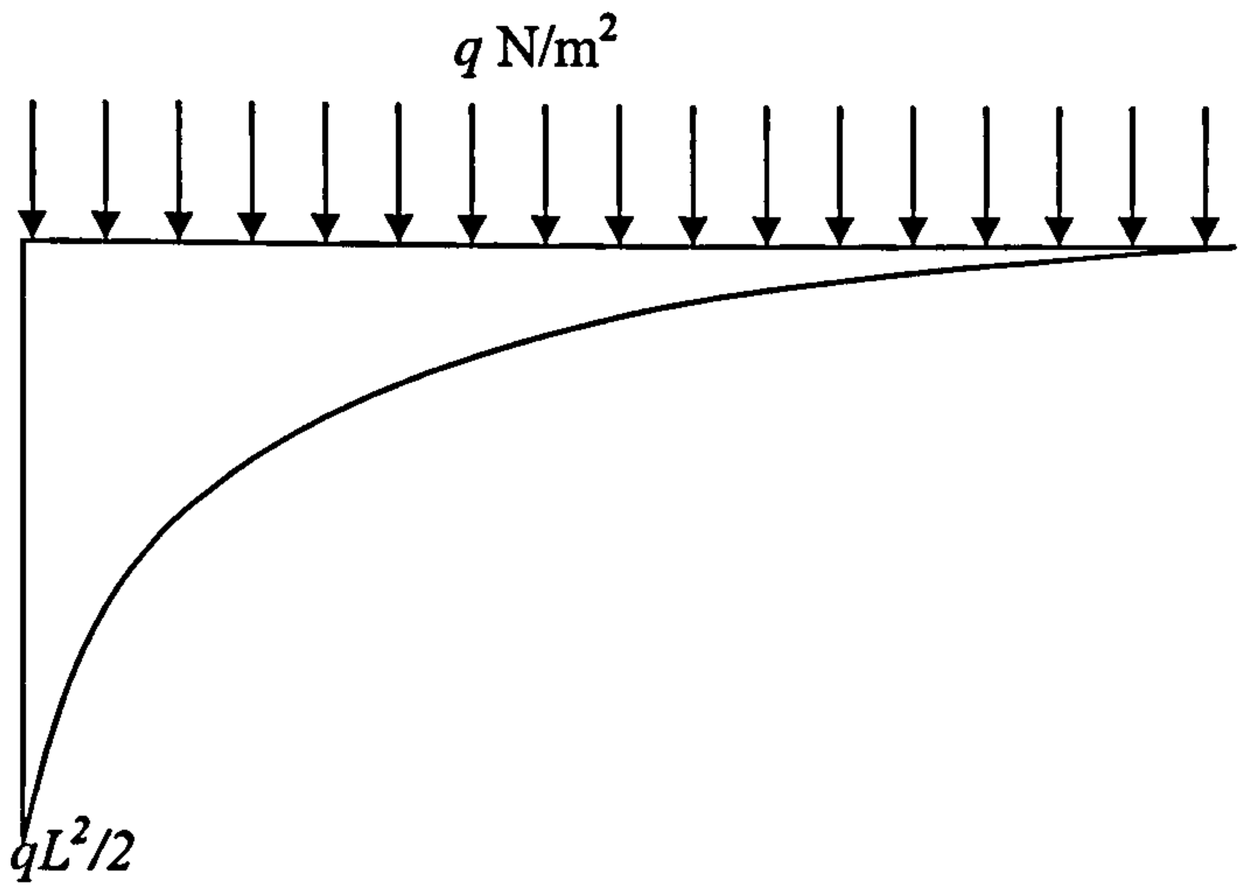

Figure 2.37 BMD for applied UDL upon a cantilever

By definition $q = r_u$ and therefore

$$M = \frac{qL^2}{2} = \frac{r_u L^2}{2} \tag{2.83}$$

Thus the ultimate load resistance, r_u is

$$r_u = \frac{2M}{L^2} \tag{2.84}$$

The equivalent elastic stiffness is given by

$$K_E = \frac{8EI}{H^4} \tag{2.85}$$

The elastic deflection, y_e, is then found as

$$y_e = \frac{r_u}{K_E} = \frac{2M}{H^2} \times \frac{H^4}{4EI} = \frac{MH^2}{4EI} \tag{2.86}$$

Using TM5-1300 the second moment of Inertia, I, and the moment, M, are found as

$$I = Fbd^3 \tag{2.87}$$

$$M = \rho_v f_{ds} d^2 = 0.005 \times 559 \times 10^6 d^2 = 2.795 \times 10^6 d^2 \tag{2.88}$$

Assuming, the percentage steel ρ_v to be 0.005. The coefficient, F is obtained from Figure 2.34 and is found as 0.245.

Upon substituting the values into the basic impulse formulas as given by (2.74) the following equation is obtained

$$\frac{3591^2}{2 \times 0.66 \times 2400d} = \frac{2M}{H^2}\left(0.3 - \frac{MH^2}{4EI}\right) \tag{2.89}$$

Further substitution gives

$$\frac{12895281}{3168d} = 92844.3d^2 - 2.037 \times 10^{-4} d \tag{2.90}$$

This simplifies to

$$1 = 22.81d^3 - 5 \times 10^{-8} d^2 \tag{2.91}$$

The depth, d is subsequently found to be 0.35 m. This is now substituted to find the following parameters

$$M = 2.795 \times 10^6 d^2 = 2.795 \times 10^6 \times 0.35^2 = 364437.5 \quad (2.92)$$

$$r_u = \frac{2 \times 364437.5}{4.25^2} = 40352.94 \quad (2.93)$$

$$K_E = \frac{8 \times 28 \times 10^9 \times 0.245 \times 1 \times 0.35^3}{4.25^4} = 7212112.9 \quad (2.94)$$

$$y_e = \frac{r_u}{K_E} = \frac{40352.94}{7212112.9} = 5.59 \times 10^{-3} \quad (2.95)$$

The total response time t_m is computed as

$$t_{\mathrm{m}} = \frac{i}{r_u} = \frac{3591}{40352.94} = 1.5758\,\mathrm{s} \quad (2.96)$$

And so the ratio of t_m to t_d is

$$\frac{t_{\mathrm{m}}}{t_{\mathrm{d}}} = \frac{1.5758}{0.0022} = 72 > 3 \quad (2.97)$$

Hence the impulsive loading is valid.

Upon substituting the values in the basic impulse equation to check blast resistance

The right hand side calculates as 11992.99 and the left hand side is 11629.94. Hence the strain energy is greater the applied kinetic energy and the structure is able to resist the load.

The required area of steel reinforcement, A_{sreq} is then found

$$A_s = 0.005 \times 350 \times 1000 = 1750\,\mathrm{mm}^2 / \mathrm{m\ width\ of\ wall} \quad (2.98)$$

To account for design variation the principal design recommendation is to provide 25% more steel.

Therefore

$$A_s = (1 + 0.25)1750 = 2187.5\ \mathrm{mm}^2 / \mathrm{m\ width\ of\ wall} \quad (2.99)$$

Adopt T32- 300 reinforcement ($A_s = 2681\ mm^2$)

The shear is found using equation (2.100).

$$v = \frac{r_u(H - d_c)}{d_c} \tag{2.100}$$

Therefore

$$v = \frac{40352.94(4.25 - 0.350)}{0.350 \times 10^6} = 0.45\ N/mm^2$$

From BS8110 the v_c value is found as 0.34, with the $100A_s/bd$ value being equal to 0.15. Since $f_{cu} = 40$ and is greater than 25, The following correction factor from the code is applied.

Hence

$$v_c = 0.34\left(\frac{f_{cu}}{25}\right)^{1/3} = 0.397 \approx 0.4$$

Therefore the following condition applies for the provision of shear reinforcement

$$0.5v_c < v < (v_c + 0.4)$$

The area of shear reinforcing steel assumed a link spacing of 300, is

$$A_{sv} = \frac{300 \times 425 \times 0.4}{0.87 \times 460} = 127.44\ mm^2$$

Hence provide R8-200 ($A_{sv} = 393\ mm^2$)

2.4.3 Simply supported floor slab using the European Code EC-2

This case study will consider a floor slab designed according to EC2. The slab is then tested for resistance to blast loading with the appropriate analysis presented.

Slab Data

Variable load = $3.0\ kN/m^2$

Floor finishes and ceiling loads = $1.0\ kN/m^2$

Imposed action or live loads = 3.0 kN/m^2

f_{ck} = 25 N/mm^2

f_{yk} = 460 N/mm^2

L = Effective span = 4.5 m

L/d_c = 21.7 Lightly stressed slab

L/d_c = 29.5 Normally reinforced slab

D_c = Density of concrete = 2400 kg/m^3

d_c = Minimum effective depth = 4500/(25.7 x c.f.)

c.f. = unity as high yield steel is being used

Hence d_c simplifies to 175 mm as a first approximation. By assuming class one exposure the cover is taken as 20 mm. Thus the overall depth of the slab is

$$H = 175 + 20 + 5 = 200\,\text{mm} \tag{2.101}$$

Where 5 mm is taken to be half the diameter of the assumed reinforcing bar.

The loading is calculated as follows. The slab self weight is computed as

$$S.W. = 200 \times 24 \times 10^{-3} = 4.8\,\text{kN/m}^2$$

By adding the loading from the floor finishes and ceiling loads the total slab permanent loading is found.

$$P.L. = 1 + 4.8 = 5.8\,\text{kN/m}^2$$

Thus for a 1m width of slab the ultimate load is calculated from equation (2.102).

$$U.L. = (1.35g_k + 1.5q_k)4.5 = 55.5\,\text{kN} \tag{2.102}$$

The maximum bending moment is then

$$M = \frac{55.5 \times 4.5}{8} = 31.2\,\text{kNm} \tag{2.103}$$

In order to provide bending reinforcement the following quantity is calculated

$$\frac{M}{bd_c f_{ck}} = \frac{31.2 \times 10^6}{1000 \times 175^2 \times 25} = 0.041 \tag{2.104}$$

The lever arm l_a = 0.96 and hence the depth of the neutral axis is

$$z = l_a d = 0.96 \times 175 = 168\,\text{mm} \tag{2.105}$$

Therefore the required area of reinforcement is

$$A_s = \frac{M}{0.87 f_{yk} z} = \frac{31.2 \times 10^6}{0.87 \times 460 \times 168} = 464\,\text{mm}^2/\text{m} \tag{2.106}$$

Adopt T10 – 150 mm bars with $A_s = 523\ \text{mm}^2/\text{m}$

To carry out a check upon the span effective depth ratio the following is calculated

$$\frac{100 A_s}{b d_c} = \frac{100 \times 523}{1000 \times 175} = 0.299 \tag{2.107}$$

This corresponds to an *L/d* ratio of 26.2. The actual ratio is

$$\frac{4500}{175} = 25.7 \tag{2.108}$$

Hence the effective depth is O.K.

The actual shear V_{sd} at the face of the support is

$$V_{sd} = \frac{55.2}{2}\left(\frac{2.25 - 0.5 \times 0.3}{2.25}\right) = 25.9\,\text{kN} \tag{2.109}$$

The allowable shear is V_{rd1}

$$V_{rd1} = [\tau_{Rd} k (1.2 + 40\rho_1)] b d \tag{2.110}$$

$$V_{rd1} = [0.3(1.6 - 0.175) \times (1.2 + 40 \times 0.0029)] \times 1000 \times 175 \times 10^{-3} = 98.7\,\text{kN} \tag{2.111}$$

Since the allowable shear is greater than the actual shear, then no shear reinforcement is needed. The end anchorage length of the reinforcing bar is calculated as follows

$$37\phi = 37 \times 10 = 370\,\text{mm} \tag{2.112}$$

Hence the required anchorage beyond the face of the support is

$$\frac{2}{3}\times 370 = 247\,\text{mm} \tag{2.113}$$

The minimum distribution steel is

$$\text{min distribution steel} = 0.0015bd = 0.001\times 1000\times 175 = 263\,\text{mm}^2/\text{m} \tag{1.114}$$

Thus provide T10-250 mm bars with $A_s = 314\ \text{mm}^2/\text{m}$

Blast Loading Analysis

The slab is now subject to a hemispherical surface, category II blast load from a 100 kgTNT bomb at a range of 4 m. The grade of the concrete is changed from 25 to 40.

The maximum deflection is

$$X_m = L\tan 4^o = 4.25\tan 4^0 = 0.297\,\text{m}$$

The ultimate resistance r_u is

$$r_u = \frac{8M}{L^2} = \frac{8\times 31.2\times 10^3}{4.25^2} = 13818.69\,\text{N/m}^2$$

Where percentage of steel, ρ_v and

$$\rho_v = \frac{A_s}{bd} = \frac{464\times 4.25}{1000\times 200} = 0.001\,\text{m}$$

The coefficient F is then found from Figure 2.34 as 0.005 with n = 7.

the dynamic stress in concrete = 560 x 10^6 N/mm^2

The equivalent elastic stiffness is

$$K_E = \frac{384EI}{5L^4} = \frac{384\times 2.8\times 10^9\times 0.005\times 1\times 0.2^3}{5\times 4.5^4} = 263647.42\,\text{N/m}^2/\text{m}$$

The elastic deflection, hence becomes

$$X_E = \frac{r_u}{K_E} = \frac{13818.69}{263647.42} = 0.05\,\text{m}$$

The required area then becomes

$$A_s = 0.005 \times 200 \times 1000 = 1000\,\text{mm}^2/\text{m}$$

Therefore adopt T20-150 bars on both top and bottom of the slab.

Hence

$$t_\text{m} = \frac{i}{r_u} = \frac{5030}{13818.69} = 0.3639\,\text{s}$$

Thus

$$\frac{t_\text{m}}{t_\text{d}} = \frac{0.3639}{0.00483} = 75 > 3$$

The impulsive load analysis is in this case valid.

The ultimate shear stress at the point d_c from the support is

$$v_\text{u} = \frac{r_u(L - d_c)}{d_c} = 1.81\,\text{N/mm}^2$$

Hence

$$v_\text{u} - v_\text{u} = 1.81 - 0.58 = 1.23\,\text{N/mm}^2$$

With $f_{cu} = 40$ N/mm^2 and $100As/bd_c = 0.52$ v_c is calculated as 0.58 N/mm^2

Taking a width of 150 mm and stirrup spacing of 300 mm the required area is

$$A_v = \frac{1.23 \times 150 \times 300}{275} = 201.3\,\text{mm}^2/\text{m}$$

where the dynamic stress of steel, $f_{ds} = 275$ N/mm^2. Adopt R10-200 stirrups with A_{vprov} = 393 mm^2

The ultimate support shear is given by

$$V_s = \frac{r_u L}{2} = 398232\,\text{Nm} = 398.232\,\text{Nmm}$$

The required area of diagonal bars at 45° is using high yield steel (f_{ds}=506 N/mm^2)

$$A_d = \frac{V_s b}{f_{ds}} = 118\,\text{mm}^2$$

Adopt T10-100 bars with A_s 285 mm^2.

The period is calculated as

$$T = 2\pi\sqrt{\frac{K_{LM} m_d}{K_E}} = 2\pi\sqrt{\frac{0.66\times 2400\times 0.4}{12.85\times 10^6}} = 0.04409 \approx 44.1\,\text{ms}$$

Using the following impulse equation with K_{LM}=0.66 and m=2400d$_c$ kg/m^2 and substituting the values the blast resistance is determined.

$$\frac{i_r^{\,2}}{2K_{LM}\rho d_c} = \frac{r_u X_E}{2} + r_u\left(X_m - X_E\right)$$

Therefore

$$\frac{5030^2}{2\times 0.66\times 2400\times 0.2} = 13818.7\left(0.297 - \frac{0.05}{2}\right)$$

The left hand side (applied kinetic energy) is worked out to be 39932 N/m and the right hand side (strain energy) is derived as 3758 N/m Hence the structure fails.

2.5 References

1. PD Smith, JG Hetherington, "Blast and Ballistic Loading of Structures", *Butterworth-Heinemann* (1994)
2. WE Baker *et al.*, "Explosions Hazards and Evaluation", *Elsevier Scientific Publishing Company* (1992)
3. MYH Bangash, "Impact and Explosions", *Blackwell* (1993)
4. GF Kinney and KJ Graham, "Explosive Shocks in Air", *Springer- Verlag* (1985)
5. MV Dharaneepathy *et al.*, "Critical Distance for Blast Resistant Design", *Computers & Structures 54 No 4 pp587-595* (1995)

6. R.B Phillips, "REN 558", *Library Archives of the Institution of Civil Engineers*, (1945)
7. TM5-1300, "Design of Structures to Resist the Effects of Accidental Explosions", *US Dept. of the Army Technical Manual* (1991)
8. MYH Bangash, "Prototype Building Structures: Analysis and Design", *Thomas Telford* (1999)

Chapter 3

Material response to explosive loads and structural strength enhancement criteria

3.1 Design of buildings

3.1.1 Introduction

Many of today's buildings are easily susceptible to many forms of malicious intent. These may include the use of toxic gas, internal and external explosion, aerial attack or even nuclear explosion. As structural engineers the greatest consideration must be given to the threat posed to buildings from bomb explosions or other forms of explosive attack. Other forms of threat are either structurally non-damaging or so damaging that no amount of cost effective design can provide purposeful protection.

The ever-increasing menace posed by various types of bomb (letter bombs, vehicle bombs or briefcase bombs) is now a serious hazard for which engineers must produce a riposte. Bombs may range from those, which are more mundane in nature to those with significant military capability. These could include incendiary devices, shaped charges, uncased high explosive and rocket propelled grenades and munitions.

In order to acquire greater blast protection some prudent measures can be incorporated into the layout of the building design. The protection from an explosion threat is categorised in two ways. Firstly there is active protection [1], which requires human intervention. This can take the form of guards, security cameras, various sensors and electrical gadgets placed at strategic or sensitive locations. Secondly there is passive protection [1], which does not require human intervention. In this instance such measures would include a perimeter wall or fencing, bollards or structural hardening.

The design of the structure itself should ensure that any sensitive or vulnerable areas within the building are as difficult to reach as possible. Measures to ensure this can include meandering pathways or restricted public access. The use of buffer zones between vulnerable areas and other parts of the building can restrict damage and loss of life in the event of an explosion. Buffer zones, for example, can be made using storage rooms. Another useful protective feature would be to restrict outside parking, thus reducing the threat from vehicle bombs. If internal parking is required by the client to be inherent in the structure then an adjacent underground structure is the best means of achieving threat reduction.

It is desirable at the design stage to include escape routes and safe havens with emergency services such as lighting to facilitate a quick safe evacuation of the building.

The larger the catchment area of the building the greater the level of protection will be. This protection is further enhanced with controlled access through a perimeter wall or fence.

3.1.2 Protection against blast loading for existing buildings

"Blastproofing" an existing structure is a costly undertaking. Engineers must therefore balance the cost against other factors such as the buildings expected lifetime, it's use and it's vulnerability of exposure to explosions.

The first step in evaluating a building's blast resistance is to consider the materials used in its construction. Masonry and brick buildings offer very little inherent resistance to blast. In such cases rather than invoking costly structural upgrading it may be more viable to change the internal use of the building, so as to mitigate the blast threat.

Cast insitu concrete or steel frames offer a higher degree of protection. In this case the first option is to consider methods of increasing the perimeter of the structure and limiting nearby parking. Once again active protection procedures can be adopted. Replacing windows with special glass such as thermally tempered or laminated glass can also be an option. Laminated glass is manufactured using a strong plastic interlayer in between the glass pieces. The most commonly used interface layers are polyvinylbutyral and acrylic [2]. Any number from two to twenty five pieces of glass has been laminated. Different types of glass including toughened and heat strengthened glass can also be laminated. In these cases the acrylic resin is used for the interface. However the cost of these options is high and is of limited use if the surrounding wall is not also strengthened.

Another measure is to surround the structure with a hardened structural wall. However this is also a costly arrangement.

A protective layer of cladding in the form of SIFCON (Slurry Infiltrated Concrete) or concrete with differing types of reinforcement would provide enhanced protection against impulsive loading. SIFCON is made by sprinkling some fibres into a mould and subsequently infiltrating them with cement based slurry. Investigations by Anderson, WF *et al.* [3] concluded that SIFCON showed greater penetration than ordinary concrete. However using 10 mm aggregate in the SIFCON improved the penetrability. Further tests by Mayhrhofer, C [4] showed SIFCON to have better load bearing capacity in both dynamic and static situations. Failure of the specimen slabs were showed to occur at 2 to 5 times the elastic limit and reinforced SIFCON slabs achieved similar bending capacity to ordinary reinforced concrete slabs with less thickness.

Bearing capacity was shown to increase significantly with the use of ribbed torsteel in ordinary concrete [5].

Fibre reinforced concrete has also been shown [6] to have higher energy absorption and reduced rear spalling in comparison to ordinary concrete when subjected to impulsive loading.

3.1.3 Structural form for blast resistance

Simple geometries are better at resisting blast loading. For example 'L' and 'U' shapes are best avoided as the blast wave becomes trapped in the re-entrant corner thus amplifying the loading intensity.

Schmitt, T [7] has investigated this phenomenon, using an experimental model. As a shock wave enters a corner a number of reflections occur of the walls. When the wave reaches the corner, a reversal of flow is induced and once again reflections occur. The last reflected shock wave is seen to undergo refraction. Hence the complex geometry and shock interaction enhances the loading and maximum blast pressure can occur as a result of the incident blast wave.

In Schmitt's experiment the analysis carried out is two-dimensional. Exact analysis for flow fields in re-entrant corners does not exist. Therefore Schmitt makes a number of assumptions to obtain peak vertex pressure and duration. These are listed below:

- The incident wave propagates normal to the wall forming the corner
- The propagation medium is a perfect gas, where specific heats are constant.
- Viscous effects are not included

- The walls are considered to be rigid and semi-infinite (i.e. the incident and reflected waves are considered to be straight and no rarefaction waves exist)

The flow field can then be modelled by combining these assumptions with initial states of temperature and pressure. The resulting flow field is idealised as a series of straight line reflections with the possibility of a final reflected shock.

Slater *et al.* [8] further investigates research into re-entrant corners. Further free field tests were carried out on full sized and scaled structures. These tests have provided a database for the load enhancement effect. Loading estimates on 2D and 3D structural configurations were initially investigated.

For more complex structures a computational fluid mechanics method has been developed [8], which provides a more elaborate analysis for blast loading. This method has been combined with a number of finite element packages and is used in the analysis of more complex blast-structure interaction schemes. Analysis using such packages has confirmed that in the case of a re-entrant corner the shock waves reflect of each wall and combine, thus resulting in enhanced shock loading. These numerical findings have been substantiated with empirical data [8]. Hence, in order to resist blast loadings it is imperative that the joints of the building structure are designed to cope with such compound shock loadings.

The orientation of a building can also help in resisting blast loading [9]. It is reported that the ground profile if raised as shown in Figure 3.1 can reduce impulse and pressures resulting from a blast. The structural forms shown in Figure 3.2 were tested and compared to cubic structure exposed to a frontal explosion. Ground zero was located 15 m from the buildings. At the front corners facing the explosion structure A showed a decrease in impulse of 70%. The triangular structure with a 60-degree apex showed a reduction in impulse of 60%. Wing planned structures with an obtuse angle facing the explosion exhibited greater reductions than did those with acute angles.

Impulse values were found to be lower at the mid-height of the structure in the case of structure's A and C. Generally it was found that the larger the angle facing the explosion the greater the reduction in impulse at the mid-height. In the case of structure's F and G these reductions were seen to be lower. The radius of the structure was noted as the main parameter in the level of impulse experienced by the structure. Structure E showed a more significant reduction and even more so the greater the elevation. Structure B was found to have greater impulse values than the reference structure.

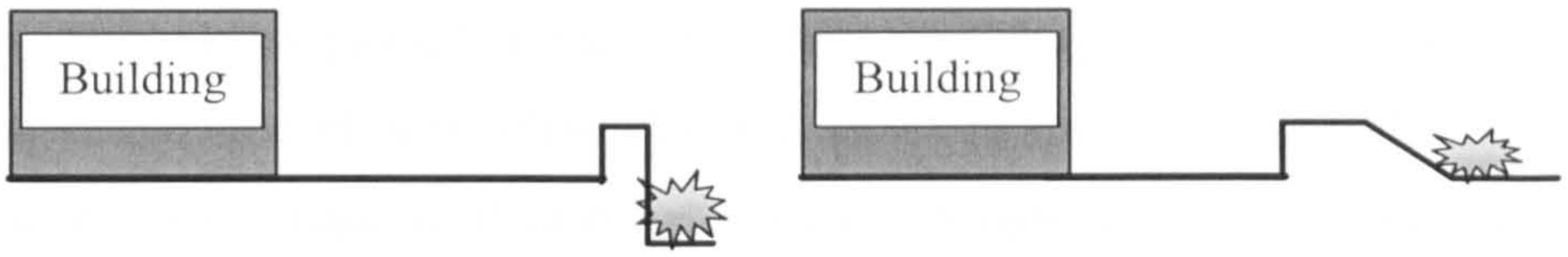

Figure 3.1 Raised ground profiles

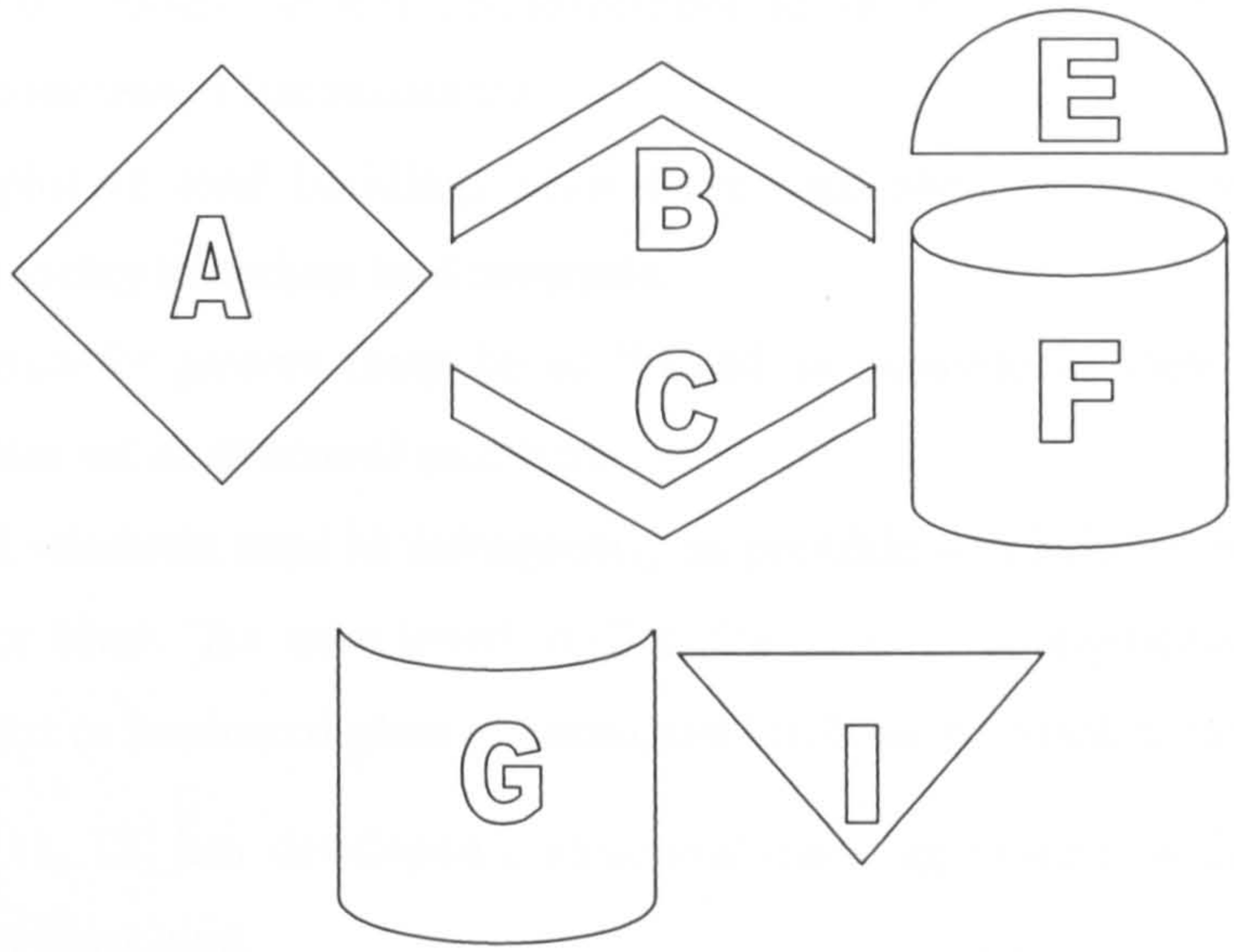

Figure 3.2 Various building geometries

Numerical investigations [9] involving stepped structures (Figure 3.3) produced the conclusion that such structures effectively reduce impulse and so lessen the chance of human injury from flying debris or glass by 'mutual shielding' of the steps (Figure 3.3)

Figure 3.3 Forms for structural protection

The interior structural layout [10] is best kept as simple as possible to avoid flying debris in an explosion situation. Mailrooms should be placed surrounded by buffer zones in order to mitigate any explosion. If this is not possible then they should be strengthened on three sides, leaving the fourth side to vent the explosion outside away from the structure. The position of the mailroom should be such as to cause minimal structural damage. Columns are best designed to span at least two floors. In the case that any floor slab failure occurs the columns are then less likely to fail. Columns can be surrounded with steel or plastic, thus enhancing confinement and shear resistance.

Greater ductility is gained if the floor slabs are designed as a two-way system. Supporting beams on each side of the slab will act as an alternate load path in the event of slab failure. The chances of slab failure can be reduced if top reinforcement is provided giving the slab greater ability to resist upward loading. Seismic detailing for the joints and continuous vertical reinforcement to increase the ultimate moment capacity will also increase blast resistance.

To resist explosive load buildings must have high shear resistance, meticulous detailing and the ability to endure load reversals.

The use of transfer girders must be as limited as possible as they transfer load bearing to a smaller set of structural members.

Smaller sized windows used as infrequently as possible will help to reduce internal loading during a blast. As mentioned earlier the use of strengthened glass such thermally tempered or laminated glass is encouraged in blast resistant design.

Shustov, V [11, 12] has developed a structural cladding system, which delays the application of any blast load.

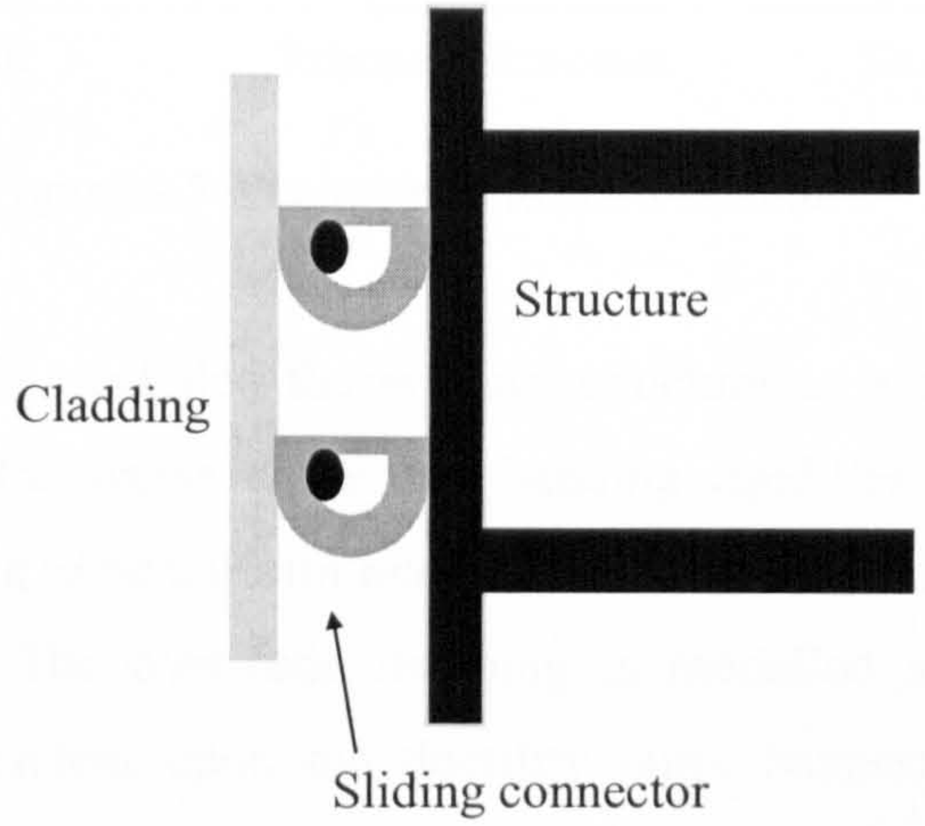

Figure 3.4 Shustov protective system [11, 12]

The kinetic energy of translation is turned into potential energy of elevation by travelling through the groove. This mitigates the blast pressure and load transfer to the surrounding walls.

3.1.4 Damage controlled structures

Today serious thought is given to controlling the damage induced upon a structure by blast loading. Damage controlled structures are those that are designed to absorb energy

such that the damage caused is minimal and can be repaired. Damage control can significantly reduce the cost of repair after any dynamic loading.

Conner, JJ *et al.* [13] investigated the potential of two independent systems in resisting dynamic loads. The primary system (Figure 3.5) carries the vertical loading and provides lateral stiffness. The secondary bracing system functions to absorb the energy.

Initial input parameters in the design are input energy of loading, lateral stiffness of the primary structure and various hysteretical parameters. An example of the latter would be the yield force over the height of the building.

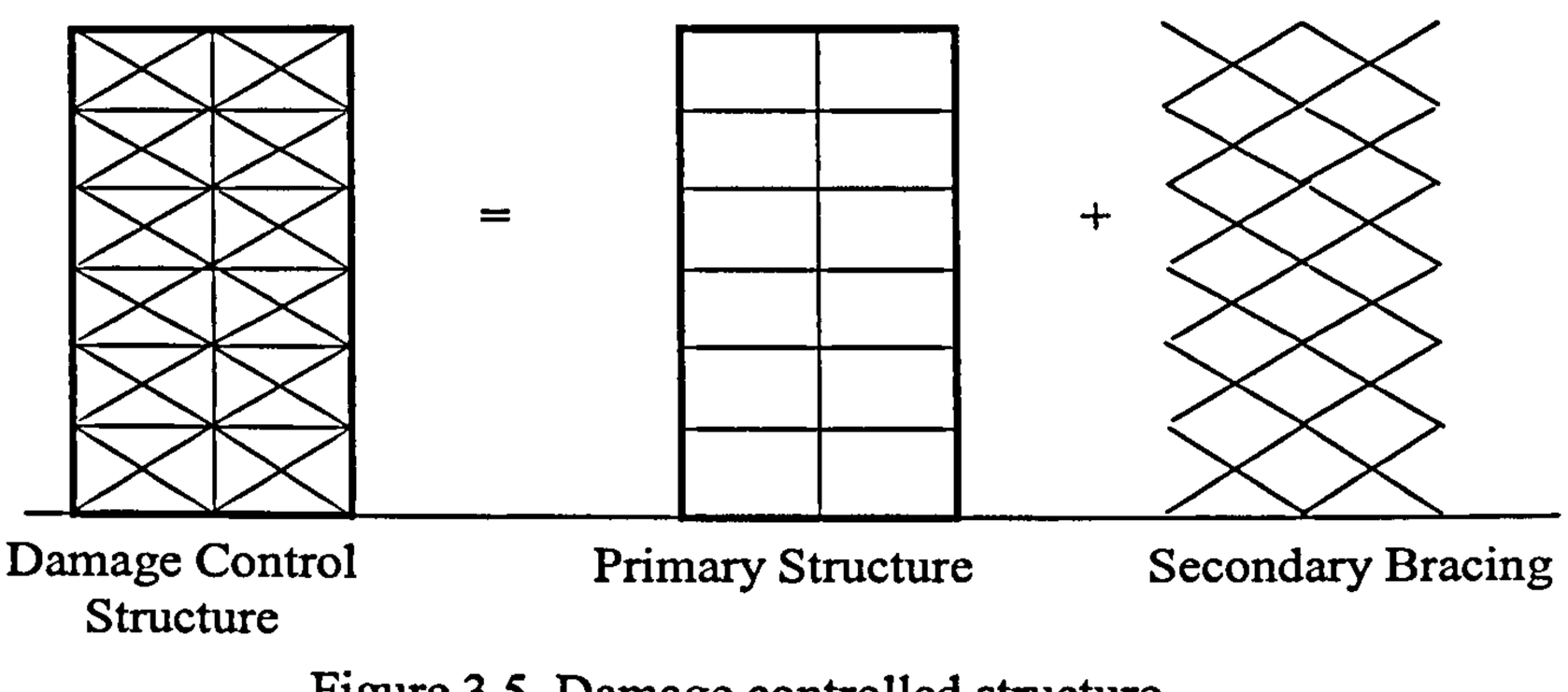

Figure 3.5 Damage controlled structure

Conner, JJ *et al.* [13] modelled the primary structure as a system of beams and columns with variable transverse shear and bending rigidities. The optimal design ensures shear and bending to be uniform over the building height. Damping is simulated using bi-linear springs. The hysteretic damping is modelled as equivalent viscous damping, which is dependent upon the ductility ratio. Numerical simulations with lumped mass models have shown that adjusting stiffness and hysteretic damping can result in the optimal stiffness distribution of a structure being achieved. Hence the response to dynamic loading can be controlled.

3.1.5 Beam column connections

The response of a full scale structure has been investigated by the USAF [14].The structure used was a full scale arched roof structure of 9.15 m high and 36.59 m long. Light reinforcement was used and the arch thickness varied from 0.46 to 0.81 m.The interior was covered with a steel plate so as to restrict flying concrete fragments on the interior and give better protection.

Results showed peak overpressure varied from 0.004 to 22 MPa. Concrete penetration was found to be 0.15 to 0.2 m and the structural acceleration was recorded at 15.9 m/s. Strong rigid connections were found to transfer very high accelerations to the structure ad therefore the use of more flexible connections were recommended in structures needing to resist blast loading.

During dynamic loading beam column connections can become crucial in resisting collapse. The ductility of these joints can result in a more ductile response of the structure capable of resisting load reversals without major collapse.

Such joints were investigated by Ha, GJ *et al.* [15]. Their experimental programme investigated various reinforcement configurations. The plastic hinge at the column - beam interface was moved a distance of 1.5h along the beam by the addition of one extra longitudinal bar as shown in Figure 3.6.

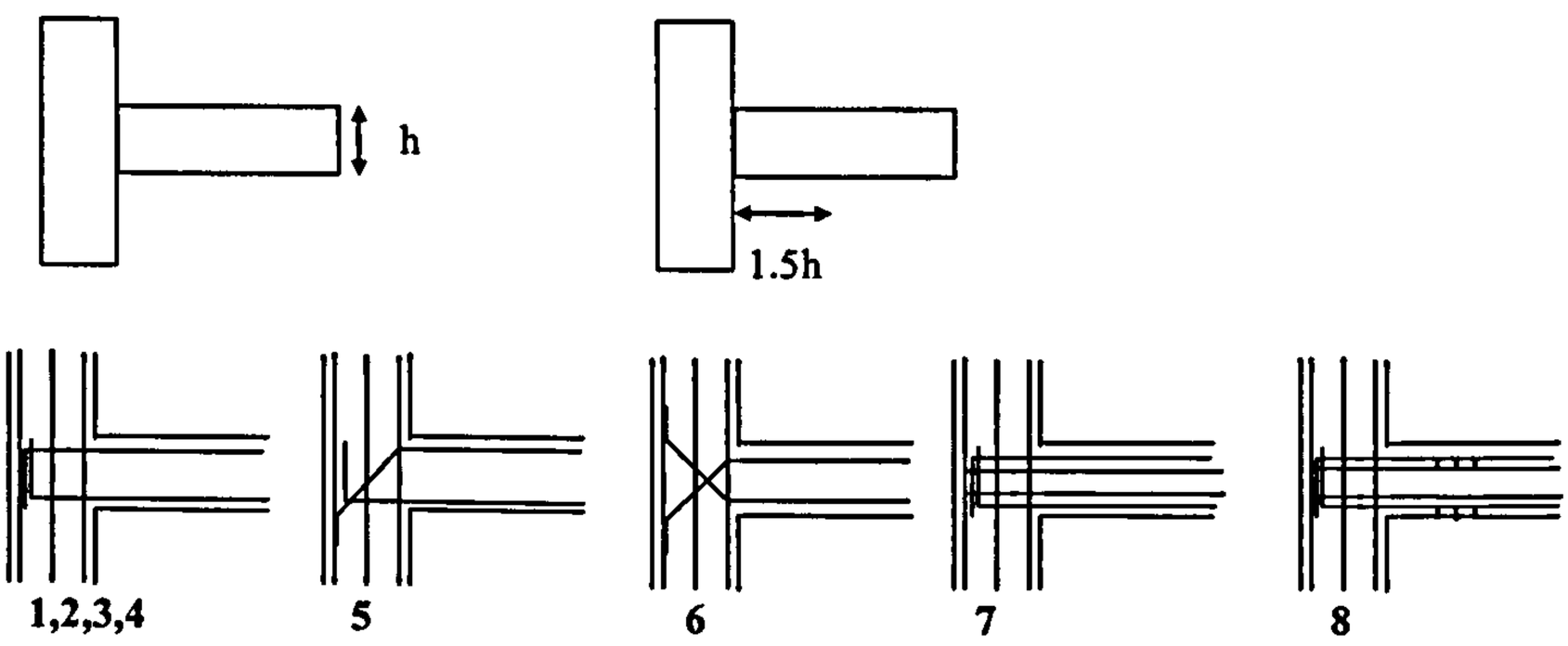

Figure 3.6 Beam joint specimens [15]

Specimens 2 and 8 showed satisfactory hysteric behaviour. Specimen 4 was satisfactory for a displacement ductility of 7 or under, whilst above this a degree of brittleness was exhibited. Specimen 5 showed a similar effect but at lower ductilities. Specimen 7 was stable. Failure patterns were similar to those shown in Figure 3.7.

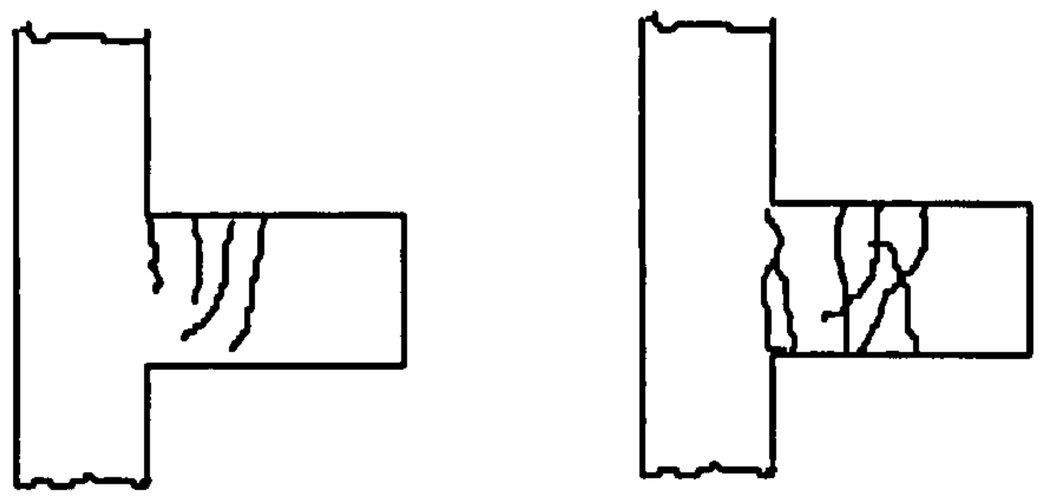

Figure 3.7 Resulting crack patterns

Specimens 2 and 4 failed with crack patterns far from the interface. Specimens 5 and 6 showed diagonal cracking at the interface with failure at displacement ductilities above 3. Specimens 7 and 8 were the only specimens to hinge at the interface.

Specimens 2, 4 and 7 maintained their yield strengths at displacement ductilities of 7 and above. Specimens 5 and 6 showed a sharp loss in yield strength on reaching the displacement ductility of 8 and 5 respectively. Both these specimens exhibited bar slippage, reduced ductility and reduced energy absorption and thus were unsatisfactory in performance.

Specimens 2, 5, 6 and 7 exhibited an increase in energy absorption. Specimen 7 and 8 (with closed stirrups) were deemed satisfactory in comparison with the conventionally reinforced specimen 4.

The net conclusion of the investigation was that a diagonal anchorage with the plastic hinge moved further along the beam would perform better under blast loading.

Beam column mechanisms were also investigated by Scott, RH [16]. Here the investigation centred upon fifteen monotonically loaded specimens, each with a beam connected to the midheight of the column. The beams were 850 mm long and 110 mm long. The columns measured 150 mm^2 in cross section with a height of 1700 mm. Beam depths were varied at either 210 mm or 300 mm and the columns were reinforced with four bars and ties. The tension reinforcement of the beam was either U-shaped, bent up or bent down in the column.

Seismic specimens had the U-shaped tension bar and extra ties to counter the effect of load reversals. Strains were measured using strain gauges in the reinforcement connected to a computer data logging system. The loading was applied through manually pumped hydraulic jacks.

The specimens were found to fail either by joint cracking or plastic hinge formation in the beam. Bars bent down in the top of the beam showed tension progressing down the vertical leg of the bar, occurring between cracking and failure. This sort of behaviour was not exhibited by the bent up bars, which showed a sudden increase in the strain at the end of the test. U-shaped bars behaved similarly to the specimens of the bent down bars.

Where the reinforcement was in the bottom of the beam, initial loadings on the column showed minor tensile strains over the column width. Loading of the beam resulted in compression along then full length of the beam. A prop was applied at the end of the beam to control beam sway. The data logger also recorded the load carried by the prop as well as the applied loads and column shear forces.

The reinforcing bars in the column under high loads were in compression. However some tension did occur under high load. Flexural cracks above and below the connection zone were observed.

With higher load and 1% tension reinforcement the bent down and U-shaped bars failed by plastic hinge formation. Lower loading resulted in failure by joint cracking. These particular specimens were found to be at or near their theoretical moment of resistance at the time of failure.

All monotonically loaded beams transferred the load by bond stresses. Bent down and U-shaped bars were found to develop bond stresses along their length after cracking in order to make up for the loss of bond within the connection zone. Bond stresses reduced outside the connection zone at each cycle of loading. This is because the required loading needed to achieve a given ductility factor is reduced. The monotonic tests showed the U-shaped bar to transfer the loading more effectively through higher bond stresses and smoother development of bond stresses, firstly in the vertical leg and then progressing into the bottom bend and finally into the horizontal leg.

In the seismic tests, reinforcing bars were physically interlocking and together with the ties kept the connection zone functioning. This behaviour resulted in limiting damage to the specimen.

Bent down bars proved to provide the highest ductility of the three tested configurations.

3.2 Strain rates

The rate of strain over a period of time, under impact is known as the strain rate. It is a very significant parameter in dynamic situations, such as blast loading. With large instantaneous loading, such as those from explosions, the material may exhibit an increase in resistance capacity compared with static loading. This occurrence is commonly referred to as the strain rate effect.

Mathematically strain rate is expressed in equation (3.1).

$$\dot{\varepsilon} = \frac{d\varepsilon}{dt} \tag{3.1}$$

where ε is strain and t is time.

The unit of strain rate is s^{-1}. For blast loading the strain rate is usually of the order of 10^3 s^{-1}. The strain rate effect was investigated by Fang,Q *et al.* [17]. They developed a rate sensitive material model based on the theory by Malvern and Perzyna. The response of an elasto/viscoplastic material is made of an elastic part and a time dependent viscoplastic part, which is related to overstress. The models for steel and concrete are shown in Figure 3.8. A uniform steady state overstress is assumed for the concrete model over the strain softening range.

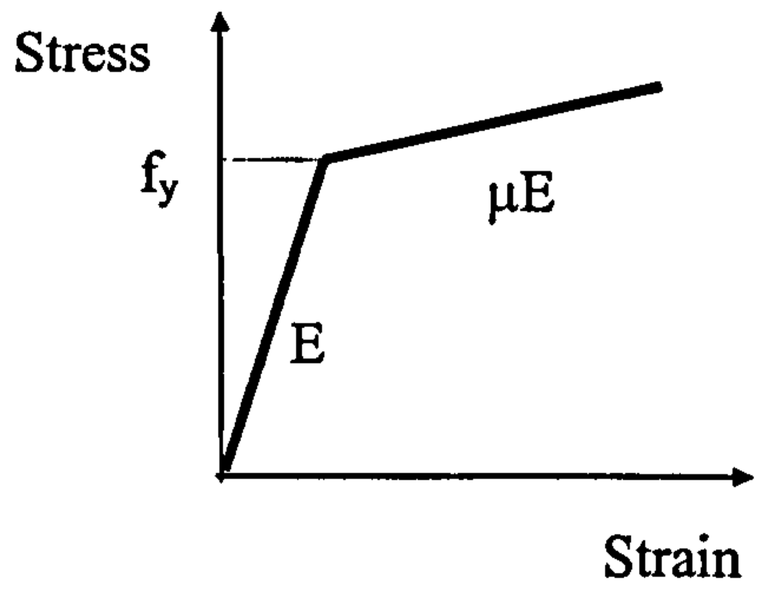

STEEL BI-LINEAR MODEL

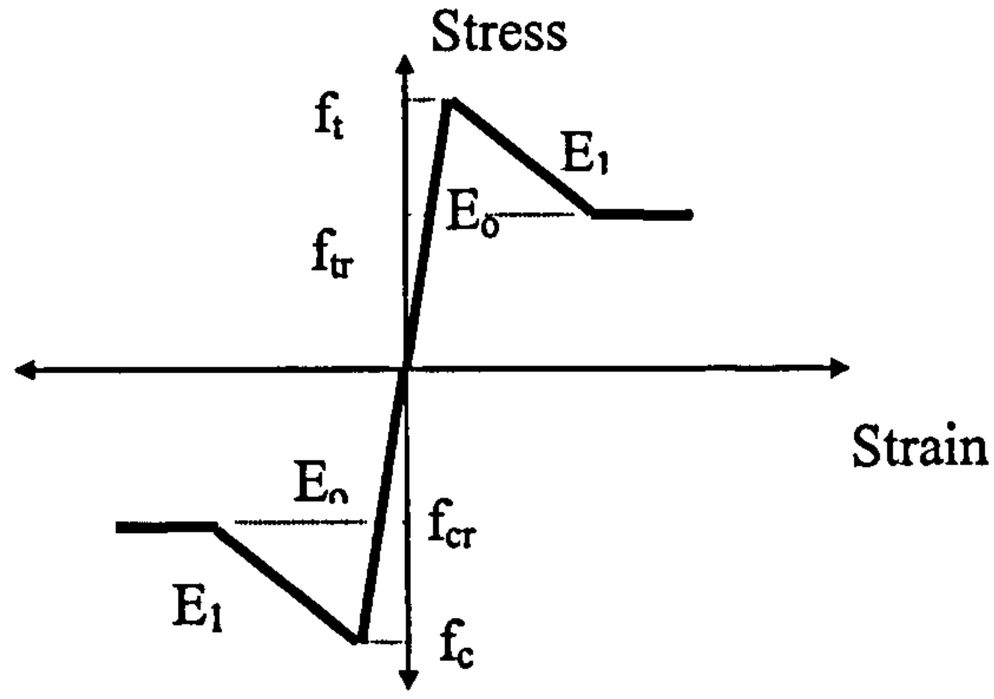

CONCRETE

Figure 3.8 Rate sensitive steel model and static concrete model [17]

The layered Timoshenko beam theory is employed. Both triangular and ramp loads are applied for four different situations. Results for rate sensitive and rate insensitive loading show a marked difference in displacement. The strain rate effect of increasing the strength has resulted in lower displacements for rate dependent loading. In conclusion the report recommends that this should be taken into account to avoid over conservative design.

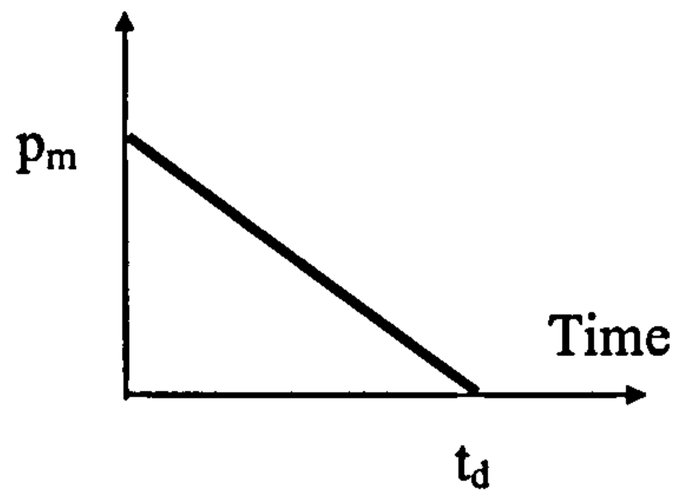

Triangle Load

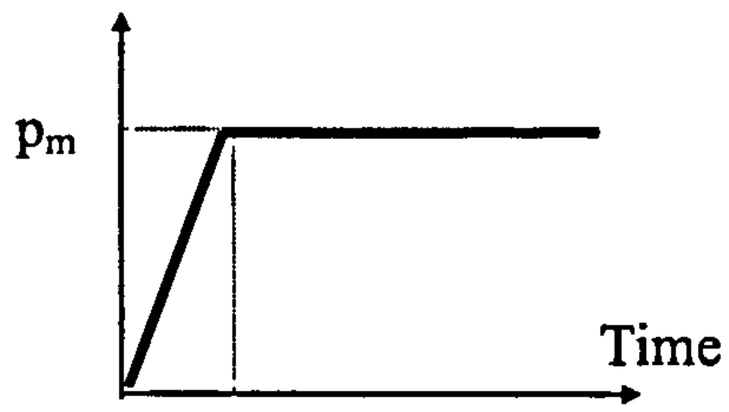

Ramp Load

Figure 3.9 Rate sensitive loading

Fang *et al.* further applied their theoretical models to various examples including a four storey reinforced concrete frame. Again rate sensitive displacements were found to be considerably less than rate insensitive displacements. They also found that in applying a tri-linear steel model a considerably larger response was observed as compared with the bi-linear model. Hence this model was recommended over the bi-linear version in measuring dynamic structural response under blast loading.

The strain rate under explosive situations lies between 10^2 and 10^5 s^{-1}.

3.3 Ductility of concrete

3.3.1 Concept of ductility

Ductility is defined as a measure of a plastic hinge's ability to sustain cyclic inelastic loading without experiencing much strength loss, i.e. it is the ability to undergo deformations without any significant strength loss. It is this property, which governs to what extent a structure has the ability to withstand blast loading. Mathematically ductility is defined by curvature ductility μ_o defined by equation (3.2).

$$\mu_o = \frac{\phi_u}{\phi_y} \tag{3.2}$$

where ϕ_u is the ultimate curvature and ϕ_y is the curvature when the tension reinforcement reaches yield.

Curvature at first yield occurs when the longitudinal tension reinforcement reaches yield strain, f_y/E_s. The curvature at ultimate strain is given by the ratio of limiting strain to neutral axis depth, ε_{cu}/c.

3.3.2 A review of recent research upon ductility of beams

The ductility of double reinforced concrete beams was investigated by Park, R *et al.* [18]. Assuming a linear strain distribution (Figure 3.10) and also that plane sections remain plane after bending, they developed a method to calculate the ductility of a beam.

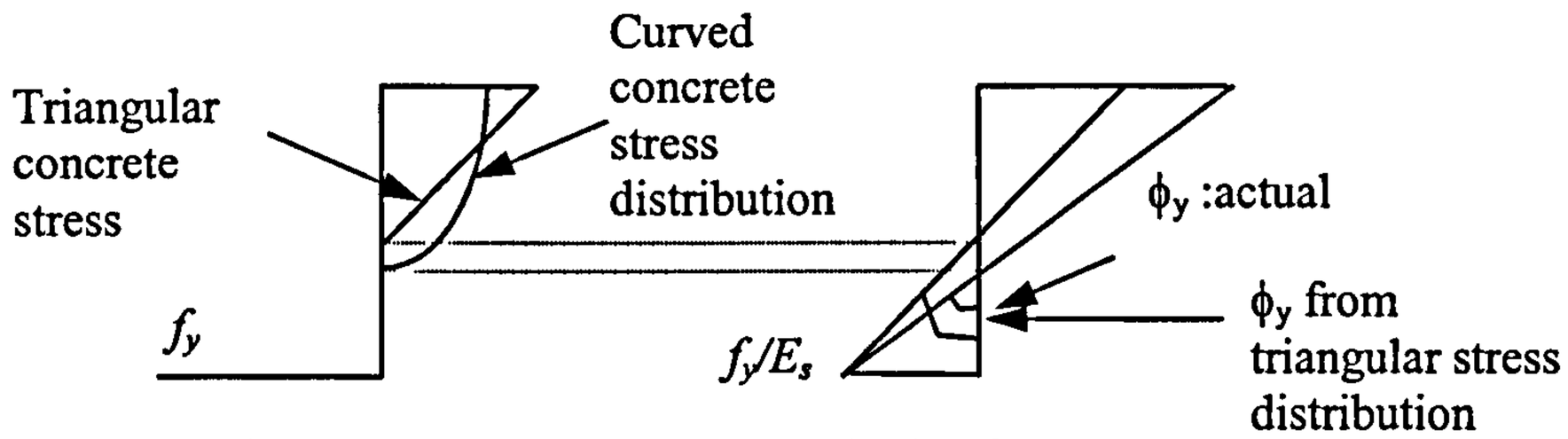

Figure 3.10 Park et al. strain distribution

It can be seen that assuming the linear stress distribution underestimates ϕ_y and thus overestimates the curvature ductility factor. The researchers cater this for by using a first approximation in their calculation of the ductility factor.

Accuracy in the estimate of the ductility of a structural member depends on the constitutive model for both steel and concrete used in the analysis. Park *et al.* assumed the following stress strain relationship for concrete (Figure 3.11).

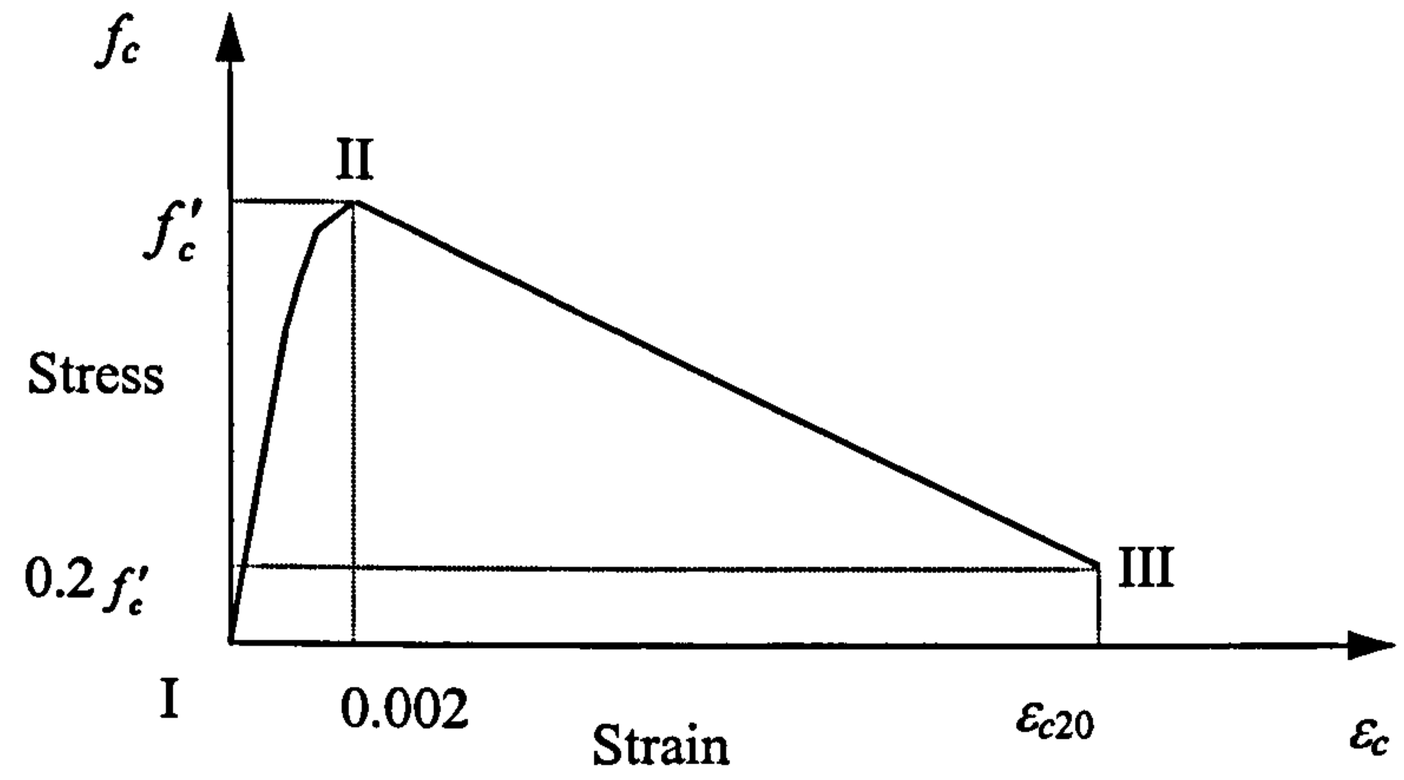

Figure 3.11 Park & Ruitong concrete model [18]

Region I-II is represented by equation (3.3).

$$f_c = f'_c\left[\frac{2\varepsilon_c}{0.002} - \left(\frac{\varepsilon_c}{0.002}\right)^2\right] \tag{3.3}$$

Region II-III is represented by equation (3.4).

$$f_c = f'_c\left[1 - z(\varepsilon_c - 0.002)\right] \tag{3.4}$$

The concrete compressive force, C_c was calculated incorporating the mean stress factor α_{ms} :

$$C_c = \alpha_{ms} f'_c bkd \tag{3.5}$$

k is the neutral axis depth factor, which is calculated using the strain distribution diagram. The equation for curvature at first yield and ultimate curvature are similarly obtained

$$\phi_y = \frac{f_y / E_s}{d(1-k)} \tag{3.6}$$

$$\phi_u = \frac{\varepsilon_{cu}}{c} \tag{3.7}$$

where, f_c = stress in concrete, f_c' = concrete compressive cylinder strength, α = depth of compressive stress block of concrete, b = width of beam section, c = distance from extreme fibre to neutral axis at ultimate curvature, kd = distance from extreme fibre to neutral axis when tension reinforcement first yields, z = a function of f_c', ε_c = compression strain in concrete, E_s = Young's modulus of elasticity for steel, and ε_{cu} = distance from extreme fibre to neutral axis at ultimate curvature of unconfined concrete.

The equations then derived were used to plot ϕ_u/ρ against tension steel ratio ρ for various ratios of compression to tension reinforcement, steel yield stresses and concrete cylinder strength. The resulting graphs show that if ρ' is increased or ρ decreased the curvature ductility increased. Also it was noted that the curvature ductility decreased if the steel yield stress was reduced or the concrete strength was increased.

Al-Hadad, MS [19] investigated the curvature ductility of beams, subjected to low and high strain rates, using the Hognestad model [20] for concrete (Figure 3.12) and the Wang *et al.* [21] model for steel.

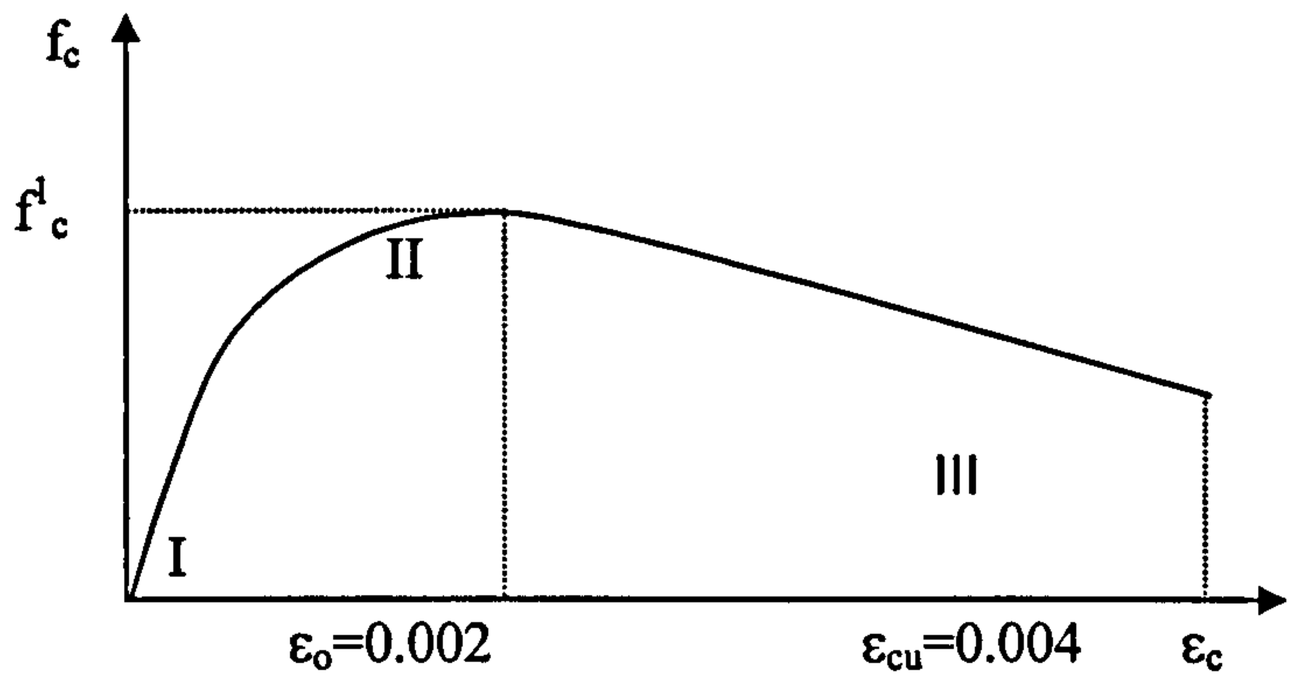

Figure 3.12 Hognestad concrete model [20]

Line I-II is represented by equation

$$f_{cs} = f_{cu}'[2\varepsilon_c / 0.002 - (\varepsilon_c / 0.002)^2] \tag{3.8}$$

Line II-III is represented by equation

$$f_{cs} = f_{cu}'[1 - Z(\varepsilon_c - 0.002)] \tag{3.9}$$

The steel is modelled over the three ranges using equations (3.10) to (3.12).

$$f_s = E_s\varepsilon_s \qquad 0 < \varepsilon_s \le \varepsilon_y \tag{3.10}$$

$$f_s = f_y \qquad \varepsilon_y < \varepsilon_s \le \varepsilon \tag{3.11}$$

$$f_s = Y(f_{su} - f_y) + f_y \qquad \varepsilon_s > \varepsilon_{sh} \tag{3.12}$$

Strain rates are modelled using the Soroushian and Obeseki formulae [22].

$$f'_y = 3.1 + 1.2f_y + (0.65 + 0.005f_y)\log\dot{\varepsilon} \ge f_y \tag{3.13}$$

$$f_u' = -20 + 2.5f_y + (-2.4 + 0.12f_y)\log\dot{\varepsilon} \tag{3.14}$$

where Z is the slope of part III of Figure 3.12, f_{cs} = concrete compressive stress, f'_{cu} = ultimate concrete compressive strength, f_s , ε_s = generic value of steel stress and strain, f_y = actual yield stress of steel, f'_y = yield strength of steel under specified strain rate, f'_u = ultimate strength of steel under specified strain rate, $\dot{\varepsilon}$ = strain rate (second^{-1}) and ε_{conc} = concrete strain

The reinforced concrete section is modelled using a number of steel and concrete layers (Figure 3.13).

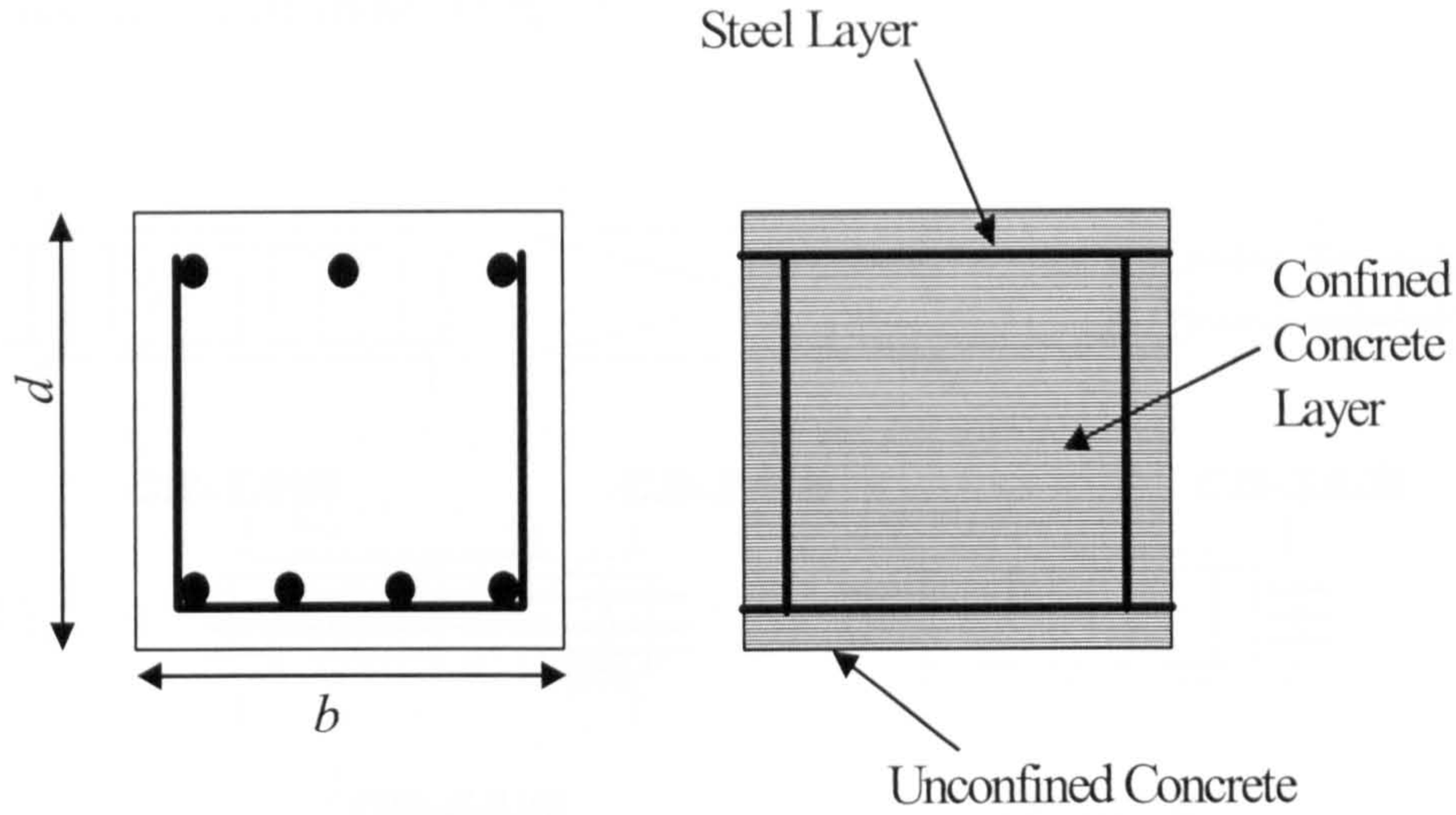

Figure 3.13 Al-Hadad RC beam layer modelling

Resulting graphs from the analysis of ductility ratio, μ_ϕ versus ρ for various steel yield strengths and strain rates revealed that u_f will increase with a decrease in the tension reinforcement. Also it was observed that μ_ϕ increases with an increase in the compression reinforcement only when $\rho > 0.005$. An increase in yield stress showed ductility to decrease. A slight increase in ductility was found to occur if the ratio of compression to tension reinforcement was increased. At a strain rate of 0.05/s (e.g. earthquake loading) a ductility reduction of 12% was observed.

3.3.3 Effect of reinforcement detailing upon the ductility of concrete beams

Moretti, M *et al.* [23] investigated into the hysteretic response of beams with various reinforcement detailing. The research mainly concerned coupling beams for shear walls. Such beams are classified according to their shear ratios. The shear ratio, α_s, is defined as: -

$$\alpha_s = \frac{M_{\max}}{Q_s h} \tag{3.15}$$

where M_{max} is the maximum Moment, Q_s is the Shear Force and H is the height of the beam.

The various layouts are shown in figure 3.14: -

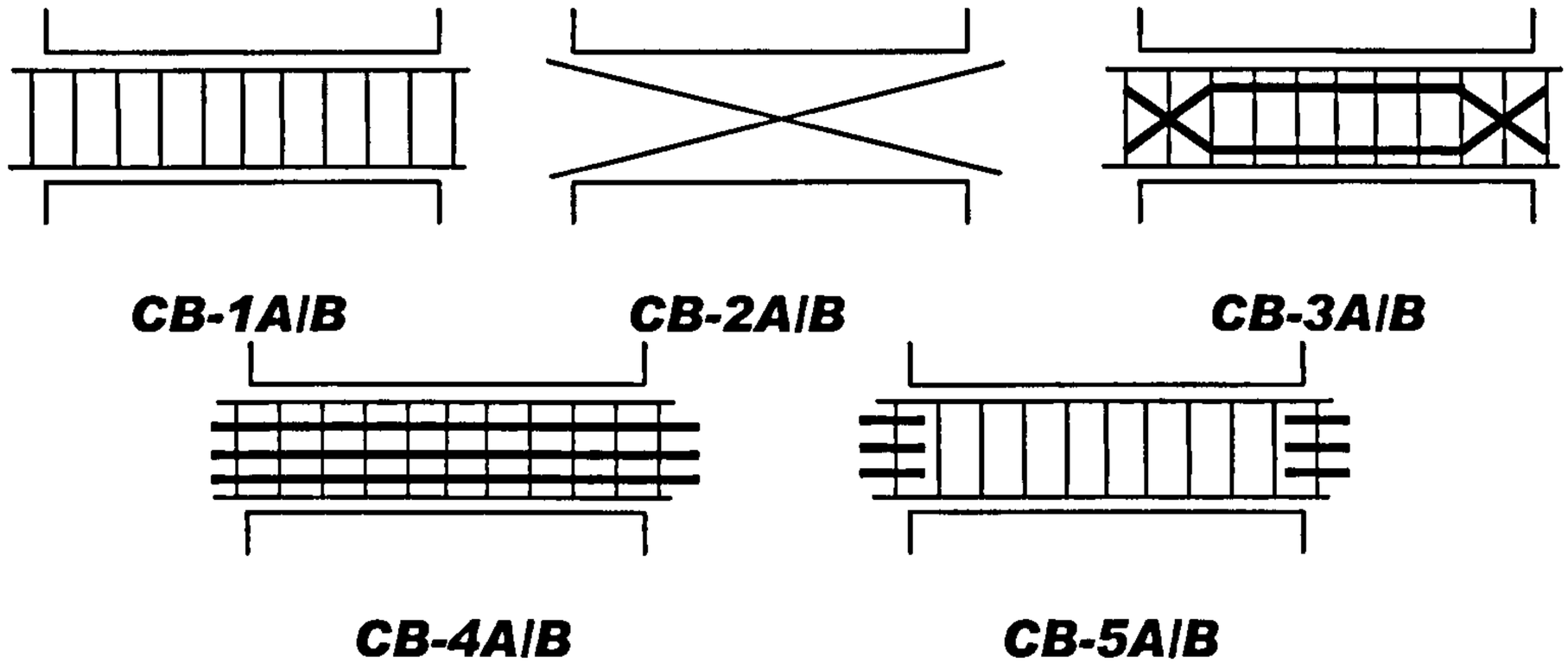

Figure 3.14 Moretti, M *et al.* concrete specimens [23]

The specimens were subjected to cyclic shear displacements with one end fixed and the other free, in order to simulate a double fixed beam coupling two walls under seismic loading. Two shear ratios of 0.5 and 0.83 were investigated. Each beam exhibited different failure patterns. These are described in the following Table 3.1:-

Table 3.1 Description of beam failure

Beam	Failure
CB-1A(as=0.5)	Failure occurred along the main diagonals in tension
CB-1B(as=0.83)	Failure occurred in shear compression at the end regions , indicating bond failure
CB-2	Failure due to buckling of reinforcements at the ends of the beams. The failure was not brittle
CB-3	Cracks occurred along the local diagonal bars. Bond failure with the main reinforcement and compression failure at the ends of the beams were also noted
CB-4	Failure occurred in the central region in shear compression
CB-5	Failure occurred in the end region also due to shear compression

Specimens CB-1/2/3-A/B with α_s=0.5 cracked along the main diagonal whereas those with α_s=0.83 exhibited cracking near the ends.

Moretti *et al.* observed that prior to the occurrence of diagonal cracking the strains along the main reinforcement agreed with theoretical predictions using flexural theory. After, however, they suggest Paulay offers a better estimate of the actual strain distribution.

The stirrups yielded mostly in all beams at cycle 4 but in CB3, CB4 and CB5 yielding did not occur at all. The authors suggest this to be due to the dowels and bent up bars transferring the shear force from the end blocks of the beam.

Beams of shear ratio 0.5 exhibited large strains in the stirrups near mid-span and those with shear ratio 0.85 showed no major strains at the centre line. Shear is found to be carried in the diagonal struts for beams with the lower shear ratio, whereas beams with the higher shear ratio the broader truss carried the shear. Beams CB-1B and CB-3B showed a shear response equal to the shear capacity of the stirrups while CB-4B and CB-5B showed no shear response. Similar results were obtained for the beams with lower shear ratio.

The authors attempted to quantify ductility in a number of ways. Firstly they calculated the displacement ductility factor μ_d as shown in Figure 3.15.

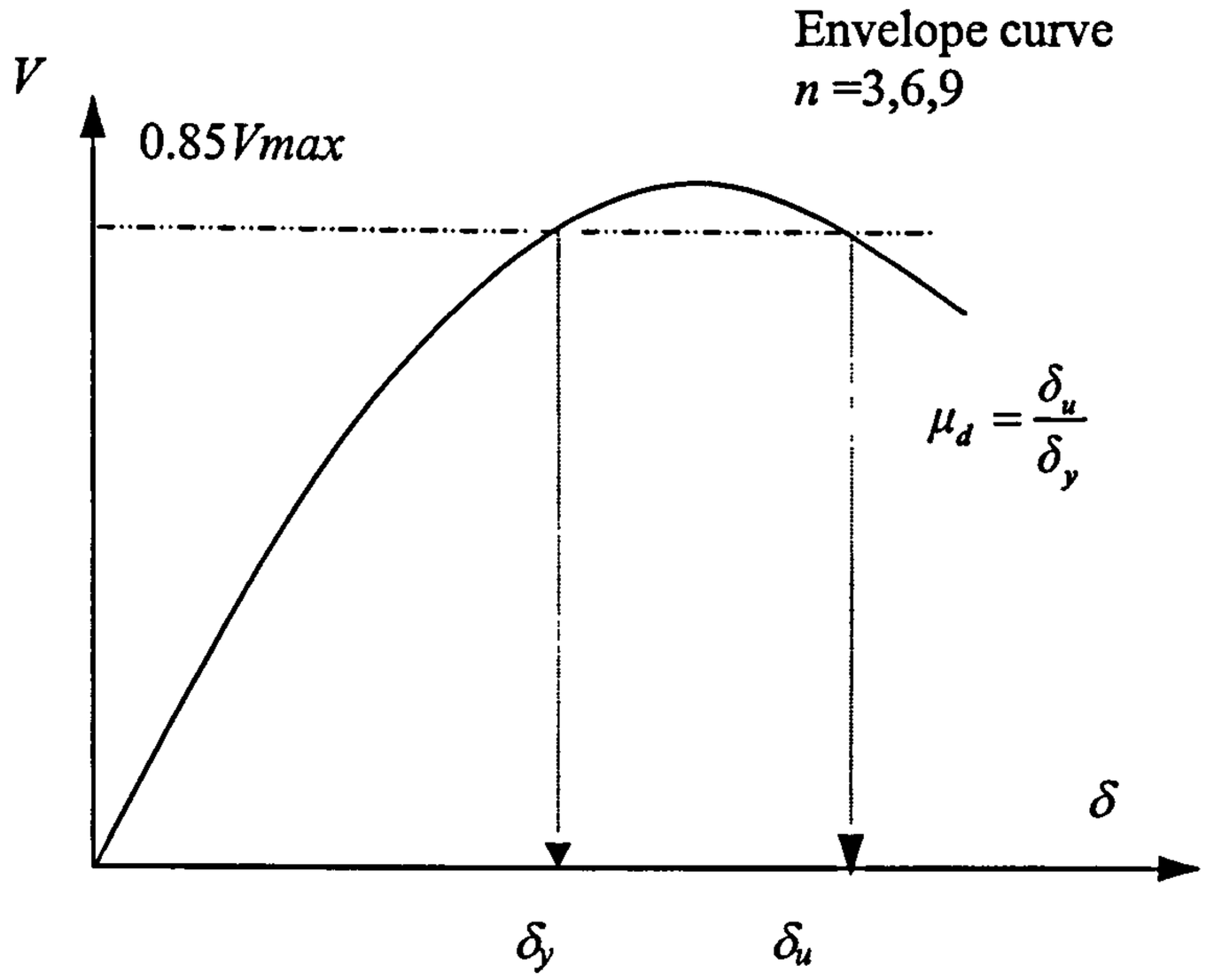

Figure 3.15 Ductility factor by Moretti *et al.* [23]

where n = number of cycles , δ = imposed displacement, δ_u= ultimate displacement of specimen, δ_y = displacement leading to yield of main reinforcement, μ_d = displacement ductility factor

μ_d was calculated at every third cycle. The authors considered the results of this not to be representative of their experimental work. Therefore use of a ductility factor in terms of stored energy was made, μ_E. The stored energy is the energy under the envelope curves while the dissipated energy is the area under the hysteretic loops (Figure 3.16).

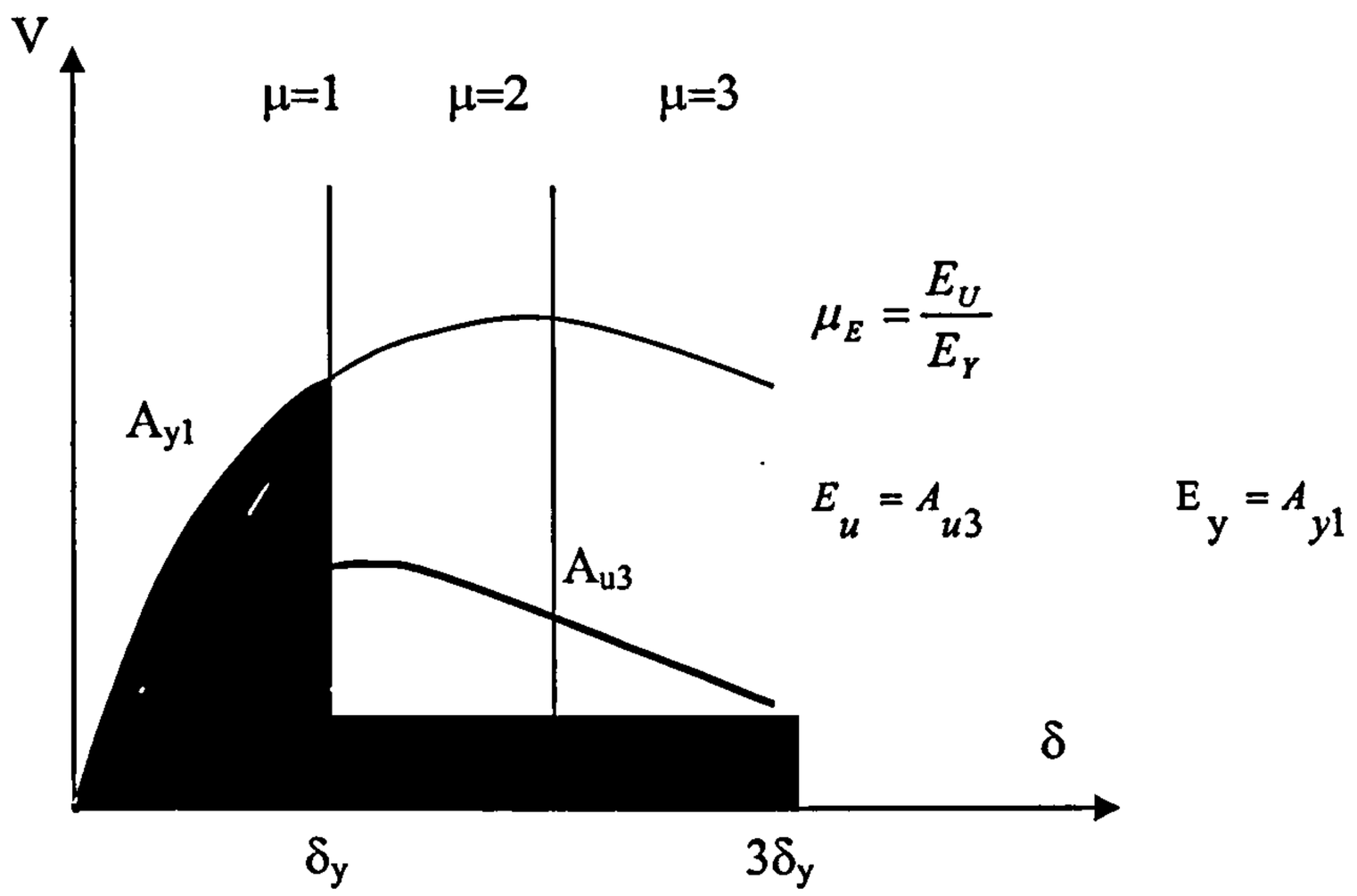

Figure 3.16 Moretti *et al.* parameter μ_E [23]

where μ_E = ductility factor in terms of stored energy μ = level of imposed displacement ductility δ/δ_y and A = area at yield/ultimate

According to the authors results here have better estimated the resistance degradation and plastic deformation of the specimens. A cyclic ductility factor was also calculated but was found to yield unrepresentative results when differing shear ratios are considered. Ductility was also quantified using "normalised shear response" and "normalised dissipated energy". These yielded accurate results.

The authors concluded that beams with conventional reinforcement to be too brittle as compared with those of bi-diagonal reinforcement. An interesting feature was the increase in ultimate capacity of beam CB-3 over the conventional of the order of 30%. Generally specimens with larger shear ratios showed less ductility. The authors suggest that to best represent ductility more than one method should be used.

Dilger, WH *et al.* [24] subjected beams of similar geometry and square cross section to strains rates ranging from 3e-05 m/m/s to 0.2 m/m/s. Their investigation considered plain beams and beams with differing transverse reinforcement. Longitudinal reinforcement was not considered.

Resulting stress strain curves were presented. As expected plain concrete prisms under the highest strain rate failed explosively. Under the lower strain rates they disintegrated slowly. The stress strain curves for the reinforced concrete showed a flat stress strain curve for the descending branch and gave no explosive failure.

The authors conclude that plain and confined concrete is similarly affected by strain rates in terms of their effect on strength. Also after peak stress in plain concrete the stress decreased rapidly. The stress-strain diagram for the concrete did not seem to be affected by the strain rate.

3.3.4 Ductility of high strength concrete

Sometimes it is possible that High strength concrete (HSC) will be used, where for aesthetic reasons more slender structural members are required.

Ashour, SA *et al.* [25] have investigated the effect on HSC ductility of compression and fibre reinforcement. Their experiments involved twelve geometrically similar beams subjected to two point loading. Some were loaded instantaneously using a hydraulic jack and the others were loaded over a period of 180 days, using iron blocks. The tension reinforcement was kept the same for all the beams, however the compression reinforcement and steel fibre content were varied for all of them.

Results indicated no significant effect on concrete compressive strength for beams with equal fibre content. Beams loaded to failure with a fibre content of at least 0.75% showed an increase in their ultimate and also their yield moments. Increasing the fibres for beams under long-term loading resulted in a decrease in the ratio of time dependent deflection to immediate deflection.

For beams with equal fibre content, compressive reinforcement was found not to appreciably affect beam deflection. They suggested the following equations for the theoretical calculation of deflection: -

$$E_c = 3200\sqrt{f_c'} + 6900 \qquad (MPa) \tag{3.16}$$

$$I_e = \left(\frac{M_{cr}}{M_a}\right)^3 I_u + \left[1 - \left(\frac{M_{cr}}{M_a}\right)^3\right] I_c \tag{3.17}$$

The increase in the second moment of inertia, due to the fibres is included using the formula

$$I_f = \sum_{n=1}^{N} m A_f d_i^{\,2} \tag{3.18}$$

where E_c = modulus of elasticity of concrete, f_c' = 28 day compressive strength of concrete, I_c = moment of inertia of cracked transformed section, I_e = effective moment

of inertia, I_f = moment of inertia by fibres, I_g = moment of inertia of gross concrete section ignoring the reinforcement, M_{cr} = cracking moment, M_a = maximum bending moment in the span, A_f = cross sectional area of one steel fibre, d = effective depth, n_f = no of effective fibres per unit area and V_f = volume fibres expressed as percentage of concrete volume

Fibres mainly improve tensile strength but have no effect on compressive behaviour. However they are known to increase the area under the stress-strain curve for HSC i.e. increase the ductility. Long term deflection is analysed using the approach by Ashour [25] where modifying parameters are introduced into the ACI code formula's for the deflection factor λ. The parameters are further modified to cater for the differences in concrete strength's between Paulson and Ashour *et al.* [25].

Comparisons between the theoretical and experimental results show deflections estimated using the second moment of inertia slightly underestimated the long and short-term deflection. Results were slightly improved by using the experimental cracking moment instead of the theoretical cracking moment. Among the conclusions reached in this investigation is that fibre content reduces the possibility of sudden failure during compression and that singly reinforced beams showed reduced deflection.

Xie, H *et al.* [26] performed an experimental investigation into the post peak behaviour and shear ductility of HSC and normal concrete beams. Shear ductility is the quantitative representation of ductility and has two definitions. Firstly (μ_1) it is the ratio of area in the descending portion of the load displacement curve up to $0.75P_{max}$ to the area up to P_{max} (Figure 3.17). The second definition (μ_2) is the ratio of the area up to $3\Delta_o$ to the area up to Δ_o.

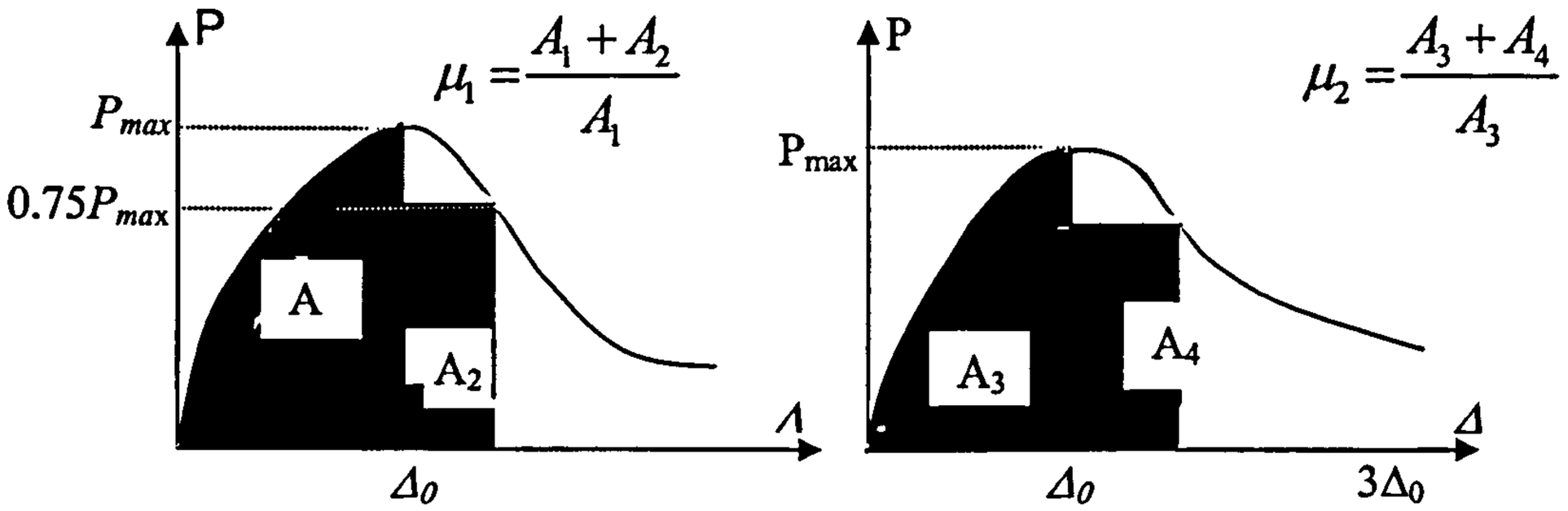

Figure 3.17 Definition of ductility ratio μ_1 and μ_2 [26]

The experiment used a purpose built energy absorbing rig and hydraulic jacks for loading fifteen shear critical beams.

Results showed that as the ratio of shear span to effective depth (a/d_e) increased the ultimate load capacity for both normal and HSC beams. Increasing the shear reinforcement decreased the slope of the post peak behaviour curve but at the same time improved load capacity.

Increasing concrete strength did not produce significant change in the shear ductility index where the *a/d* ratio was 2 or above. Where it equalled 1 significant change was observed. HSC beams exhibited near plastic post peak behaviour when twice the minimum shear reinforcement (as recommended by ACI318-89) was provided. μ_2 was lower for beams with a/d_e=2 than for a/d_e=1 or 3.

When shear reinforcement was increased beams with a/d_e=1 or 3 showed little response. With a/d_e=2 significant increase in the shear ductility index occurred. A further increase with a/d_e=3 did show substantial increase in the shear ductility. Further increases had no effect. Therefore beams with a/d_e=3 proved to have significant energy absorption ability.

3.4 Confinement of concrete

Confinement of concrete can help to increase resistance to blast and impact loading. The following gives details of recent research into confinement of concrete.

3.4.1 Internal confinement

Column confinement using stirrups can produce planes of weakness between the concrete core and the concrete cover. Alsayed, SH [27] has suggested that use of steel fibres may result in the provision of better strength enhancement and ductility.

Alsayed investigated fourteen specimens. He varied the aspect ratio of the steel and volume fraction of the fibre. The resulting load curves showed significant strength and ductility increases for simple reinforcement layout with a large fibre quantity. Larger diameter bars were more efficient than thinner bars of the same length. The addition of silicon fibre to concrete did increase the strength, ductility and confining pressure. The load carrying contribution is dependent on the volume fraction and aspect ratio. The behaviour of fibrous and non-fibrous concrete was found to be similar until about 60-80% of ultimate load.

Ahmad, SH [28] have compared the various models for confined concrete. Table 3.2 show comparisons of some models for confined concrete.

Table 3.2 Various models for confined concrete

	Ivenger et al.	*Fafihs & Shah*	*Ahmad& Shah Simple*	*Ahmad & Shah detail*	*Martinez et al.*
volumetric ratio of confined concrete core	*	*	*		
plain concrete strength	*	*	*		*
concrete strain					*
yield strength of spiral steel	*	*	*		
dilation characteristics of plain concrete					
ratio spacing and diameter of lateral steel				*	*
plain concrete stress strain curve				*	

The investigations by Martinez predicted peak stress very well. Ahmad and Shah overestimated the peak strength and strain as did Fafhis and Shah.

Stress strain curves, however were not predicted very well by any of the models particularly post peak behaviour, Ahmad and Shah's results were found to most closely mirror the results of this investigation.

Once inclined cracking (Figure 3.18) has occurred as a result of the action of the lugs against the concrete, stresses are transferred by inclined compression thus creating an internal pressure inside the concrete causing failure by concrete splitting.

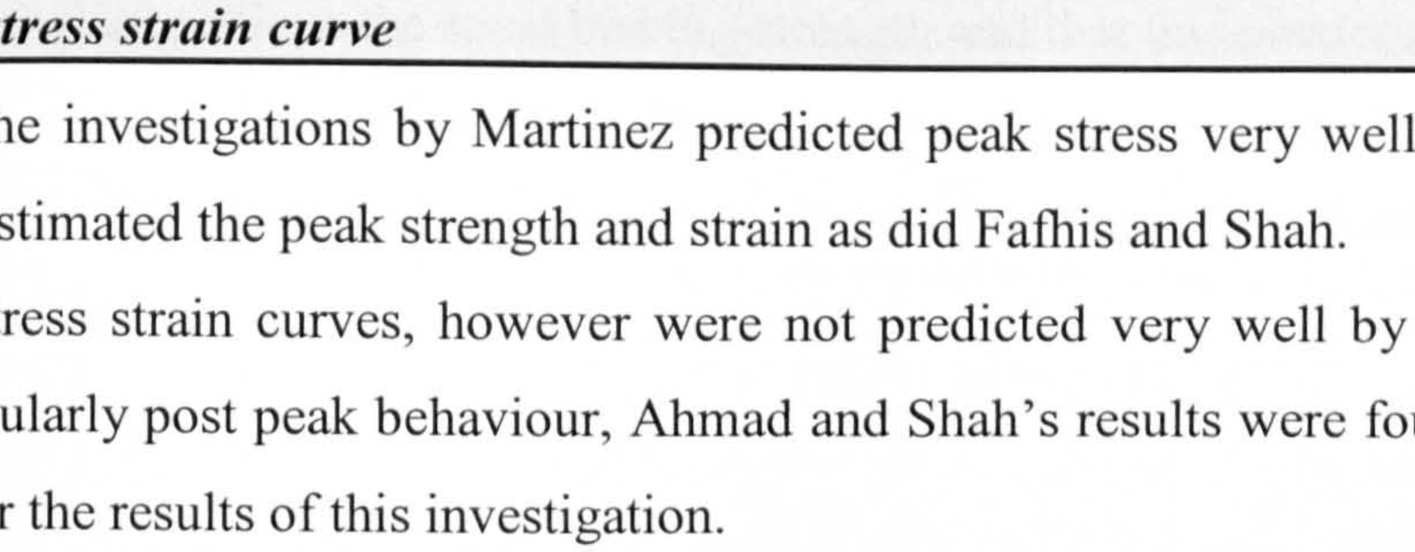

Figure 3.18 Inclined Cracking at Bond Surface

Aslani S *et al.* [29] suggest that sufficient confinement across the splitting may prevent 'pull out' failure of the reinforcing bar. Investigations by them involved a partially bonded bar of 8mm diameter. A plastic sheet was placed outside the confined area to simulate the cracking that would occur due to the bonding stresses of the adjacent bars. Transverse reinforcement and compressive strength were varied. A hydraulic activator was used to pull the bar out at one end.

Plain concrete specimens failed by brittle split cracking. The addition of confining steel resulted in failure by pull out and did have some effect on stopping the cracks from widening.

Split cracks ran parallel to the plane of the confining steel and transverse steel is thought to not to provide any more restraint if vertical reinforcement is present in the joint. Therefore confinement was found to have no influence on local bonding in such situations. There was found to be no major difference in bond slip characteristics, whatever the spacing of the transverse reinforcement. However the ultimate bond strength increases proportionately to the square root of the concrete compressive strength.

Karabinis, AI *et al.* [30] stated that similar circular concrete columns of differing size may not achieve the same bearing strength and that this phenomena was not catered for in current design formulae. They presented a more general approach based on plasticity. Elastic behaviour of concrete is taken as linear. The loading/failure function was defined as:

$$F = \sqrt{J_{2D}} + \theta J_1 - \kappa = 0 \tag{3.19}$$

where κ is the strain hardening function defined in terms of strain trajectory, θ is the frictional coefficient, J_1 and J_{2D} are the first and second invariance of the stress tensor respectively

$$\dot{\varepsilon} = \int \sqrt{d\varepsilon^{pT} d\varepsilon^{p}} \tag{3.20}$$

where ε^T is the plastic strain trajectory. The p denotes irrecoverable deformation. The plastic strain evolution is described using the flow rule

$$d\varepsilon^p = d\lambda \frac{dG}{d\bar{\sigma}} \tag{3.21}$$

The consistency equation is used to ensure plastic loading maintaining stress on the loading surface:

$$dF = \frac{\partial F^T}{\partial \bar{\sigma}} d\sigma + \frac{\partial F}{\partial \dot{\varepsilon}} d\varepsilon^T = 0 \tag{3.22}$$

Concrete material properties are obtained from simple unconfined compression tests. The theory is tested against some published experimental data and yields reasonable agreement.

3.4.2 Internal confinement of high strength concrete

High strength concrete is not much better than normal concrete in resisting crack propagation and also has a lower capacity to transfer shear, as the crack surface is smooth.

Cusson, J *et al.* [31] reports that current stress strain models do not accurately predict the post peak behaviour of HSC columns, since strain localisation occurs after peak stress in confined concrete and produces a shear failure plane. Also elastic unloading of the undamaged concrete occurs.

Tests at LCPC [32] revealed shorter columns to have greater ductility and post peak behaviour not to be influenced by slenderness ratio.

Cusson, J *et al.* continues to report that the ties become significant only after spalling of the concrete occurs due to the Poisson's ratio effect. The core of the concrete can develop higher strength than in unconfined concrete if the area of transverse reinforcement is sufficient enough to do this. The confinement pressure of a concrete core is proportional to the size of the smallest confined concrete area and is governed by the distribution of reinforcement around the concrete core. Cusson, J derived the effective confinement index to represent the confinement efficiency in HSC columns.

$$CI = \frac{\text{Effective Confinement Pressure}}{\text{Unconfined Concrete Strength}} \tag{3.23}$$

After peak stress has occurred a shear plane will form in an HSC column dividing it into two wedges. These wedges are restrained from sliding by the longitudinal and transverse reinforcement and concrete friction. It was observed that HSC columns did exhibit softening and decreasing axial capacity as axial displacement increases. This was thought to be because of instant unloading due to tie rupture or buckling of longitudinal bars thus causing sliding of the wedges relative to each other.

Nagashima, T *et al.* [33] noted pronounced post peak softening when high strength ties were used. Larrard, D *et al.* [34] reported the opposite with low strength ties. Therefore it is known that high strength ties can have an adverse effect on the post peak axial strength of columns. This was thought to be because highly stressed ties may open more quickly after failure of the concrete or because high strength steel ruptures at an earlier strain than ordinary concrete.

Twelve confined HSC columns were tested [34] and were found to exhibit little softening at large axial displacements using normal strength steel spirals. They also found ultimate strength to increase along with the confining reinforcement almost independently of concrete compressive strength. It was also noted that higher ultimate to maximum strength ratio's occur in normal concrete than in HSC. The use of ties with hooks produced softening at large displacements. Nagashima's results confirm this.

Cusson *et al.* [35] tested twenty seven columns with varying concrete compressive strength, transverse reinforcement ratio's, tie spacing, longitudinal reinforcement ratios and concrete cover.

Loading was applied concentrically to the columns with concrete strength ranging from 60-120 MPa. The longitudinal reinforcement was provided by deformed bars and the lateral reinforcement by plain steel bars.

Test results showed during initial pre-peak loading confinement did not show significant influence. After peak the concrete cover starts to crack and the transverse reinforcement is at approximately half its yield stress. As the concrete cover spalls the column loses 10-15% of maximum axial load. At this instant the confinement results in an increase in lateral concrete strain. In this state of loading the best confined specimens reach yield stress. The final state of the specimens included longitudinal bar buckling, ruptured ties and inclined shear plane formation.

HSC showed less lateral expansion to occur than in normal concrete mainly due to greater modulus of elasticity and less internal microcraking. Compressive concrete strength and toughness is found to be enhanced with lateral reinforcement and even more enhanced when normal strength concrete is used.

Yield strength of the steel confinement dictates concrete confinement pressure. Increases in yield strength were not found to significantly affect strength of the column.

The confinement efficiency is greater with smaller tie spacings. Increases in longitudinal reinforcement were found to be effective only if the transverse reinforcement was also increased.

Therefore concrete spalling reduces column axial capacity before confinement exhibits any effect in increasing strength or ductilty. Well confined specimens showed strength enhancements of 50-100% and ductility increases of 10-20 times the original.

3.4.3 External confinement

Hybrid construction is known to increase strength energy absorption and ductility through enhanced confinement. It also provides a greater stiffness for the concrete in the axial direction.

Li, MW *et al.* [36] suggested the use of 100 mm wide fibre straps made either of E-glass or carbon fibre to provide external confinement (Figure 3.19). These can provide greater ductility and strength as they have a high strength to weight ratio. Added advantages of such a system is they can be made very thin to wrap around any column and are not too detrimental to the aesthetics of a structure. They are also not prone to corrosion, but do need a special coating to protect from ultra-violet radiation.

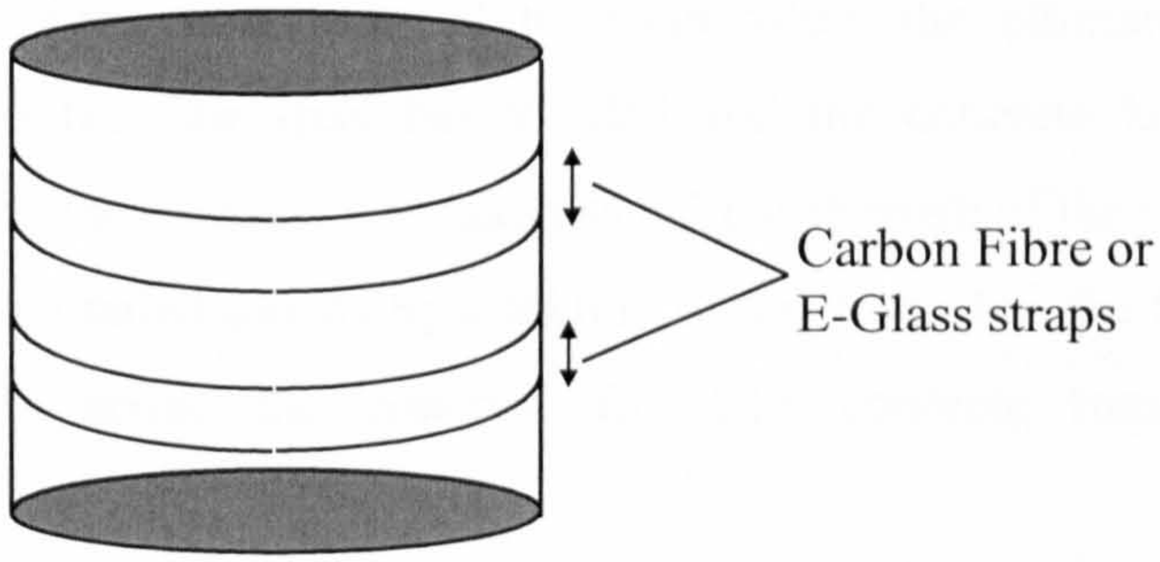

Figure 3.19 External confinement [36]

Li *et al.* investigation derived models for both rectangular and circular columns in which the effective pressure was defined as

$$f_t^{'} = f_l.k_e \tag{3.24}$$

where f_l is the transverse pressure from the reinforcement, f_t' is the effective lateral confining pressure and k_e is the confinement effectiveness coefficient.

The composite strap is known to behave linearly until failure. The parameter studies showed, in the case of circular columns, that the provision of straps increases the column load capacity. The increase is larger if carbon fibre is used. It was also found that the ductility factor increased with increasing strap thickness but decreased if the spacing between the straps was increased.

Li *et al.* concluded that straps provided increases in compressive strength and strain at failure. Also carbon fibre was known to be more effective than E-glass. It was also observed that maximum moment capacity did not increase as much the ultimate axial load and ductility factor. This is beneficial for dynamic loading, as it will produce flexural failure as opposed to brittle shear failure.

Usami, T [37] carried out investigations concerning dynamic loading of steel jacketed columns Stiffened and unstiffened columns were designed as fixed at bottom and free at the top. The varied parameters were length of filled concrete, column slenderness ratio and flange plate width thickness. The final parameter mentioned was varied within a moderate range, as larger values are known to give structural damage under dynamic loading. Concrete fill was between 0.3 and 0.5 the length of the column.

Loading was through hydraulic jacks. Both horizontal and vertical movements were recorded. Each specimen underwent a horizontal displacement history whilst under constant axial load. Failure was assumed to occur when the ultimate moment of resistance was reached (i.e. the steel has yielded and the concrete has cracked in tension). The strength of the concrete was taken as 0.7 the strength of the cylinder.

The unfilled columns failed mostly by buckling of the walls, but the filled columns showed buckling only above the concrete fill. The concrete remained mostly undamaged.

Results for columns with concrete infill show the highest energy absorption capacity and ductility, since local plate buckling was prevented by the concrete. However greater thickness/width ratios and longer columns proved more ductile.

The buckling could cause partial separation between the steel and the concrete. To avoid this external confinement with fibre composites has been suggested by Miraman, A *et al.* [38]. They investigated thirty different cylindrical specimens with three differing strengths and varying water content. Each specimen had a different jacket thickness. Axial and lateral strains were recorded with data acquisition system. The specimens were found to fail suddenly at the midheight of the tube.

Lateral expansion of the concrete encased tubes is defined by rate of change of volumetric strain ε_v.

$$\varepsilon_v = \varepsilon_1 + 2\varepsilon_r \tag{3.25}$$

where ε_v are the volumetric strains, ε_l are the axial strains and ε_r are the lateral strains Confinement depends on the concrete dilation under load and it's radial stiffness (Figure 3.20).

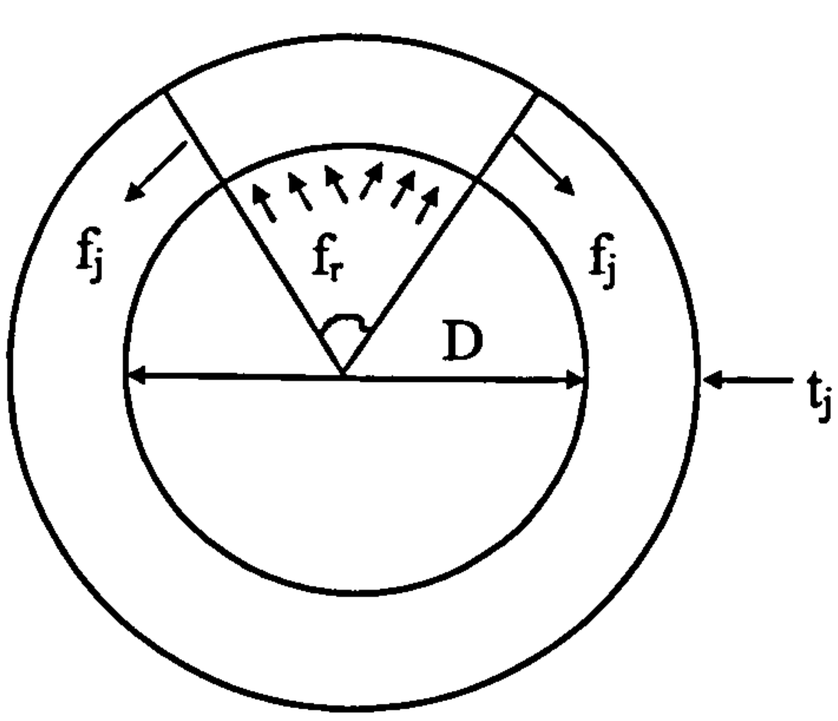

Figure 3.20 Radial stiffness

where f_r is the confining pressure and f_j is the hoop stress.

Formation of the first hoop was taken as failure of the jacket. Fibre wraps were found to be more effective in reducing lateral strains [39]. Comparison of this model and current models showed current models to overestimate dilatancy of fibre wrapped columns, suggesting therefore that they are inadequate.

Dropping weights on specimens confined with either PVC or steel show an increase in the contact force of 20 % for the former and 100% for the latter [40]. Steel specimens used in these tests showed no cracking in the top face while PVC specimens showed minor cracking.

3.4.4 Effect of confinement at higher temperatures

Various studies on plain concrete at elevated temperatures showed increases in ductility, uniaxial strength and modulus of elasticity. Studies concerning confined concrete at ambient temperatures also revealed increases in ductility and strength.

Hamoush *et al.* [41] investigated plain concrete specimens and two specimens of differing confinement under temperatures of 700 degrees using a muffle furnace.

The authors concluded a decrease in compressive strength along with an increase in crushing strain and strain at ultimate strength in plain concrete specimens. This produced an increase in ductility and a lower modulus of elasticity. Cyclic heating regimes increased strain even further. Increasing the number of cycles resulted in increased compressive strength up to the temperature of 400°C. After this concrete began to lose it's integrity.

In the case of confined concrete the greater the confinement the greater the improvement in strength up to certain limits, particularly at temperatures greater than 400°C.

The confinement produced a 'stitching effect' to repair any cracks resulting from thermal gradients, thus producing stronger concrete.

3.5 Response of structures to transient and impulsive loading

Forces in contact with a structure are known as impact loads. At the moment of impact stress waves propagate from the impacted region of the structure through to distant parts of the structure. As stated earlier the rate of straining can alter the mechanical properties of concrete. To what extent they develop depends on the size of the impact, relative masses and stiffnesses. Takeda *et al.* [42] report that structural response to impact loads is a combination of a primary and a secondary response. The primary response involves the incident stress waves and results in the cracking, spalling and fracture of the impacting zone. The secondary response is the elastoplastic response of the rest of the structure.

Their investigations reveal a multitude of response mechanisms, mainly due to the fact that primary and secondary responses develop independently of each other. However the response depends considerably on the rate effect and incident stress waves. Further tests carried out by Takeda *et al.* [43] showed maximum shear to occur at lower strains for high rate loading. However the yield stress of the reinforcement increased.

Continued research by Takeda *et al.* [44] produced formula's for the depth of penetration due to missile impact and depth of a crater resulting from explosion damage.

The depth of penetration was found to be

$$X_m = \frac{\alpha}{\beta+1}.v_o^{\beta+1} \tag{3.26}$$

$$\alpha = \frac{2^n m^{1-n}}{c\varphi} \tag{3.27}$$

$$\beta = 1-2n \tag{3.28}$$

where X_m = max depth of penetration (cm), m = mass of projectile, V_o = impact velocity, φ = periphery of Projectile, C *and* n = constants

The depth of a crater was found to be

$$D_c = \sqrt{\frac{QL}{v_o T_1 D}} \tag{3.29}$$

where D_c = depth of crater, L = weight of explosives, v_o = specific volume of gases, T_1 = explosion temperature, D = detonation velocity and Q = constant

The only current existing code of practice for blast load design is TM5-1300 ("Structures to resist the effect of accidental explosion"). It utilises the single degree of freedom lumped mass system with viscous damping. Alternatively multi degree of freedom systems could be employed.

Transient loads are usually of short duration and last no more than a few milliseconds. The force-time function and the velocity-time functions are shown in Figure 3.21.

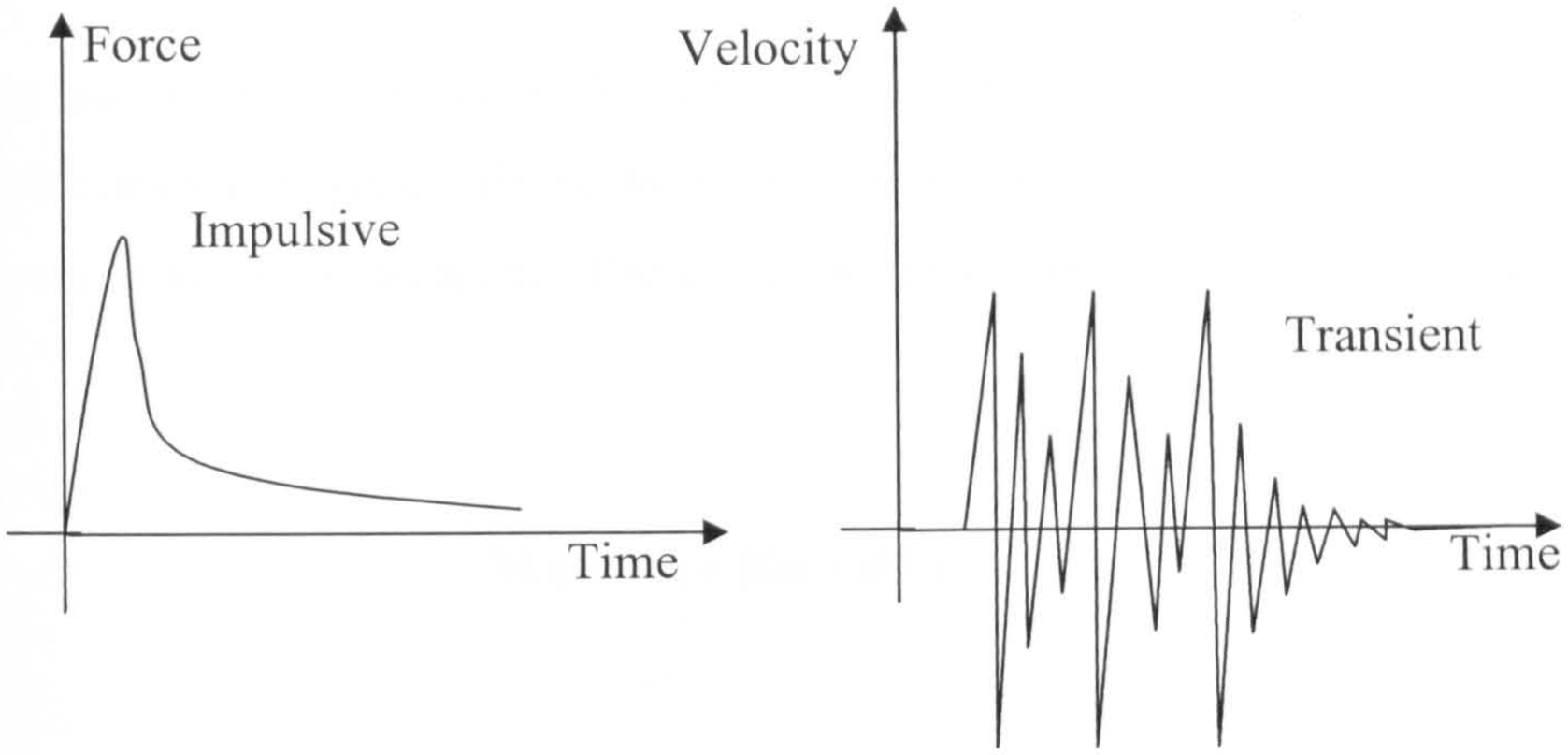

Figure 3.21 Transient and impulsive loading

The resulting vibration from transient loading of a structure can be either be forced or free [45]. Free vibration occurs when the structure is initialised with a velocity by the transient load, and the ensuing vibration will depend on the damping of the structure. Forced vibrations are usually due to a time dependent applied force. The case where the forcing frequency equals the applied structures natural frequency is known as resonance. This will cause the amplitude of the response to increase to infinity resulting in the development of enormous stresses, possibly leading to structural failure. The equation of motion of a SDOF system (Figure 3.22) is

$$M\ddot{x} + c\dot{x} + kx = P(t) \tag{3.30}$$

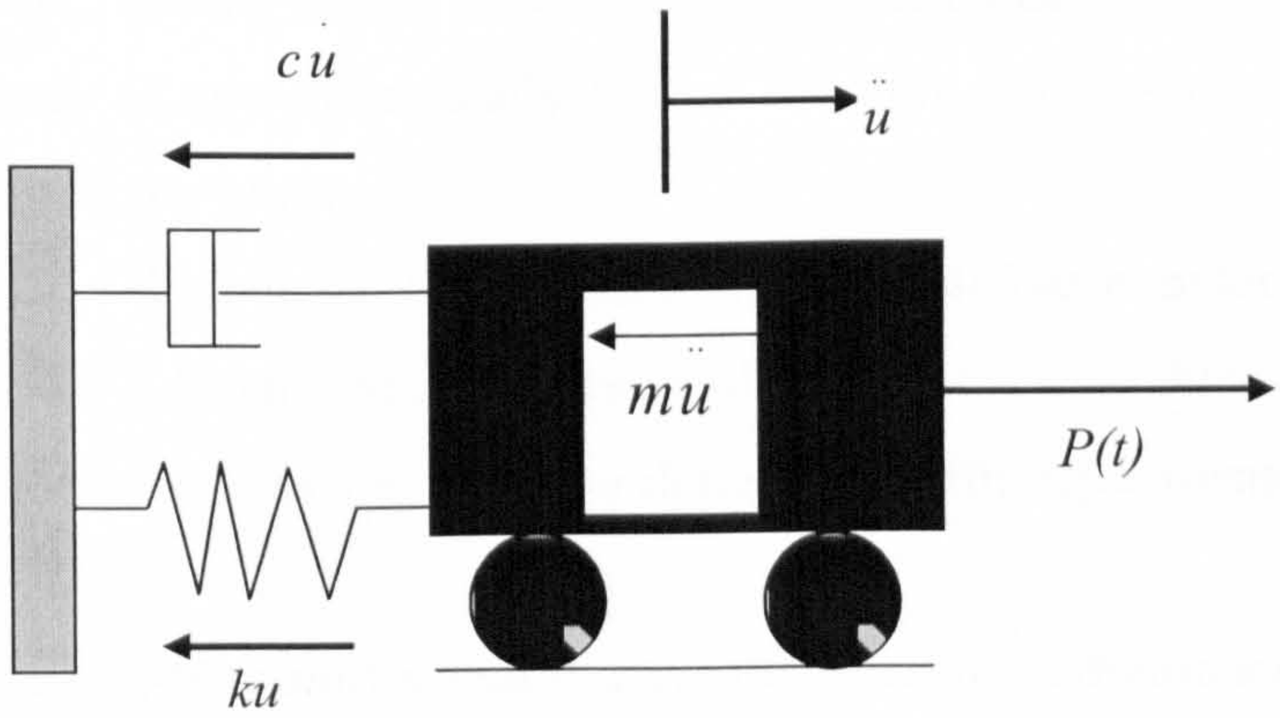

Figure 3.22 Viscous damping, inertia, spring and applied forces in an SDOF system

In the case of a free vibration the RHS is made equal to zero. MDOF systems will have a stiffness and mass matrix of the n^{th} dimension where as in SDOF systems these matrices are of the dimension 1x1. The equation of motion for an MDOF system is

$$\mathbf{M}\ddot{\mathbf{u}} + \mathbf{C}\dot{\mathbf{u}} + \mathbf{K}\mathbf{u} = \mathbf{P}(t) \tag{3.31}$$

where, **M** is the mass matrix, **C** is the viscous damping matrix, **K** is the stiffness matrix and **u** is the displacement matrix.

These equations of motion are either solved by Direct Integration schemes or by the modal superposition method [46]. The latter method involves transforming the equations of motion into a set of decoupled SDOF equations. The process involves the calculation of modal shapes and frequencies. The advantage of this method is that only the first few modes need be calculated to obtain a reasonable accurate response.

There are numerous direct integration schemes available. These involve the calculation of velocity, displacement and acceleration while marching in time.

Tests carried out using 800 mm long beams with 100x42 mm cross section subjected to a 78g explosive charge showed failure to occur in a conical plug with inclined cracking. Among the conclusions reached was that the inclined cracks were initiated by shear. Further more, investigations by Krauthammer, T [47] have shown that the frequency of any dynamically loaded structure is closely related to the shear transfer capacity of any joint.

Krauthammer, T [47] modelled the response of a concrete beam under transient loading using Timoshenko's Beam theory. Reasonable accuracy was shown to be obtained using this method by comparing resulting deflections with experimental data for beams and slabs.

Luckyram *et al.* [48] reported that if shear deformation is dominant, it can affect the overall flexural collapse of a slab. Flexural deformation can also affect shear, thus resulting in a softer target. The interaction of shear flexure interactions modelled by Luckyram *et al.* using the Binary Response Mode as shown in Figure 3.23.

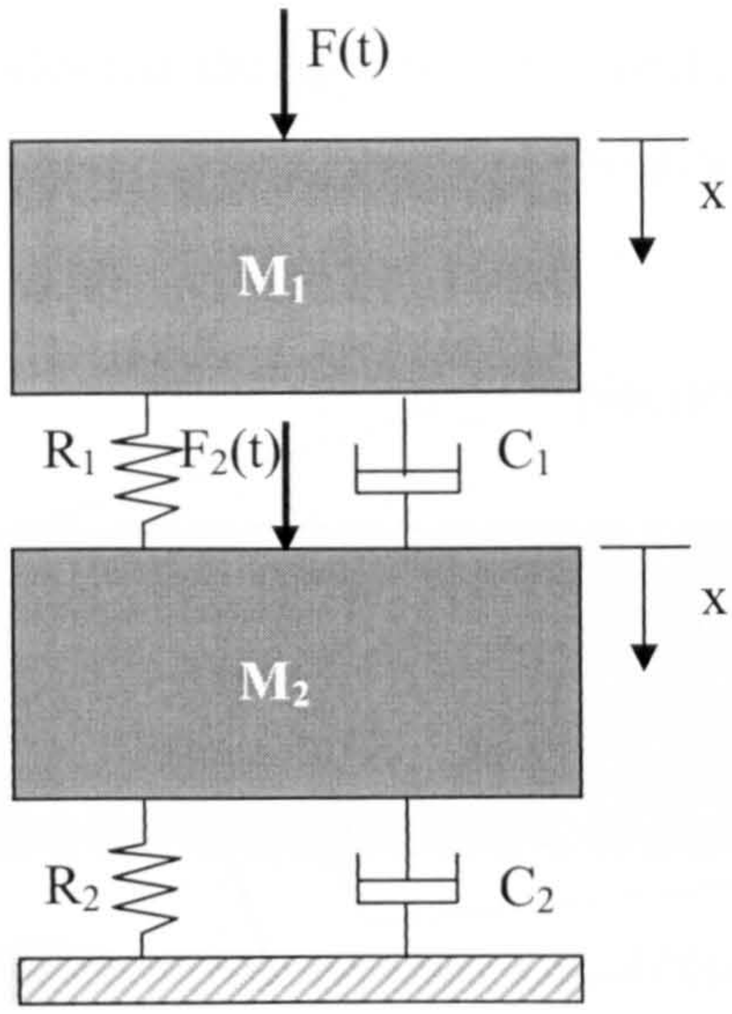

Figure 3.23 Binary response model [48]

R denotes the spring resistance and C denotes the damping of the dashpots. The governing equation of motion in matrix form is

$$\mathbf{M}\Delta a = \mathbf{C}\Delta v + \mathbf{K}\Delta x = \mathbf{F} \tag{2.32}$$

Figure 3.24 shows the resistance functions employed in the tests on the slabs:

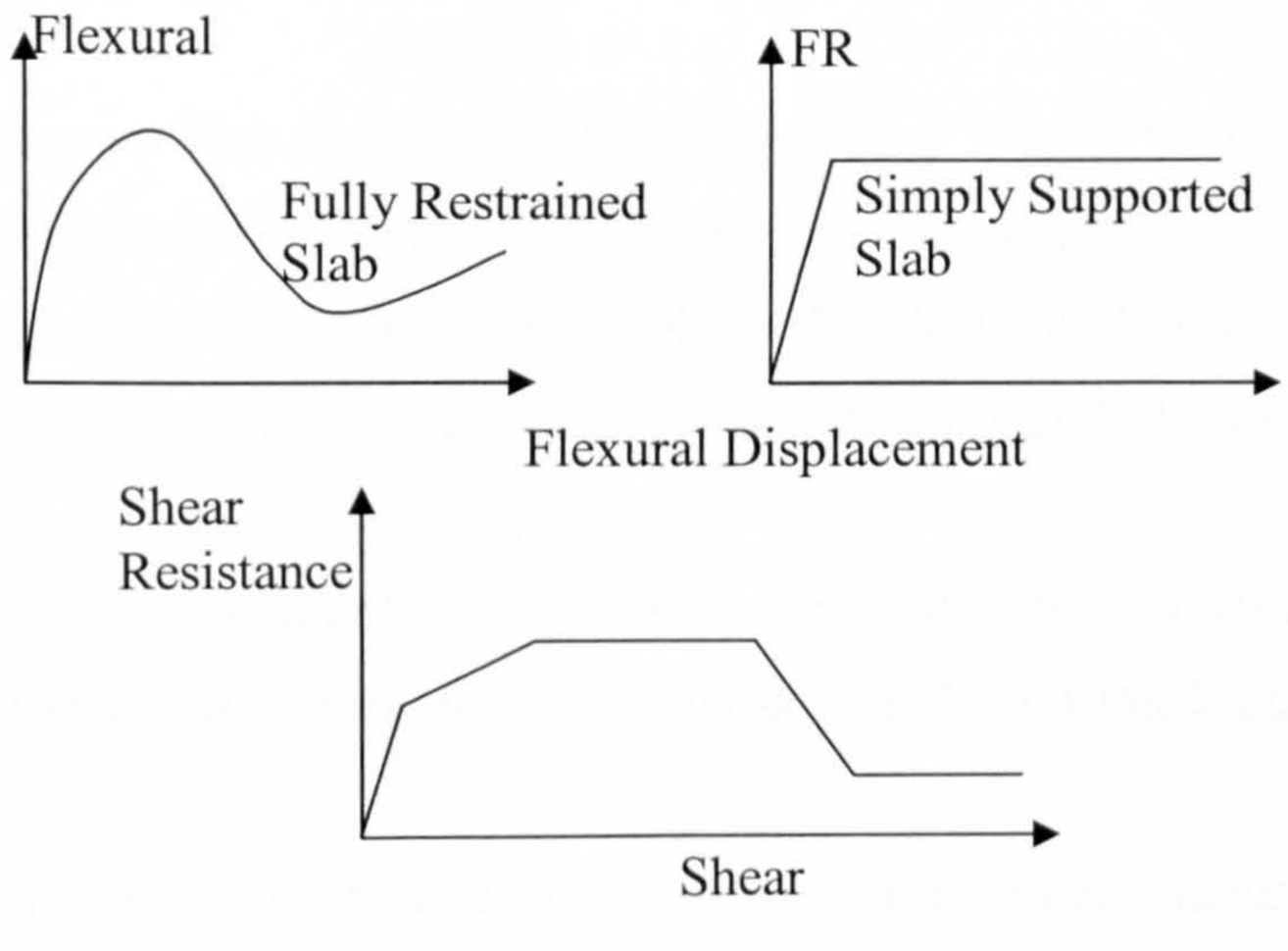

Figure 3.24 Krauthammer's resistance function

Time steps were taken to be the least of :

$$\frac{\text{Shear Mass}}{40}, \frac{\text{Flexural Mass}}{40} \text{ and } \frac{\text{Event Duration}}{40}.$$

Results yielded higher deformation than the ordinary SDOF model.

The importance of shear flexure interaction was further established by The Defense Research Agency [49] has adopted the approach of combining local perforation and global flexural collapse using mass-spriong models. The mechanism is shown in Figure 3.25.

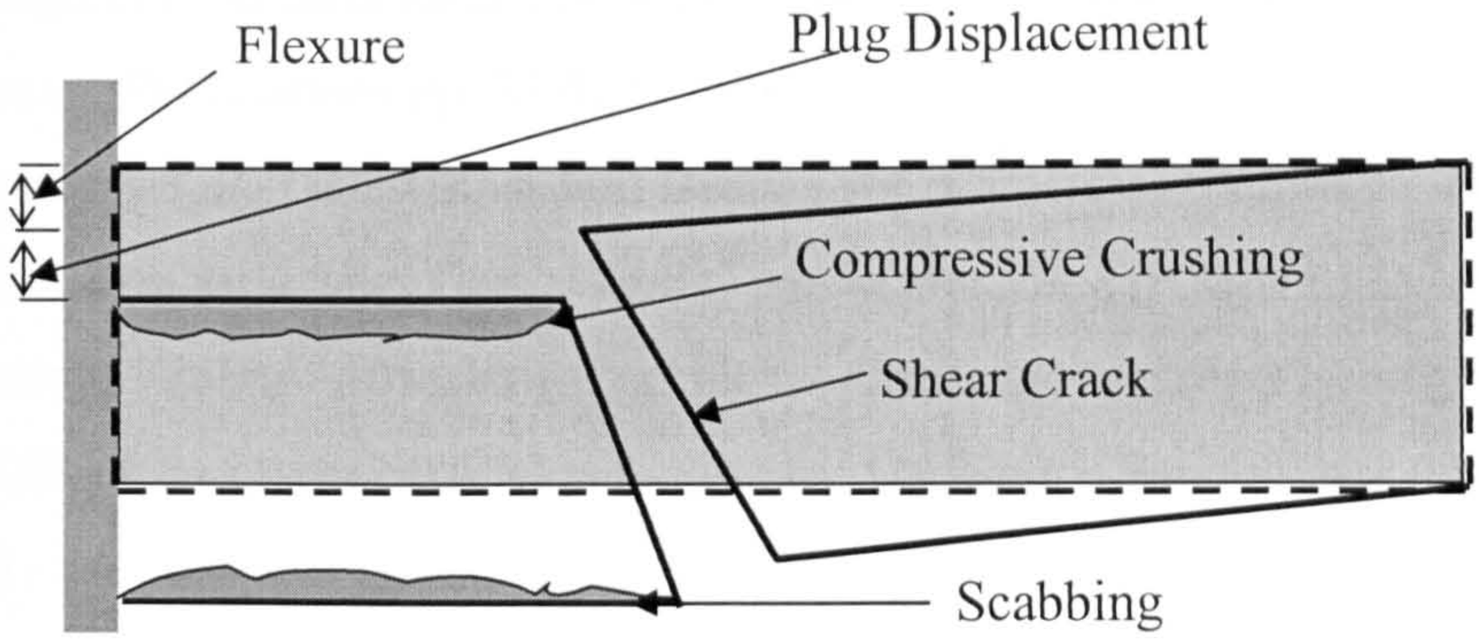

Figure 3.25 DRA model for shear flexure interactive response [49]

Crushing results in a surface crater occuring from the incident plastic shock waves. Brisance then results in shear cracking and following this scabbing occurs at the rear.

3.6 References

1. DJ Hammond, "Lessons from the Oklahoma City Bombing" *ASCE Press* (1996)
2. "Structural Use of Glass in Buildings" Inst. Struct. Eng, London (1999)
3. WF Anderson *et al.*, "The Resistance of SIFCON to High Velocity Impact", *Structures Under Shock and Impact II, Computational Mechanics Publications pp 89-98* (1992)
4. C Mayhrhofer, "Response of Reinforced SIFCON-slabs under Blast Loading" *Structures under Shock and Impact III, Computational Mechanics Publications pp 139-147* (1994)
5. St Soretz, "Impact Tests on RC Beams", *Proceedings BAM Concrete Structures under Impact and Impulsive Loadings June 2-4 pp 296-303* (1982)
6. A Stilp *et al.*, "Behaviour of Fibre Reinforced Concrete Slabs Under Impact Loading", *Proceedings BAM Concrete Structures under Impact and Impulsive Loadings June 2-4 pp 322-328* (1982)
7. T Schmitt, "Shock Wave Propagation in a Re-entrant Corner" *Jour Physics and Fluids* ***24(9)*** (1981)

8. JE Slater *et al.*, "Development of Computational Methods and Conduct of Experimental Tests for Blast Loading Analysis" *Structures under Shock and Impact III, Computational Mechanics Publications pp 383-392* (1994)
9. M Barakat *et al.*, "New Architectural Forms to Reduce the Effects of Blast Waves and Fragments on Structures", *Structures under Shock and Impact V Computational mechanics Publications pp 53-61* (1998)
10. M Ettouney *et al.*, "Blast Resistant Design of Commercial Buildings" *Practice Periodical on Structural Design and Construction Feb* (1996)
11. V Shustov, "Energy Absorbing Technique: Challenge of Proportioning", *Structures under Shock and Impact III, Computational Mechanics Publications pp 479-485* (1994)
12. V Shustov, "Shock Evader", *Structures under Shock and Impact III, Computational Mechanics Publications pp 485-494* (1994)
13. JJ Connor *et al.*, "Damage Controlled Structures I: Preliminary Design Methodology for Seismically Active Regions", *Jour Struct. Eng. **123** No 4 pp 423-431* (1997)
14. EH Bultmann Jnr, "Full Scale Field Test of a Blast resistant Structure", *Paper 17 pp 163-170 Proc. Structural Designs for Hazardous Loads E & FN Spon Brighton* (1991)
15. GJ Ha, "Response of Reinforced HSC Beam Column Joints under Load Reversals", *Mag Conc. Res. 44 No 160 pp 175-184* (1992)
16. RH Scott, "Intrinsic Mechanisms in RC Beam Column Connection Behaviour", *ACI Structural Jour. **93** No 3 pp 336-346* (1996)
17. Q Fang *et al.*, "Rate Sensitive Analysis of Framed Structures part II: implementation and Application to steel and RC frames ", *Jour. Struct. Eng and Mech **5** No 3 pp 239-256* (1997)
18. R Park *et al.*, "Ductility of Doubly Reinforced Concrete Beam Sections", *ACI Structural Jour. pp 217-225* (1988)
19. MS Al-Hadad, "Curvature Ductility of RC Beams under Low and High Strain Rates", *ACI Structural Jour. pp 526-534* (1995)
20. E Hognestad *et al.*, "Concrete Stress Distribution in Ultimate Stress Design", *ACI Jour. **52** No6 pp 455-479* (1955)

21. P Wang *et al.*, "High Strength Concrete in Ultimate Strength Design", *ACI Structural Jour. **104** No87 pp 1761-1773* (Nov 1978)
22. P Soroushian and H Obeseki , "Strain Rate –Dependent Interaction Diagrams for RC Sections", *ACI Jour. **83** No1 pp 108-116* (1986)
23. M Moretti *et al.*, "On the Behaviour and Ductility of RC Coupling Beams of Shear Walls", *ACI Structural Jour. **93** No 6 pp 711-720* (1996)
24. WH Dilger *et al.*, "Ductility of Plain and Confined Concrete Under Different Strain Rates", *ACI Structural Jour. pp 73-81* (1984)
25. SA Ashour *et al.*, "Influence of Steel Fibres and Compression Reinforcement on Deflection of HSC Beams", *ACI Structural Jour. **94** No 6 pp 611-624* (1997)
26. H Xie *et al.*, "Shear Ductility of RC Beams of Normal and HSC", *ACI Struct Jour March April **91** No 2 pp140-149* (1994)
27. SH AlSayed, "Confinement of RC Columns by Rectangular Ties and Steel Fibres", *Mag Conc. Res. 44 No 161 pp 265-270* (1992)
28. SH Ahmad, "A Comparative Study of models for Confinement of Concrete by Circular Spirals" *Mag Conc Res. **46** No 166 pp 49-56* (1994)
29. S Aslani *et al.*, "Bond of Deformed Bars to Concrete: Effects of Confinement and Strength", *ACI Materials Jour V 88 No 3 May June* 1991
30. AI Karabinis *et al.*, "Effects of Confinement on Concrete on Concrete Columns: Plasticity Approach", *Jour Struct. Eng. **120** No 9 pp 2747-2767* (1994)
31. J Cusson *et al.*, "Strain Localisation in Confined HSC Columns", *Jour Struct Eng. **122** No 9 pp 1055-1061* (1996)
32. F D Larrard *et al.*, "Post –Failure Behaviour of High or very High Performance Concrete in Compression", *Bulletin de Liaison des Laboratoires des Ponts et Chauseees. 179 pp 11-20* (1992)
33. Nagashima T *et al.*, "Monotonic axial Compression Test on Ultra High Strength Concrete tied Columns", *10th World Conf.on Earthquake Eng. Rotterdam The Netherlands pp 2983-2988* (1992)
34. De Larrard, "Engineering Properties of High Performance Concretes", *High Performance Concrete from Material to Structure. pp 85-114* (1992)
35. D Cusson *et al.*, "High Strength Concrete Columns confined by Rectangular Ties", *Jour Struct Eng. **120** No 3 pp 783-804* (1994)
36. MW Li *et al.*, "Strength and Ductility of Concrete Columns Externally Reinforced with Fibre Composite Straps", *ACI Struct.Jour.. Eng. **91** No 4 pp 434-447* (1994)

37. T Usami, "Ductility of Concrete Steel Box Columns under Cyclic Loading", *Jour Struct. Eng. 120 No 7 pp 2021-2039* (1994)

38. A Mirmiran *et al.*, "Behaviour of Concrete Columns Confined by Fiber Composite", *Jour Struct. Eng. 123 No 5 pp 583-590* (1997)

39. H Saadatmanesh, "Strength of Ductility of Concrete Columns Externally Reinforced with Fibre Composite Straps", *ACI Structural Jour. 91 No 4 pp 434-447* (1994)

40. SJ Pritchard, "Hard Impact Testing of Confined Concrete Cylinders", *Structures under Shock and Impact V Computational mechanics Publications pp 493-502* (1998)

41. A Hamoush, "Effect of Siliceous Aggregate Concrete Subjected to Elevated Temperature and Cyclic Heating", *ACI Materials Jour. 94 No 2 pp 83-89* (1997)

42. Takeda *et al.*, "Basic Concept on the Response of Structural Members and Structures under Impact or Impulsive Loadings ", *Proceedings BAM Concrete Structures under Impact and Impulsive Loadings June 2-4 pp 13-18* (1982)

43. Takeda *et al.*, "Mechanical Properties of Concrete and Steel in RC Structures", *Proceedings BAM Concrete Structures under Impact and Impulsive Loadings June 2-4 pp 266-278* (1982)

44. Takeda *et al.*, "Fracture of RC Structural Members and Structures subjected to Impact or Explosion", *Proceedings BAM Concrete Structures under Impact and Impulsive Loadings June 2-4 pp 289-295* (1982)

45. MB Kanchi, "Matrix Methods of Structural Analysis", *2nd Edition Wiley Eastern Ltd* (1993)

46. JL Humar, "Dynamics of Structures", *Prentice Hall* (1993)

47. T Krauthammer *et al.*, "Impulsive Concrete interface Shear Transfer", *Paper 30 pp 305-312 Proc. Structural Designs for Hazardous Loads E & FN Spon Brighton* (1991)

48. J Luckyram *et al.*, ("Blast Loaded RC Slabs: A Binary Response Model for Shear and Flexure Interaction", *Structures Under Shock and Impact II, Computational Mechanics Publications pp 177-188* (1992)

49. AJ Sheridan *et al.*, "An Analysis of Shear /Flexure Coupling Applied to Failure of RC Structures", *Structures Under Shock and Impact II, Computational Mechanics Publications pp 189-198* (1992)

Chapter 4

Numerical investigation into the rotational capacity of reinforced concrete elements

4.1 Introduction

The challenges of modern civil engineering necessitate a thorough and complete understanding of concrete's structural response to both static and dynamic loads. Concrete's enormously complex response pattern can be attributed to any one of the following:

- It's non-linear stress strain behaviour under complex loading
- It's cracking phenomena with and without aggregate interlocking effects
- It's relationship to the reinforcing steel – bonded and unbonded
- It's strain rate effect under blast loading

These response phenomena are the subject of continual research.

The failure of singular reinforced concrete beams has been the subject of much controversy in recent years. The controversy centres over the effect of beam size upon the rotational capacity. The influence of the way in which size effects the rotational capacity is important since most structural testing is done upon elements much smaller in size than those used in building structures. Hence a thorough understanding of the size effect is necessary to assess concrete behaviour under loading.

In this chapter strain localisation is investigated and a simple constitutive law for the failure of concrete is proposed. It is intended for use in the combined FEM/DEM code to numerically assess the structural response to blast loading. There are also wider implications of the research here presented since all limit state design codes depend on inelastic rotational capacity of the hinging regions in RC members.

4.2 Effects upon rotational capacity of a R.C. failure

Corley, W [1] investigated the effect of beam size on the beam's rotational capacity. His investigation centred on a series of fourty beams of varying geometries and reinforcement, subjected to single point loading as shown in Figure 4.1.

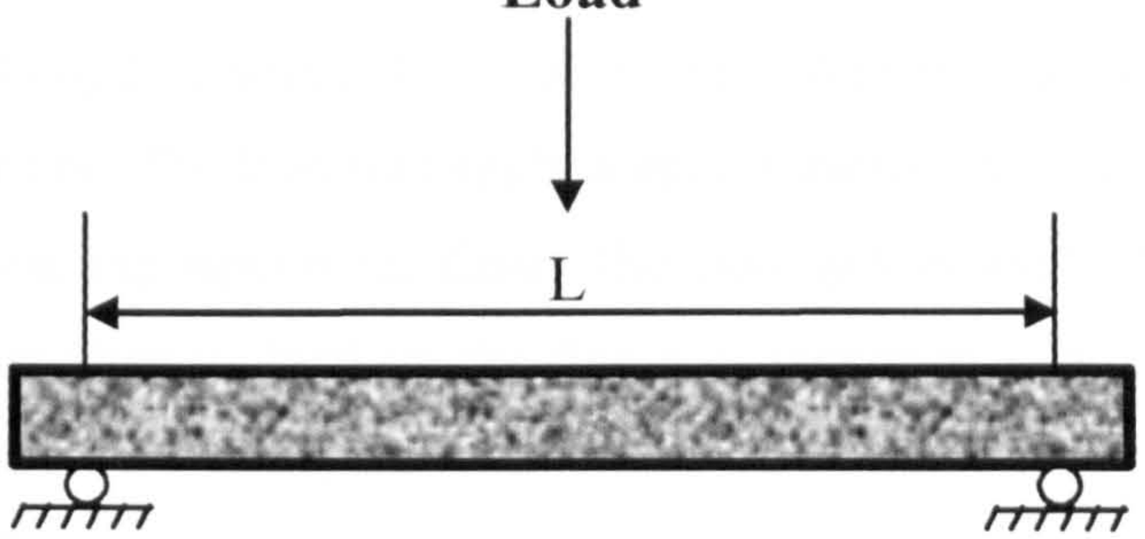

Figure 4.1 Beam loading for experiments by Corley

The differing beams sections, section properties, span lengths and reinforcement layout is given in Figure 4.2.

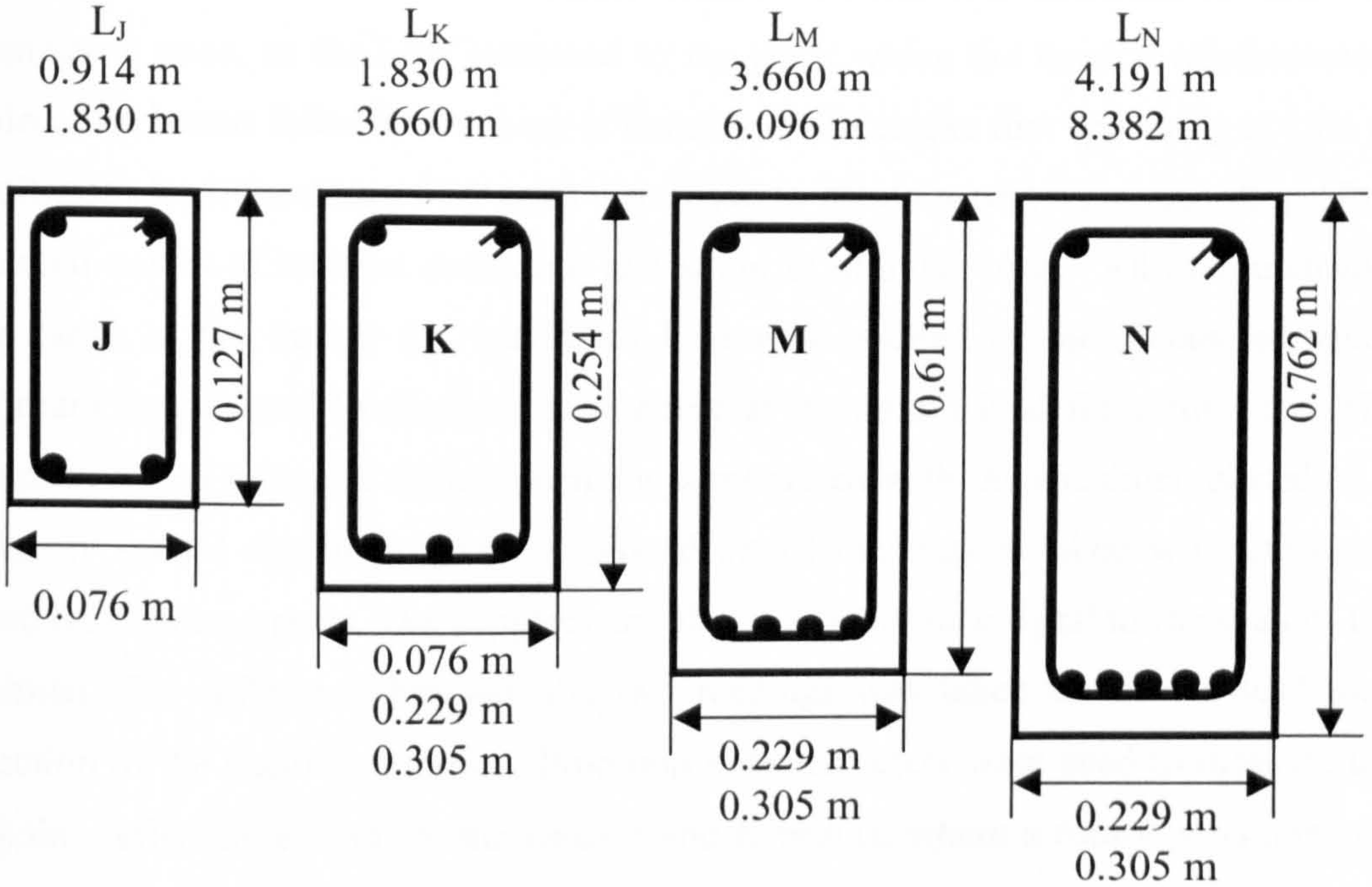

Figure 4.2 Beam sections for experiments by Corley

The amount of tension reinforcement was varied between 1% and 3% and the binding reinforcement was varied between 0.3% and 9%. The yield stress tension and compression reinforcement was 10.5 MN/m^2 (60 ksi). For the shear reinforcement this figure was 8.8 MN/m^2 (50 ksi).

The concrete mix used yielded a nominal cylinder strength of 27.5 MPa (4000 psi) at 28 days. Specimens were cast in plastic coated plywood forms and were subsequently compacted by a high frequency vibrator. The specimens were stored at 21.1^{0}C for the first three days after which they were uncovered and stored at 21.1^{0}C with relative humidity kept at 50%. Tests were done 28 to 31 days after casting.

The beams had the same nominal yield stress for the compression steel and the same concrete cylinder strength. During the loading tests, free rollers placed at each end supported the test beams. The load was applied upon various plates placed on the beam, by hydraulic rams reacting against the floor. The loading was applied in increments of 15% of the calculated ultimate load for the first four increments and increments of 5% thereafter. Each increment was applied over one minute and held constant for a further fourteen minutes. Most of the test required approximately 12 increments taking three hours to complete.

All the beams were under-reinforced and failed by crushing of concrete after yielding of the tension reinforcement had occurred. Flexural cracks were first visible at 15%to 30% of the ultimate load. These cracks widened and extended towards the compression zone, as the load increased to the point where the tension reinforcement yielded. The beams failed by crushing of concrete, with cracks first appearing at 15% of the ultimate load. Sandborn 67A units were used to obtain a continuos recording of all measured values of rotation deflection and strain at ultimate load. All measurements were taken at the instant the maximum load was reached or the instant at which maximum load started to decrease after being at maximum load for some time. The deflection of the midpoint of the specimen is measured with the specimen placed on a uniformly spaced styrofoam pads. A second set of readings is taken with the beam placed on round supports. The supports are placed at a distance equal to the span of the specimen. The difference between the two readings was taken to be the dead load deflection of the beam in question. Precision potentiometers were used to measure the midpoint deflection except for the series J and K beams, where a rotary potentiometer was used.

In order to investigate the effect of size on the rotational capacity the maximum concrete compressive strain of those beams with similar width to half span ratios and similar stirrups were compared. Since the values were found to be similar it was concluded that size has no direct effect upon the rotational capacity of the hinging

regions. It was however concluded that by decreasing the stirrup spacing the rotational capacity was found to significantly increase.

However this conclusion is contradicted by Hillerborg, A [2,3]. His theoretical model proposed that the complete stress strain curve in concrete is described by combing the ascending portion of a stress strain curve with the descending portion of a stress- deformation curve as shown in Figure 4.3. This was justified since such a curve shows additional deformation occuring due to crack formation within the fracture zone. Hillerborg suggests that localisation occurs after the peak point is reached. He further suggests that this needs to be accounted for in an approximate way.

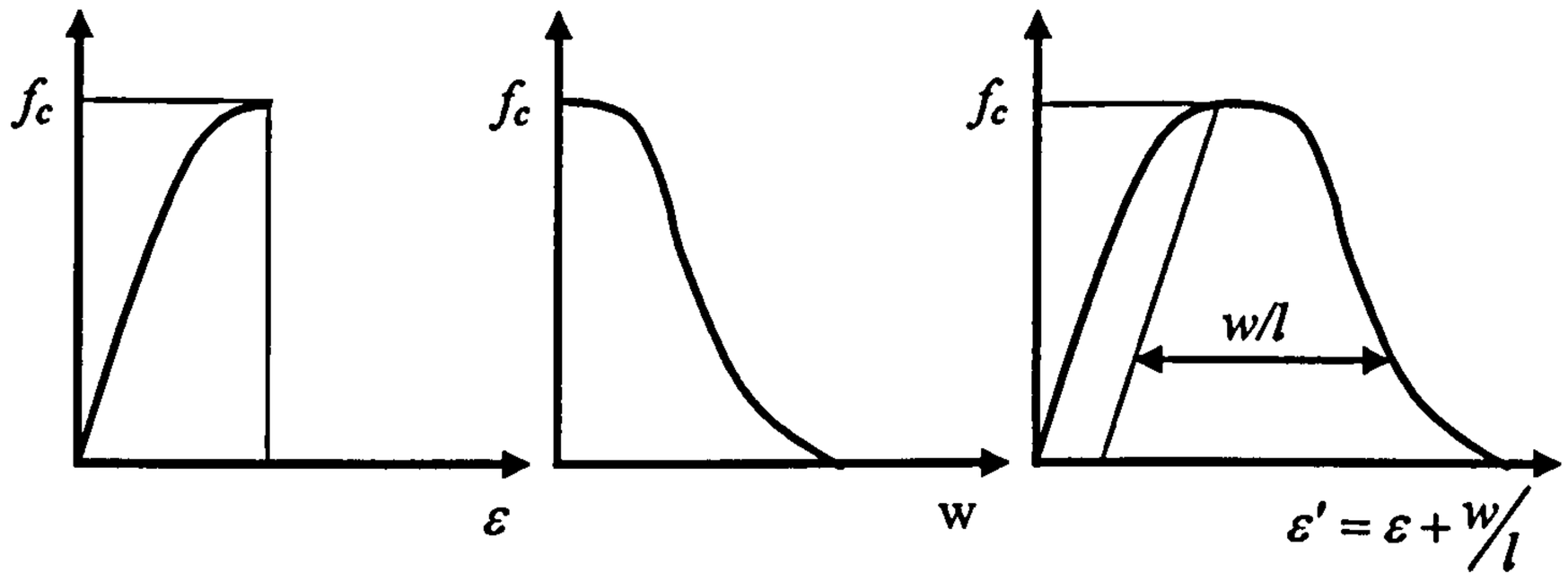

Figure 4.3 Complete stress- strain relationship proposed by Hillerborg

Thus the complete stress strain relationship can be represented by

$$\varepsilon' = \varepsilon + w/l \tag{4.1}$$

By assuming plane sections remain plane and combining this equation with equation (4.1) Hillerborg suggests a realistic prediction results providing that the beam length, l is chosen appropriately. Hillerborg suggests that for a rectangular beam

$$l = \beta \varepsilon d \tag{4.2}$$

where εd is the depth of the compression zone and β is a constant of proportionality equal to 0.8.

By assuming the stress strain relationships to be linear, Hillerborg derives a relationship between rotational capacity and the depth of a beam as given by

$$\theta_{max} = \frac{0.4w}{\omega d} \tag{4.3}$$

where ω, the mechanical reinforcement ratio is given by

$$\omega = \frac{A_s f_s}{bdf_c} \tag{4.4}$$

This equation shows the rotational capacity to be inversely proportional to the beam depth, thus finding beam size to directly influence the rotational capacity. Hillerborg also suggests that just prior to failure localisation of the strains in the compression part of the concrete takes place thus considerably influencing the ductility (energy dissipation prior to failure). However, Hillerborg does emphasize the need for further research to uphold his theoretical findings.

The effect of size upon the rotational plastic hinge capacity of a reinforced concrete beam subjected to pure bending has been further investigated by Alca, N et.al.[4]. Their results suggest that localisation does not occur and that the rotational capacity is not a function of depth.

The ACI code for concrete [5] allows for redistribution of moments between members and sections. The authors state for this to occur there must be adequate deformation capacity of the plastic hinging region.

Alca et.al.'s approach first assumed no tension carried in the concrete such that the stress and strain distributions are as shown in Figure 4.4.

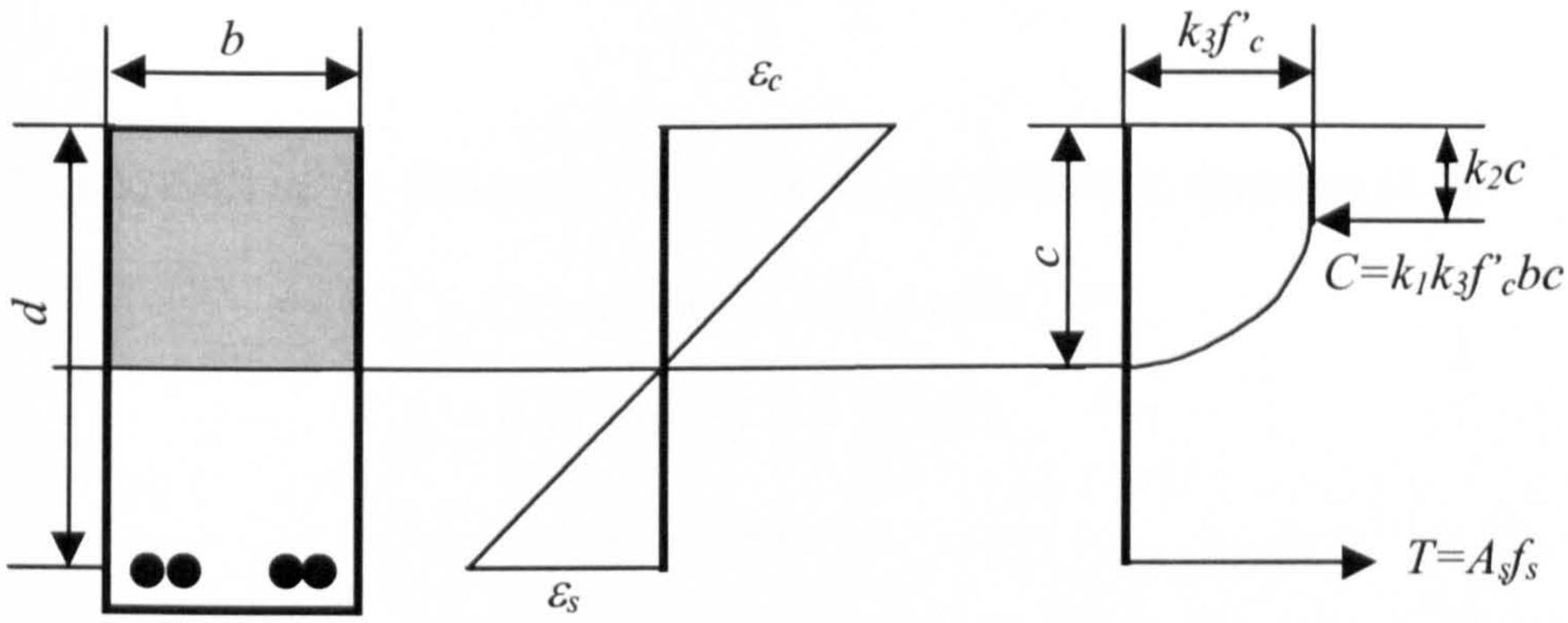

Figure 4.4 Reinforced concrete beam with cross section

Furthermore the ultimate moment and ultimate rotation are assumed to correspond to the same point on the load deformation relationship, thus the ultimate curvature ψ_u, and ultimate rotation, θ_u are defined as follows:

$$\psi_u = \frac{\varepsilon_{c\theta u}}{c_{\theta u}} \tag{4.5}$$

$$\theta_u = \psi_u 1 \tag{4.6}$$

where

$$c_{\theta u} = \frac{A_s f_s}{k_1 k_3 f'_c b} \tag{4.7}$$

$\varepsilon_{c\theta u}$ = the extreme compression fibre strain at ultimate rotation, $c_{\theta u}$ = neutral axis depth at ultimate rotation, A_s = area of steel, f_s = stress in steel at ultimate rotation, k_1 = ratio of the average stress to the maximum stress, k_3 = ratio of the maximum stress in the compression zone to the cylinder strength f'_c, b = width of the compression zone, l=length over which the curvature is measured, d = effective depth and m = dimensionless constant.

The mechanical reinforcement ratio at ultimate rotation, ω is given by

$$\omega = \frac{A_s f_s}{f'_c bd} \tag{4.8}$$

By substituting equation (4.5) and (4.8) into (4.6) the following relationship is derived

$$\theta_u \omega = m k_1 k_3 \varepsilon_{c\theta u} \tag{4.9}$$

The ACI code dictates the following values for the parameters in equation (4.9).

$$k_1 = 0.85 \text{ where } f'_c < 27.6 \text{ MPa}$$

$$k_1 = 0.65 \text{ where } f'_c > 55 \text{ MPa}$$

$$k_3 = 0.85$$

$$\varepsilon_{c\theta u} = 0.003$$

Hence Alca et. al. proposes that equation (4.9) suggests that concrete sections with the same concrete strength and the same ω will have the same ultimate rotation. Hence the normalised ultimate rotation $\theta_u \omega$ is constant for any hinging section of the same concrete strength.

The experimental program set up by Alca et.al. involved twelve high strength concrete reinforced beams being subjected to two point loading as shown in Figure 4.5. Three depths of 230, 360 and 515 mm were used as well as two concrete strengths of 50 and 90 MPa (at 56days). Two examples of each beam were cast and scaled geometrically in all respects except aggregate size. The beams were cast such that the concrete in the compression zone would reach the peak of the stress strain curve while the steel was still in its yield plateau. Hence the descending zone of the concrete in compression would dominate behaviour.

Two letters and a number designate each beam. The first letter S, M or L refers to the small, medium or large beam. The second letter L or H refers to low or high strength concrete and the number refers to the first and second beam of the same type. Concrete cylinder tests showed failure for the high strength concrete to occur between the aggregate and mortar, whereas the failure plane dissected through the aggregate and mortar in the high strength concrete. The lower strength concrete used four bars of reinforcement while the higher strength concrete beams used eight bars.

The loading set up is shown in Figure 4.5 and the specimen beams are described in Table 4.1.

Table 4.1 Beam specimen description

Specimen	Φ mm	b mm	d mm	h mm	L mm	Stirrups in Shear Span
SL1/2	16	150	230	282	3740	#10@115 mm
SH1/2	16	150	230	302	3740	#10@115 mm
ML1/2	25.2	235	360	443	5860	#10 @ 160 mm
MH1/2	25.2	235	360	475	5860	#15 @ 160 mm
LL1/2	35.7	335	515	630	8380	#15 @ 230 mm
LH1/2	35.7	335	515	678	8380	#15 @ 115 mm

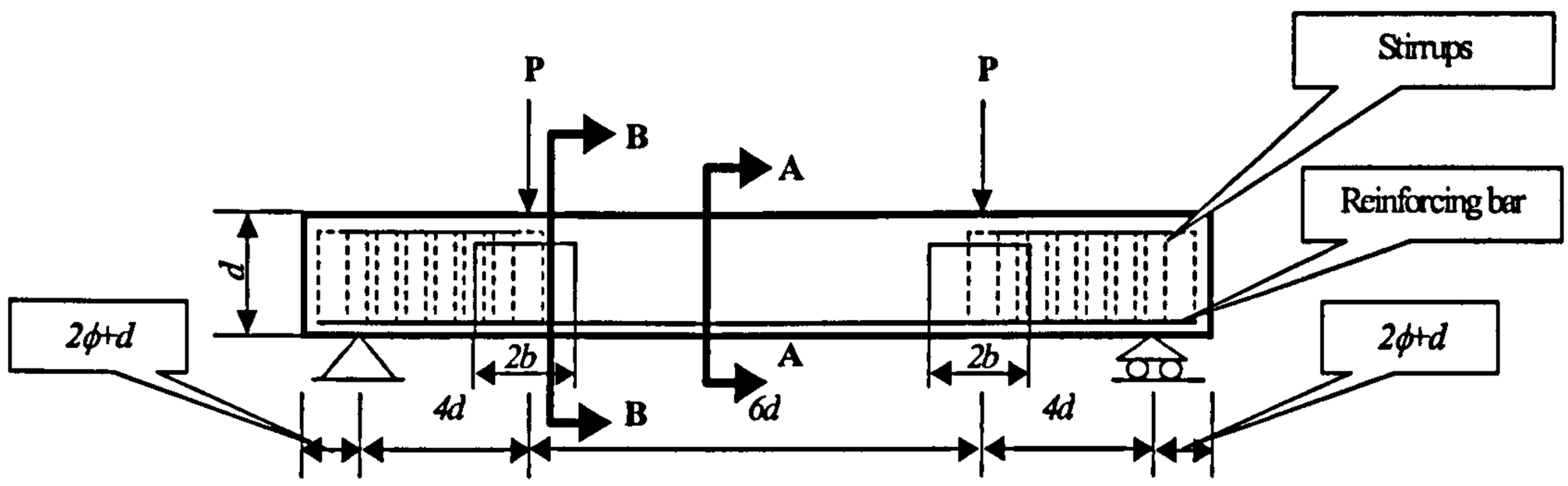

Figure 4.5 Loading arrangement for the beams

Loading has been provided by two 1780 kN jacks. Loading at both pcints was maintained equal. The centreline deflections and the change in shear spans due to deflections were measured with cable transducers. The rotation meters were measured with rotation meters embedded a distance of 0.26*d* from the top surface. The distance between the rotation meters is 3.7*d*. The opposite side has five pairs of LVDT's to measure the longitudinal average strains. The strain distribution is assumed to be linear. Top surface strains were measured with a 2 in demec gage. Strains in the longitudinal reinforcement were measured with 5 mm foil strain gages attached to the top and bottom of every bar at the midspan. To reduce the effect of tension stiffening a transverse notch was formed at the position of the gage.

The loading was applied in between ten to fifteen steps with each step taking about fifteen minutes. Time to reinforcement yield was approximately three to four hours. Tests took about eight to twelve hours to complete depending upon the deformation capacity of the beam. The dead weight of the beam is not accounted for in the tests, since initial readings were taken after the beams were aligned in the test frame.

Table 4.2 Material properties of Alca's beam specimens

Beam	f'_c MPa	Age days	f'_t MPa	Age days	G_F N/m	Age days	f_y MPa	f_s MPa	ρ %	ω
SL1	51.1	56	4.6	90	178.5	138	410	410	2.32	0.186
SL2	51.1	56	4	83	182.7	131	410	410	2.32	0.186
ML1	52.7	56	4.3	106	193	104	409	409	2.36	0.184
ML2	54.1	37	3.7	99	233.5	97	404	404	2.36	0.177
LL1	54.2	52	4.2	85	219.2	160	409	428	2.32	0.183
LL2	43.8	44	3.8	70	218.4	145	409	410	2.32	0.217
MH2	73.4	73	4.6	78	211.9	76	402	402	4.73	0.259
SH1	90.1	56	6.5	76	216.5	124	410	410	4.64	0.211
SH2	85.6	56	5.5	69	193.9	117	410	410	4.64	0.222
MH1	90.3	56	6.2	92	255.7	90	402	402	4.73	0.21
LH1	90.3	46	5.6	62	224.2	137	406	426	4.64	0.219
LH2	87.8	47	5.2	55	233.4	130	412	432	4.64	0.229

The yield moment and rotation for the lower strength beams are defined as M_y and θ_y respectively. For the higher strength concrete the yield moment is defined as the load at which both layers of reinforcement have yielded. The yield rotation is calculated by averaging the deformations corresponding to the yielding of the first and second layers. The ultimate moment M_u is the peak moment capacity of the beam and occurs at peak rotation θ_{Mu}. The ultimate deformation is the load at which the load starts to drop significantly.

All specimens exhibited similar behaviour. At 5 –10% of ultimate load primary cracks appeared extending rapidly toward the compression zone in the first few load steps. Strain distributions showed no significant variation throughout the length of the test region. Near the yield load secondary cracks appeared extending to the same level of the primary cracks in the first few load steps.

Post yield behaviour showed some widening in the cracks with some horizontal cracking appearing. Different crack failure patterns were shown by the low and high strength concrete.

In the low strength beams the primary cracks divided into branches. Secondary cracks extended vertically. The strain increased in part of the beam whilst in the other sections of the beam the strain remained near constant. As loading increased, the non-linearity in strain distribution also increases. The beams would start to spall at the corners followed by cracks propagating at the top surface. At this stage the compression fibre strains were measured as being between 300-3800 microstrain and local strains were recorded as high as 5300 microstrain. The centreline deflections were between 65-75% of the failure deflections. The small and large beams failed locally where a primary crack existed. The medium strength beams failed with primary branch cracks connecting to form a failure plane with crushing at a particular section. Failure was not explosive with the failure planes running between mortar and aggregate, similar to the cylinder tests.

The higher strength concrete beams did not show any primary branching, All cracks propagated to approximately the same distance from the top surface. At first spalling the extreme compression fibre strains were 3400-4100 microstrain with local strains reaching 4600 microstrain. The centre line deflection were 60-80% of the failure deflections. Prediction of the locality of the failure was not possible as failure was explosive and sudden. Hence the readings from the demec's were stopped at $0.75\theta_u$. No stirrup reinforcement was provided in the test region.

A summary of results is presented in Table 4.3.

The peak strain from the cylinder tests (2500-3200 microstrain) provided an indication as to the point at which strain localisation should start. It was noticed, however that at 60-70% of θ_u even the smallest strain exceeded this value.

The authors also noticed that if strain localisation was to occur in a section of the beam, the concrete adjacent to the section, which has not softened, should show a reduction in stress with a reduction in strain. This is found not to be the case. The authors cite some reasons for this. Firstly the localisation as defined by Hillerborg occurs over the whole beam. Secondly discrete strain localisation may occur closer than 2 in (50.8 mm) apart (distance of demec gages). Thirdly that the stress strain relationship obtained from the cylinder test is unrepresentative of the actual behaviour.

To further test for the third possibility, Alca et.al employ a method developed by Smith and Orangun [6] to obtain estimates of the stress strain relationship curve. The tensile strength is neglected. Every load step requires the moment, extreme fibre strain, ε_c and neutral axis depth, c at each load step.

Table 4.3 Summary of experimental results

Beam	M_y kNm	θ_y deg	M_u kNm	θ_{Mu} deg	ε_{Mu} με	$M_{\theta u}$ kNm	θ_{Mu} deg	$\varepsilon_{c\theta u}$ με	$\varepsilon_{\theta u}$ mm
SL1	65.3	0.922	68.8	1.919	3197	68.7	2.567	3962	75.1
SL2	64.9	0.905	69.4	3.289	4647	69	3.461	4818	67.9
ML1	248.2	0.888	256.2	2.378	3901	255.5	2.544	4097	122.9
ML2	250.6	0.888	275.1	4.051	5217	275.1	4.051	5217	98.1
LL1	755	0.911	774	2.962	4830	774	2.962	4830	178.2
LL2	720.2	0.945	747.6	2.137	3979	739.4	2.2	4081	202.2
MH2	475.5	1.152	476.6	1.639	4003	474.5	1.713	4142	184.6
SH1	128.2	1.094	136.5	2.813	4771	134.8	2.968	4906	80.5
SH2	128.8	1.094	134.2	2.687	4886	134.2	2.687	4886	88.5
MH1	493.8	1.02	521.8	2.693	4936	519.8	2.756	5012	138.6
LH1	1432	1.089	1546	2.962	5003	1546	2.962	5003	184.4
LH2	440	1.089	1566	3.077	5089	1566	3.077	5089	180.6

The concrete stress block is represented by a polynomial given by

$$f_c' = a_1\varepsilon + a_2\varepsilon^2 + a_3\varepsilon^3 + \ldots + a_n\varepsilon^n \qquad (4.10)$$

The average extreme fibre strain was measured with a demec gage and valued for ε_c were estimated. The values of ε_c were estimated using equation (4.10) and the rotations were found by the rotation meters. The resulting curves show that the low strength concrete shows some descending branch activity. However this is reported as not fully represented by the experimental results, which shows the strain distribution to be minimal but not to the extent as to imply strain localisation of the whole hinging region. The high strength beam showed no real descending activity. Hence failure is deemed to occur without any strain localisation being developed. This conclusion is verified by the experiment.

The authors conclude that the size of the beams did not exhibit any effect on the rotational capacity of the beams when subjected to pure bending. Secondly the extreme fibre strains measured indicate that the high strength beams were as deformable as the low strength beams. The failure pattern in the low strength concrete was mainly bond type failure, whereas the high strength beams showed failure to occur through aggregate failure. The high strength beams were observed to fail explosively. Finally the authors note that the stress strain curve for concrete in flexure may be different to the stress strain curve for a uniaxially loaded concrete cylinder.

4.3 Numerical modelling

The beams used in the experiment by Alca,N et. al. are adopted for use in the numerical simulation. The aim of the numerical simulation is to investigate the effects of size on rotational capacity and to propose a constitutive failure law for concrete for hazardous loading conditions.

4.3.1 Numerical modelling of the concrete stress and strain curves

The concrete is stress strain curve is modelled using the following formula [7]

$$z = 1 - \left(\frac{a+b-1}{a+b}\right) e^{D[(a+cb)/(a+b)(1-a-b)]} \times a(1-d) + b(1-D)^c \qquad (4.11)$$

where $a = 0.63$, $b = 1.8$, $c = 6.0$ and D is given by

$$D = \frac{\varepsilon_c - \varepsilon_{cp}}{\varepsilon_{cb} - \varepsilon_{cp}} \tag{4.12}$$

where ε_c = strain in the concrete, ε_{cp} = peak strain in the concrete and ε_{cb} = concrete breaking strain.

For the range of concrete stress between zero and peak stress the concrete is calculated from

$$\sigma_c = \sigma_{cp}\left[\frac{2\varepsilon_c}{\varepsilon_{cp}} - \left(\frac{\varepsilon_c}{\varepsilon_{cp}}\right)^2\right] \tag{4.13}$$

If the stress in the concrete is in between the peak and the breaking strain then the stress is calculated from

$$\sigma_c = \sigma_{cp} \times z \tag{4.14}$$

The stress strain curves obtained for each of the Alca beams is shown in Figure 4.6 and compared with the experimental results.

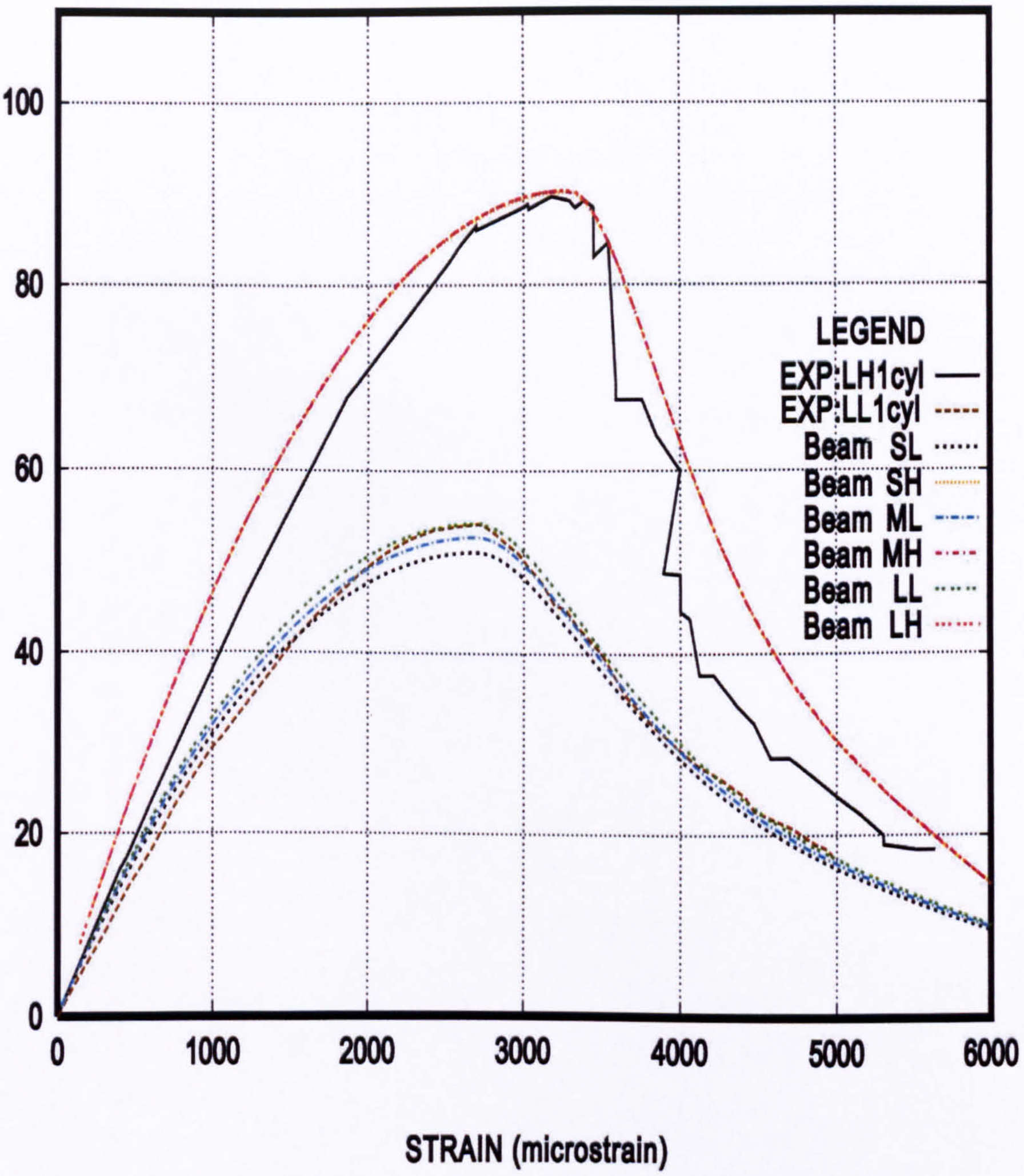

Figure 4.6 Numerical and experimental stress strain curves for the Alca beams

The results obtained from the experiment are plotted for beams LH and LL. As is seen from Figure 4.6 a good agreement between the numerical and experimental results is obtained. For the purposes of clarity experimental results for the other beams are not plotted. The numerically obtained curves are shown and they too are found to agree well with experimentally obtained results.

4.3.2 Stress and strain curve for reinforcing steel

The generalised stress strain curve is shown in Figure 4.7.

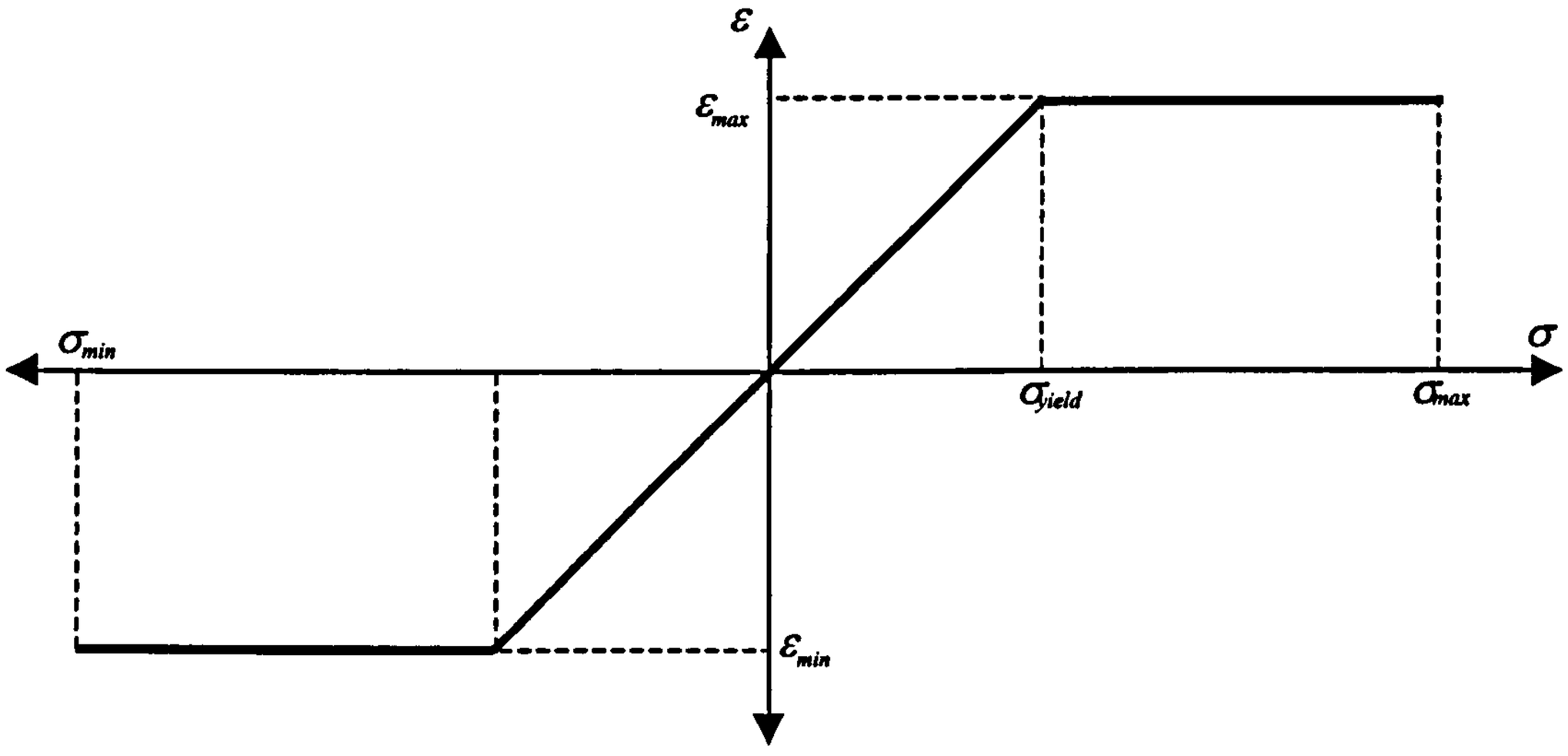

Figure 4.7 Stress strain curve for reinforcing steel

In order to model this stress strain relationship, the following steps have been taken:

(i)

$$\varepsilon_s = \varepsilon_{TOT} - \varepsilon_p \tag{4.15}$$

where, ε_s = elastic strain, ε_{TOT} = total strain and ε_p = plastic strain.

(ii) In the range where the total strain in the concrete is below the strain hardening of concrete $\varepsilon_{TOT} < \varepsilon_H$

$$\sigma_{max} = \sigma_y \tag{4.16}$$

where, σ_{max} = minimum stress in the steel and σ_y = stress in the steel at yield

(iii) In case the case where the total strain is less than the yield stain of steel $\varepsilon_{TOT} < \varepsilon_y$

$$\sigma_{max} = \sigma_y + (\varepsilon_{TOT} - \varepsilon_H)H \tag{4.17}$$

where, ε_H = strain hardening of the steel and H = Modulus of Hardening

(iv) In all other cases the steel is taken to have ruptured

$$\sigma_{max} = 0 \tag{4.18}$$

(v) In the case $\sigma_s > \sigma_{max}$ then

$$\sigma_s = \sigma_{\max} \tag{4.19}$$

$$\varepsilon_s = \sigma_{\max} / E_s \tag{4.20}$$

$$\varepsilon_p = \varepsilon_{TOT} - \varepsilon_s \tag{3.21}$$

where E_s = Young's Modulus of Steel and H = Modulus of Hardening

(vi) In the case $\sigma_s < \sigma_{min}$ then

$$\sigma_s = \sigma_{\min} \tag{4.22}$$

$$\varepsilon_s = \sigma_{\min} / E_s \tag{4.23}$$

$$\varepsilon_p = \varepsilon_{TOT} - \varepsilon_s \tag{3.24}$$

4.3.3 Numerical modelling of Moment-Curvature relation

The beam cross section is divided into a number of segments, *N*. The size of each segment is taken as

$$\Delta x = \frac{d}{N} \tag{4.25}$$

where N is the number of segments, which was taken to be 3000.

The value of κ is initially set. For this value of κ, the value of x, the distance of the neutral axis to the tensile reinforcement, is computed such that the tensile force in the steel, f_s equals the compressive force in the concrete, f_c.

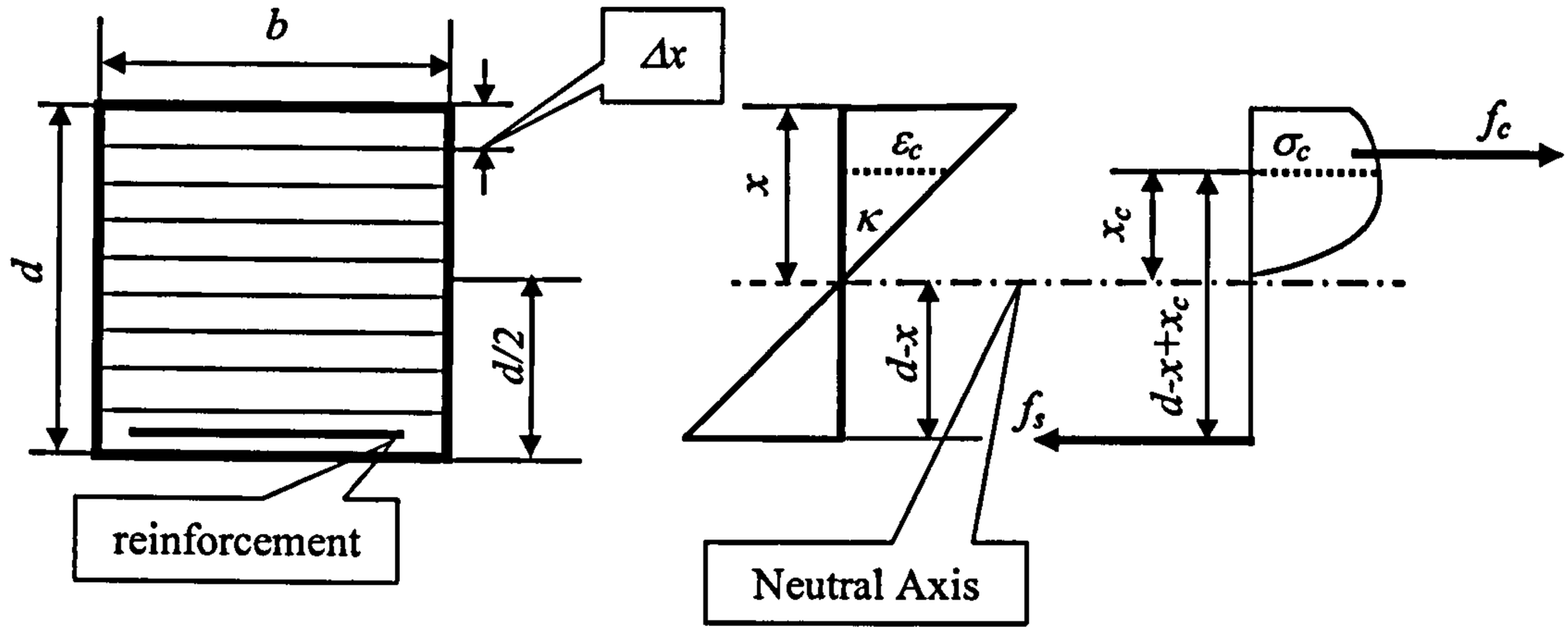

Figure 4.8 Concrete beam cross section with stress and strain blocks

The position of x for each value of κ can be calculated in one of either two methods. The first is regular falci. If it is assumed that the position of x is at the top of the beam cross section (Figure 4.9) i.e. at x_n, then the concrete force, f_c will be equal to zero.

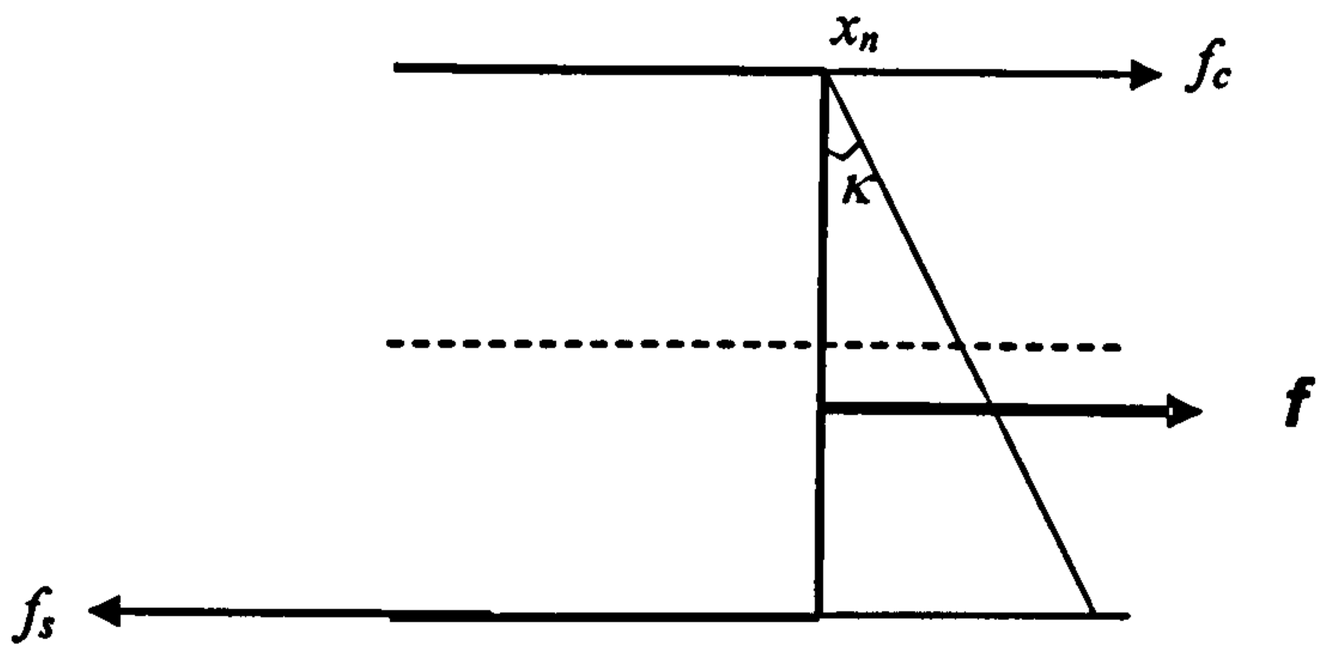

Figure 4.9 Force in the concrete is zero

Since

$$f_c = 0 \tag{4.26}$$

the resulting force, f will be less than zero as the concrete force, f_c is equal to zero.

$$f = (f_c - f_s) < 0 \tag{4.27}$$

If it is assumed that the position of x is at the bottom of the beam cross section i.e. at x_p, then the force in the steel, f_s will equal zero (Figure 4.10).

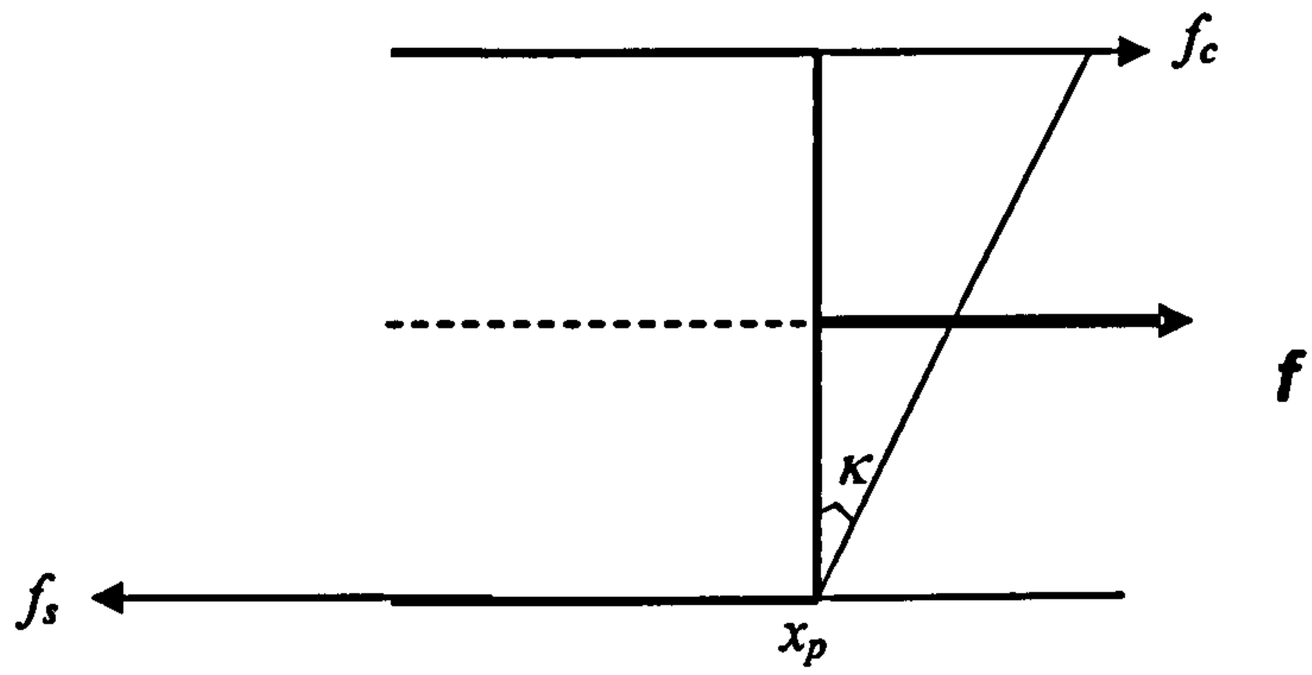

Figure 4.10 Force in the steel is zero

Since

$$f_s = 0 \tag{4.28}$$

The resulting force is greater than zero as given by

$$f = (f_c - f_s) > 0 \tag{4.29}$$

Hence the equilibrium position of x, where $f_c = f_s$, lies in between the two extremes. Thus for the first iteration it is assumed, where ε_{av} is initially supplied as zero.

$$x = d - \frac{\varepsilon_{av}}{\kappa} \tag{4.30}$$

The total strain is found then as

$$\varepsilon_{total} = \kappa(d - x) \tag{4.31}$$

Hence using this value of strain the corresponding value of stress, σ_s can be calculated from the stress strain function for steel. The force in the steel becomes

$$f_s = \sigma_s A_s \tag{4.32}$$

To account for the effect of compression steel the distance of the compression steel to the neutral axis is given by

$$d_{na} = x - d_{cr} \tag{4.33}$$

Therefore the strain in the compression steel is given by

$$\varepsilon_{tc} = -\kappa d_{na} \tag{4.34}$$

The stress strain relationship of the steel is used to obtain the corresponding stress in the steel, σ_{cs} Thus the force in the compression steel is worked out from

$$f_{cs} = \sigma_{sc} A_{cs} \tag{4.35}$$

The contribution provided by the steel top the total moment, M_{cs} is then found from

$$M_{cs} = d_{na} f_{cs} \tag{4.36}$$

The new value of the x_c is now found from

$$x_c = x - 0.5dx \tag{4.37}$$

The strain in the concrete, ε_c, for each segment is given by

$$\varepsilon_c = x_c \kappa \tag{4.38}$$

The corresponding stress is given by the stress strain relationship for concrete Thus for the same segment the force in the concrete is given by

$$f_c = \sigma_c b \Delta x \tag{4.39}$$

Hence the contribution of the concrete to the total moment is found from the summation of the forces for each segment multiplied by the lever arm as given by

$$\sum_{i=0}^{N} M = f_c(x_c + d - x) = \sigma_c b(x_c + d - x)\Delta x \tag{4.40}$$

The new value of strain is now calculated from the strain velocity, ε_v

$$\varepsilon_v = f \times \Delta t \tag{4.41}$$
$$\varepsilon_{av} = \varepsilon_v \times \Delta t$$

A new value of x_c is now obtained using equation (4.30).When the force and stresses in the concrete are calculated, the total force, f is then found as

$$f = f_c - f_s - f_{cs} \tag{4.42}$$

The second method of obtaining the position of x is by use of dynamic relaxation.

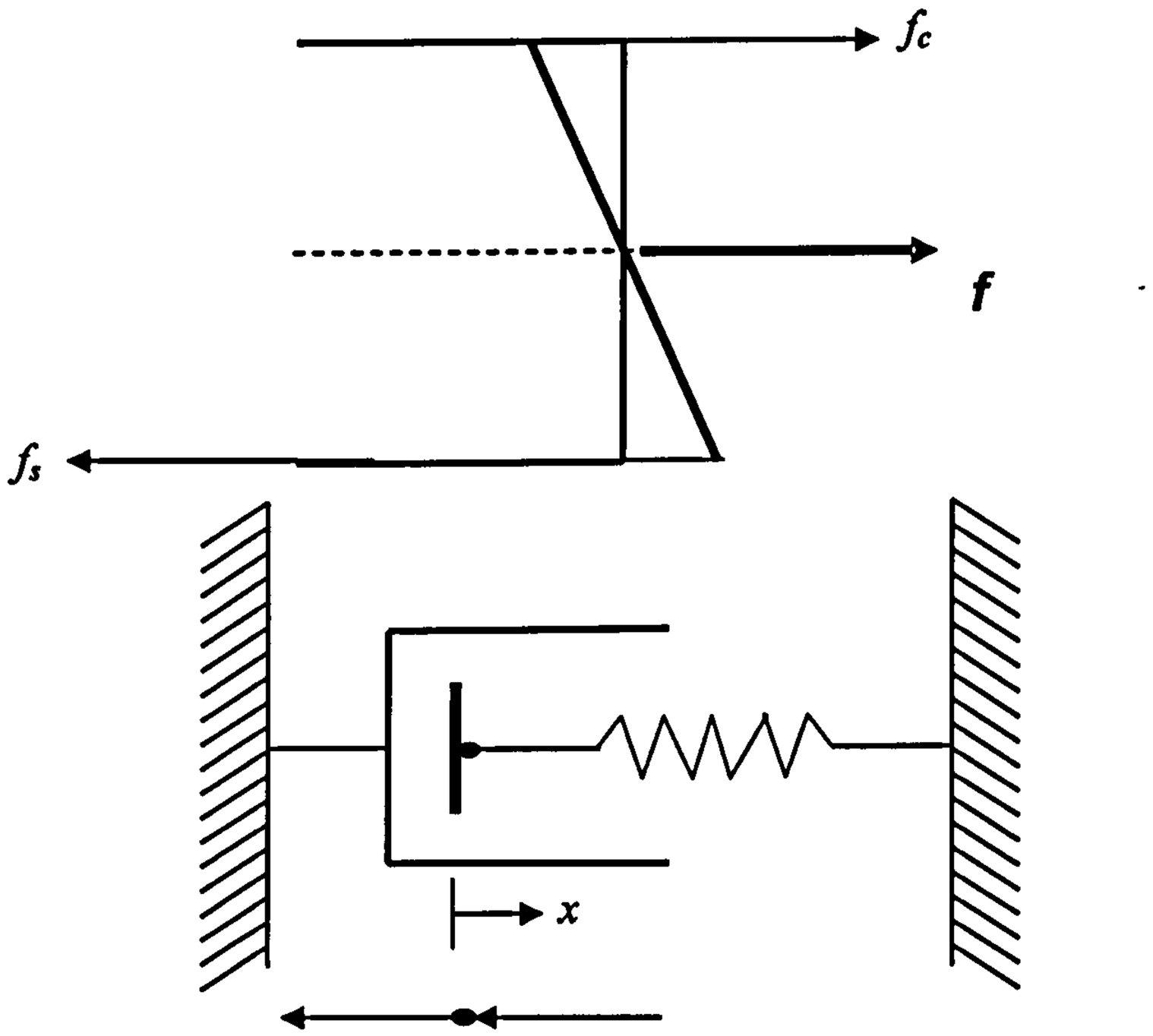

Figure 4.11 Rheological model: spring dashpot model

The force is related to the average strain rate by the damping constant c as given by

$$f = c\dot{\varepsilon}_{av} \tag{4.43}$$

This can be written in the form

$$f = c\frac{d\varepsilon_{av}}{dt} \tag{4.44}$$

Which reduces to

$$\frac{f}{c} = \dot{\varepsilon}_{av} \tag{4.45}$$

Hence

$$\Delta\varepsilon_{av} = \frac{f}{c}\Delta t \tag{4.46}$$

Thus the new

$$\Delta\varepsilon_{av(new)} = \Delta\varepsilon_{av(old)} - \frac{f}{c}\Delta t \tag{4.47}$$

Hence the strain is found from summing the individual strains for each of the segments

$$\sum_{i=0}^{N}\varepsilon_{av} = \frac{f}{c}\Delta t \tag{4.48}$$

The time step,Δt is calculated from

$$\Delta t = \sqrt{\frac{1}{bdE}} \tag{4.49}$$

Where E is the modulus of concrete and was taken as 20.5 N/mm^2.

The time step has to be within the following limits to provide a stable solution

$$\Delta t < \frac{c}{k} \tag{4.50}$$

The forces is found by summing the individual forces over the whole of the cross section

$$\sum_{i=0}^{N} f = f_c - f_s \tag{4.51}$$

The value of ε_{av} will be seen to converge to the correct value from which the value of x at which equilibrium of forces exists, can be calculated. This is shown in Figure 4.12

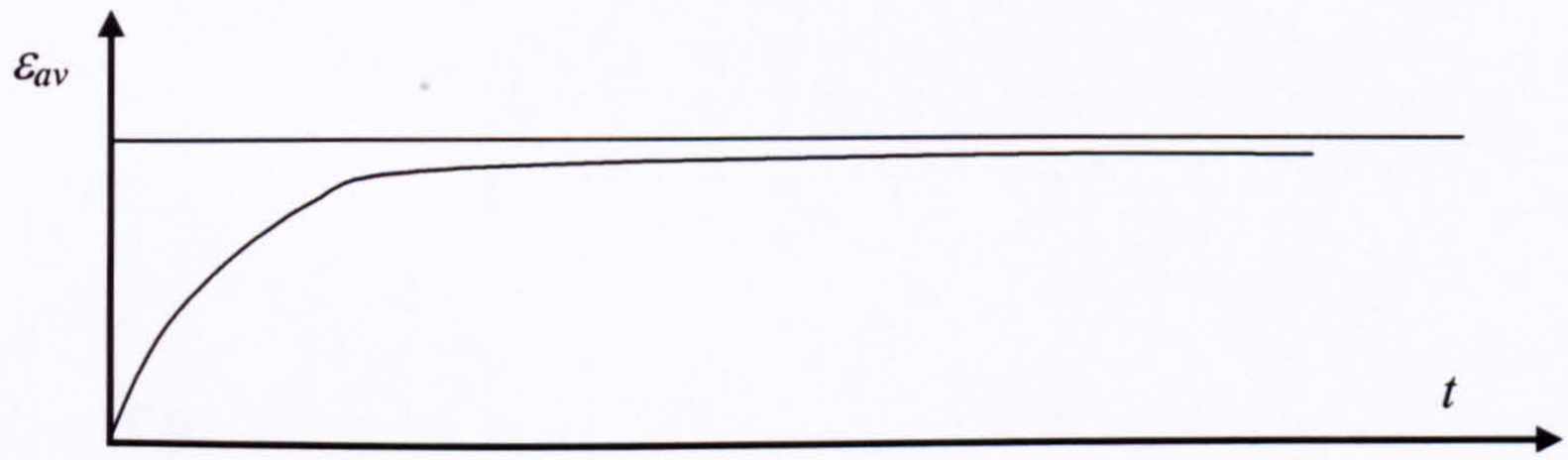

Figure 4.12 Convergence to give ε_{av}

The resulting moment curvature curve is shown in Figure 4.13

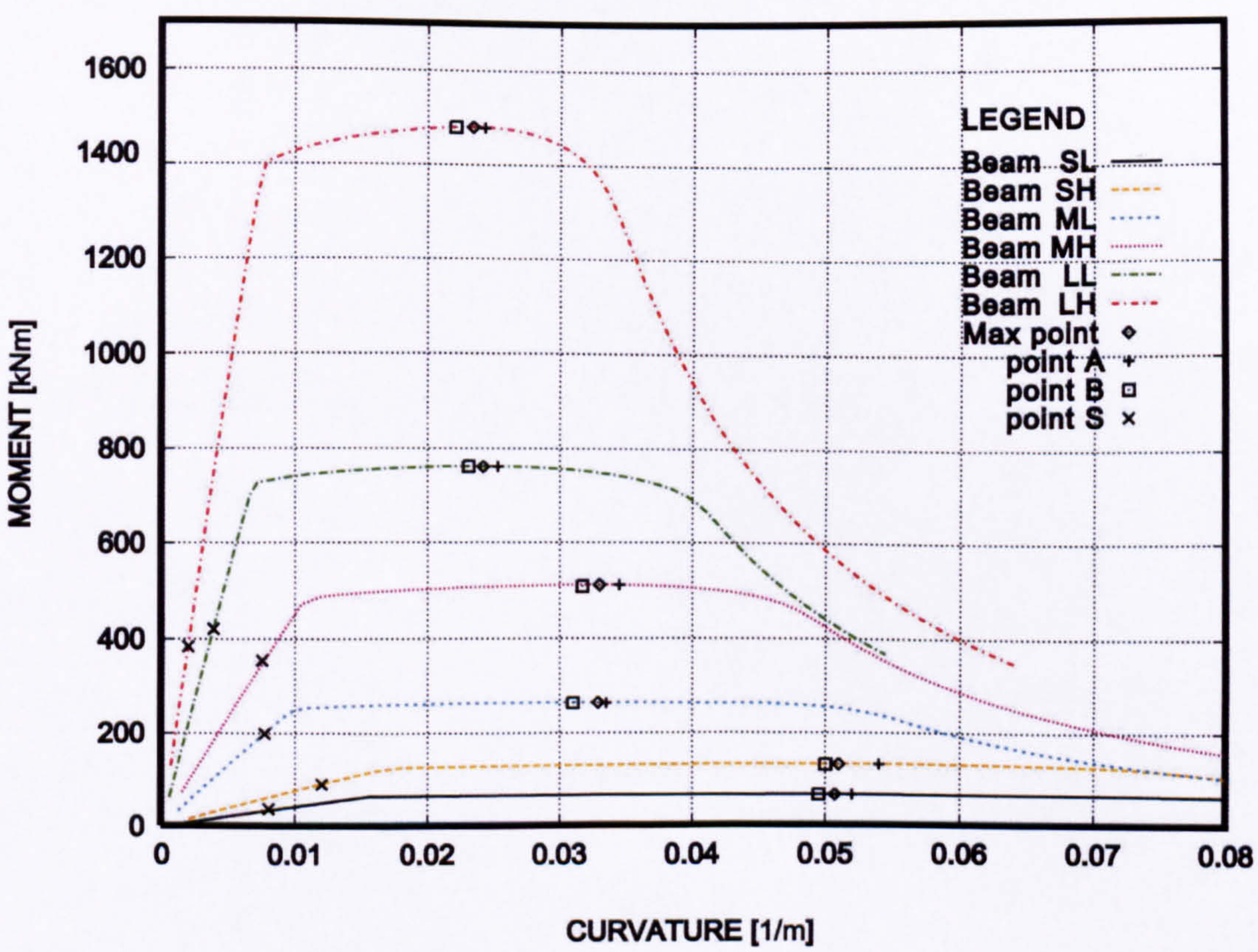

Figure 4.13 Moment - Curvature relation

4.3.4 Moment Rotation relationship

The rotation was measured a distance of $3.7d$ across the centre line of the beam, where d is the depth of the beam.

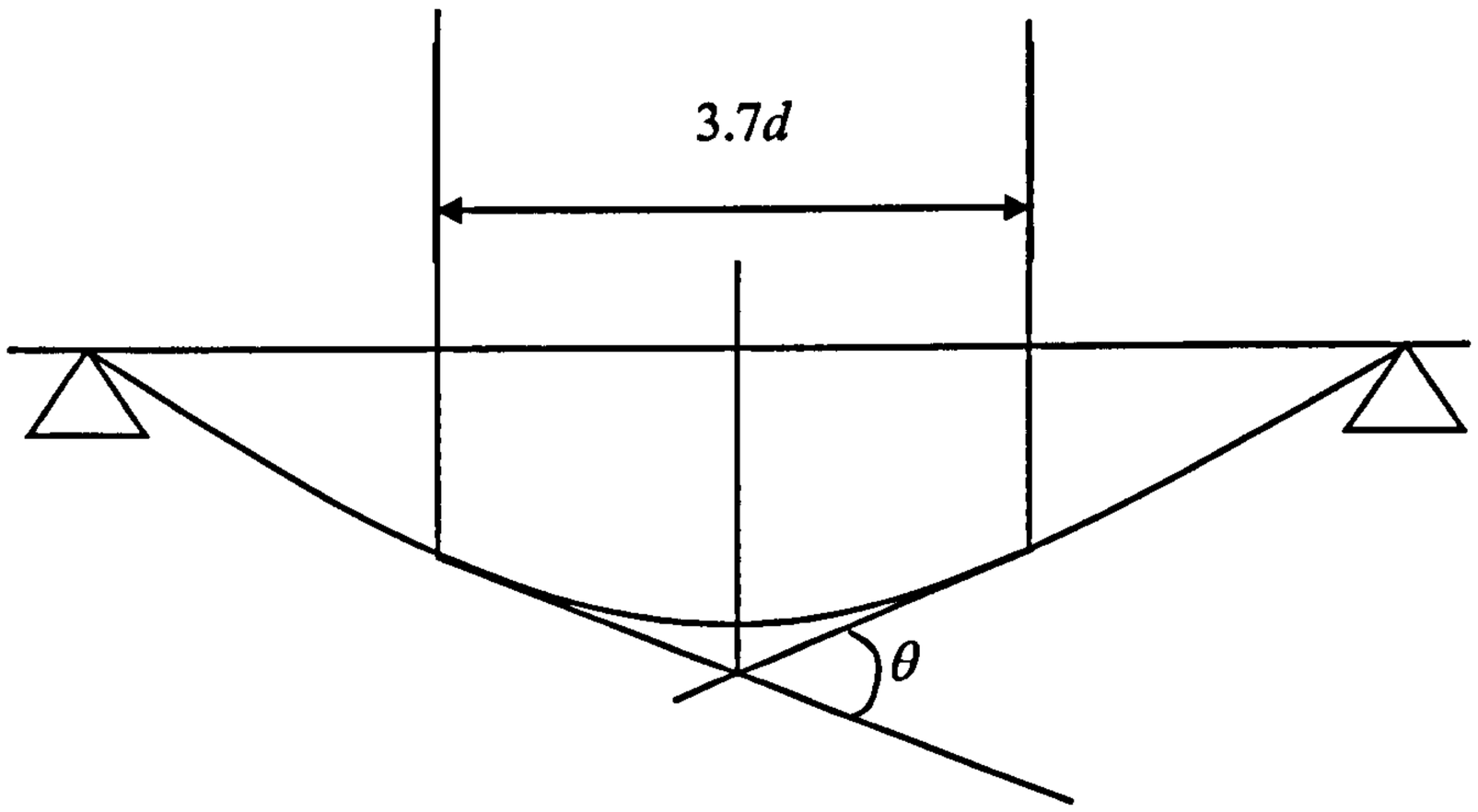

Figure 4.14 Distance across which rotation of the beam was measured

The distance along which the rotation is measured is divided into a number of segments, n, between a minimum value of x and a maximum value of x (Figure 4.15).

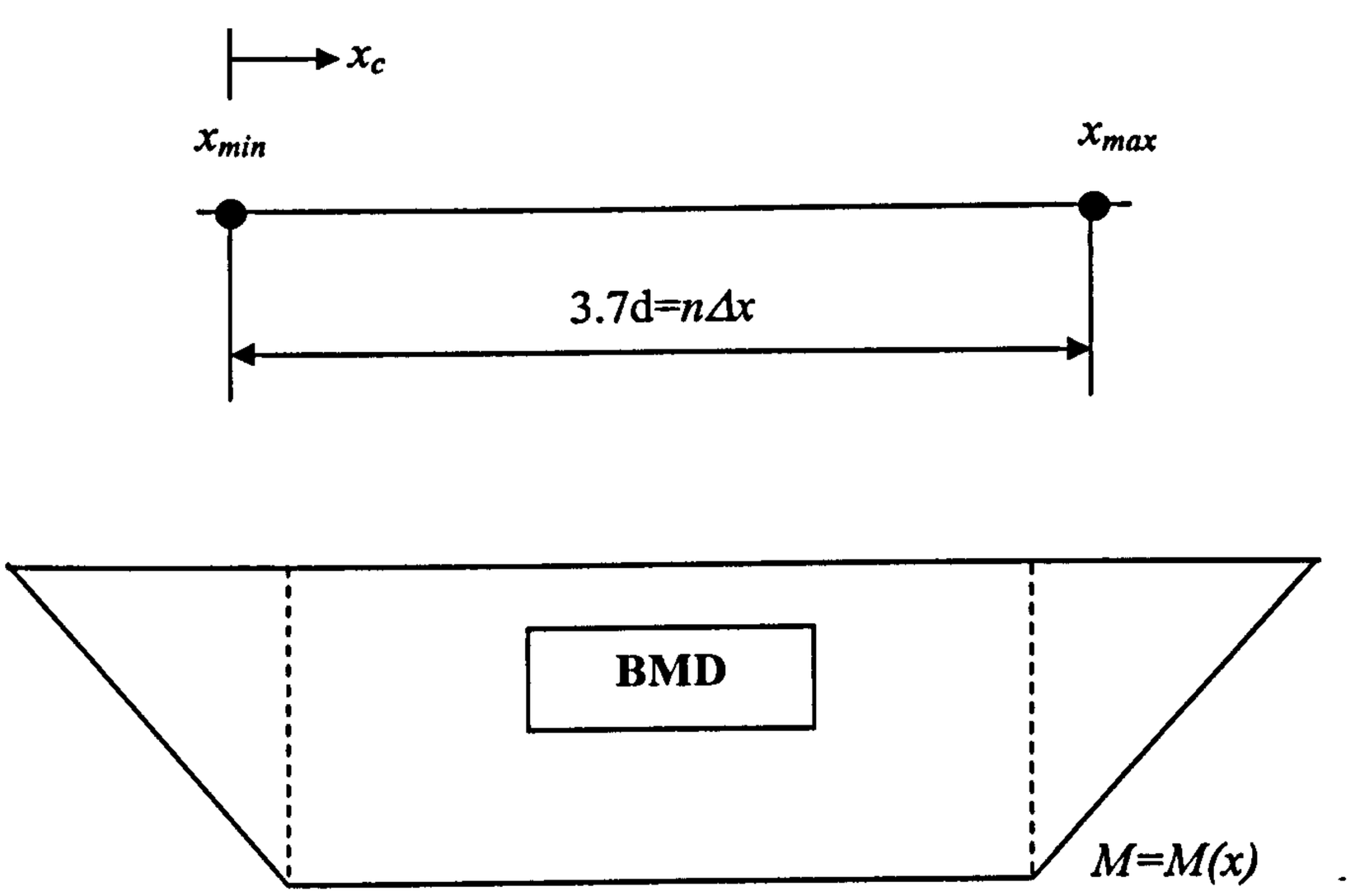

Figure 4.15 Beam bending moment function for

The size of the segment. Δx is then calculated from

$$\Delta x = \frac{x_{max} - x_{min}}{n} \tag{4.52}$$

The current value of x, x_c is then found from

$$x_c = x_{\min} + \frac{\Delta x}{2} \tag{4.53}$$

The current moment is then interpolated from the bending moment diagram.

The current value of curvature for this moment is then found from the inputted M-κ curve for each segment. Thus the total rotation is found by summation over the segments

$$\theta = \int_{x\min}^{x\max} \kappa(x)\, dx \tag{4.54}$$

The resulting moment-curvature and moment rotation curves are shown in Figure 4.16. As is seen there is good agreement between the experimental and the numerical results for the moment rotation curves.

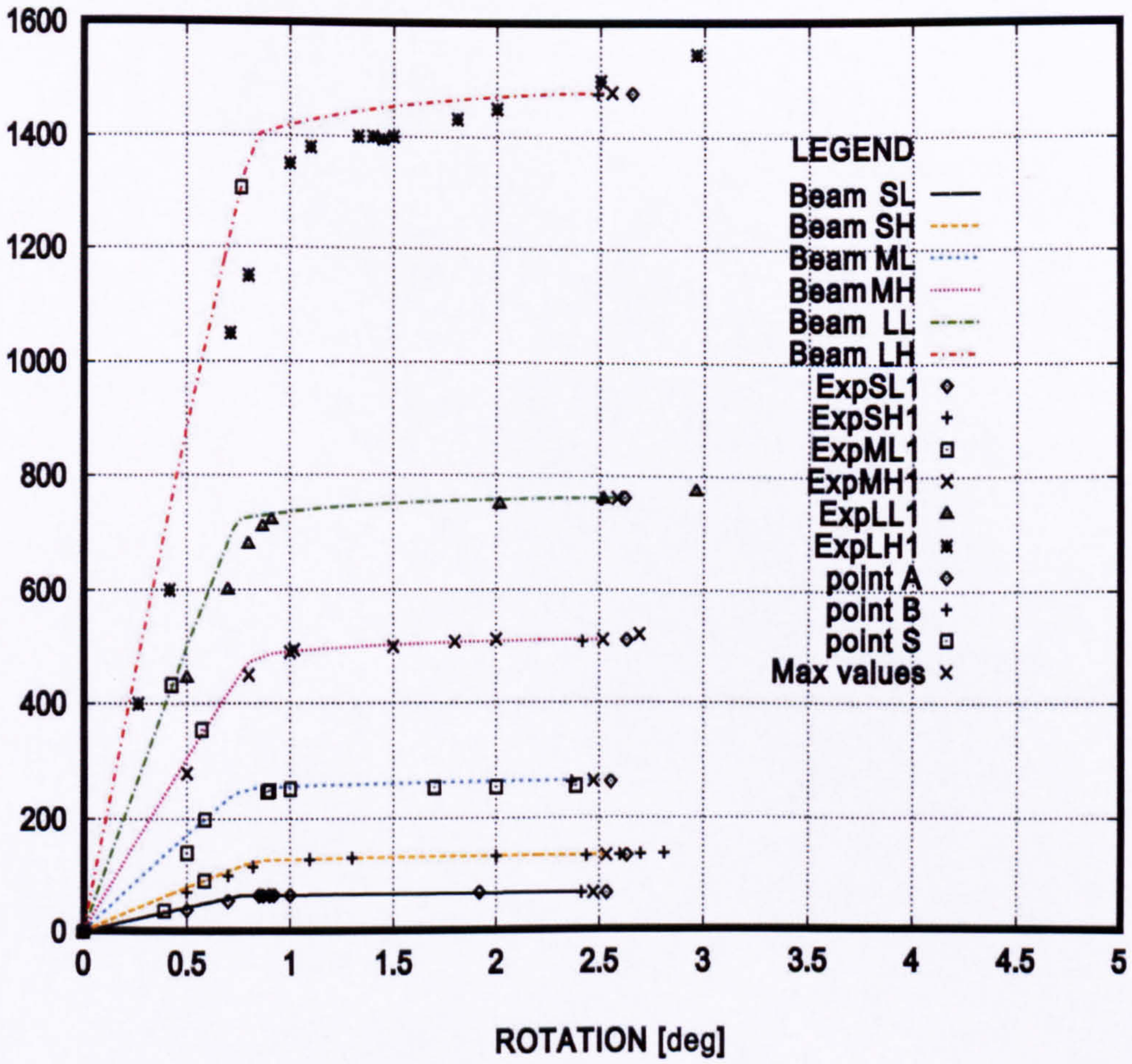

Figure 4.16 Moment rotation curves

4.3.5 Calculation of shear

A strip of width Δx is shown in Figure 4.17.

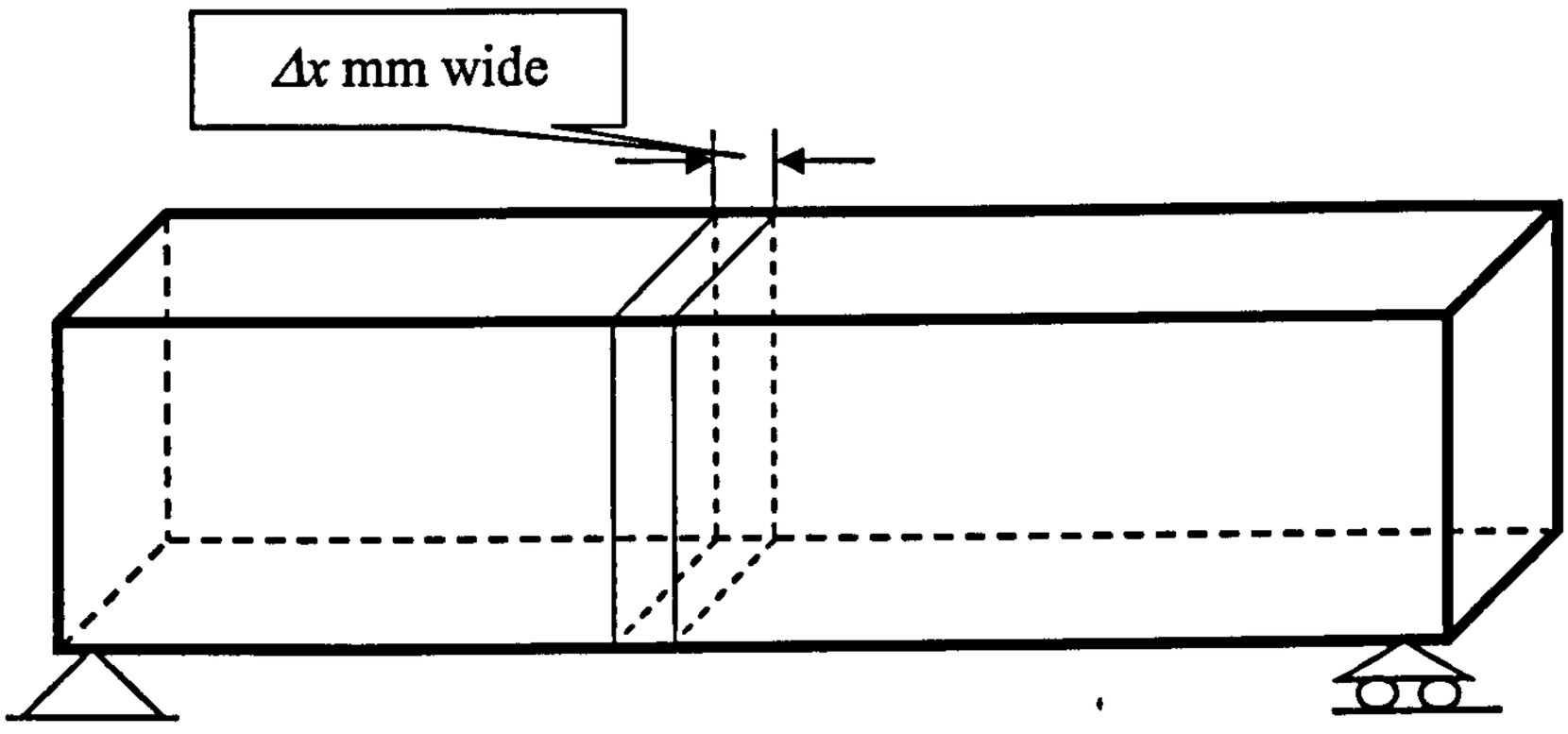

Figure 4.17 Strip of beam

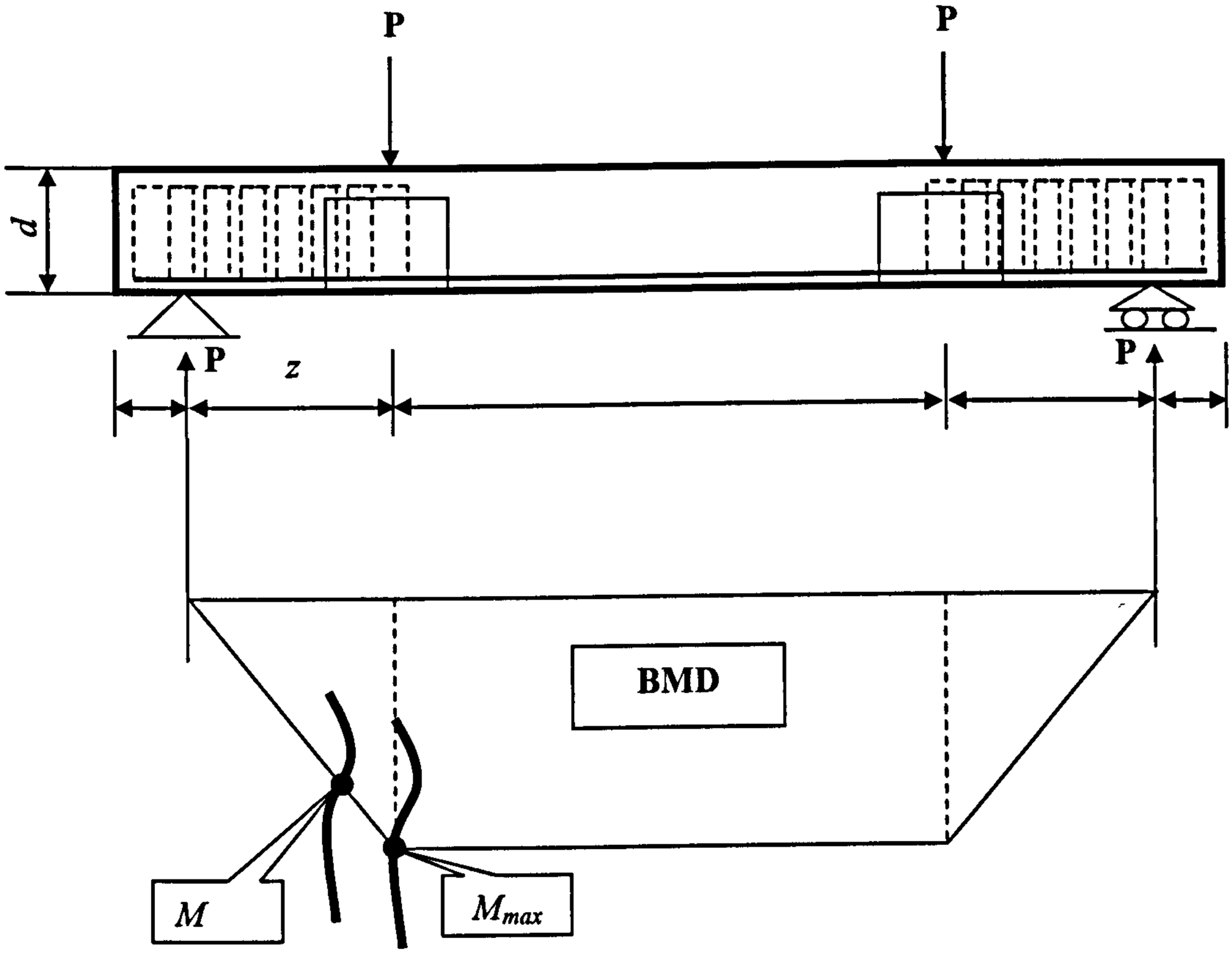

Figure 4.18 Bending moment across strip

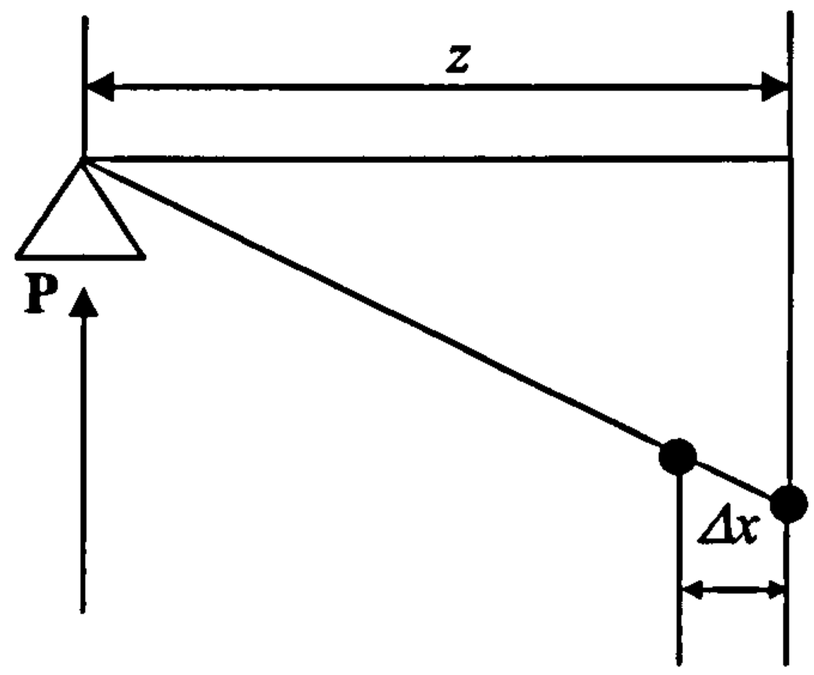

Figure 4.19 Partial bending moment diagram

The moments on either side of the strip are calculated as follows.

The maximum moment, M_{max} is given by

$$M_{\max} = Pz \tag{4.55}$$

The moment M is given by

$$M = P(z - dx) = M_{\max} - \frac{M_{\max}}{z}\Delta x \tag{4.56}$$

Each of these moments will result in a stress distribution on either side of the strip. However since the moments are unequal the stress distributions will also be unequal.

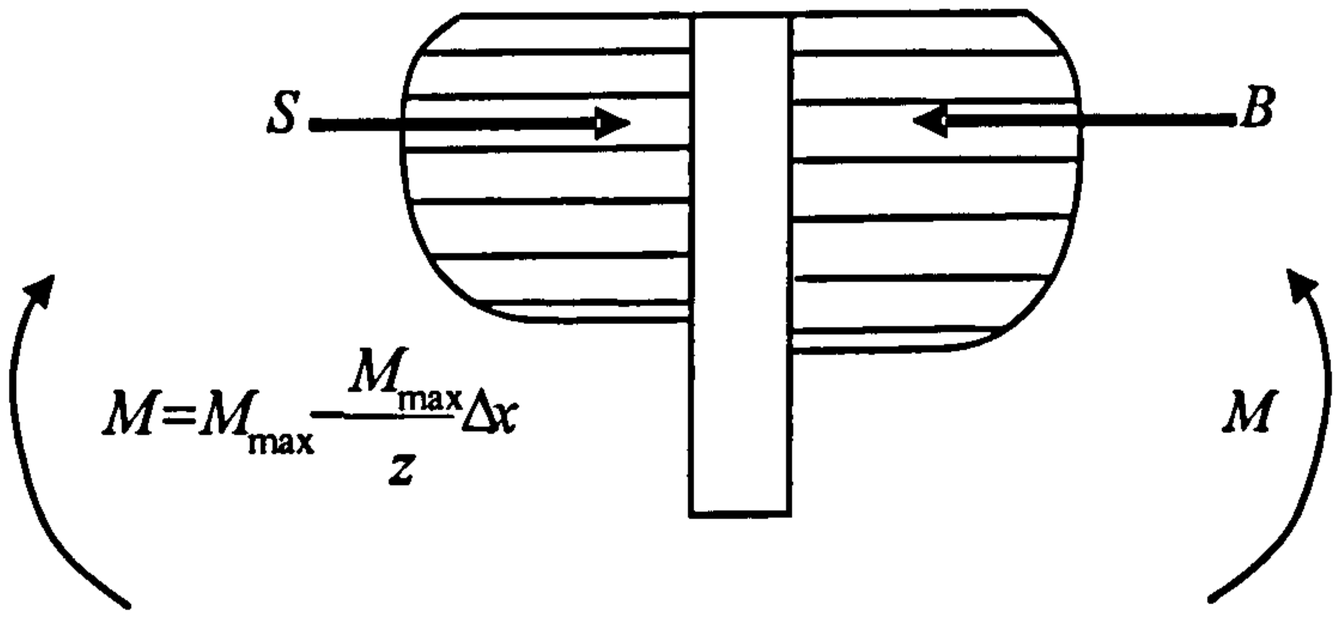

Figure 4.20 Stress distributions on either side of the strip

If the stress distribution is arbitrarily cut as shown in Figure 4.21.

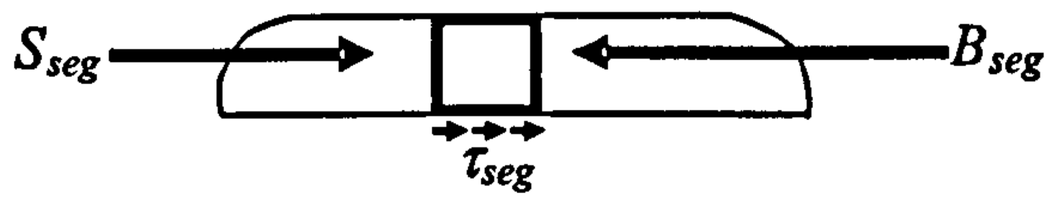

Figure 4.21 Arbitrary cut of stress distribution diagrams

The forces resulting from the stress distributions are given by

$$B = \sum B_{seg} = \int_0^N \sigma_B dA \tag{4.57}$$

$$S = \sum S_{seg} = \int_0^N \sigma_S dA$$

where dA is the area of the segment under consideration and N is the number of segments.

The total shear force, τ, is calculated from the following

$$\tau = \sum_0^N \left(\frac{B_{seg} - S_{seg}}{b\Delta x} \right) \tag{4.58}$$

The stress and strain distributions obtained from the numerical model are shown in Figure 4.22 to Figure 4.39.

Figure 4.22 shows the normal stress distribution for beam SL

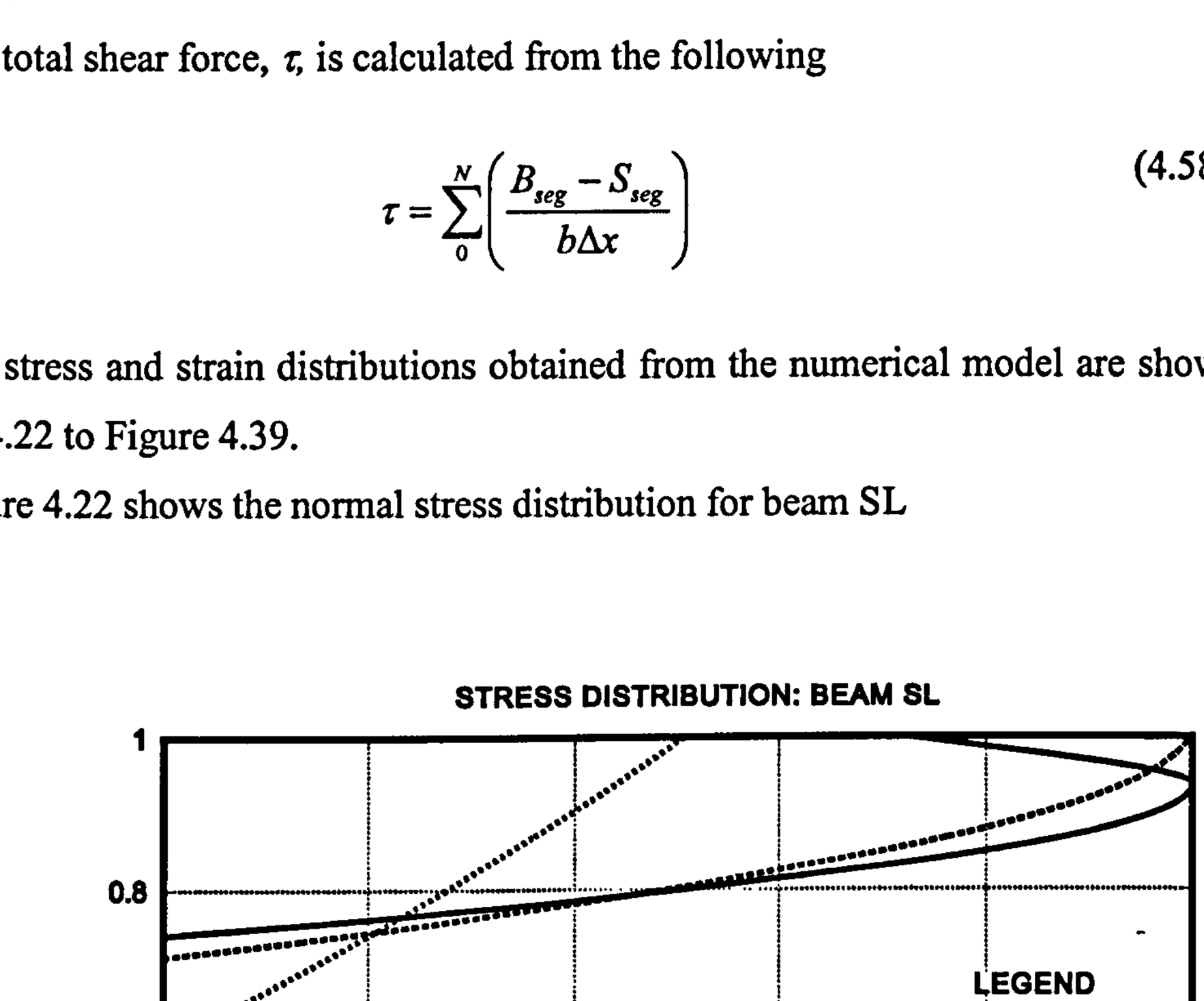

Figure 4.22 Normal stress distribution for beam SL

Figure 4.23 shows the normal stress distribution for beam SH

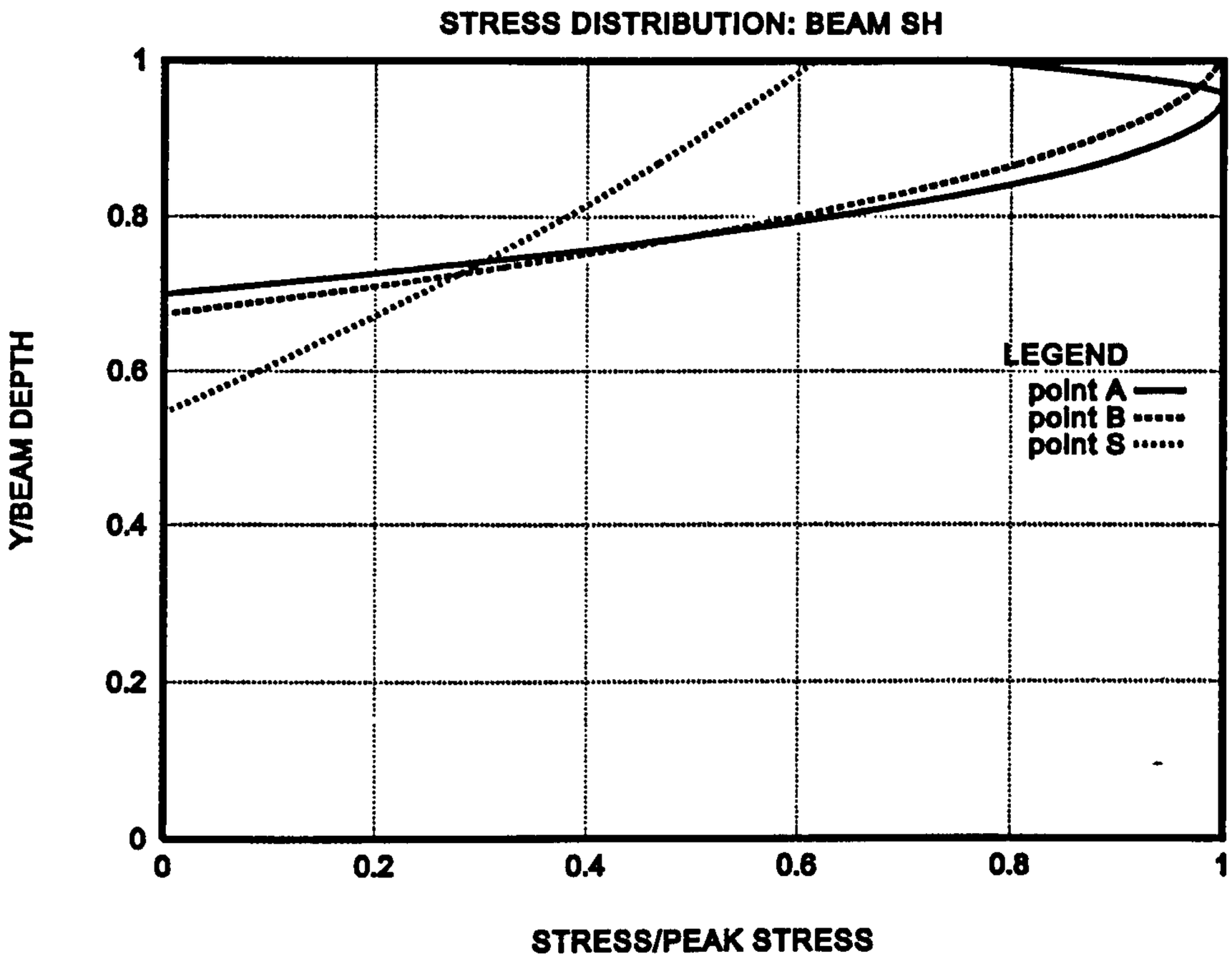

Figure 4.23 Normal stress distribution for beam SH

Figure 4.24 shows the normal stress distribution for beam ML

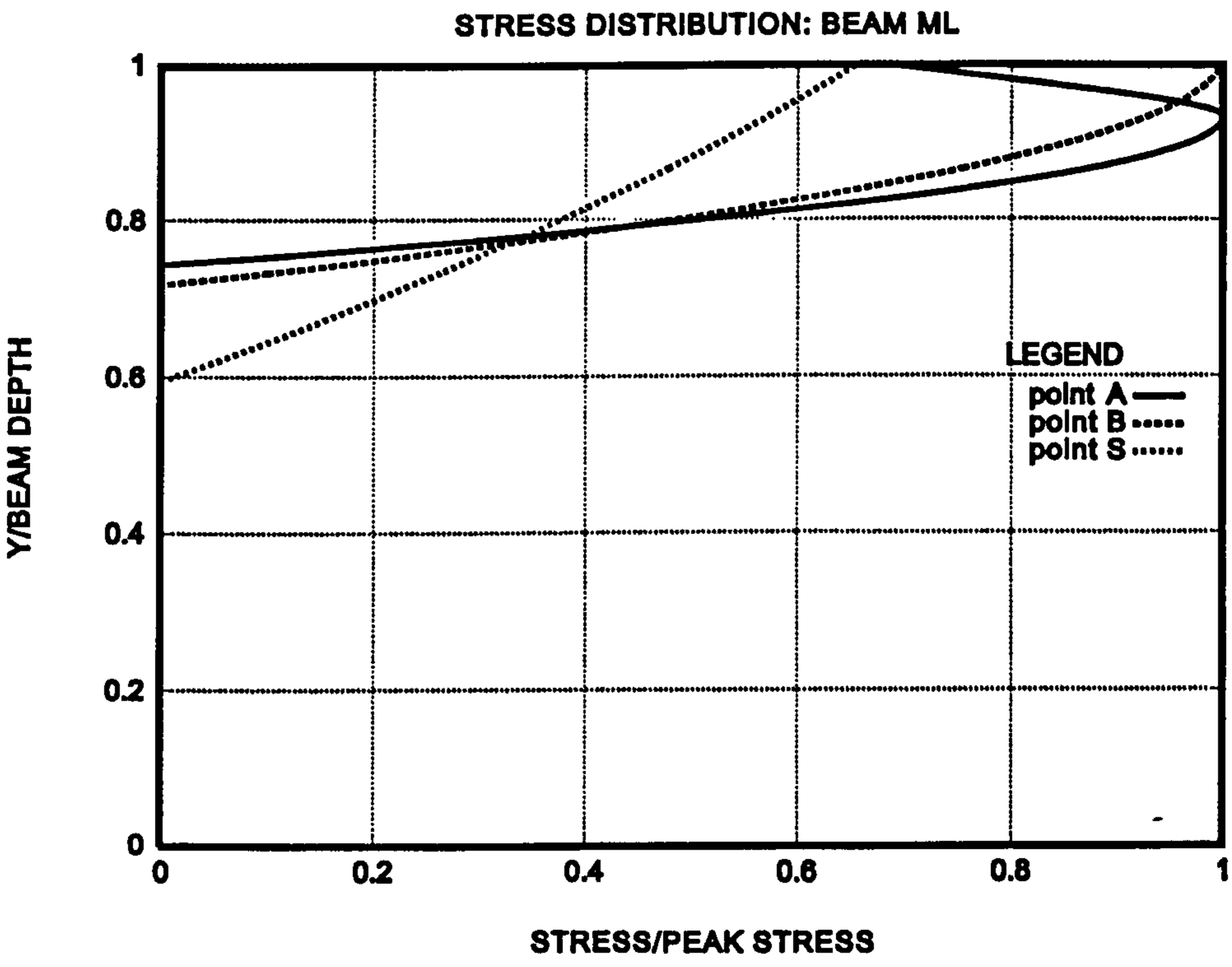

Figure 4.24 Normal stress distribution for beam ML

Figure 4.25 shows the normal stress distribution for beam MH

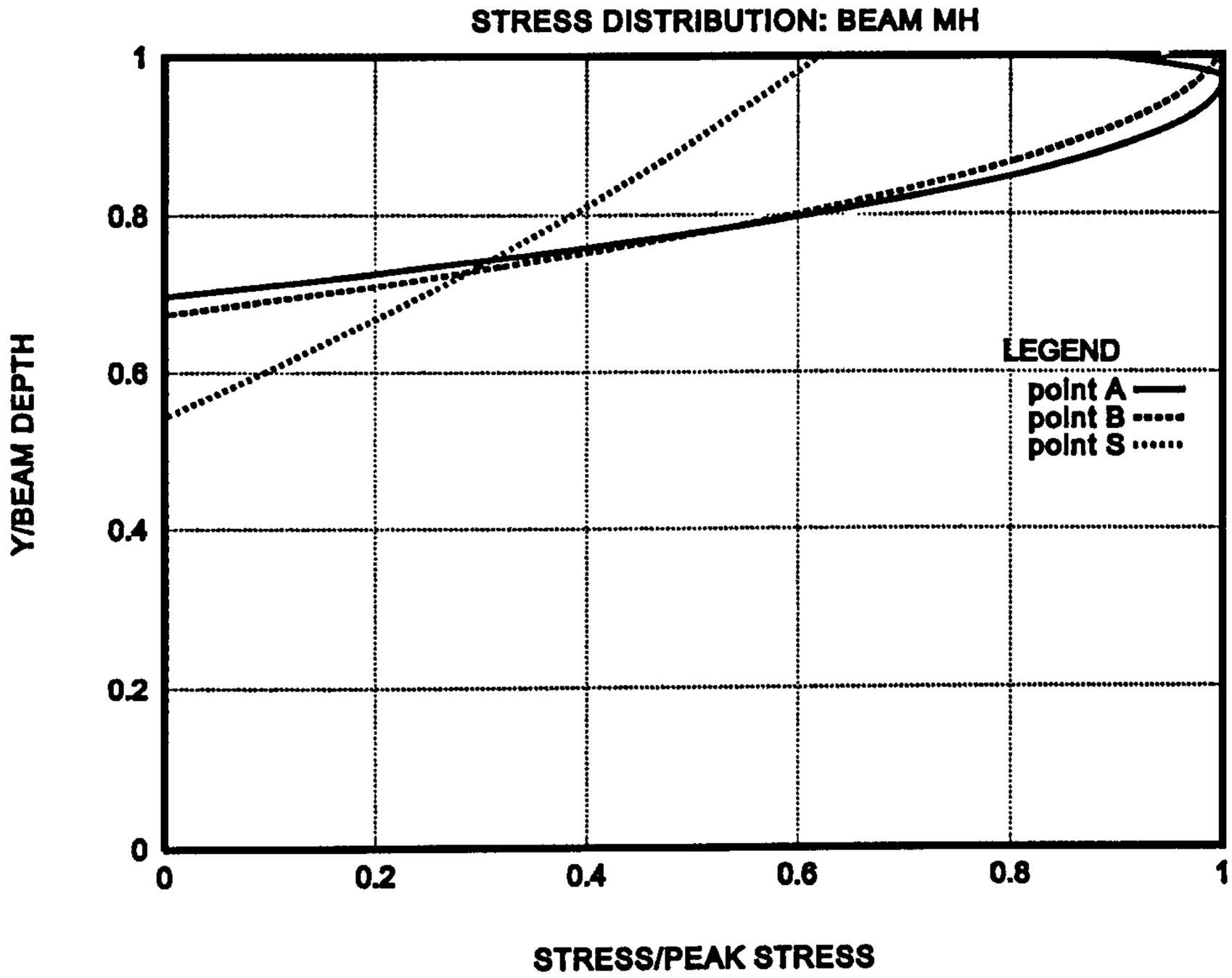

Figure 4.25 Normal stress distribution for beam MH

Figure 4.26 shows the normal stress distribution for beam LL

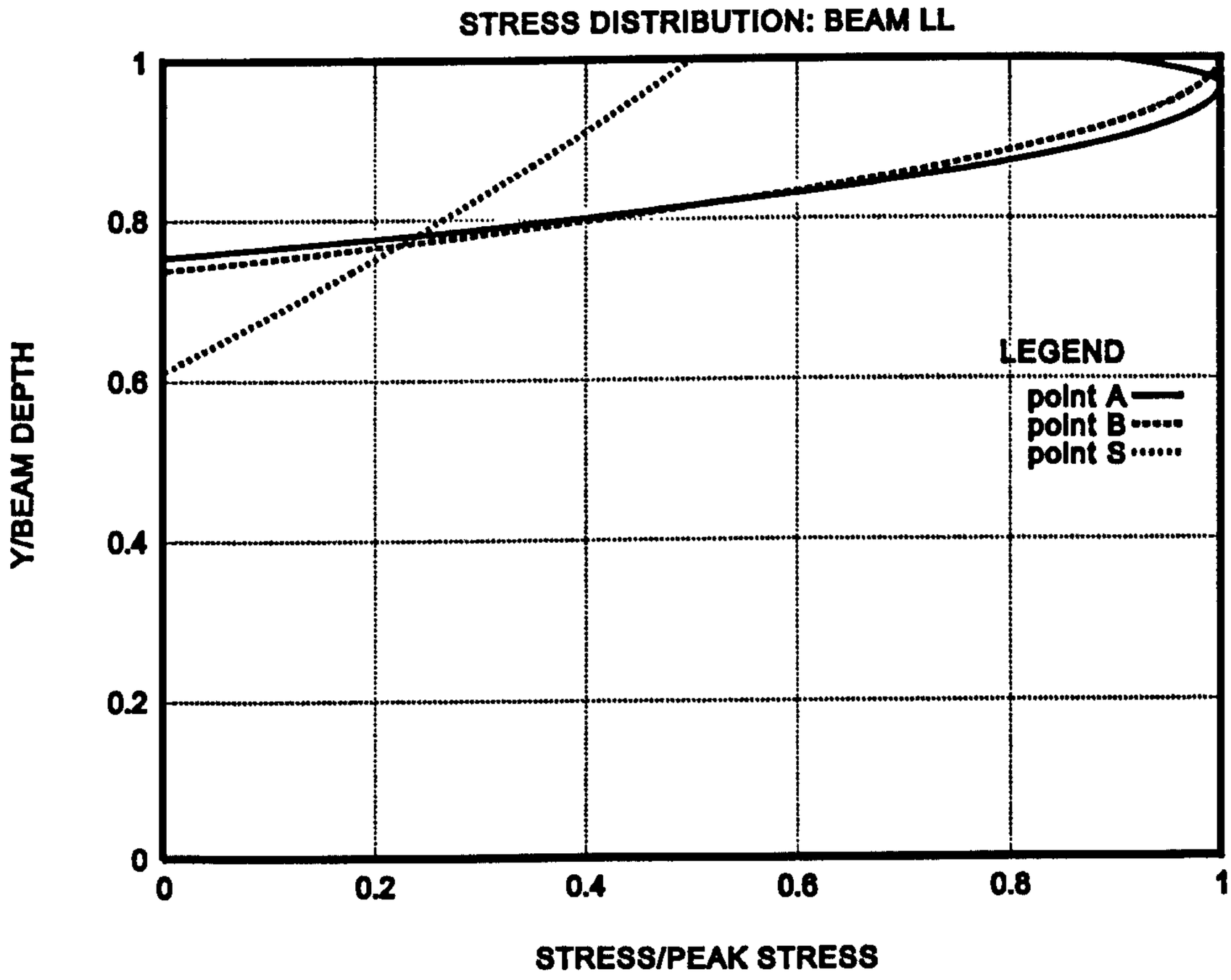

Figure 4.26 Normal stress distribution for beam LL

Figure 4.27 shows the normal stress distribution for beam LH

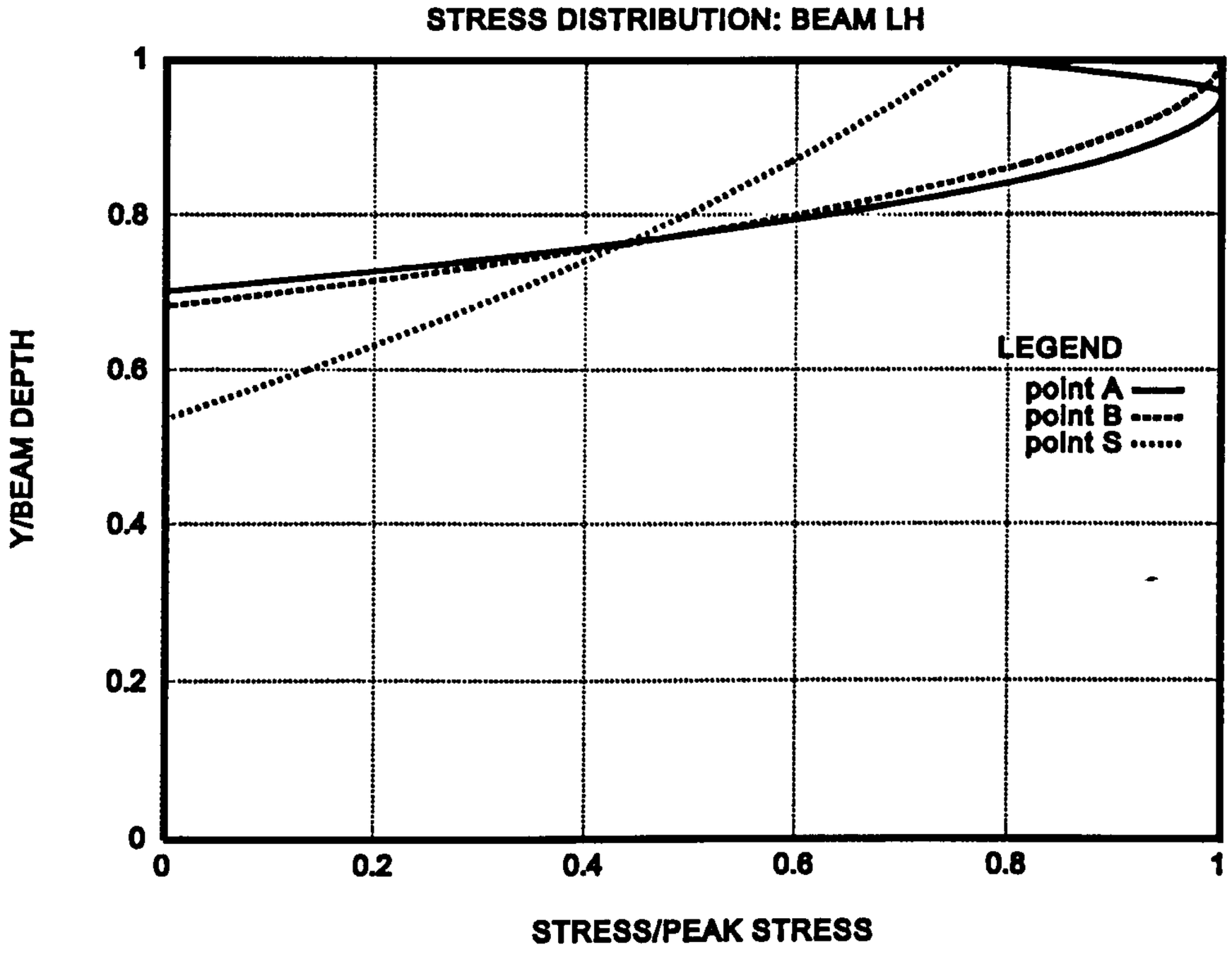

Figure 4.27 Normal stress distribution for beam LH

From Figure 4.22 to Figure 4.27 it is seen that at point B no softening in the compression zone of the concrete is evident. However at point A softening seems to be apparent.

Figure 4.28 shows the shear stress plots for points S and B for beam SL

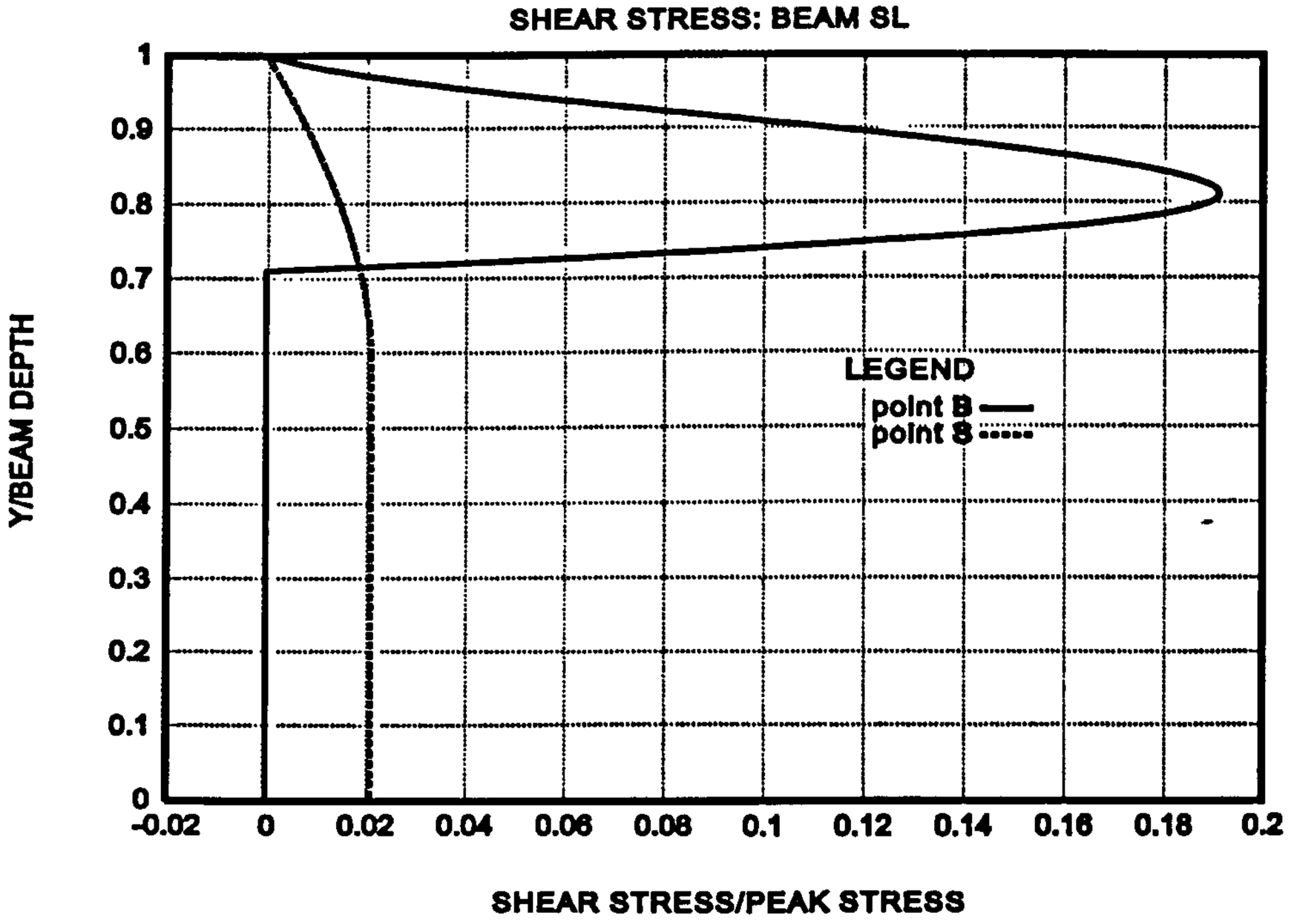

Figure 4.28 Shear stress distribution for points S and B for beam SL

Figure 4.29 shows the shear stress plots for points S and B for beam SH

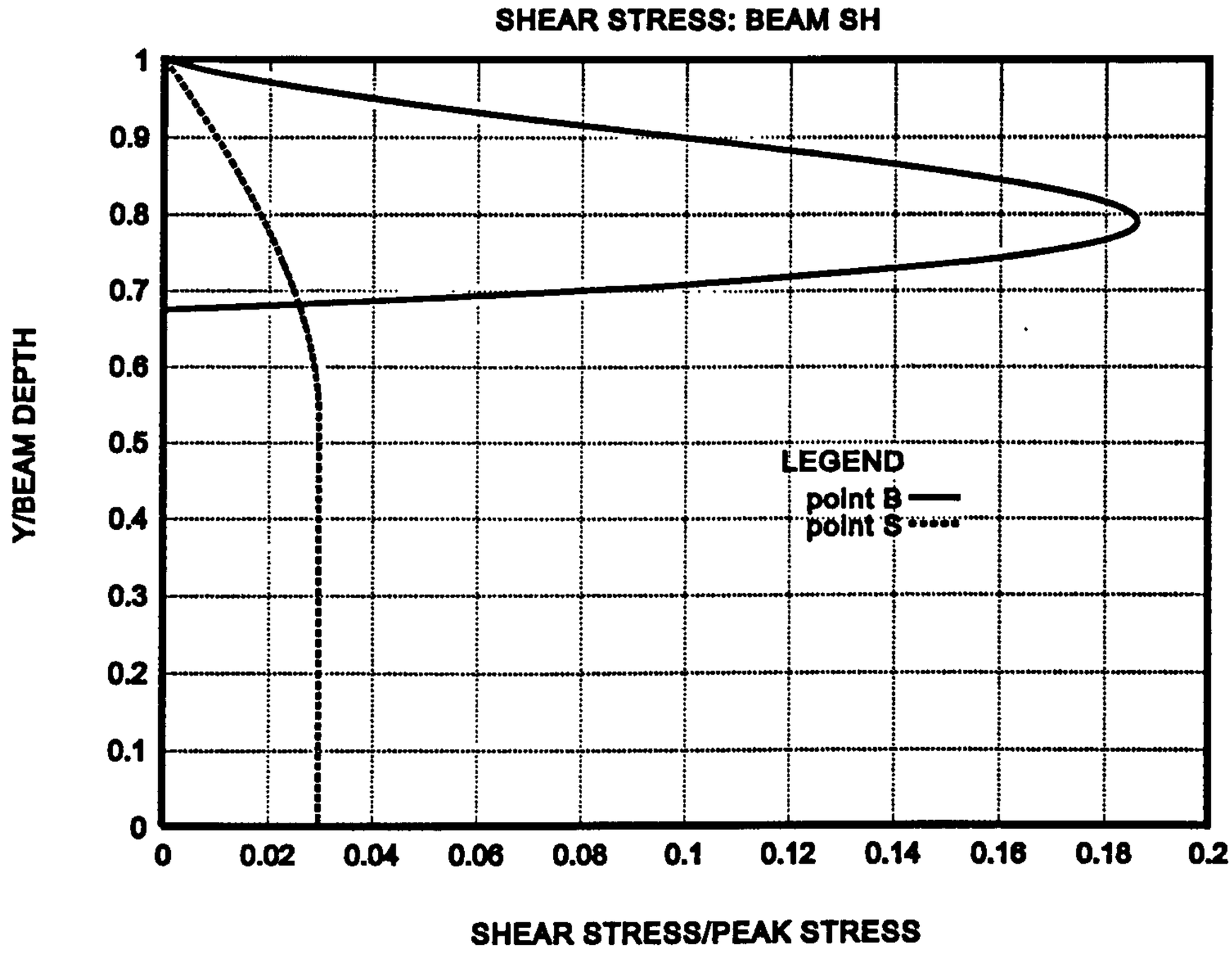

Figure 4.29 Stress distribution for points S and B for beam SH

Figure 4.30 shows the shear stress plots for points S and B for beam ML

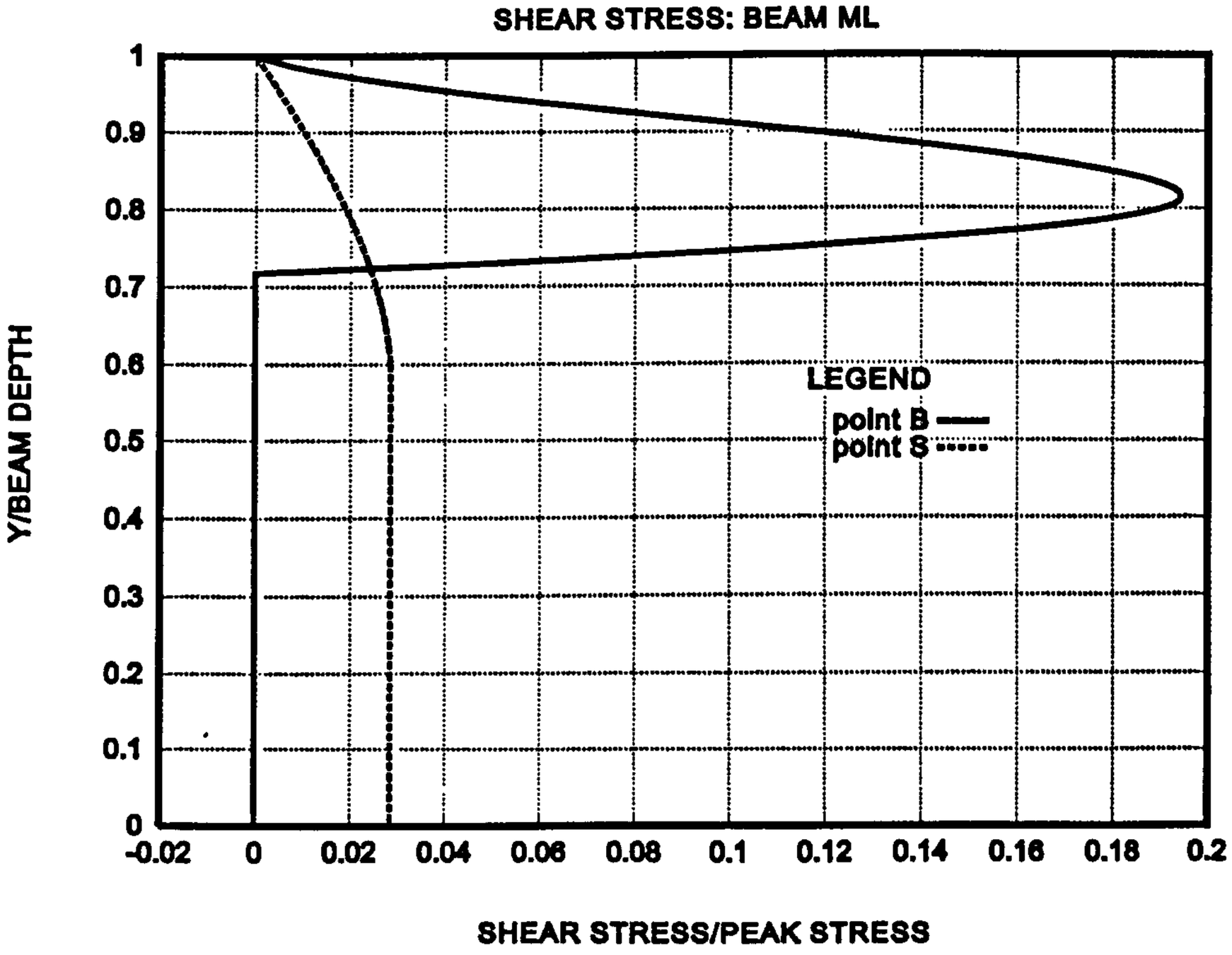

Figure 4.30 Stress distribution for points S and B for beam ML

Figure 4.31 shows the shear stress plots for points S and B for beam MH

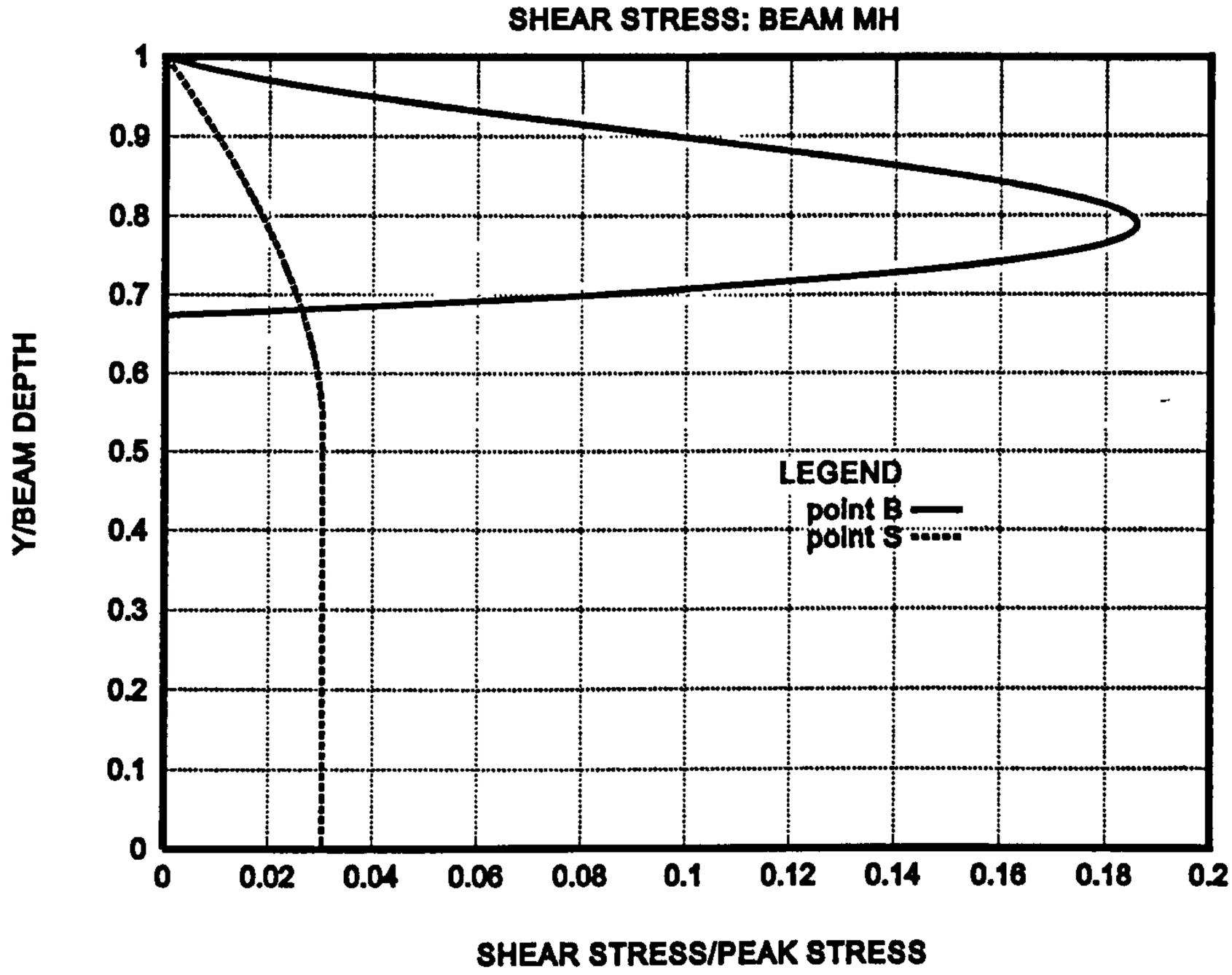

Figure 4.31 stress distribution for points S and B for beam MH

Figure 4.32 shows the shear stress plots for points S and B for beam LL

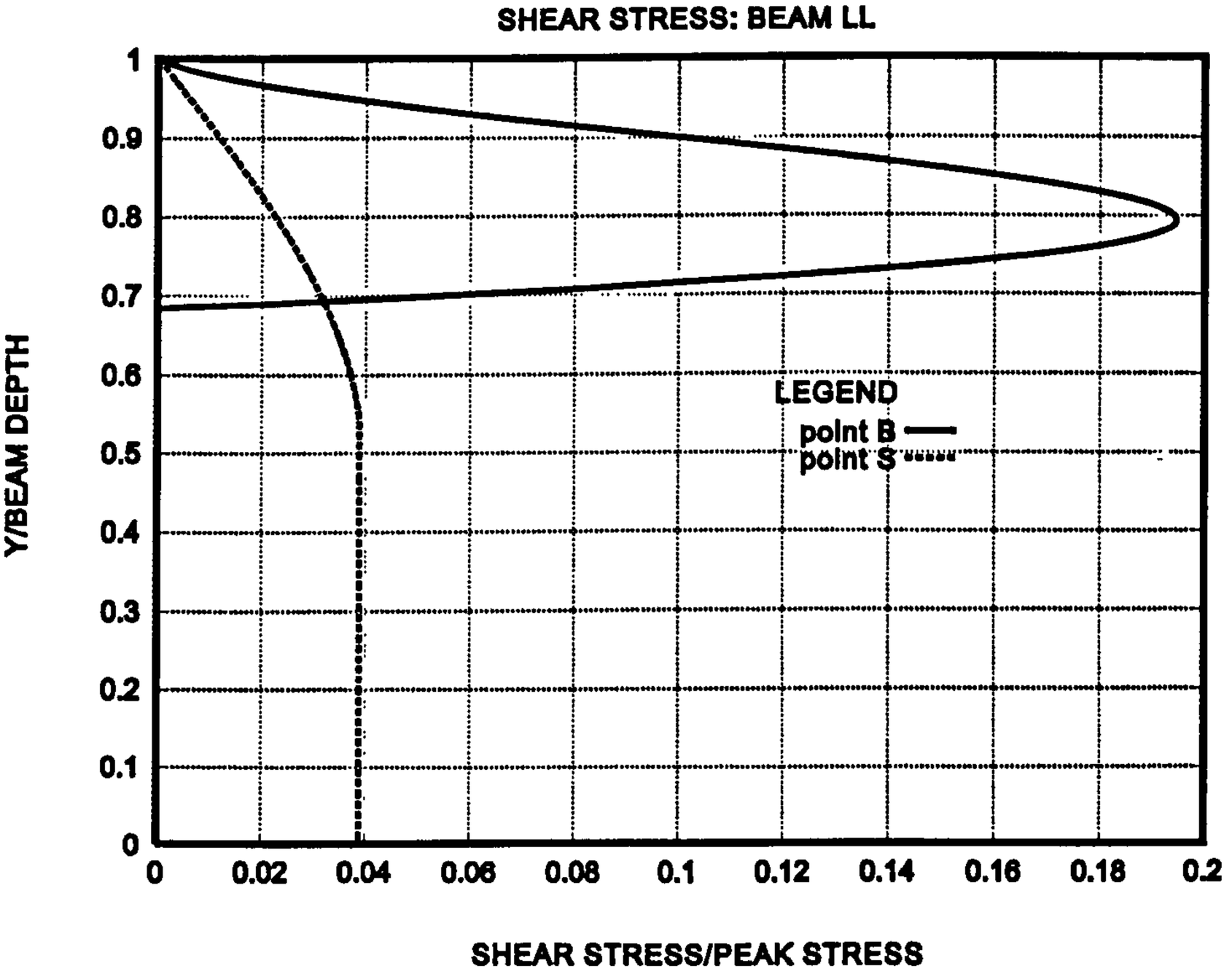

Figure 4.32 Stress distribution for points S and B for beam LL

Figure 4.33 shows the shear stress plots for points S and B for beam LH

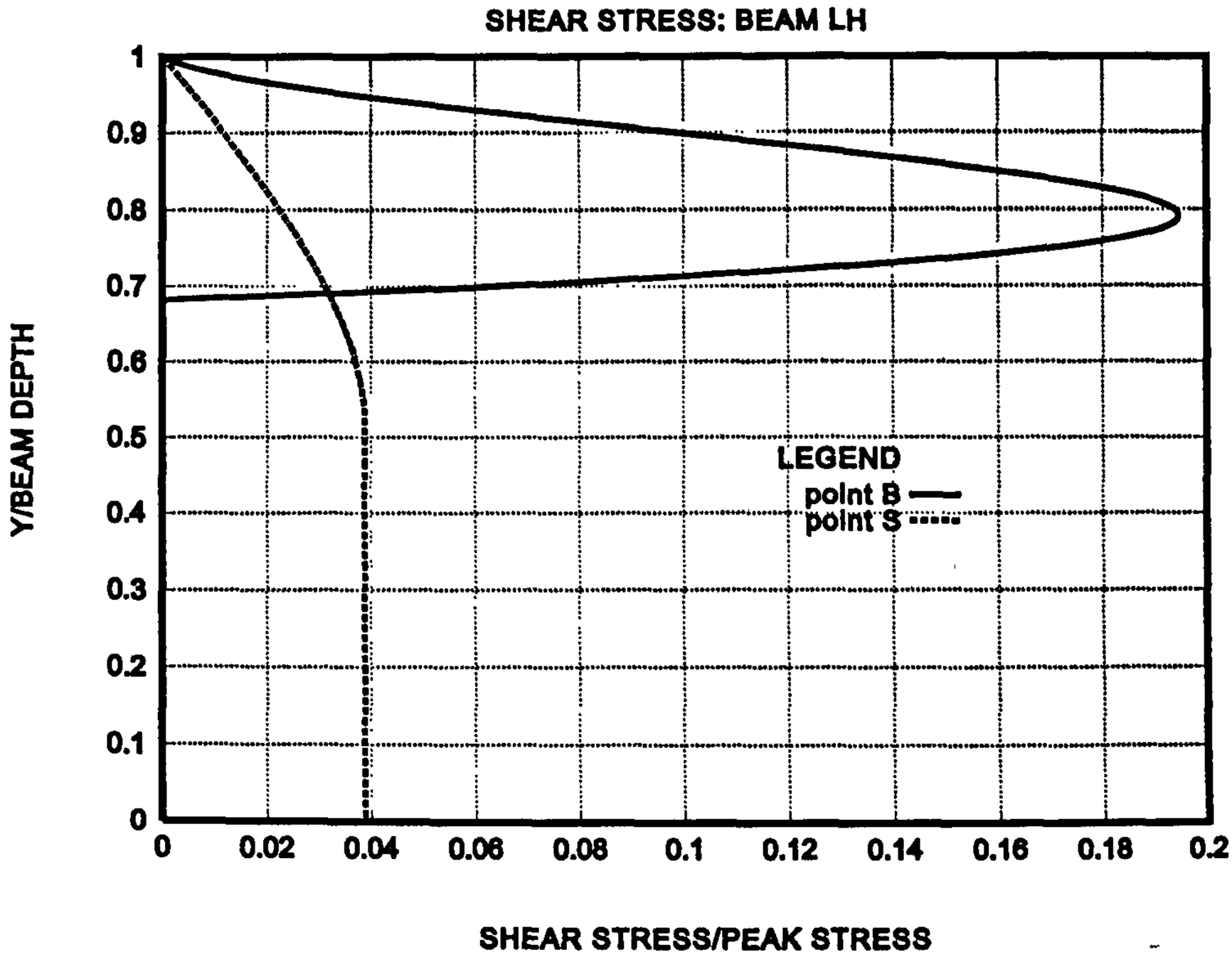

Figure 4.33 Stress distribution for points S and B for beam LH

Figure 4.28 to Figure 4.33 indicate that at point S very minimal shear stresses are endured by the beams. At point B the shear stresses carried is relatively moderate.

Figure 4.34 shows the shear stress plots at the point A for beam SL

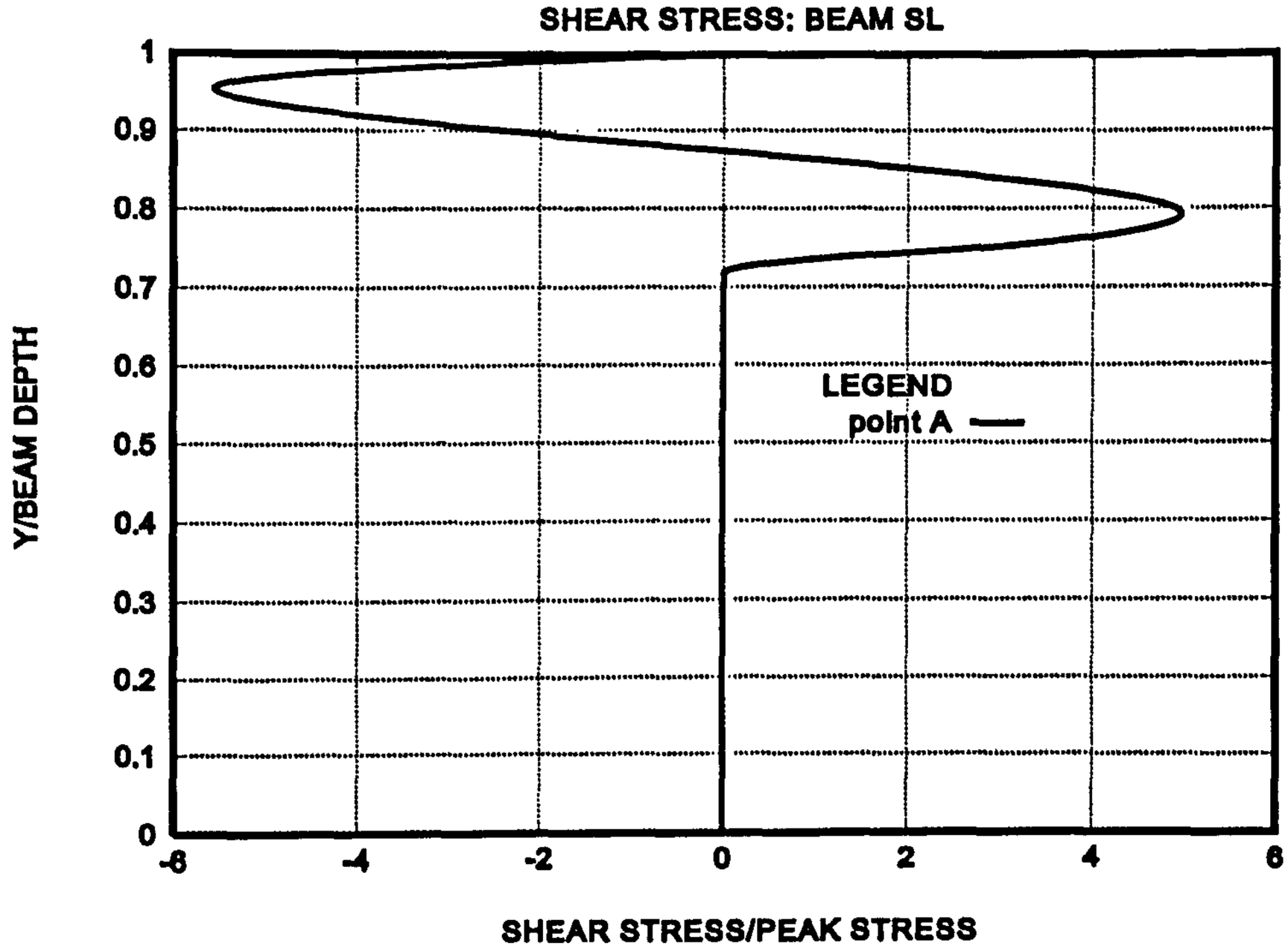

Figure 4.34 Shear stress distribution at the point A for beam SL

Figure 4.35 shows the shear stress plots at the point A for beam SH

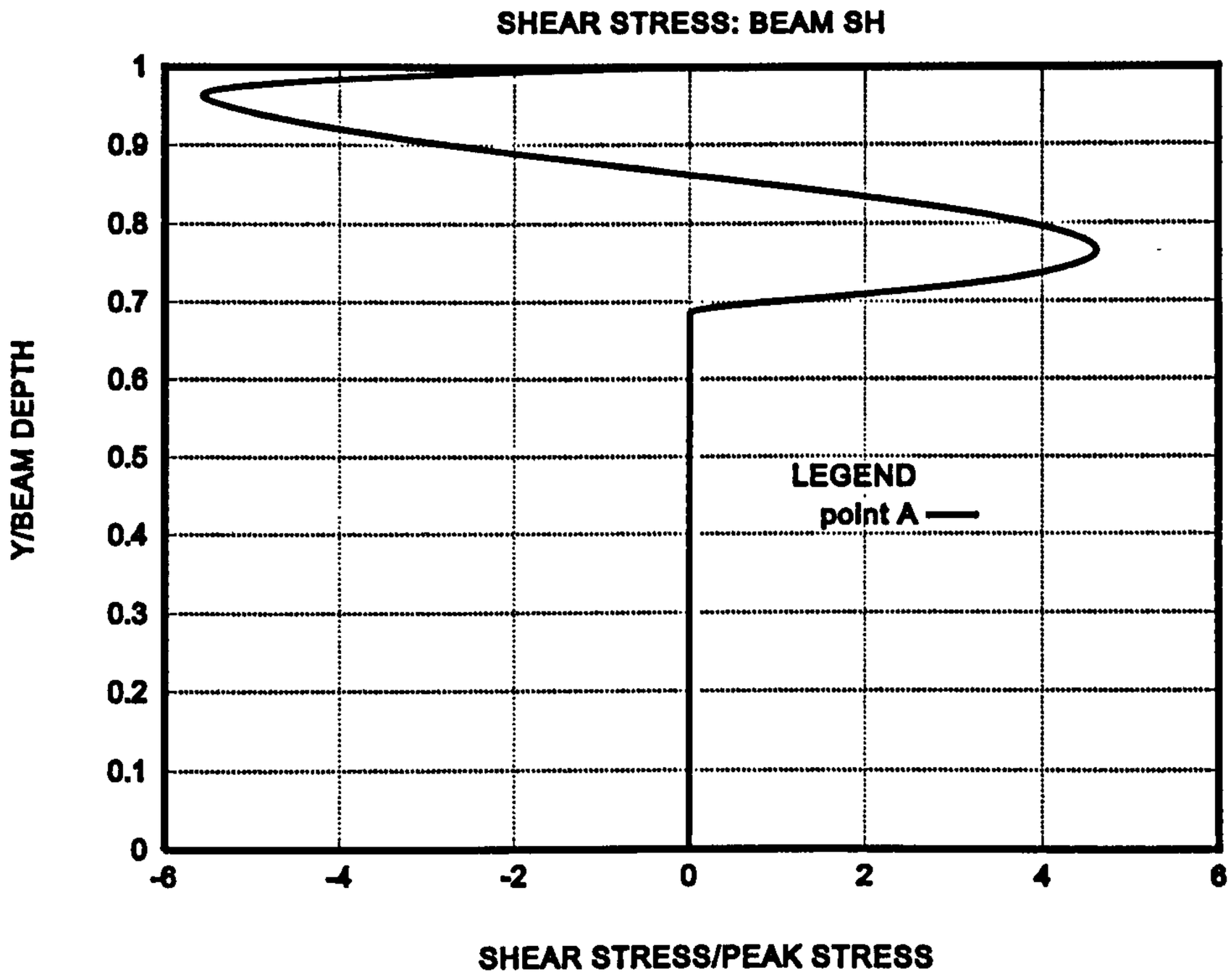

Figure 4.35 Shear stress distribution at the point A for beam SH

Figure 4.36 shows the shear stress plots at the point A for beam ML

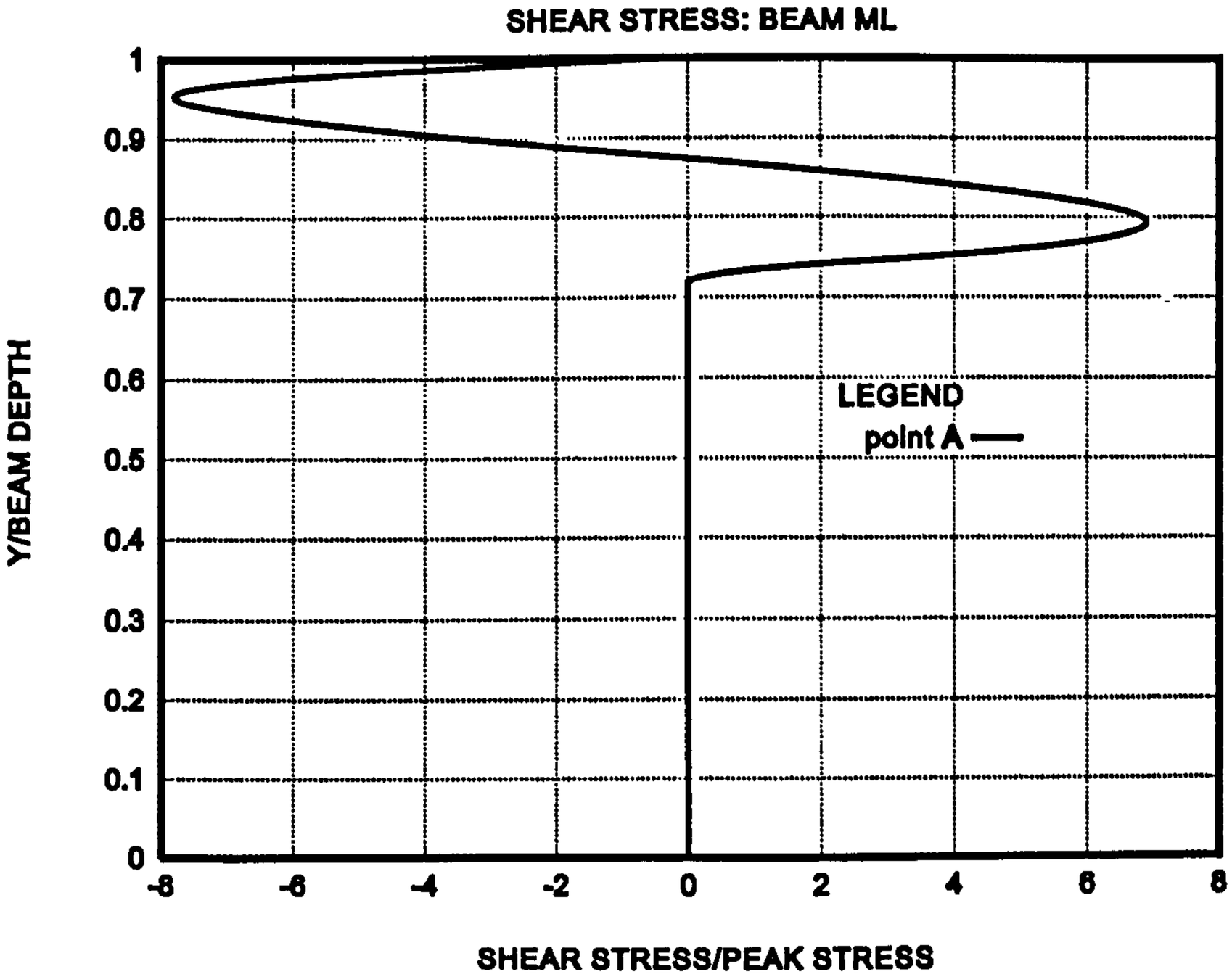

Figure 4.36 Shear stress distribution at the point A for beam ML

Figure 4.37 shows the shear stress plots at the point A for beam MH

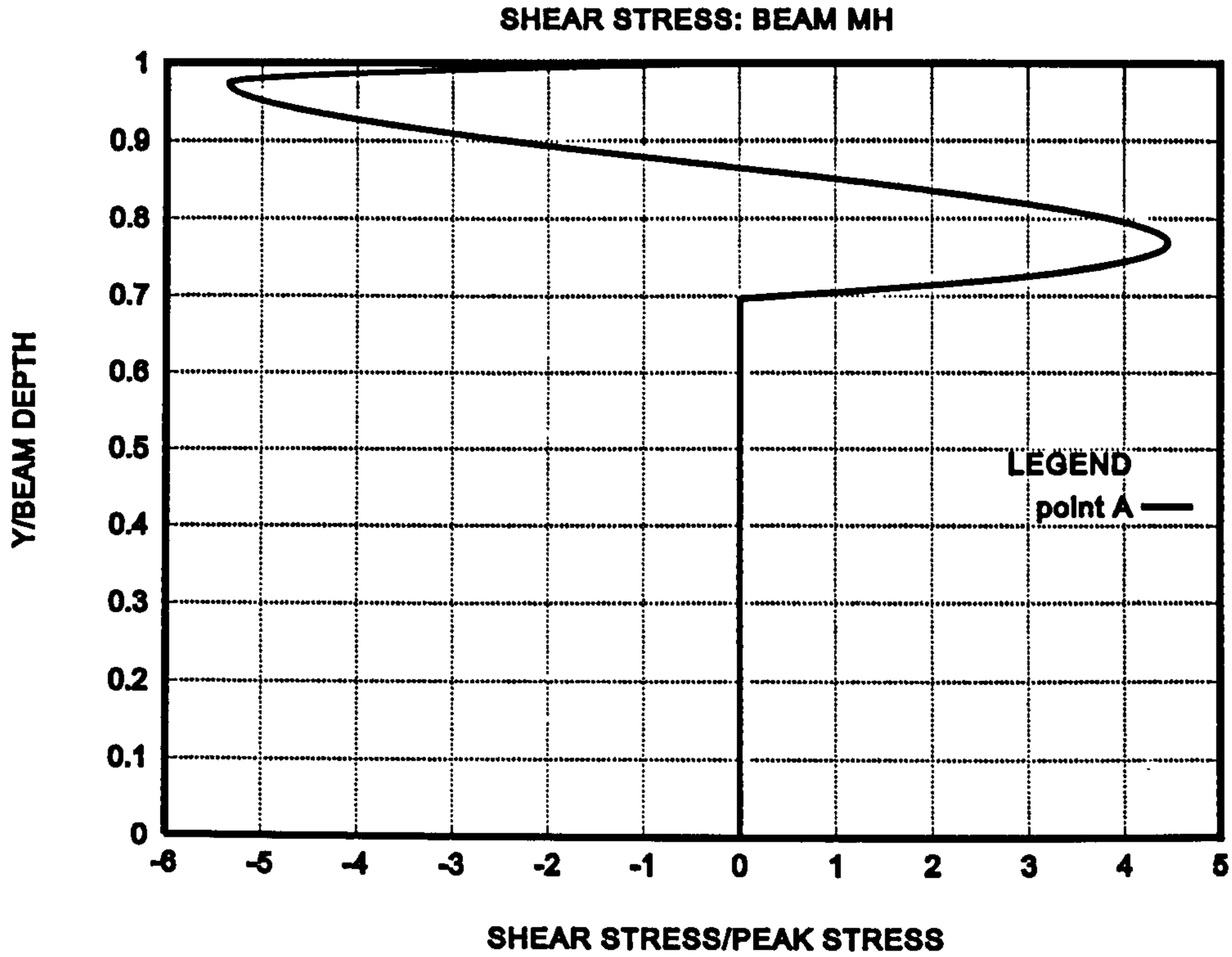

Figure 4.37 Shear stress distribution at the point A for beam MH

Figure 4.38 shows the shear stress plots at the point A for beam LL

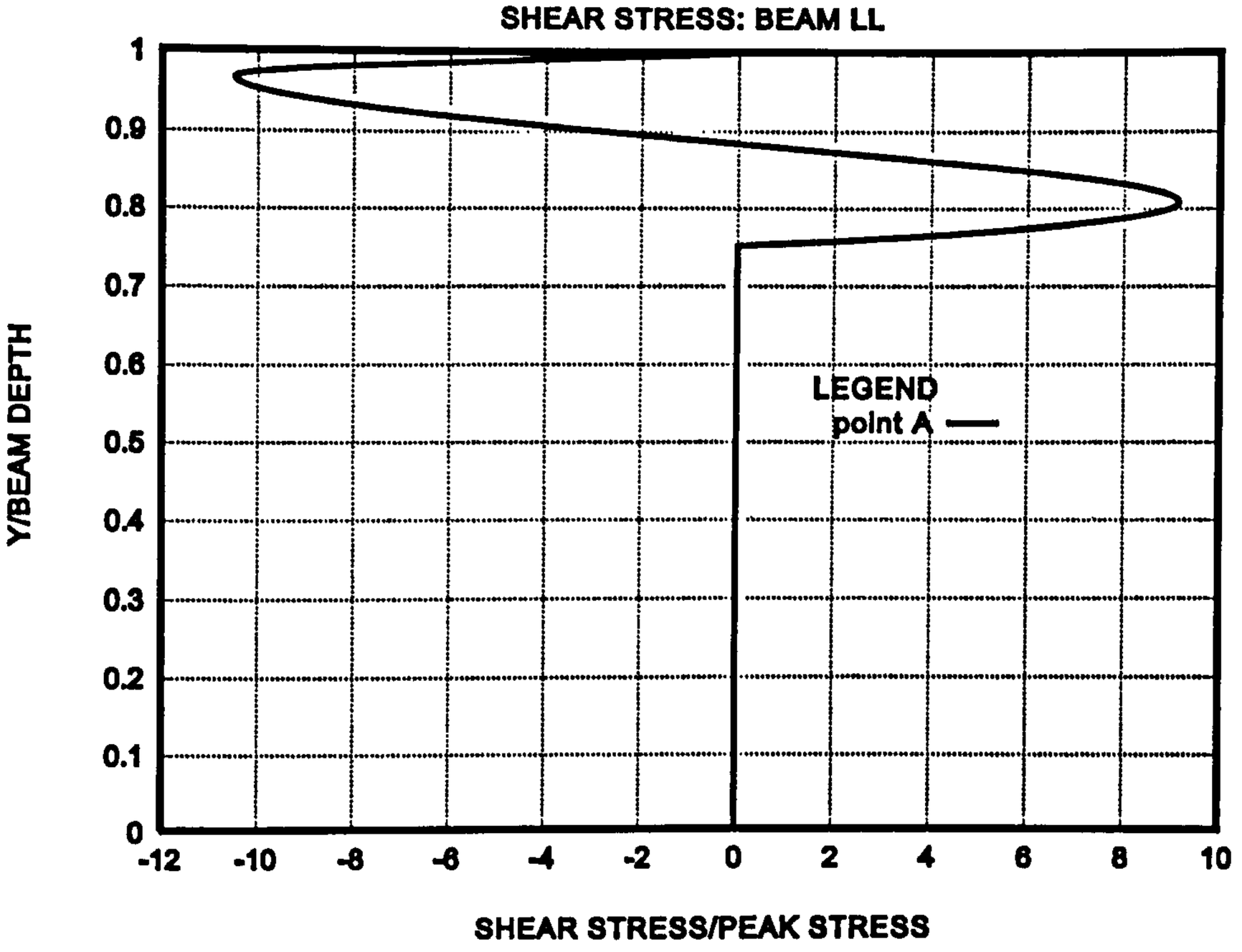

Figure 4.38 Shear stress distribution at the point A for beam LL

Figure 4.39 shows the shear stress plots at the point A for beam LH

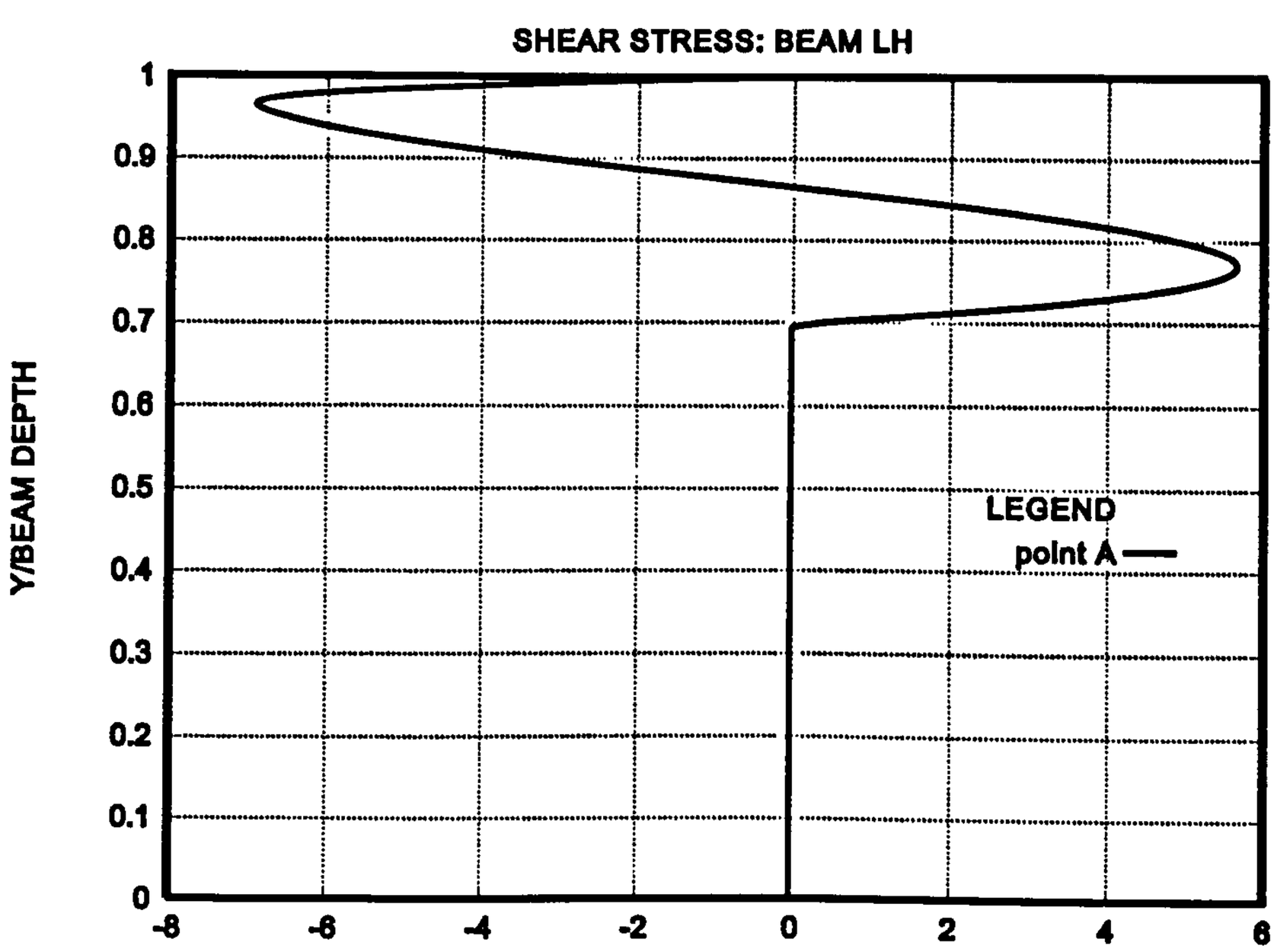

Figure 4.39 Shear stress distribution at the point A for beam LH

Figure 4.34 to Figure 4.39 show that an enormous increase in shear stress occurs. The concrete beams cannot carry such a large shear stress. This indicates that any softening in concrete occurs due to shear rather than large nominal stress as pointed out by Hillerborg [2]. In other words the plane sections theory is no longer valid. However a significant redistribution of stress is equally not possible because it requires extensive shear stress. The logical conclusion is, therefore that immediately after point B is reached the concrete fails.

Figure 4.40 shows the energy increases non-linearly with increased rotation initially after which the increase is seen to be linear

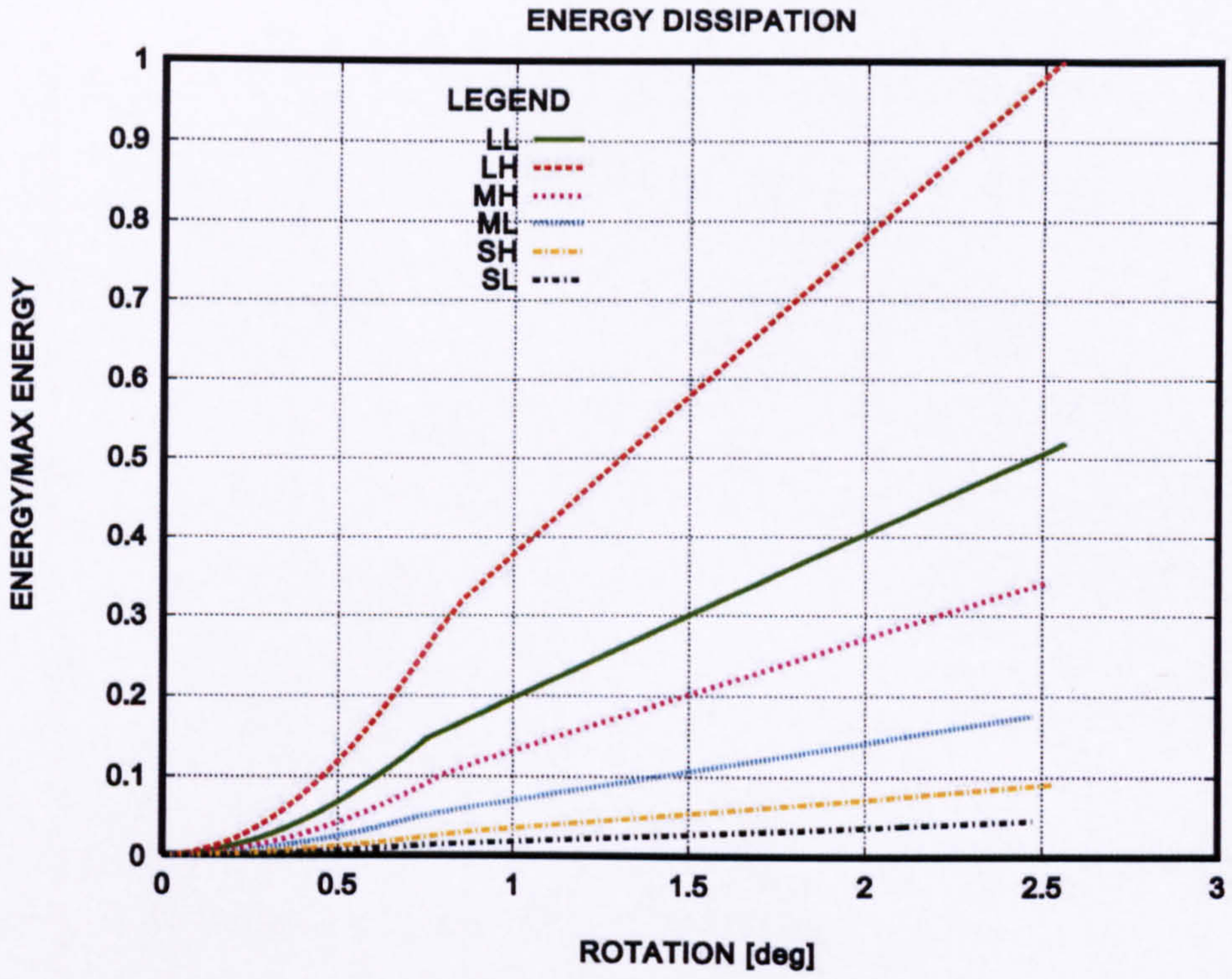

Figure 4.40 Energy dissipation in all the beams

The energy for both low strength and high strength beams shows a bi-linear increase with increasing depth size (Figure 4.41 and Figure 4.42). The change in linearity seen to occur at a depth of about 360 mm.

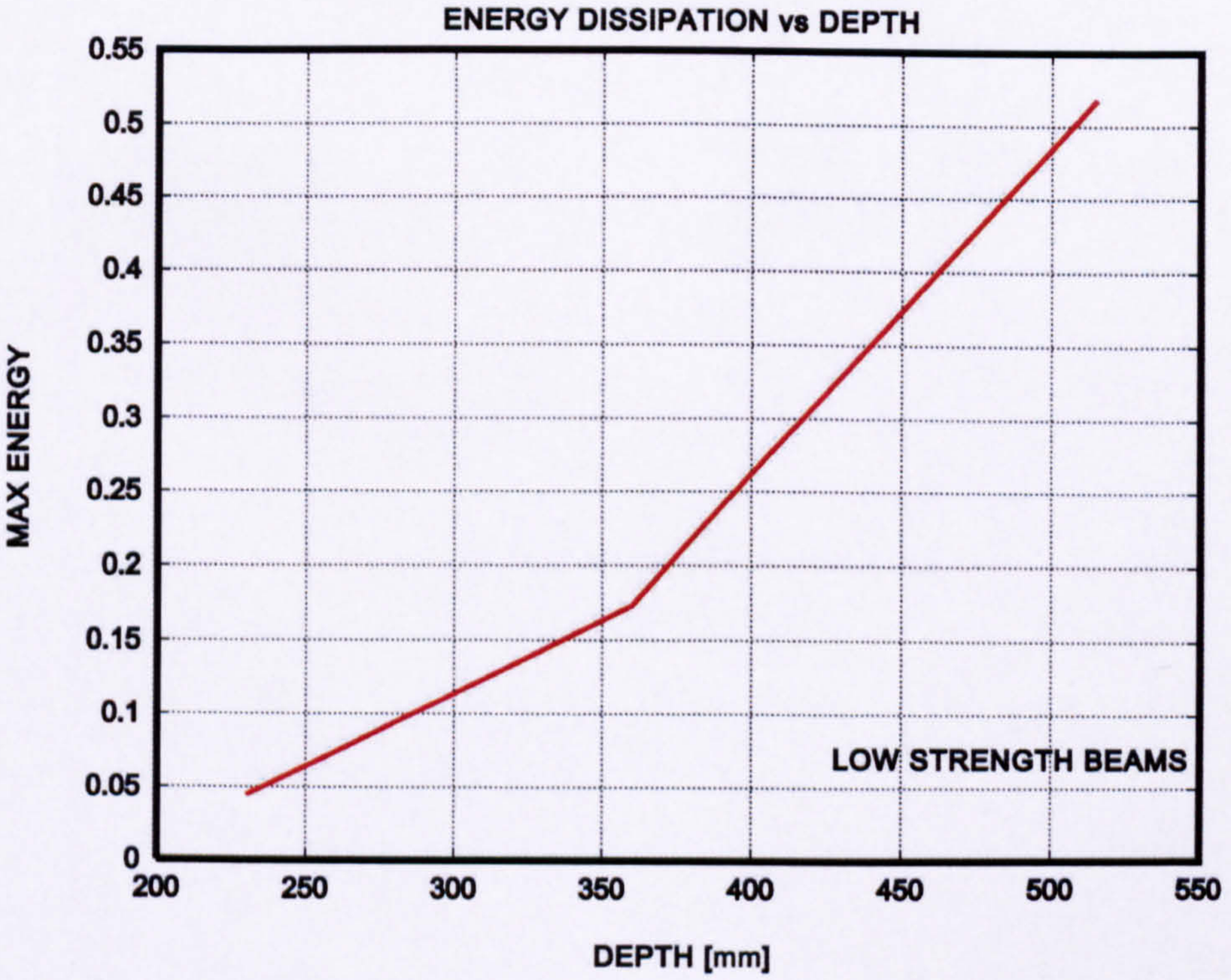

Figure 4.41 Energy dissipation vs beam depth for low strength beams

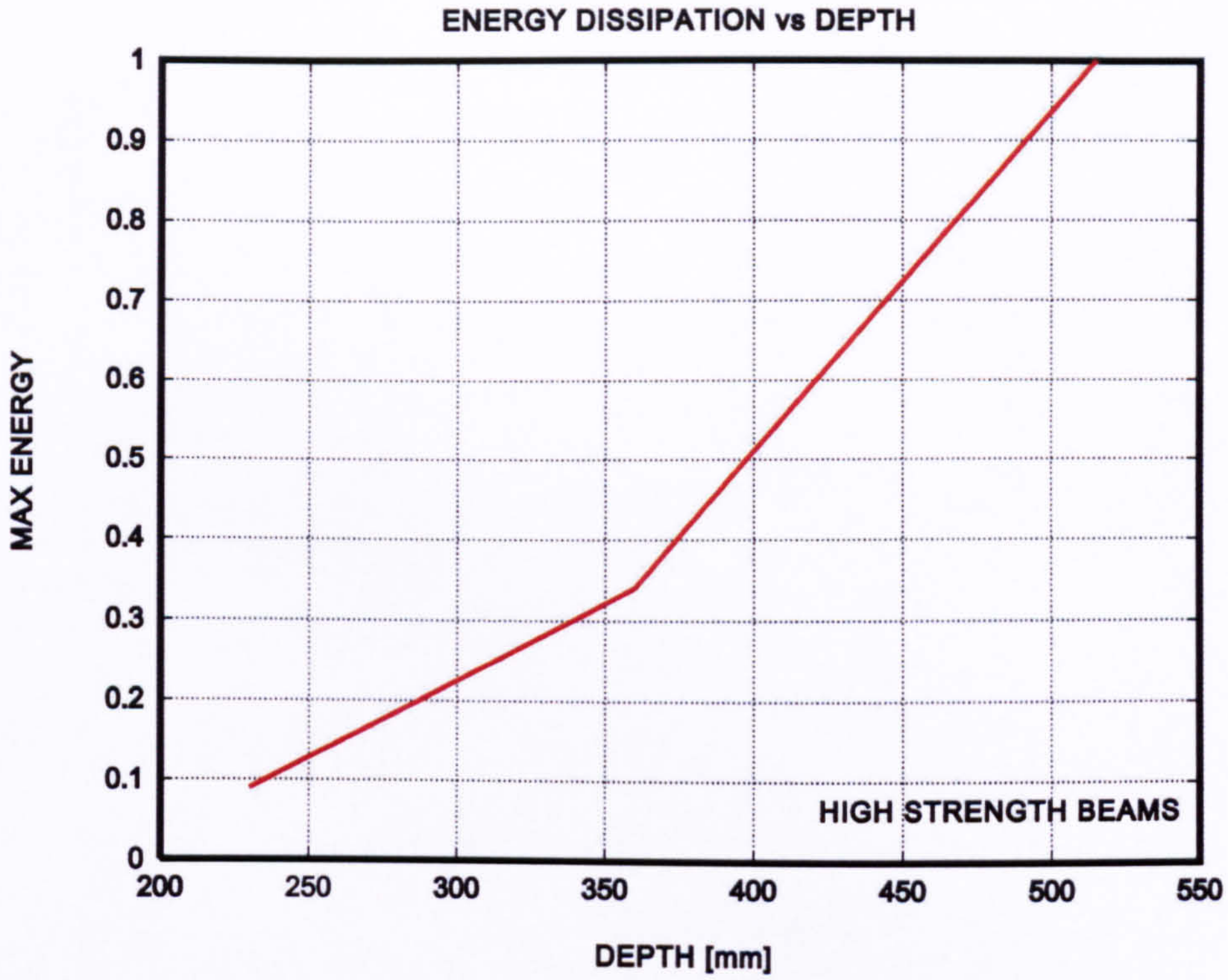

Figure 4.42 Energy dissipation vs beam depth for high strength beams

4.3.6 Numerical investigation with column loading

Further investigations were carried out into the effect of axial loading upon the resulting moment curvature relationship.

For investigations with axial column loading, P_{col} the column load was added to the force in the steel such that the force in the steel was given by

$$f_s = f_s + P_{col} \tag{4.59}$$

The maximum column load was calculated from

$$P_{col} = \sigma_{peak} A_{bcs} \tag{4.60}$$

Where A_{bcs} is the cross sectional area of the beam. Thus in order to account for axial column loading equation (4.36) will read as

$$M_{cs} = d_{na} f_{cs} - P_{col} \frac{d}{2} \tag{4.61}$$

Where P acts at the centre of the cross section thus having a lever arm of $d/2$.

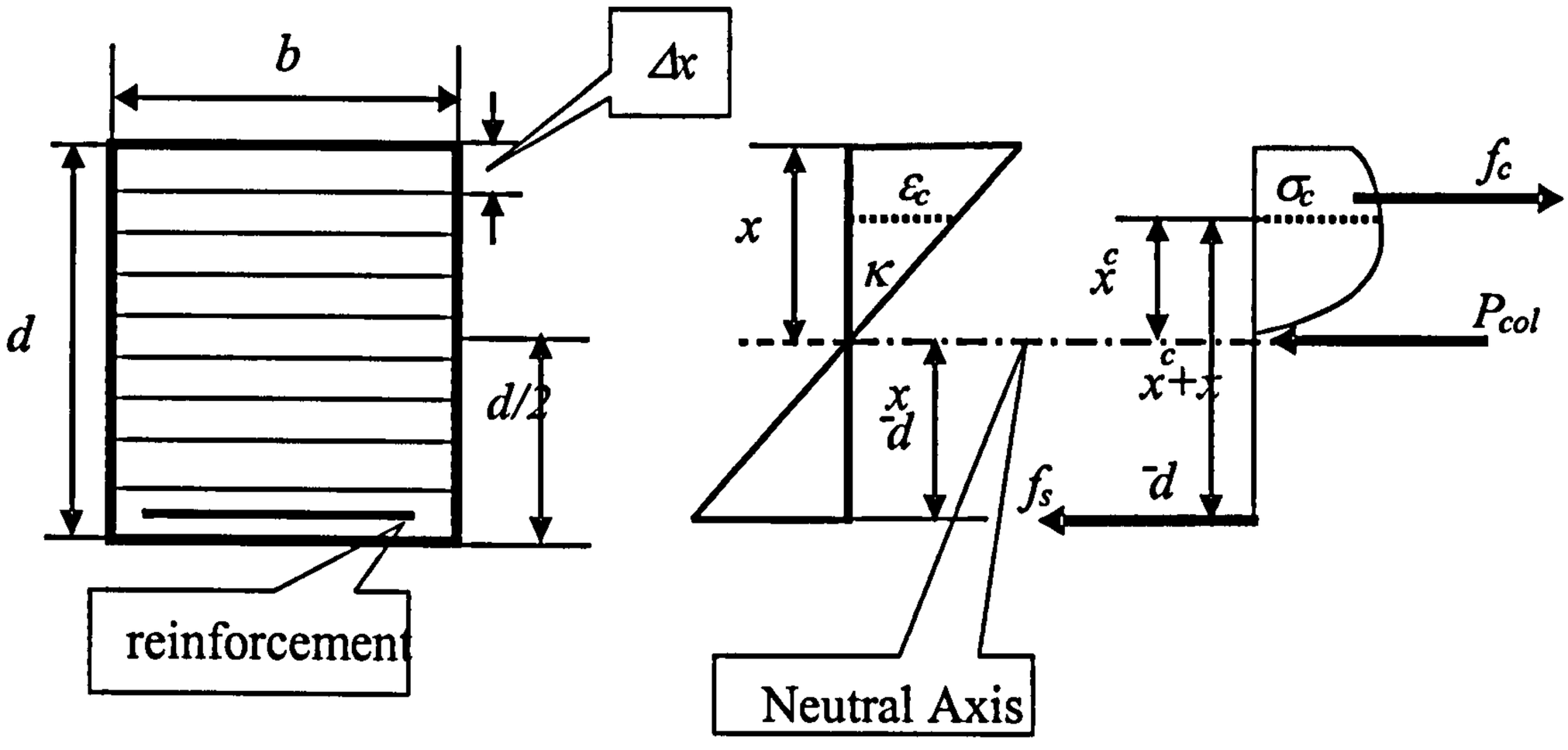

Figure 4.43 Beam cross section with stress and strain distribution

The maximum column load for Beam LL is calculated from

$$N_{\max} = \sigma A_s = 50 \times 0.24069 = 12121830\,\text{N} \tag{4.62}$$

The full area of steel is 4000 mm^2 (F). This value is reduced to 2000 mm^2 (H) for investigations using half the reinforcement and further dropped to 1334 mm^2 (T) for investigations using one third of the reinforcement.

The Moment-Curvature plots are shown for varied axial loading in Figure 4.44 to Figure 4.48

Figure 4.44 shows the Moment-Curvature relationship for beam LL with zero axial loading.

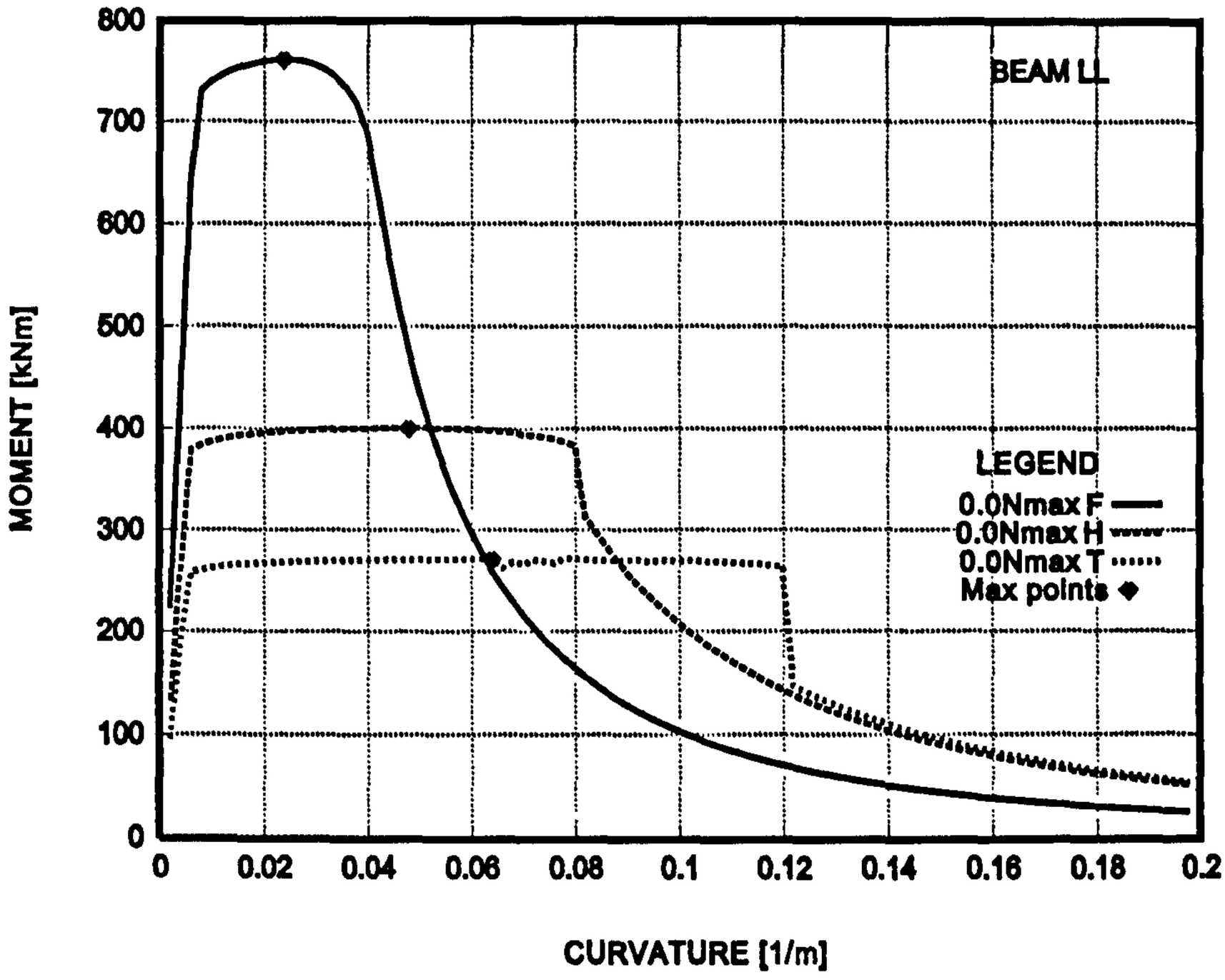

Figure 4.44 Moment-Curvature relationship for beam LL with $0.0N_{max}$

Figure 4.45 shows the Moment-Curvature relationship for beam LL with $0.1N_{max}$ column loading.

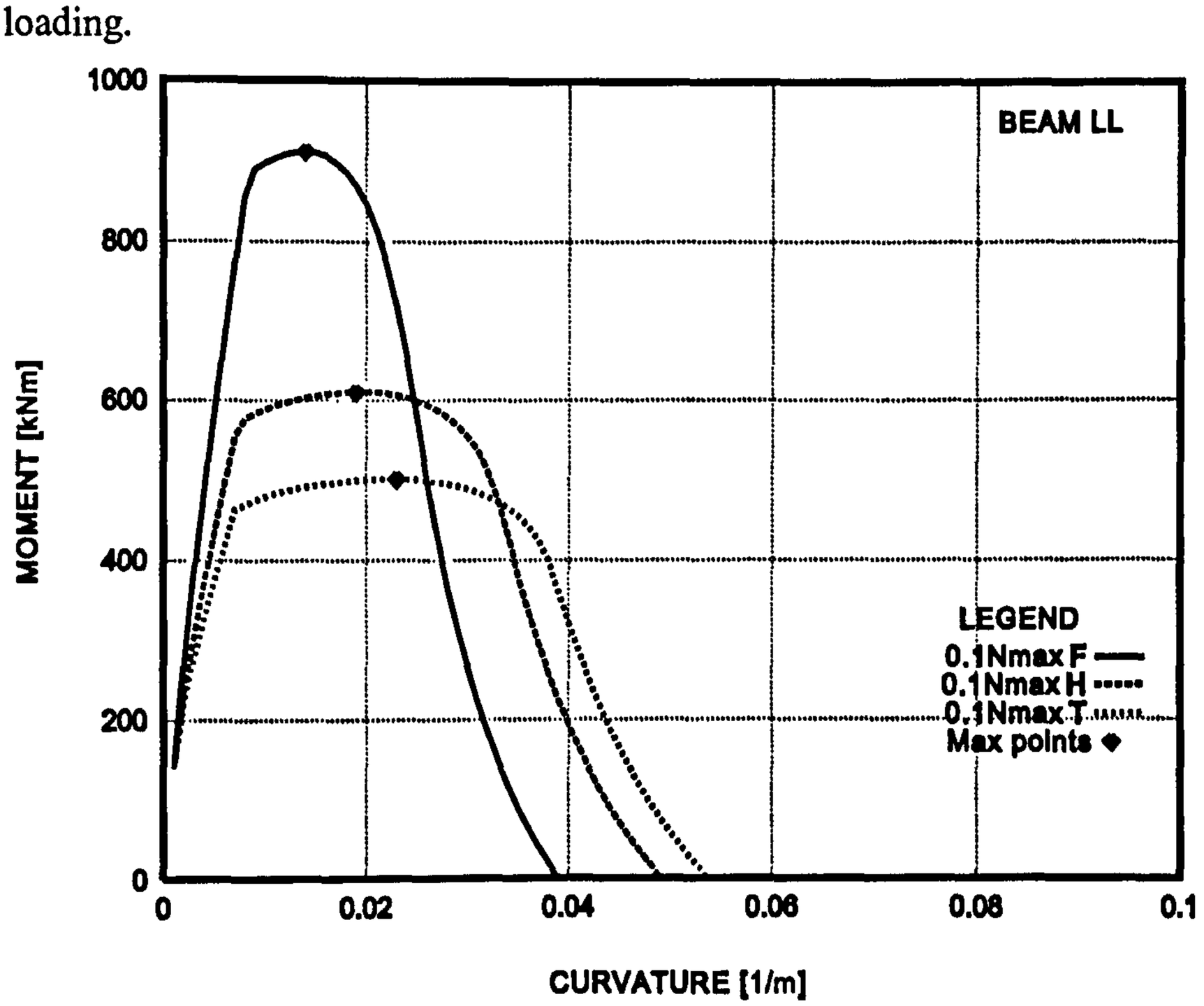

Figure 4.45 Moment-Curvature relationship for beam LL with $0.1N_{max}$

Figure 4.46 shows the Moment-Curvature relationship for beam LL with $0.2N_{max}$ column loading.

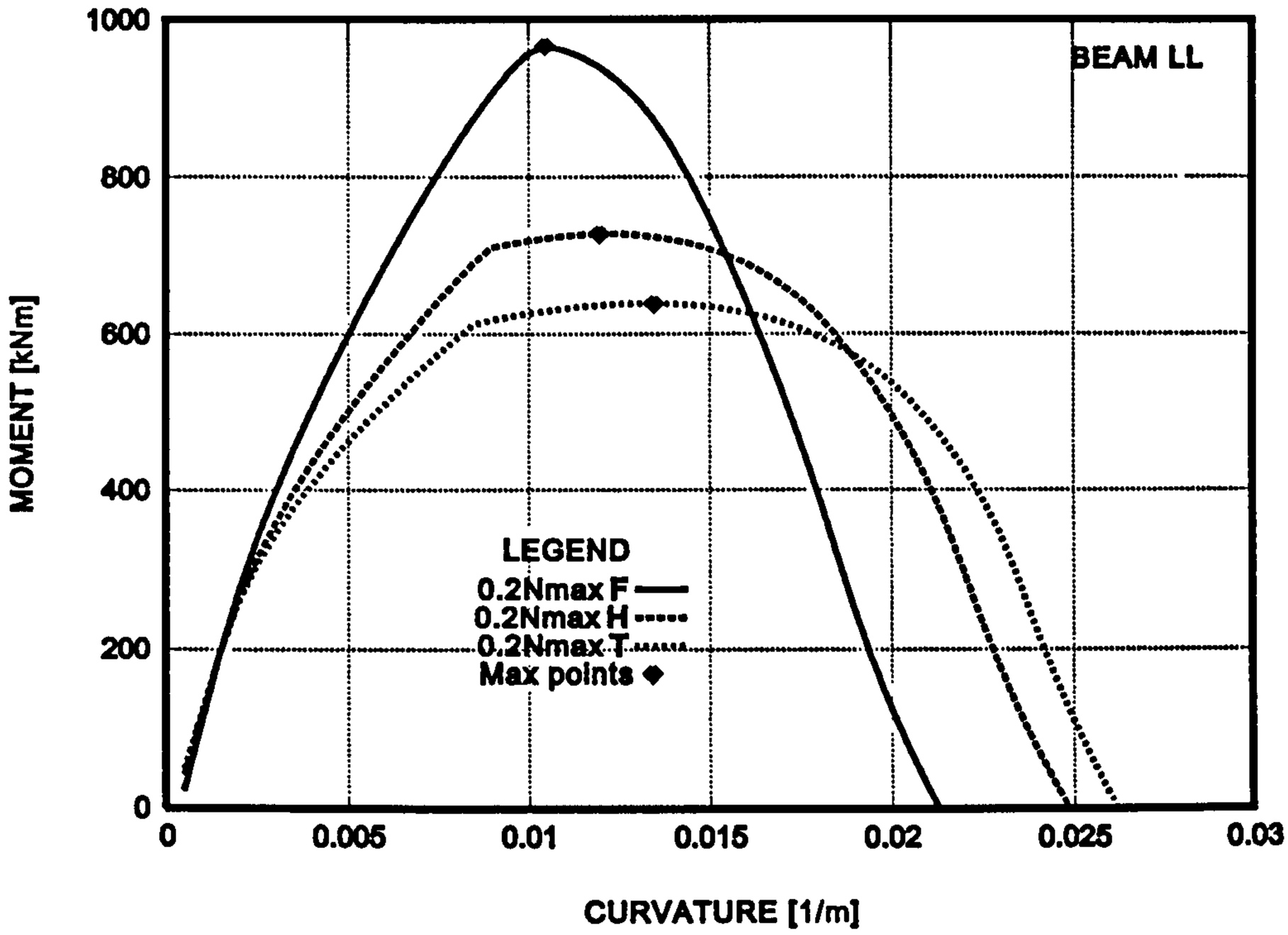

Figure 4.46 Moment-Curvature relationship for beam LL with $0.2N_{max}$

Figure 4.47 shows the Moment-Curvature relationship for beam LL with $0.4N_{max}$ column loading.

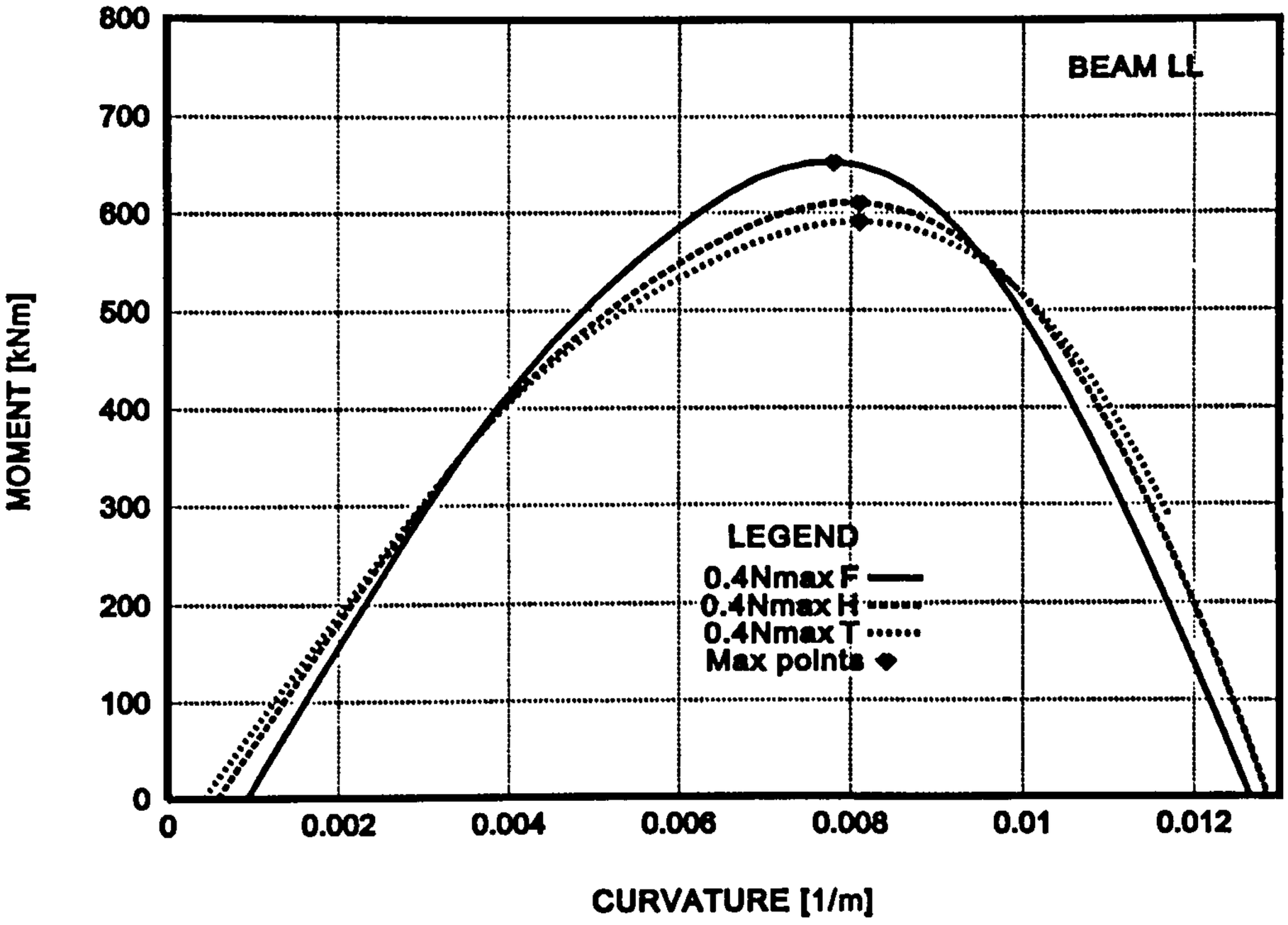

Figure 4.47 Moment-Curvature relationship for beam LL with $0.4N_{max}$

Figure 4.48 shows the Moment-Curvature relationship for beam LL with $0.6N_{max}$ column loading.

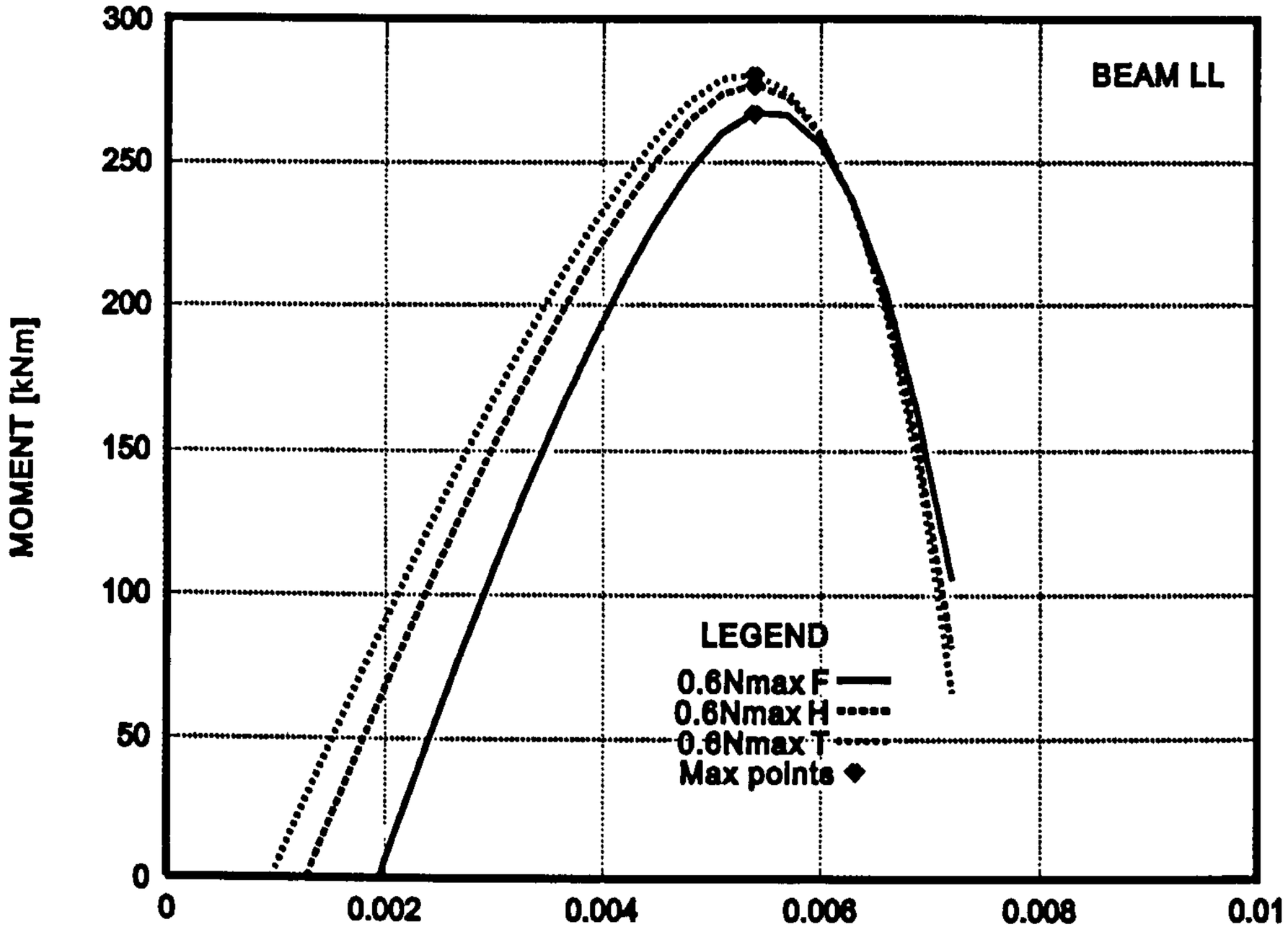

Figure 4.48 Moment-Curvature relationship for beam LL with $0.6N_{max}$

Figure 4.48 show the maximum moment to increase up to a loading of $0.2N_{max}$ after which the maximum moment is found to fall below the values obtained for the case with zero axial loading. The range of curvature is also seen to reduce with increased axial loading. This indicates a reduction in the energy absorption of the beams with higher axial loading. This is shown in Figure 4.49. Hence a reduction in the ductility of concrete beams is seen to occur with increasing axial loading.

Figure 4.50 shows that for axial loading equal to or below 0.1Nmax the energy reduces with an increase in reinforcement ratio. For values above this loading the energy is found to remain constant with increasing reinforcement ratio.

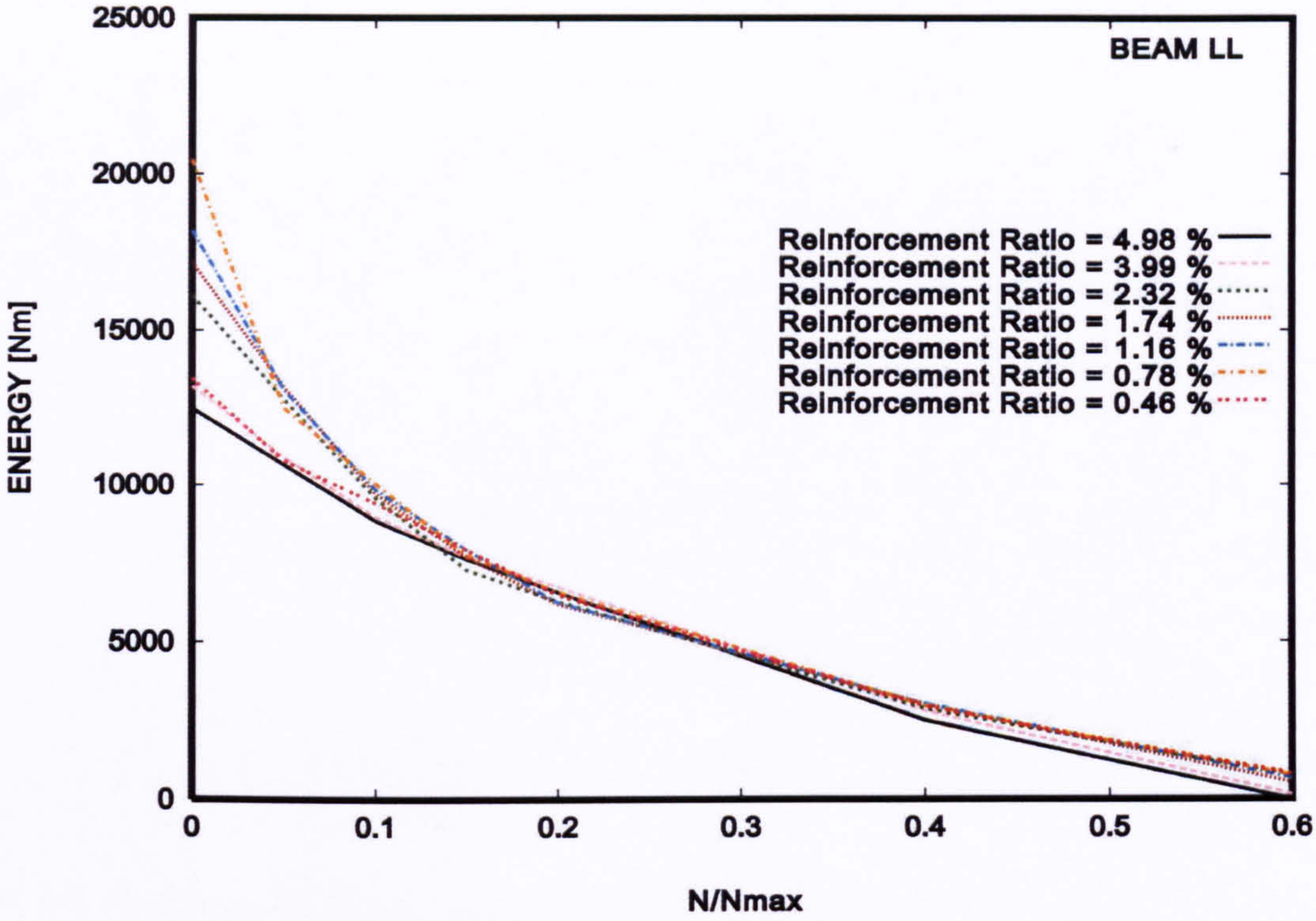

Figure 4.49 Variation in energy absorption with column loading

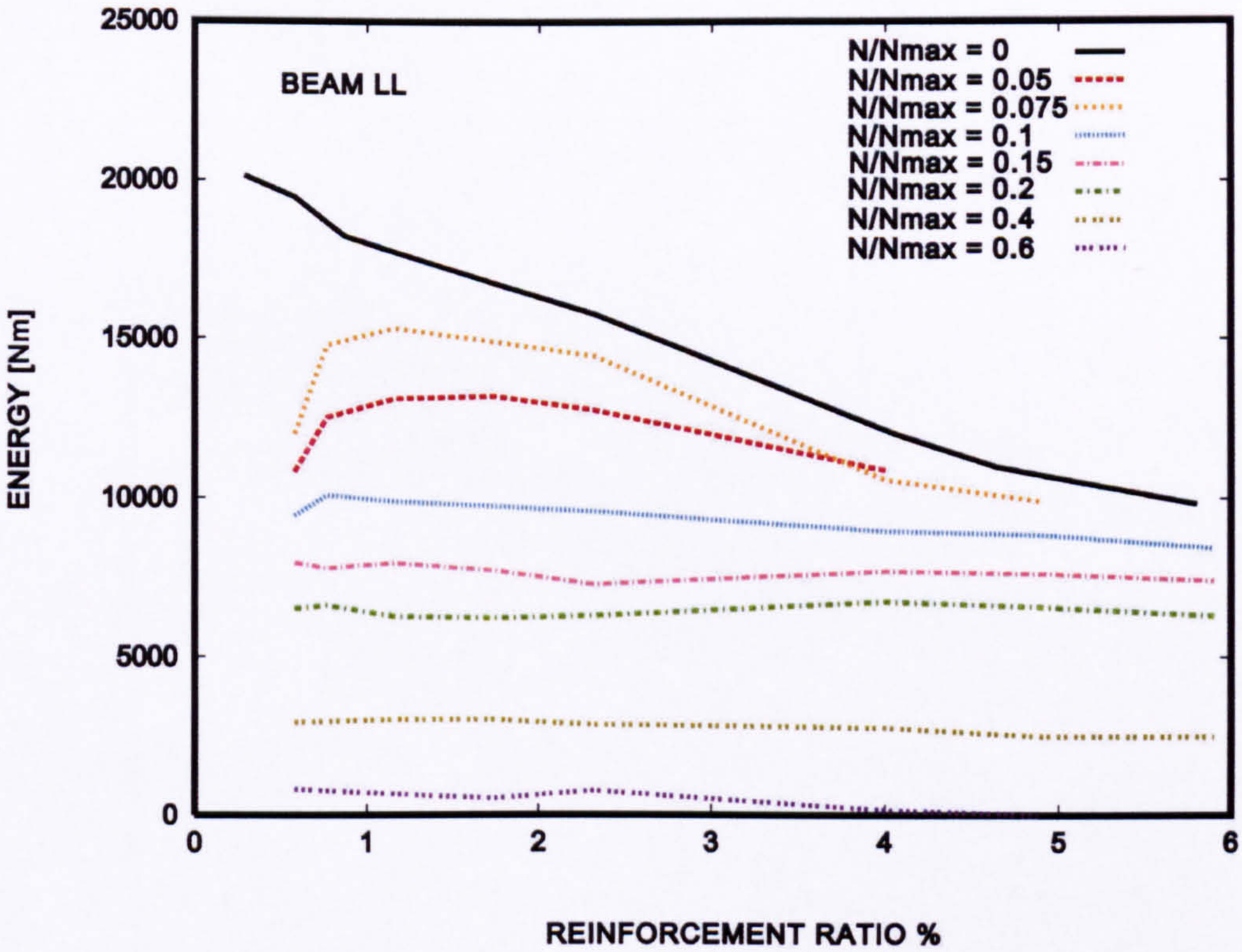

Figure 4.50 Variation in energy absorption with reinforcement ratio

4.3.7 The effects of strain rates

To account for the effects of strain rate in the concrete the concrete function is modified such that the peak stress is higher as shown in Figure 4.51.

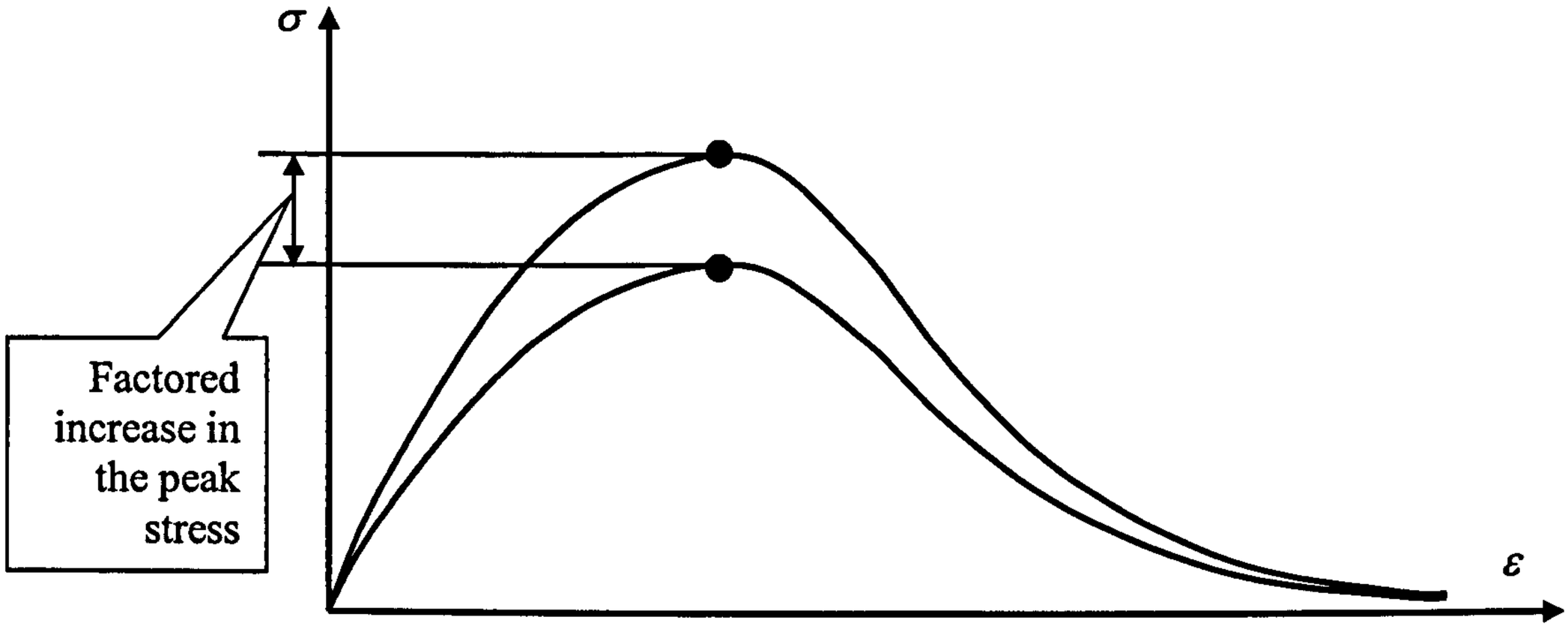

Figure 4.51 Stress-strain curves for concrete modified to account for strain rate

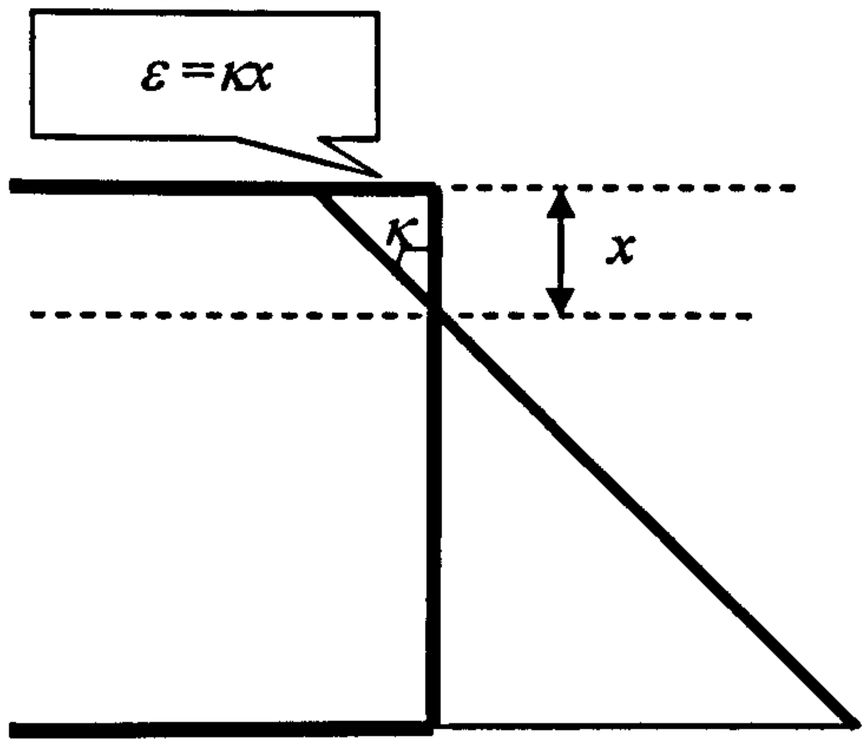

Figure 4.52 Curvature rate

As the stress is induced the curvature will change at a certain rate (Figure 4.52). This will be refered to as the curvature rate, $\dot{\kappa}$, The strain rate is calculated by multiplying the curvature rate by x as follows

$$\dot{\varepsilon} = \dot{\kappa} x \tag{4.63}$$

Figure 4.53 shows the Moment – Curvature relationship for beam LH at various strain rates.

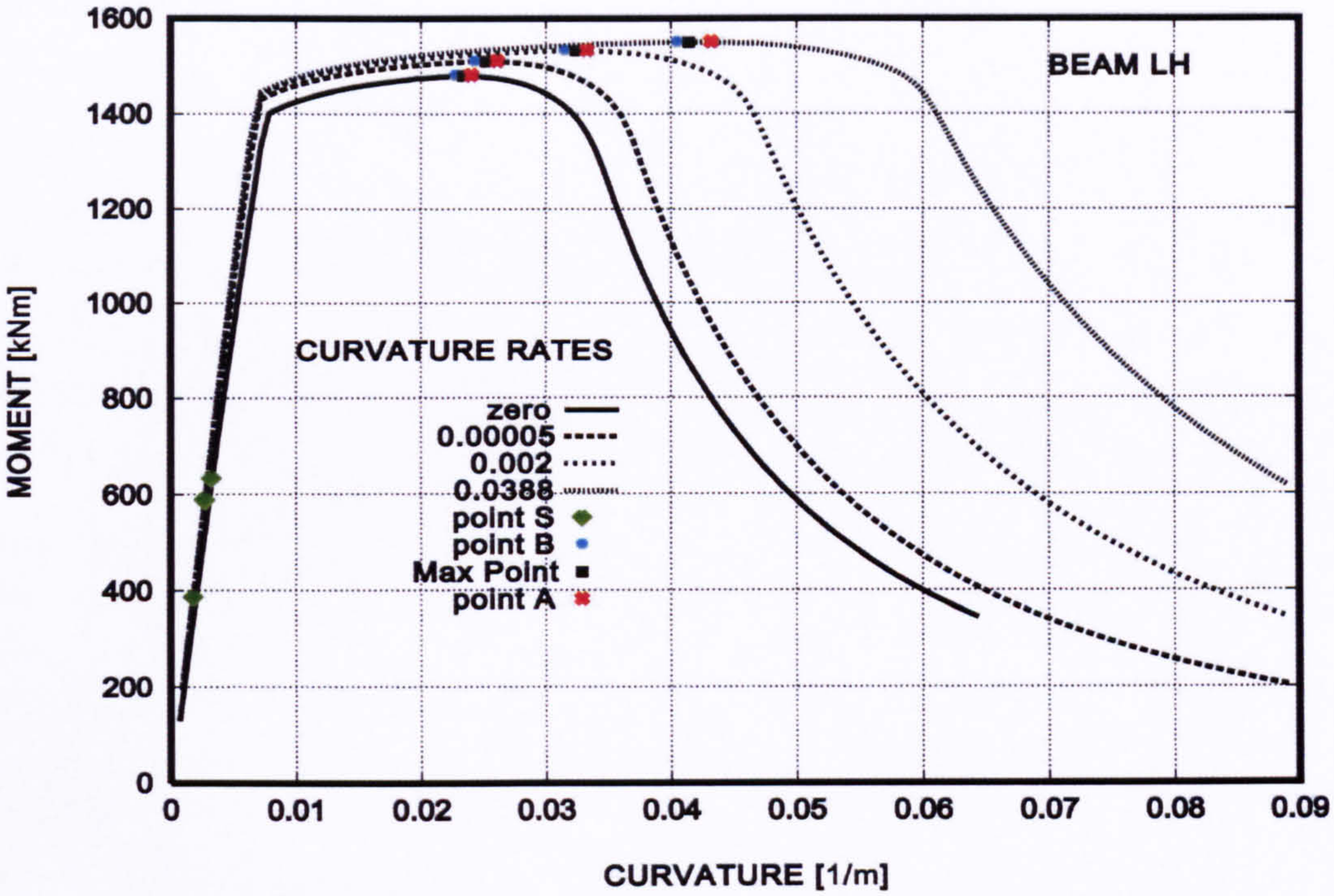

Figure 4.53 Moment-Cuvature at various strain rates for beam LH

Figure 4.54 shows the shear stress plots obtained at a strain rate of 0.00005 for points S,B,M and A, where point M relates to the maximum point.

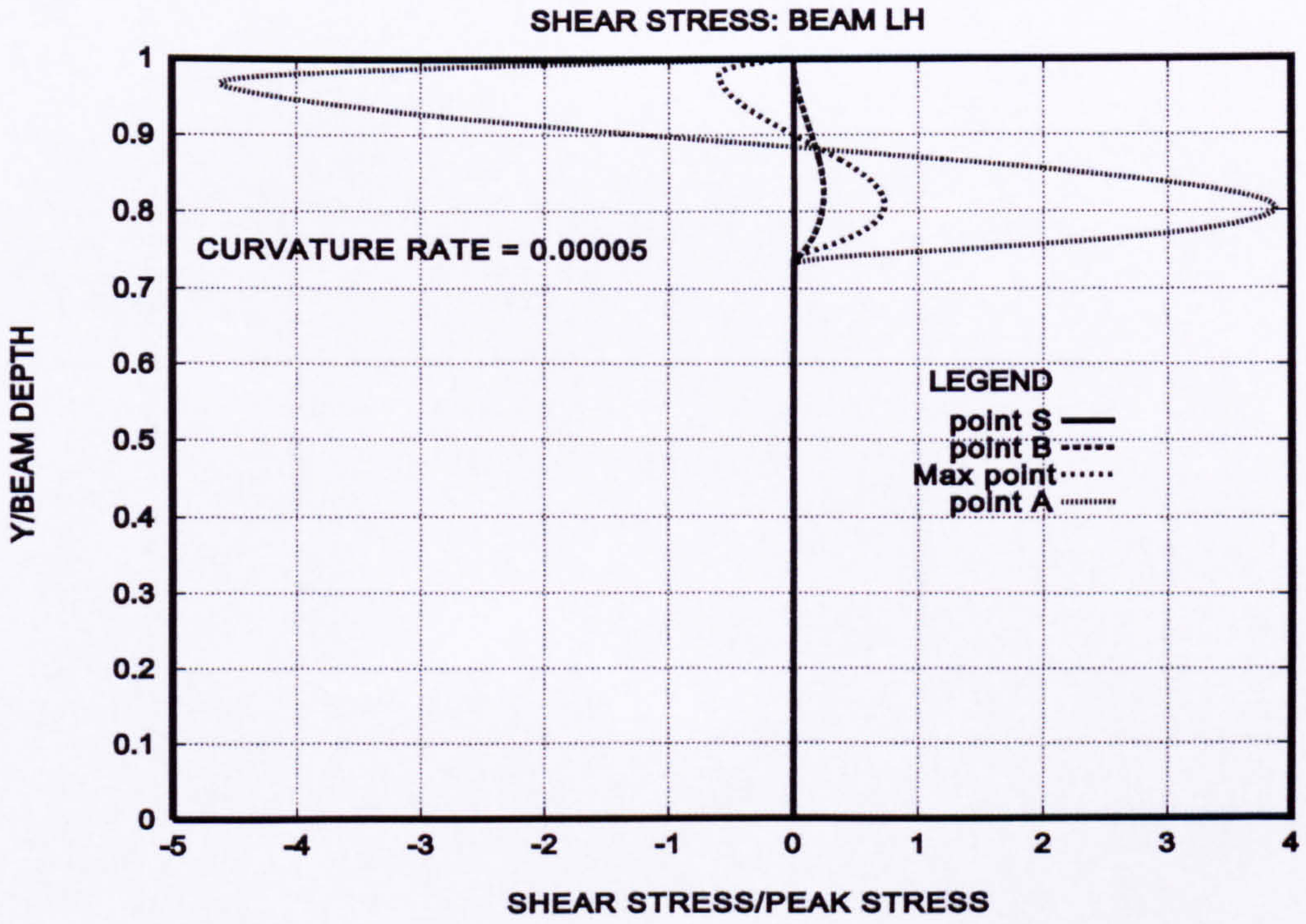

Figure 4.54 Shear stress distribution at κ =0.00005 for beam LH

Figure 4.55 shows the shear stress plots obtained at a strain rate of 0.002 for points S,B,M and A.

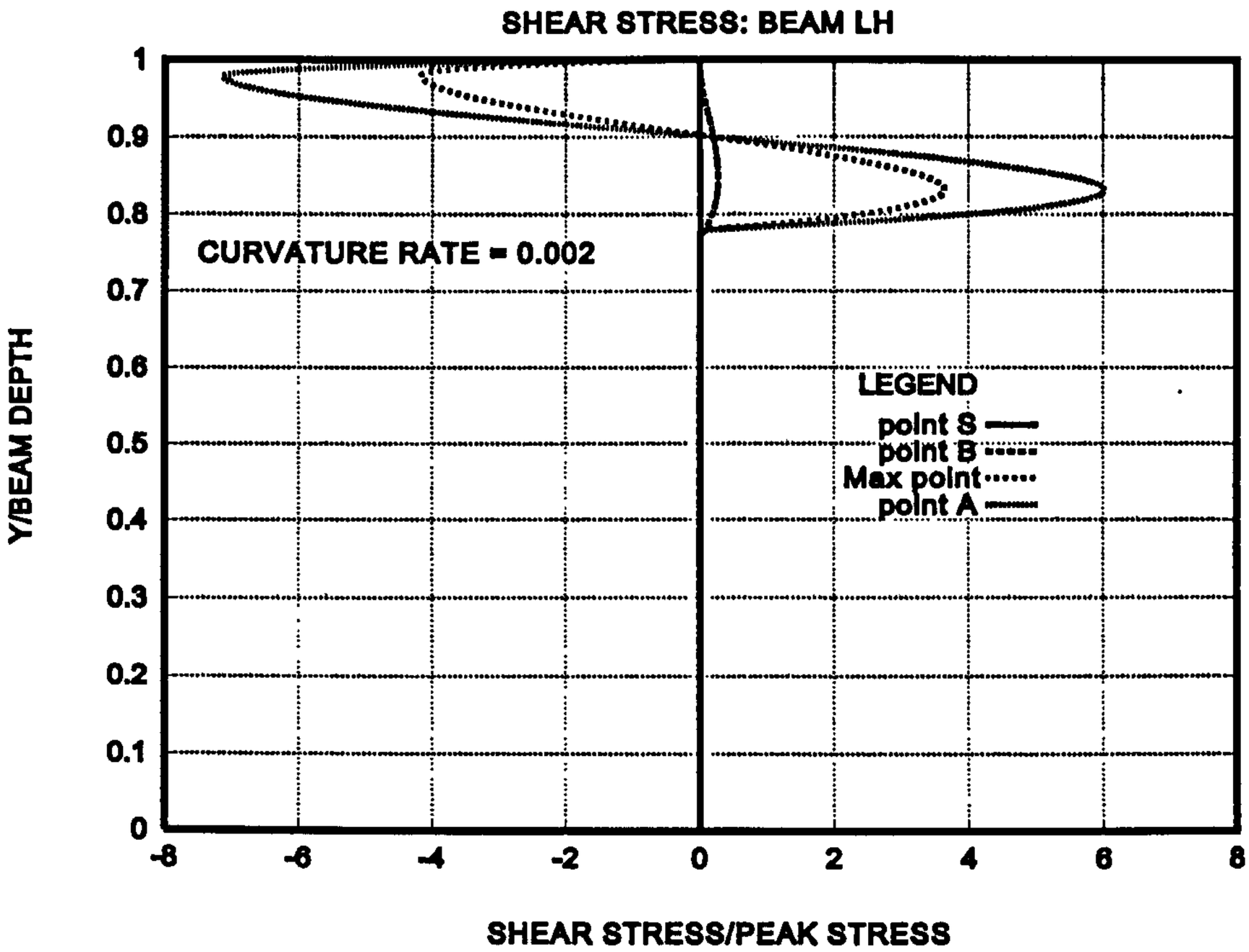

Figure 4.55 Shear stress distribution at $\dot{\kappa}$ =0.002 for beam LH

Figure 4.56 shows the shear stress plots obtained at a strain rate of 0.0388 for points S,B,M and A.

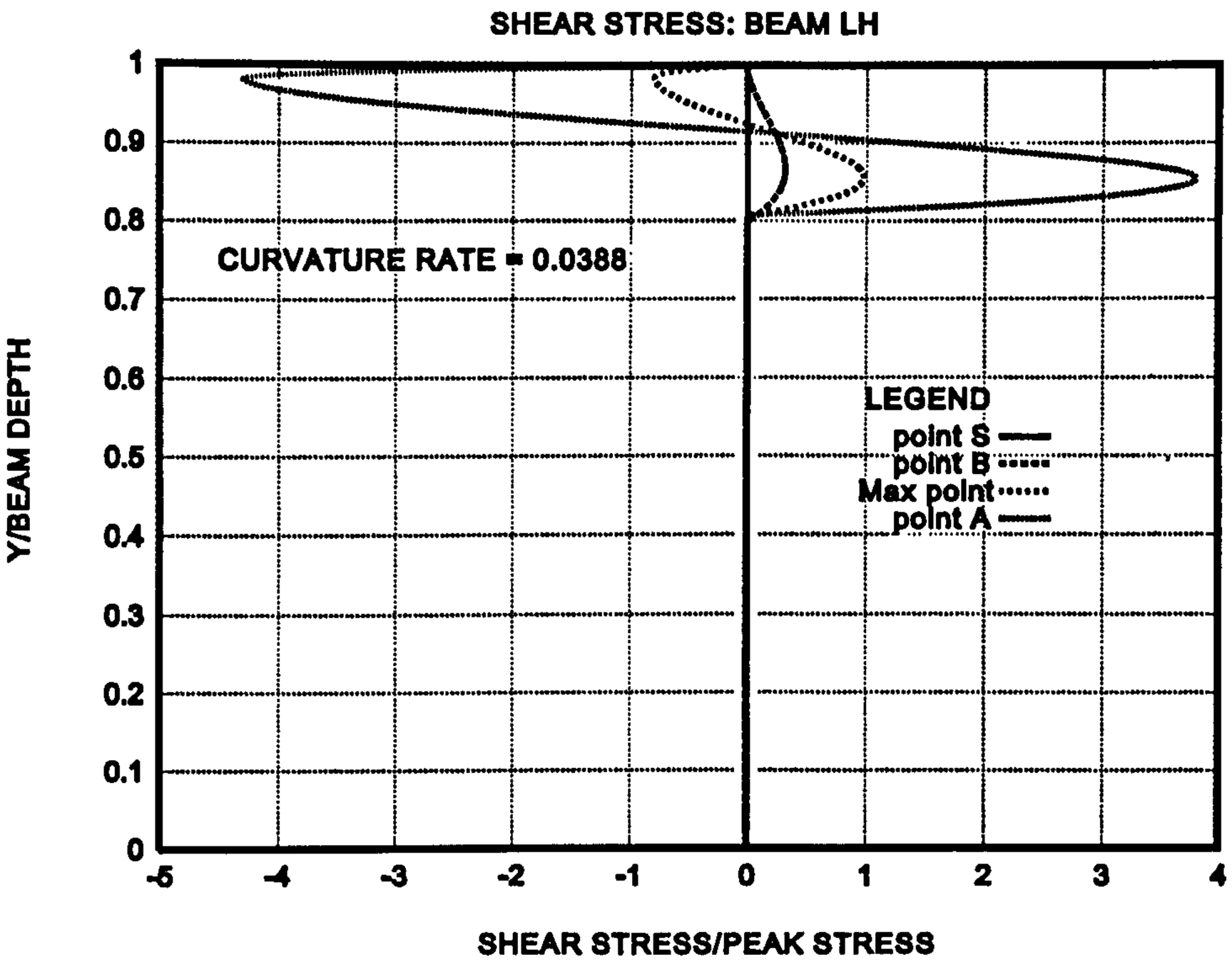

Figure 4.56 Shear stress distribution at $\dot{\kappa}$ =0.0388 for beam LH

Figure 4.57shows the normal stress distribution obtained at a strain rate of 0.00005 for points S,B,M and A.

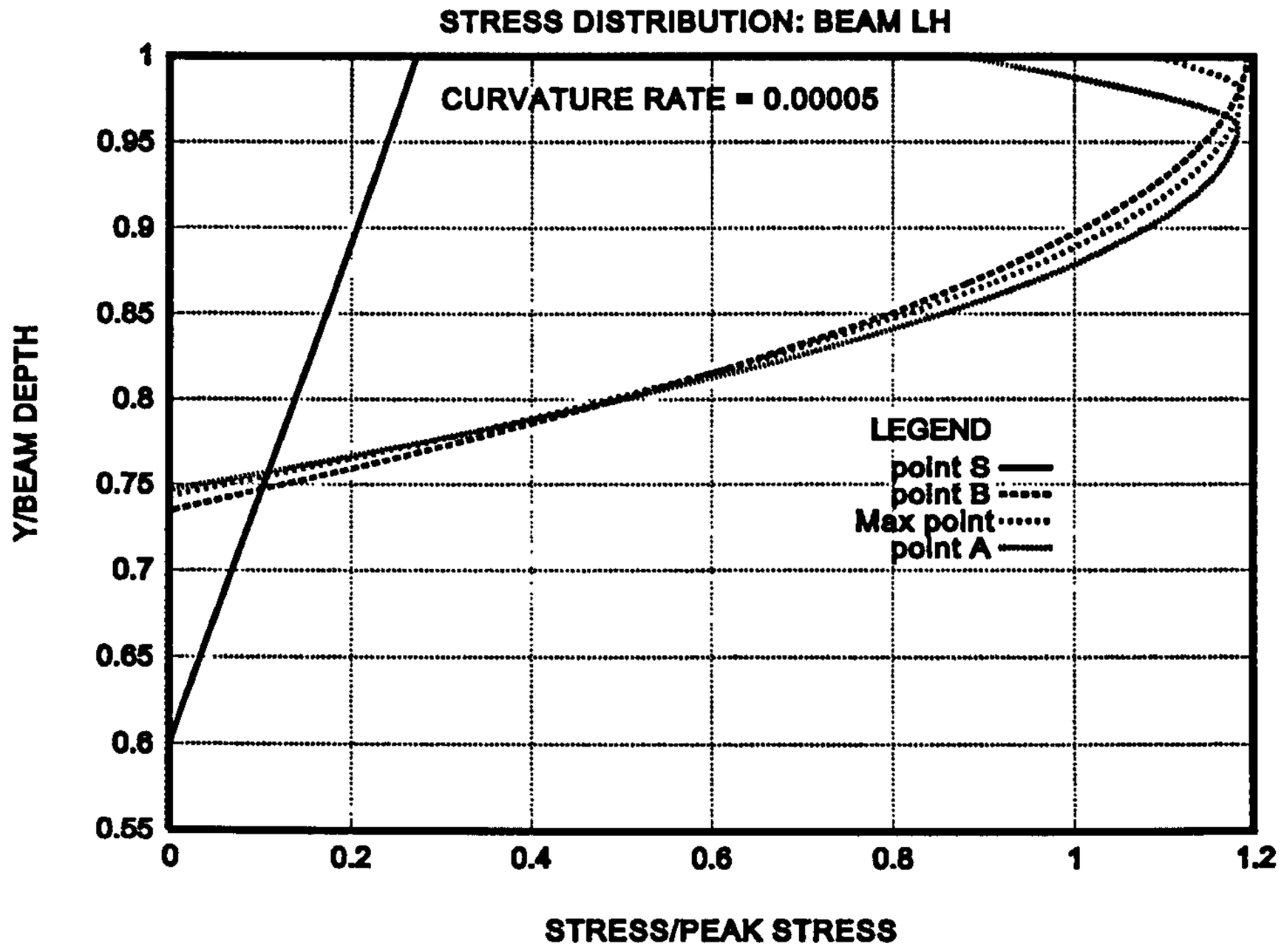

Figure 4.57 Normal stress distribution at $\dot{\kappa}$=0.00005 for beam LH

Figure 4.58 shows the normal stress distribution obtained at a strain rate of 0.002 for points S,B,M and A.

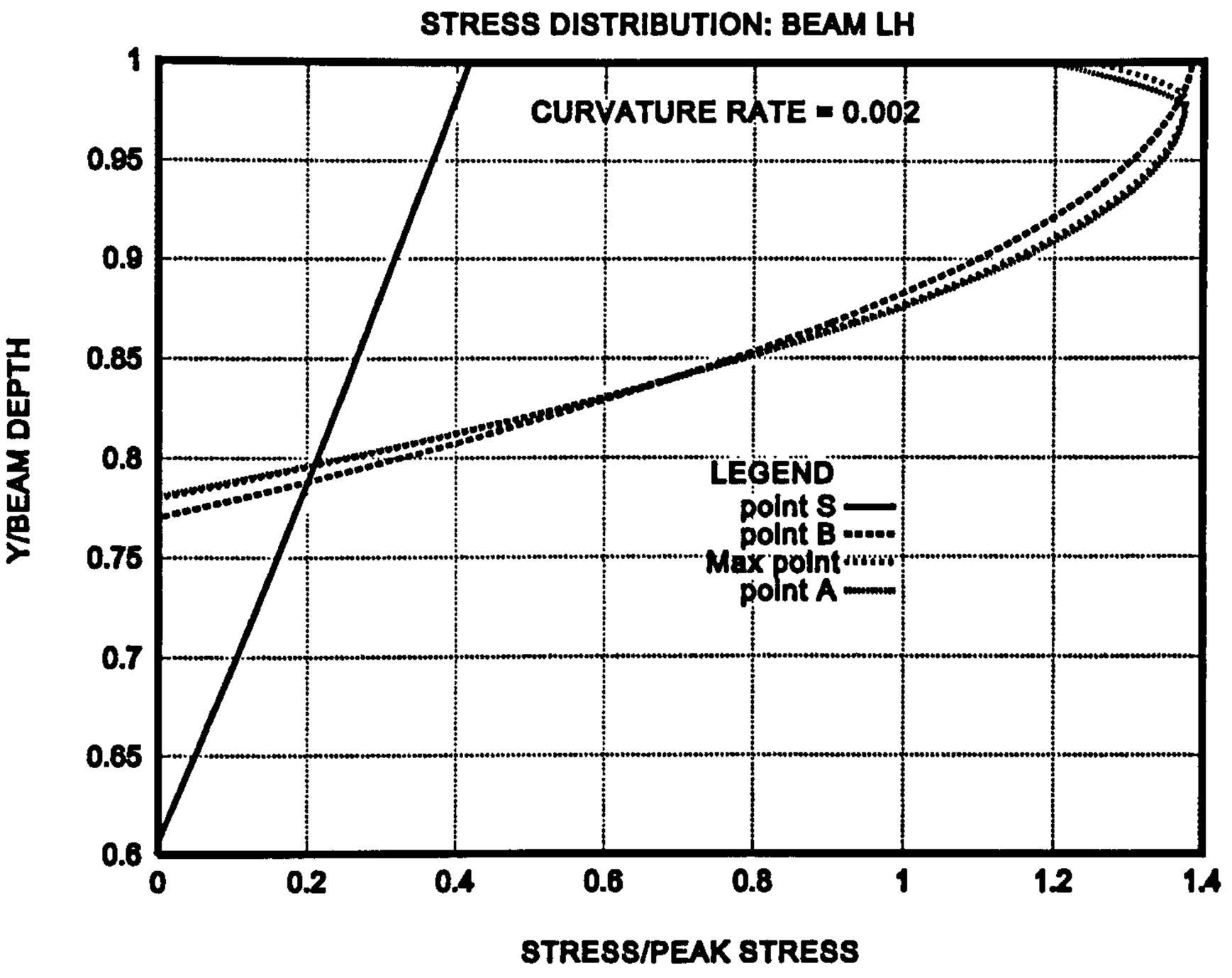

Figure 4.58 Normal stress distribution at $\dot{\kappa}$=0.002 for beam LH

Figure 4.59 shows the normal stress distribution obtained at a strain rate of 0.0388 for points S,B,M and A.

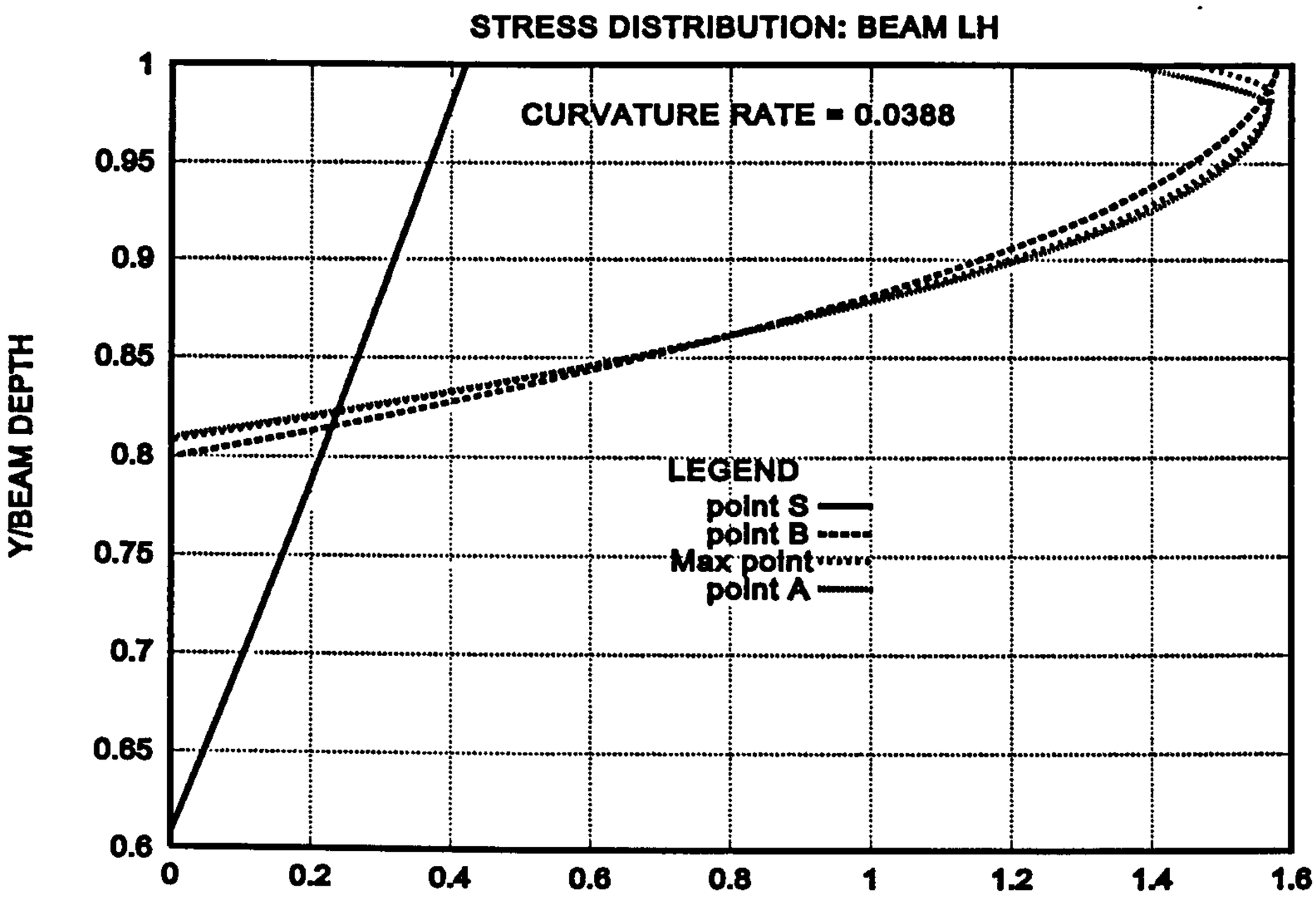

Figure 4.59 Normal stress distribution at $\dot{\kappa}$ =0.0388 for beam LH

In considering strain rates it is evident from the stress distribution curves that no strain softening occurs up to point B. At the maximum point moderate strain softening is seen to occur from the stress plots. At point A the strain softening is more pronounced.

The shear stress plots show that moderate shear stresses are carried up to and until point M. At point A the shear stress is far to high to be carried by concrete. Hence indicating concrete fails in shear and confirming the bi linear curvature relationship for Moment-Curvature still applies, when strain rates are taken into account.

A parametric study was carried out to investigate the effect of varying the curvature rate, reinforcement and column loading in combination. Beam LL was adopted for this part of the investigation.

Investigations were carried out using a value for the area of steel reinforcement of 4000 mm^2 (here on referred to as full reinforcement, F). The area of reinforcement was then lowered to a value of 2000 mm^2 (here on referred to as half reinforcement, H), which was then subsequently further lowered to a value of 1334 mm^2 (here on referred to a third reinforcement, T). The axial loads considered were zero, $0.12N_{max}$, $0.2N_{max}$, $0.4N_{max}$, $0.6N_{max}$ and N_{max}. The curvature rates considered were 0.0005, 0.002 and 0.0388. The normal stress and shear stress distributions are presented for the $0.1N_{max}$ and $0.6N_{max}$ cases only.

Figure 4.60 to Figure 4.72 show the results for the case where full reinforcement was used.

Figure 4.60 shows the Moment-Curvature relationship for full Reinforcement with curvature rate of 0.00005 at various column loadings.

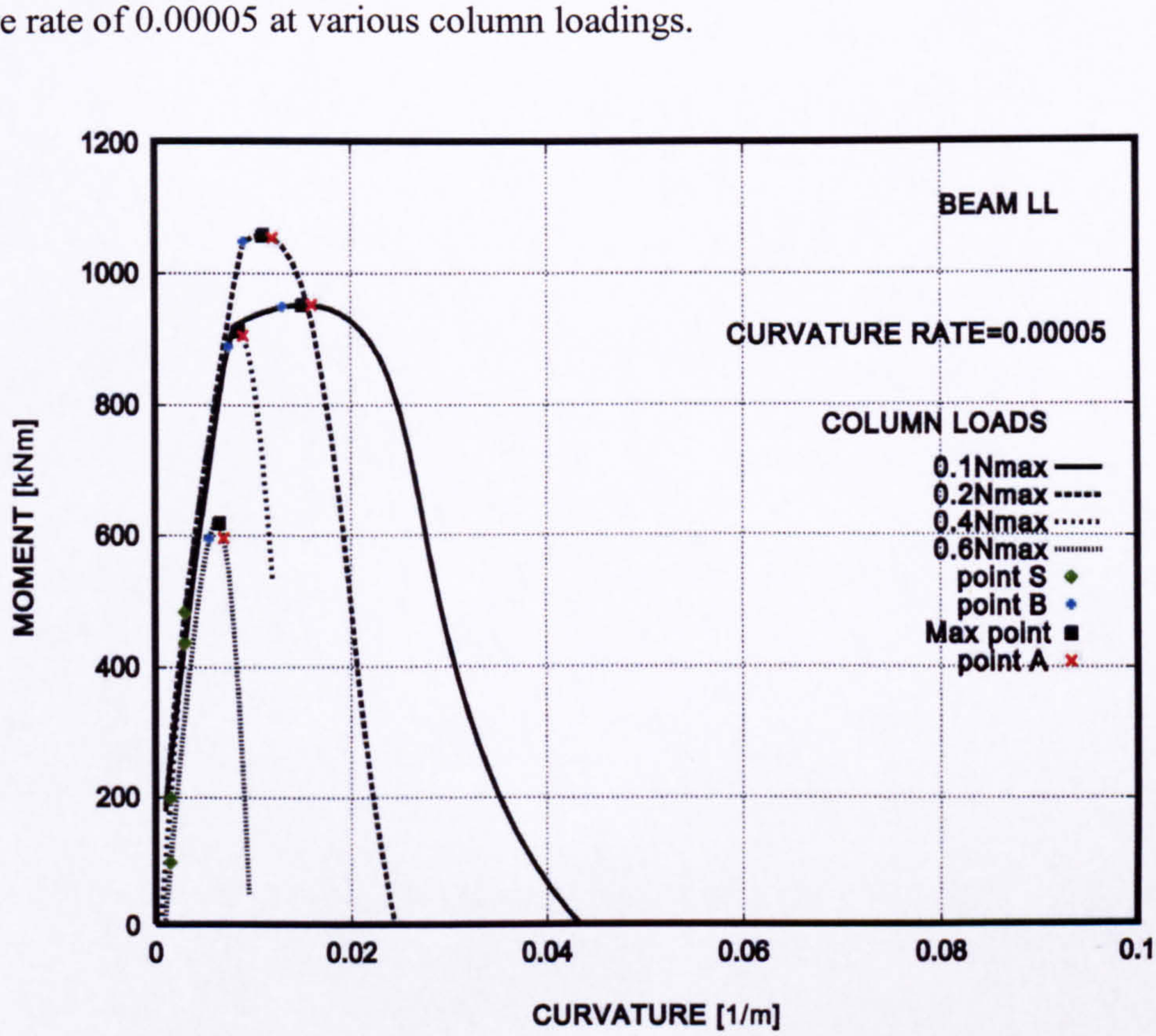

Figure 4.60 Moment-Curvature at κ =0. 00005 for various column loadings, (F)

Figure 4.61 shows the Moment-Curvature relationship for full Reinforcement with curvature rate of 0.002 at various column loadings

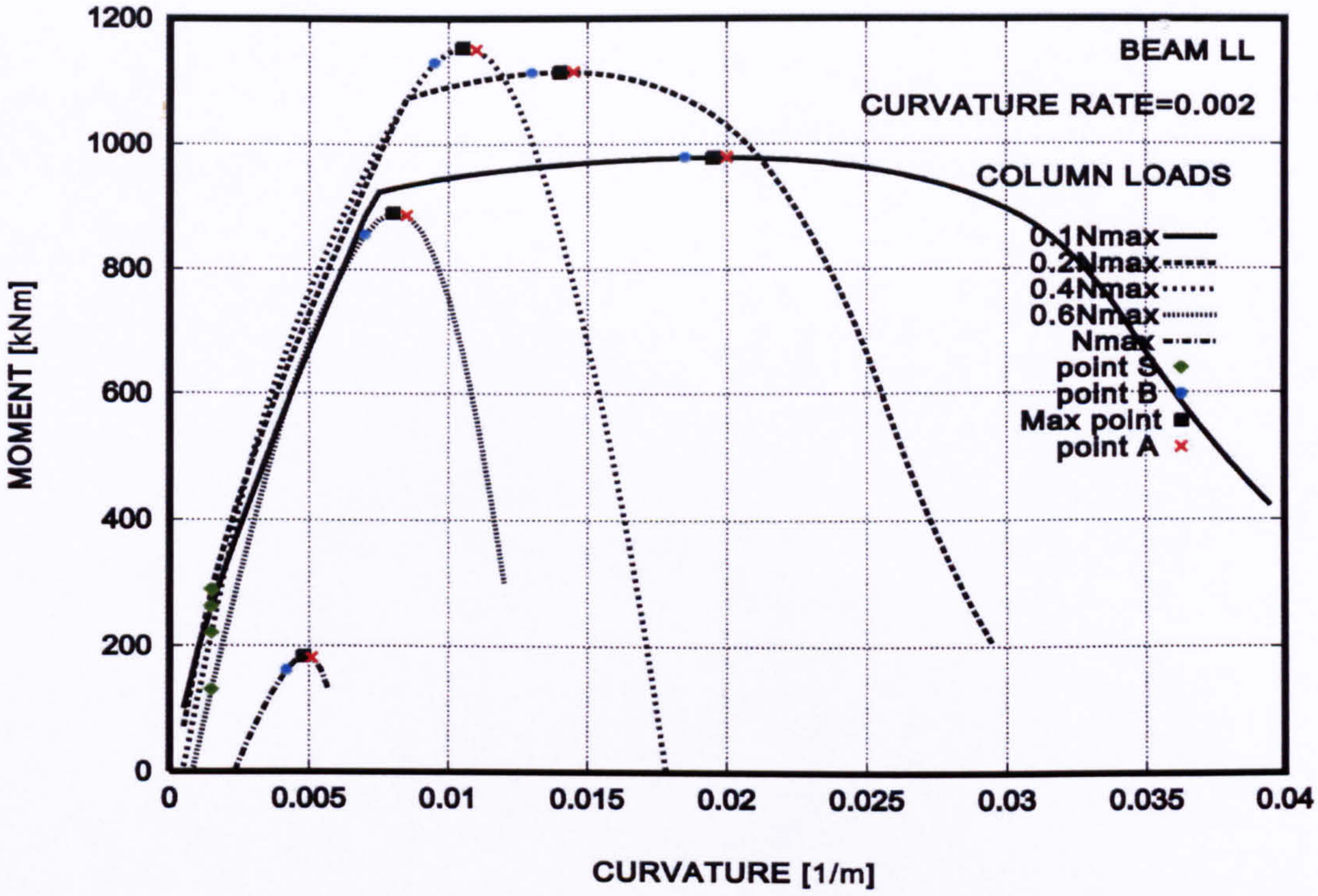

Figure 4.61 Moment-Curvature at κ=0. 002 for various column loadings (F)

Figure 4.62 shows the Moment-Curvature relationship for full Reinforcement with curvature rate of 0.0388 at various column loadings

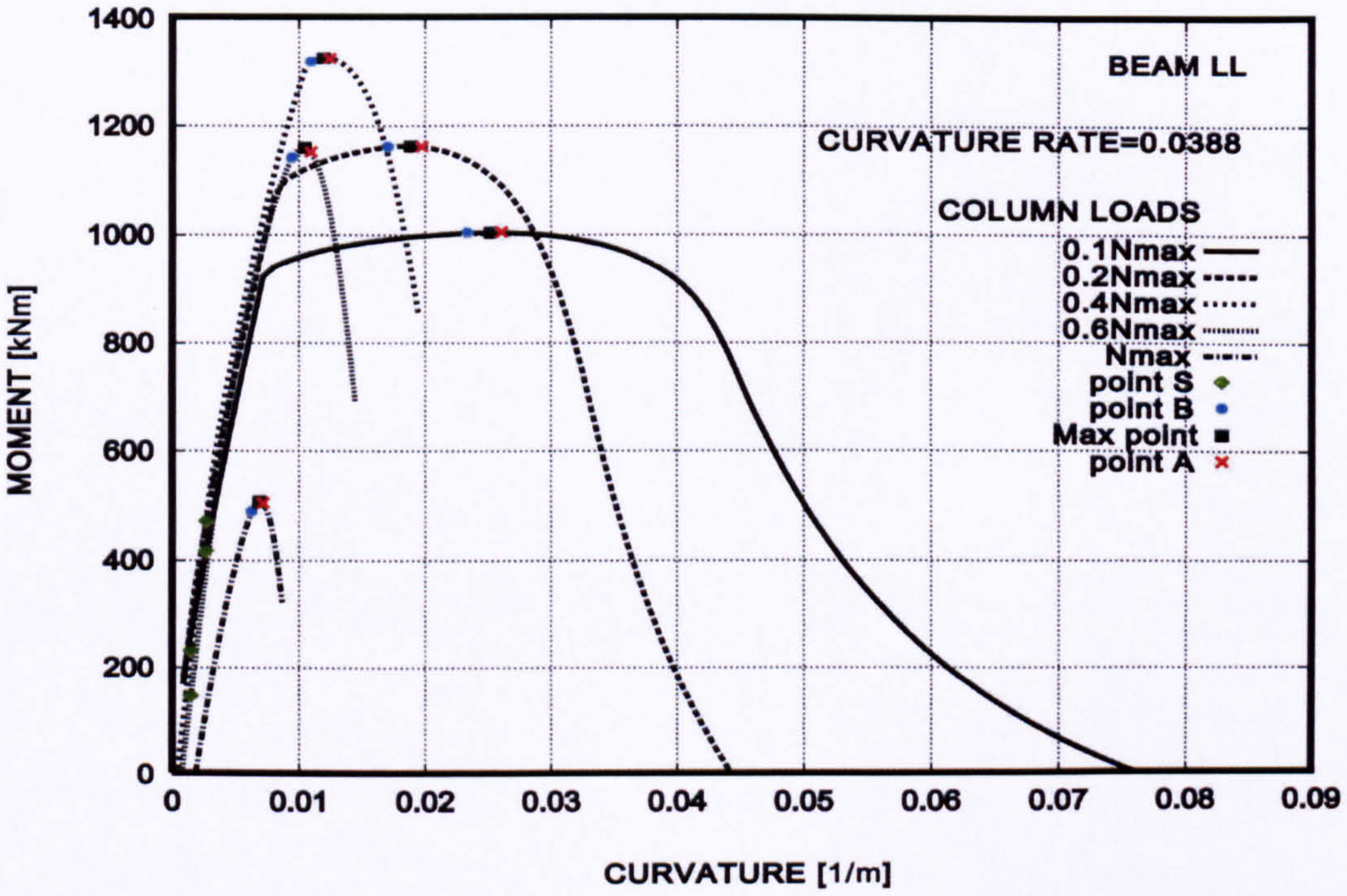

Figure 4.62 Moment-Curvature at κ=0. 0388 for various column loadings (F)

Figure 4.60 to Figure 4.62 show a decrease in ductility as the column load is increased. However an increase in ductility is apparent as the curvature rate is increased.

Figure 4.63 shows the normal stress distribution for beam LL with full reinforcement, an axial loading of $0.1N_{max}$ and a curvature rate of 0.00005.

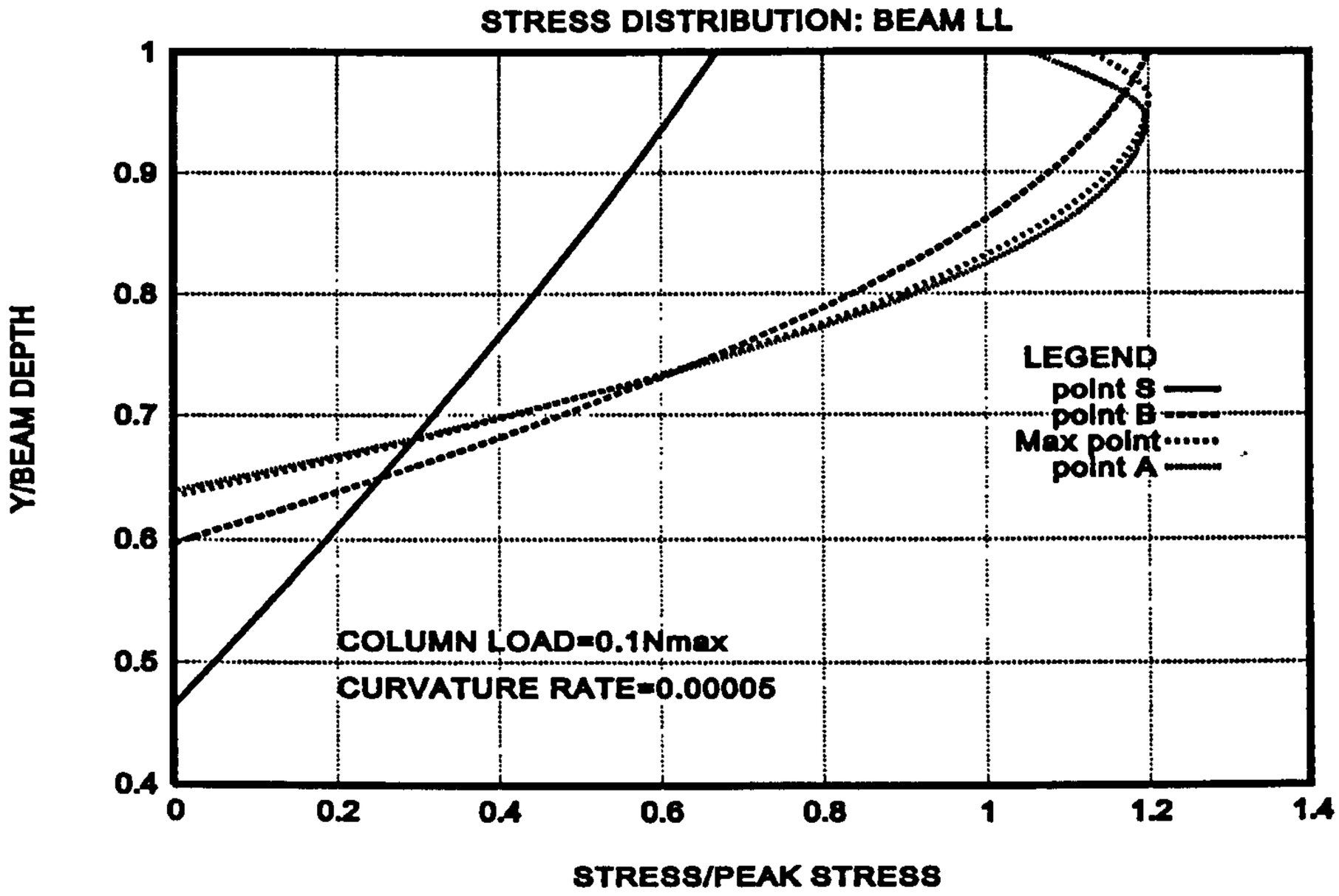

Figure 4.63 Normal stress distribution at $0.1N_{max}$ and κ =0. 00005 (F)

Figure 4.64 shows the shear stress distribution for beam LL with full reinforcement, an axial loading of $0.1N_{max}$ and a curvature rate of 0.00005.

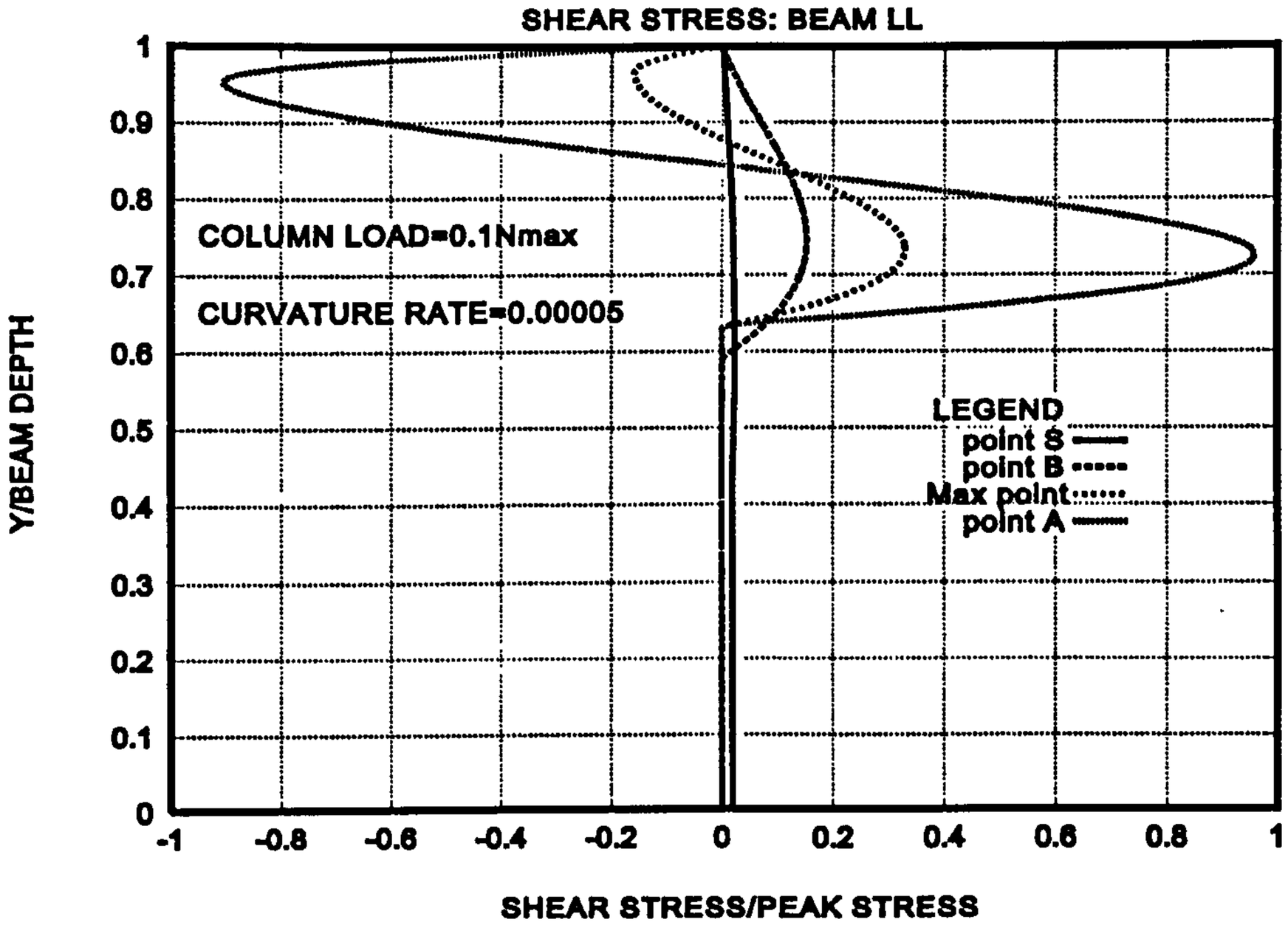

Figure 4.64 Shear stress distribution at $0.1N_{max}$ and κ =0. 00005 (F)

Figure 4.65 shows the normal stress distribution for beam LL with full reinforcement, an axial loading of $0.1N_{max}$ and a curvature rate of 0.002.

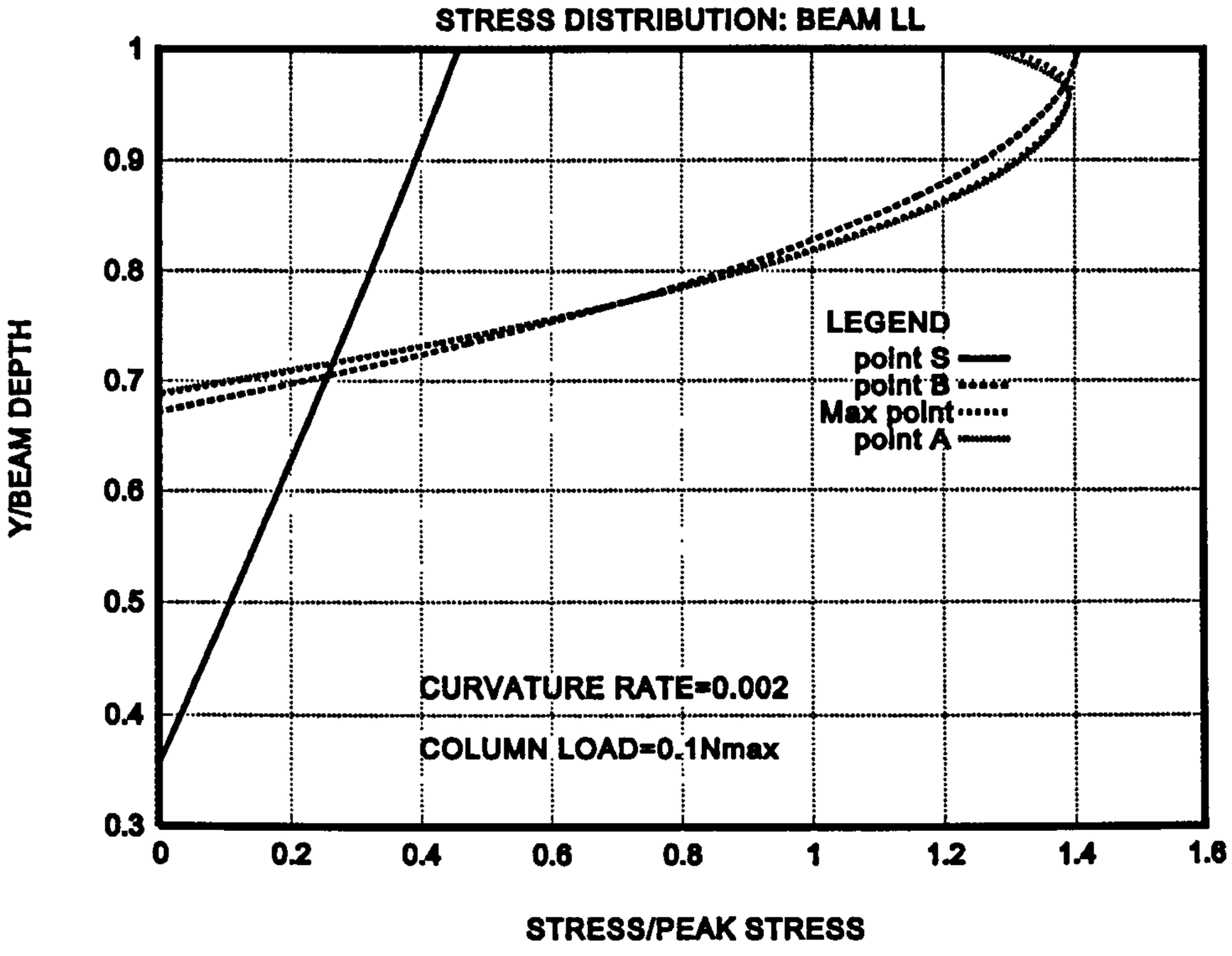

Figure 4.65 Normal stress distribution at $0.1N_{max}$ and $\dot{\kappa}$ =0. 002 (F)

Figure 4.66 shows the shear stress distribution for beam LL with full reinforcement, an axial loading of $0.1N_{max}$ and a curvature rate of 0.002.

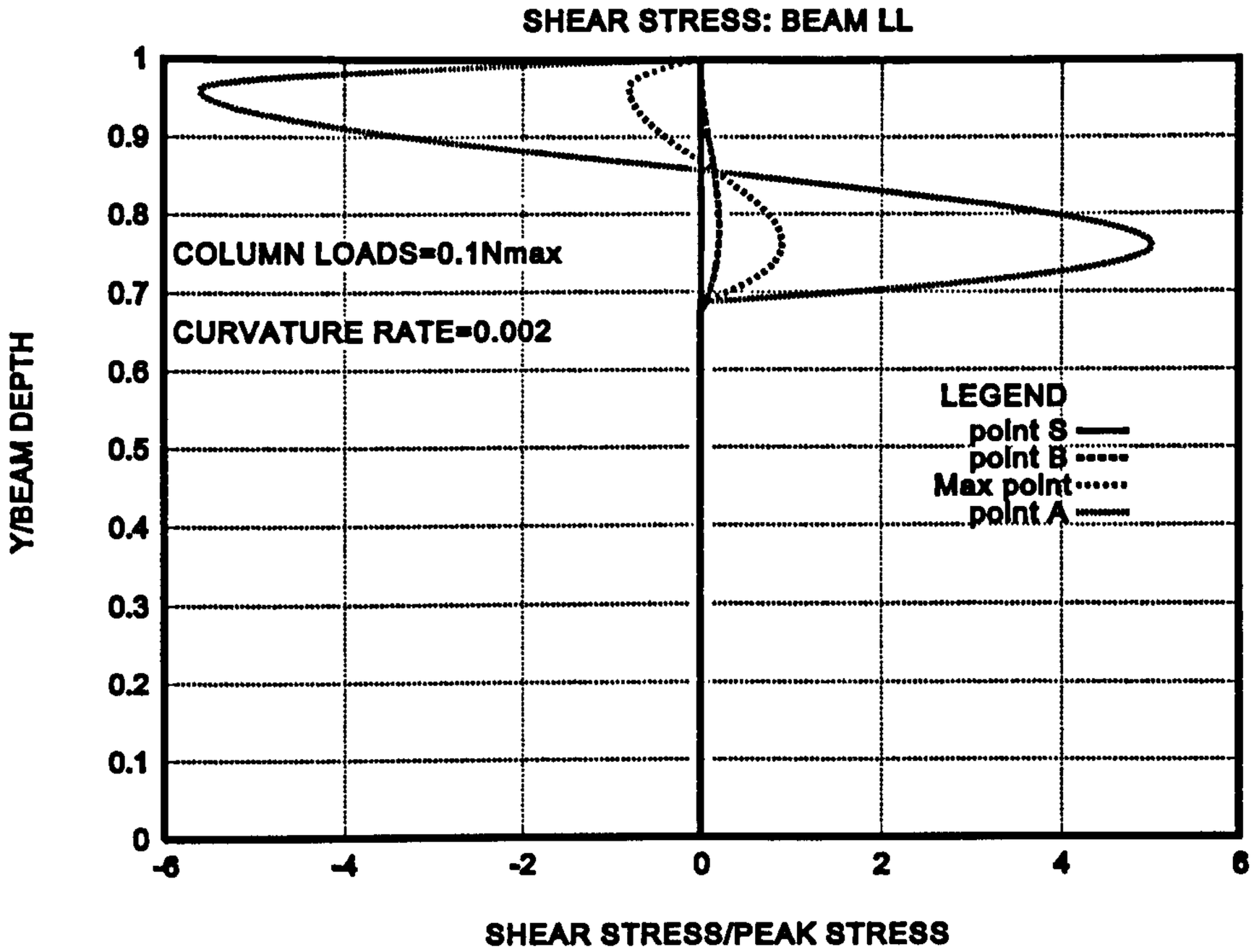

Figure 4.66 Shear stress distribution at $0.1N_{max}$ and $\dot{\kappa}$ =0. 002 (F)

Figure 4.67 shows the normal stress distribution for beam LL with full reinforcement, an axial loading of $0.1N_{max}$ and a curvature rate of 0.0388.

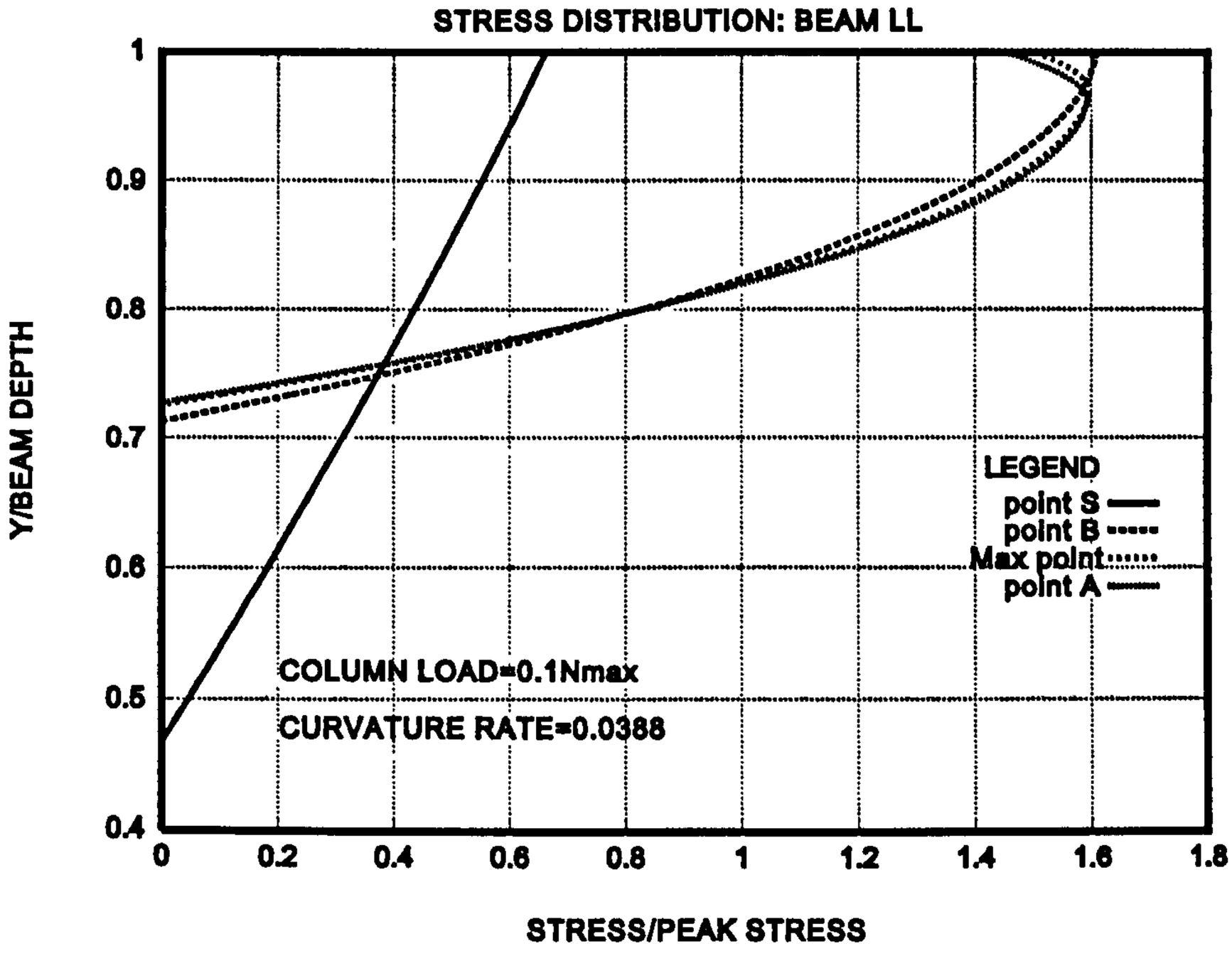

Figure 4.67 Normal stress distribution at $0.1N_{max}$ and $\dot{\kappa}$ =0. 0388 (F)

Figure 4.68 shows the shear stress distribution for beam LL with full reinforcement, an axial loading of $0.1N_{max}$ and a curvature rate of 0.0388.

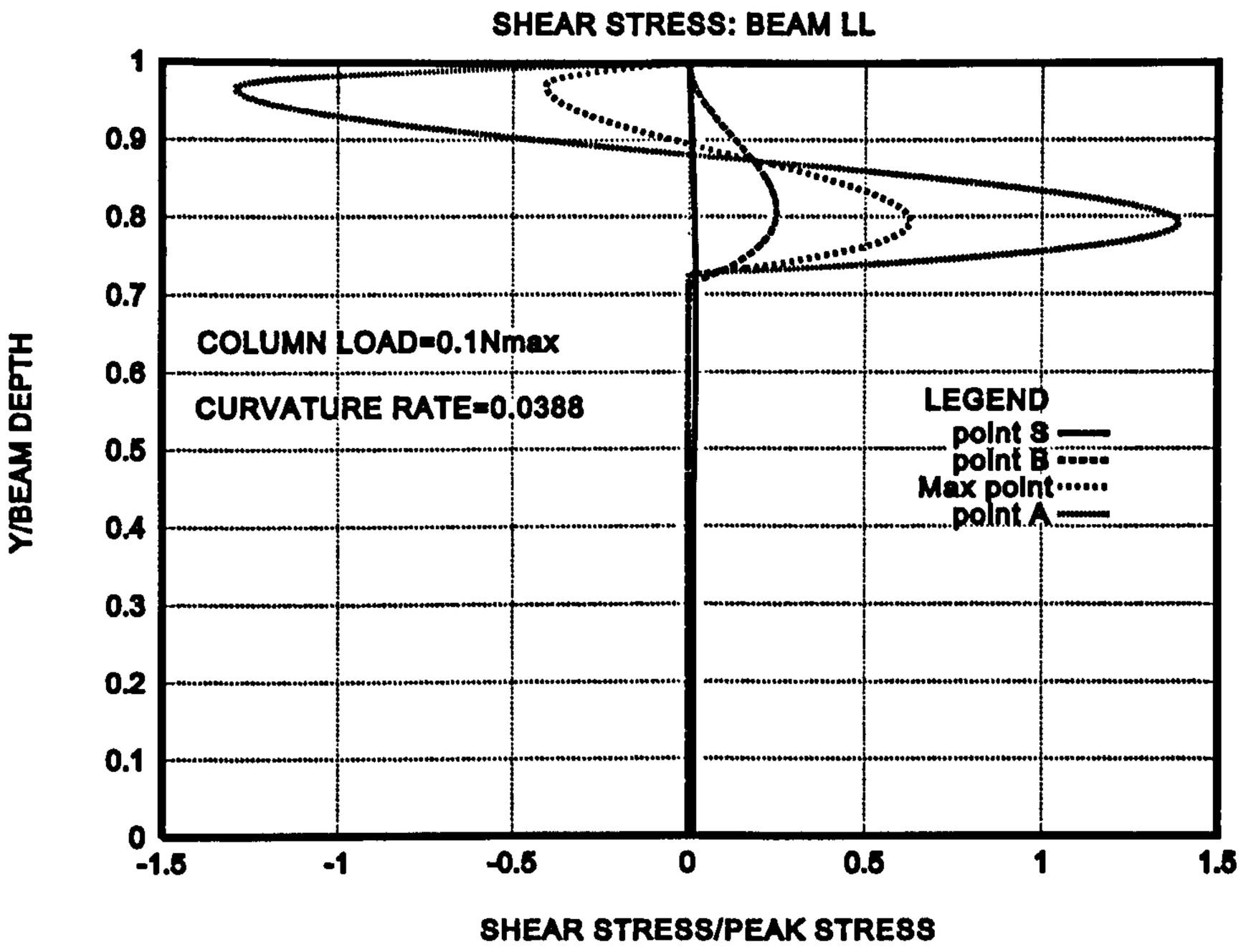

Figure 4.68 Shear stress distribution at $0.1N_{max}$ and $\dot{\kappa}$ =0. 0388 (F)

Figure 4.69 shows the normal stress distribution for beam LL with full reinforcement, an axial loading of $0.6N_{max}$ and a curvature rate of 0.002.

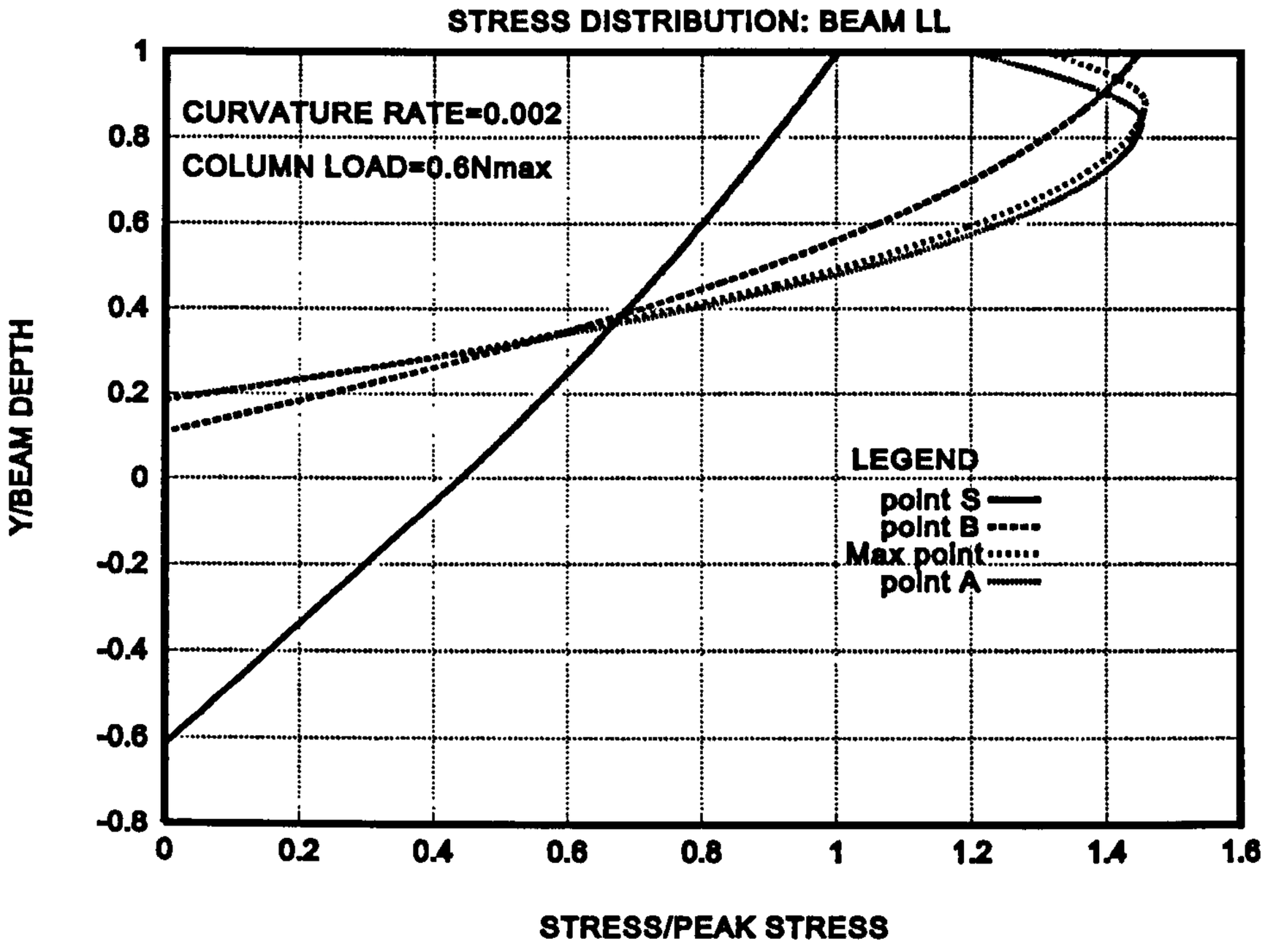

Figure 4.69 Normal stress distribution at $0.6N_{max}$ and $\dot{\kappa}$ =0. 002 (F)

Figure 4.70 shows the shear stress distribution for beam LL with full reinforcement, an axial loading of $0.6N_{max}$ and a curvature rate of 0.002.

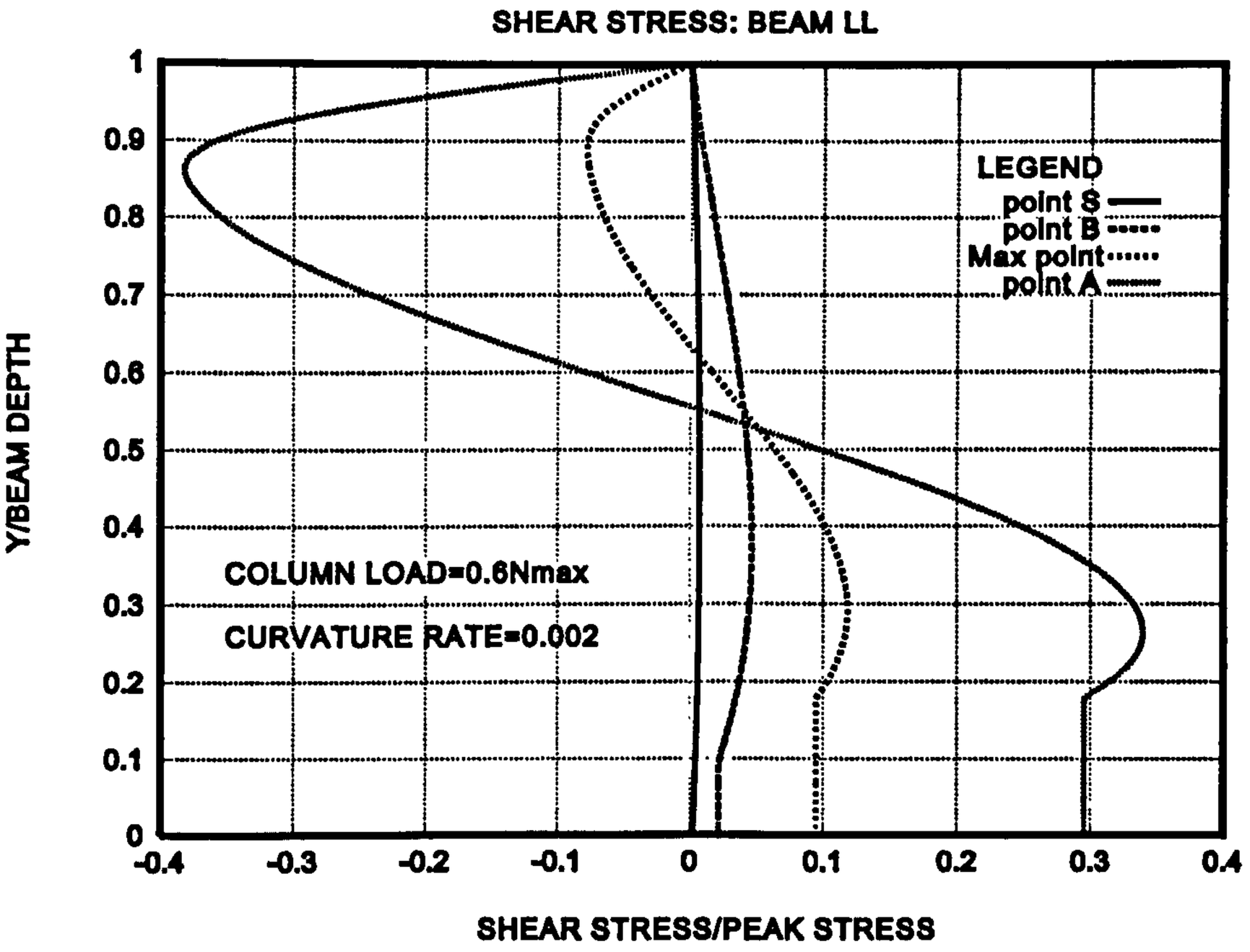

Figure 4.70 Shear stress distribution at $0.6N_{max}$ and $\dot{\kappa}$ =0. 002 (F)

Figure 4.71 shows the normal stress distribution for beam LL with full reinforcement, an axial loading of $0.6N_{max}$ and a curvature rate of 0.0388.

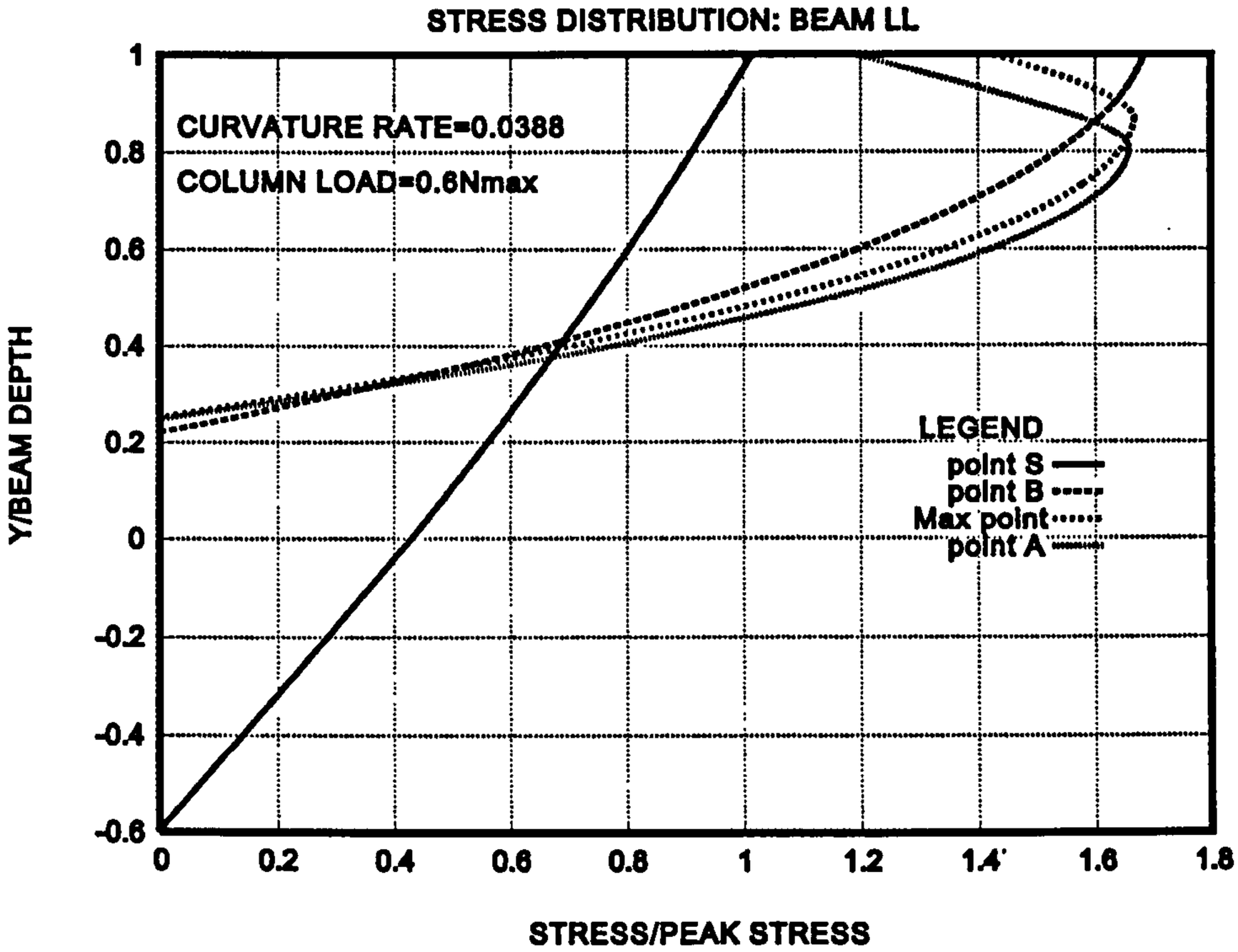

Figure 4.71 Normal stress distribution at $0.6N_{max}$ and $\dot{\kappa}$ =0. 0388 (F)

Figure 4.72 shows the shear stress distribution for beam LL with full reinforcement, an axial loading of $0.6N_{max}$ and a curvature rate of 0.0388.

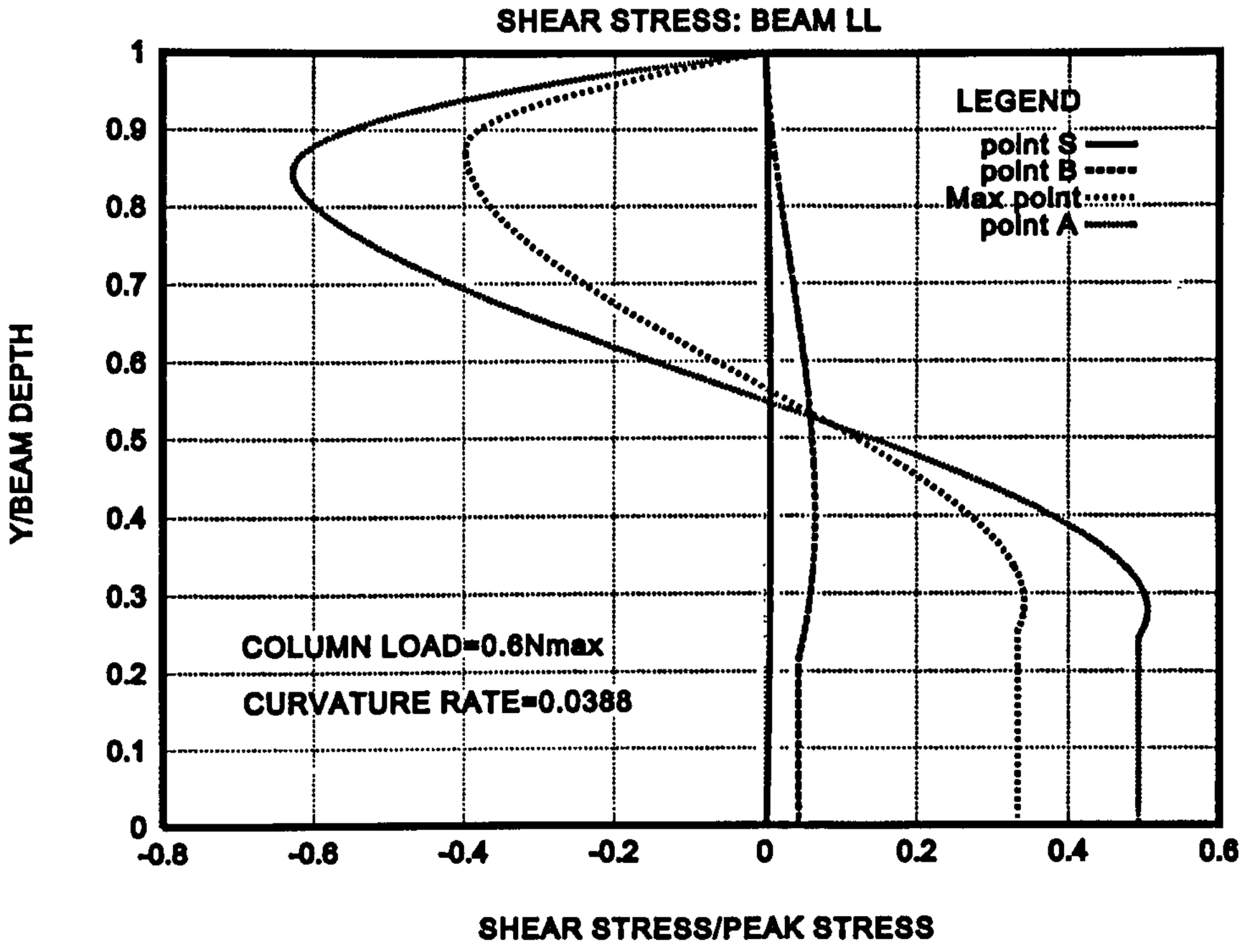

Figure 4.72 Shear stress distribution at $0.6N_{max}$ and $\dot{\kappa}$ =0. 0388 (F)

The normal stress distribution plots show that noticeable softening occurs at point A, where full reinforcement is adopted. However the shear stress plots show that the shear stresses developed at point A are too high for concrete to bear and hence failure by this point has to have occurred. The shear stress increases for both $0.1N_{max}$ and 0.6 N_{max} axial loading cases. In the case of the lower axial load the shear stress is seen to increase with curvature rate up to a curvature rate of 0.002 and then decreases with a curvature rate of 0.0388. The shear stresses are seen to be smaller with the higher axial load. However the shear plots for the higher axial load show a more pronounced S shape. This shows the higher axial loading has produced a compressive crushing effect in a greater length of the beam. This is consistent with what is to be expected as the axial load is increased.

Figure 4.73 to Figure 4.87 show the results obtained for the case where half reinforcement was used.

Figure 4.73 shows the Moment-Curvature relationship for half Reinforcement with curvature rate of 0.00005 at various column loadings.

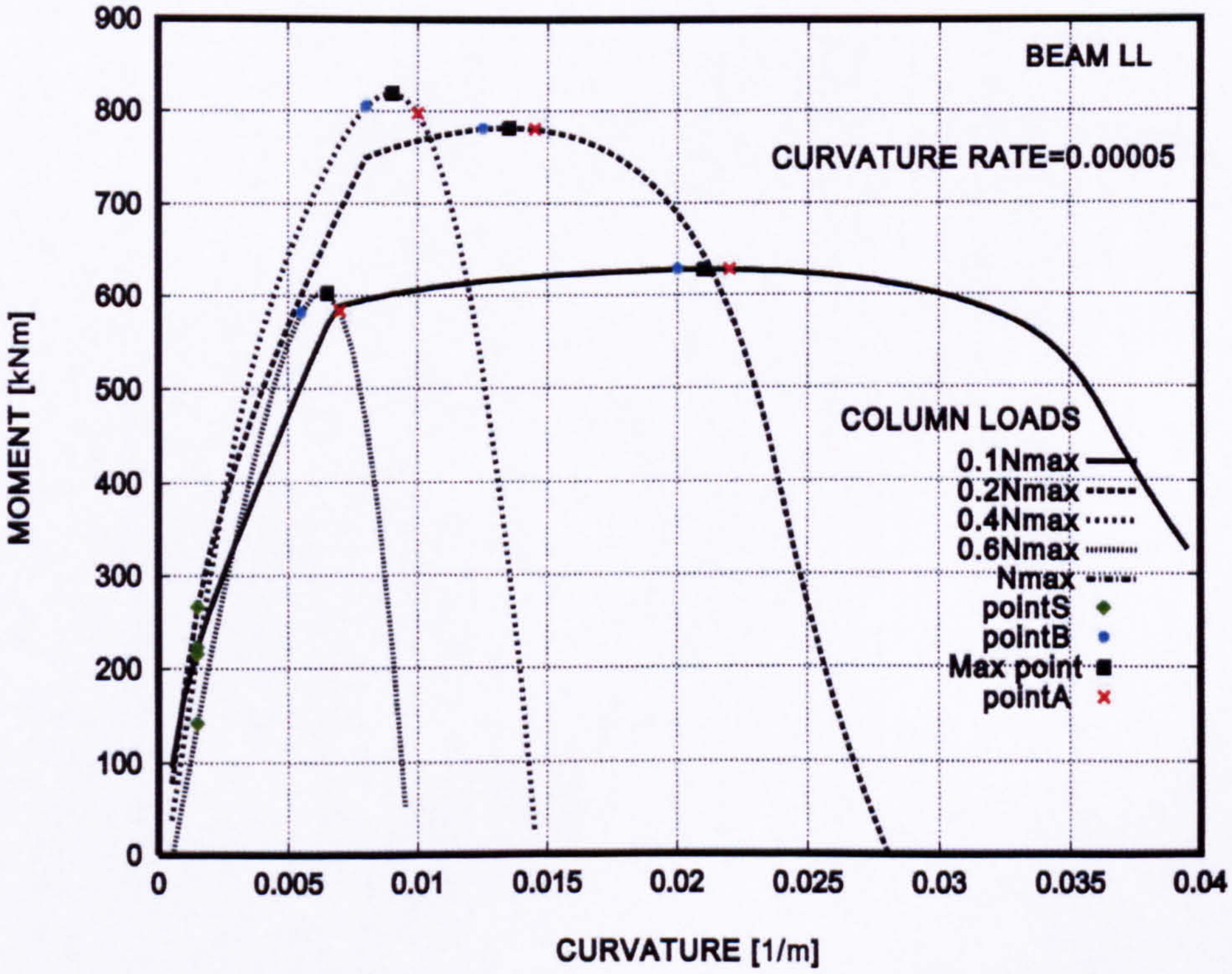

Figure 4.73 Moment-Curvature at κ =0. 00005 for various column loadings, (H)

Figure 4.74 shows the Moment-Curvature relationship for half Reinforcement with curvature rate of 0.002 at various column loadings

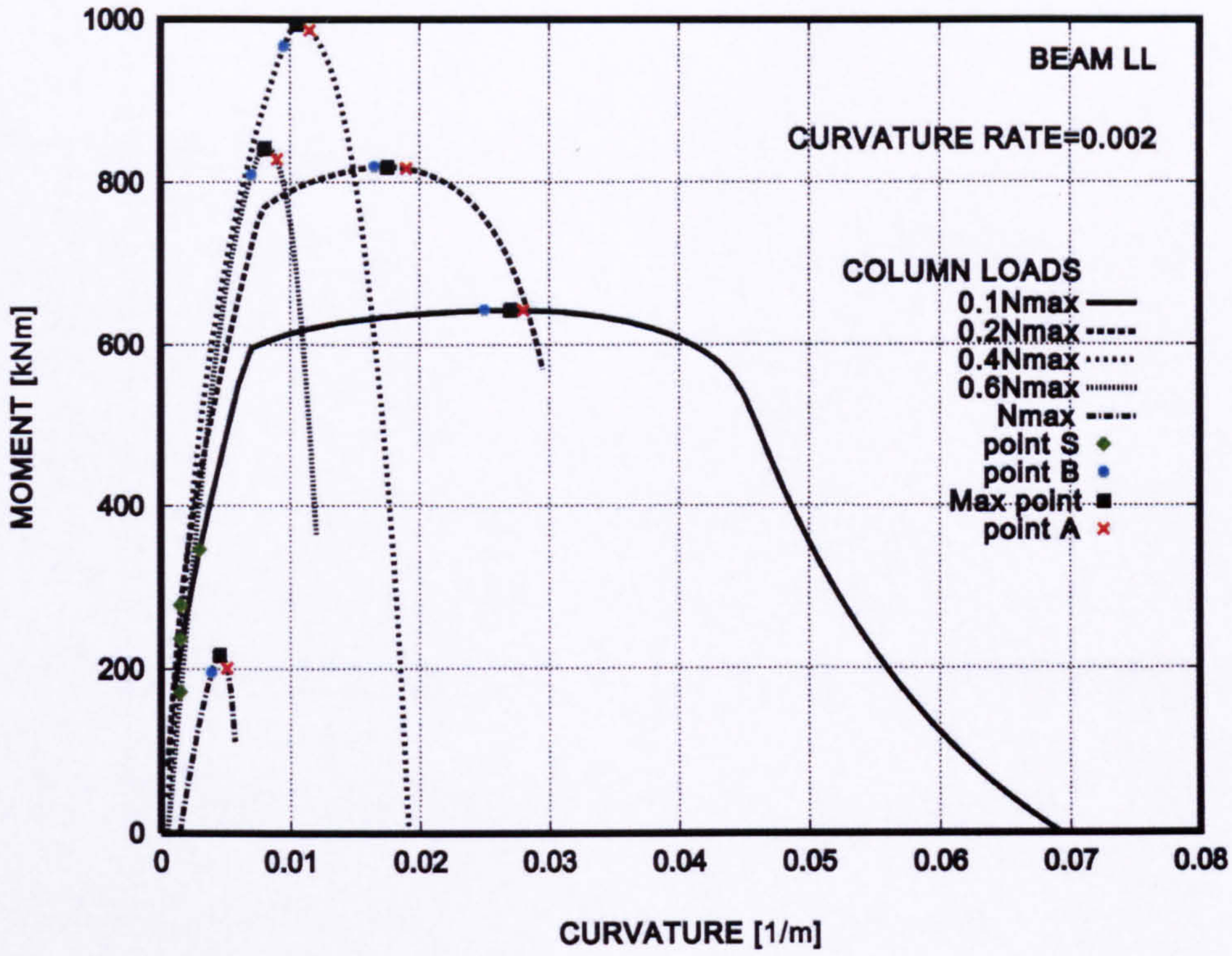

Figure 4.74 Moment-Curvature at κ =0. 002 for various column loadings (H)

Figure 4.75 shows the Moment-Curvature relationship for half Reinforcement with curvature rate of 0.0388 at various column loadings

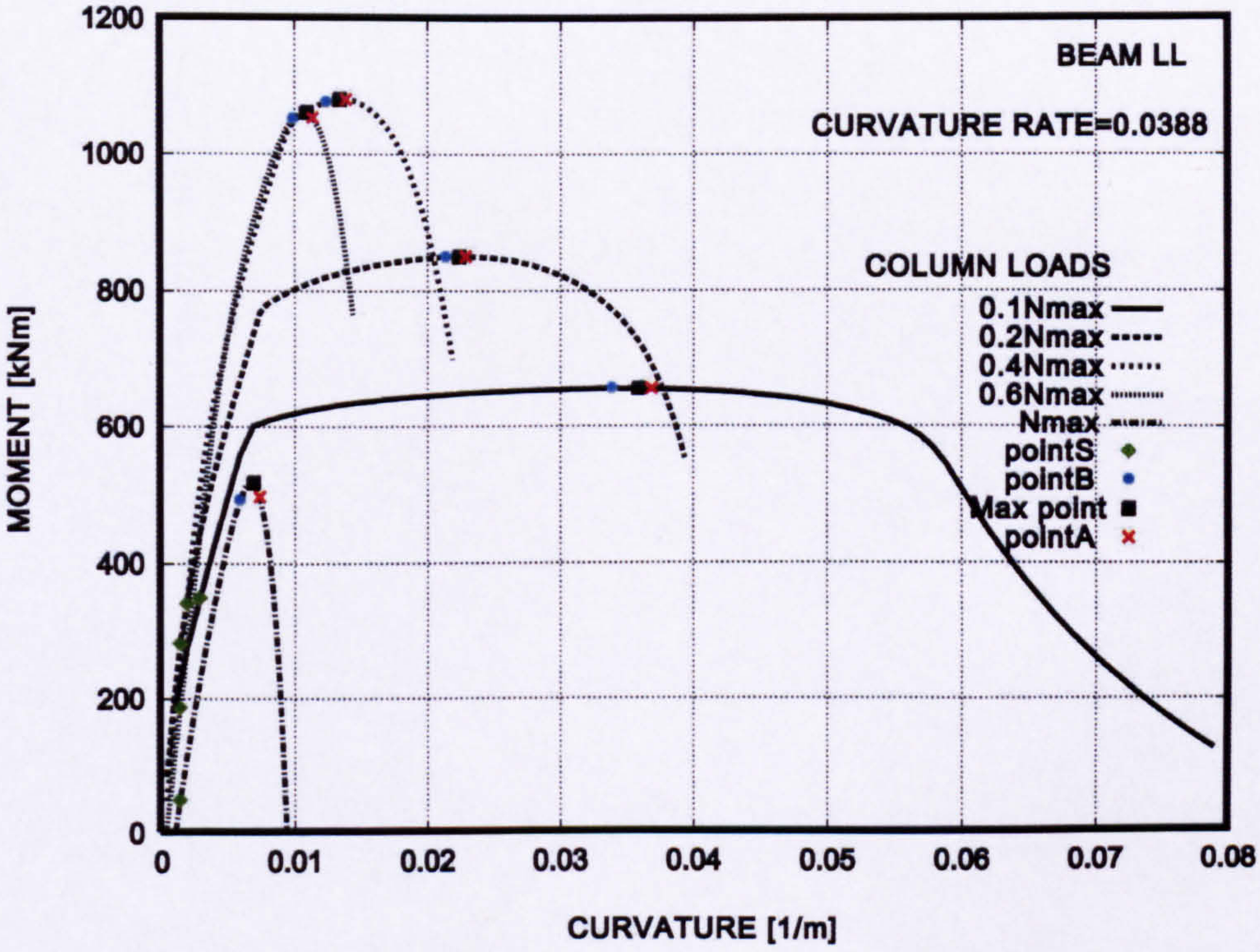

Figure 4.75 Moment-Curvature at κ =0. 0388 for various column loadings (H)

Figures show a similar pattern of decreasing ductility with increasing axial load. A reduction is seen with increasing curvature rates as compared with the case where full reinforcement was investigated.

Figure 4.76 shows the normal stress distribution for beam LL with half reinforcement, an axial loading of $0.1N_{max}$ and a curvature rate of 0.00005.

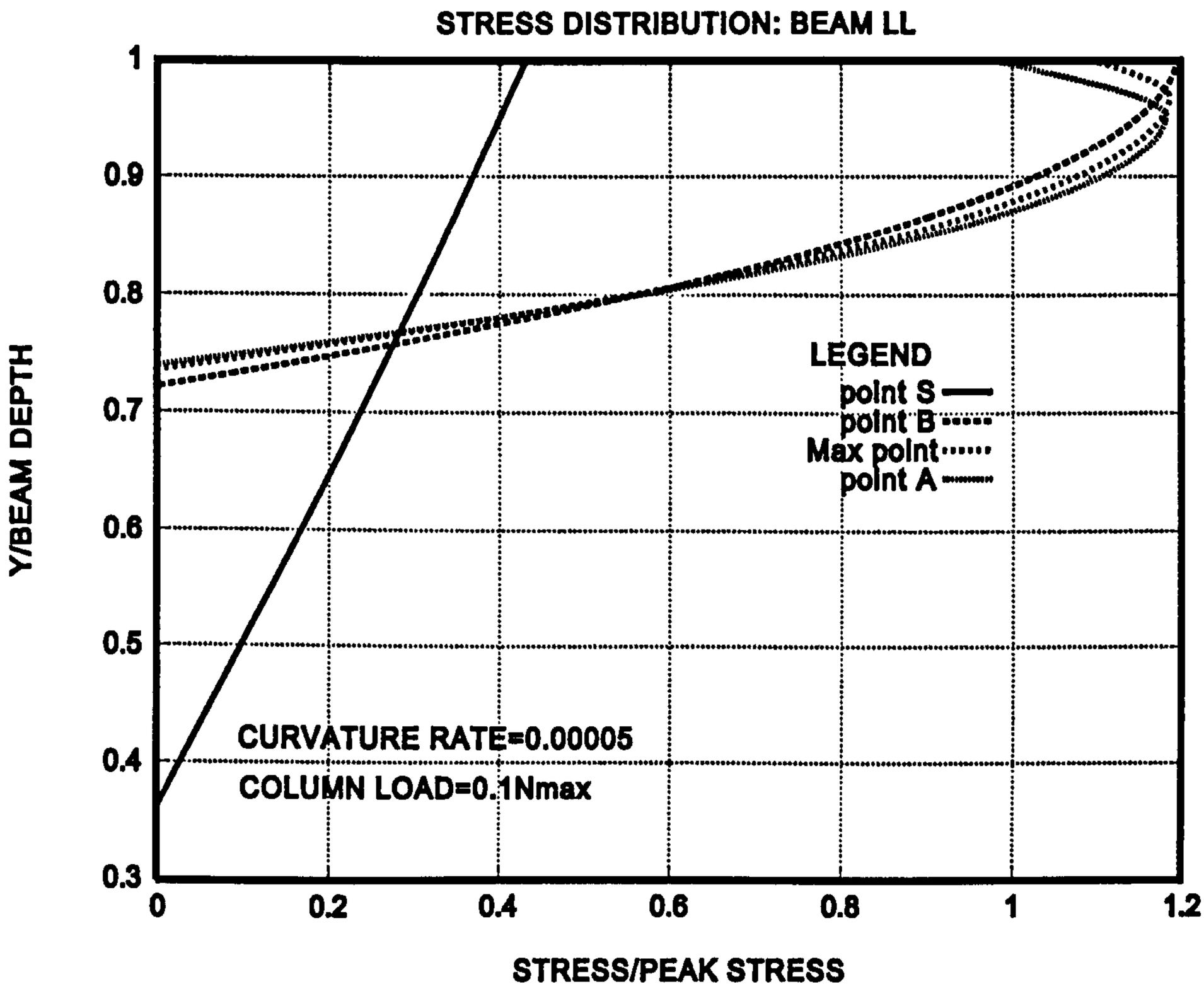

Figure 4.76 Normal stress distribution at $0.1N_{max}$ and $\dot{\kappa}$ =0. 00005 (H)

Figure 4.77 shows the shear stress distribution for beam LL with half reinforcement, an axial loading of $0.1N_{max}$ and a curvature rate of 0.00005.

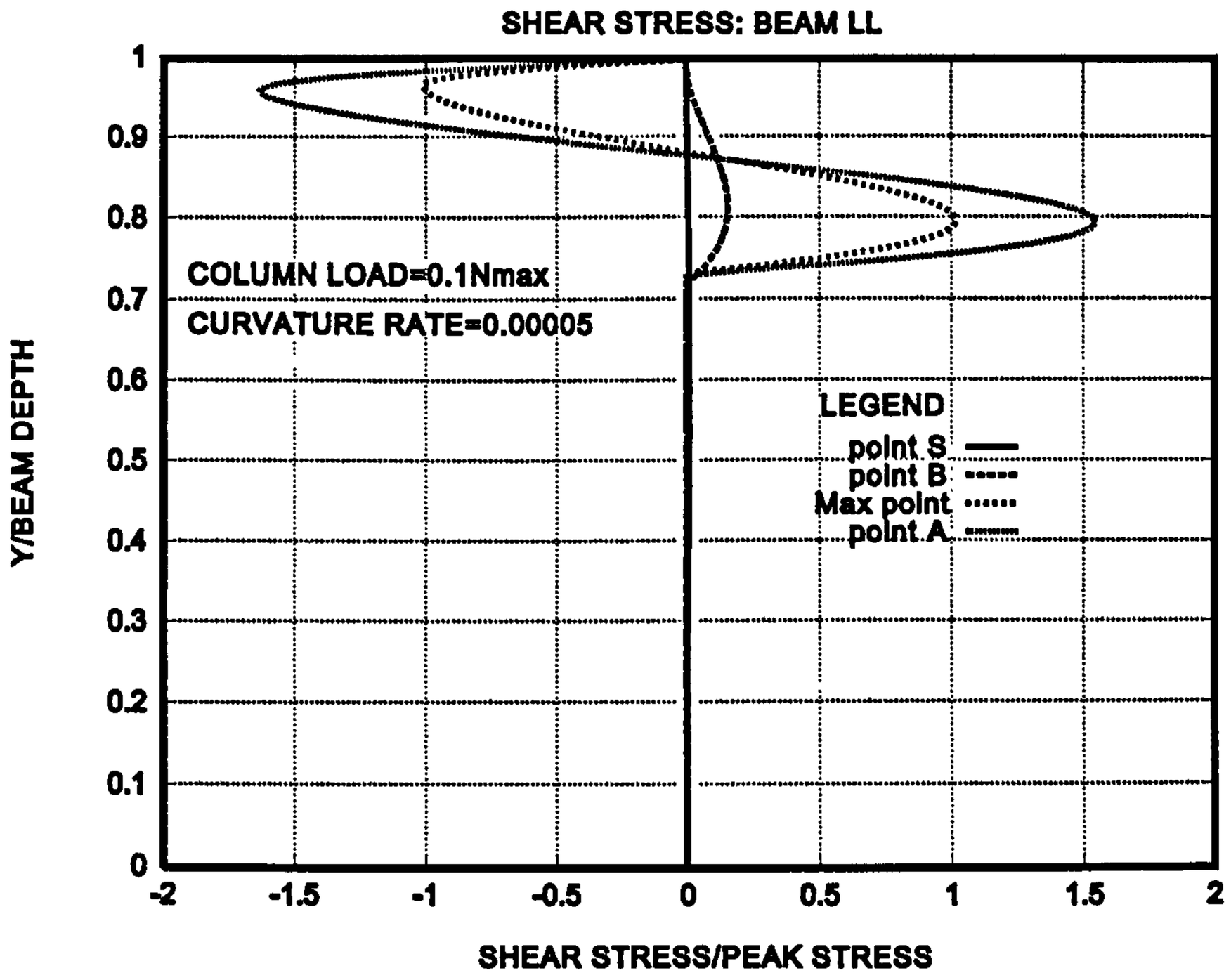

Figure 4.77 Shear stress distribution at $0.1N_{max}$ and $\dot{\kappa}$ =0. 00005 (H)

Figure 4.78 shows the normal stress distribution for beam LL with half reinforcement, an axial loading of $0.1N_{max}$ and a curvature rate of 0.002.

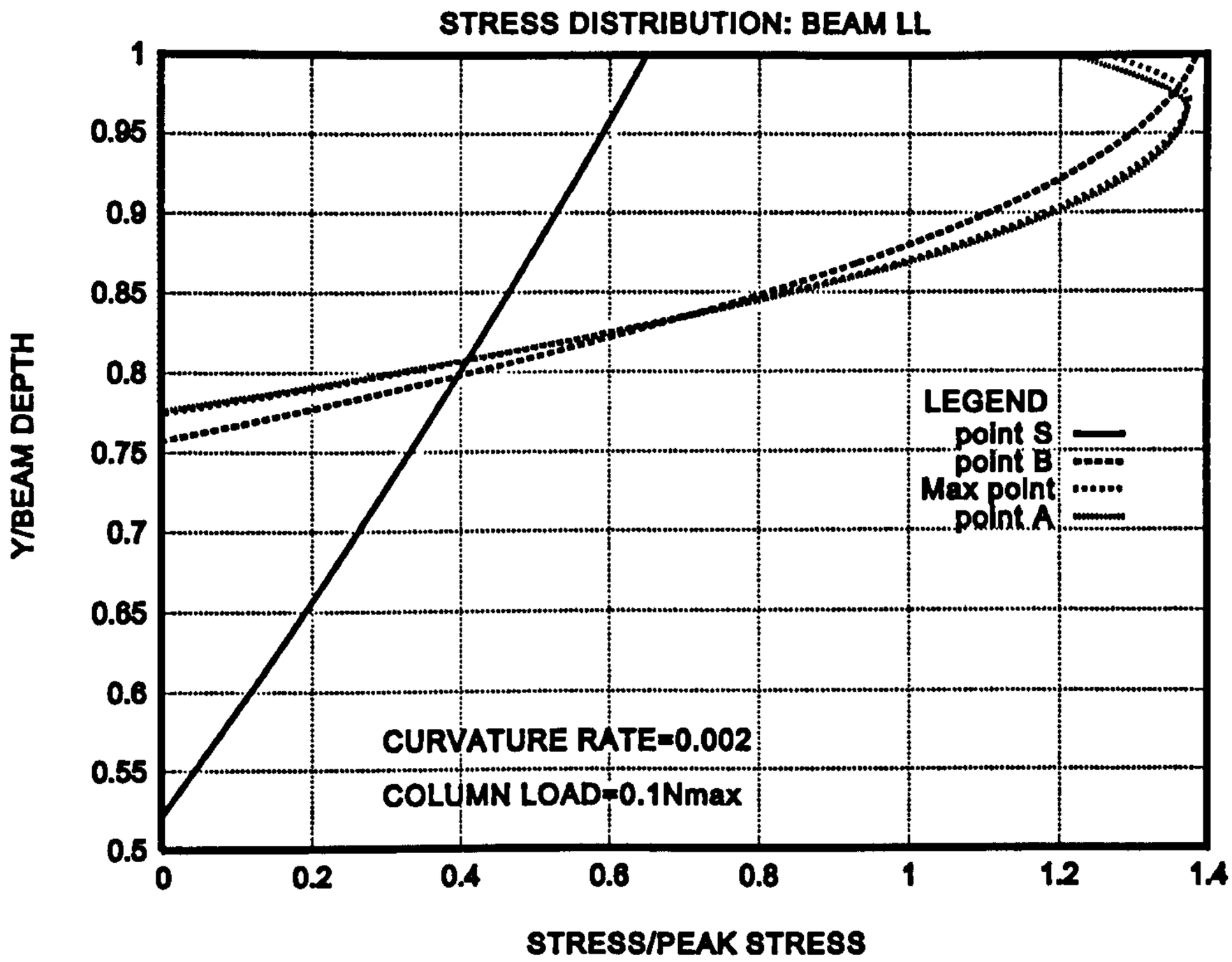

Figure 4.78 Normal stress distribution at $0.1N_{max}$ and $\dot{\kappa}$ =0. 002 (H)

Figure 4.79 shows the shear stress distribution for beam LL with half reinforcement, an axial loading of $0.1N_{max}$ and a curvature rate of 0.002.

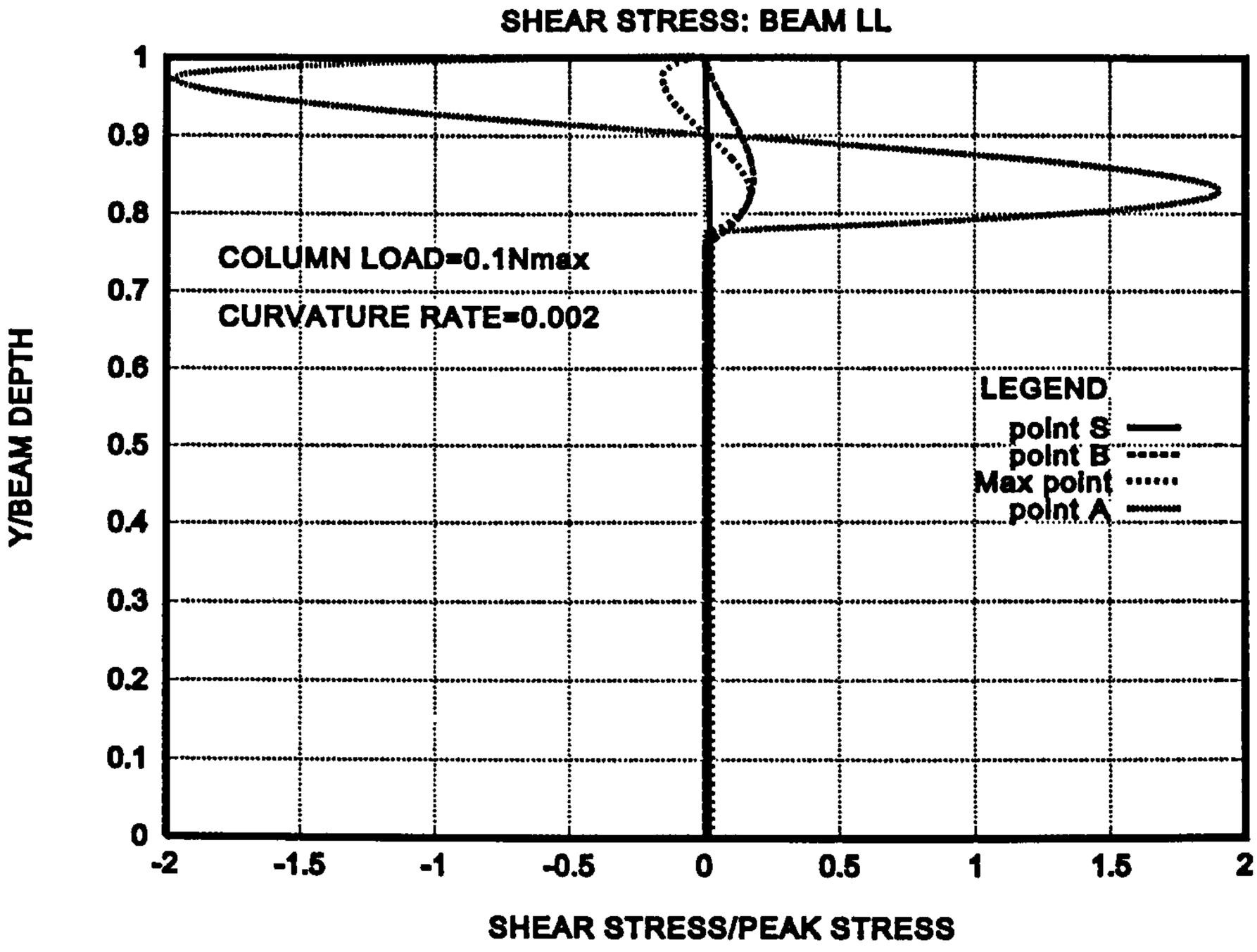

Figure 4.79 Shear stress distribution at $0.1N_{max}$ and $\dot{\kappa}$ =0. 002 (H)

Figure 4.80 shows the normal stress distribution for beam LL with half reinforcement, an axial loading of $0.1N_{max}$ and a curvature rate of 0.0388.

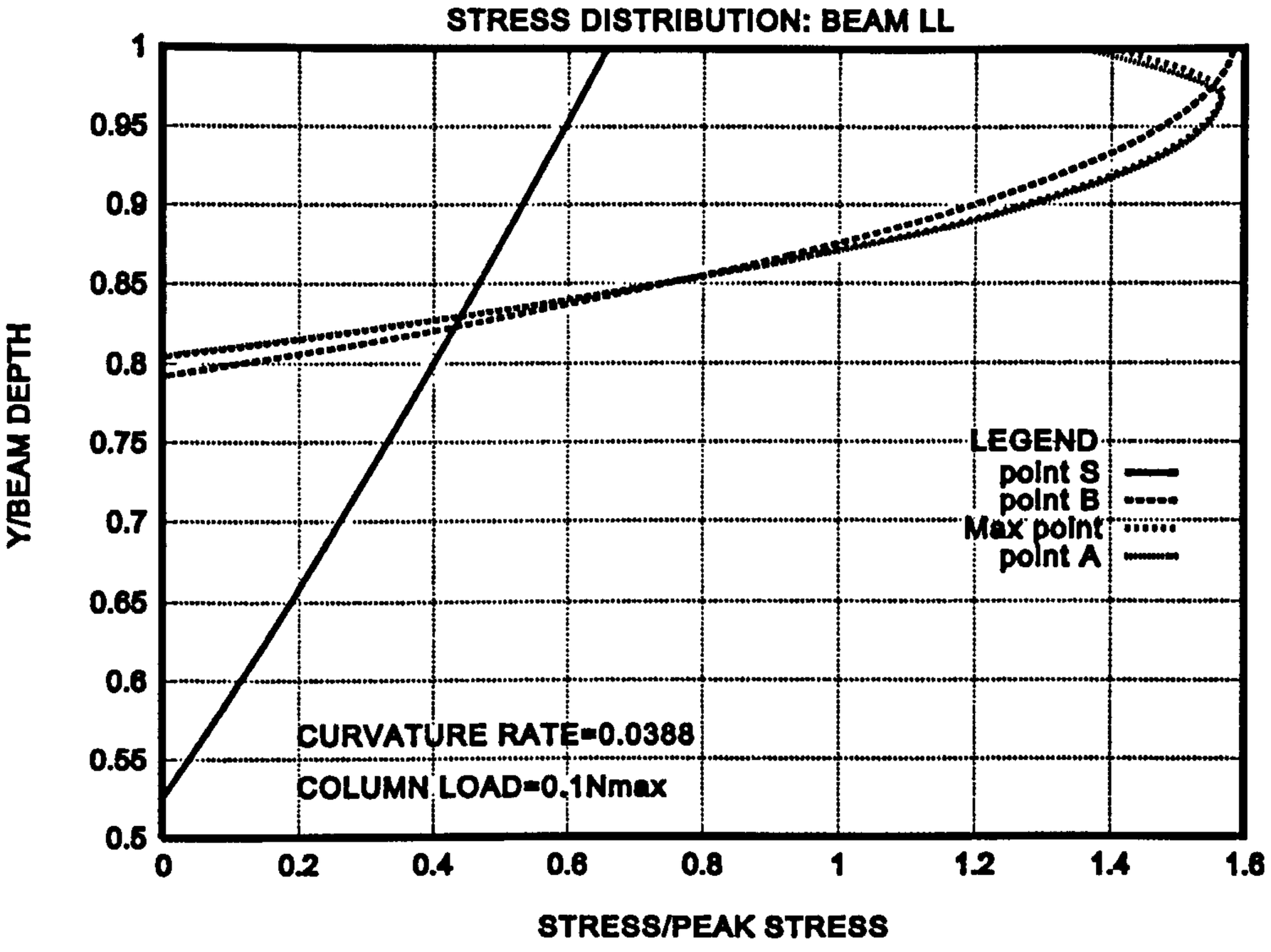

Figure 4.80 Normal stress distribution at $0.1N_{max}$ and $\dot{\kappa}$ =0. 0388 (H)

Figure 4.81 shows the shear stress distribution for beam LL with half reinforcement, an axial loading of $0.1N_{max}$ and a curvature rate of 0.0388.

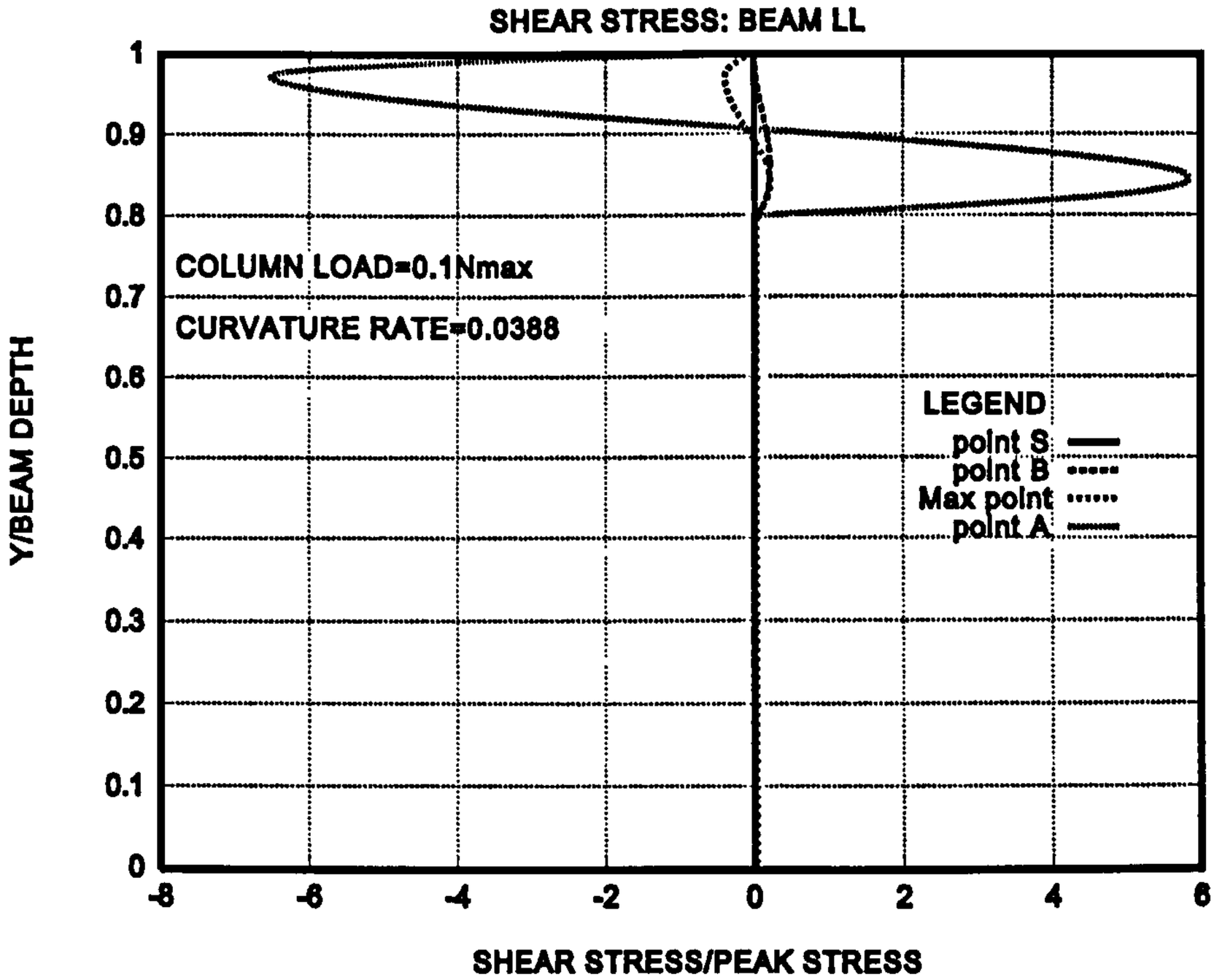

Figure 4.81 Shear stress distribution at $0.1N_{max}$ and $\dot{\kappa}$ =0. 0388 (H)

Figure 4.82 shows the normal stress distribution for beam LL with half reinforcement, an axial loading of $0.6N_{max}$ and a curvature rate of 0.00005.

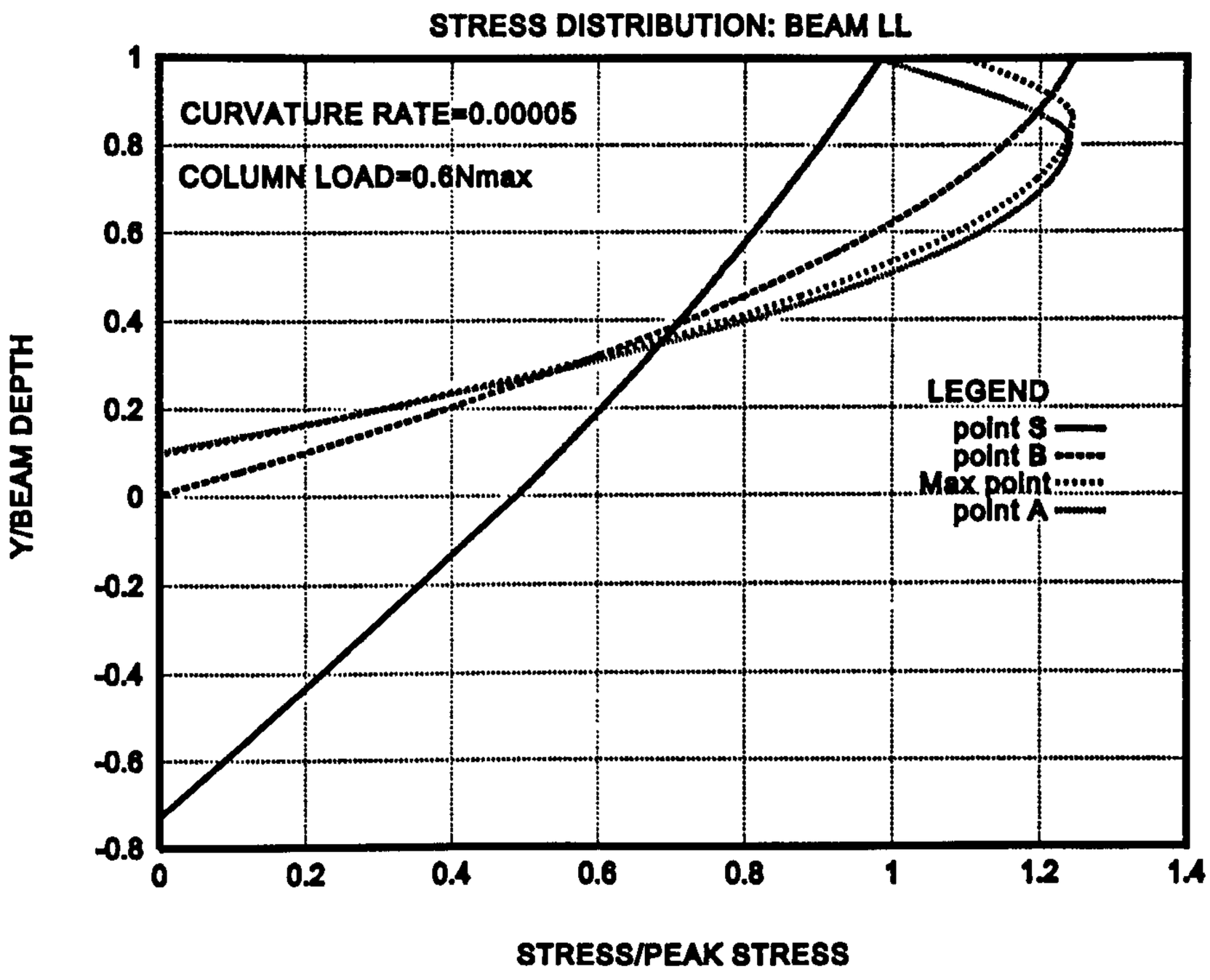

Figure 4.82 Normal stress distribution at $0.6N_{max}$ and $\dot{\kappa}$ =0. 00005 (H)

Figure 4.83 shows the shear stress distribution for beam LL with half reinforcement, an axial loading of $0.6N_{max}$ and a curvature rate of 0.00005.

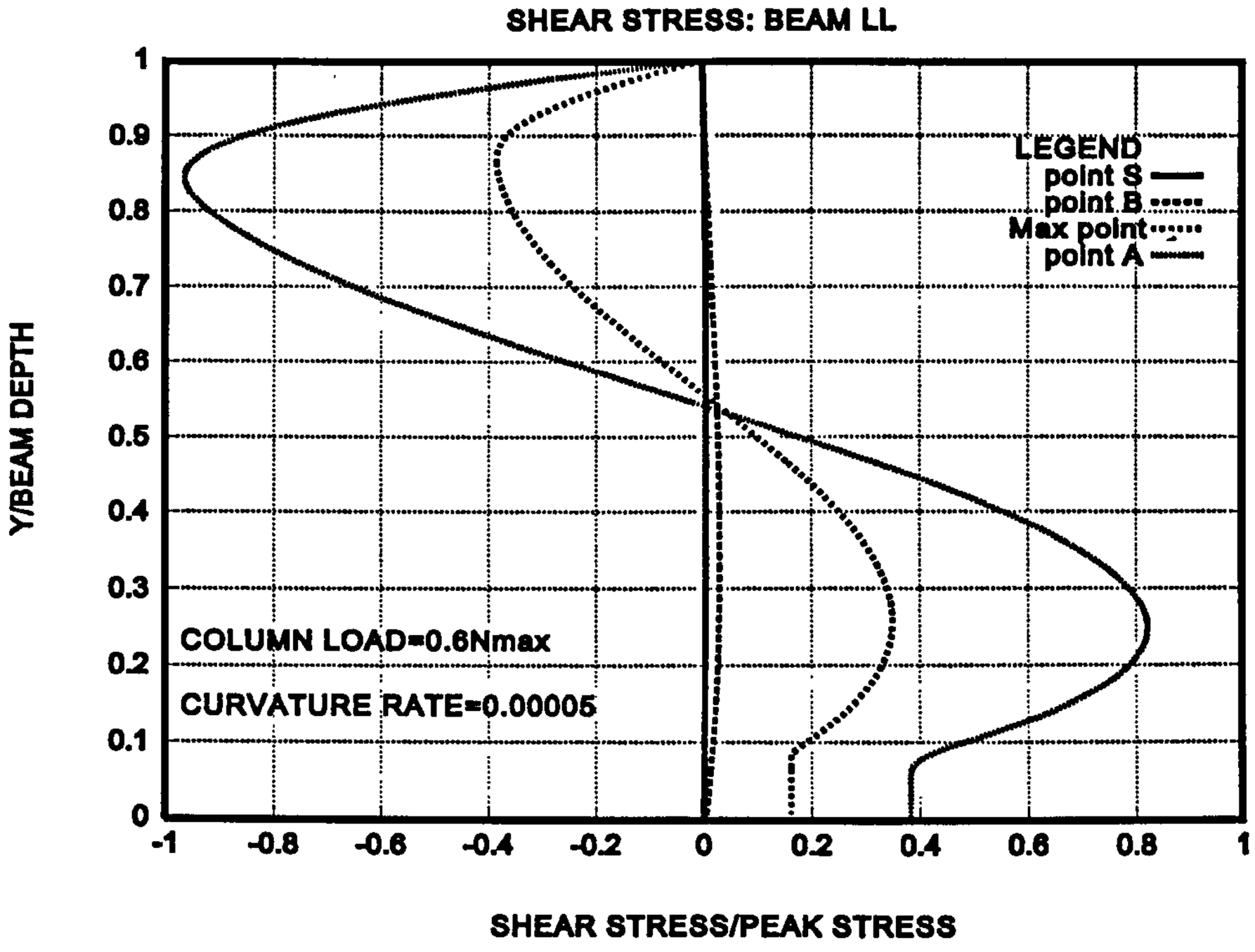

Figure 4.83 Shear stress distribution at $0.6N_{max}$ and $\dot{\kappa}$ =0. 00005 (H)

Figure 4.84 shows the normal stress distribution for beam LL with half reinforcement, an axial loading of $0.6N_{max}$ and a curvature rate of 0.002.

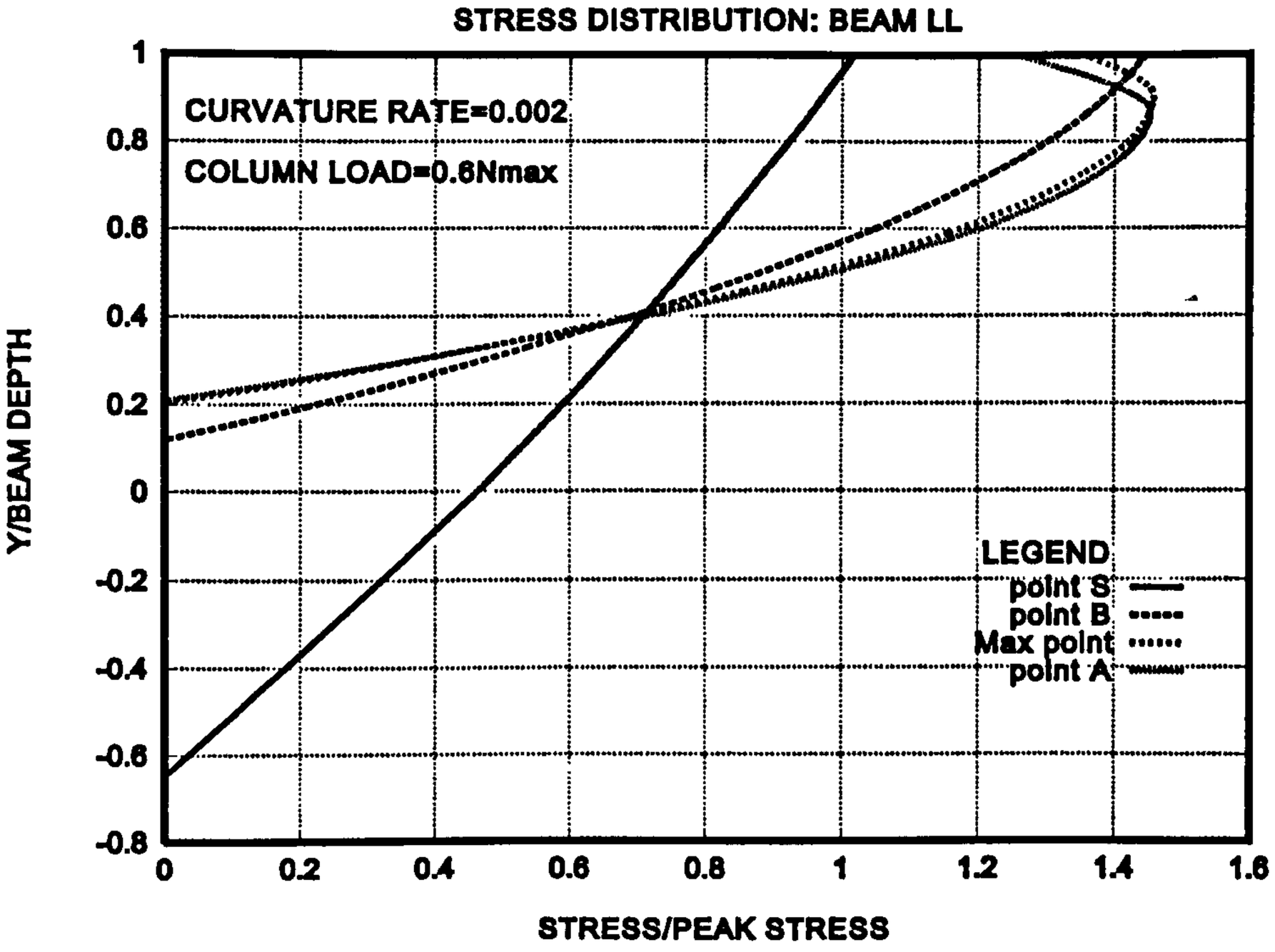

Figure 4.84 Normal stress distribution at $0.6N_{max}$ and $\dot{\kappa}$ =0. 002 (H)

Figure 4.85 shows the shear stress distribution for beam LL with half reinforcement, an axial loading of $0.6N_{max}$ and a curvature rate of 0.002.

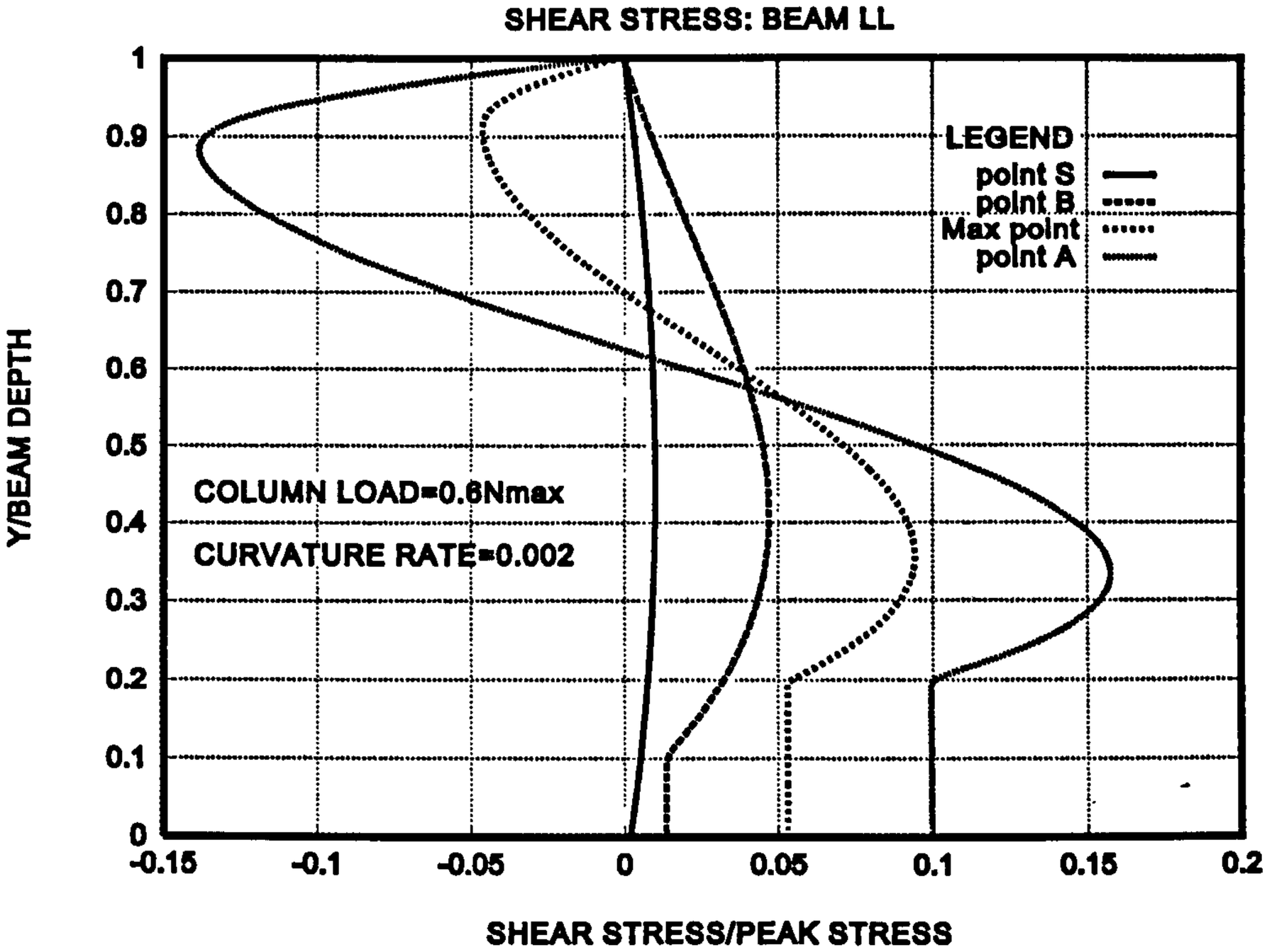

Figure 4.85 Shear stress distribution at $0.6N_{max}$ and $\dot{\kappa}$ =0. 002 (H)

Figure 4.86 shows the normal stress distribution for beam LL with half reinforcement, an axial loading of $0.6N_{max}$ and a curvature rate of 0.0388.

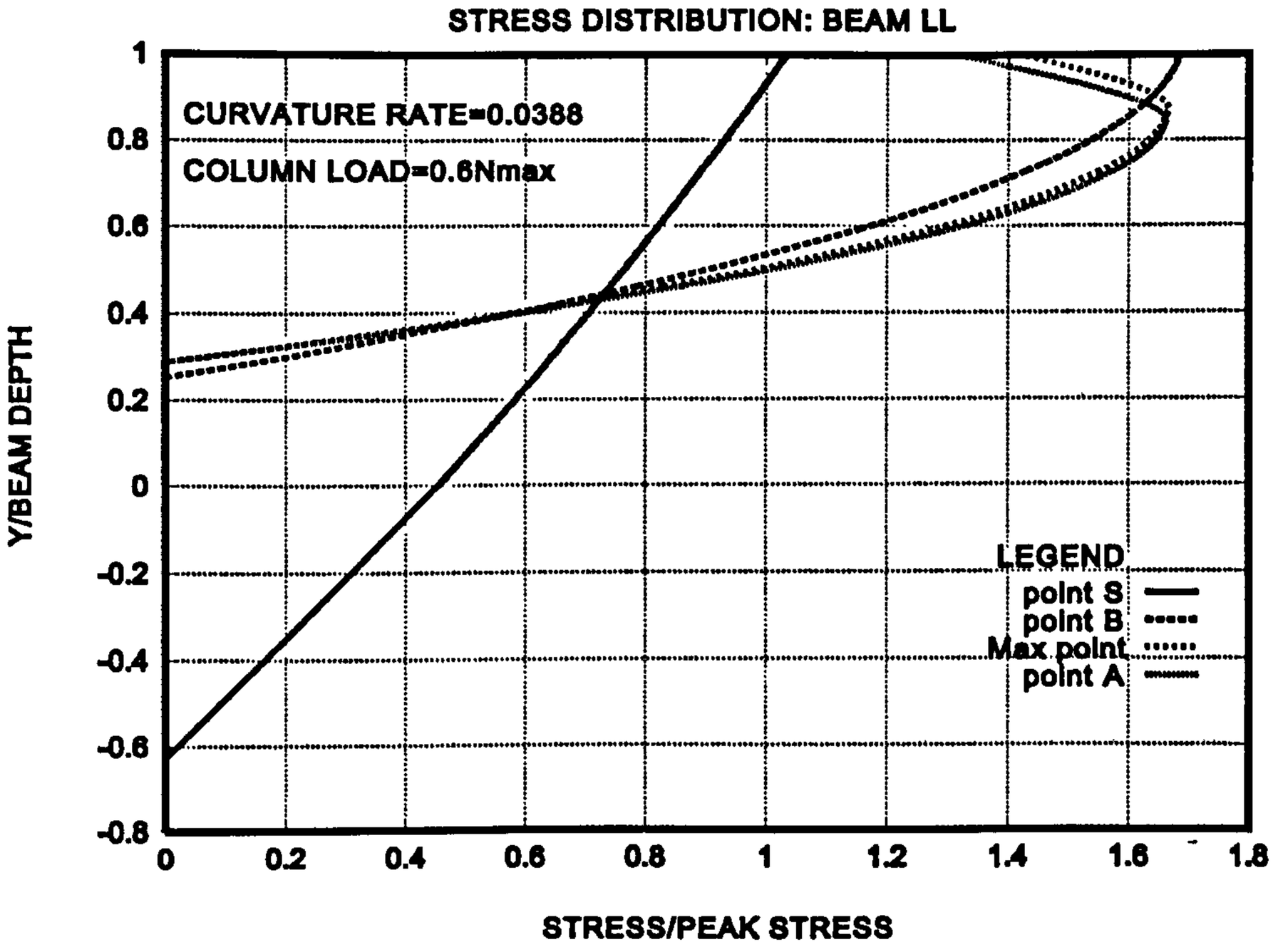

Figure 4.86 Normal stress distribution at $0.6N_{max}$ and $\dot{\kappa}$ =0. 0388 (H)

Figure 4.87 shows the shear stress distribution for beam LL with half reinforcement, an axial loading of $0.6N_{max}$ and a curvature rate of 0.0388.

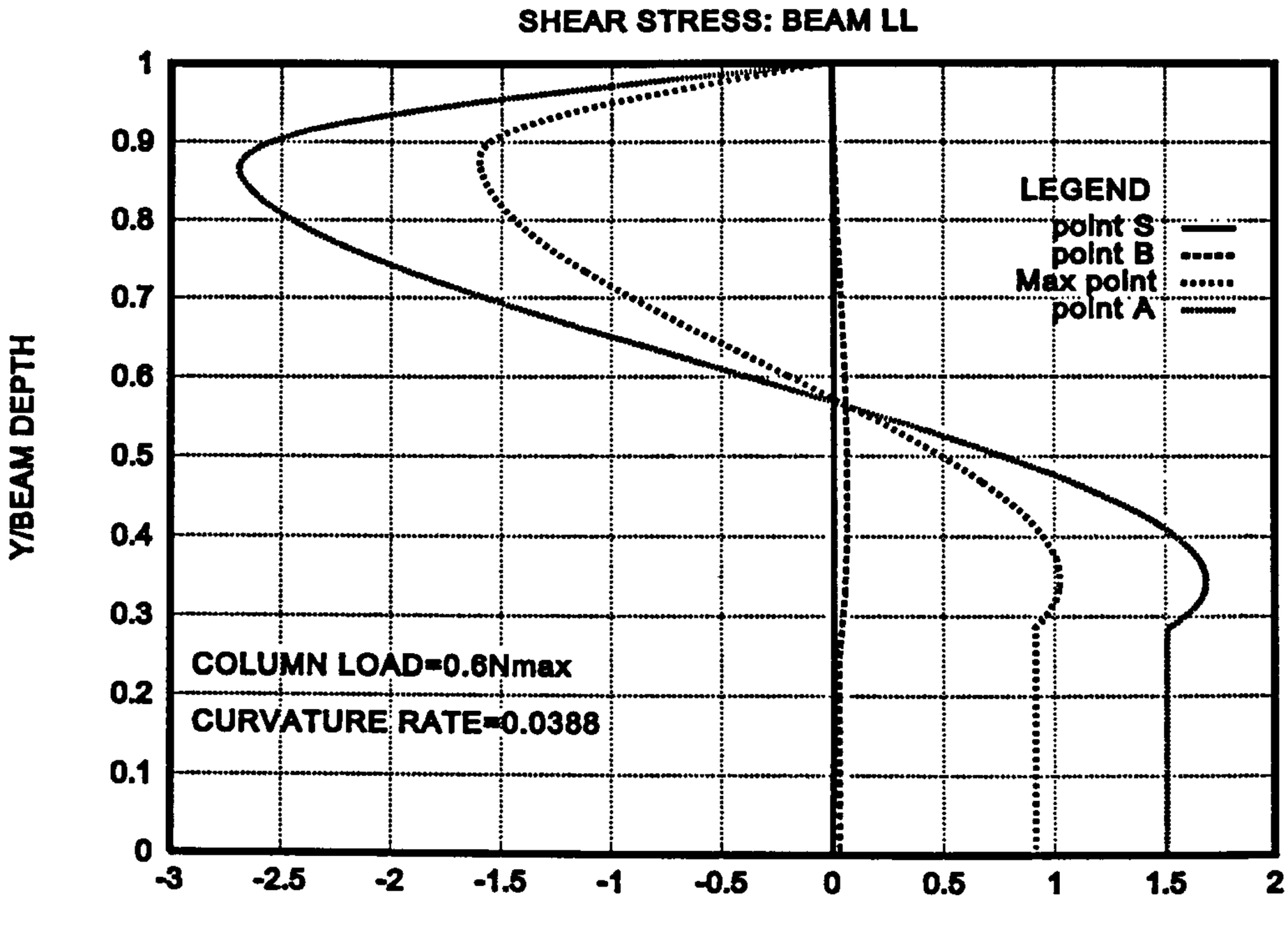

Figure 4.87 Shear stress distribution at $0.6N_{max}$ and $\dot{\kappa}$ =0. 0388 (H)

Figure 4.73 to Figure 4.87 show an increase in shear and normal stresses as the curvature increases for the lower axial loading case of 0.1 N_{max}. In this case half the reinforcement is used. The normal stresses are observed to increase with increasing curvature rate for both cases of axial loading. With the lower axial load the shear stresses are observed to increase with higher curvature rate. For the higher axial loading the shear stresses are observed to reduce from rates 0.0005 to 0.002 before increasing at the rate of 0.0388. Again a more pronounced S shape shear is seen in the case of the higher axial loading. This is consistent with increased axial loading for reasons described earlier.

Figure 4.88 to Figure 4.102 show the results obtained for the case where third reinforcement was used.

Figure 4.88 shows the Moment-Curvature relationship for third Reinforcement with curvature rate of 0.00005 at various column loadings

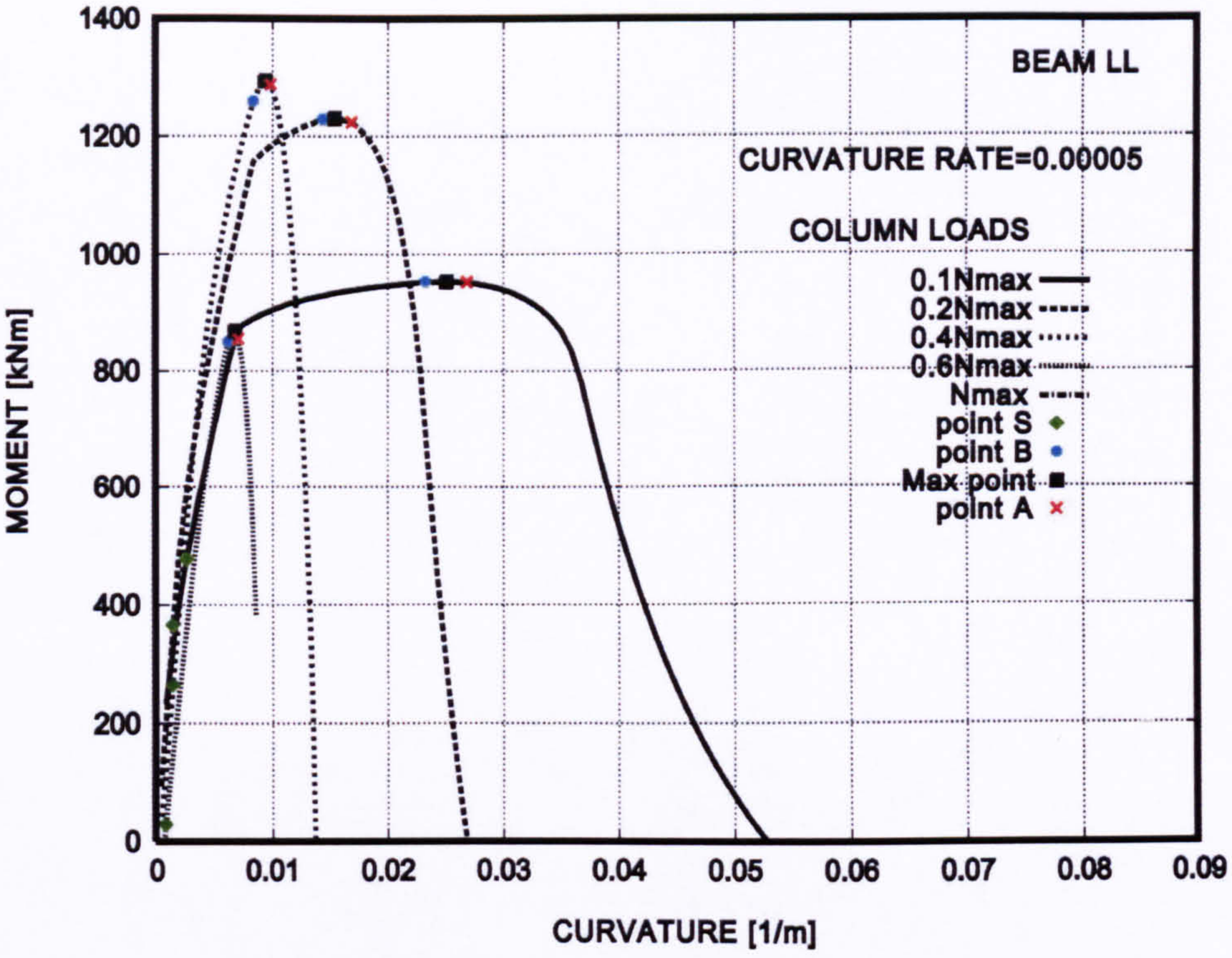

Figure 4.88 Moment-Curvature at κ =0. 00005 for various column loadings, (T)

Figure 4.89 shows the Moment-Curvature relationship for third Reinforcement with curvature rate of 0.002 at various column loadings

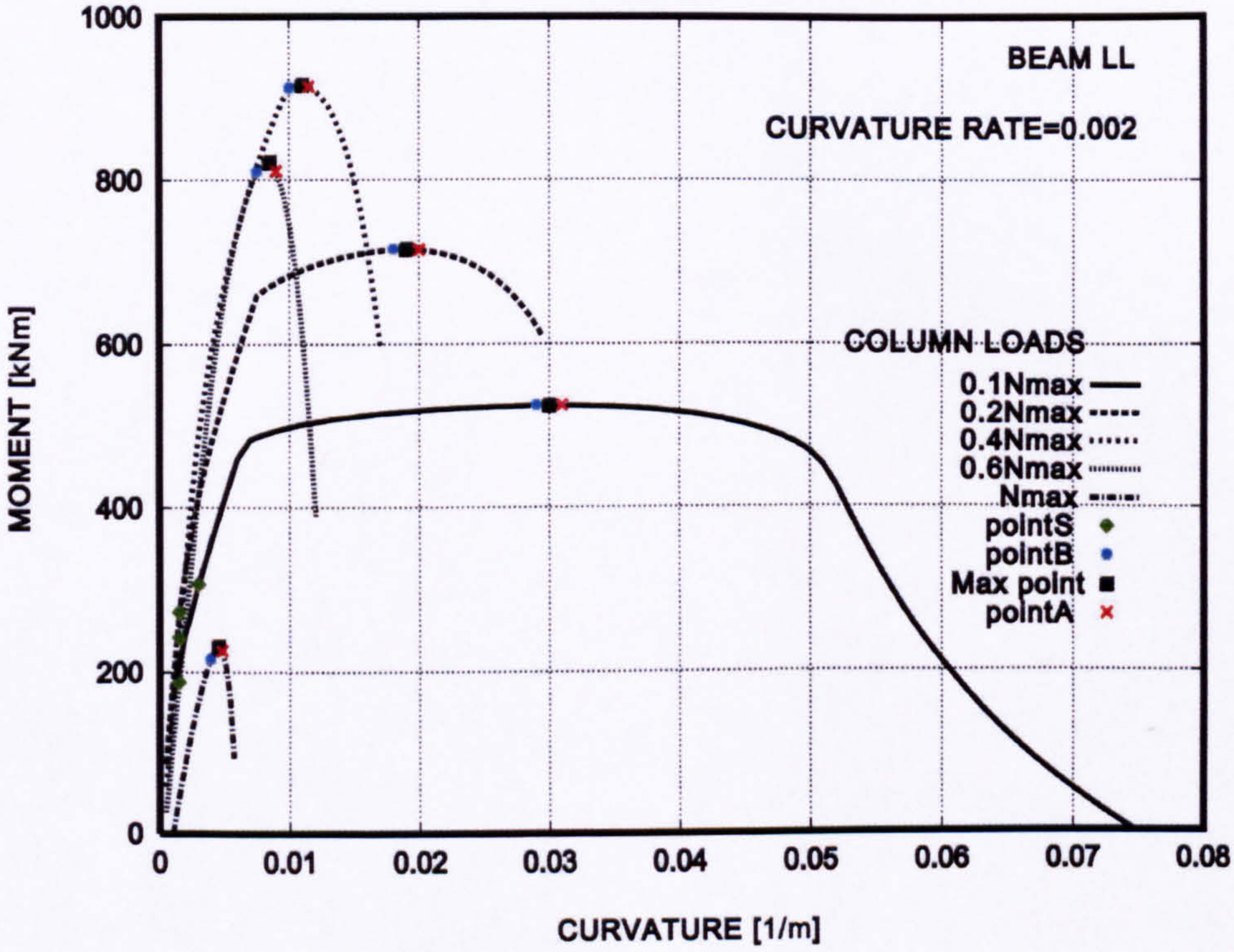

Figure 4.89 Moment-Curvature at κ =0. 002 for various column loadings (T)

Figure 4.90 shows the Moment-Curvature relationship for third Reinforcement with curvature rate of 0.0388 at various column loadings

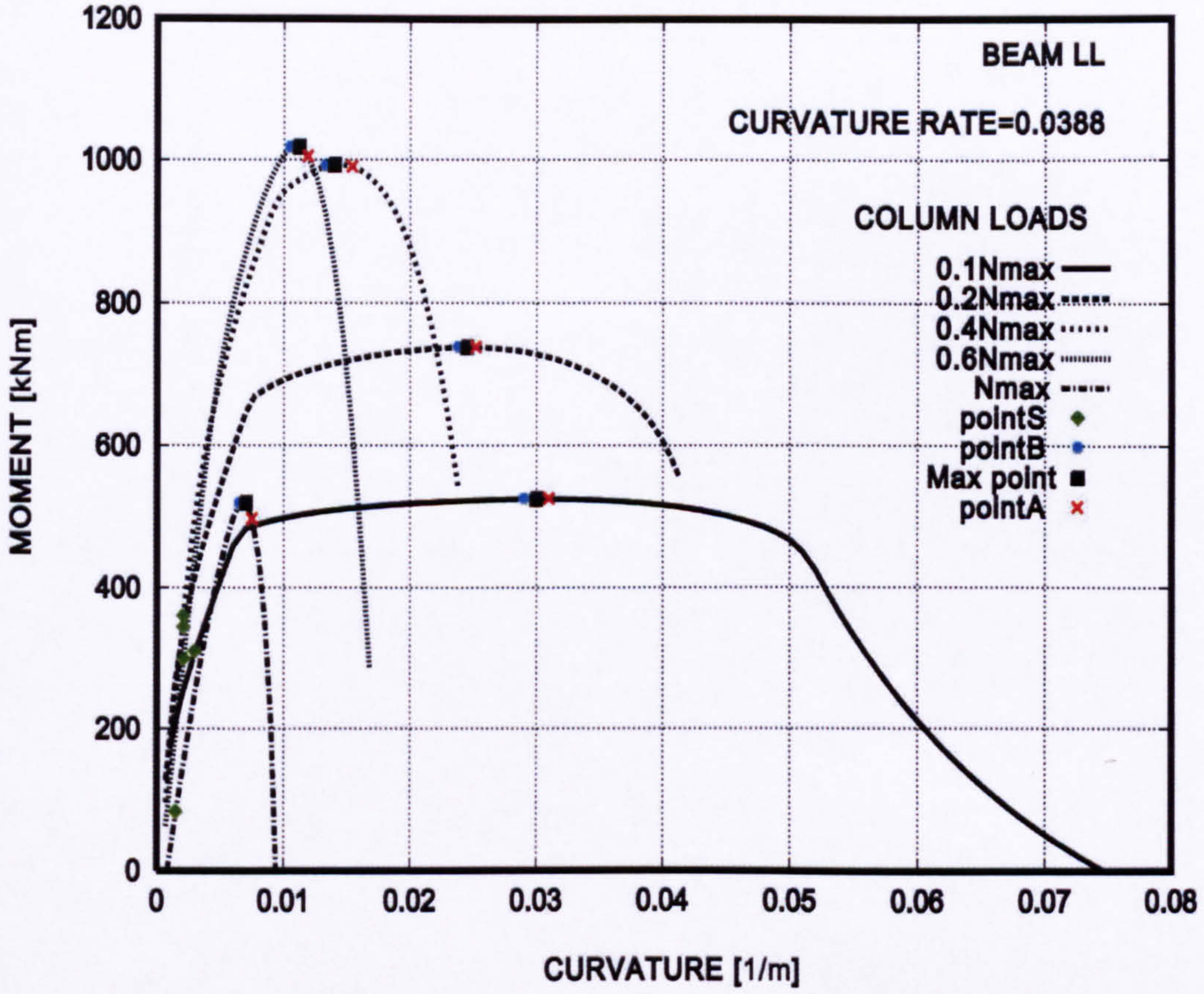

Figure 4.90 Moment-Curvature at κ=0. 0388 for various column loadings (T)

Figure 4.88 to Figure 4.90 show a similar relationship between ductility and axial loading. However in this case the ductility is found to be lower than that for the case with half reinforcement.

Figure 4.91 shows the normal stress distribution for beam LL with third reinforcement, an axial loading of $0.1N_{max}$ and a curvature rate of 0.00005.

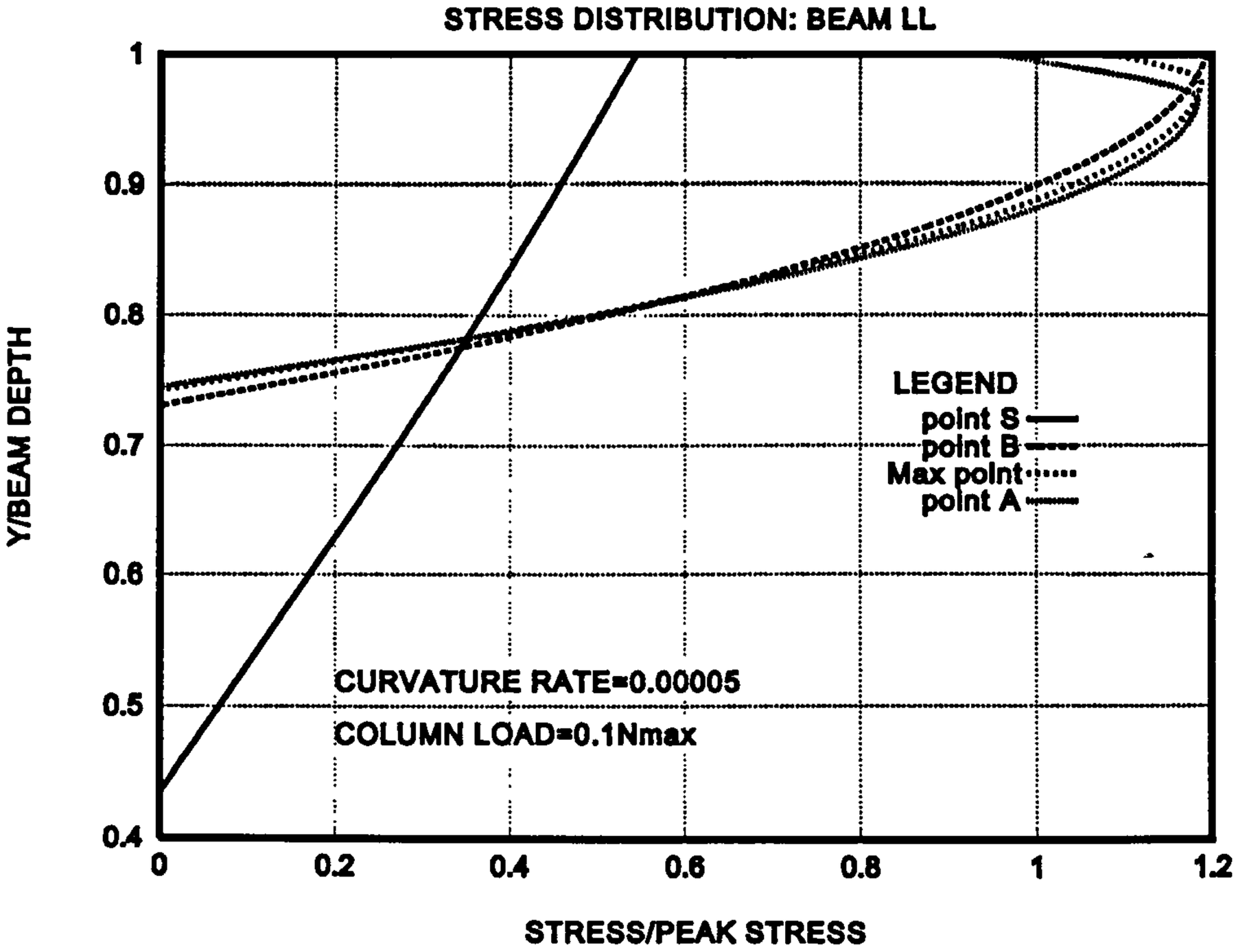

Figure 4.91 Normal stress distribution at $0.1N_{max}$ and κ =0. 00005 (T)

Figure 4.92 shows the shear stress distribution for beam LL with third reinforcement, an axial loading of $0.1N_{max}$ and a curvature rate of 0.00005.

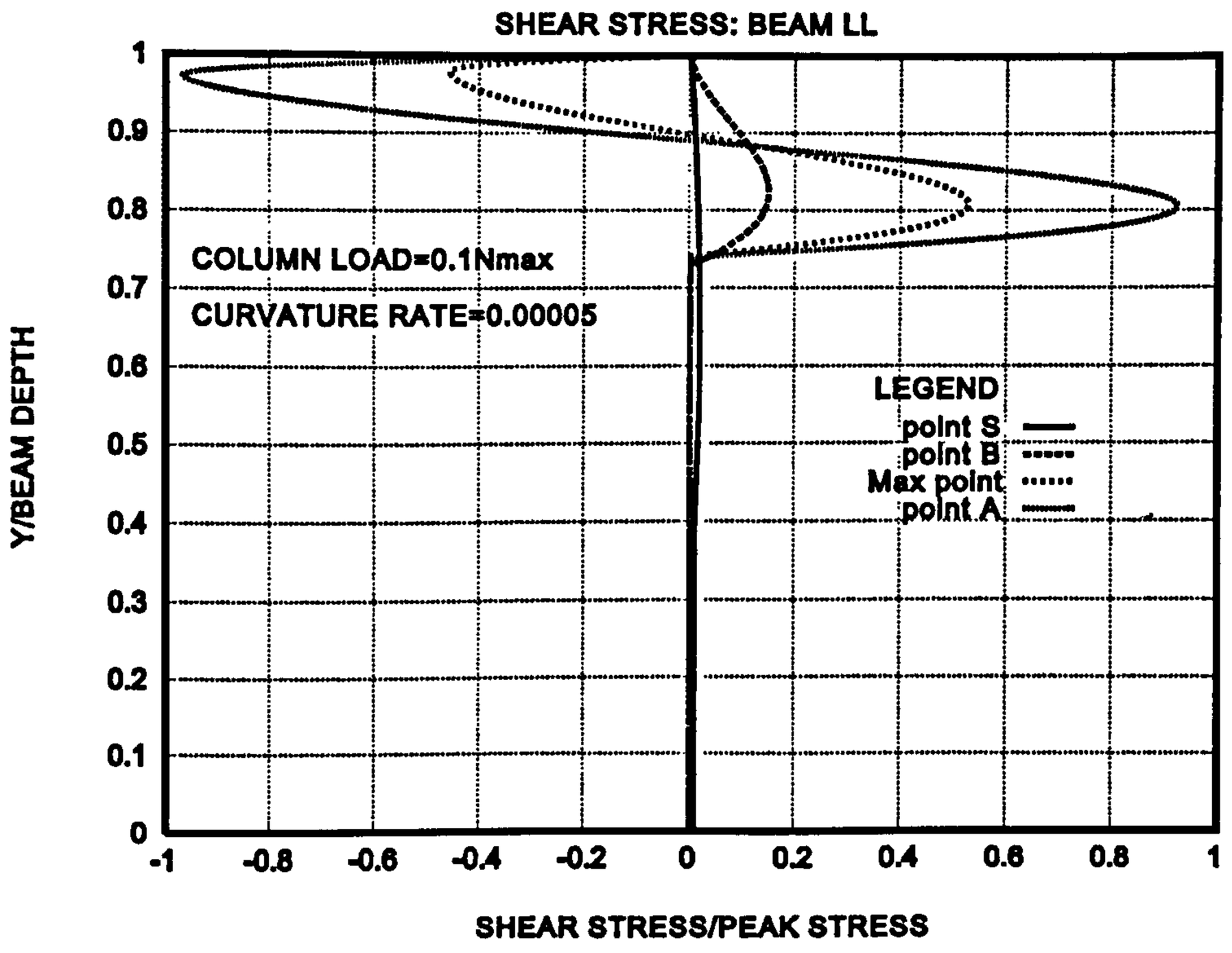

Figure 4.92 Shear stress distribution at $0.1N_{max}$ and κ =0. 00005 (T)

Figure 4.93 shows the normal stress distribution for beam LL with third reinforcement, an axial loading of $0.1N_{max}$ and a curvature rate of 0.002.

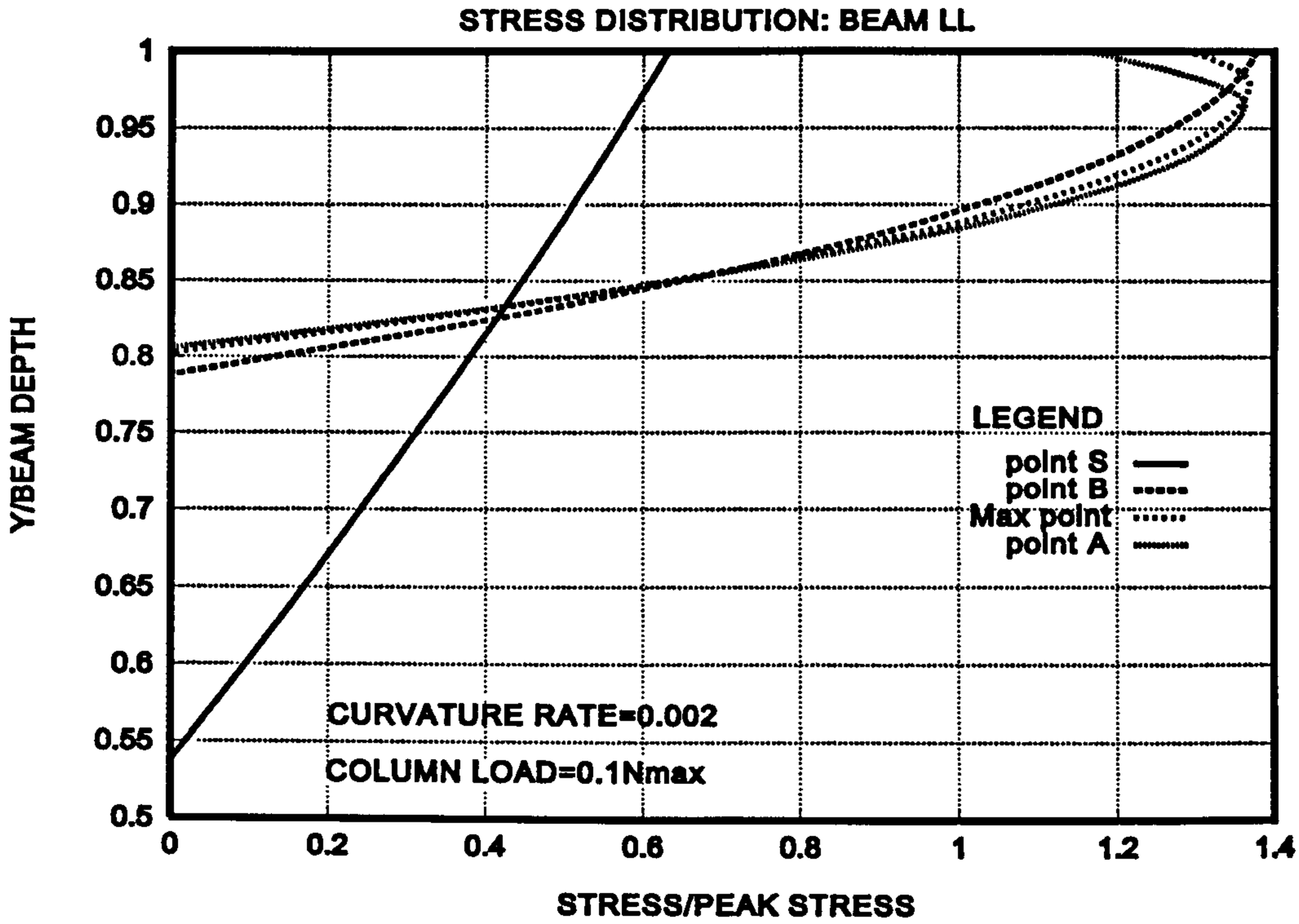

Figure 4.93 Normal stress distribution at $0.1N_{max}$ and $\dot{\kappa}$ =0. 002 (T)

Figure 4.94 shows the shear stress distribution for beam LL with third reinforcement, an axial loading of $0.1N_{max}$ and a curvature rate of 0.002.

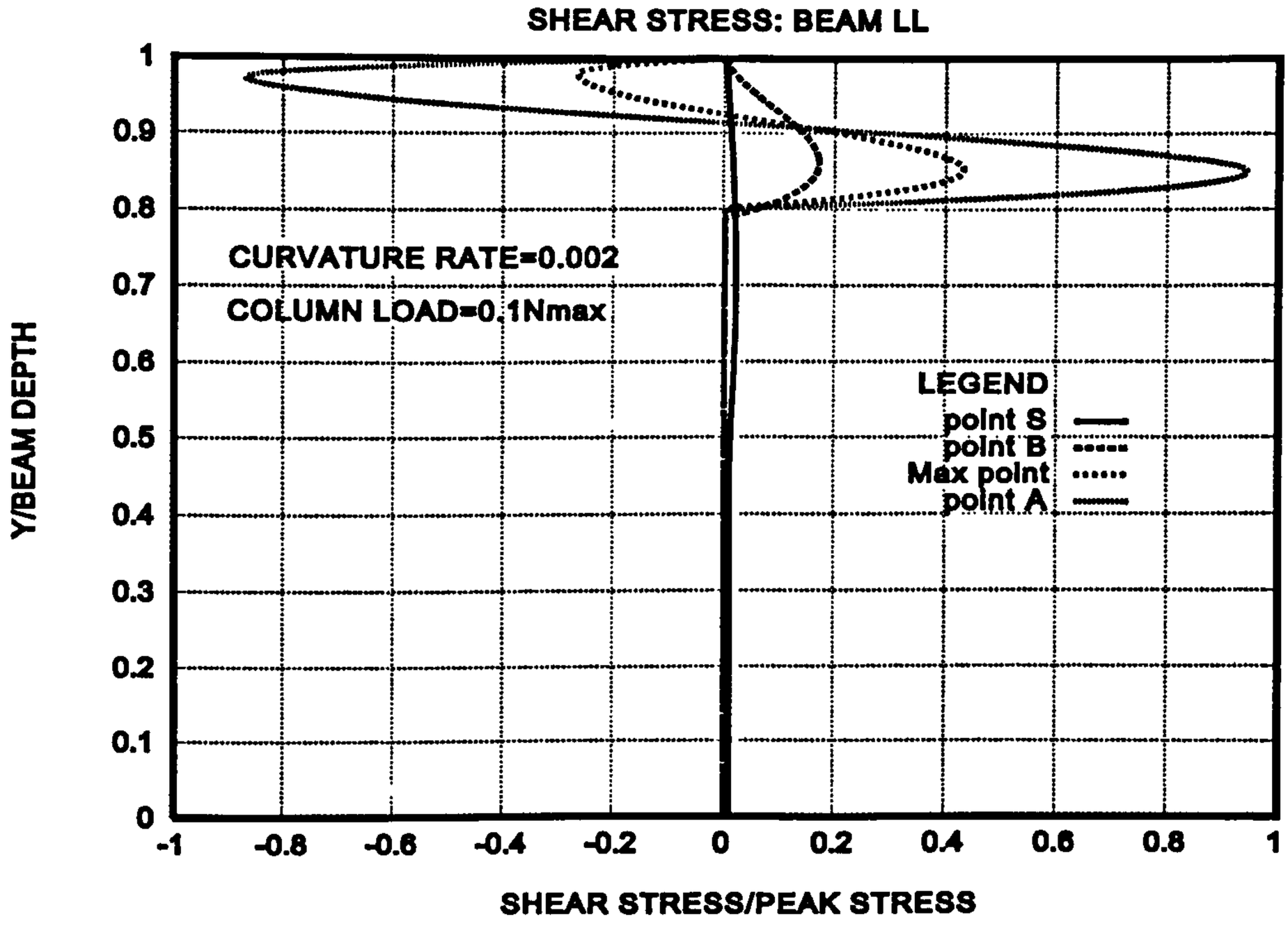

Figure 4.94 Shear stress distribution at $0.1N_{max}$ and $\dot{\kappa}$ =0. 002 (T)

Figure 4.95 shows the normal stress distribution for beam LL with third reinforcement, an axial loading of $0.1N_{max}$ and a curvature rate of 0.0388.

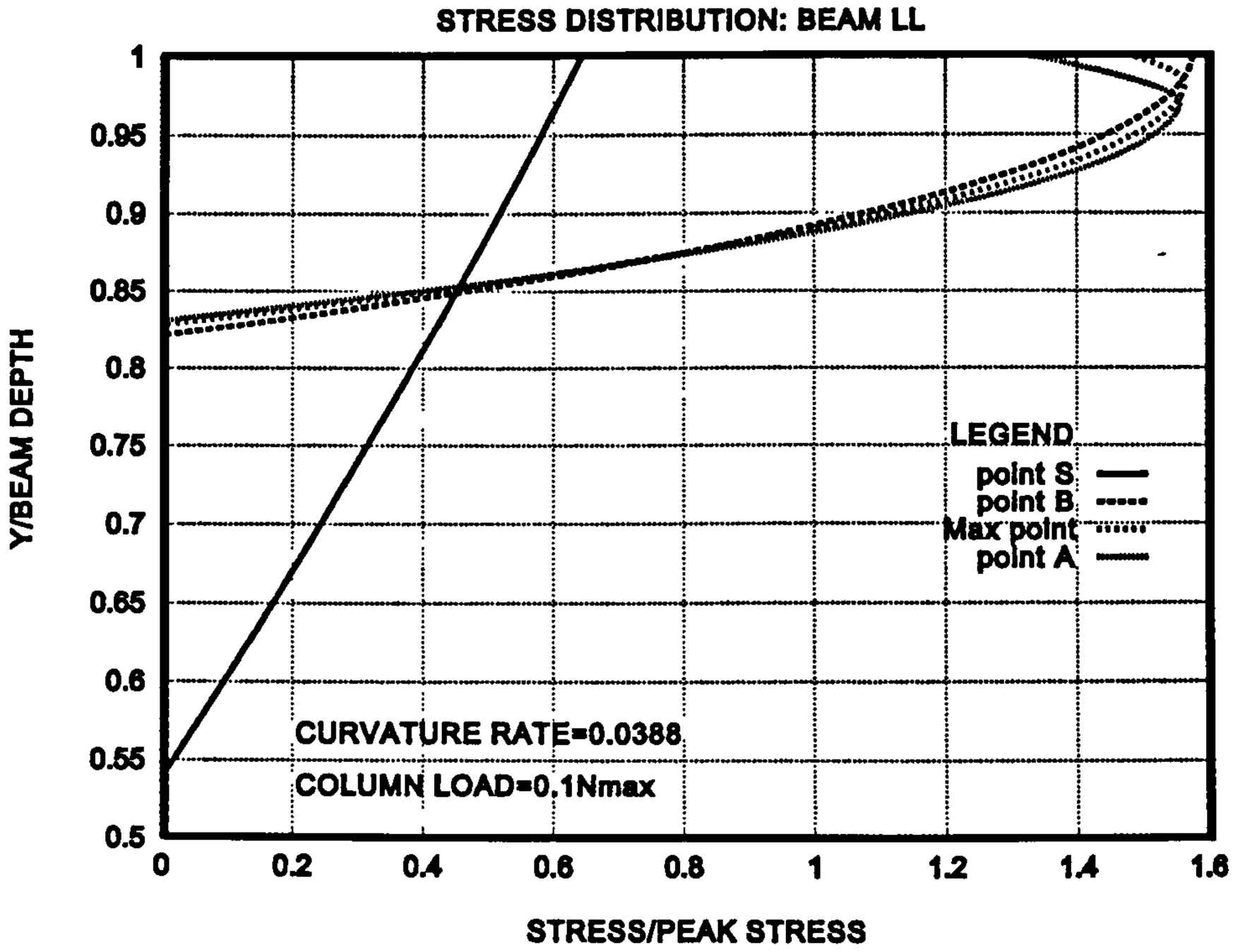

Figure 4.95 Normal stress distribution at $0.1N_{max}$ and $\dot{\kappa}$ =0. 0388 (T)

Figure 4.96 shows the shear stress distribution for beam LL with third reinforcement, an axial loading of $0.1N_{max}$ and a curvature rate of 0.0388.

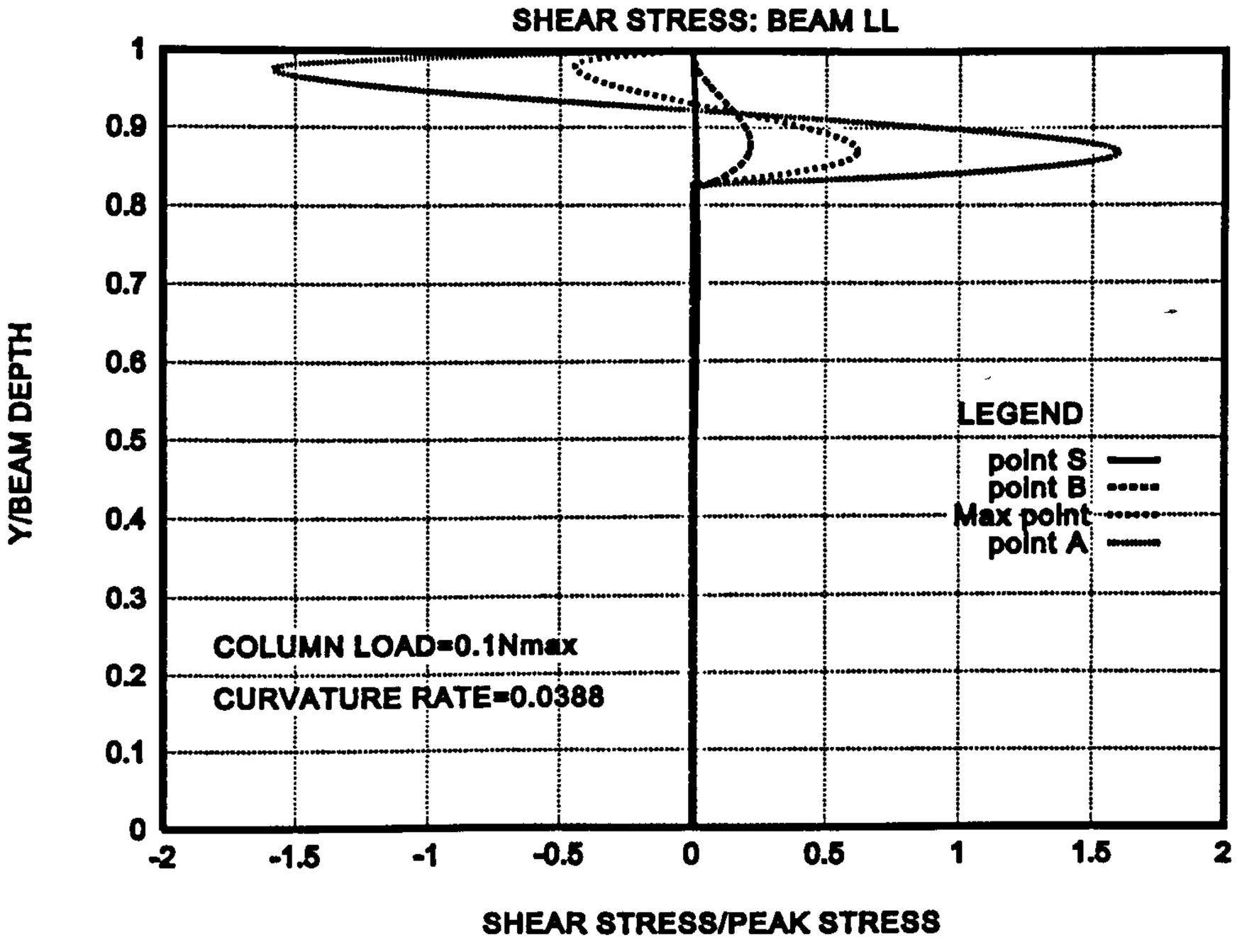

Figure 4.96 Shear stress distribution at $0.1N_{max}$ and $\dot{\kappa}$ =0. 0388 (T)

Figure 4.97 shows the normal stress distribution for beam LL with third reinforcement, an axial loading of $0.6N_{max}$ and a curvature rate of 0.00005.

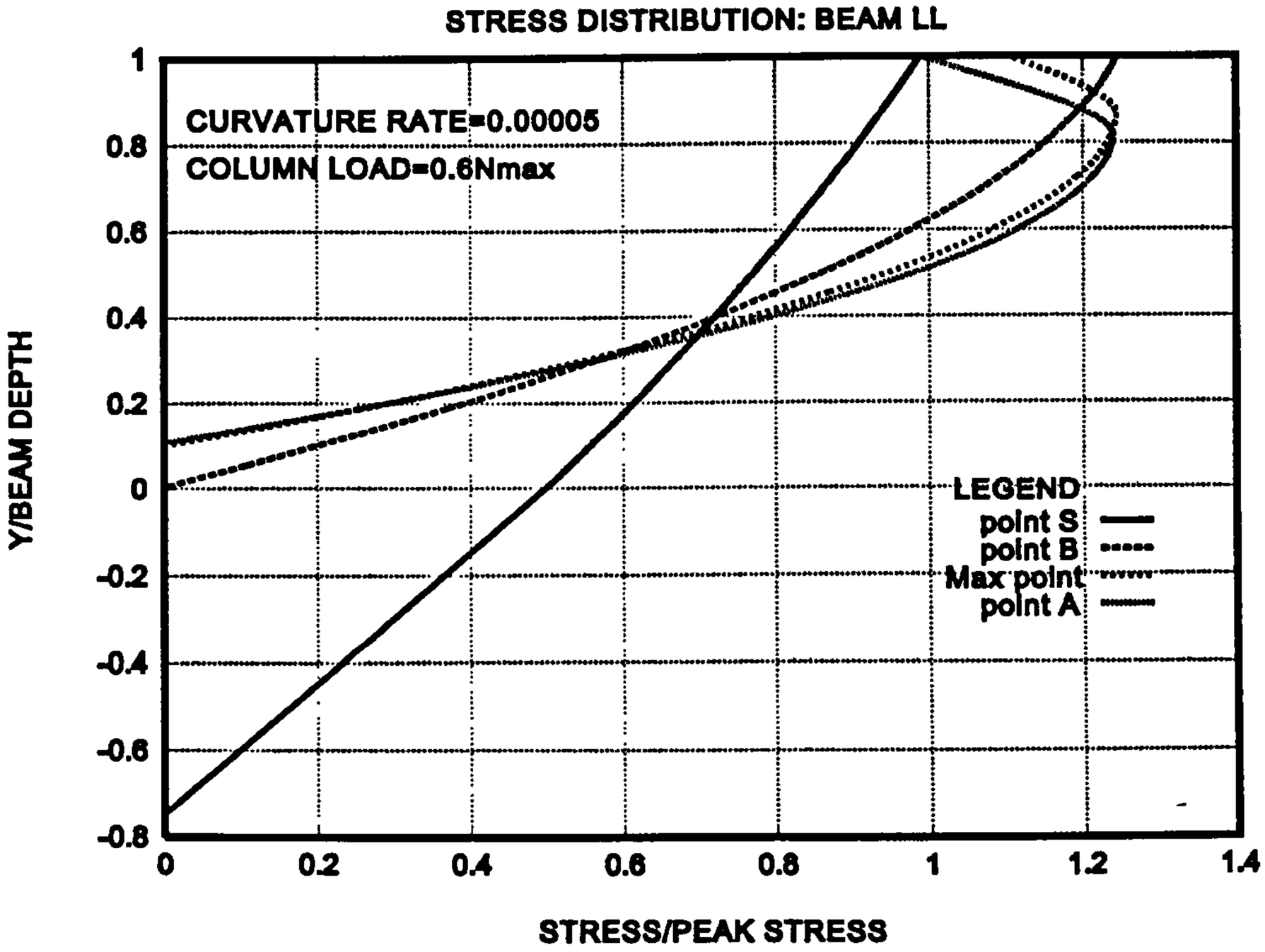

Figure 4.97 Normal stress distribution at $0.6N_{max}$ and $\dot{\kappa}$ =0. 00005 (T)

Figure 4.98 shows the shear stress distribution for beam LL with third reinforcement, an axial loading of $0.6N_{max}$ and a curvature rate of 0.00005.

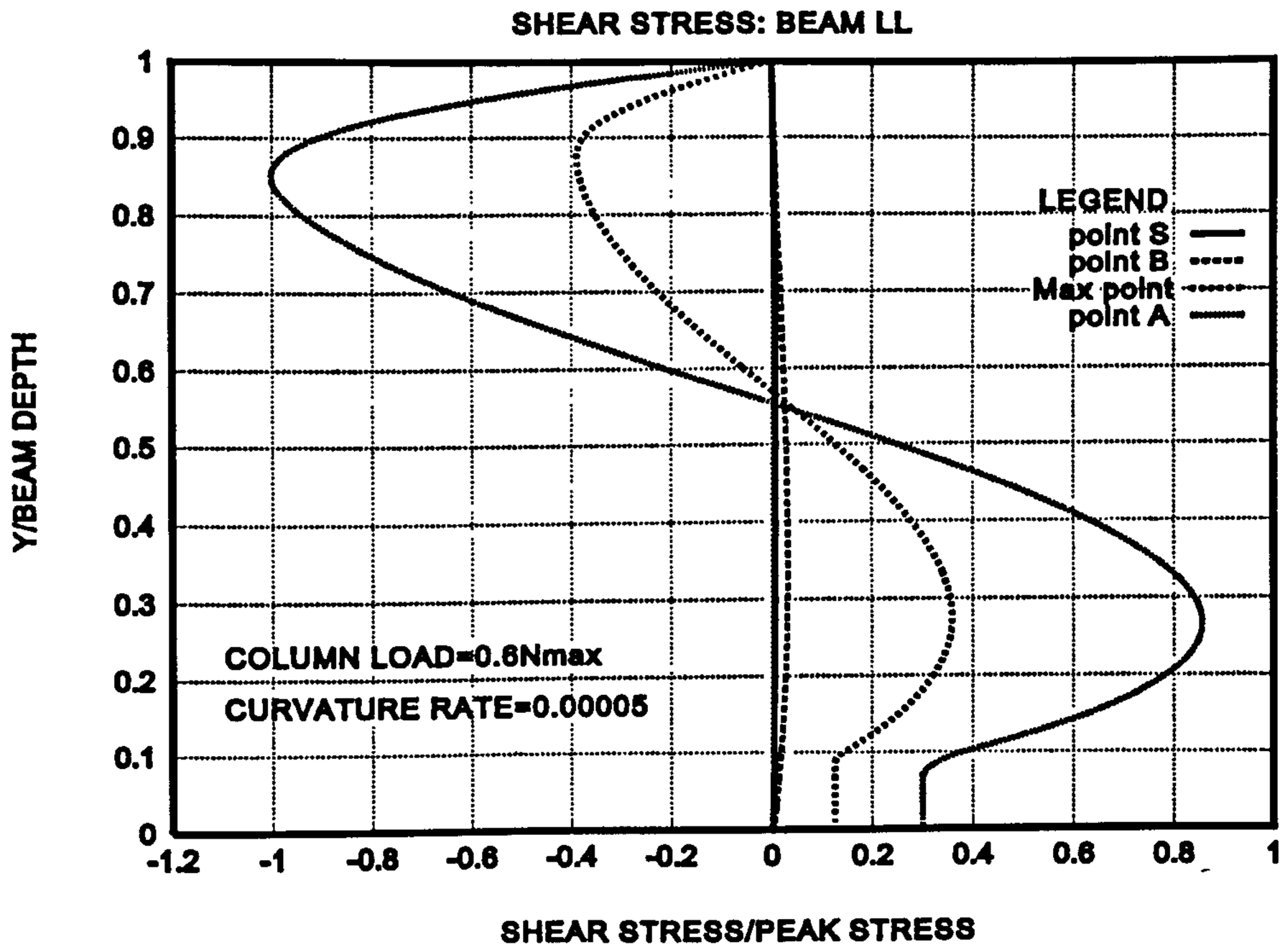

Figure 4.98 Shear stress distribution at $0.6N_{max}$ and $\dot{\kappa}$ =0. 00005 (T)

Figure 4.99 shows the normal stress distribution for beam LL with third reinforcement, an axial loading of $0.6N_{max}$ and a curvature rate of 0.002.

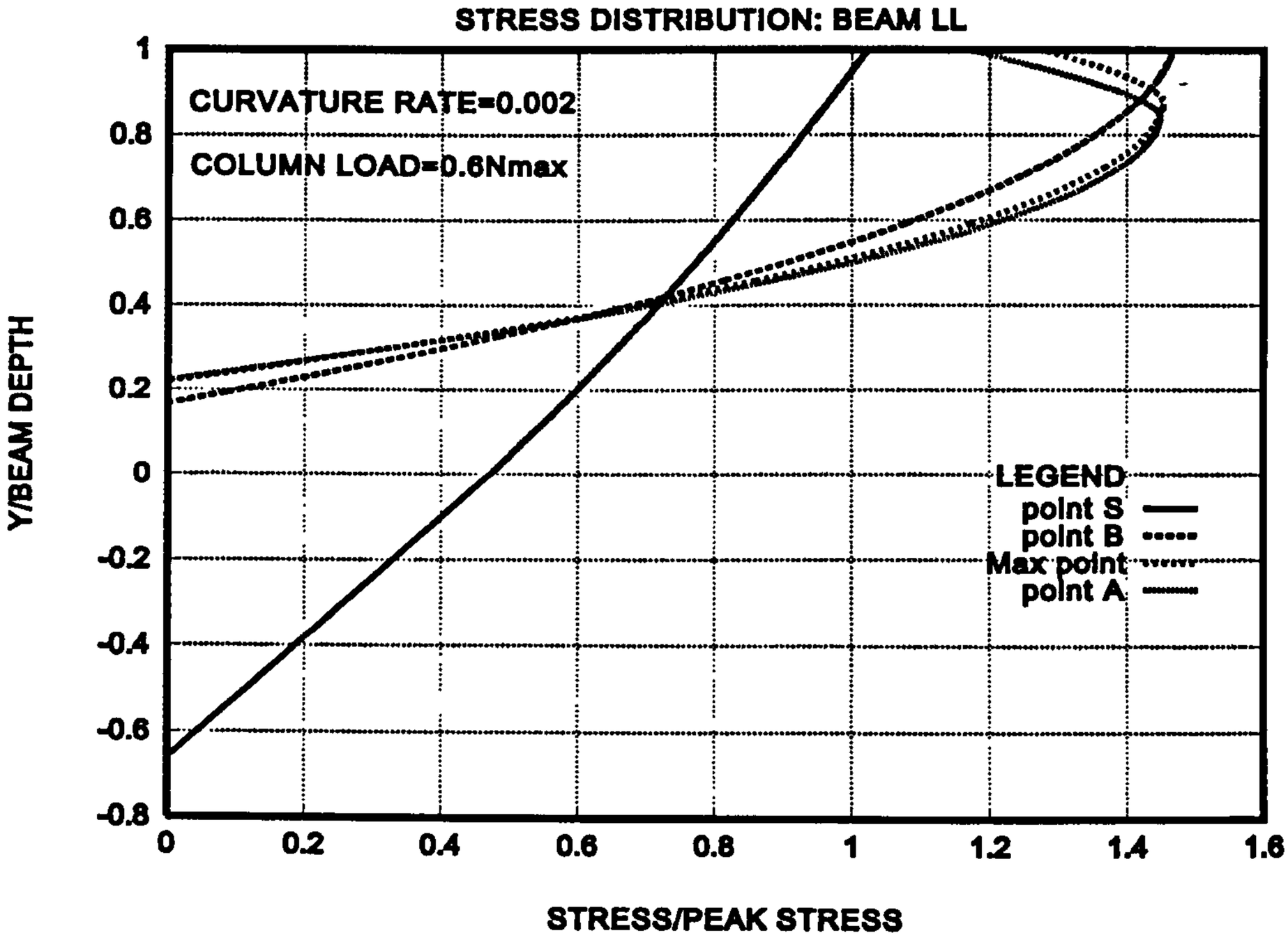

Figure 4.99 Normal stress distribution at $0.6N_{max}$ and $\dot{\kappa}$ =0. 002 (T)

Figure 4.100 shows the shear stress distribution for beam LL with third reinforcement, an axial loading of $0.6N_{max}$ and a curvature rate of 0.002.

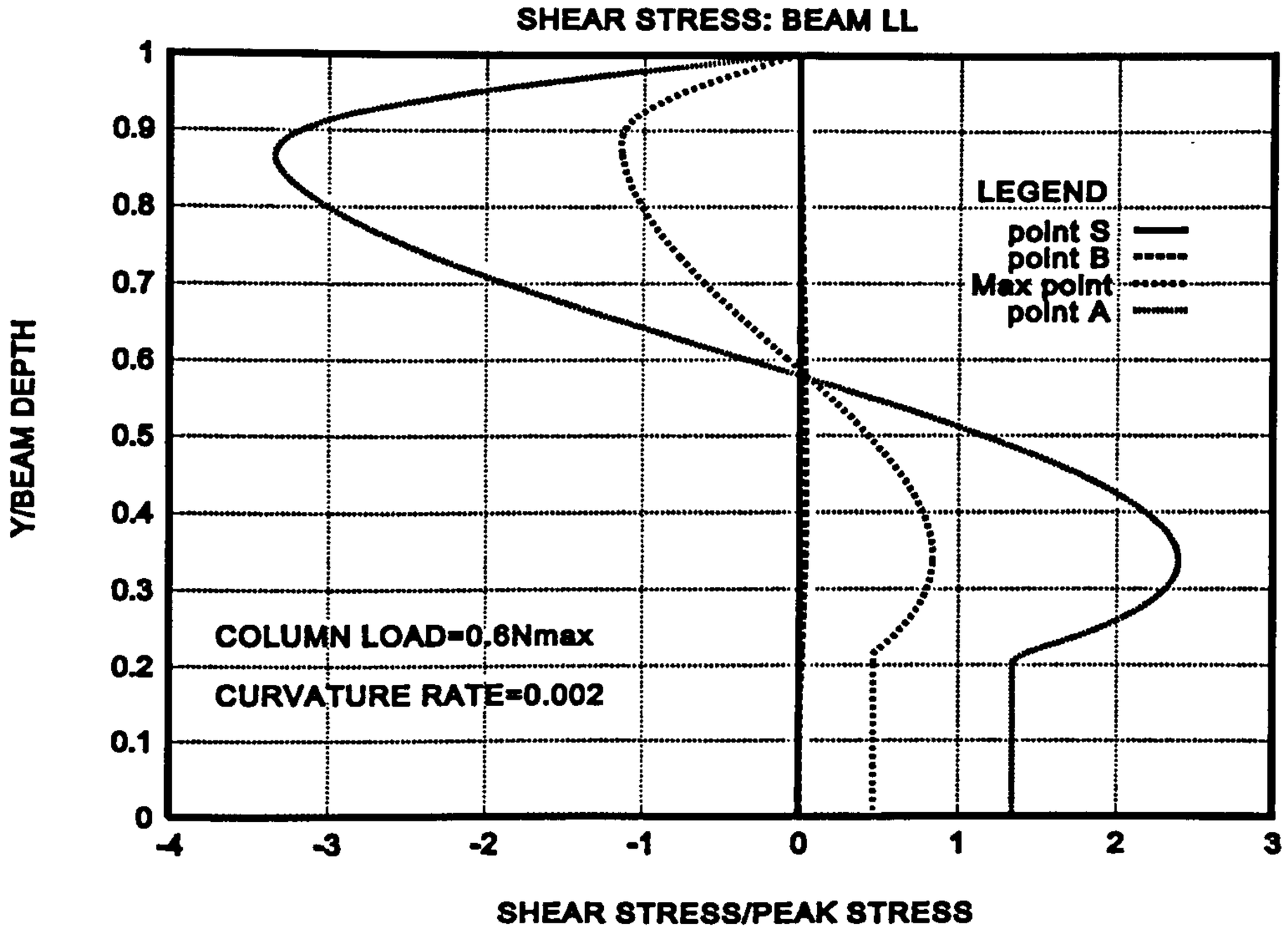

Figure 4.100 Shear stress distribution at $0.6N_{max}$ and $\dot{\kappa}$ =0. 002 (T)

Figure 4.101 shows the normal stress distribution for beam LL with third reinforcement, an axial loading of $0.6N_{max}$ and a curvature rate of 0.0388.

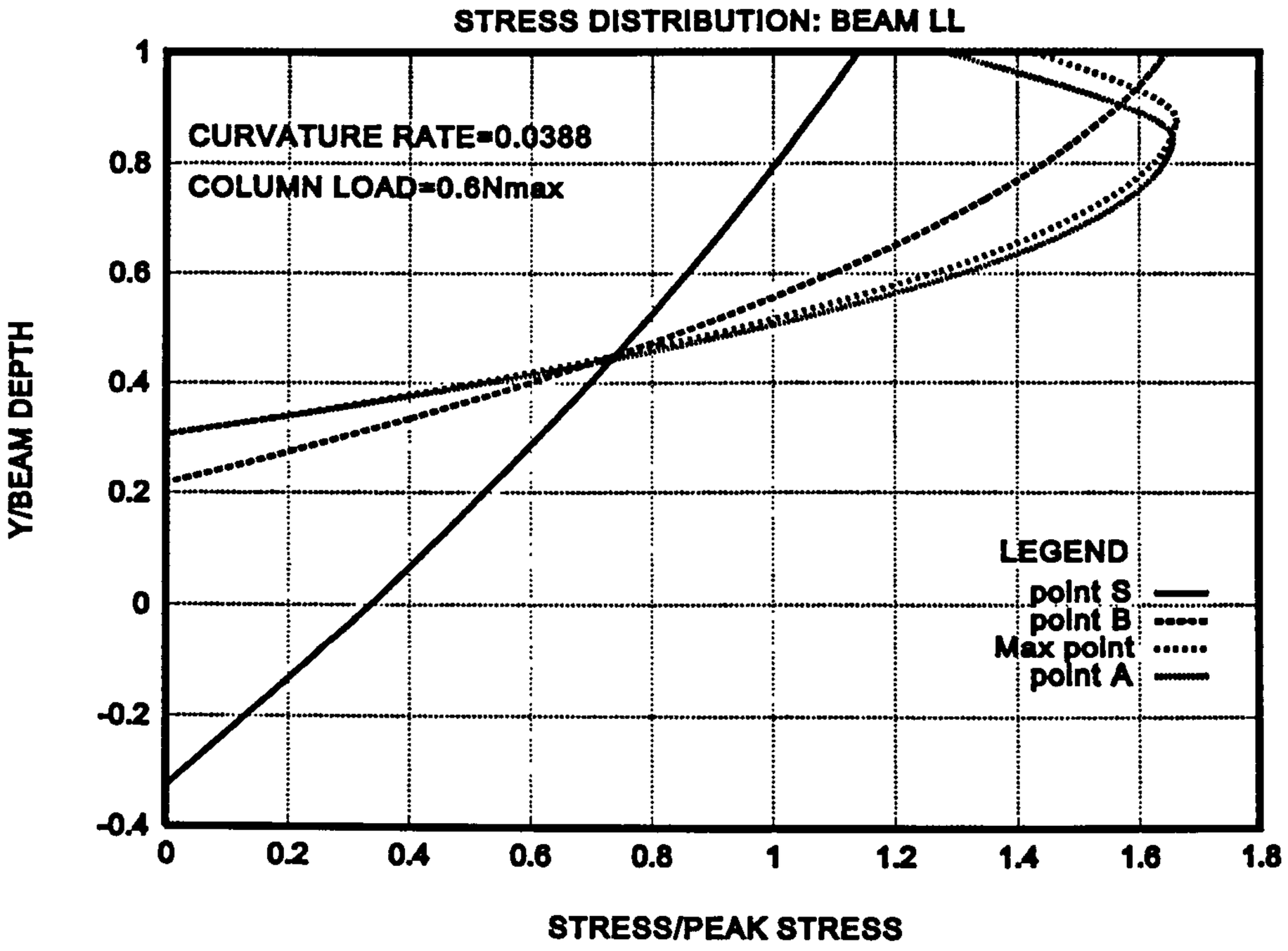

Figure 4.101 Normal stress distribution at $0.6N_{max}$ and $\dot{\kappa}$ =0. 0388 (T)

Figure 4.102 shows the shear stress distribution for beam LL with third reinforcement, an axial loading of $0.6N_{max}$ and a curvature rate of 0.0388.

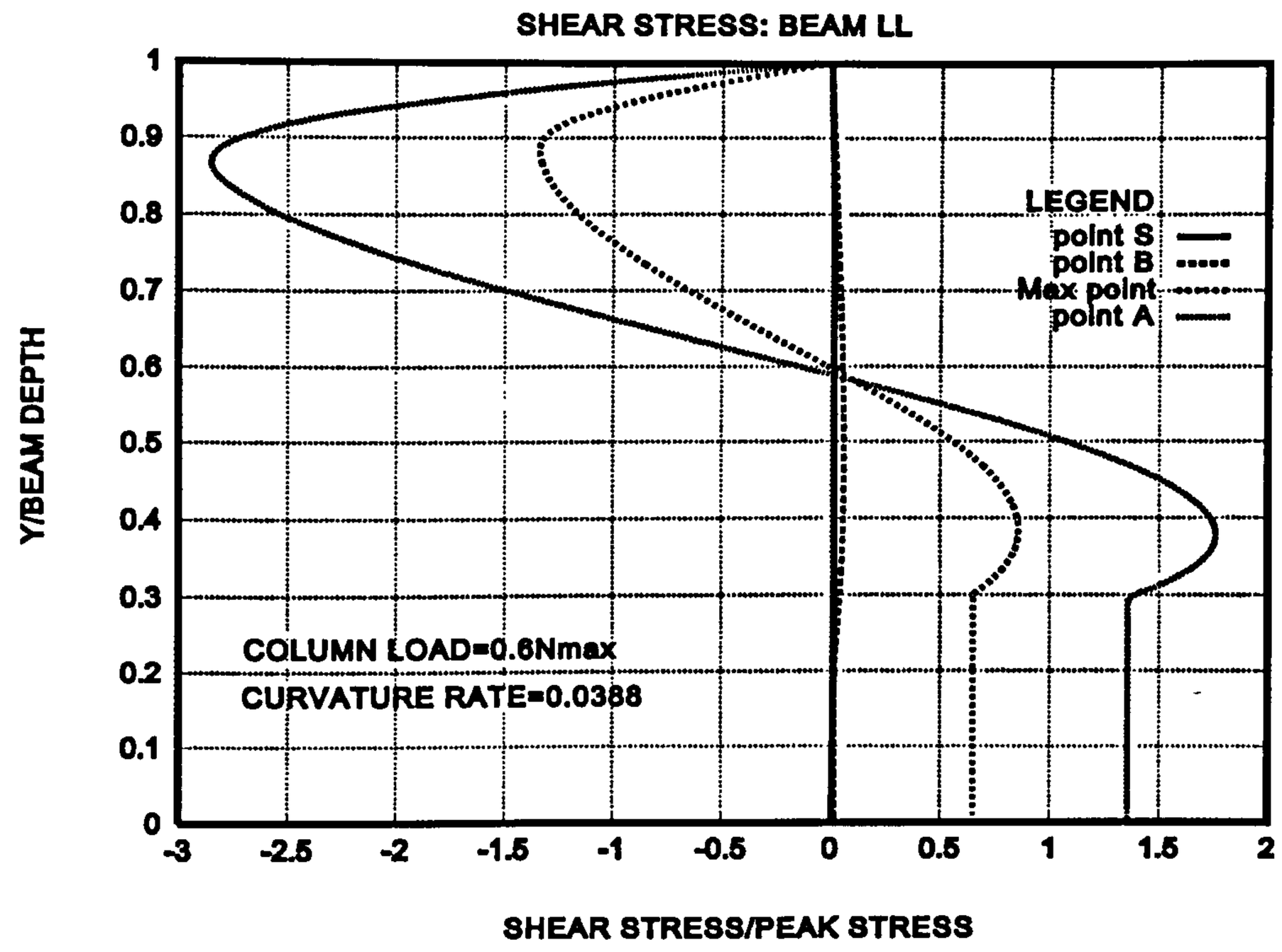

Figure 4.102 Shear stress distribution at $0.6N_{max}$ and $\dot{\kappa}$ =0. 0388 (T)

Normal shear stress distribution show that noticeble softening occurs at point A and the shear stress distributions show that the shear developed at this point is too high for concrete to endure, thus again indicating failure must have occurred. The normal stresses are seen to increase with higher curvature rates for both the loading cases. For the lower axial loading the shear stresses are seen to increase with the curvature rate. For the higher axial loading the more pronounced S shape shear plots are obtained. However the shear increases with curvature rate up to a rate of 0.002 but decreases for the rate of 0.0388. In this case the shear stresses produced are similar to that of the case where half the reinforcement was used. However the more pronounces S shape indicates these stresses are endured along a greater length of the beam.

4.4 Conclusions

Research was carried out to investigate the effects of beam size upon localised failure of concrete beams. Initial results obtained showed that at point B no softening of the concrete had occurred and that only moderate shear stresses were developed up to this point. However, beyond this at point A the concrete developed enormous shear stresses, which is too high for concrete to bear. Thus the concrete cannot fail in localisation, instead shear failure must occur.

A section of beam is taken where the moments are different on both sides as shown in Figure 4.103.

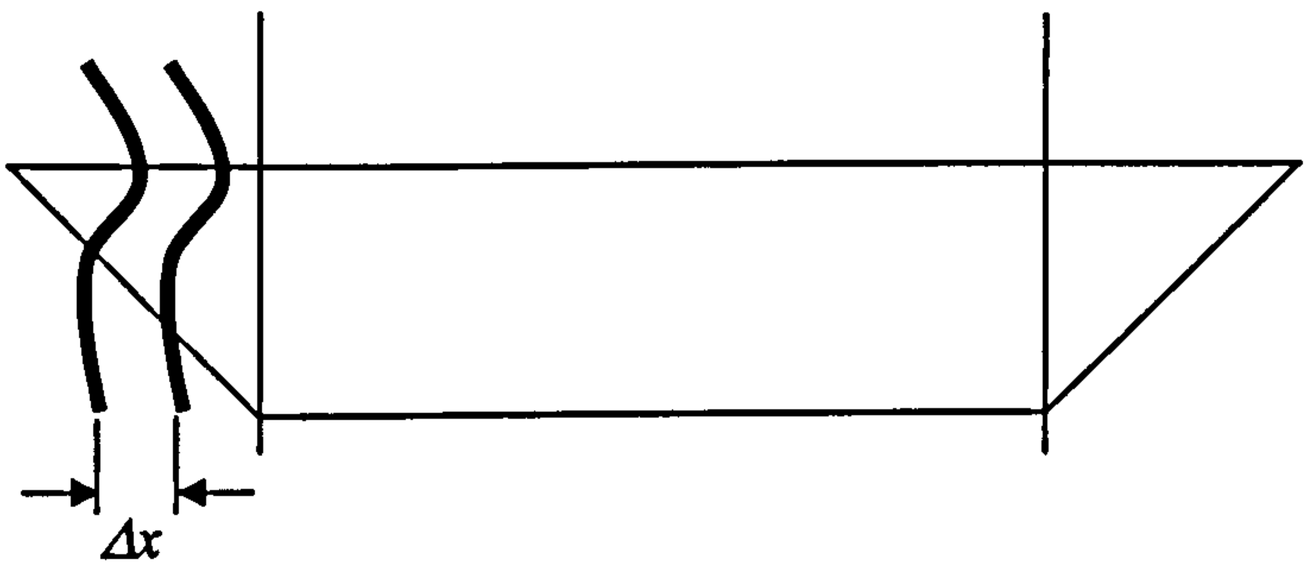

Figure 4.103 Beam section across bending moment diagram

The stress distributions on both sides are shown in Figure 4.104

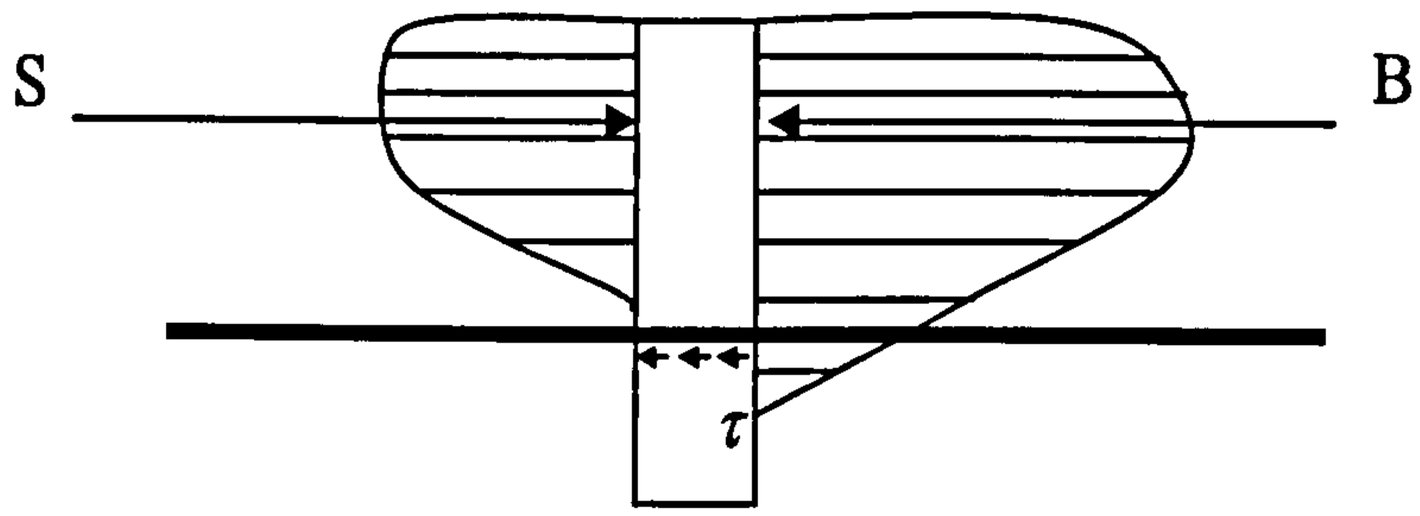

Figure 4.104 Stress distribution on either side of beam strip

The moment on the one side of the strip has not softened but on the other side the moment has softened. Hence the curvature will be different on either side. This will result in differing stress distributions on either side of the strip, as shown in Figure 4.104. Equilibrium can only be kept by the shear force τ. However, τ is too large and hence shear failure will occur. A small softening will occur until the shear reaches full value to cause shear failure.

If the strip of beam considered has moments that are equal on both sides, the corresponding curvatures will be different for each moment. One will be produced with a curvature in the softening region and one will be produced with a curvature in the non-softened region. This will result in differing stress distributions on either side of the strip. In this case the equilibrium can only be maintained by the shear forces. However these are too large and shear failure of the beam occurs.

It is pointed out that at point B there is no softening in compression, while at point A the concrete section would have already failed. Hence any redistribution of shear and normal stresses due to softening of concrete would have very little effect on the curvature and rotation i.e. the ductility of the beam. In summary the shape of the softening curve or the size of the beam would not influence the ductility of concrete beams. It would be a function of the ultimate strain at which the peak strength of concrete is reached and properties of reinforcement. For e.g. the reinforcement ratio and the confinement.

Thus a bi-linear moment curvature law would apply as advocated by Alca et all [4]. In addition, this would be influenced by shear reinforcement, confinement and strain rate effects.

The effects of varying the reinforcement, strain rates and axial loading were also investigated. The results showed the concrete to fail in a similar manner developing huge shear stresses at point A, thus confirming the bi-linear moment curvature law. It was noted however that the ductility was seen to reduce with increasing axial lading. Reducing the area of reinforcement used was seen to reduce ductility. Increasing the curvature rate in all three cases of reinforcement was seen to reduce the concrete ductility.

4.5 References

1. W.G.Corley, "Rotational capacity of Reinforced Concrete Beams", *Jour. Of the Structural Division, Proc. ASCE pp 4939-4941* (1966).
2. A.Hillerborg, "Fracture Mechanics Concepts applied to Moment Capacity and Rotational Capacity of Reinforced Concrete Beams" *Engineering Fracture Mechanics, 35(1/2/3) pp 233-240* (1990).
3. A.Hillerborg, "Fracture Mechanics Concepts applied to Moment Capacity and Rotational Capacity of Reinforced Concrete Beams" *Proc. of the Inter. Conf. On Fracture of Concrete and Rock, July 4-6* (1988).
4. N.Alca, D.B.A.Scott, J.G.MacGregor, "Effect of Size on Flexural Behaviour of High Strength Concrete Beams" *ACI Structural Journal* **94(1)** *pp 59-67* (1997).
5. ACI Committee 318 "Building Code Requirements for Reinforced Concrete and Commentary", *ACI 318-890/ACI318R-89,ACI Detroit pp 4939-4941* (1989).
6. R.G.Smith, C.O.Orangun, "Evaluation of the Stress-Strain Curve of Concrete in Flexure Using the Method of Least Squares", *ACI Journal* **66(7)** *pp 553-559* (1969).
7. P.H.Evans, M.S.Marthe, "Microcracking and stress strain curves for concrete in tension", *Mater. Struct.(RILEM)* **1** *pp 61-64* (1968).

Chapter 5

Discrete element technology

5.1 Introduction

The combined finite-discrete element method is a recently developed numerical method aimed at modelling failing, fracturing and/or fragmenting solids. The method combines aspects of both finite elements and discrete elements

Solid domains are discretized into finite elements in the usual way dictated by the finite element method. However finite (as opposed to small) rotations and finite displacements are assumed a priori. It is also assumed that solid domains can fail, fracture or fragment. Thus a single domain represented by a single finite element mesh is transformed into a number of interacting domains, each of which is represented by its own separate finite element mesh.

In this chapter a simple element is introduced which can be used in the discretization of structural elements.

A structural beam is shown in Figure 5.1. It's orientation is described by local element axis **a1** and **a2**.

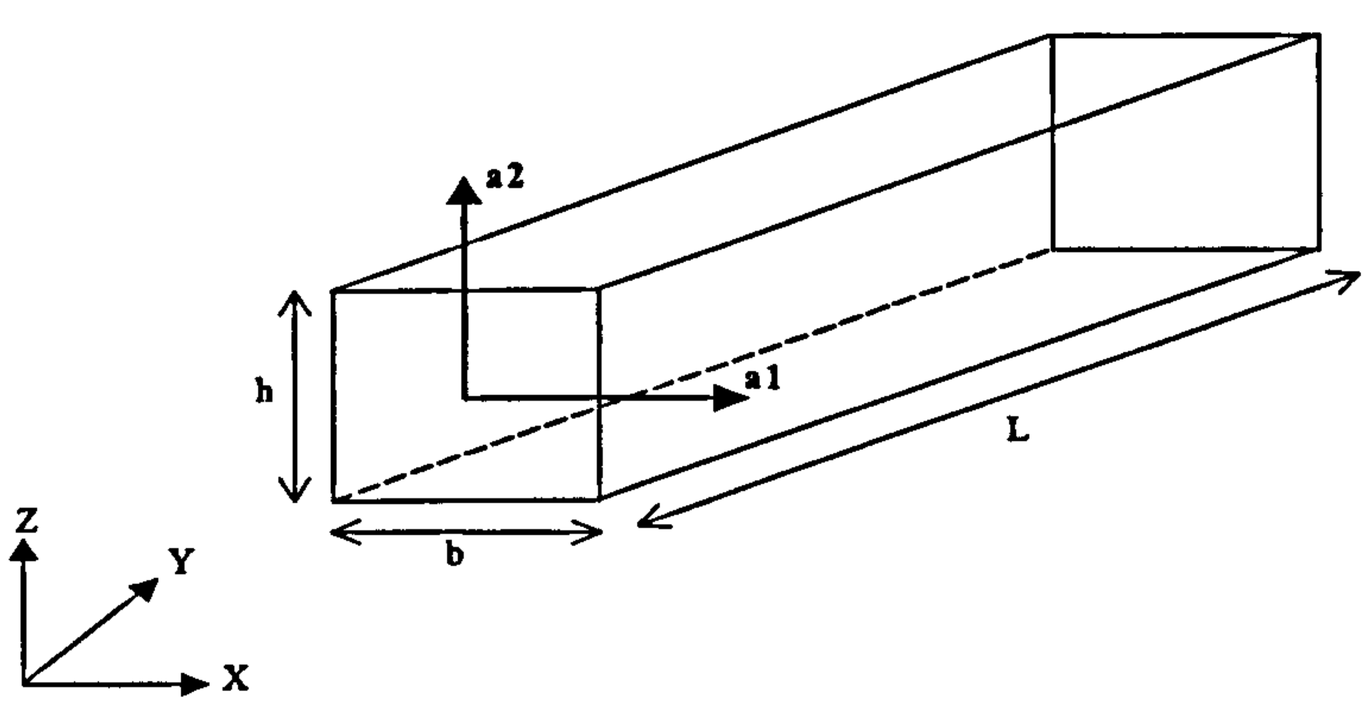

Figure 5.1 Beam structural element

This beam can be discretised into nodes and elements as shown in Figure 5.2.

Figure 5.2 Discretised beam structural element

The mass of each node is taken to act across half of the adjoing elements to either side of the node, as shown in Figure 5.3.

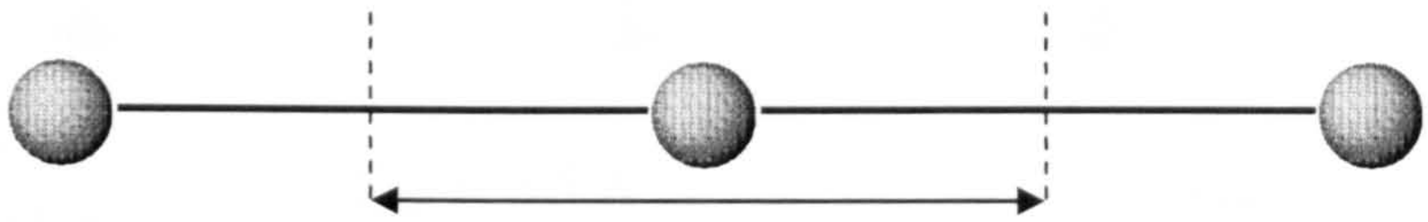

Figure 5.3 Area over which mass of node acts

Each element has end nodes i and j at either end. The local orientation of the nodes is described by the local nodal axis. For example, at node i this would be $e_{1(i)}$and $e_{2(i)}$. The element length is represented by vector r_i . r(i) and r(j) are the respective nodal vectors in the global axis as illustrated by Figure 5.4.

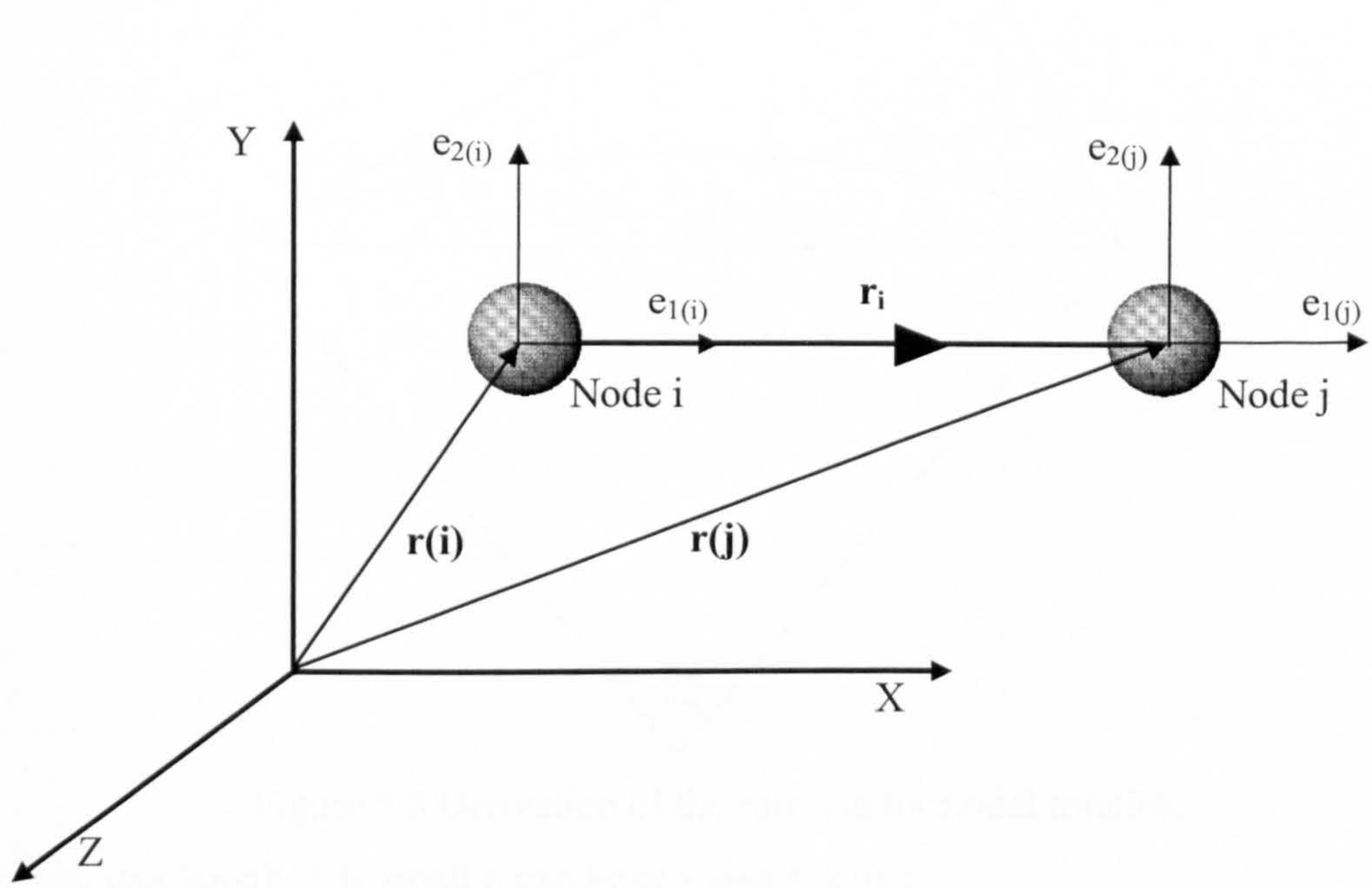

Figure 5.4 Typical element with nodes - showing local nodal and global axis

This element can then be used to discretise walls, beams, columns and slabs, as illustrated with a simple structure as shown in Figure 5.5.

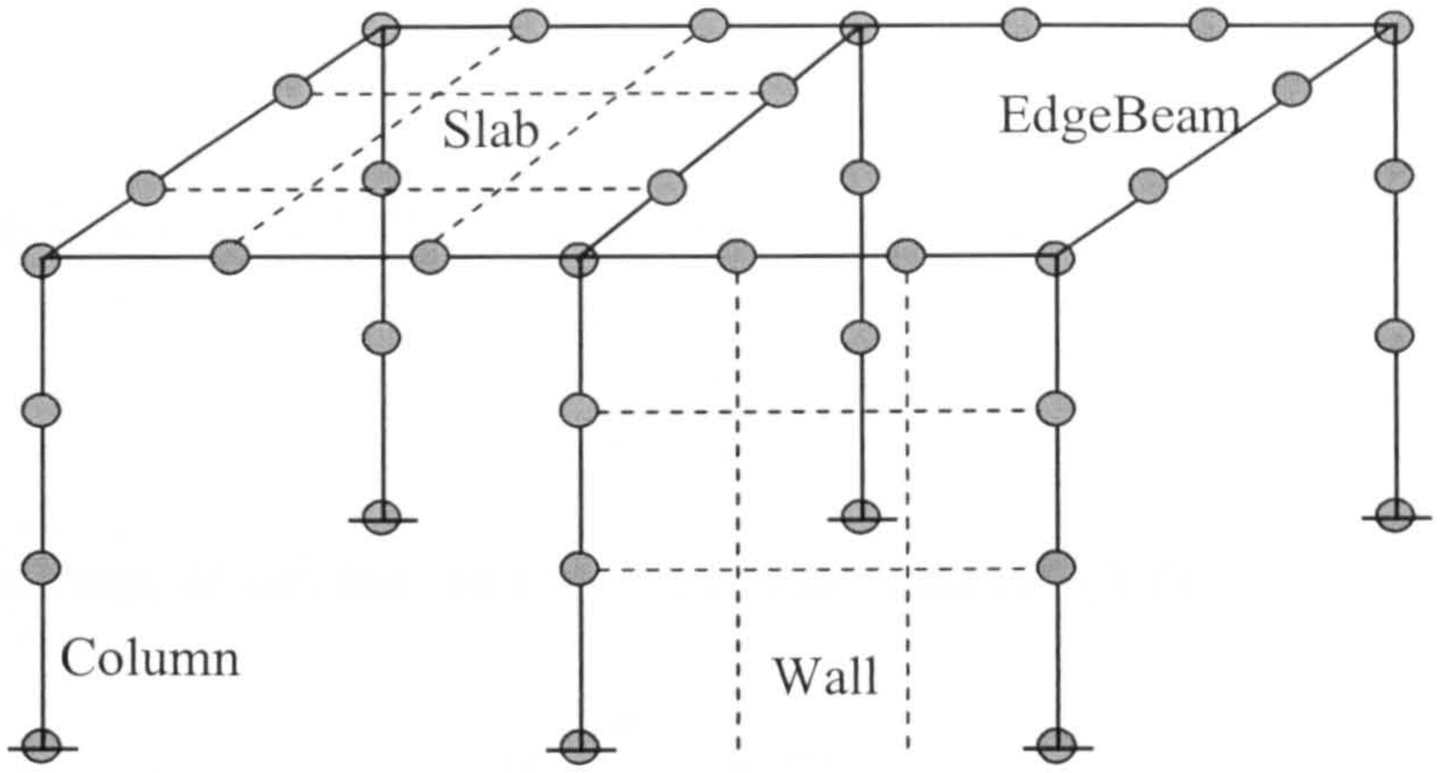

Figure 5.5 A simple discretised structure

The nodal rotation is found as follows. Figure 5.6 shows a simple element with applied moments at each node. The nodal orientations are thus found.

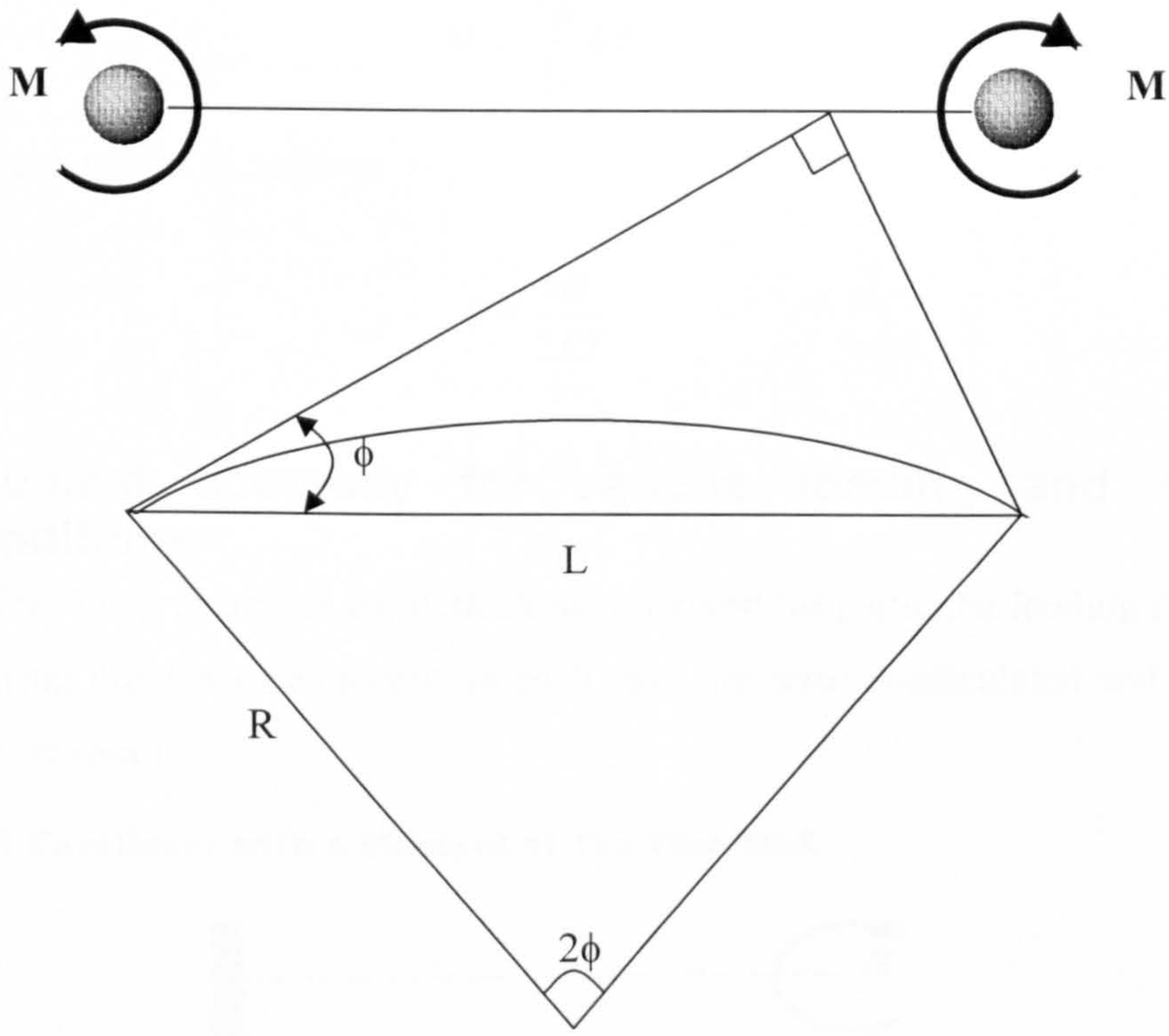

Figure 5.6 Derivation of the formula for nodal rotation

If the element length, L is small it can be can asserted that

$$L = 2\phi R \tag{5.1}$$

where ϕ is the angle and R is the radius of curvature. Rearanging equation (5.1) gives equation (5.2).

$$\frac{1}{R}=\frac{2\phi}{L} \tag{5.2}$$

The first term in equation (5.2) is equal to the curvature ϕ_u.

$$\phi_u=\frac{1}{R} \tag{5.3}$$

Hence the moment, M can then be computed using equation (5.3).

$$M=\frac{EI}{R}=\phi_u EI \tag{5.4}$$

Therefore by substituting equations (5.2) and (5.3) into equation (5.4), the expression for moment can be given as

$$M=\frac{2\phi}{L}EI \tag{5.5}$$

Rearranging equation (5.5) gives

$$\phi=\frac{ML}{2EI} \tag{5.6}$$

5.2 Element accuracy for various loading and support conditions

In the following examples the deflection is derived for particular loading cases, each with a varying number of elements. In each case the error is calculated and compared with the exact result.

Example 1 Cantilever with a Moment at the Free End

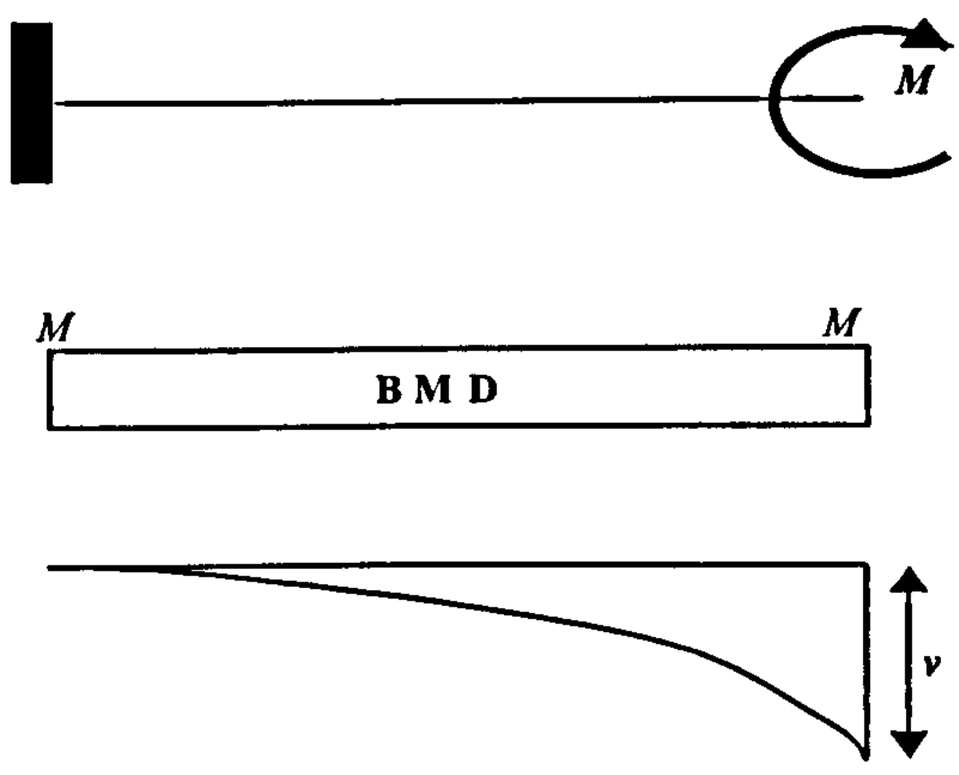

Figure 5.7 The BMD and deflected shape for a cantilever with end moment

The exact deflection, v in the standard case is given by equation (5.7).

$$v = \frac{ML^2}{2EI} \tag{5.7}$$

Case with 1 Element

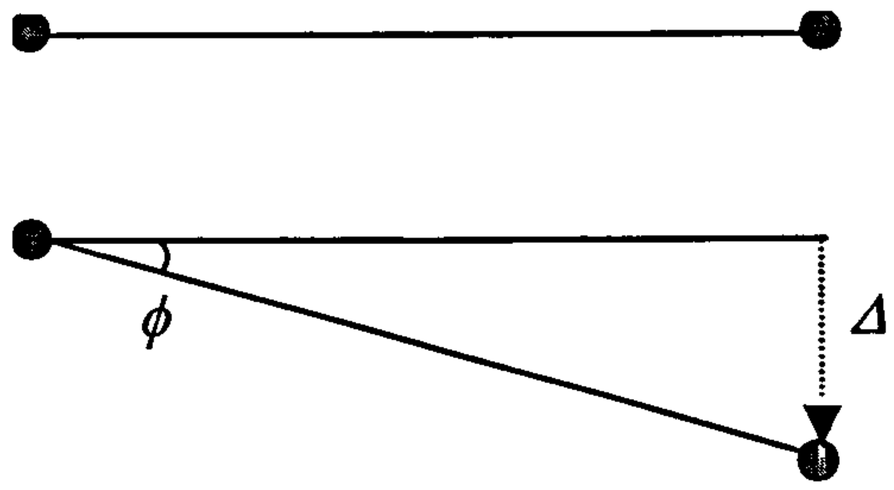

Figure 5.8 Deflection using one element

The angle ϕ is found using equation (5.6).

$$\phi = \frac{ML}{2EI} \tag{5.8}$$

The deflection, as given in equation (5.9) is derived by multiplying the angle ϕ with the length of the element, which in this particular case is L

$$\Delta = \frac{ML}{2EI}.L = \frac{ML^2}{2EI} \tag{5.9}$$

where

Δ = the deflection in our case, E = the Youngs modulus of elasticity, I = the second moment of inertia

As is seen this expression for deflection is the same as the theoretical prediction for the deflection and hence no error is found.

Case with 2 Element

A similar principle is employed for the case where two elements are used, to calculate the deflections Δ_1 and Δ_2 of the first and second elements respectively.

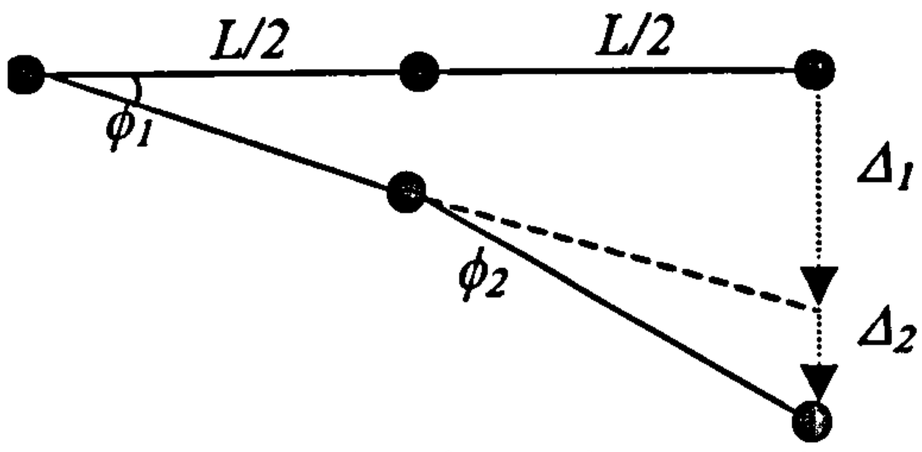

Figure 5.9 Deflection using two elements

For equilibrium at the middle node as shown in Figure 5.10, the following conditions apply.

$$\alpha = \beta \text{ and } \beta = 0.5\gamma \tag{5.10}$$

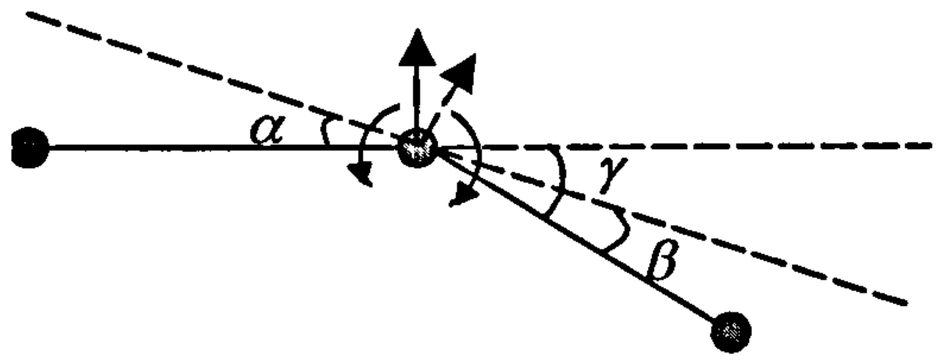

Figure 5.10 Moment equilibrium at middle node

The respective element rotations ϕ_1 and ϕ_2 are obtained using equation (5.6) and is shown in equations (5.11) and (5.12).

$$\phi_1 = \frac{M}{2EI}\frac{L}{2} = \frac{ML}{4EI} \tag{5.11}$$

$$\phi_2 = \frac{M}{2EI}\frac{L}{2} = \frac{ML}{4EI} \tag{5.12}$$

The respective element deflections are Δ_1 and Δ_2 are obtained using equation (5.9) and is shown in equations (5.13) and (5.14).

$$\Delta_1 = \frac{ML}{2EI}.\frac{L}{2} = \frac{ML^2}{4EI} \tag{5.13}$$

$$\Delta_2 = \frac{ML}{2EI}.\frac{L}{2} = \frac{ML^2}{4EI} \tag{5.14}$$

Therefore the total deflection is found from the sum of the individual element deflections.

$$\Delta = \Delta_1 + \Delta_2 = \frac{ML^2}{4EI} + \frac{ML^2}{4EI} = \frac{ML^2}{2EI} \tag{5.15}$$

As in the first case a zero percent error is found to exist between the obtained and exact deflection values.

Example 2 Cantilever with an End Point Load

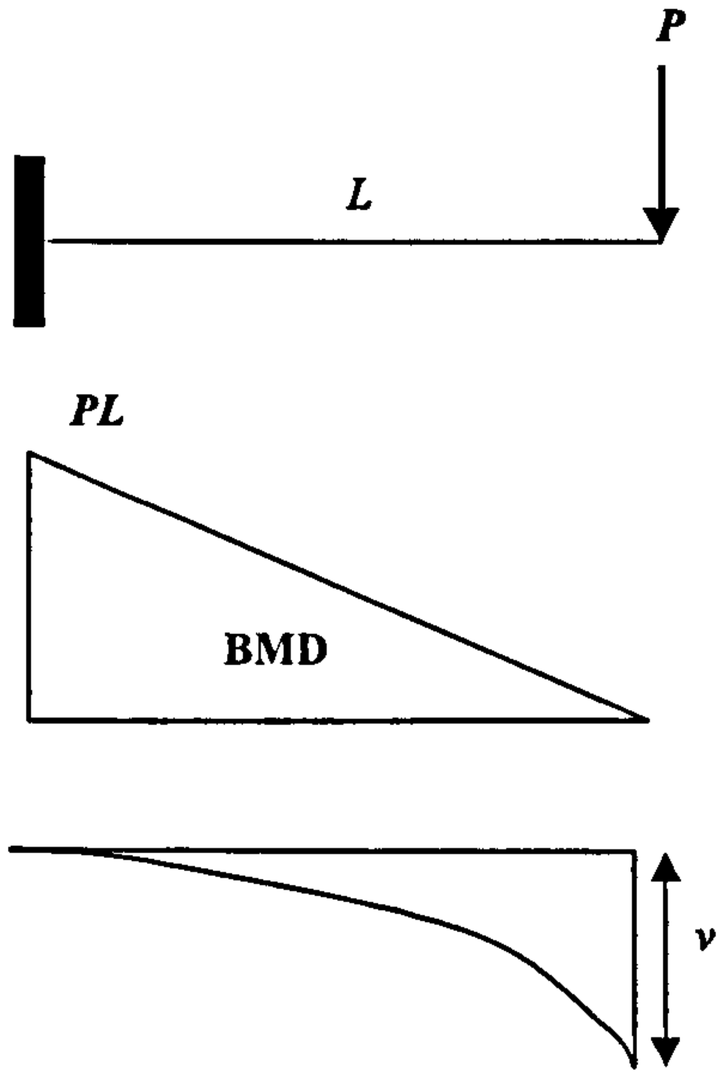

Figure 5.11 The BMD and deflected shape for a cantilever with end point load

The exact deflection, v in the standard case is given by equation (5.16).

$$v = \frac{PL^3}{3EI} \tag{5.16}$$

Case with 1 Element

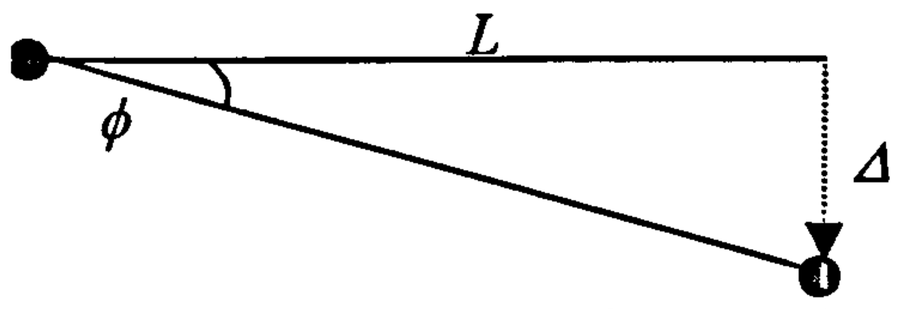

Figure 5.12 Deflection using one element

The moment, M is calculated as

$$M = P.L \tag{5.17}$$

Hence referring to equation (5.6), the element rotation is calculated according to equation (5.18).

$$\phi = \frac{PL}{2EI} L = \frac{PL^2}{2EI} \tag{5.18}$$

Thus the deflection is found as

$$\Delta = \frac{PL^2}{2EI} L = \frac{PL^3}{2EI} \tag{5.19}$$

The error between the obtained deflection and the exact deflection is now calculated

$$\left| \frac{\frac{PL^3}{2EI} - \frac{PL^3}{3EI}}{\frac{PL^3}{3EI}} \right| \times 100 = \left| \frac{3}{2} - 1 \right| \times 100 = 50\% \tag{5.20}$$

Case with 2 Elements

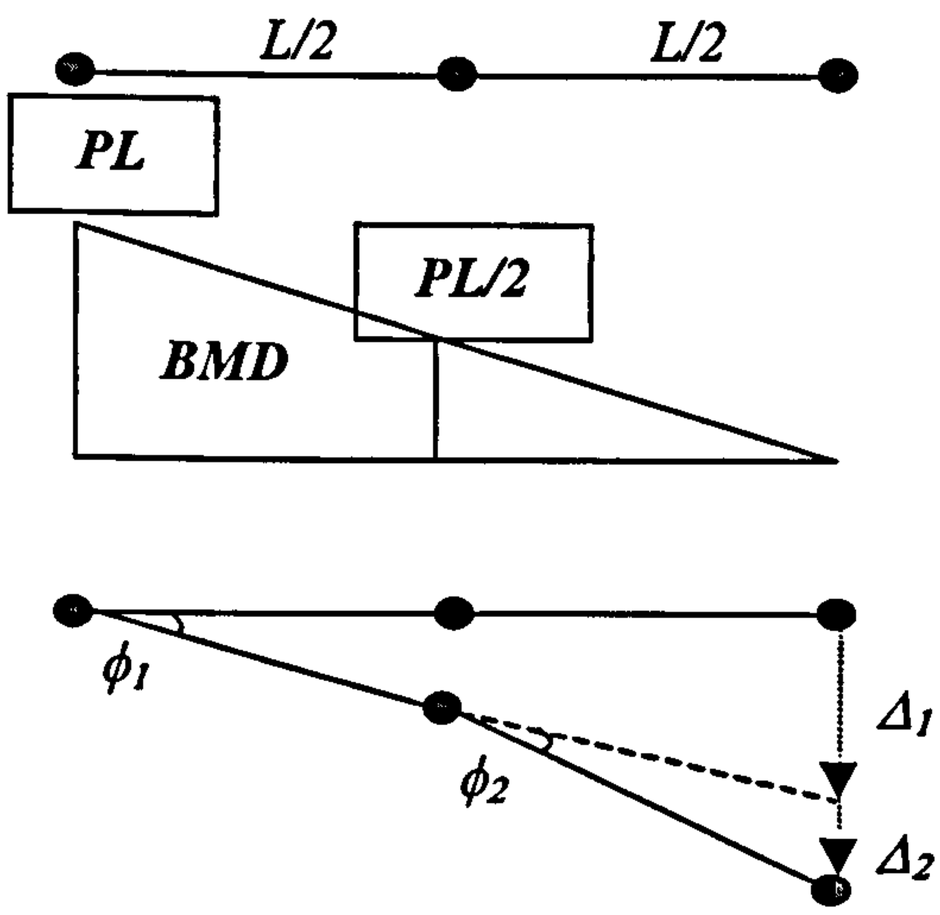

Figure 5.13 Deflection using two elements

Using the above procedures the element angles and deflections are as follows. The element length in this case is L/2.

$$\phi_1 = \frac{PL}{2EI} \frac{L}{2} = \frac{PL^2}{4EI} \tag{5.21}$$

For the second element a moment of *PL/2* acts at the node. Hence accounting for this in the calculation for the element rotation ϕ_2 gives

$$\phi_2 = \frac{1}{2} \frac{PL}{2EI} \frac{L}{2} 2 = \frac{PL^2}{4EI} \tag{5.22}$$

The deflections are found by multiplying the element rotations by the distance of the rotated node to the deflected end of the beam

$$\Delta_1 = \frac{PL^2}{4EI} \cdot L = \frac{PL^3}{4EI} \tag{5.23}$$

$$\Delta_2 = \frac{PL^2}{4EI} \cdot \frac{L}{2} = \frac{PL^3}{8EI} \tag{5.24}$$

The total deflection is then found to be as

$$\Delta = \Delta_1 + \Delta_2 = \frac{PL^3}{4EI} + \frac{PL^3}{8EI} = \frac{3PL^3}{8EI} \tag{5.25}$$

The error between the deflection given in equation (5.25) and the exact deflection is

$$\left| \frac{\frac{3}{8} - \frac{1}{3}}{\frac{1}{3}} \right| \times 100 = 12.5\% \tag{5.26}$$

Case with 4 Elements

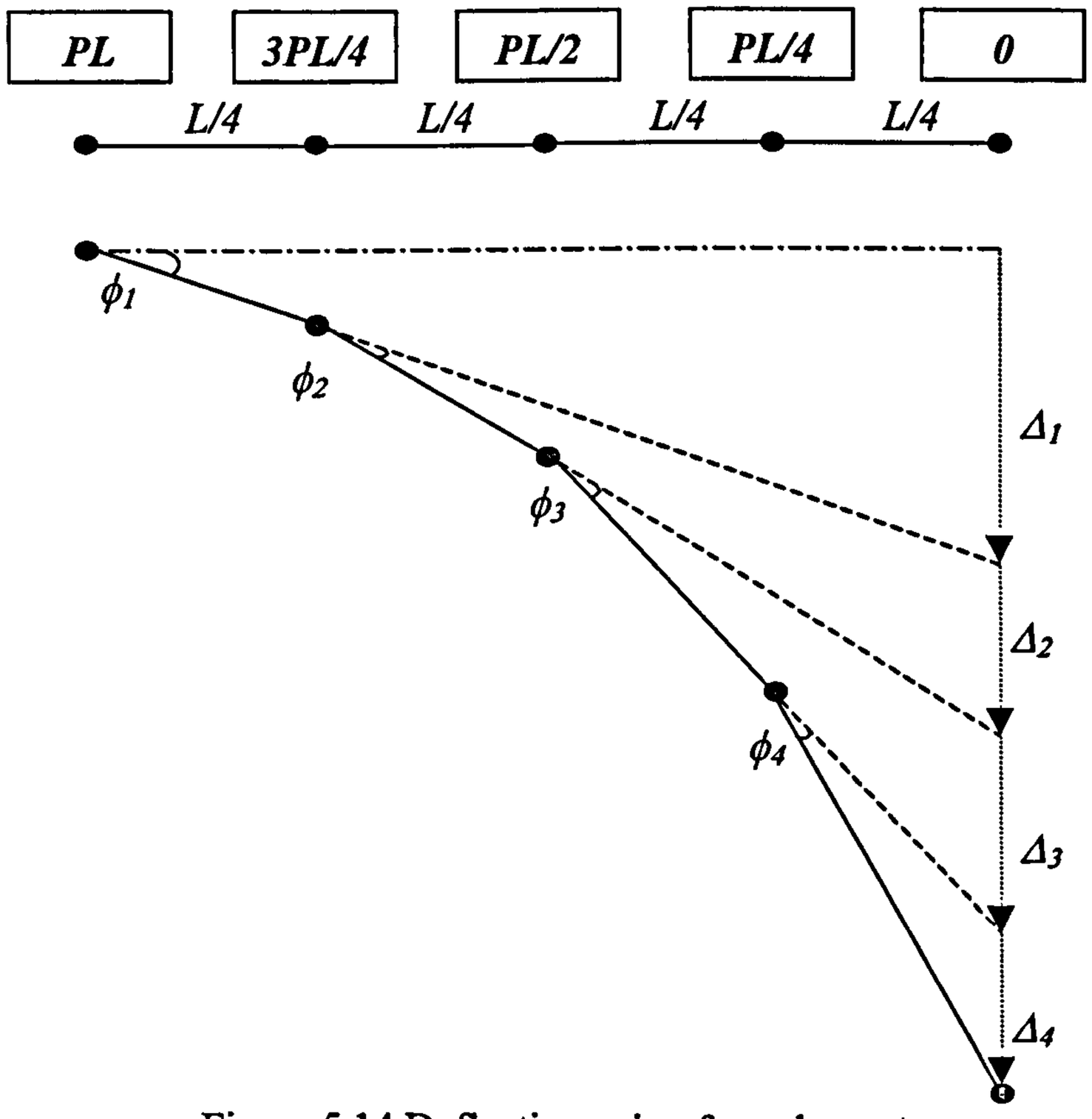

Figure 5.14 Deflection using four elements

Each element length is now *L/4*. The bending moments at each node are shown in bold in the boxes in Figure 5.14. The respective element rotations and displacements are given in equations (5.27) to (5.34).

$$\phi_1 = \frac{PL}{2EI}\frac{L}{4} = \frac{PL^2}{8EI} \tag{5.27}$$

$$\phi_2 = \frac{1}{2}\frac{3PL}{4EI}\frac{L}{4}2 = \frac{3PL^2}{16EI} \tag{5.28}$$

$$\phi_3 = \frac{1}{2}\frac{PL}{2EI}\frac{L}{4}2 = \frac{PL^2}{8EI} \tag{5.29}$$

$$\phi_4 = \frac{1}{2}\frac{PL}{4EI}\frac{L}{4}2 = \frac{PL^2}{16EI} \tag{5.30}$$

$$\Delta_1 = \frac{PL^2}{8EI}L = \frac{PL^3}{8EI} \tag{5.31}$$

$$\Delta_2 = \frac{9PL^3}{64EI} \tag{5.32}$$

$$\Delta_3 = \frac{PL^3}{16EI} \tag{5.33}$$

$$\Delta_4 = \frac{PL^3}{64EI} \tag{5.34}$$

Hence the total deflection will be

$$\Delta = \Delta_1 + \Delta_2 + \Delta_3 + \Delta_4 = \frac{11PL^3}{32EI} \tag{5.35}$$

The error in this case is calculated as previously and found to be 3.125%.

$$\left|\frac{\frac{11}{32}-\frac{1}{3}}{\frac{1}{3}}\right|\times 100 = 3.125\% \tag{5.36}$$

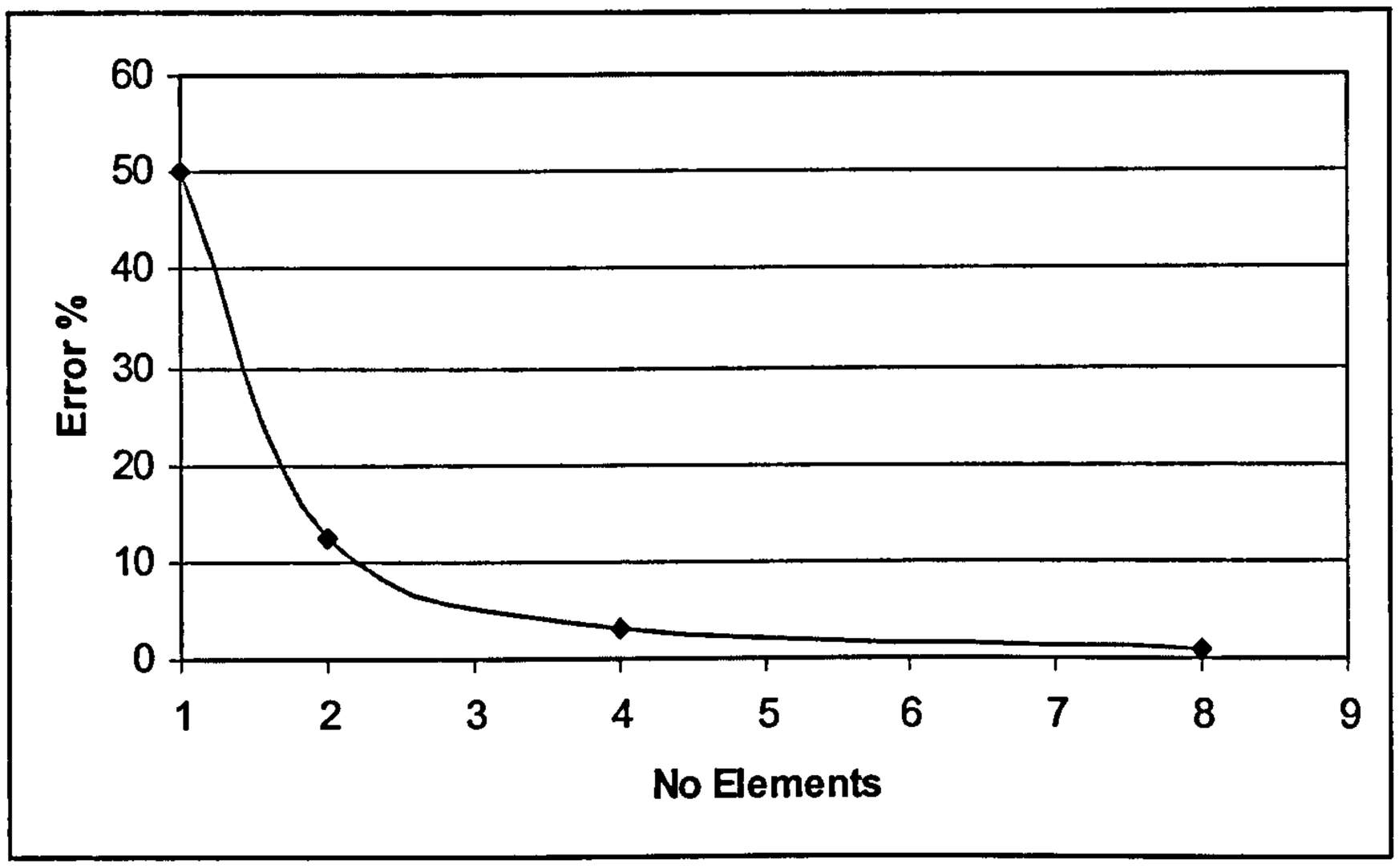

Figure 5.15 Error v No elements

The error is estimated to be of the order of L^2.

Example 3 Cantilever with a Distributed Load

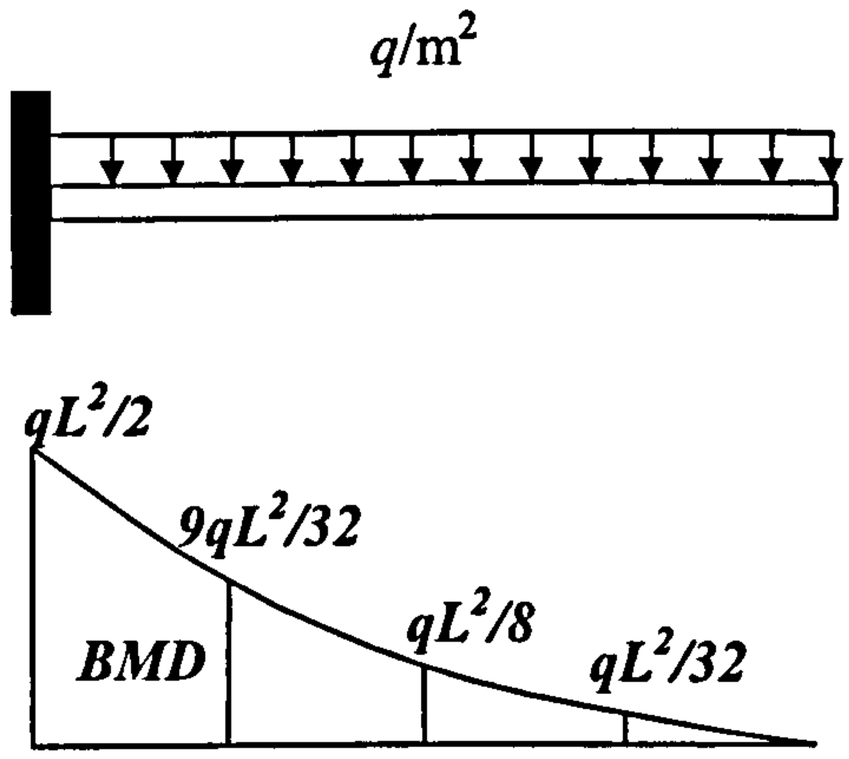

Figure 5.16 The BMD for a cantilever with distributed load

The exact deflection, v in the standard case is given by equation (5.37).

$$v = \frac{qL^4}{8EI} \tag{5.37}$$

Case with 1 Element

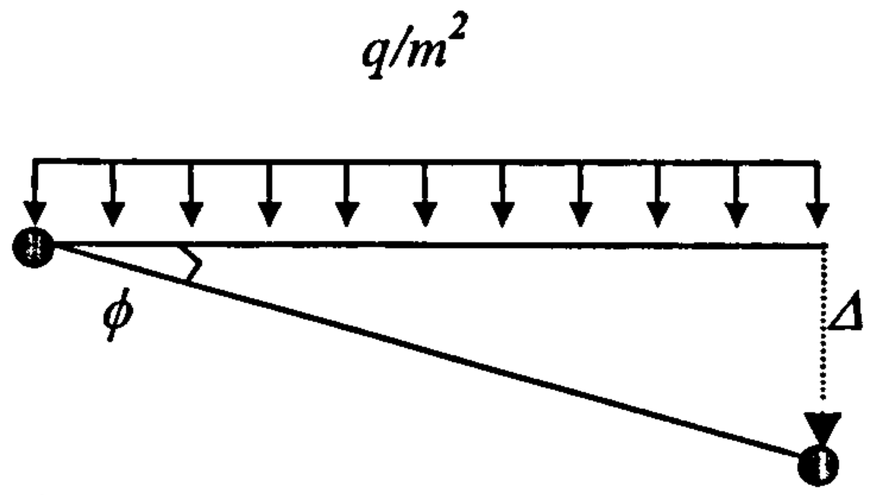

Figure 5.17 Deflection using one element

Referring to equation (5.6), the element rotation is calculated according to equation (5.38).

$$\phi = \frac{qL^2}{2}\frac{1}{2EI}L = \frac{qL^3}{4EI} \tag{5.38}$$

From this we can find the deflection to be as per equation (5.39).

$$\Delta = \frac{qL^3}{4EI}L = \frac{qL^4}{4EI} \tag{5.39}$$

The error difference is calculated as

$$\left|\frac{\frac{1}{4}-\frac{1}{8}}{\frac{1}{4}}\right| \times 100 = 50\% \tag{5.40}$$

Case with 2 Elements

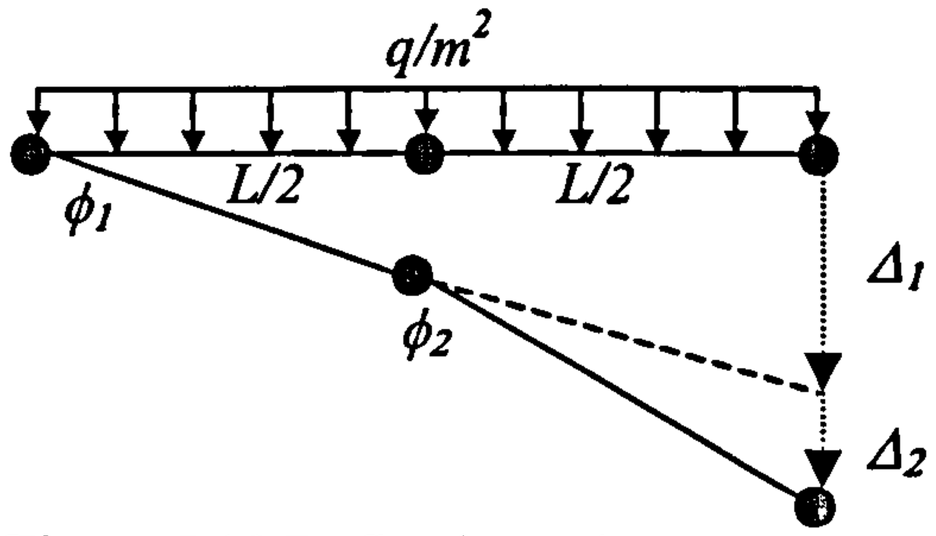

Figure 5.18 Deflection using two elements

The element angles and deflections are derived as shown in equations (5.41) to (5.44).

$$\phi_1 = \frac{qL^2}{2}\frac{1}{2EI}\frac{L}{2} = \frac{qL^3}{8EI} \tag{5.41}$$

$$\phi_2 = \frac{qL^2}{8}\frac{1}{2EI}\frac{L}{2}2 = \frac{qL^3}{16EI} \tag{5.42}$$

$$\Delta_1 = \frac{qL^4}{8EI} \tag{5.43}$$

$$\Delta_2 = \frac{qL^4}{32EI} \tag{5.44}$$

The total deflection is then found to be as per equation (5.45).

$$\Delta = \Delta_1 + \Delta_2 = \frac{5qL^4}{32EI} \tag{5.45}$$

The error between the deflection and the exact deflection is

$$\left|\frac{\frac{5}{32}-\frac{1}{8}}{\frac{1}{8}}\right| \times 100 = 25\% \tag{5.46}$$

Case with 4 Elements

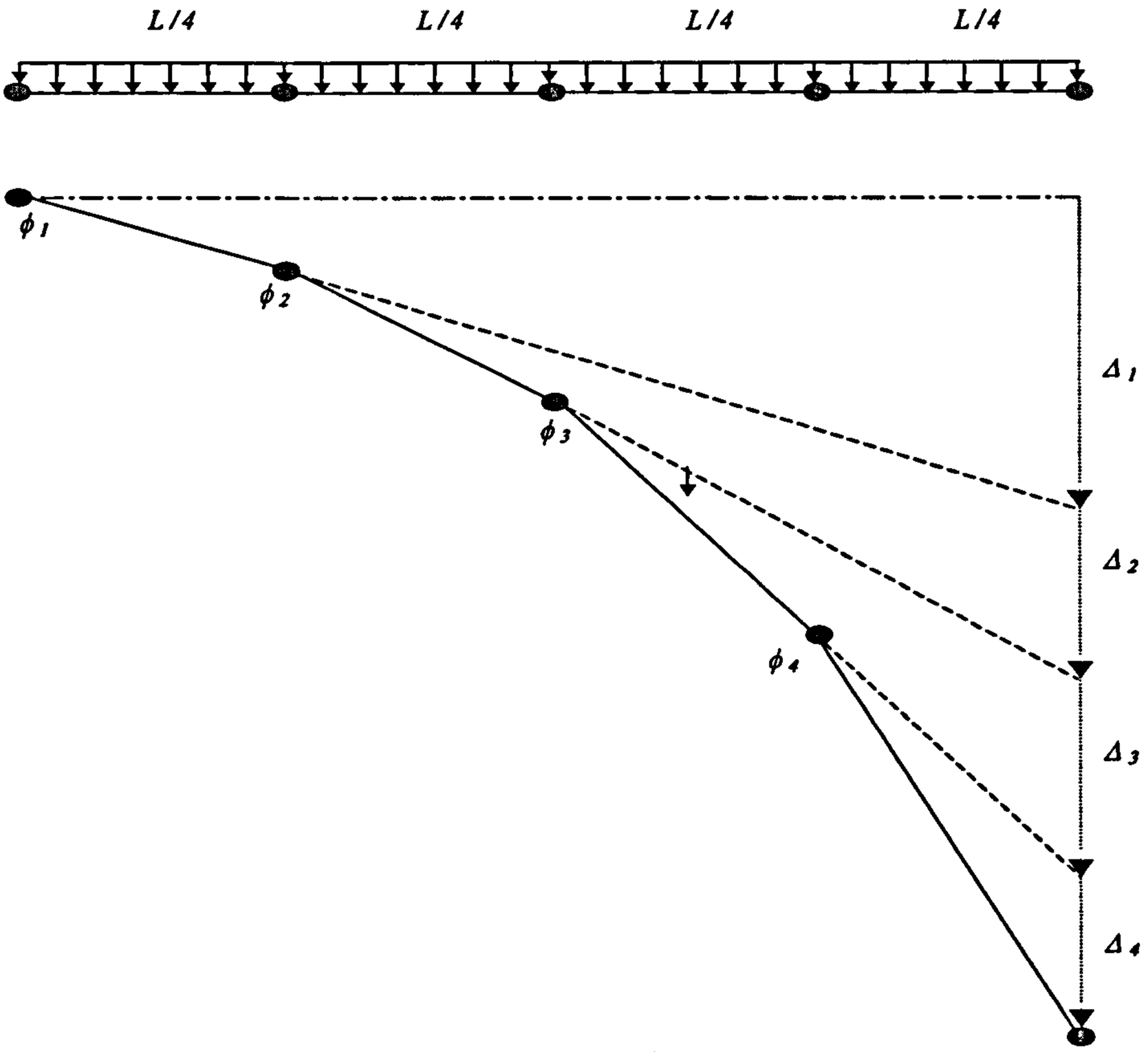

Figure 5.19 Deflection using four elements

The element angles and rotations for this case is described as per equations (5.47) to (5.54).

$$\phi_1 = \frac{qL^2}{2}\frac{1}{2EI}\frac{L}{4} = \frac{qL^3}{16EI} \tag{5.47}$$

$$\phi_2 = \frac{9qL^2}{32}\frac{1}{2EI}\frac{L}{4}2 = \frac{9qL^3}{128EI} \tag{5.48}$$

$$\phi_3 = \frac{qL^2}{8}\frac{1}{2EI}\frac{L}{4}2 = \frac{qL^3}{32EI} \tag{5.49}$$

$$\phi_4 = \frac{qL^2}{32}\frac{1}{2EI}\frac{L}{4}2 = \frac{qL^3}{128EI} \tag{5.50}$$

$$\Delta_1 = \frac{qL^4}{16EI} \tag{4.51}$$

$$\Delta_2 = \frac{27qL^4}{512EI} \tag{5.52}$$

$$\Delta_3 = \frac{qL^4}{64EI} \tag{5.53}$$

$$\Delta_4 = \frac{qL^4}{512EI} \tag{5.54}$$

Hence the sum of the individual deflections gives the total deflection

$$\Delta = \Delta_1 + \Delta_2 + \Delta_3 + \Delta_4 = \frac{17qL^4}{128EI} \tag{5.55}$$

The error in this case is

$$\left| \frac{\frac{17}{128} - \frac{1}{8}}{\frac{1}{8}} \right| \times 100 = 6.25\% \tag{5.56}$$

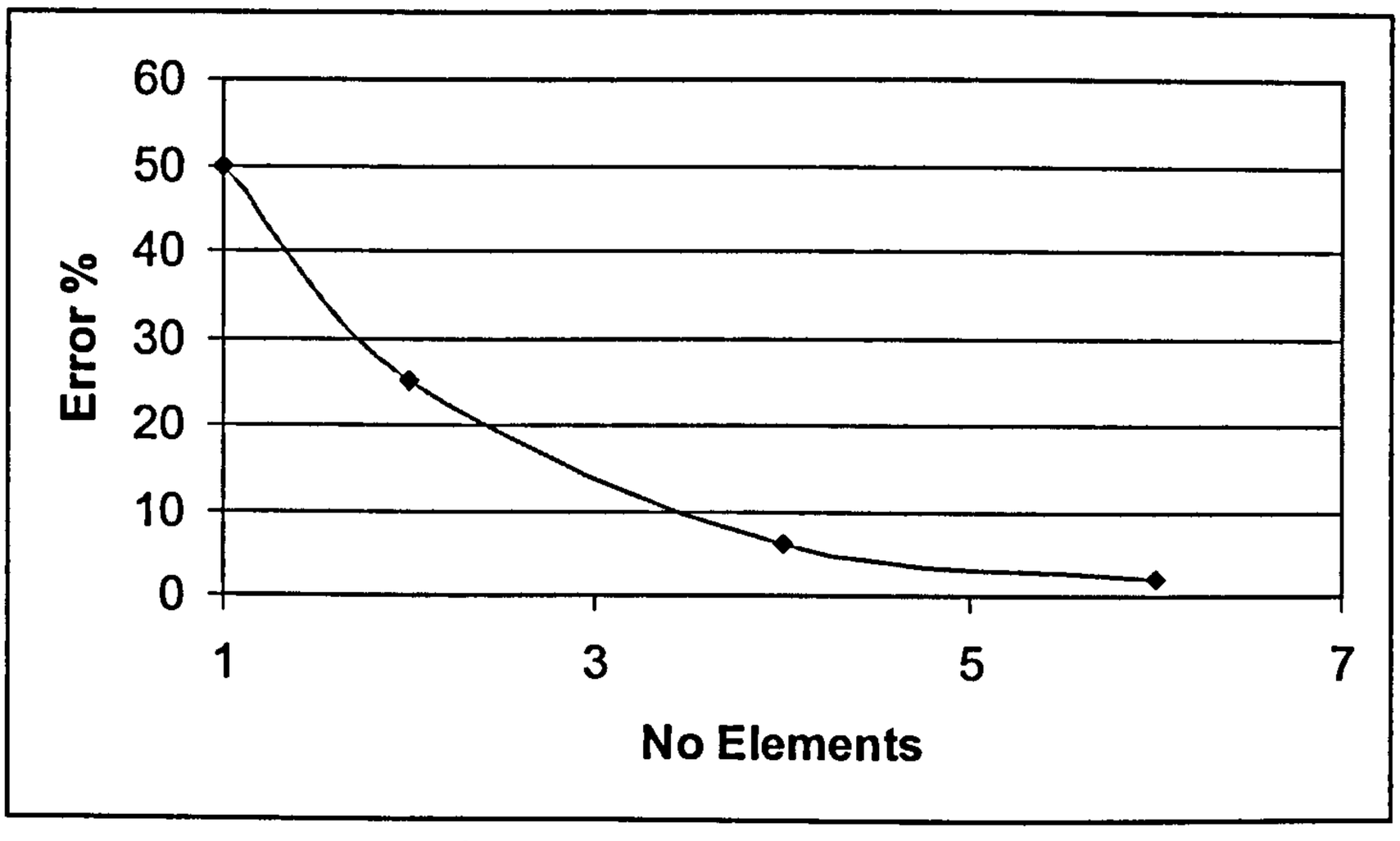

Figure 5.20 Error v No elements

The error in all cases so far reduces as the number of elements employed is increased and appears to be converging to the exact result.

In the subsequent examples the bending moments are calculated at the nodal points and compared to the standard result

Example 4 A Simply Supported Beam under Distributed Load

Case with 2 Elements

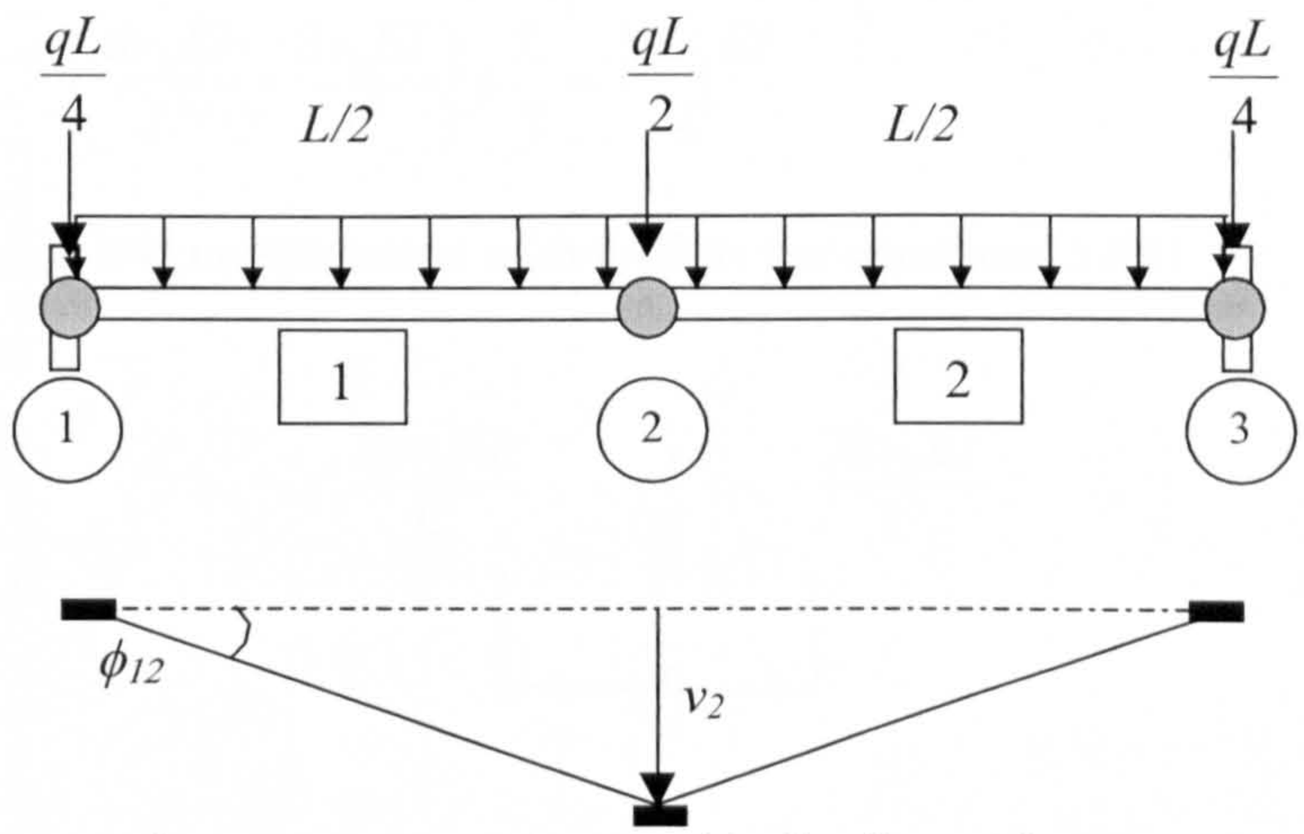

Figure 5.21 Simply supported beam with distributed load using two elements

The distributed load is made equivalent to point loads using the equivalent load theorem [3].

Assuming rotations are small the angle ϕ_{12} is found to be

$$\phi_{12} = \frac{v_2}{(L/2)} = \frac{2v_2}{L} \tag{5.57}$$

The moment M_{12} is found as

$$M_{12} = \frac{2EI}{L}\phi = \frac{2EI}{(L/2)}\frac{2v_2}{L} = \frac{8v_2EI}{L^2} \tag{5.58}$$

By symmetry M_{12} is equal to M_{32}. Therefore the provisional bending moment diagram in terms of deflections will be as shown in Figure 5.22.

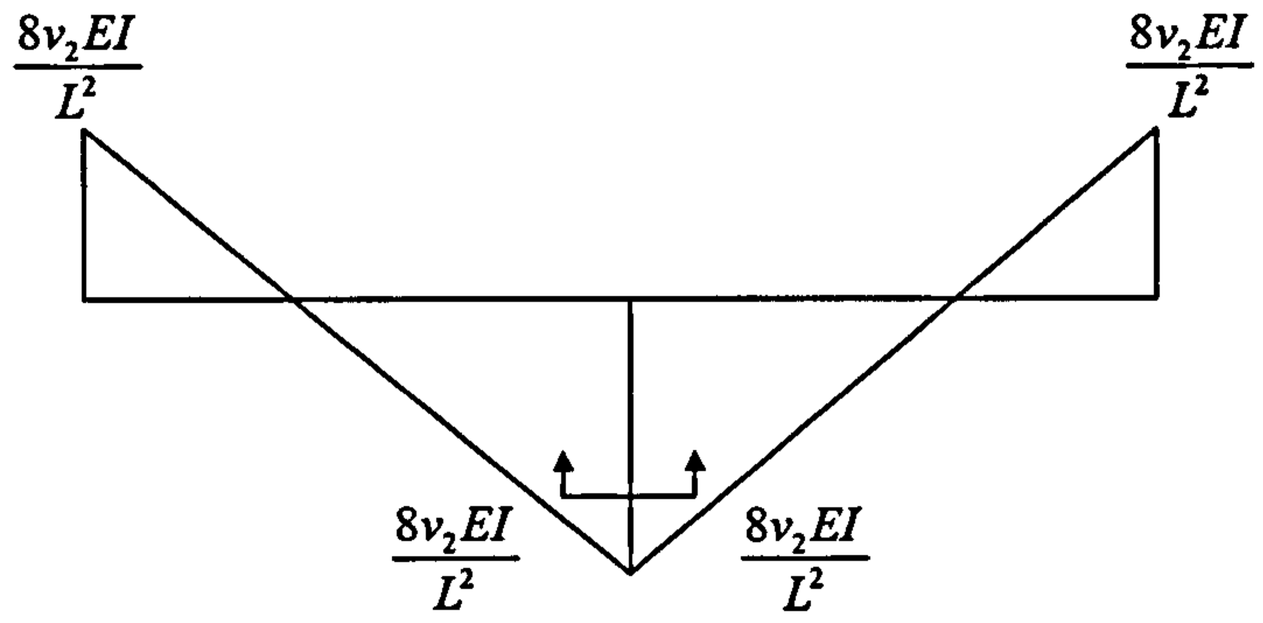

Figure 5.22 Provisional BMD for simply supported beam with distributed load using two elements

The shear at node 2 is given by equation (5.59).

$$\left(\frac{8v_2EI}{L^2}+\frac{8v_2EI}{L^2}\right)\div\frac{L}{2}=\frac{32v_2EI}{L^3} \tag{5.59}$$

The shear at node 2 is now equated with load as per equation (5.60).

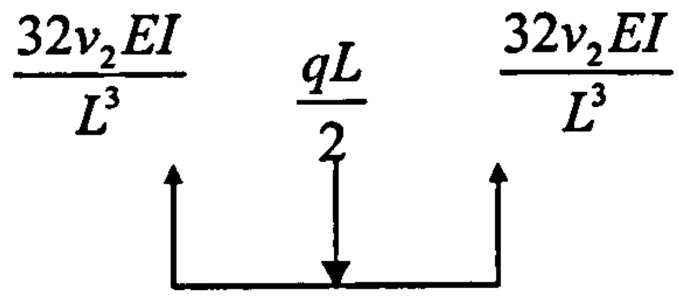

$$2\left(\frac{32v_2EI}{L^3}\right)=\frac{qL}{2} \tag{5.60}$$

Rearaanging equation (5.60) gives the deflection v_2 as

$$v_2=\frac{qL^4}{128EI} \tag{5.61}$$

Therefore equation (5.61) is substituted into the values shown in Figure 5.22 to produce the final bending moment diagram illustrated in Figure 5.23.

$$M=\frac{8EI}{L^2}\frac{qL^4}{128EI}=\frac{qL^2}{16} \tag{5.62}$$

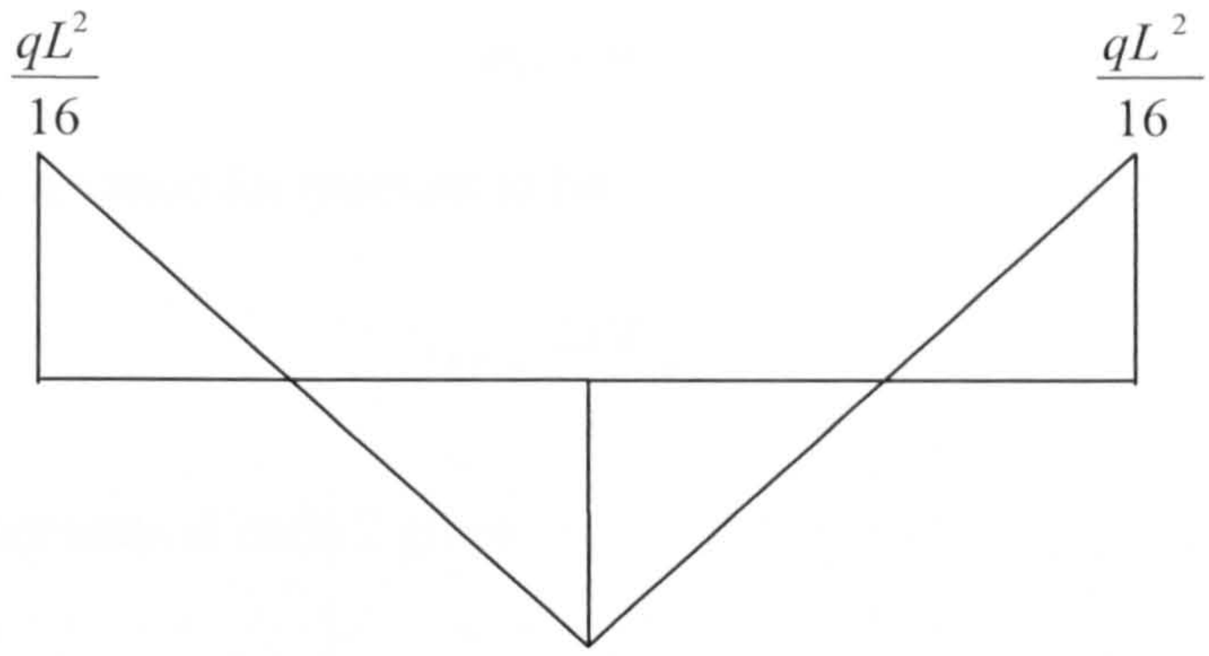

Figure 5.23 Final BMD for simply supported beam with distributed load using two elements

The end moments are found to differ from the exact result by 25% and the centre moment is found to differ by 50%.

Case with 3 Elements

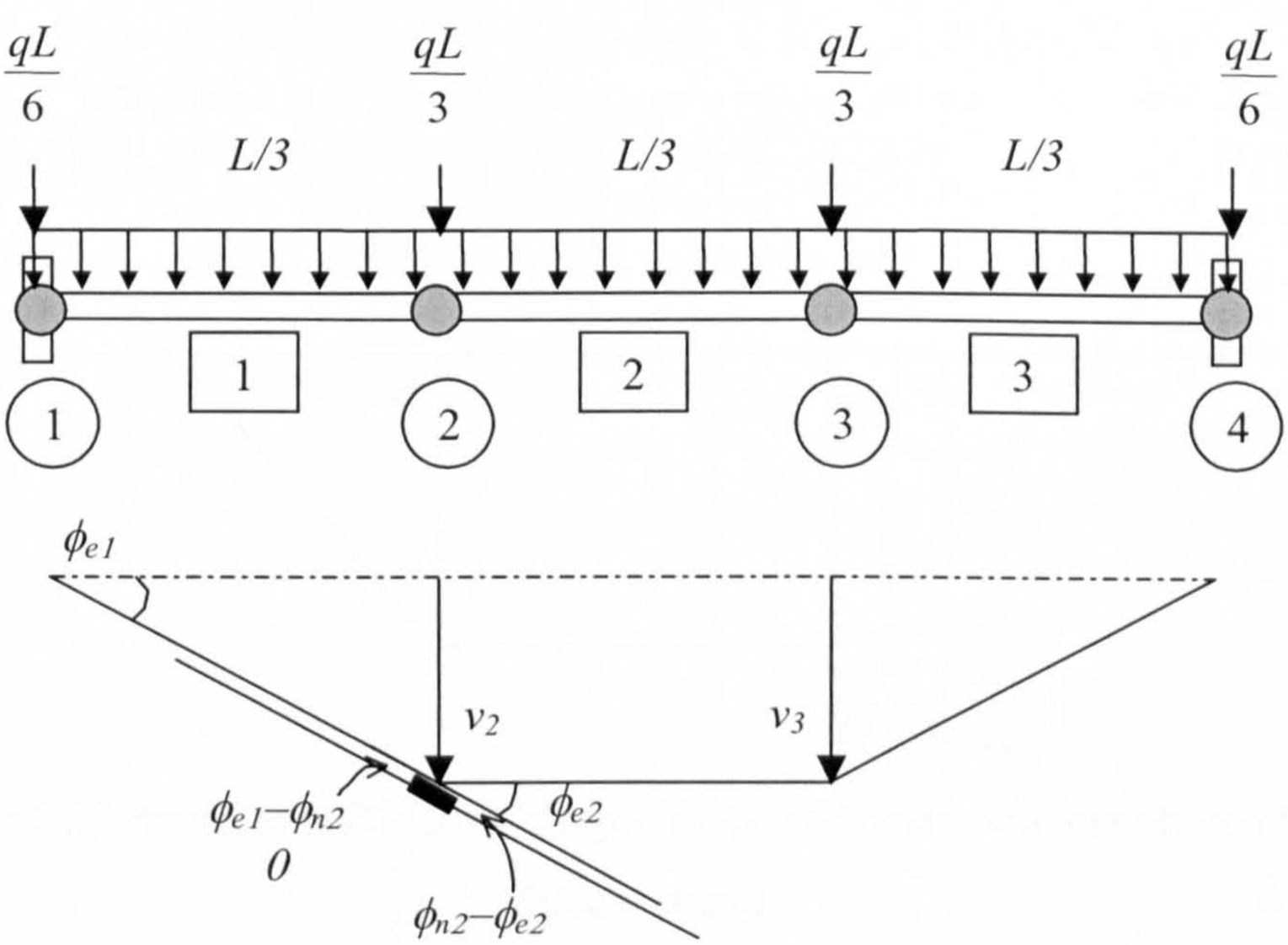

Figure 5.24 Simply supported beam with distributed load using three elements

Once again rotations are assumed small, hence the rotation of element one ϕ_{e1} is

$$\phi_{e1} = \frac{3v_2}{L} \tag{5.63}$$

The nodal rotation at 2 is represented as ϕ_{n2}. The rotation of element 2 is zero, hence

$$\phi_{e2} = 0 \tag{5.64}$$

Taking the basic equation for moment to be

$$M = \frac{2EI}{L}\phi \tag{5.65}$$

And equating moments at node 2 gives

$$\frac{2EI}{(L/3)}\left(\frac{3v_2}{L} - \phi_{n2}\right) = \frac{2EI}{(L/3)}\phi_{n2} \tag{5.66}$$

This gives the nodal rotation at 2, ϕ_{n2} as

$$\phi_{n2} = \frac{3v_2}{2L} \tag{5.67}$$

Therefore our provisional BMD in terms of deflections is shown in Figure 5.25.

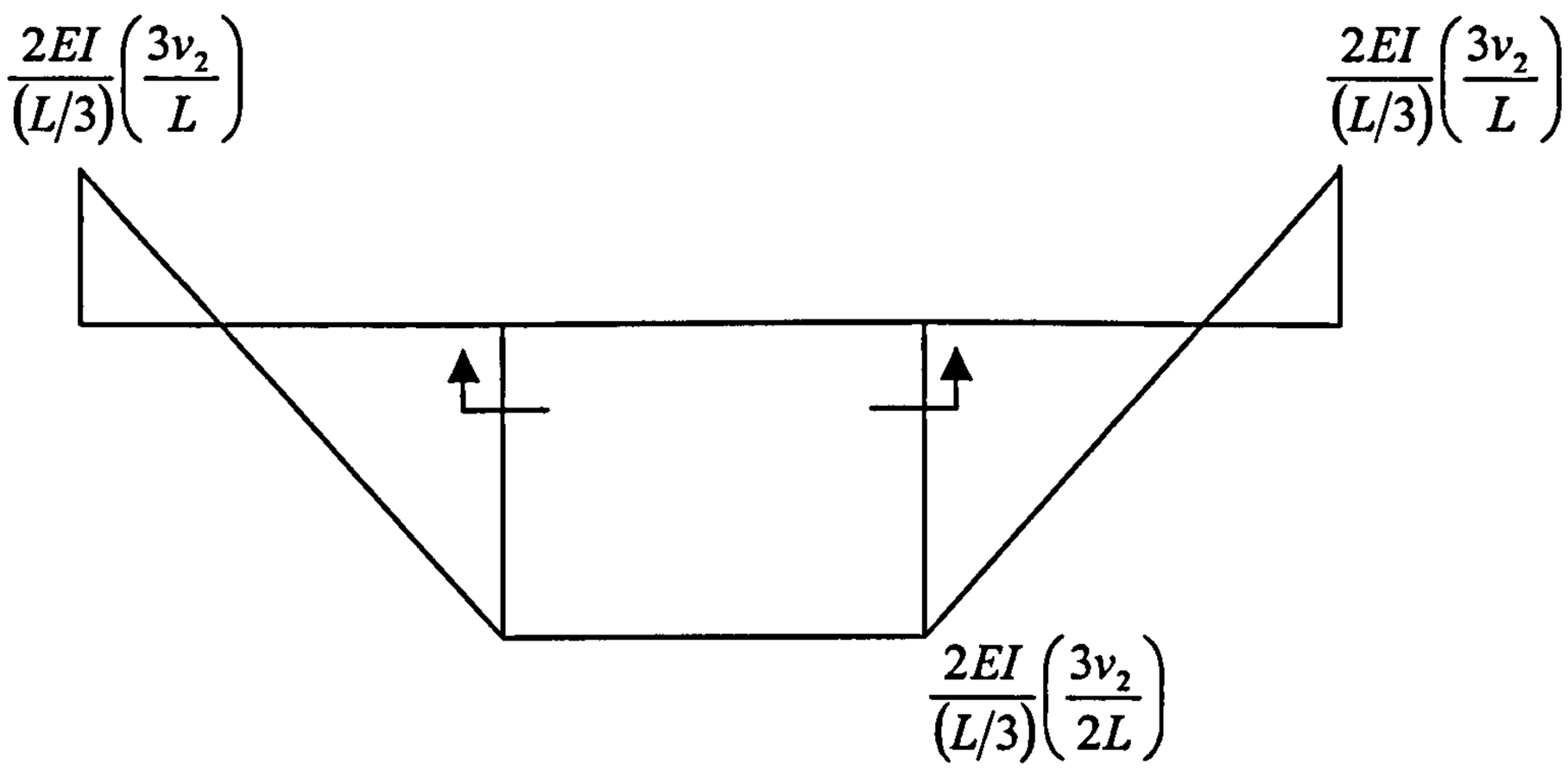

Figure 5.25 Provisional BMD for simply supported beam with distributed load using three elements

The shear at 2 is

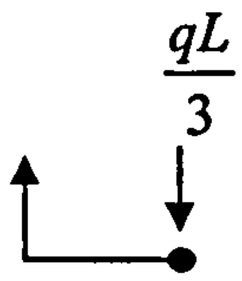

$$\left(\frac{9v_2EI}{L^2}+\frac{18v_2EI}{L^2}\right)\frac{3}{L}=\frac{qL}{3} \tag{5.68}$$

Hence

$$\left(\frac{27v_2EI}{L^2}\right)\frac{3}{L}=\frac{qL}{3} \tag{5.69}$$

By rearanging equation (5.68) the deflection v_2 will be

$$v_2=\frac{qL^4}{243EI} \tag{5.70}$$

Combining this result with the provisional bending moment diagram in Figure 5.25 results in the final BMD as illustrated in Figure 5.26.

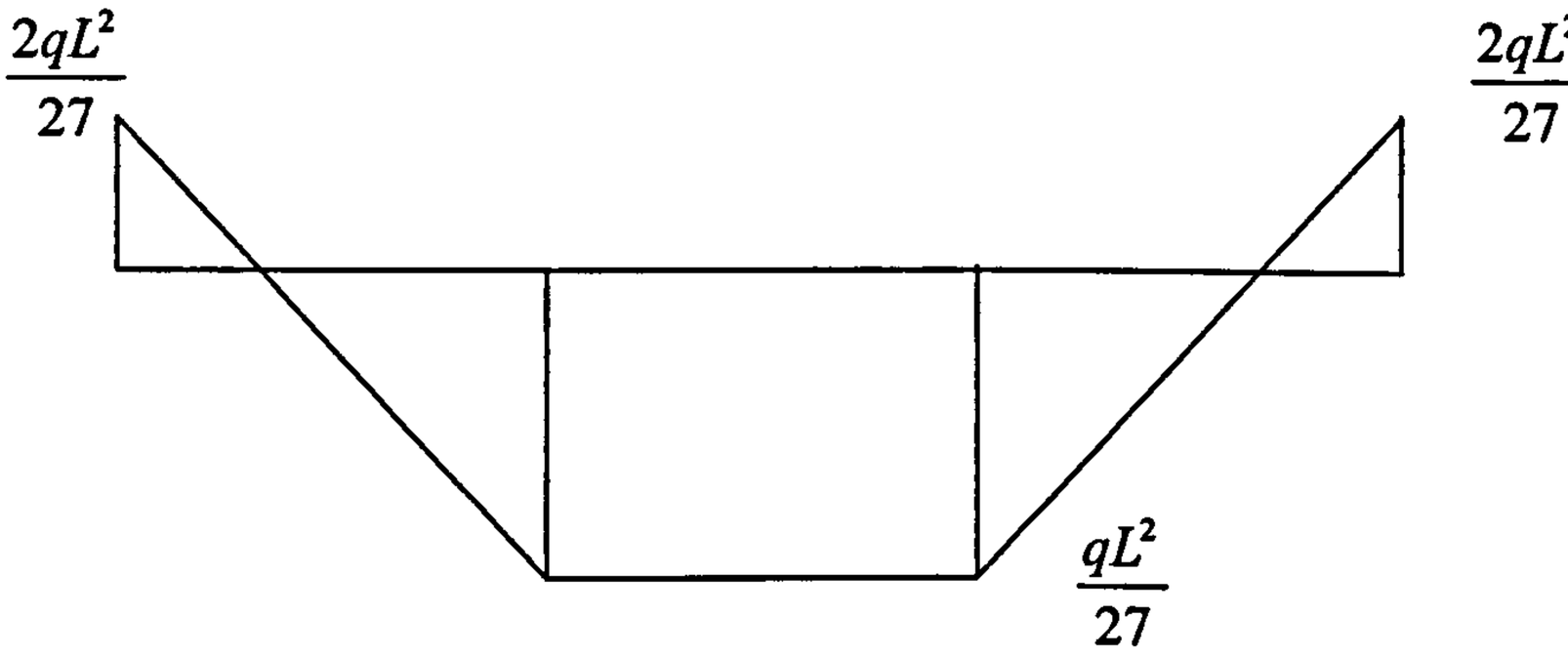

Figure 5.26 Final BMD for simply supported beam with distributed load using three elements

The error at node 1 is

$$\left|\frac{\frac{2}{27}-\frac{1}{12}}{\frac{1}{12}}\right|\times 100=11\% \tag{5.71}$$

The error at node 3 is

$$\left|\frac{\frac{2}{27}-\frac{1}{12}}{\frac{1}{12}}\right|\times 100 = 14\% \tag{5.72}$$

The error is seen to reduce significantly by just adding one element to the analysis.

Case with 4 Elements

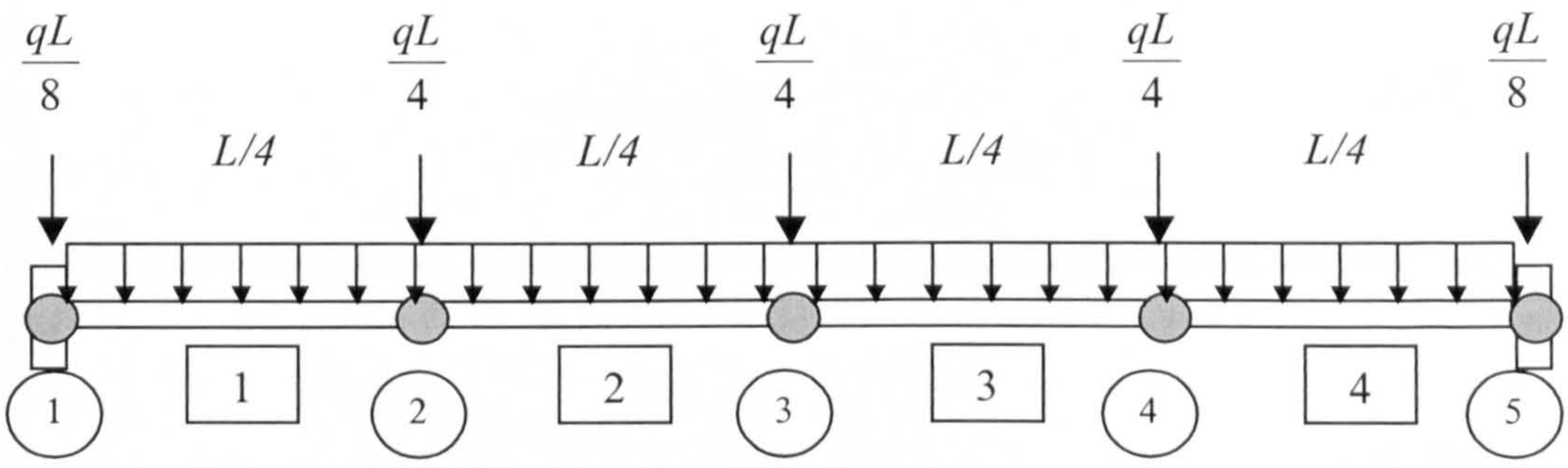

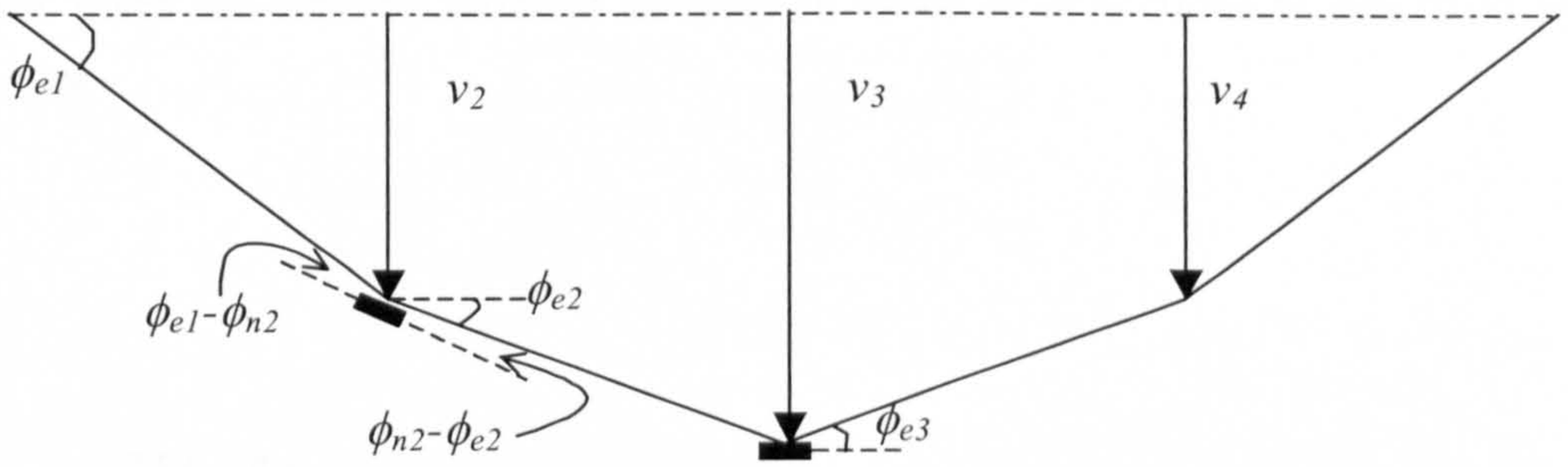

Figure 5.27 Simply supported beam with distributed load using four elements

The rotated angles are calculated as follows

$$\phi_{e1} = \frac{4v_2}{L} \tag{5.73}$$

$$\phi_{e2} = \frac{v_3 - v_2}{(L/4)} = \frac{4}{L}(v_3 - v_2) \tag{5.74}$$

As the equation is the same on both sides the rotation at node three is zero.

$$\phi_{n3} = 0 \tag{5.75}$$

By equating moments at node two

$$\frac{2EI}{L/4}\left(\frac{4v_2}{L} - \phi_{n2}\right) = \frac{2EI}{L/4}\left(\phi_{n2} - \frac{4}{L}(v_3 - v_2)\right) \tag{5.76}$$

This gives

$$\phi_{n2} = \frac{2v_3}{L} \tag{5.77}$$

Equating moments about node three proves that our assumption in equation (5.76) is correct

$$\frac{2EI}{L/4}\left(\frac{4}{L}(v_3 - v_2)\right) = \frac{2EI}{L/4}\left(\frac{4}{L}(v_3 - v_2)\right) \tag{5.78}$$

This now gives the bending moment diagram in terms of deflections as described by Figure 5.28.

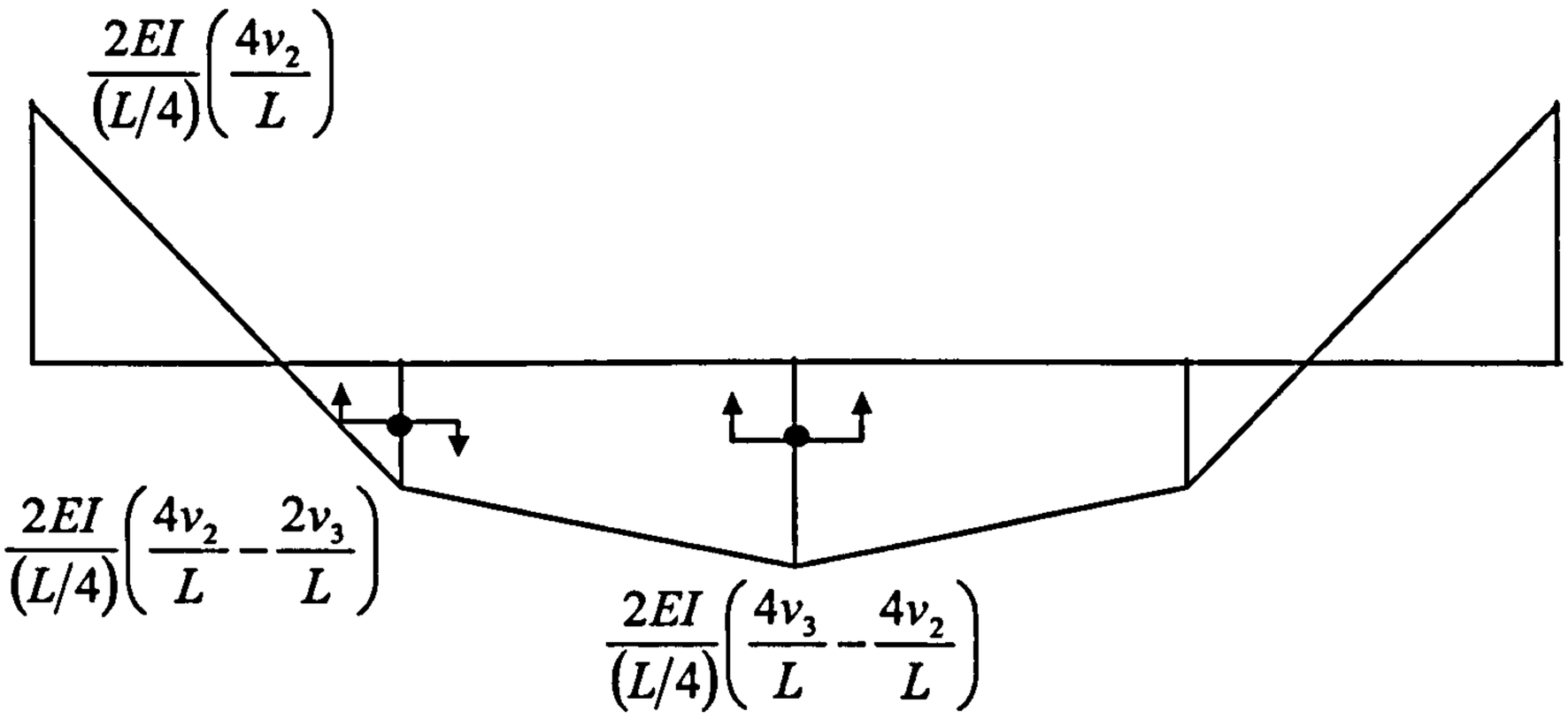

Figure 5.28 Provisional BMD in terms of deflection using four elements

The shear on the left of node 2 is found as

$$\left[\frac{32EI}{L^2}+\frac{8EI}{L^2}(4v_2-2v_3)\right]\frac{4}{L} \tag{5.79}$$

Which gives

$$\left[\frac{64EIv_2}{L^2}-\frac{16EIv_3}{L^2}\right]\frac{4}{L} \tag{5.80}$$

The shear on the right of node 2 is found as

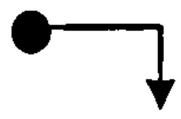

$$\left[\left(\frac{8EI}{L^2}(4v_3-4v_2)\right)-\left(\frac{8EI}{L^2}(4v_2-4v_3)\right)\right]\frac{4}{L} \tag{5.81}$$

which gives

$$\left[\frac{8EI}{L^2}(6v_3-8v_2)\right]\frac{4}{L} \tag{5.82}$$

By subtracting equation (5.80) from equation (5.82) and subsequently equating them with the load gives

$$\left[\frac{8EI}{L^2}(6v_3-8v_2)\right]\frac{4}{L} \tag{5.83}$$

This simplifies to

$$128v_2-64v_3=\frac{qL^4}{16EI} \tag{5.84}$$

Equating the shear with load at node three gives

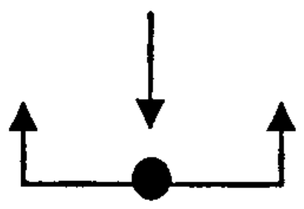

$$\left[\left(\frac{8EI}{L^2}(6v_3 - 8v_2)\right)\frac{4}{L}\right]2 = \frac{qL}{4} \tag{5.85}$$

This simplifies to

$$96v_3 - 128v_2 = \frac{qL^4}{16EI} \tag{5.86}$$

Solving equations (5.84) and (5.86) will give us v_2 and v_3.

$$v_2 = \frac{5qL^4}{2048EI} \tag{5.87}$$

$$v_3 = \frac{qL^4}{256EI} \tag{5.88}$$

Combining these results with the provisional BMD in Figure 5.28 give the final BMD as shown in Figure 5.29

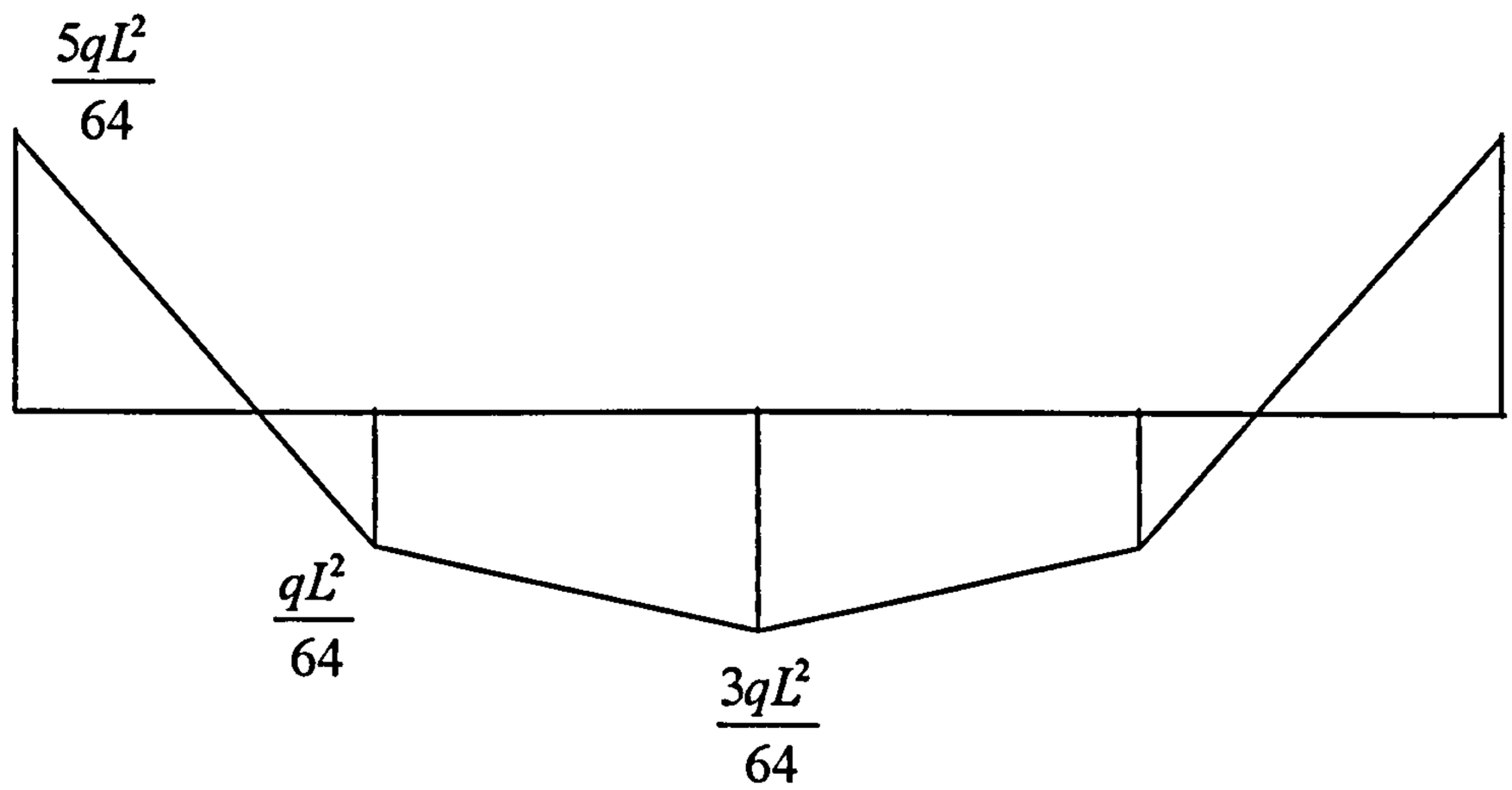

Figure 5.29 Final BMD using four elements

The end moment error is

$$\left|\frac{\frac{5}{64}-\frac{1}{12}}{\frac{1}{12}}\right|\times 100 = 6.25\% \tag{5.89}$$

The centre moment error is

$$\left|\frac{\frac{3}{64}-\frac{1}{12}}{\frac{1}{12}}\right|\times 100 = 12.5\% \tag{5.90}$$

They are again seen to converge to the exact result.

Case with 5 Elements

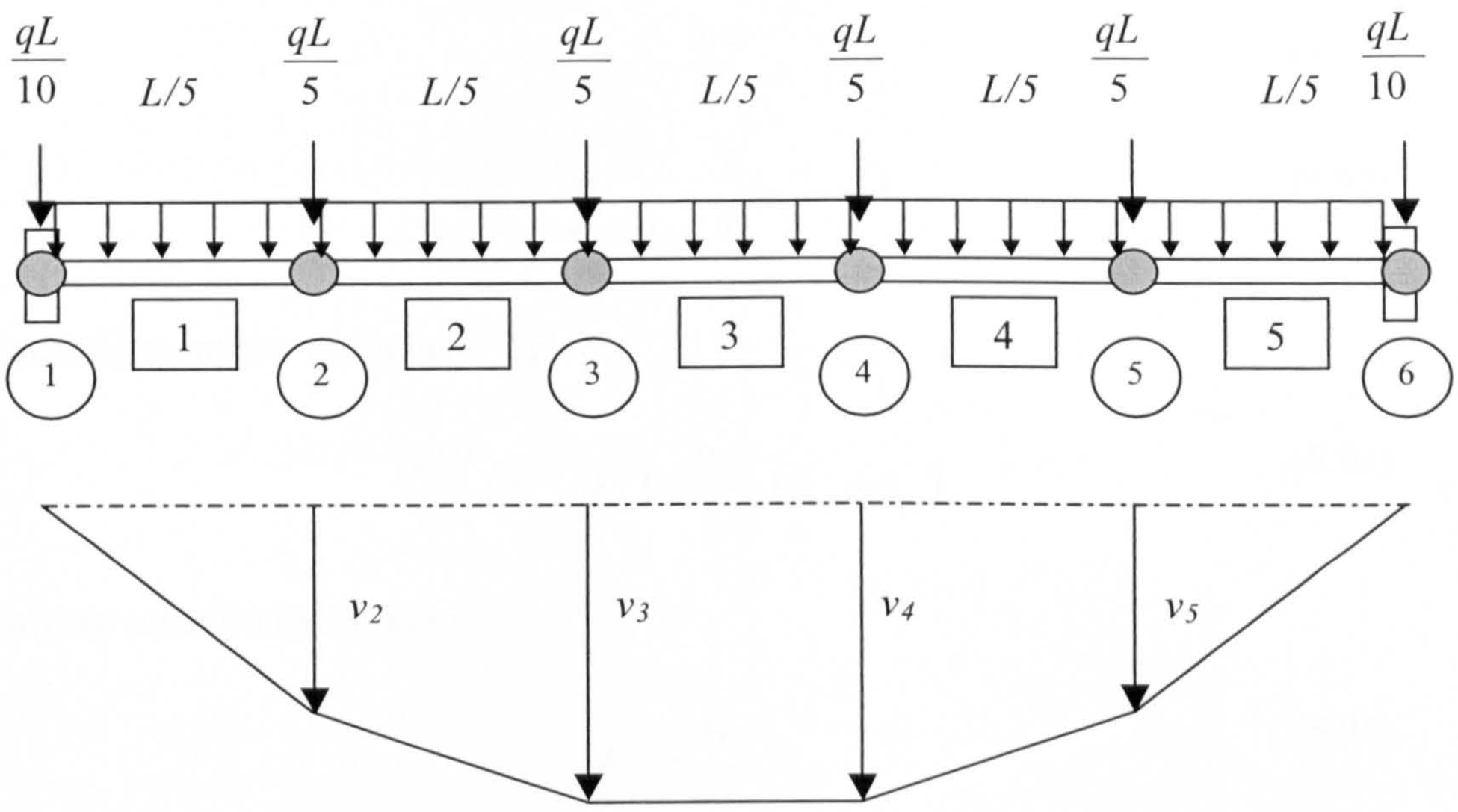

Figure 5.30 Simply supported beam with distributed load using five elements

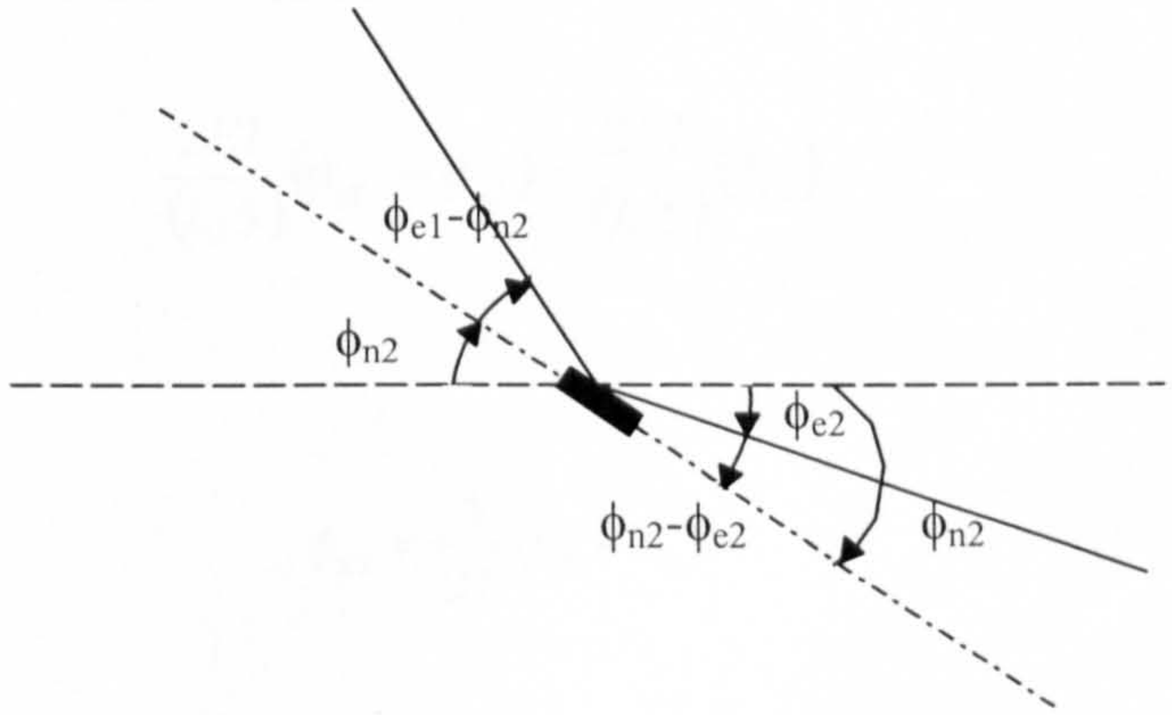

Figure 5.31 Rotation at node 2

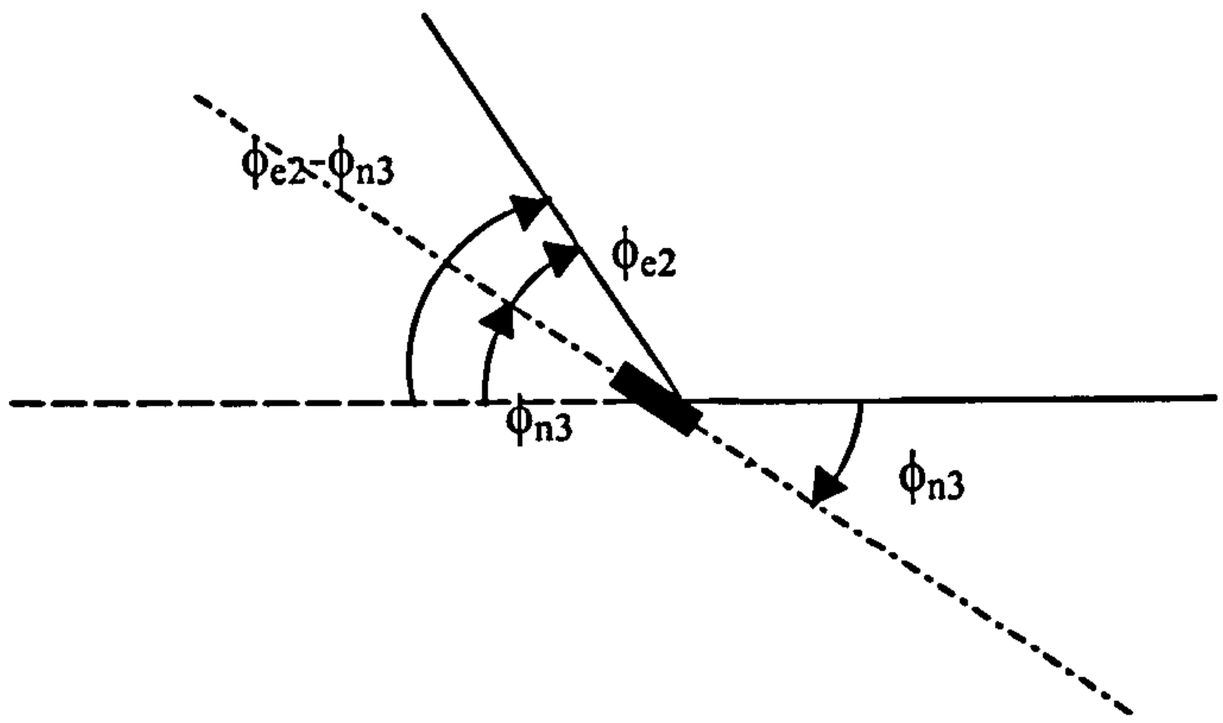

Figure 5.32 Rotation at node 3

The rotations are given in equations (5.91) and (5.92).

$$\phi_{e1} = \frac{5v_2}{L} \tag{5.91}$$

$$\phi_{e2} = \frac{v_3 - v_2}{(L/5)} = \frac{5}{L}(v_3 - v_2) \tag{5.92}$$

Equating moments about node 2 gives

$$\frac{2EI}{L/4}(\phi_{e1} - \phi_{n2}) = \frac{2EI}{L/4}(\phi_{n2} - \phi_{e2}) \tag{5.93}$$

Solving equation (5.93) gives

$$\phi_{n2} = \frac{5v_3}{2L} \tag{5.94}$$

Equating moments about node three

$$\frac{2EI}{(L/5)}(\phi_{e2} - \phi_{n3}) = \frac{2EI}{(L/5)}(\phi_{n3}) \tag{5.95}$$

Solving this gives

$$\phi_{n3} = \frac{5}{2L}(v_3 - v_2) \tag{5.96}$$

Therefore the provisional bending moment diagram in terms of deflections is as shown in Figure 5.33.

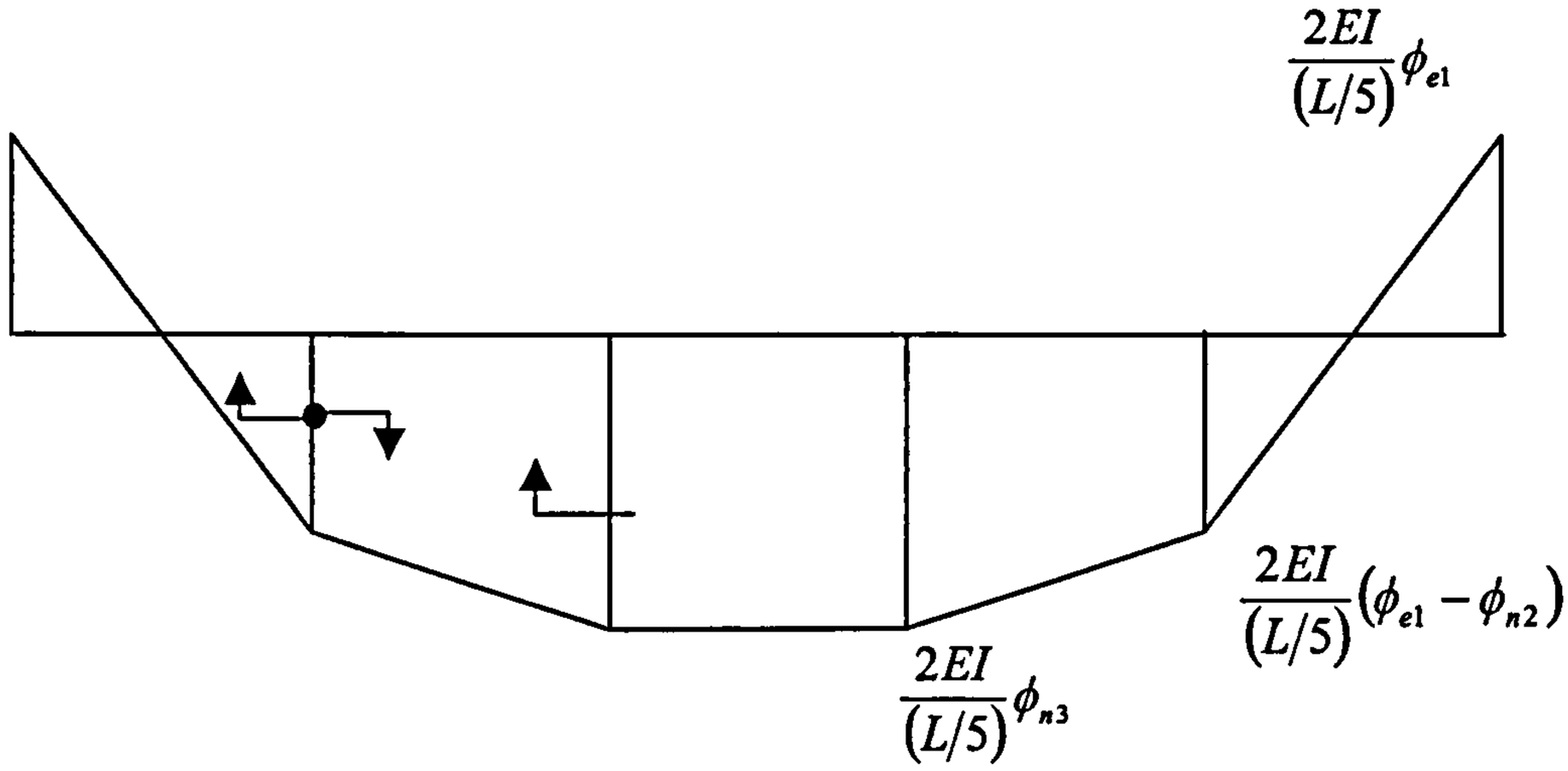

Figure 5.33 Provisional BMD in terms of the deflections

The shear on the left of node 2 is found as

$$\left[\frac{50EIv_2}{L^2}+\frac{50EI}{L^2}\left(v_2-\frac{v_3}{2}\right)\right]\frac{5}{L} \tag{5.97}$$

Which gives

$$\frac{125EI}{L^3}[4v_2-v_3] \tag{5.98}$$

The shear on the left of node 2 is found as

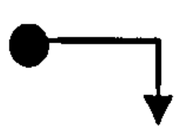

$$\left[\left(\frac{25EI}{L^2}(v_3-v_2)\right)-\left(\frac{50EI}{L^2}\left(v_2-\frac{v_3}{L}\right)\right)\right]\frac{5}{L} \tag{5.99}$$

Which gives

$$\frac{125EI}{L^3}[3v_3-3v_2] \tag{5.100}$$

By subtracting equation (5.100) from equation (5.98) and equating them with the load gives

$$\frac{125EI}{L^3}(7v_2 - 3v_3) = \frac{qL}{5} \tag{5.101}$$

This simplifies to

$$7v_2 - 3v_3 = \frac{qL^4}{625EI} \tag{5.102}$$

Equating the shear with load at node three gives

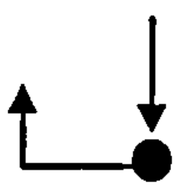

$$\frac{125EI}{L^3}(2v_3 - 3v_2) = \frac{qL}{5} \tag{5.103}$$

This simplifies to

$$2v_3 - 3v_2 = \frac{qL^4}{625EI} \tag{5.104}$$

Solving equations (5.102) and (5.104)will give us v_2 and v_3.

$$v_2 = \frac{qL^4}{625EI} \tag{5.105}$$

$$v_3 = \frac{2qL^4}{625EI} \tag{5.106}$$

Combining these results with the provisional bending moment diagram gives the final bending moment diagram as illustrated in Figure 5.34.

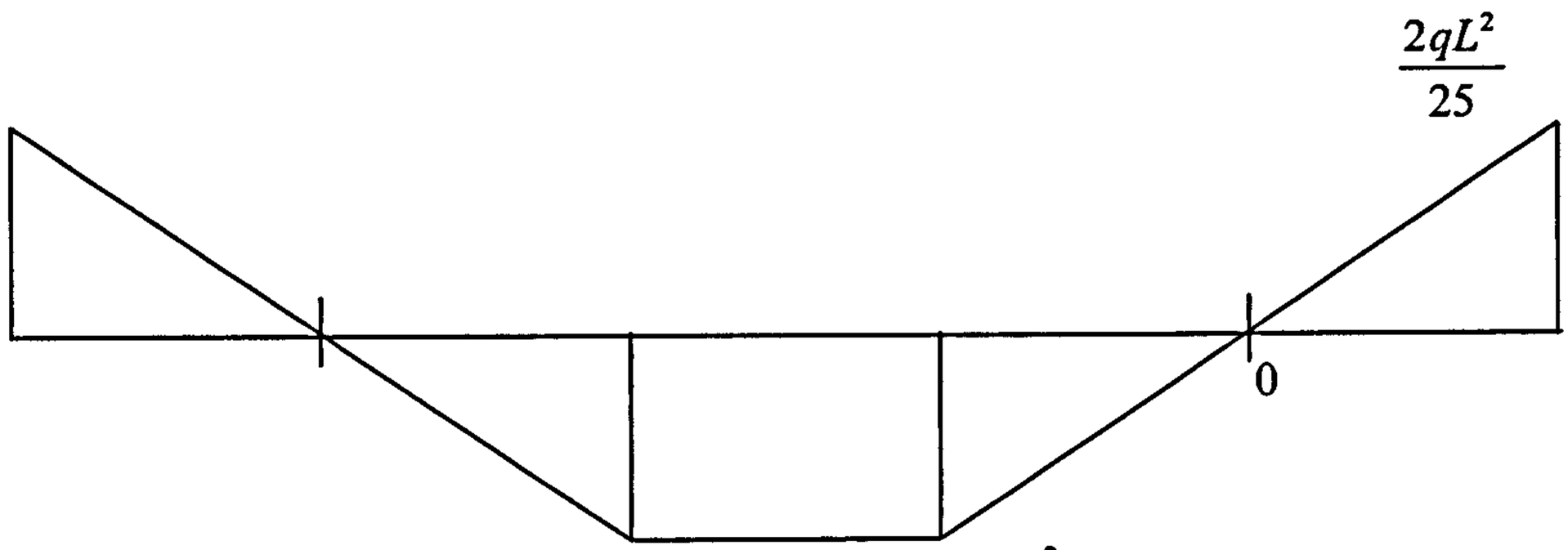

Figure 5.34 The BMD and deflected shape for a cantilever with end moment

The end moment error is

$$\left|\frac{\frac{2}{25}-\frac{1}{12}}{\frac{1}{12}}\right|\times 100 = 4\% \qquad (5.107)$$

The centre moment error is

$$\left|\frac{\frac{1}{25}-\frac{1}{12}}{\frac{1}{12}}\right|\times 100 = 4\% \qquad (5.108)$$

With the use of just five elements it is seen that the error has become insignificant.

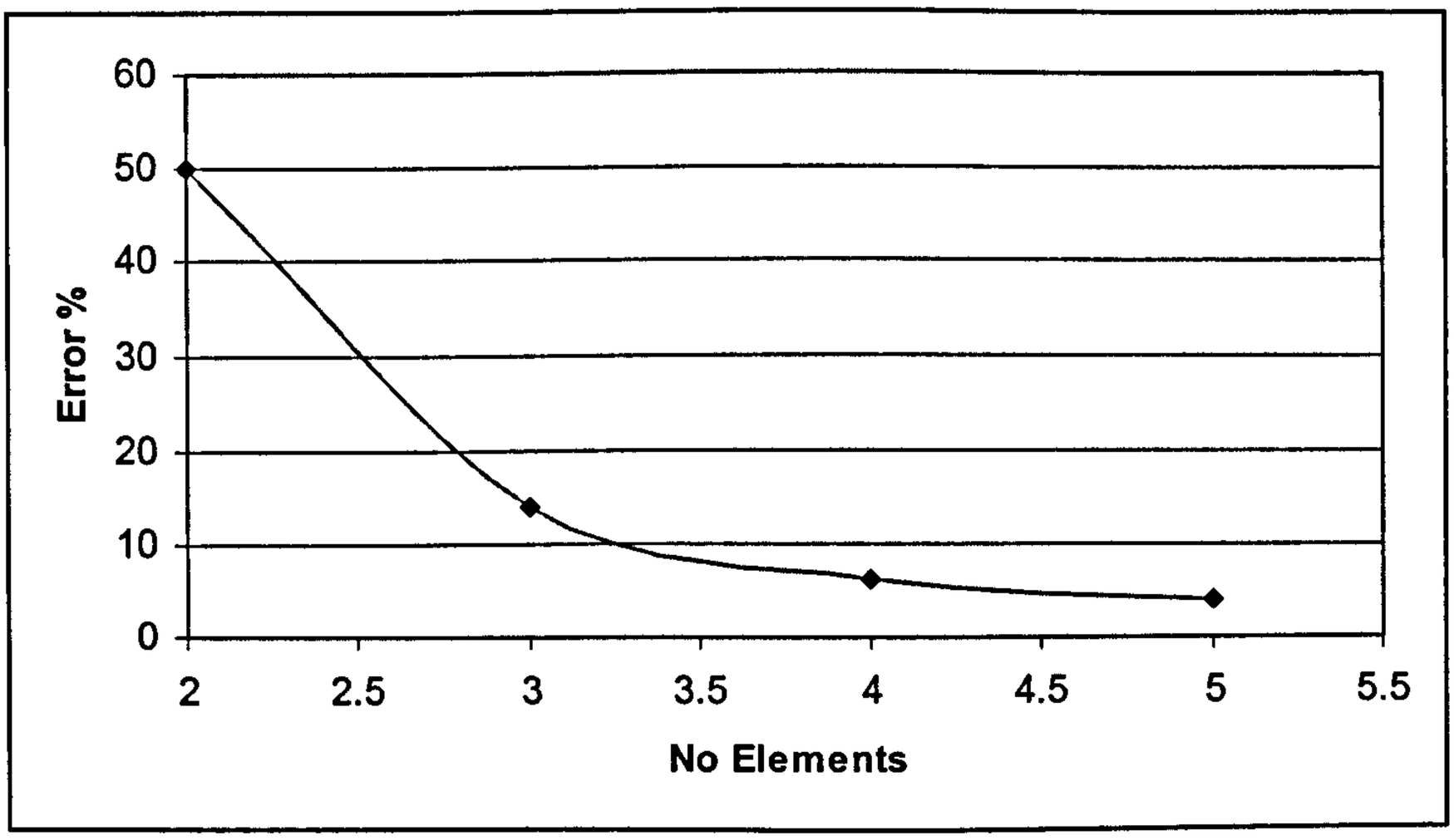

Figure 5.35 Centre Moment Error v No Elements

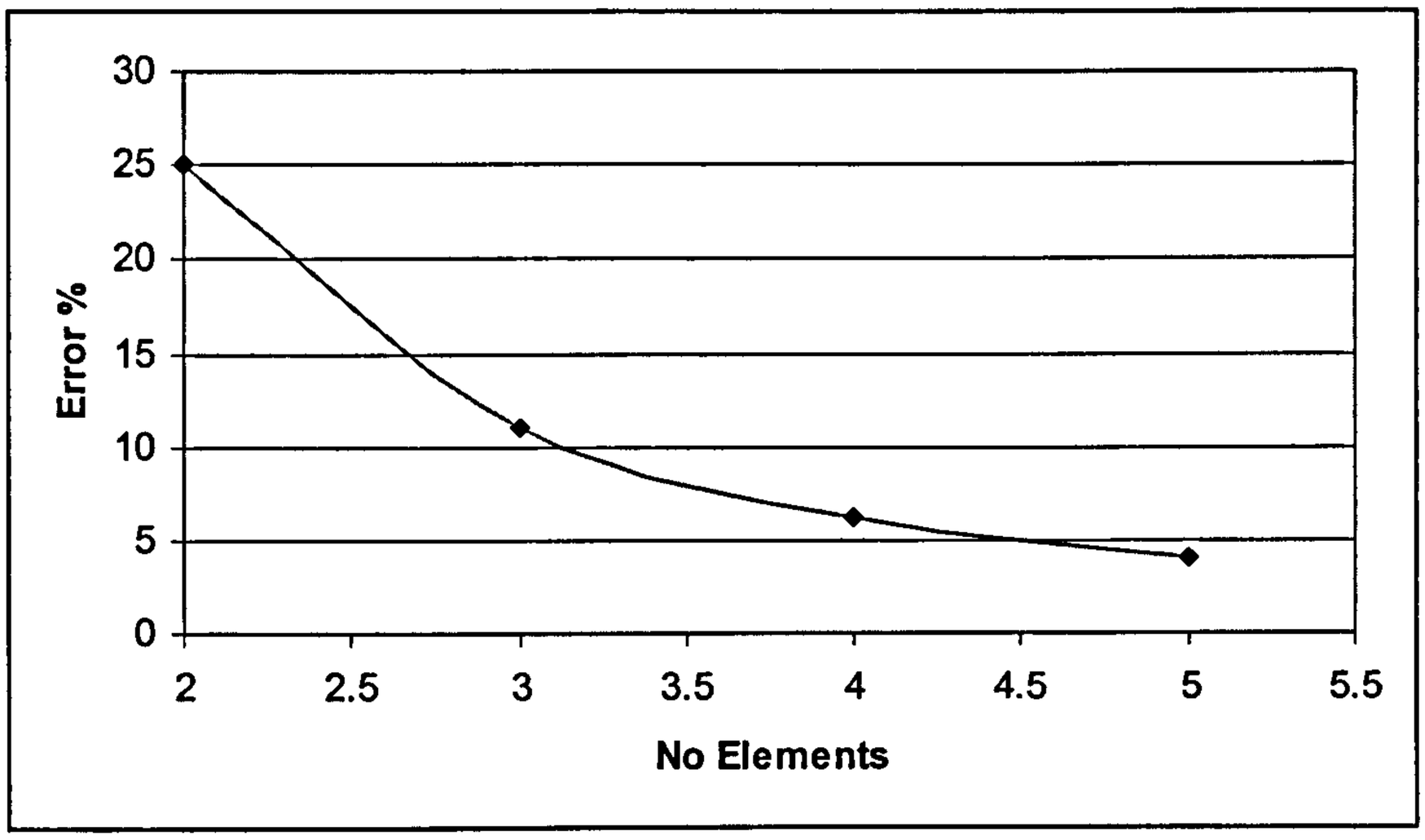

Figure 5.36 End Moment Error v No elements

Figure 5.35 and Figure 5.36 show a decrease in the difference between the exact moment and computed moment as the number of elements is increased. Thus the accuracy is seen to increase with the number of elements used.

5.3 Static condensation

Let us say that our applied load is p and that our equation of motion is given in equation (5.109)

$$\mathbf{K}\mathbf{x} + \mathbf{M}\ddot{\mathbf{x}} = \mathbf{p} \tag{5.109}$$

Equation (5.109) can be written more fully as

$$\begin{bmatrix} \mathbf{M}_{tt} & \mathbf{0} \\ \mathbf{0} & \mathbf{0} \end{bmatrix} \begin{bmatrix} \ddot{\mathbf{x}}_t \\ \ddot{\mathbf{x}}_\theta \end{bmatrix} + \begin{bmatrix} \mathbf{k}_{tt} & \mathbf{k}_{t\theta} \\ \mathbf{k}_{\theta t} & \mathbf{k}_{\theta\theta} \end{bmatrix} \begin{bmatrix} \mathbf{x}_t \\ \mathbf{x}_\theta \end{bmatrix} = \begin{bmatrix} \mathbf{p} \\ \mathbf{0} \end{bmatrix} \tag{5.110}$$

The suffix t denotes translation and rotation is referred to using suffix θ. $\mathbf{k}_{tt}$ are the forces on the translational degrees of freedom due to translation. $\mathbf{k}_{t\theta}$ are the forces on translation degrees of freedom due to rotation. Other **k** matrices are thus easily inferred. The rotational degrees of freedom in the mass matrix can be eliminated by static condensation, because the kinetic energy corresponding to the rotational degrees of freedom is insignificant compared with those corresponding to translation. This assumes that there are no loads in the rotational degrees of freedom and hence no spring forces along these degrees of freedom.

Equation (5.100) can now be written as

$$\mathbf{M}_{tt}\,\ddot{\mathbf{x}}_t + \mathbf{k}_{tt}\mathbf{x}_t + \mathbf{k}_{t\theta}\mathbf{x}_{t\theta} = \mathbf{p} \tag{5.111}$$

And

$$\mathbf{k}_{\theta t}\,\mathbf{x}_t + \mathbf{k}_{\theta\theta}\,\mathbf{x}_\theta = \mathbf{0} \tag{5.112}$$

Therefore

$$\mathbf{M}_{tt}\,\ddot{\mathbf{x}}_t + \mathbf{k}^*\mathbf{x}_t = \mathbf{p} \tag{5.113}$$

k* is the condensed stiffness matrix, given by

$$\mathbf{k}^* = \mathbf{k}_{tt} - \mathbf{k}_{t\theta}\,\mathbf{k}_{\theta\theta}{}^{-1}\mathbf{k}_{\theta t} \tag{5.114}$$

The stiffness matrix for a general element shown in Figure 5.37 will now be derived.

Figure 5.37 Simple general element

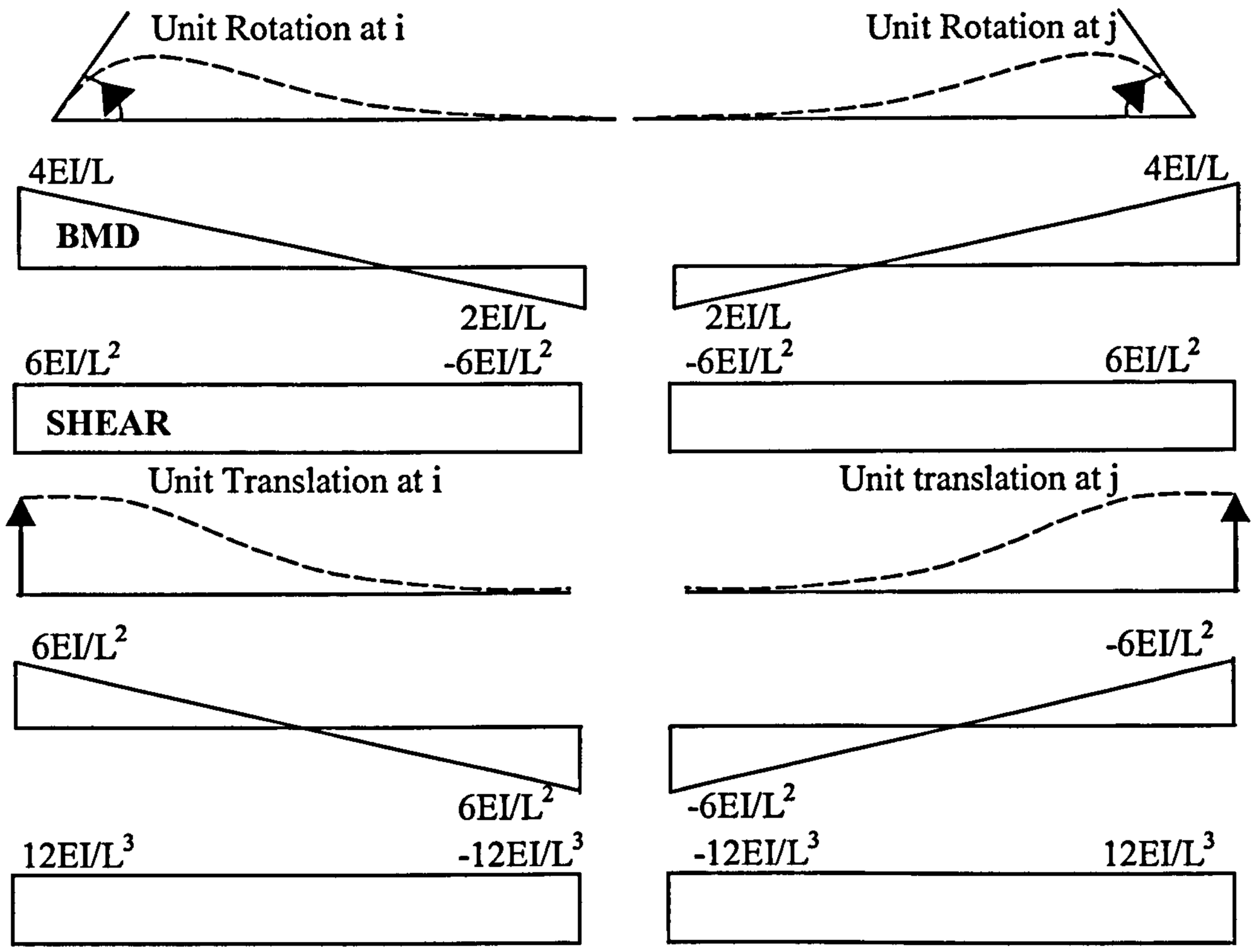

Figure 5.38 Bending moment and shear diagrams due to unit translation and rotation at each node

The force displacement relationship is now given in equation (5.115).

$$\begin{bmatrix} F_1 \\ F_2 \\ M_1 \\ M_2 \end{bmatrix} = \begin{bmatrix} 12EI/L^3 & -12EI/L^3 & 6EI/L^2 & -6EI/L^2 \\ -12EI/L^3 & 12EI/L^3 & -6EI/L^2 & 6EI/L^2 \\ 6EI/L^2 & -6EI/L^2 & 4EI/L & 2EI/L \\ 6EI/L^2 & -6EI/L^2 & 2EI/L & 4EI/L \end{bmatrix} \begin{bmatrix} X_1 \\ X_2 \\ \phi_1 \\ \phi 2 \end{bmatrix} \quad (5.115)$$

Referring to Figure 5.37 the force displacement relationship for the adopted element will now be derived.

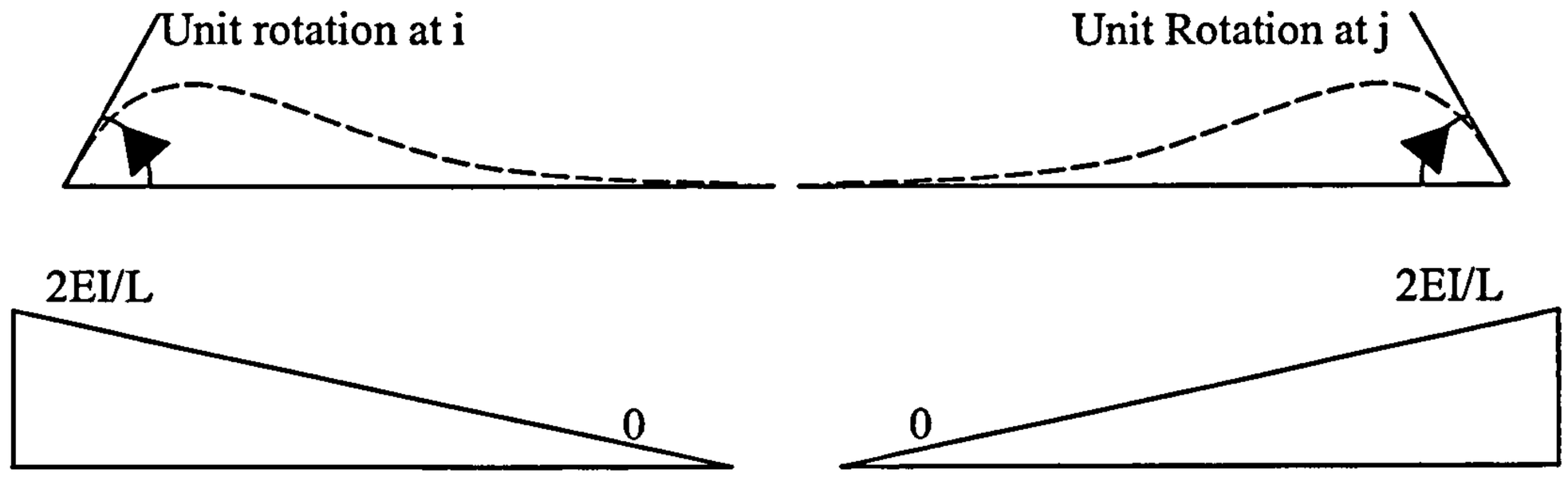

Figure 5.39 Bending moment and shear diagrams due to unit translation and rotation at each node

The force displacement relationship for this element is

$$\begin{bmatrix} F_1 \\ F_2 \\ M_1 \\ M_2 \end{bmatrix} = \begin{bmatrix} 4EI/L^3 & -4EI/L^3 & 2EI/L^2 & -2EI/L^2 \\ -4EI/L^3 & 4EI/L^3 & 2EI/L^2 & -2EI/L^2 \\ 2EI/L^2 & -2EI/L^2 & 2EI/L & 0 \\ 2EI/L^2 & -2EI/L^2 & 0 & 2EI/L \end{bmatrix} \begin{bmatrix} X_1 \\ X_2 \\ \phi_1 \\ \phi_2 \end{bmatrix} \quad (5.116)$$

It can be seen from equation (5.115) that the $\mathbf{k}_{\theta\theta}$ part of the global stiffness matrix is completely full. Inverting this to obtain the condensed stiffness will require complex coding and take up much CPU time.

As shown in Figure 5.38 the element used will assume zero moment at the opposite end to the applied moment. Equal moments at each end will be assumed for applied translation. This results in the $\mathbf{k}_{\theta\theta}$ matrix being diagonal. Hence it is much simpler to invert. Using the lumped mass matrix also contributes to saving on computation.

Taking the five element beam which has already been dealt with earlier the condensed stiffness matrix can be derived as follows.

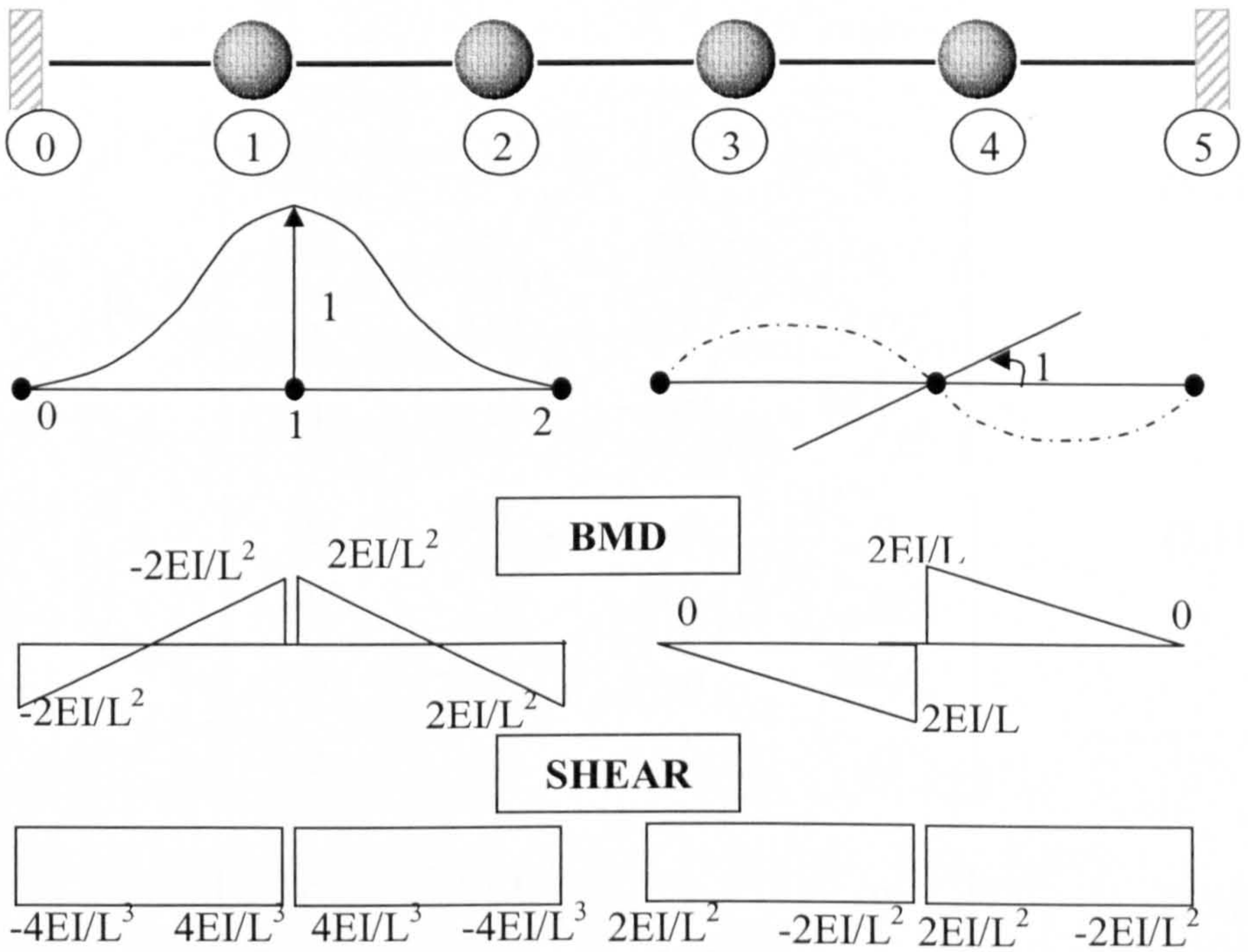

Figure 5.40 Unit translation and rotation at node 1 of the five element beam

Figure 5.40 shows the unit translation and rotation as applied to node one. The unit translations and rotations as applied to the other nodes will result in similar bending moment and shear diagrams.

For the example under consideration the global stiffness matrix is described by equation (5.117).

$$\begin{bmatrix} F_1 \\ F_2 \\ F_3 \\ F_4 \\ M_1 \\ M_2 \\ M_3 \\ M_4 \end{bmatrix} = \begin{bmatrix} \mathbf{k}_{tt} & \mathbf{k}_{t\theta} \\ \mathbf{k}_{\theta t} & \mathbf{k}_{\theta\theta} \end{bmatrix} \begin{bmatrix} X_1 \\ X_2 \\ X_3 \\ X_4 \\ \phi_1 \\ \phi_2 \\ \phi_3 \\ \phi_4 \end{bmatrix} \tag{5.117}$$

where

$$[\mathbf{k}_{tt}] = \begin{bmatrix} 8EI/L^3 & -4EI/L^3 & 0 & 0 \\ -4EI/L^3 & 8EI/L^3 & -4EI/L^3 & 0 \\ 0 & -4EI/L^3 & 8EI/L^3 & -4EI/L^3 \\ 0 & 0 & -4EI/L^3 & 8EI/L^3 \end{bmatrix} \tag{5.118}$$

$$[\mathbf{k}_{t\theta}] = \begin{bmatrix} 0 & 2EI/L^2 & 0 & 0 \\ -2EI/L^2 & 0 & 2EI/L^2 & 0 \\ 0 & -2EI/L^2 & 0 & 2EI/L^2 \\ 0 & 0 & -2EI/L^2 & 0 \end{bmatrix} \tag{5.119}$$

$$[\mathbf{k}_{\theta t}] = \begin{bmatrix} 0 & -2EI/L^2 & 0 & 0 \\ 2EI/L^2 & 0 & -2EI/L^2 & 0 \\ 0 & 2EI/L^2 & 0 & -2EI/L^2 \\ 0 & 0 & 2EI/L^2 & 0 \end{bmatrix} \tag{5.120}$$

$$[\mathbf{k}_{\theta\theta}] = \begin{bmatrix} 4EI/L & 0 & 0 & 0 \\ 0 & 4EI/L & 0 & 0 \\ 0 & 0 & 4EI/L & 0 \\ 0 & 0 & 0 & 4EI/L \end{bmatrix} \tag{5.121}$$

Substituting for equations (5.118) to (5.120) in equation (5.114) will give the condensed stiffness matrix as in equation (5.122).

$$[\mathbf{k}^*] = \frac{EI}{L^3}\begin{bmatrix} 7 & -4 & 1 & 0 \\ -4 & 6 & -4 & 1 \\ 1 & -4 & 6 & 0 \\ 0 & 1 & -4 & 7 \end{bmatrix} \qquad (5.122)$$

This example has shown the relative ease with which the condensed stiffness matrix is obtained. Thus the main advantage of this new simple element is the fact that static condensation is easily performed to eliminate the rotational degrees of freedom with the need for for complex matrix inversion. This reduces the overall CPU time without any appreciable loss in accuracy providing a suitable number of elements are used.

5.4 Forces and moments along the element

The element presented is intended for use in the numerical simulation of structures and structural elements subjected to hazardous loading. Such hazardous loading will induce stresses and forces along the length of the element. They are calculated as follows.

Vector $\mathbf{r_i}$ represents an element in it's initial position, with coordinates α, β, γ in the global axis. The local axis is shown as e1, e2 and e3.

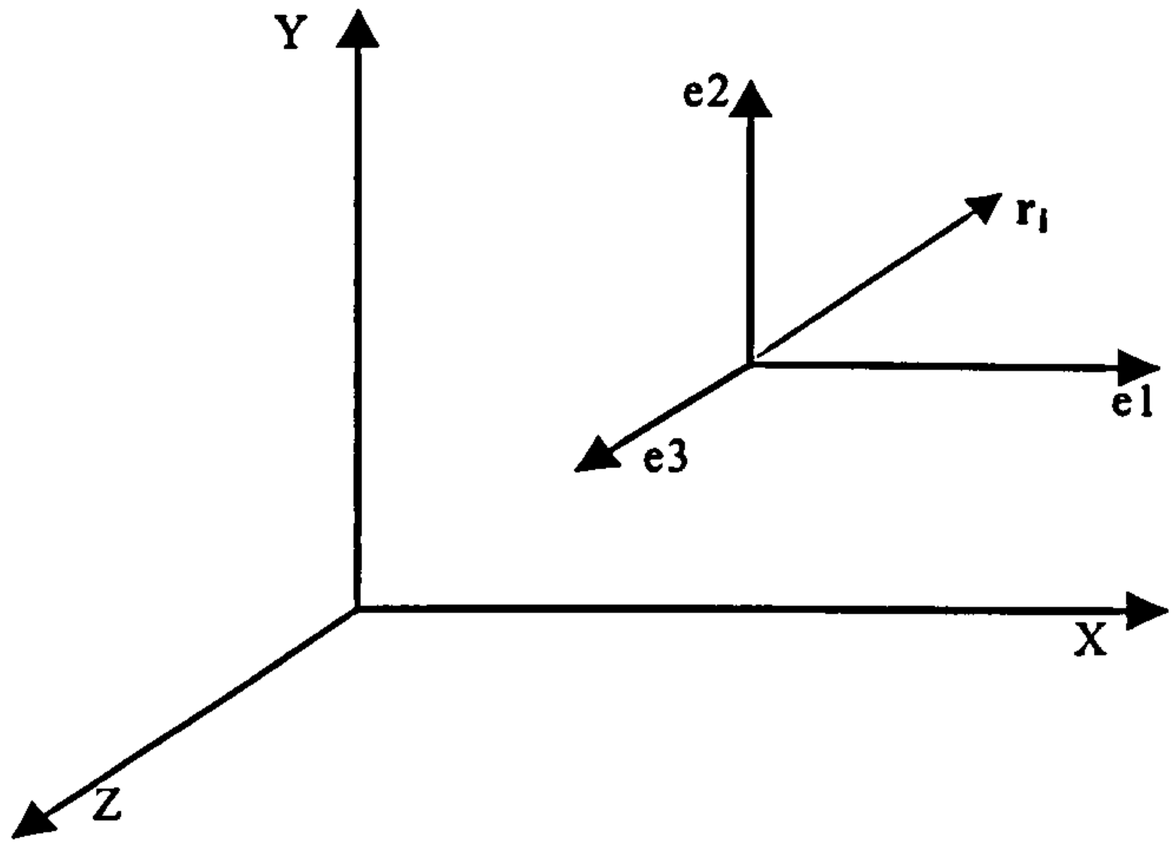

Figure 5.41 Initial Vector in the Local and Global Axis

Initially the projection of $\mathbf{r_i}$ on to the local axis is the same as it's projection on to the global axis. Therefore initially

$$\mathbf{r}_i = \alpha \mathbf{e}_1 + \beta \mathbf{e}_2 + \gamma \mathbf{e}_3 = \alpha \mathbf{X} + \beta \mathbf{Y} + \gamma \mathbf{Z} \tag{5.123}$$

Once **r** has rotated the coordinates will change only in the global axis, provided that there is no relative rotation between the node and the element.

The current position of vector $\mathbf{r}_c$ can be found from

$$[\mathbf{r}_c] = \begin{bmatrix} e_{x1} & e_{x2} & e_{x3} \\ e_{y1} & e_{y2} & e_{y3} \\ e_{z1} & e_{z2} & e_{z3} \end{bmatrix} \begin{bmatrix} \alpha \\ \beta \\ \gamma \end{bmatrix} = \begin{bmatrix} e_{x1} & e_{x2} & e_{x3} \\ e_{y1} & e_{y2} & e_{y3} \\ e_{z1} & e_{z2} & e_{z3} \end{bmatrix} \begin{bmatrix} r_x \\ r_y \\ r_z \end{bmatrix}_i \tag{5.124}$$

The **e** matrix is known as the rotation matrix where $\mathbf{e}_{x1}$ is the projection of e1 on to the x axis, $\mathbf{e}_{x2}$ is the projection of e1 on to the y axis and $\mathbf{e}_{x3}$ is the projection of e1 on to the z axis. Thus the others are similarly inferred.

Therefore since the initial projection on to the local axis is the same as to the global axis the initial rotation matrix [**R**] for the element is

$$\begin{bmatrix} 1 & 0 & 0 \\ 0 & 1 & 0 \\ 0 & 0 & 1 \end{bmatrix} \tag{5.125}$$

If we now assume that along with stretching of the element there is relative rotation of the node, then the calculation to obtain $\mathbf{r}_c$ is as follows

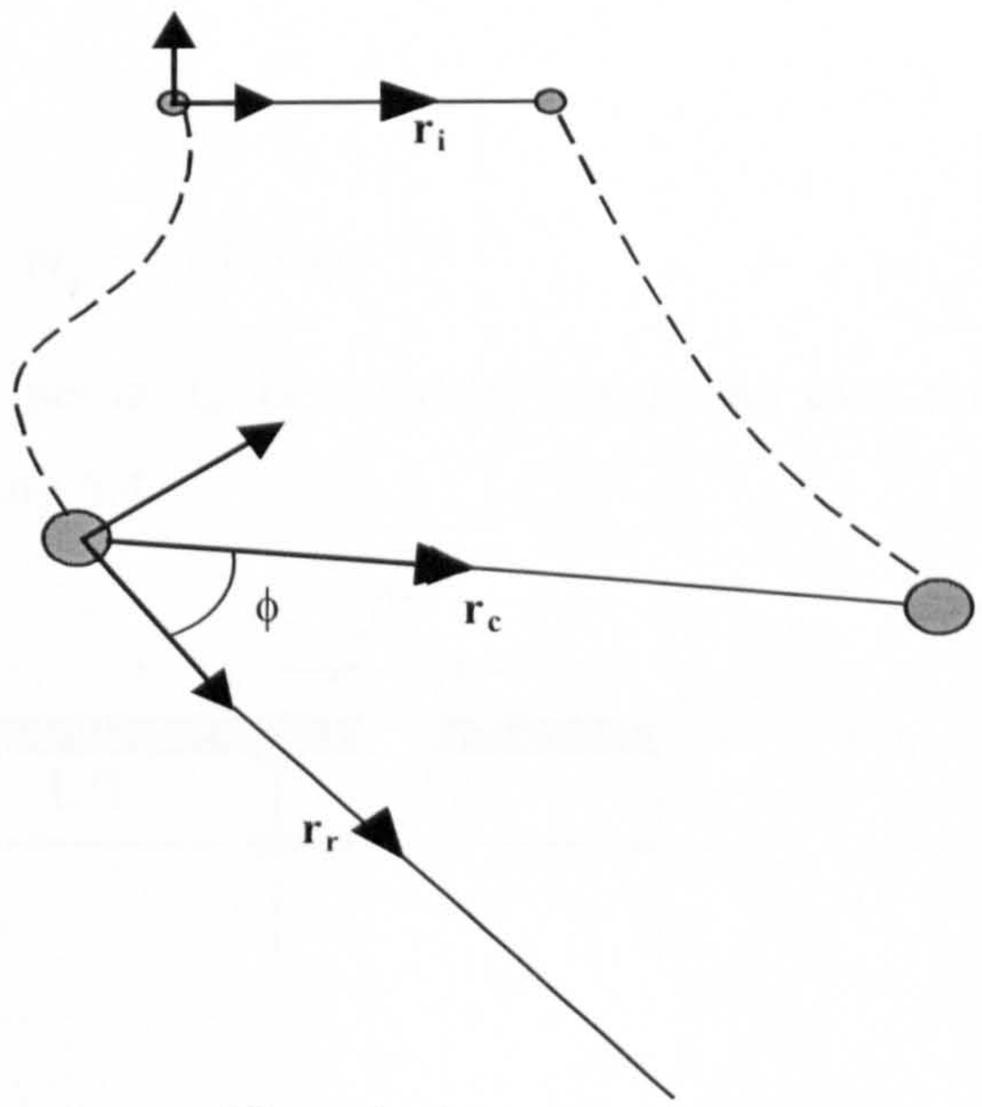

Figure 5.42 Current Position of Stretched Element with Relative Nodal Rotation

Figure 5.42 shows that the element has moved to it's current position, $\mathbf{r_c}$ but the node has also rotated to vector $\mathbf{r_r}$. This can be substantiated from the coordinates of the nodes.

$$[\mathbf{r_r}] = [\mathbf{R}][\mathbf{r_i}] \tag{5.126}$$

where **[R]** is the rotation matrix.

The vector $\mathbf{r_r}$ is used to calculate $\mathbf{r_c}$ using vector product. The cross product of $\mathbf{r_r}$ and $\mathbf{r_c}$ will produce a vector acting out of the plane of paper. If this is taken as a unit vector, then the sin of the angle between $\mathbf{r_r}$ and $\mathbf{r_c}$ is derived as follows

$$\sin\phi = \frac{\mathbf{r_r} \times \mathbf{r_c}}{(r_r)(r_c)} \tag{5.127}$$

As the angle is considered small the sin ϕ can be taken as ϕ, thus giving

$$\phi = \frac{\mathbf{r_r} \times \mathbf{r_c}}{(r_r)(r_c)} \tag{5.128}$$

After obtaining the $\mathbf{r_i}$, $\mathbf{r_r}$ and $\mathbf{r_c}$ the nodal mass, m_n for both nodes are subsequently calculated from

$$m_n = r_i \times 0.5A\rho \tag{5.129}$$

The second moment of inertia, I_n, is found by integrating over the length of half the element as shown in Figure 5.43

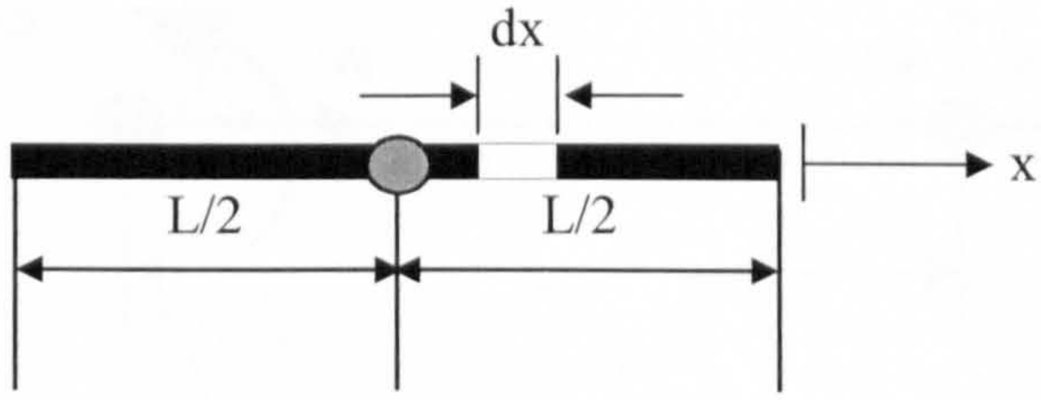

Figure 5.43 Element Rotational Velocity

$$I_n = \int_0^{L/2} x^2 \rho A \quad dx = \left[\rho A \frac{x^3}{3} \right] = \frac{\rho A L^2}{24} \tag{5.130}$$

In this case the initial length of the element is r_i thus the equation (5.130) becomes

$$I_n = \frac{A \rho r_i^3}{24} \tag{5.131}$$

The next step is to calculate the relative velocity of the nodes along the element, v_a, and then to calculate the damped axial force, f_a.

$$v_a = (v_{rx} \times r_{cx}) + (v_{ry} \times r_{cy}) + (v_{rz} \times r_{cz}) \tag{5.132}$$

where v_{rx} is the relative velocity of the two nodes of the element and r_{cx} is the component of the $\mathbf{r_c}$ vector projected on to the x axis. The other notations of equation (5.133) are similarly inferred.

The axial force is given by

$$f_a = EA \times \left(\frac{\mathbf{r_c} - \mathbf{r_i}}{r_i} \right) \tag{5.133}$$

Cross product of the $\mathbf{r_c}$ and $\mathbf{r_r}$ vectors will give the rotation ϕ in the global system.

$$\boldsymbol{\varphi} = \mathbf{r_c} \times \mathbf{r_i} \tag{5.134}$$

The rotation vector is then found in the local element coordinate system to give ϕ_L.

The local element rotations are then obtained

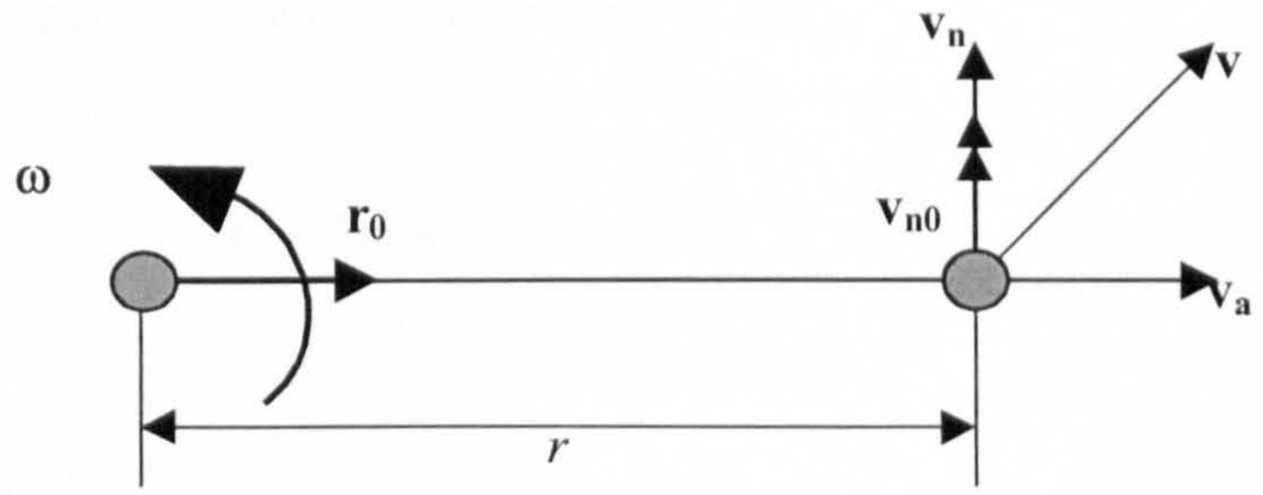

Figure 5.44 Element Rotational Velocity

The cross product of the unit vectors $\mathbf{v_{n0}}$ and $\mathbf{r_0}$ will give the direction of the element rotational velocity. The magnitude is found by multiplying by the ratio v_n/r

$$\boldsymbol{\omega} = (\mathbf{r_o} \times \mathbf{v_{no}})(\frac{v_n}{r}) \tag{5.135}$$

This therefore gives

$$\boldsymbol{\omega} = (\mathbf{r_o} \times \mathbf{v_n})(\frac{1}{r}) \tag{5.136}$$

The horizontal component of velocity, v_a has no influence on the rotational element velocity and hence is not included.

The resultant rotational velocity of the nodes, $\boldsymbol{\omega_{res}}$ is then found

$$\boldsymbol{\omega}_{res} = \boldsymbol{\omega}_1 - \boldsymbol{\omega}_0 \tag{5.137}$$

The local moments, M, at any point along the element, in each of the axis direction is calculated using

$$M = \frac{2\phi EI}{r_i} \tag{5.138}$$

If node one is assumed to rotate by 1 then the stiffness of the node is

$$k_i = \frac{2EI}{r_i} \tag{5.139}$$

The moment due to the rotational velocity is damped by multiplying it by equation (5.140). The final equation is shown in equation (5.145).

$$C = 2m\omega \tag{5.140}$$

Since

$$\omega = \sqrt{\frac{k}{m}} \tag{5.141}$$

The damping coefficient C is given by

$$C = 2m\sqrt{\frac{k}{m}} \tag{5.142}$$

Taking the equivalent mass to be given by (5.130) and combing it with equation (5.139) gives

$$C = \sqrt{\frac{A\rho EIr_i^2}{3}} \tag{5.143}$$

A parameter s is introduced to the equation. At $\xi = 0$ the damping is non-existent and at $\xi = 1$ the damping is critical.

$$C = \xi\sqrt{\frac{A\rho EIr_i^2}{3}} \tag{5.144}$$

The local moments are thus calculated

$$M = C\omega r_i \tag{5.145}$$

These local moments are then found in the global system, $\mathbf{M_G}$. Shear is found from

$$\mathbf{s} = \mathbf{M_G} \cdot \frac{\mathbf{1}}{\mathbf{r_c}} \tag{5.146}$$

This procedure is first applied to node 0 and then to node 1. Then nodal forces and moments are then updated with the calculated moments, shear and axial forces. A generalised flow chart is shown in Figure 5.

5.4.1 Damping of the stretching movement of the element

Damping is introduced when the element is stretched. The element is assumed to be equivalent to a node attached to a spring as shown in Figure 5.45.

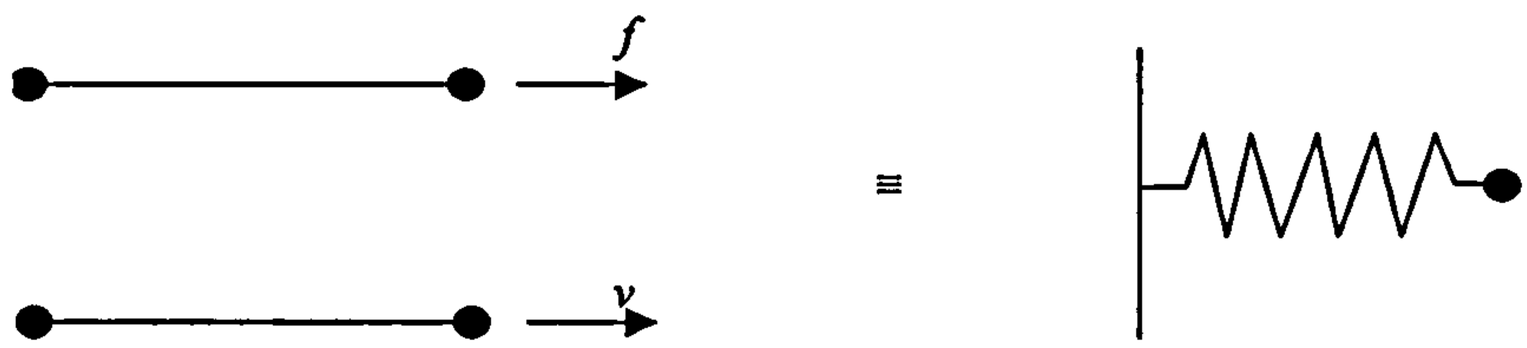

Figure 5.45 Equivalent Spring and Node

The force f is found from

$$f = \frac{\Delta EA}{L} \tag{5.147}$$

The element forces and moments can now be calculated. A flow chart showing the algorithmic procedure has been carefully devised and is shown in Figure 5.46.

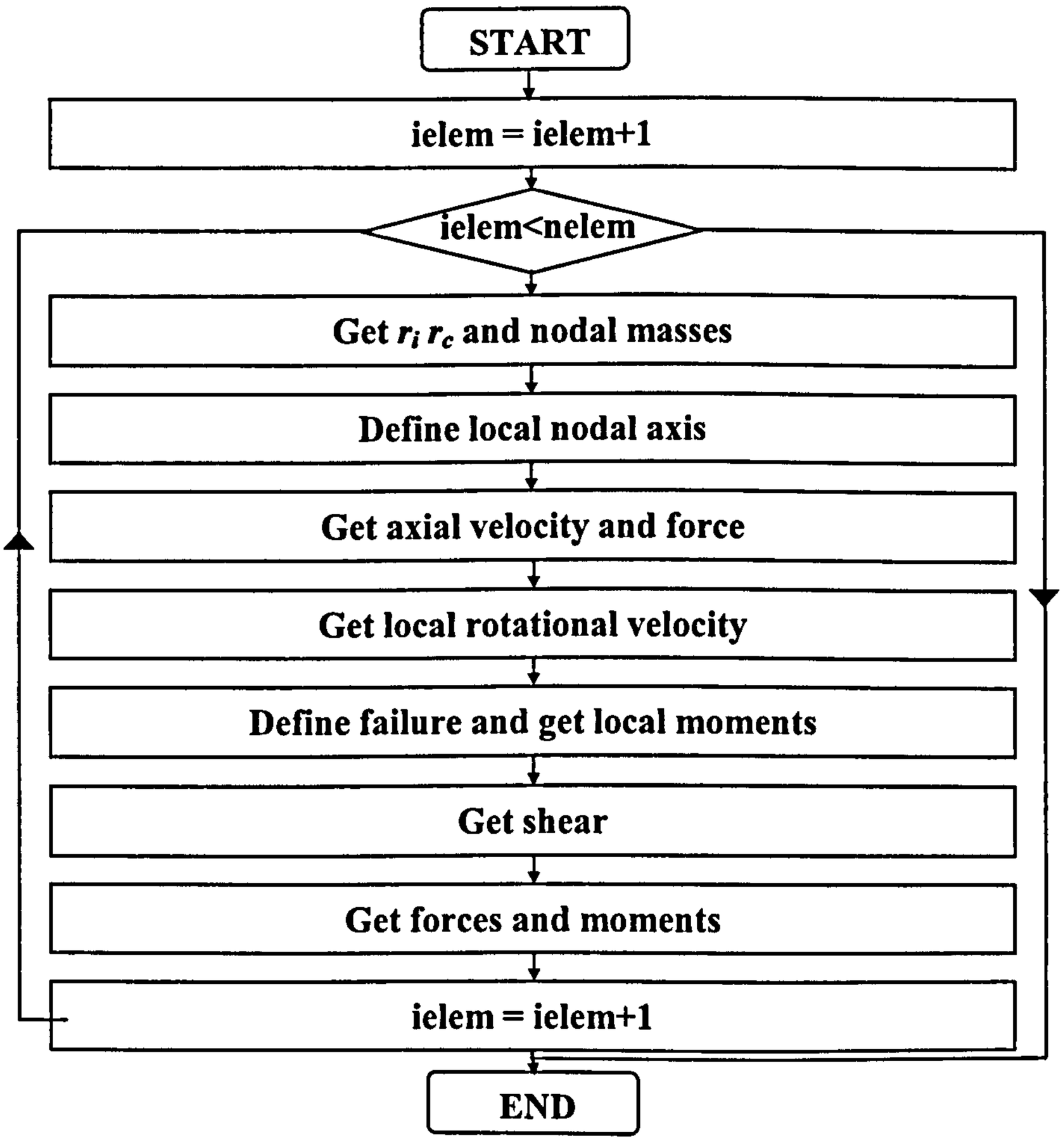

Figure 5.46 Generalised Flow Chart to Calculate Element Forces and Moments

The applied nodal velocities can be split as shown if Figure 5.47. The bending component does not contribute to the stretching of the element and therefore we will ignore it for now. The velocity of stretch, v_s, is found from the dot product of the resultant velocity with $\mathbf{r_c}$.

$$\mathbf{v_s} = (\mathbf{v_1} - \mathbf{v_2}).\mathbf{r_c} \tag{5.148}$$

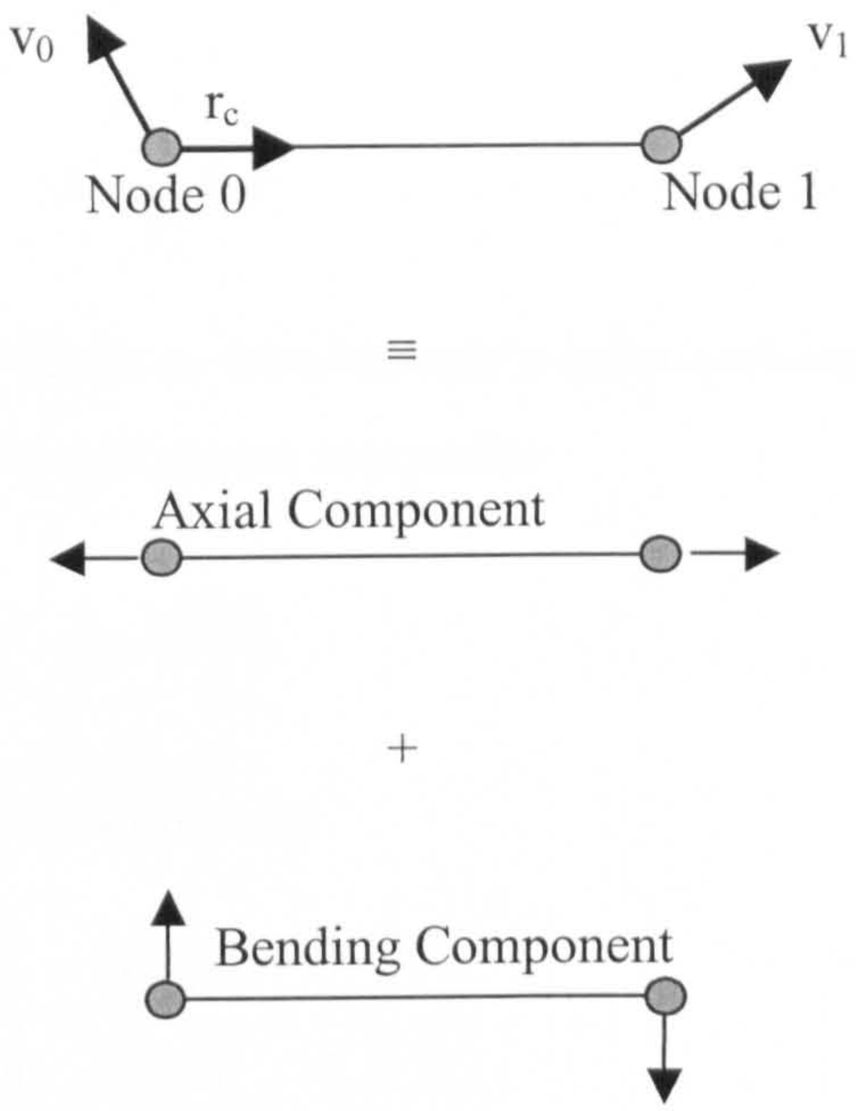

Figure 5.47 Components of Applied Velocity

Let us now assume that the axial velocity components are the equivalent of one node moving away from a fixed node as shown in Figure 5.48.

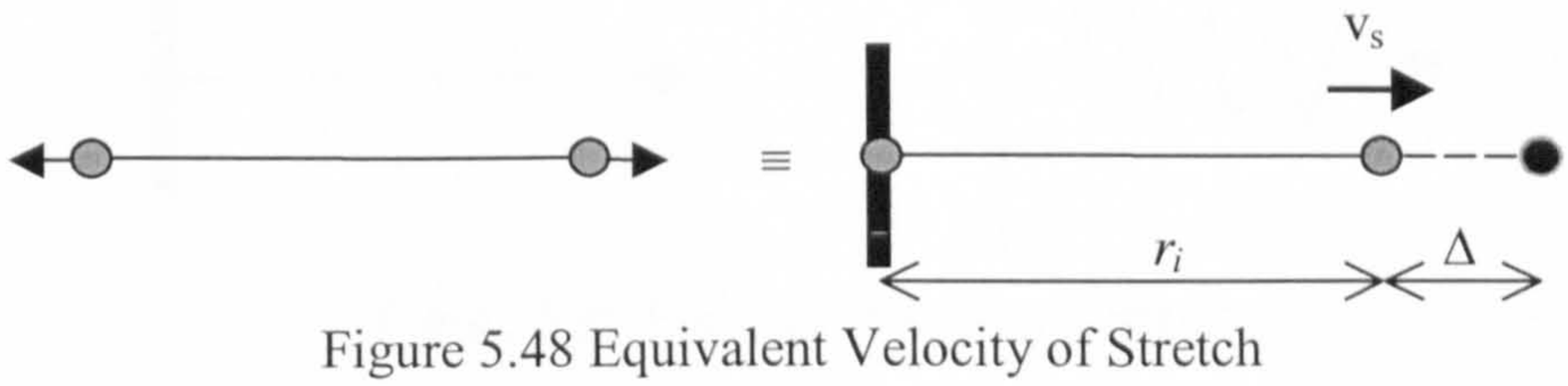

Figure 5.48 Equivalent Velocity of Stretch

The velocity of stretch will move the node in one second a displacement of Δ .

$$\Delta = v_s .dt \tag{5.149}$$

where *dt* is the time step.

The strain rate can be calculated as

$$\dot{\varepsilon} = \frac{d\varepsilon}{dt} = \frac{v_s}{r_i} \tag{5.150}$$

The stress can be found from

$$\sigma = \dot{\varepsilon}\, c \tag{5.151}$$

where c is the damping constant. If the initial displacement is one then the stiffness is calculated as

$$k = \frac{1}{r_i} EA \tag{5.152}$$

The mass of each node is taken as the elements's cross sectional area multiplied by its initial length and its density split across two nodes

$$m = \frac{Ar_i \rho}{2} \tag{5.153}$$

Hence the frequency ω, will be given by

$$\omega = \sqrt{\frac{k}{m}} = \sqrt{\frac{2EA}{r_i A\rho}} = \frac{1}{r_i}\sqrt{\frac{2E}{\rho}} \tag{5.154}$$

The element is now replaced with a spring system.

Figure 5.49 Equivalent Spring System

The equation of motion of such a system is

$$kx + m\ddot{x} + c\,\dot{x} = 0 \tag{5.155}$$

Critical damping will occur when the damping coefficient $c=2m\omega$. Equation (5.155) is divided through by m giving

$$\frac{k}{m}x+\frac{m}{m}\ddot{x}+\frac{2m\omega}{m}\dot{x}=0 \tag{5.156}$$

Since

$$\frac{k}{m}=\omega^2 \tag{5.157}$$

Equation (5.155) reduces to

$$\omega^2 x+\ddot{x}+2\omega\dot{x}=0 \tag{5.158}$$

If

$$x=e^{\lambda t} \tag{5.159}$$

Then

$$\dot{x}=\lambda e^{\lambda t} \text{ and } \ddot{x}=\lambda^2 e^{\lambda t} \tag{5.160}$$

Therefore

$$\omega^2+\lambda^2+2\omega\dot{\lambda}^2=0 \tag{5.161}$$

The solution of the quadratic equation becomes

$$x=-e^{\omega t} \tag{5.162}$$

This shows that at critical damping there is no oscillation. Therefore for one element there would be no oscillation if the critical damping were:

$$c_{crit}=2m\omega=2\cdot\frac{Ar_i\rho}{2}\cdot\frac{1}{r_i}\sqrt{\frac{2E}{\rho}}=A\sqrt{2E\rho} \tag{5.163}$$

The force due to damping is found as

$$f = A\dot{\varepsilon}c = A.\frac{v_s}{r_i}c = A.\frac{1}{r_i}.c.\dot{x} \tag{5.164}$$

where

$$v_s = \dot{x} \tag{5.165}$$

Therefore the critical force at which damping will occur is

$$f_{crit} = A\frac{1}{r_i}c_{crit}\dot{x} \tag{5.166}$$

Hence say

$$f_{crit} = C_{crit}\dot{x} = 2m\omega\dot{x} \tag{5.167}$$

Thus

$$f_{crit} = 2\frac{A\rho r_i}{2} \times \frac{1}{r_i}\sqrt{\frac{2E}{\rho}}\dot{x} = A\sqrt{2E\rho}\dot{x} \tag{5.168}$$

Hence critical damping at which no oscillation occurs is

$$A\sqrt{2E\rho}\dot{x} = \frac{A}{r_i}c_{crit}\dot{x} \tag{5.169}$$

Which gives

$$c_{crit} = r_i\sqrt{2E\rho} \tag{5.170}$$

The actual damping force, f is then given as

$$f_{crit} = Ar_i\sqrt{2E\rho}\dot{x} \tag{5.171}$$

ξ is assigned a value of zero if there is no damping or 1 if damping is critical.

The equivalent mass can be found from.

$$I_m = \frac{A\rho r^3}{24} \tag{5.172}$$

The rotational stiffness is given by

$$k = \frac{2EI}{r_i}\phi \tag{5.173}$$

where I is the second moment of Inertia.

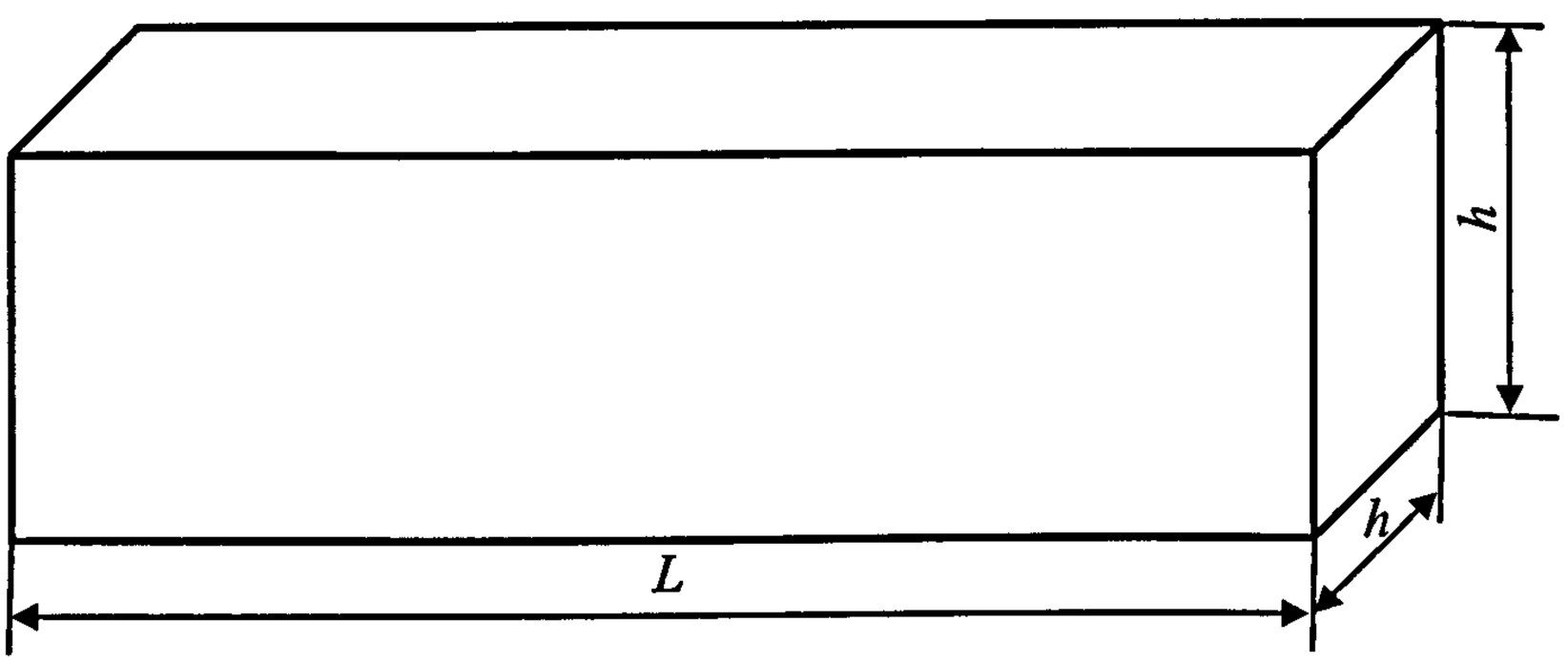

Figure 5.50 Structural beam member

If the rotational and axial displacements are one then the axial and rotational velocities are calculated as follows.

The second moment of inertia, I is

$$I = \frac{bh^3}{12} = \frac{h^4}{12} \tag{5.174}$$

The stiffness of the beam element is then

$$k = 2EI\frac{\phi}{L} = 2EI\frac{1}{L} = \frac{2h^4}{12}\cdot\frac{1\cdot E}{h} = \frac{Eh^3}{6} \tag{5.175}$$

The generalised mass, m_g can be taken as

$$m_g = \frac{A\rho h^3}{24} \tag{5.176}$$

Hence the rotational velocity, ω_ϕ is found from

$$\omega_\phi = \sqrt{\frac{k}{m_g}} = \frac{2}{h}\sqrt{\frac{E}{\rho}} \tag{5.177}$$

A similar approach is taken to calculate the rotational velocity along the axis, ω_a. Assuming the mass to be split equally across the two end nodes of the beam this becomes

$$m = \rho A \frac{h}{2} \tag{5.178}$$

The stiffness, k is found from

$$k = \varepsilon A = \frac{1}{h} E h^2 = Eh \tag{5.179}$$

Hence ω_a becomes

$$\omega_a = \sqrt{\frac{k}{m}} = \frac{1}{h}\sqrt{\frac{2E}{\rho}} \tag{5.180}$$

The above calculations are now repeated for the situation where the cross sectional width is now reduced to h/2. Therefore ω_a is found from

$$m = \rho A \frac{h}{2} = \rho \frac{h}{2} \cdot \frac{h^2}{2} = \frac{\rho h^3}{4} \tag{5.181}$$

$$k = \varepsilon A = \frac{1}{h} E \frac{h^2}{2} = \frac{Eh}{2}$$

$$\omega_a = \sqrt{\frac{k}{m}} = \frac{1}{h}\sqrt{\frac{2E}{\rho}}$$

The value of ω_ϕ is found as follows

$$I = \frac{bh^3}{12} = \frac{h}{2} \cdot \frac{h^3}{12} = \frac{h^4}{24} \tag{5.182}$$

$$k = 2EI\frac{\phi}{L} = 2EI\frac{1}{h} \cdot \frac{h^2}{24} = \frac{Eh^3}{12}$$

$$m_g = \frac{A\rho r^3}{24} = \frac{h^2}{2}\rho h^3 \cdot \frac{1}{24} = \frac{\rho h^5}{48}$$

$$\omega_\phi = \sqrt{\frac{k}{m_g}} = \frac{2}{h}\sqrt{\frac{E}{\rho}}$$

The values for ω_ϕ and ω_a obtained are exactly the same as in the first case. The values of area and mass have reduced in proportion.

It is also seen that ω_a is less than ω_ϕ. In this instance rotation will govern the time step. Therefore the time step 1/2mω will be smaller resulting in greater CPU time.

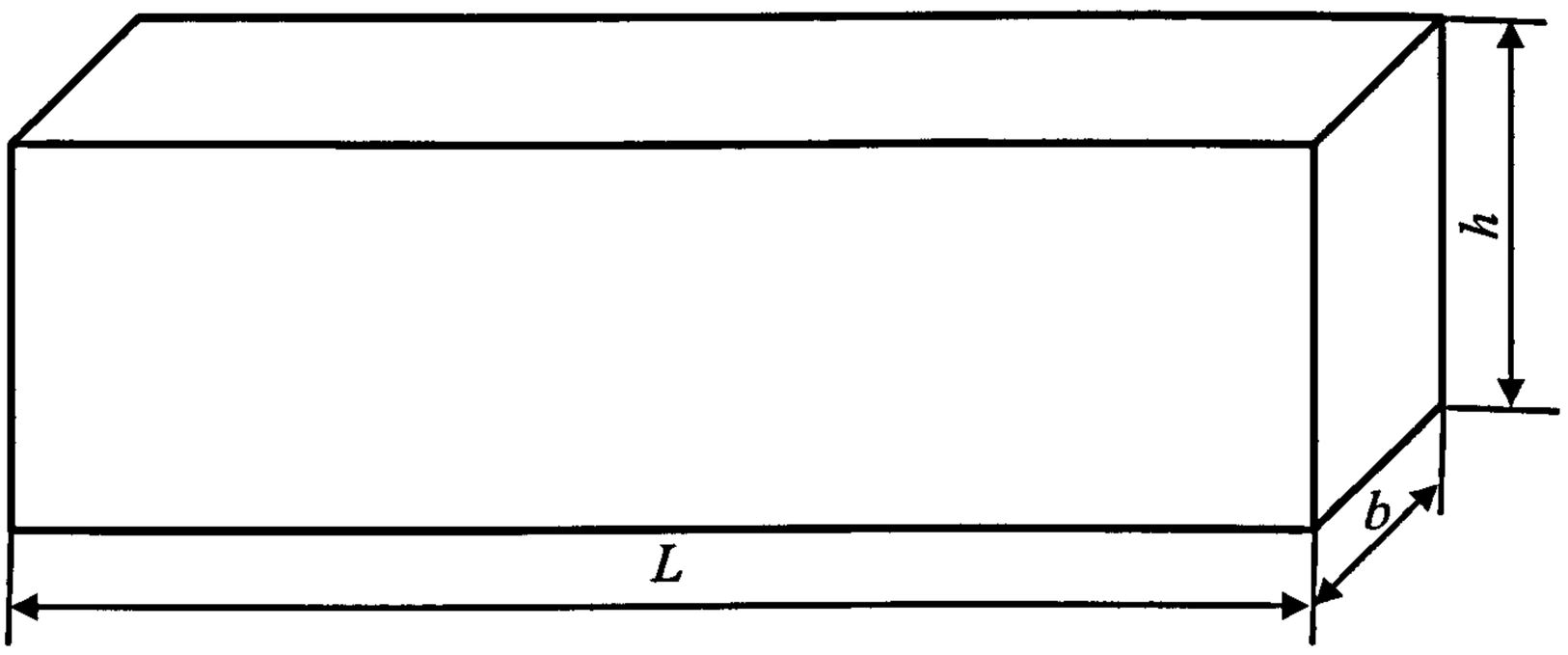

Figure 5.51 Structural beam member

If the dimensions are as shown in Figure 5.51 ω_a and ω_ϕ are calculated as follows

$$k = \frac{2EI\phi}{L} = \frac{2Ebh^3}{12L} \tag{5.183}$$

$$m_g = \frac{A\rho L^3}{24}$$

$$\omega_\phi = \sqrt{\frac{k}{m_g}} = \sqrt{\frac{4Eh^2}{\rho L^4}}$$

$$k = \frac{Ebh}{L} \tag{5.184}$$

$$m_g = \frac{\rho bhL}{2}$$

$$\omega_a = \frac{1}{L}\sqrt{\frac{2E}{\rho}}$$

If they are both made equal then

$$\omega_\phi = \omega_a \tag{5.185}$$

$$\sqrt{\frac{4Eh^2}{\rho L^4}} = \sqrt{\frac{2E}{\rho L^2}}$$

Thus

$$L = h\sqrt{2} \tag{5.186}$$

Therefore as long as $L>h\sqrt{2}$ axial rotation will govern and ω_ϕ will have no effect on the time step.

5.5 References

1. A. Munjiza, D.R.J. Owen, N. Bicanic, "A combined finite-discrete element method in transient dynamics of fracturing solids", *Int. J Engineering Computations,* **12**, *pp 145-174* (1995).
2. Humar , "Dynamics of Structures", *Butterworth-Heinemann* (1992)
3. Kong et all, "Structural Analysis", *Nelson Publishing Company* (1984)
4. Bangash MYH, "Manual of Numerical methods in Concrete-", *Thomas Telford Publishing* (2002)
5. Timoshenko, "Mechanics of Materials", *Chapman and Hall* (1990)
6. Kanchi M B, "Matrix Methods of Structural Analysis", *Wiley Eastern* (1993)
7. Atkins K E, "Numerical Analysis, *Wiley* (1989)
8. Dawe D J, "Matrix Finite Element Displacement Analysis of Structures", *Wiley* (1984)

Chapter 6

Discrete element methods and contact detection

6.1 Introduction

The combined finite-discrete element method is a recently developed numerical method aimed at modelling failing, fracturing and/or fragmenting solids. The method combines aspects of both finite elements and discrete elements [1].

Discrete Element Method relies on the free interaction of a large number of separate and unconnected bodies. Each body can then be discretized using the finite element method. The number of discrete elements, their density and their shape will change in time. Solid domains are discretized into finite elements in the usual way dictated by the finite element method. However finite (as opposed to small) rotations and finite displacements are assumed a priori. It is also assumed that solid domains can fail, fracture or fragment. Thus a single domain represented by a single finite element mesh is transformed into a number of interacting domains, each of which is represented by its own separate finite element mesh. This is usually performed through, what is termed, transition from continua to discontinua algorithms.

Thus in order to avoid two separate discretizations (one for contact and the other for deformation), in this work contact discretization is conveniently assumed to coincide with the finite element discretization, resulting in each structural member being discretized into a relatively large number of finite elements. In this context it is an imperative to employ the simplest possible finite element in order to improve CPU efficiency. This is achieved through formulation of the previously described two noded

finite element with simplified stiffness matrix, enabling elimination of rotational degrees of freedom (static condensation) without a need for matrix inversion.

In the combined finite-discrete element method, contact between interacting domains is defined in a similar way to the discrete element method. The major difference arises from the fact that the finite element discretization of the solid domains is also conveniently used to discretize the contacting domains. Thus discretized contact solutions are used for both contact detection and contact interaction [2, 3, 4, 5, 6].

Hence the essence of the combined finite-discrete element method is incorporation of the contact detection and contact interaction aspects of the discrete element method into the finite element method. Contact interaction requires accurate representation of the geometry of the contacting domains. In the combined finite-discrete element method this is achieved through so called discretized contact solutions, where a relatively fine discretization characterised by a large number of nodal points is usually employed. Contact detection is a set of procedures and algorithms aimed at discovering those domains which are close enough for contact to occur.

Various contact detection algorithms are suited only to particular problems such as quasi-static or dense packing. Most algorithms are suited to quasi-static problems where the relative motion of the bodies is restricted. Dynamic problems, however, involve a large number of bodies with no significant restriction on their motion. This will inevitably increase the CPU time, T (total detection time), generated by such algorithms, as contact detection will now be performed a number of times as opposed to just the single occasion for quasi-static problems.

Hence the optimum algorithm would need to minimise the CPU time and memory requirements, M, in terms of the number of elements and their packing density, It will also need to be flexible enough to account for the change in M and T with packing density.

Most of the algorithms referred to above have total detection time T directly proportional to

$$T \propto N \ln(N) \tag{6.1}$$

where, N is the total number of discrete elements.

In the case of the NBS algorithm the time T is found to be directly proportional to the number of bodies, N.

$$T \propto N \tag{6.2}$$

The memory requirements are

$$M \propto N\frac{1}{\sqrt[2]{\rho}} \quad \text{for 2D} \tag{6.3}$$

$$M \propto N\frac{1}{\sqrt[2]{\rho}} \quad \text{for 2D} \tag{6.4}$$

$$M \propto N\frac{1}{\sqrt[3]{\rho}} \quad \text{for 3D} \tag{6.5}$$

where ρ is the packing density.

The NBS algorithm is equally effective for dense and loose packing, while CPU time is not influenced by packing density. For example in the case of 3D a 125 fold decrease in packing gives a less than 5 fold increase in memory requirement.

This chapter presents the NBS algorithm as applied to problems of a multidimensional nature. Examples are run on a medium size workstation for purposes of algorithm demonstration.

6.2 NBS contact detection for problems of a 2D nature

The reader is referred to reference 1, where a more detailed delineation of this topic is presented.

In this instance the system will consist of a number of discs, which represent the discrete element system, within a defined rectangular shape. The rectangle is then divided into smaller shapes of dimension *ncelx* by *ncely*.

Each disc will have its centre within one of the smaller rectangular shapes (Figure 6.1).

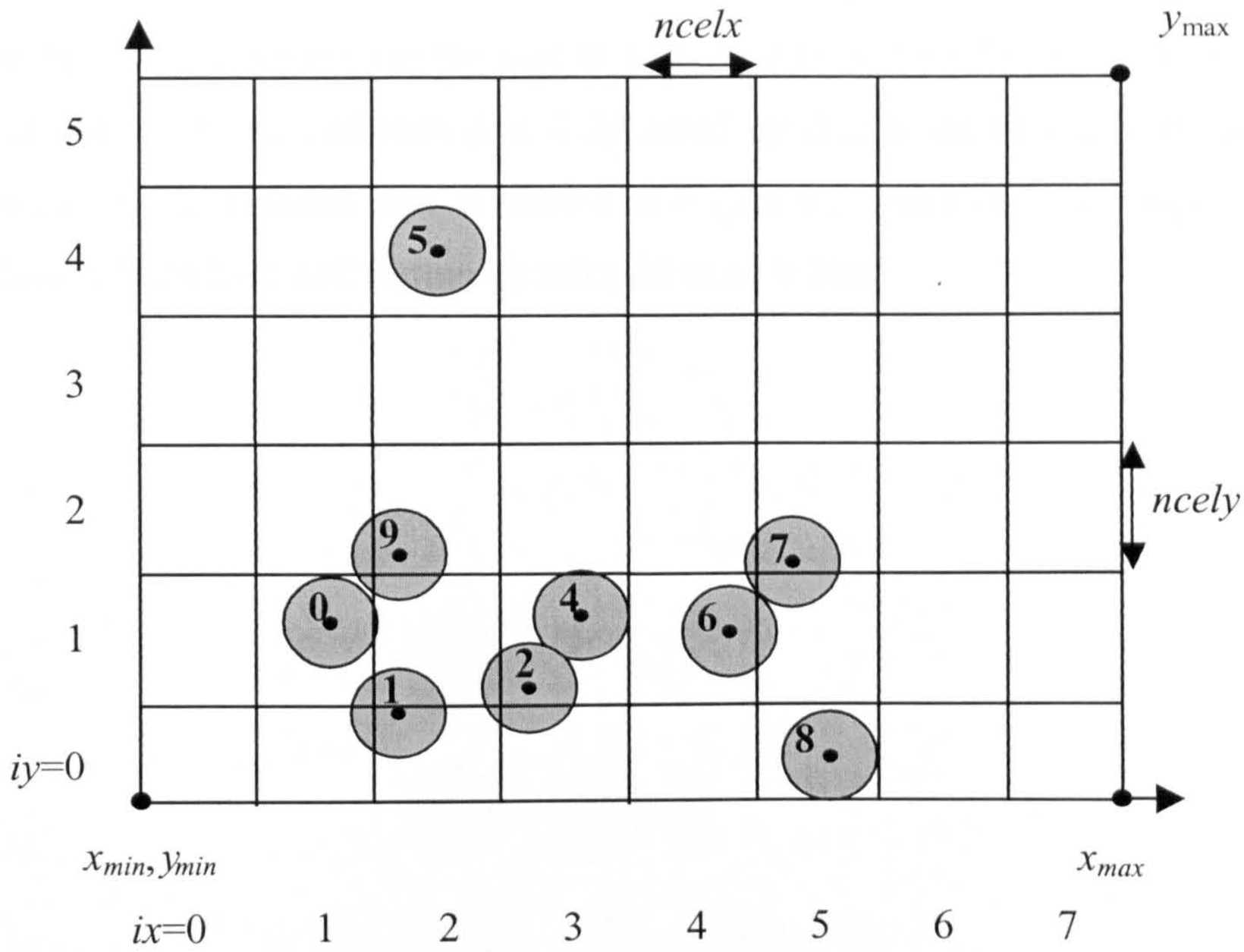

Figure 6.1 Mapping of discs onto cells

Each of the numbered discs is mapped

$$E = \{0,1,2,3,.....N\} \tag{6.6}$$

to the set of cells

$$C = \begin{Bmatrix} (0,0) & (0,1) & ..... & (0, ncely-1) \\ (1,0) & (1,0) & ..... & (1, ncely-1) \\ (ncelx-1,0) & (ncelx-1,1) & .....(ncelx-1, ncely-1) \end{Bmatrix} \tag{6.7}$$

For example the cell (ix,iy) may have disc with centre coordinates (x,y)

Therefore from Figure 6.1 we may say disc 5 is assigned to cell (2,4). The discs are numbered and then assigned to a particular row and then to a particular column of cells.

Incorporating the use of linked lists reduces memory requirements. Firstly each disc is looped over in ascending numerical order and it's integerised *iy* coordinate is found. Therefore from figure we can see the disc 0 is the first to be found when *iy*=1. The next disc found will be disc 2 and then disc 4 followed by disc 6. At each disc is found, it will push along the previous disc as shown in Figure 6.2. Here only the sequence for *iy*=1 is shown. Such lists will further be referred to as Y lists.

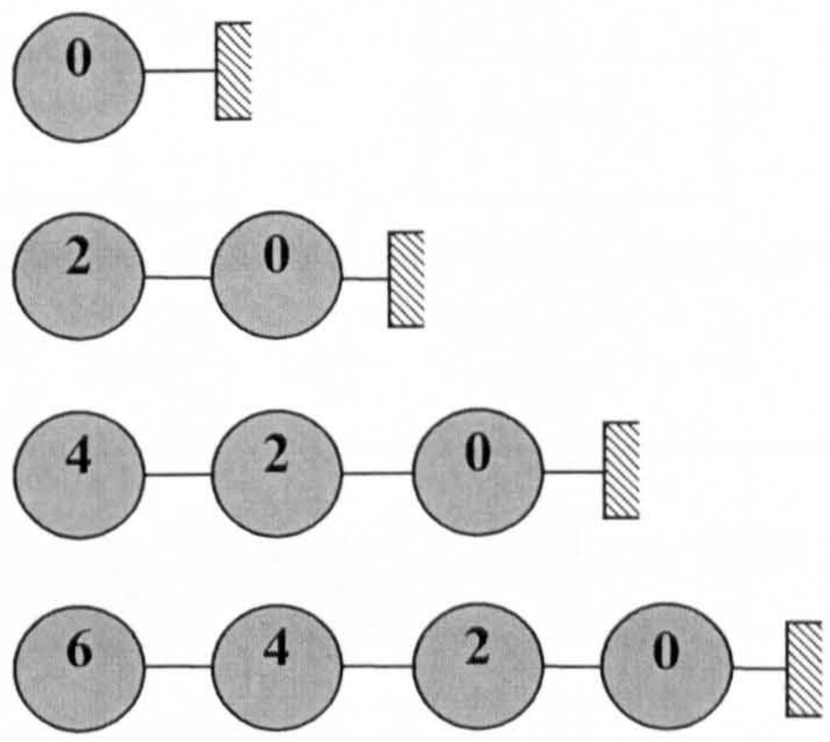

Figure 6.2 List formation sequence for *iy*=1

This process is effectuated by the use of two single dimension arrays as shown in Figure 6.3. The negative one indicates the end of the list.

The heady array is *ncely* large and the nexty array is N large, where *ncely* is the number of cells in the y direction. In the case of *iy*=1 the head array begins as heady[1]=6. The nexty array represents the next disc in the list for *iy*=1.Therefore it can be read as nexty[6]=4, nexty[4]=2, nexty[2]=0 and nexty[0]=-1.

A loop over each particular Y list is now performed in order to create a 2D (X,Y) list by checking it's integerised *ix* coordinate. Each disc for the Y_1 list is placed by it's integerised *ix* coordinate thus creating a 2D list as illustrated in Figure 6.4

	heady		nexty
	0	0	-1
	6	1	-1
	-1	2	0
		3	-1
	-1	4	-1
	-1	5	1
	-1	6	4

Figure 6.3 Numerical representation of single dimension arrays used for the 2D case

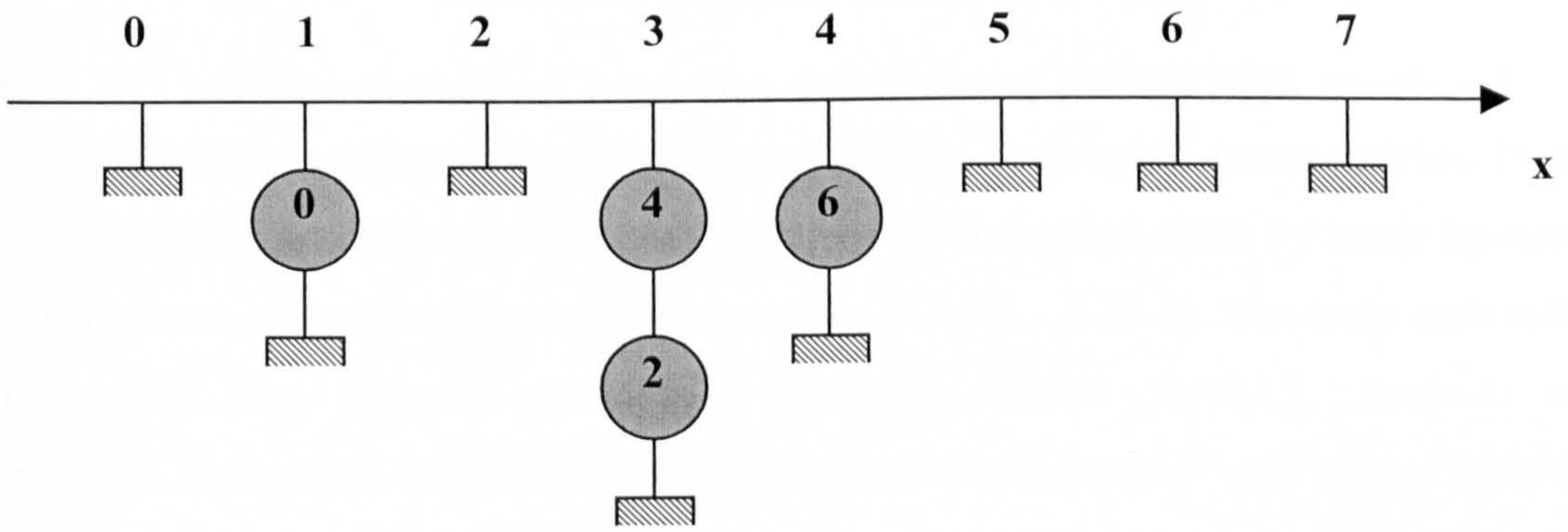

Figure 6.4 2D (X,Y) list

As no loops over cells is carried out we can assume that CPU time required is not a function of *ncelx* or *ncely* and hence not a function of packing density ρ.

Contact detection is carried out where the cell has one or more discs mapped to it. A check of the neighbouring cells for contact detection is then carried out. Once again in all operations involved T is not a function of *ncelx* or *ncely*.

As no loop over the cells is performed at any stage we can assume CPU time, T to be directly proportional to the number of discs, N.

6.3 NBS contact detection algorithm for 3D problems

The NBS algorithm for three dimensions replaces the discs with spheres in a finite defined cubic system as shown in the Figure 6.5. The boundaries are defined by x_{min}, y_{min}, z_{min}, x_{max}, y_{max} *and* z_{max}.. The centres of each sphere will never fall outside these

boundaries. Once again the NBS algorithm will find spheres with distances between their closest points less than or equal to zero, i.e. they touch or they overlap.

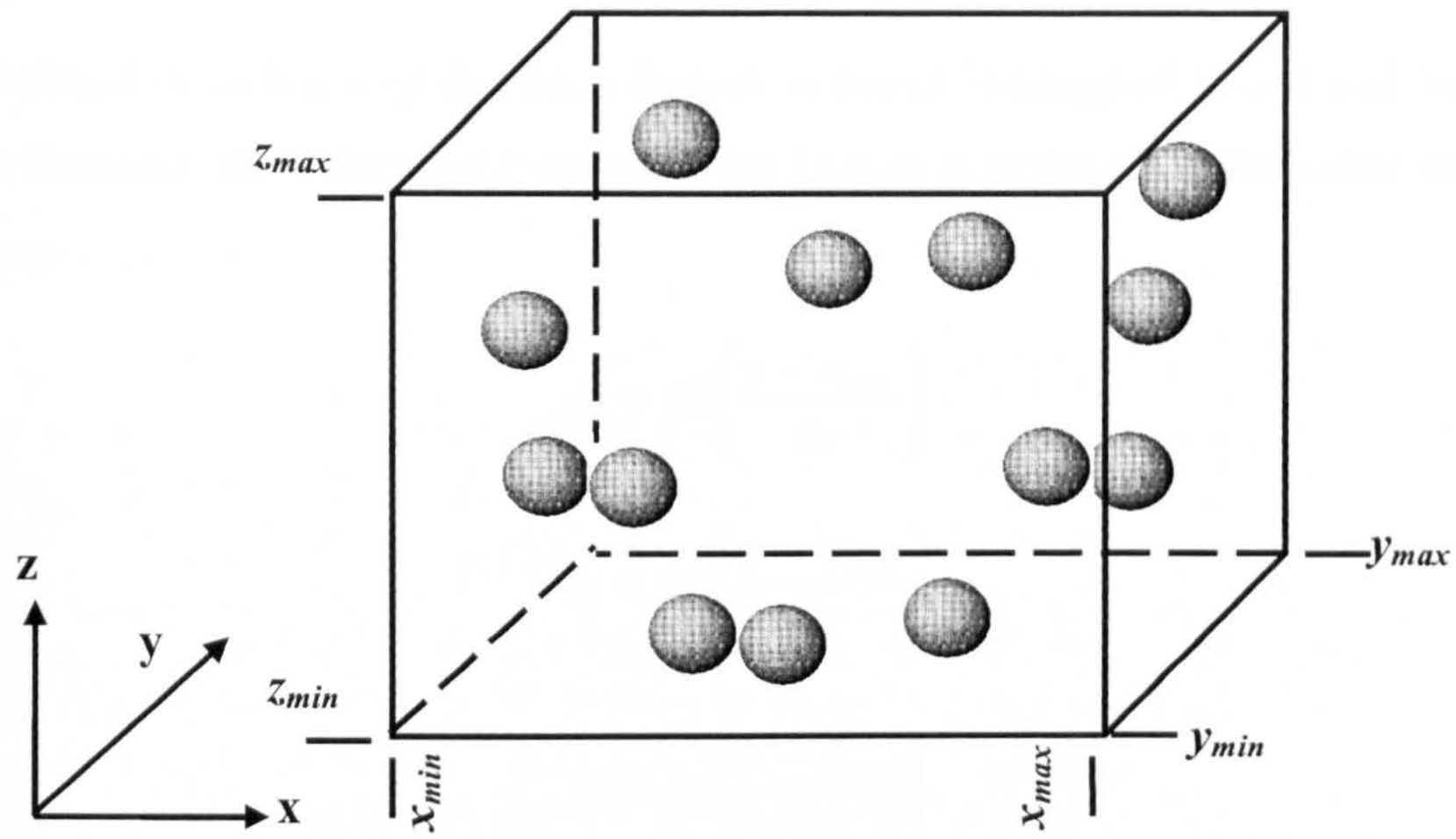

Figure 6.5 3D Contact detection problem

6.4 3D Implementation into the combined FEM/DEM method

The NBS algorithm as has been shown [1] relies upon space decomposition. In this case the cube is subdivided into smaller cubes of dimension *ncelx* by *ncely* by *ncelz*. Each sphere is identified by an integer number {0,1,2,3,…..,N-1}. Similarly each cell is recognised by integer co-ordinates (*ix,iy,iz*), where *ix*=0,1,2,…*ncelx*-1 and *iy*=0,1,2,…….*ncely*-1 and *iz*=0,1,2,……*ncelz*-1. *ncelx*-1 ,*ncely*-1 and *ncelz* -1 are the maximum number of cubes in the x, y and z directions.

$$ncelx = \frac{x_{\max} - x_{\min}}{2r} \tag{6.8}$$

$$ncely = \frac{y_{\max} - y_{\min}}{2r} \tag{6.9}$$

$$ncely = \frac{z_{\max} - z_{\min}}{2r} \tag{6.10}$$

where r is the radius of the sphere

Mapping from the set of spheres

$$E = \{0,1,2,3,.....N\} \tag{6.11}$$

to the set of cubes

$$C = \left\{ \begin{matrix} (0,0,0) & (0,1,0) & ..... & (0, ncely-1, ncelz-1) \\ (1,0,0) & (1,0,0) & ..... & (1, ncely-1, ncelz-1) \\ (ncelx-1,0,0) & (ncelx-1,1,1) & .....(ncelx-1, ncely-1, ncelz-1) \end{matrix} \right\} \quad (6.12)$$

is defined in such a way that each discrete element is assigned to one and only one cell. For instance, the sphere with co-ordinates (x,y,z) is assigned to the cubic cell (*ix,iy,iz*), where

$$ix = Int\left(\frac{x - x_{min}}{2r}\right) \quad (6.13)$$

$$iy = Int\left(\frac{y - y_{min}}{2r}\right) \quad (6.14)$$

$$iz = Int\left(\frac{z - z_{min}}{2r}\right) \quad (6.15)$$

iz,iy and *iz* are said to be integerised relative co-ordinates, here on referred to as integerised co-ordinates. For example sphere eight can be seen to map on to layer 1, column 3 and cell (3,0,1), Figure 6.6

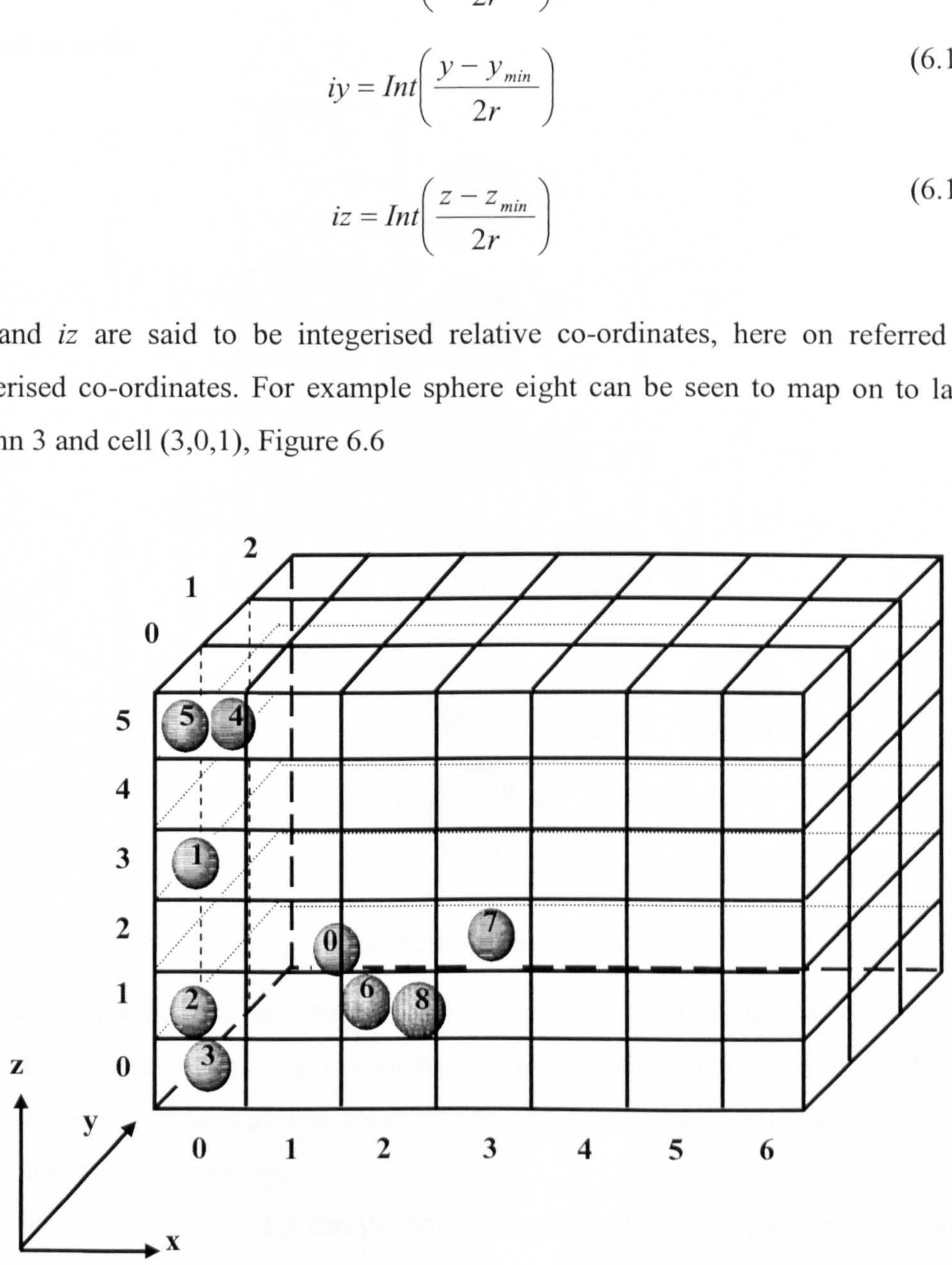

Figure 6.6 Mapping of spheres on to cubic cells

Mapping may also be represented by a 3D array

$$ncel = ncelx.ncely.ncelz \tag{6.16}$$

This undoubtedly would require increased memory, especially for cases where the number of spheres is thinly spread over the cubic space.

This problem is solved, as in the two dimensional case, by using linked lists. Firstly the spheres are mapped on to layers in the z direction. For each layer in the z direction a linked list *iz* is constructed. This is shown in Figure 6.7. For example layer *iz* = 2 is referred to as Z_2 .

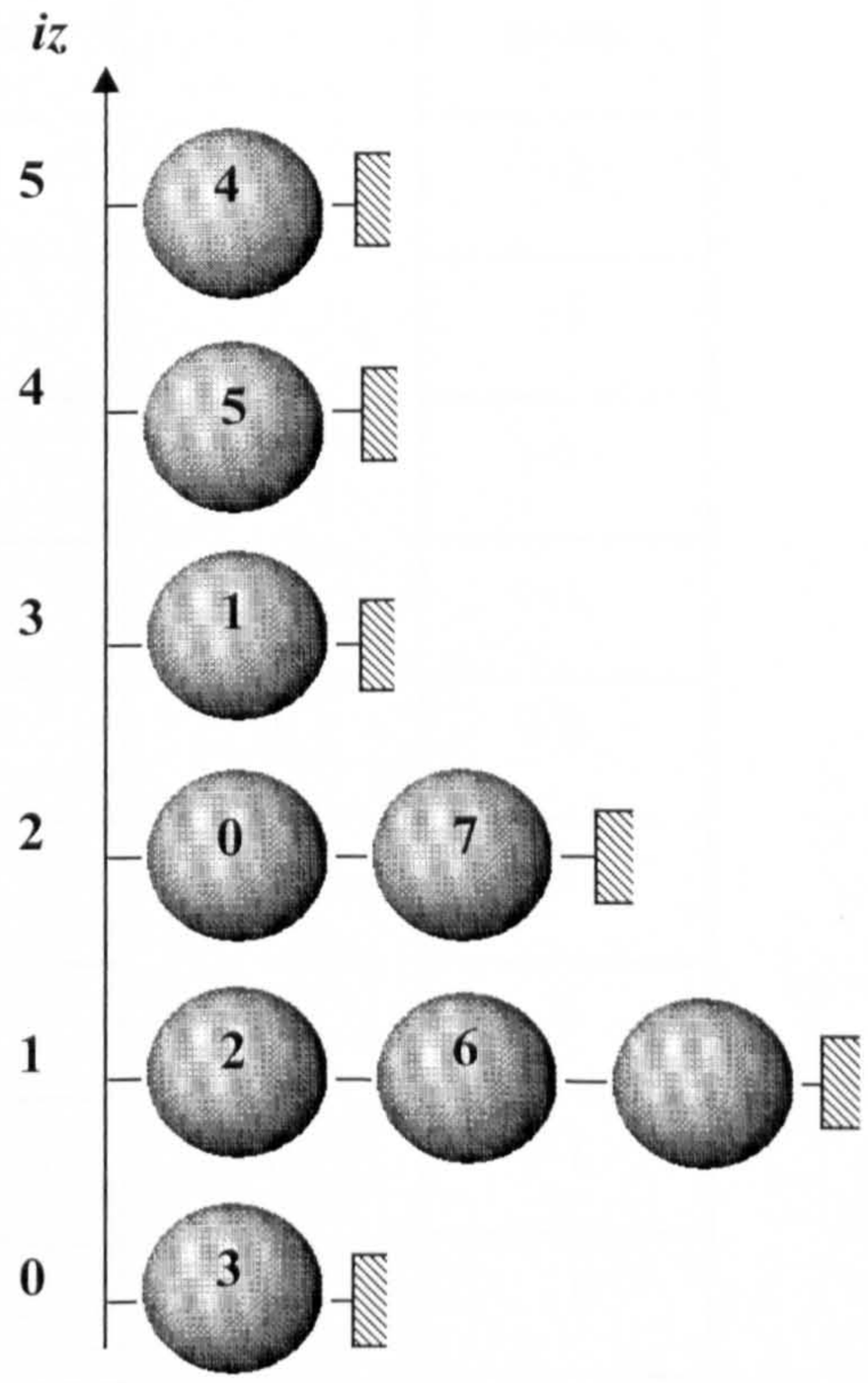

Figure 6.7 Linked lists, Z_i

A loop over each of the spheres is used to place them on to their respective z layer by ascertaining the integerised *iz* coordinate. For example when iz =1 i.e. Z_1 ,the sphere 8 is first placed and then pushed along by sphere 6 and further pushed along by sphere 2 once found to lie on this layer.

This done using two 1D arrays which we will call headz and nextz as shown in Figure 6.8. Hence for *iz* = 1 headz[1]=2, nextz[2]=6, nextz[6]=8 and nextz[8]= -1. Similar analogous methods are used to form X ,Y and lists for any other dimension.

Loops over the non empty Z lists are done to obtain a list of spheres in the y direction-Y list. These will be placed according to their integerised *iy* co-ordinate. A loop over the non empty Y lists is next performed to place each sphere onto an X list by using its *ix* value. By this procedure each individual sphere is placed onto a list in each of the axis directions.

Once the X, Y and Z or N then the head and next arrays are reset to –1 indicating no spheres present. The subsequent layer is then formed. It can be seen no loop over the cubic cells is carried out and so the CPU time is not a function of *ncelx*, *ncely* or *ncelz* and so is not a function of the packing density ρ.

	headz	**nextz**
0	-1	-1
1	2	-1
2	-1	6
3	-1	-1
4	-1	2
5	-1	4
6	-1	8
7	-1	-1
8	-1	-1

Figure 6.8 Formation of linked list Z_1

6.5 NBS algorithm – detection of contact

Each sphere can only be mapped on to a single cubic cell and only neighbouring cells can have any contact. The next stage is to detect contact between the spheres. Once the sphere has been mapped it is marked so that the check against neighbouring cells is not repeated in the loop.

The next step is to search for contacts with spheres in surrounding cubic cells. For example (0,0,2) will check itself against cells (0,0,2), (0,0,1), (1,0,1) and (2,0,1). It will

also check itself against all the cells directly beneath each of it's neighbouring cells lying on the same layer.

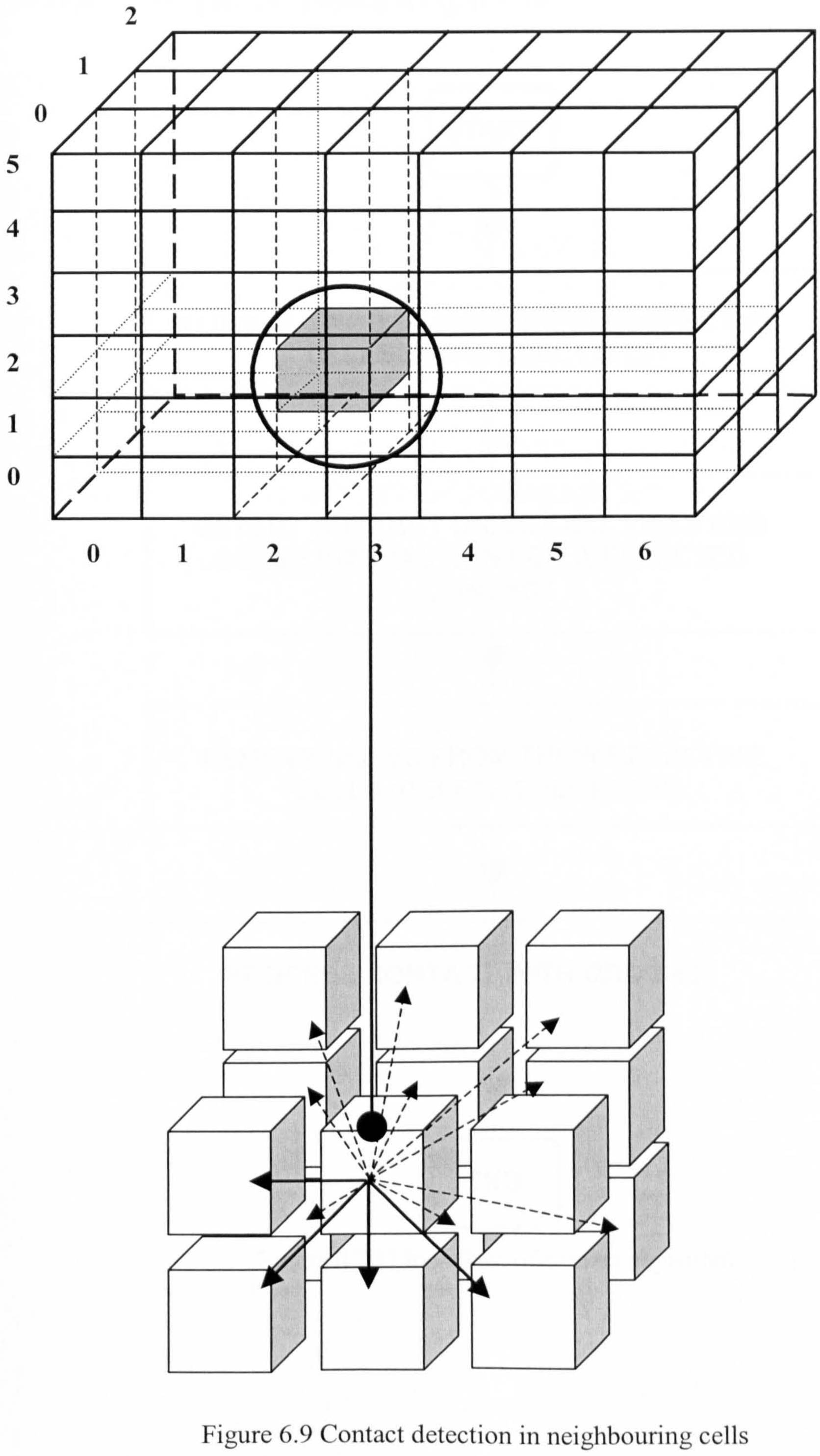

Figure 6.9 Contact detection in neighbouring cells

6.6 3D NBS algorithm – implementation

The code is able to identify which particular nodes are in contact with each other. A flow chart of the algorithm is shown in Figure 6.10.

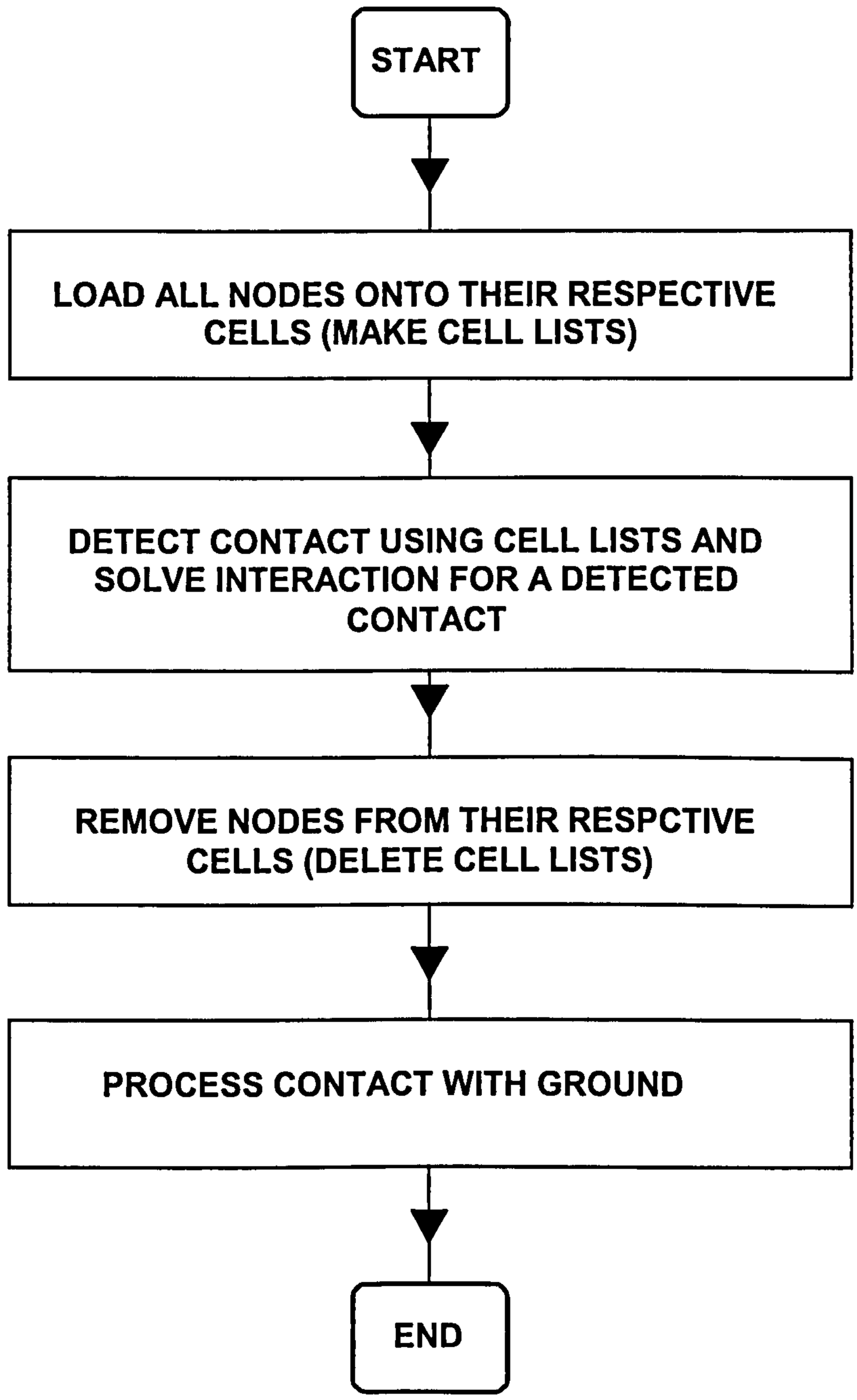

Figure 6.10 Flow chart of contact algorithm

This algorithm ensures no cell is checked twice, thus keeping CPU time to an optimum.

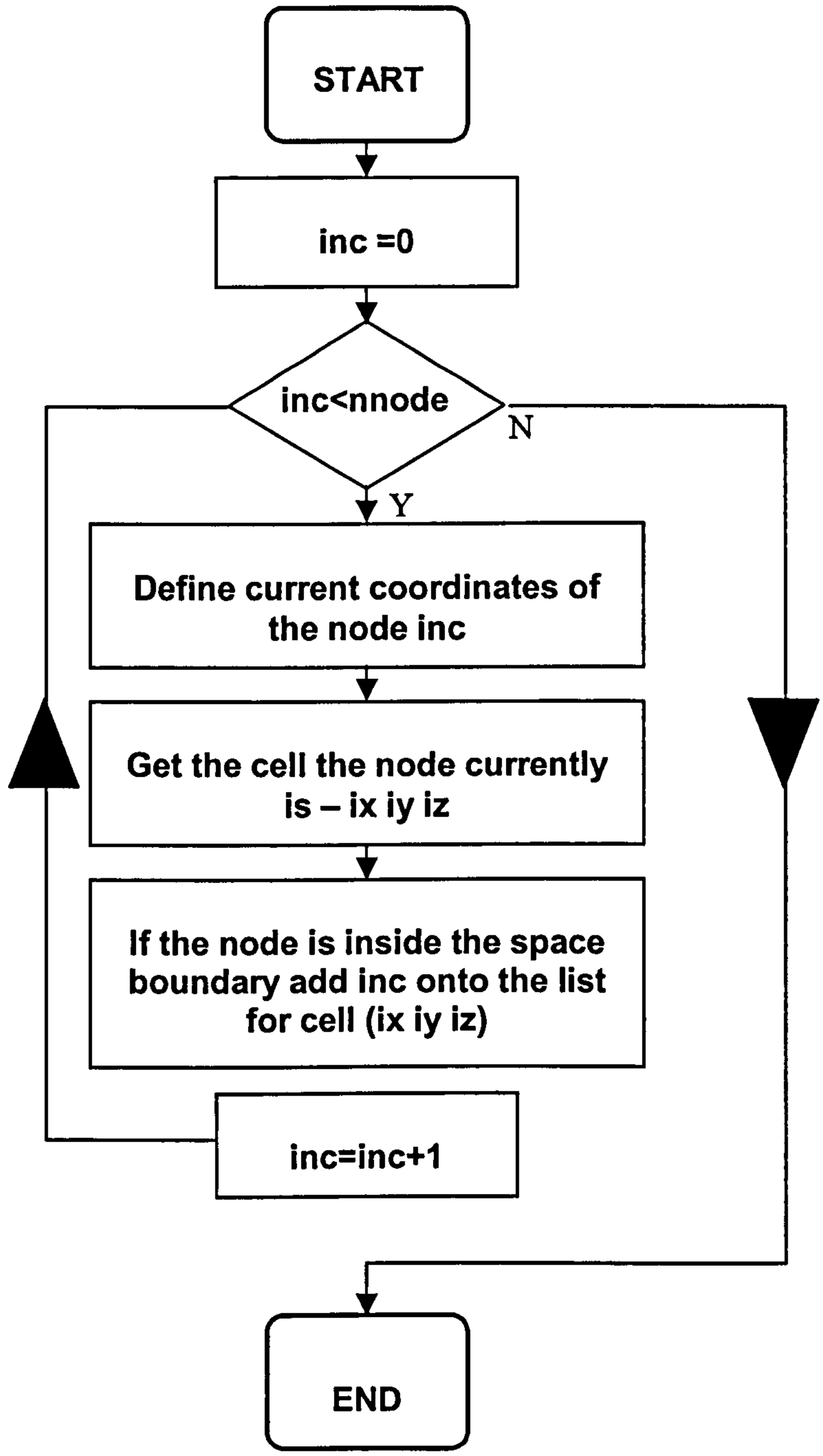

Figure 6.11 Flow chart detailing the procedure for creating nodal lists for each cell

The algorithm, next processes the interaction between the "contactor" node and the "target" node, once they have been found.

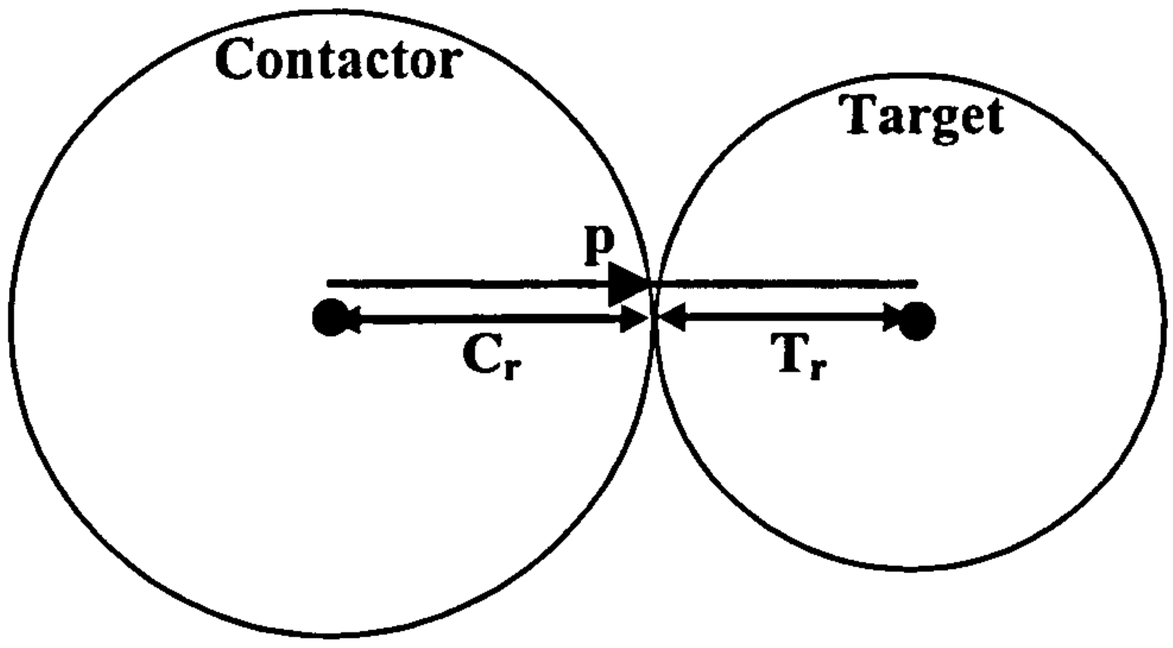

Figure 6.12 Contact between contactor and target node

The vector **p** is found by adding the vector radii of the two nodes.

$$\mathbf{p} = \mathbf{C}_r + \mathbf{T}_r \tag{6.17}$$

It is then transformed into a unit vector.

Contact will occur if there is overlap between the two nodes and **p** is less than the sum of the vector radii.

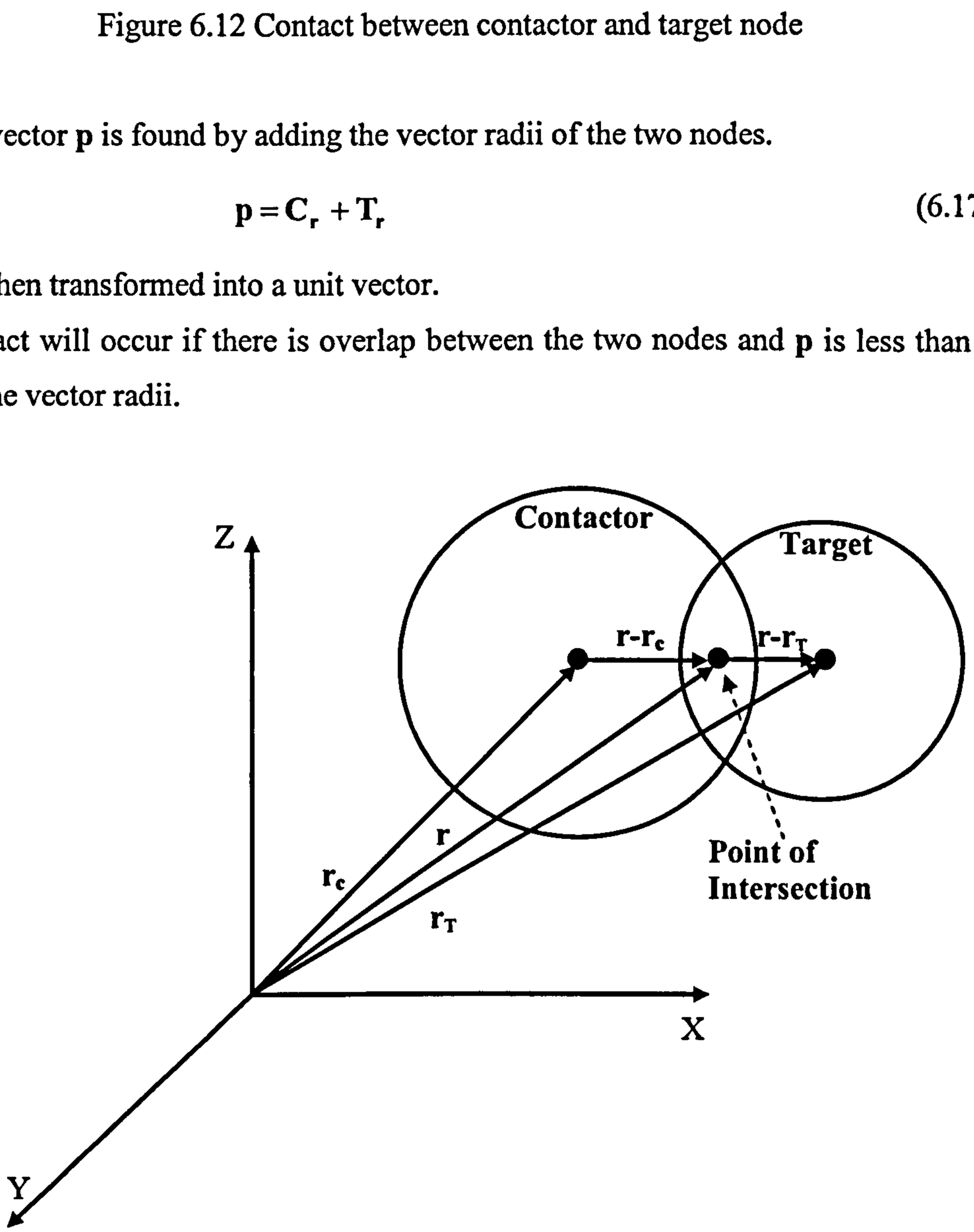

Figure 6.13 Point of intersection between contacting nodes

The **r** vector at the point of intersection is obtained from the vectors $\mathbf{r_C}$ and $\mathbf{r_T}$. The component of rotational velocity for both nodes contributing to contact is obtained by cross product of the rotational velocity and the respective **r** vector. This is shown in equation (6.18).

$$\mathbf{h_C} = \omega_C \times (\mathbf{r} - \mathbf{r_C}) \tag{6.18}$$

A similar equation applies for the target .

$$\mathbf{h_T} = \omega_T \times (\mathbf{r} - \mathbf{r_T}) \tag{6.19}$$

These components are then combined with the translational velocities to obtain the relative velocities in the x, y and z directions (equation (6.20)).

$$\mathbf{v} = \mathbf{h_C} + \mathbf{v_C} - \mathbf{h_T} - \mathbf{v_T} \tag{6.20}$$

Dot product between the relative velocities and the unit vector **p** will give axial component of velocity in the direction of **p**, v_n.

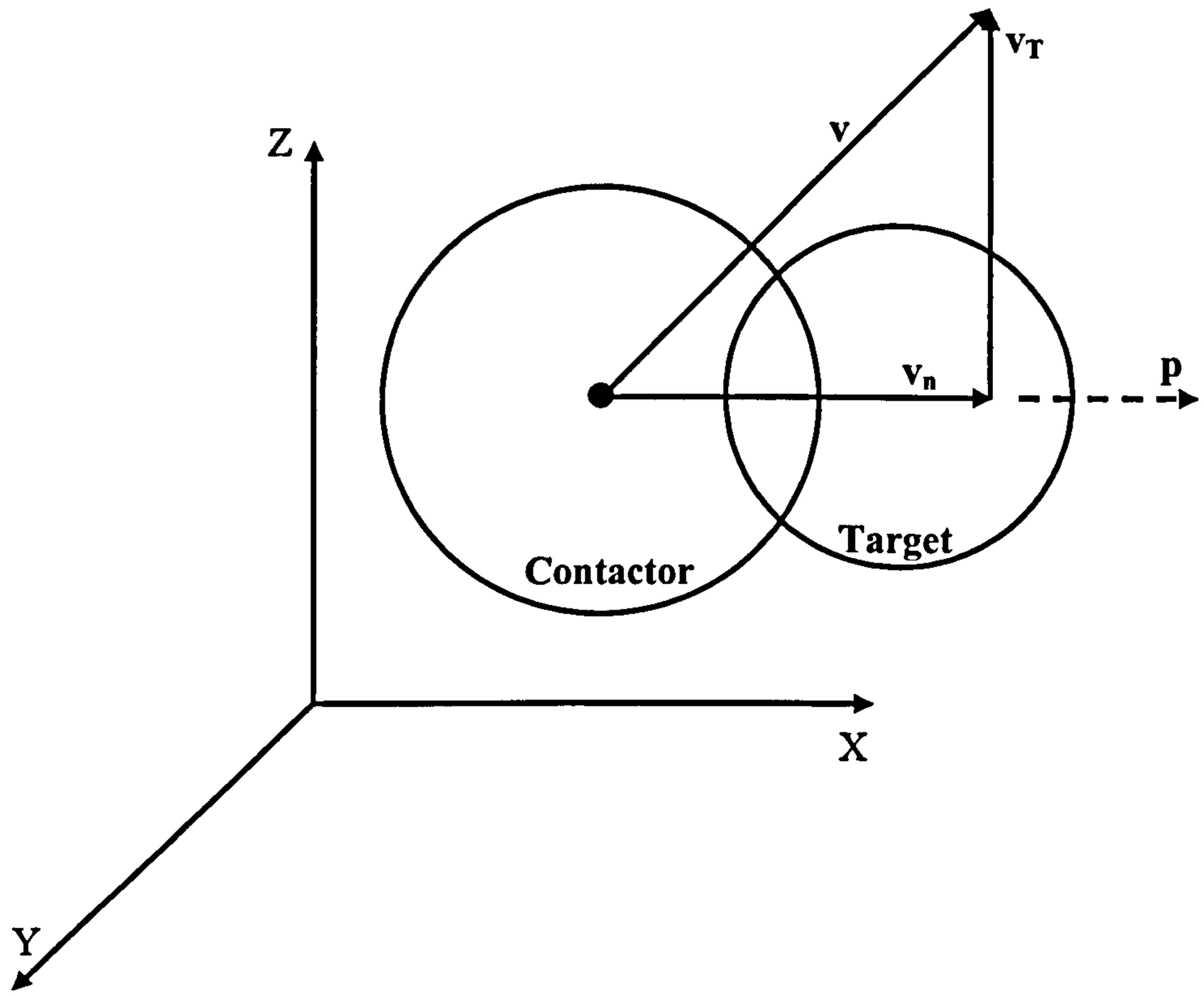

Figure 6.14 Tangential and axial components of relative velocity

$$v_n = \mathbf{v}.\mathbf{p} \tag{6.21}$$

The tangential velocity, $\mathbf{v_T}$ in the x,y and z directions is found from

$$\mathbf{v}_T = \mathbf{v} - \mathbf{v}_n . \mathbf{p} \tag{6.22}$$

The next step is to obtain the frictional and normal forces ($\mathbf{f_f}$ and $\mathbf{f_n}$ respectively), from the penalty function method [7].

The penalty function method in simple form is

$$f = \alpha \times \Delta \tag{6.23}$$

where Δ is the overlap and α is the penalty function parameter. In our case let us assume the overlaping spheres to be represented by a cuboid.

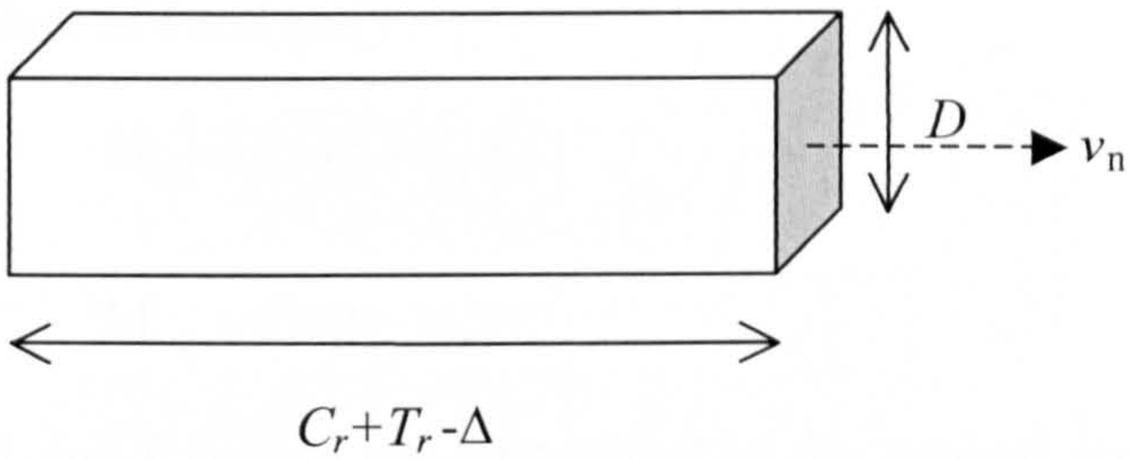

Figure 6.15 Cuboid representation of contacting spheres

Where

$$D = C_r + T_r \tag{6.24}$$

Assuming the overlap is small the force is easily calculated as

$$f = ED\Delta \tag{6.25}$$

The damped force is calculated as

$$f_d = cv_n \tag{6.26}$$

where ξ is the damping ratio. When $\xi = 1$ damping is critical and when x = 0 damping does not exist.

However we know the frequency of the couple in contact is given by

$$\omega = \sqrt{k/m} \tag{6.27}$$

where the stiffness can be approximated by

$$k = \frac{1}{\mathrm{D}} D^2 E = DE \text{ (if the displacement is 1)}$$

The damping is therefore expressed in terms of the critical damping $c = \xi 2m\omega$

where m is the mass of the sphere. Equation (6.26) becomes

$$f_d = \left(2\xi\sqrt{DEm}\right)v_n \tag{6.28}$$

The normal force is multiplied by **p** to give it direction. The friction force is multiplied by $\mathbf{v_T}$ to obtain it's direction. The result is then combined to obtain the force vector **f**.

$$\mathbf{f} = \mathbf{f_n}.\mathbf{p} - \mathbf{f_f}.\mathbf{v_T} \tag{6.29}$$

where **v** is the velocity vector.The contribution of each node to the moment are then found by Cross product of **f** and and **r**.

$$\mathbf{M_{tC}} = \mathbf{f} \times (\mathbf{r} - \mathbf{r_{Cr}}) \tag{6.30}$$

$$\mathbf{M_{tT}} = \mathbf{f} \times (\mathbf{r} - \mathbf{r_{Tr}})$$

The resulting **M** and **f** vectors are then added to the applied moments and forces respectively to update the global force and moment vectors.

The procedure is illustrated in the flow charts of Figure 6.16 and Figure 6.17.

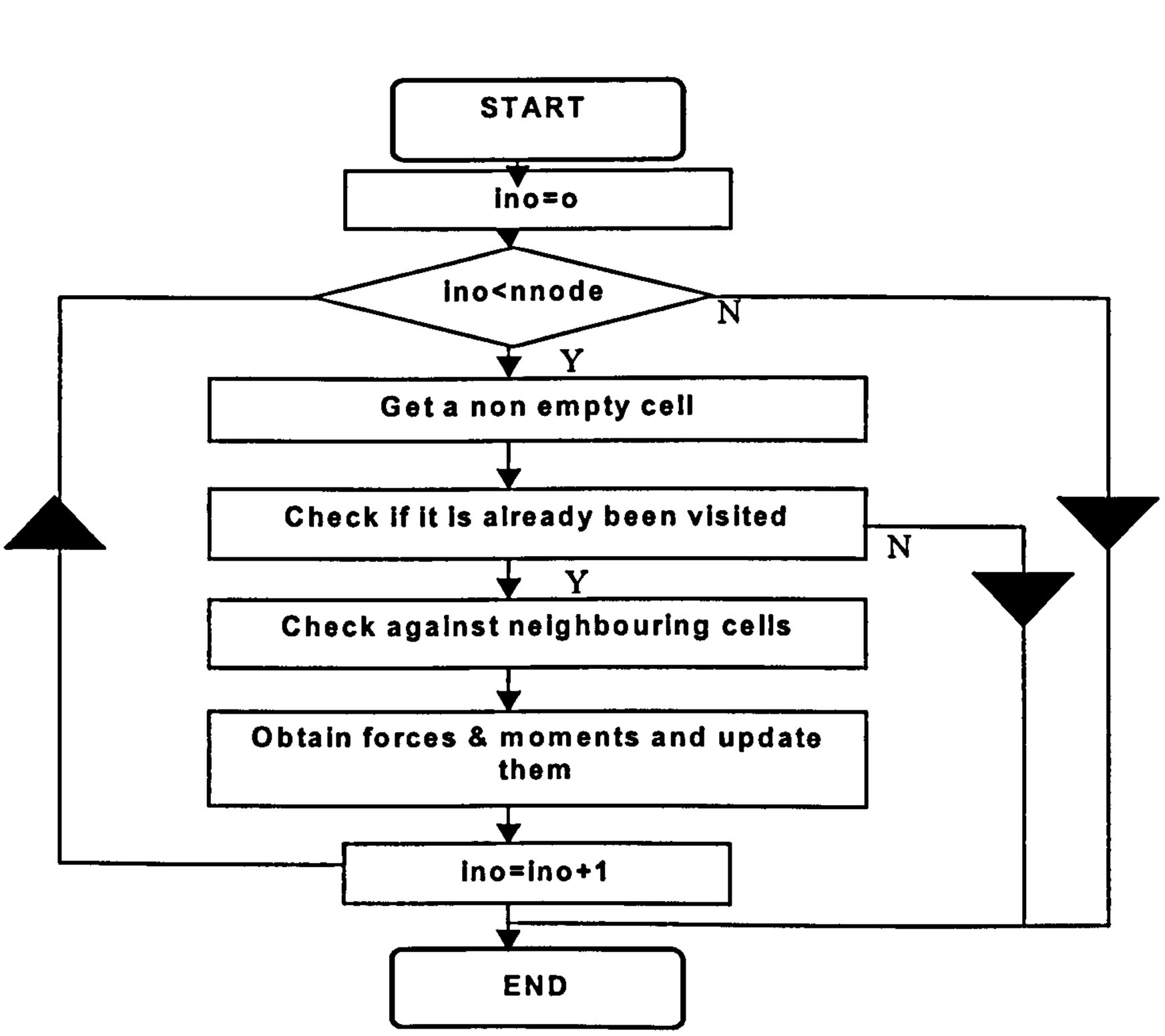

Figure 6.16 Detecting contact between spheres

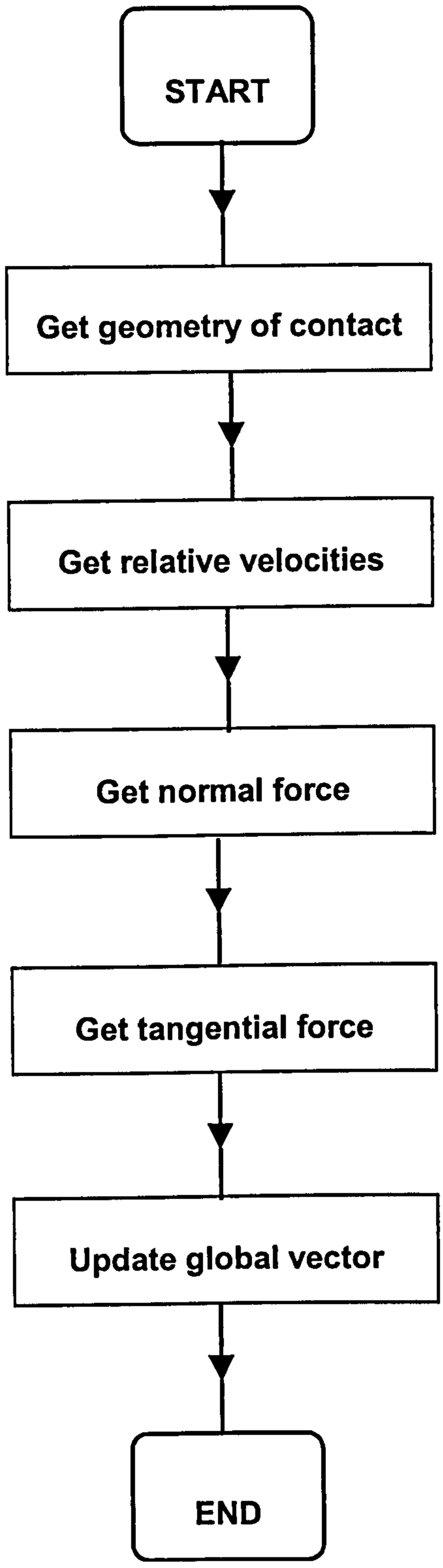

Figure 6.17 Procedure to update global force and moment vector

At this point contact with the wall of the box needs to be considered. To do this the lists for each cell must first be deleted as shown in Figure 6.18.

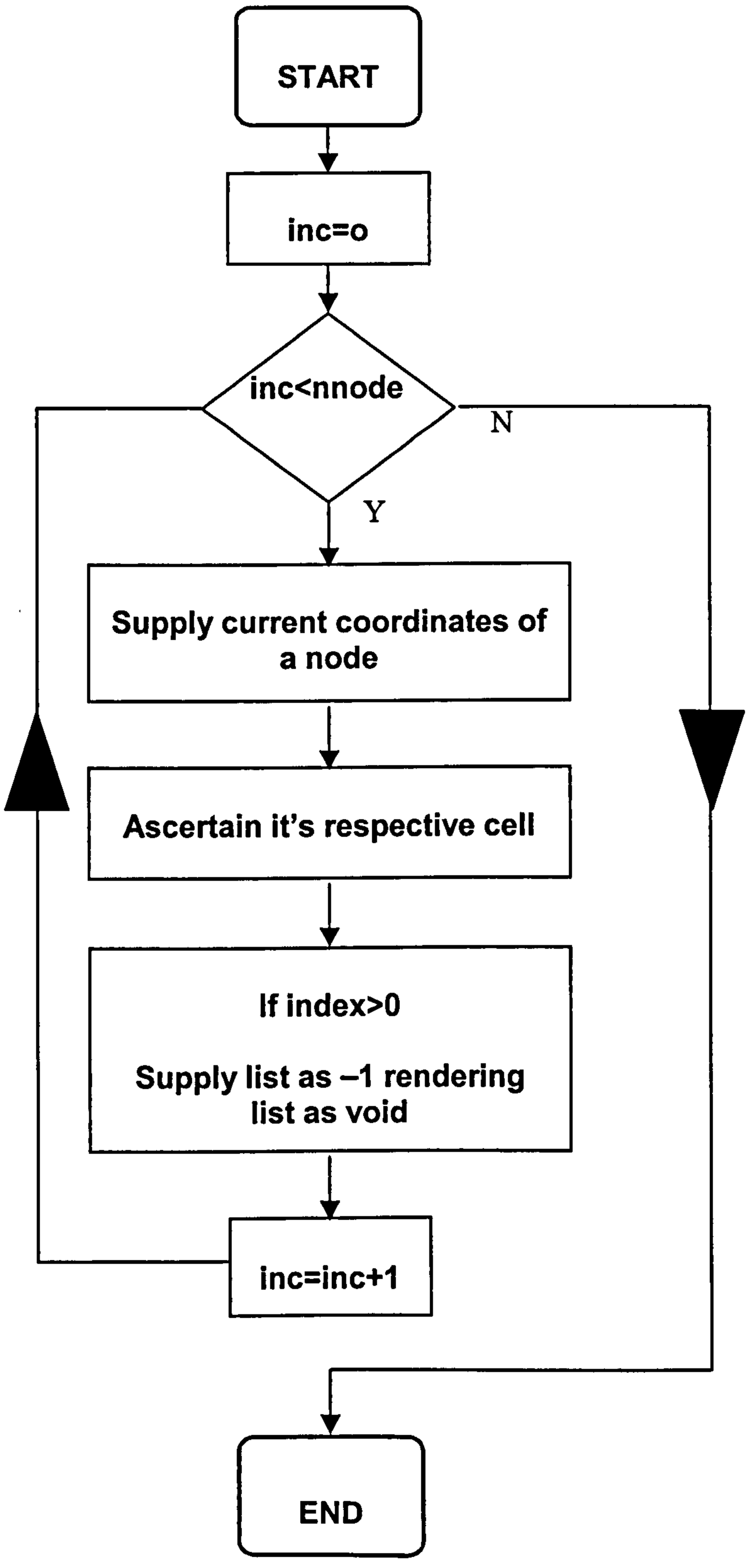

Figure 6.18 Deleting cell lists

In the case of contact with the the box wall the node is now regarded as the target. A similar procedure, as outlined before, is followed to obtain the friction and normal forces. A force vector is then obtained using equation (6.29). The moments are obtained using the second equation numbered (6.30). The global target force and moment vector is then updated. The procedure is shown in figure Figure 6.20.

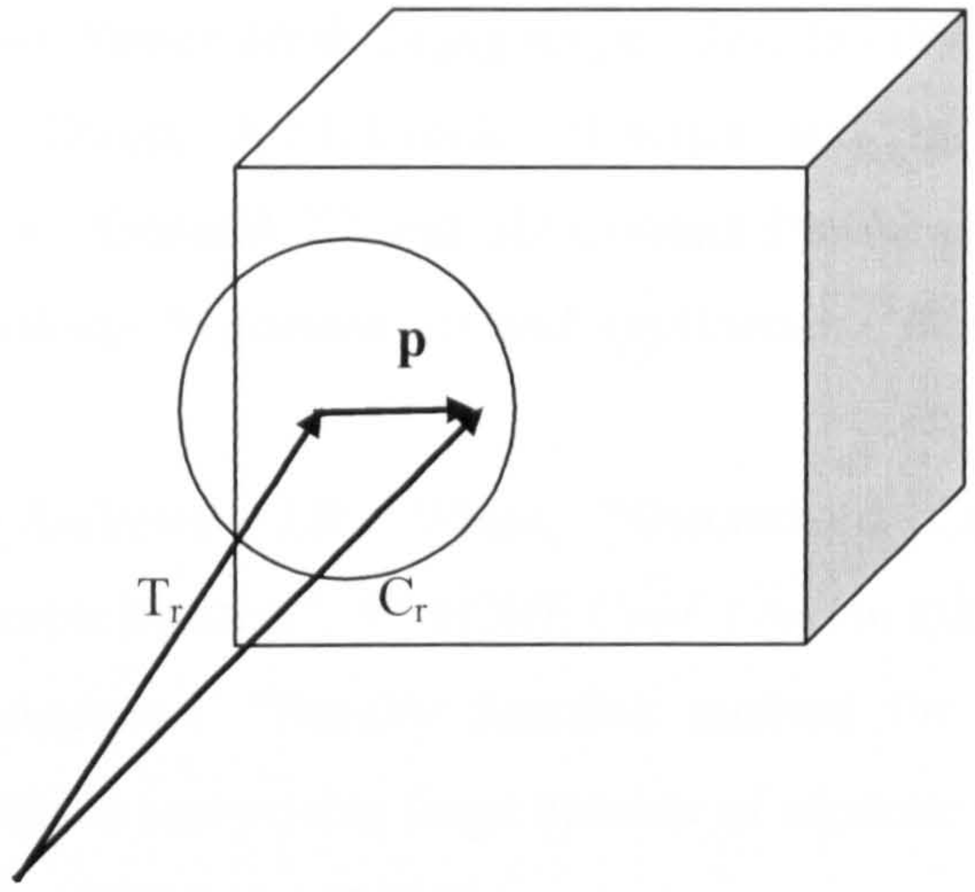

Figure 6.19 Contact with the box

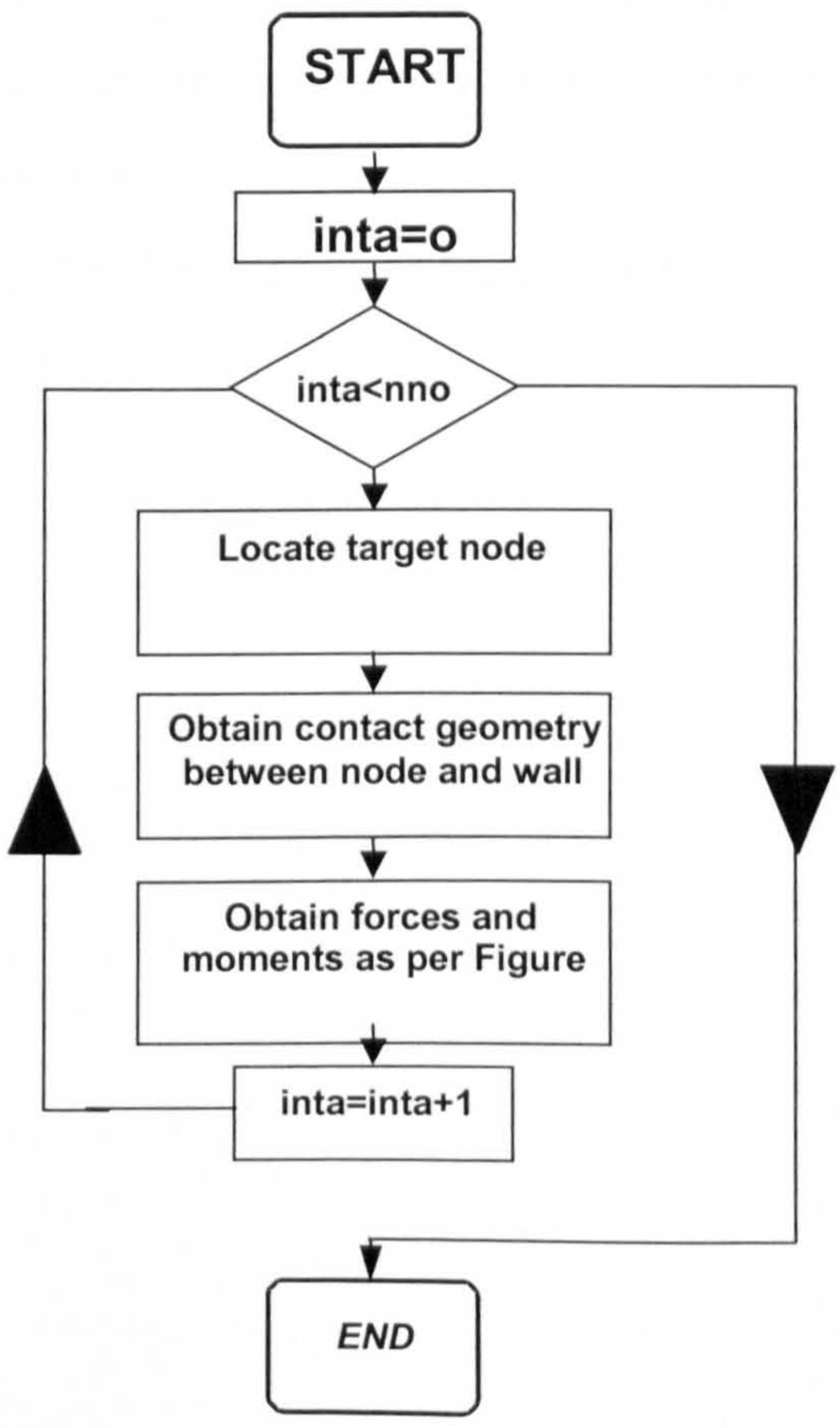

Figure 6.20 Flow chart for contact with the box

6.7 References

1. A. Munjiza, D. R. J. Owen, N. Bicanic, "A Combined Finite- Discrete Element Method in Transient Dynamics of Fracturing Solids", *Int Jour Eng Comput* **12**, *pp 145-174* (1995)
2. A. Munjiza, K. R. F. Andrews, " NBS Contact Detection Algorithm for Bodies of a Similar Size" *Int Jour Numer Meth Engng* **43** *pp 131-149* (1998)
3. A.Munjiza, D.R.J. Owen, A.J.L.Crook, "Energy and Momentum Preserving Contact Algorithm for General 2D and 3D Contact Problems", *Proc 4th Int. Conf Computational Plasticity- Fundementals and Applications, Barcelona pp 829-841* 3 –6 April (1995)
4. A.Munjiza, K.R.F.Andrews, J.R. White, "Discretized Contact Solution for combined finite-discrete Method", *5th ACME Conf. London UK pp 96-100*, (1997).
5. A.Munjiza, K.R.F.Andrews, "Penalty function method for in combined finite-discrete element systems comprising large number of separate bodies", *Int. J. Num. Methods Eng.*, **49**, *pp 1377-1396*, (2000)
6. J.Williams, E.Perkins, "Cgrid- Neighbour search for Many Body Simulation" *Proc. 4th Int. Conf. Discontinuous Deformation Analysis ,University of Glasgow, pp 427-439* 6th–8th June (2001)
7. O. C. Zienkiewizc, "The Finite Element Method in Engineering Science", MacGrawhill (1971)

Chapter 7

Validation of the finite/discrete element using R.C. static loading experiments

7.1 Introduction

A combined finite-discrete element model for failure and collapse of structural systems comprising of reinforced concrete beam or column type structural members has been developed and implemented into a combined finite–discrete element code.

The proposed solutions meet standard criteria required for combined finite-discrete element implementations, which can be summarised as follows:

- Finite element discretizations must be able to capture pre-failure behaviour accurately
- After the failure and collapse has occurred, the same finite element discretization must be able to capture interaction between failing and collapsing structural elements.

Hence the use of a very inexpensive (in terms of CPU time) two noded finite element described in Chapter 5 together with numerical integration, enabling the non-linear behaviour of both concrete and reinforcement to be captured. Experimental verification of the proposed numerical solution for non-linear behaviour and collapse has been done using the results from experiments undertaken at the University of Alberta, Canada [2]. The results obtained using the proposed model, are compared with analytical and experimental results. In addition the rotational capacities obtained are found to be in good agreement with published experimental results [2].

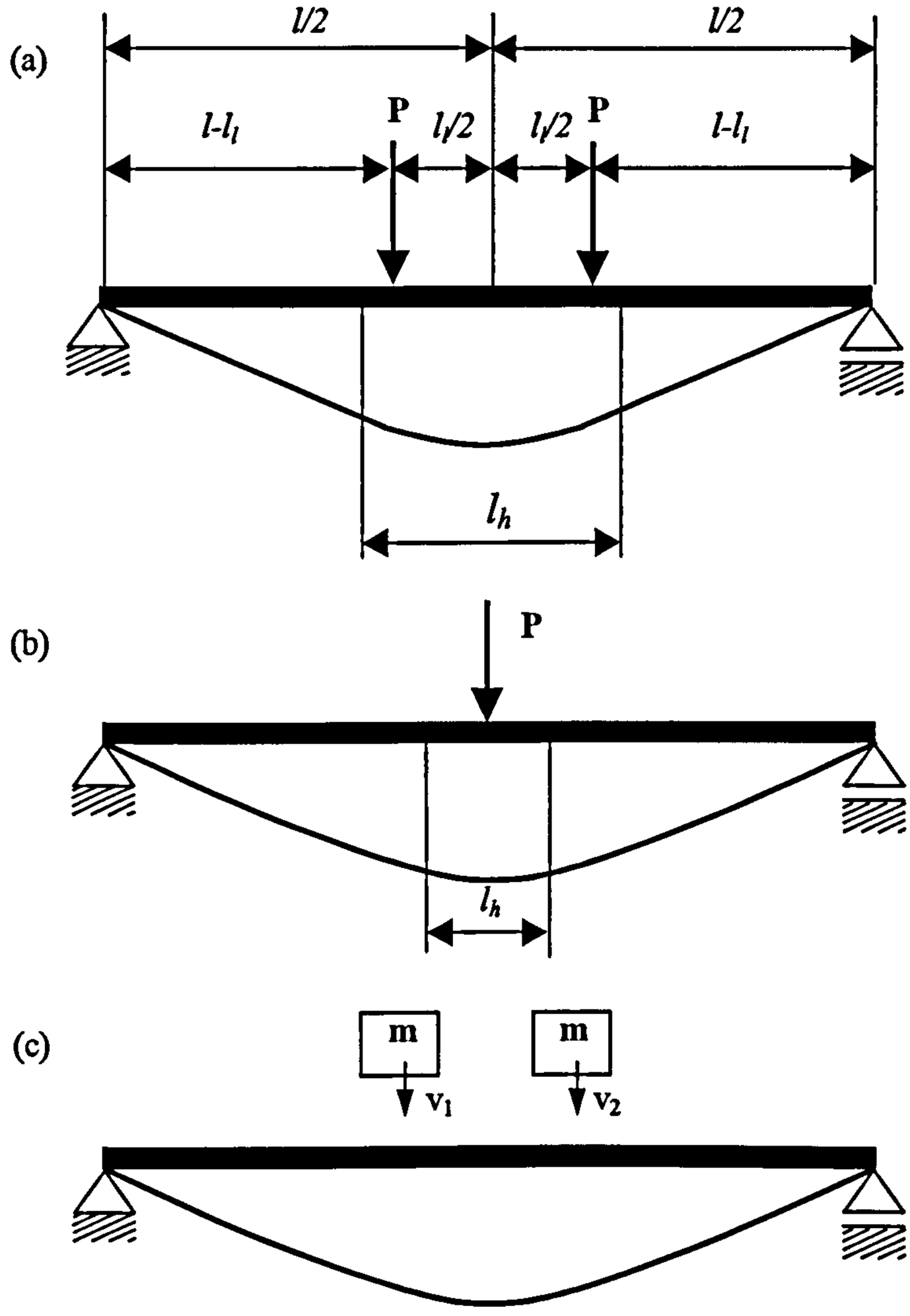

Figure 7.1 Plastic hinge length, a) a two point loading, b) a single concentrated load, c) a dynamic load

7.2 Developed numerical model

Failure of reinforced concrete beams is characterised by the formation of zones of highly localised plastic strains, also called plastic hinges. The size of the plastic hinge is usually much smaller than the length of the beam. However, it is also a function of the load applied. This is illustrated by an example of a simply supported beam shown in Figure 7.1. In Figure 7.1(a) the beam subjected to two concentrated loads P at a distance $l_l/2$ from the centre of the beam is shown. Experimental investigations [2] have shown that the length of the plastic hinge, l_h, is controlled by the distance between these two concentrated loads. Thus the length of the plastic hinge in this particular case can be relatively large. On the other hand for a single concentrated load, shown in Figure

7.1(b) the plastic hinge is for this load reduced to a narrow area close to the applied load. In short, for the same structural system the size of the plastic hinge varies significantly with loading.

The length of the plastic hinge directly controls energy dissipation prior to failure and thus directly influences the extent of moment redistribution in the case of static loading. Under transient dynamic loading (blasts, impacts) the ultimate failure is governed by the ability of the material to dissipate energy. This is illustrated in Figure 7.1(c), where two masses with constant velocity impact the beam. The dynamic response results in straining of the material with the kinetic energy being either transformed into potential energy or dissipated. Most of energy dissipation occurs through the plastic straining of the material and the state of rest is reached only after all initial kinetic energy has been dissipated. Thus it is important to model the stress and strain fields and energy dissipation mechanisms in the region of the plastic hinge accurately. In this context, either *p* or *h* finite element refinements can be employed, i.e. higher order elements can be adopted or a larger number of lower order finite elements can be used. This is illustrated in Figure 7.2. In Figure 7.2(a) the plastic hinge is modelled using a single high order element (i.e. the plastic hinge is incorporated into the finite element). In Figure 7.2(b) the same plastic hinge is modelled using a number of lower order finite elements.

The essence of the combined finite-discrete element method is incorporation of the contact detection and contact interaction aspects of the discrete element method into the finite element method. Contact interaction requires accurate representation of the geometry of the contacting domains. In the combined finite-discrete element method this is achieved through so called discretized contact solutions, where a relatively fine discretization characterised by a large number of nodal points is usually employed.

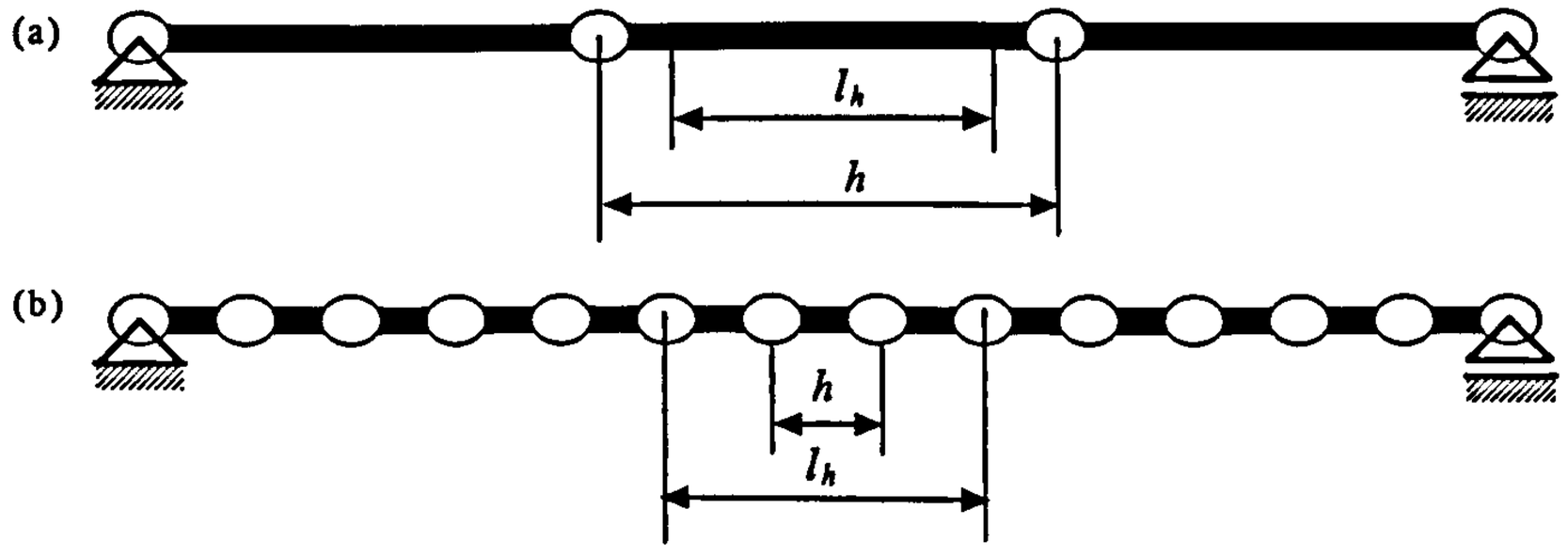

Figure 7.2 Plastic hinge approximation, a) using a single higher order element, b) using a number of lower order elements

7.3 Reinforced concrete section.

The assumption of a linear relationship between bending moment and curvature does not hold for reinforced concrete as illustrated by a typical moment-curvature graph shown in Figure 7.3.

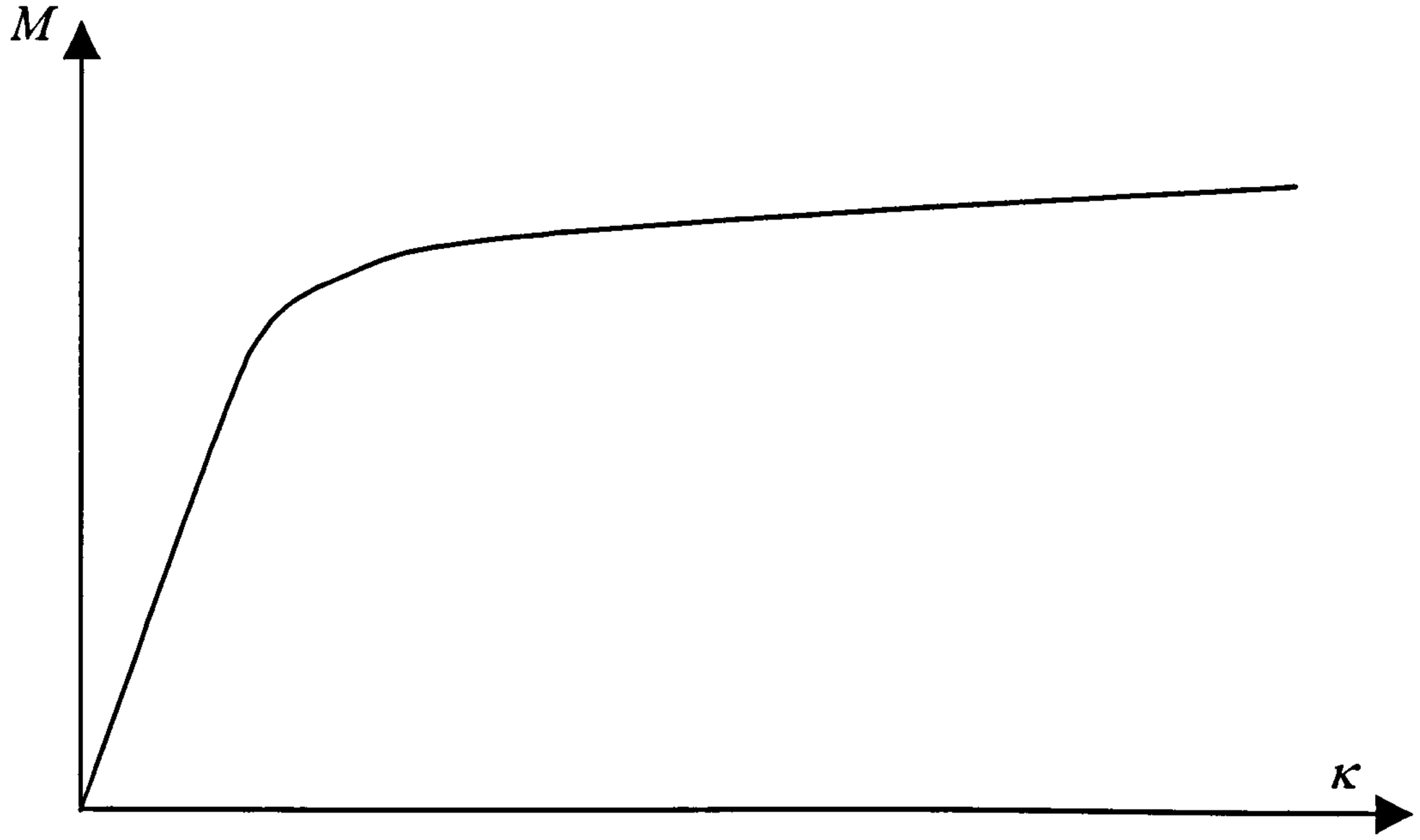

Figure 7.3 A typical moment curvature graph for a reinforced concrete section

Thus the stiffness matrix has to be modified to take into account the nonlinear characteristics of the reinforced section in bending. The simplest approach is to supply the moment curvature relation. However for multi-axial bending combined with an axial force the moment curvature relation is a function of nonlinear properties of both steel and concrete and is therefore for a general case difficult to obtain in a closed form. Hence numerical integration over the cross section of the beam is adopted in this work. To facilitate this the cross section of the beam is replaced by the idealised section shown in Figure 7.4. The beam reinforcement is assumed to consist of four bars placed in the four corners of the beam. The total area of steel A_s is given by

$$A_s = A_{s1} + A_{s2} + A_{s3} + A_{s4} \tag{7.1}$$

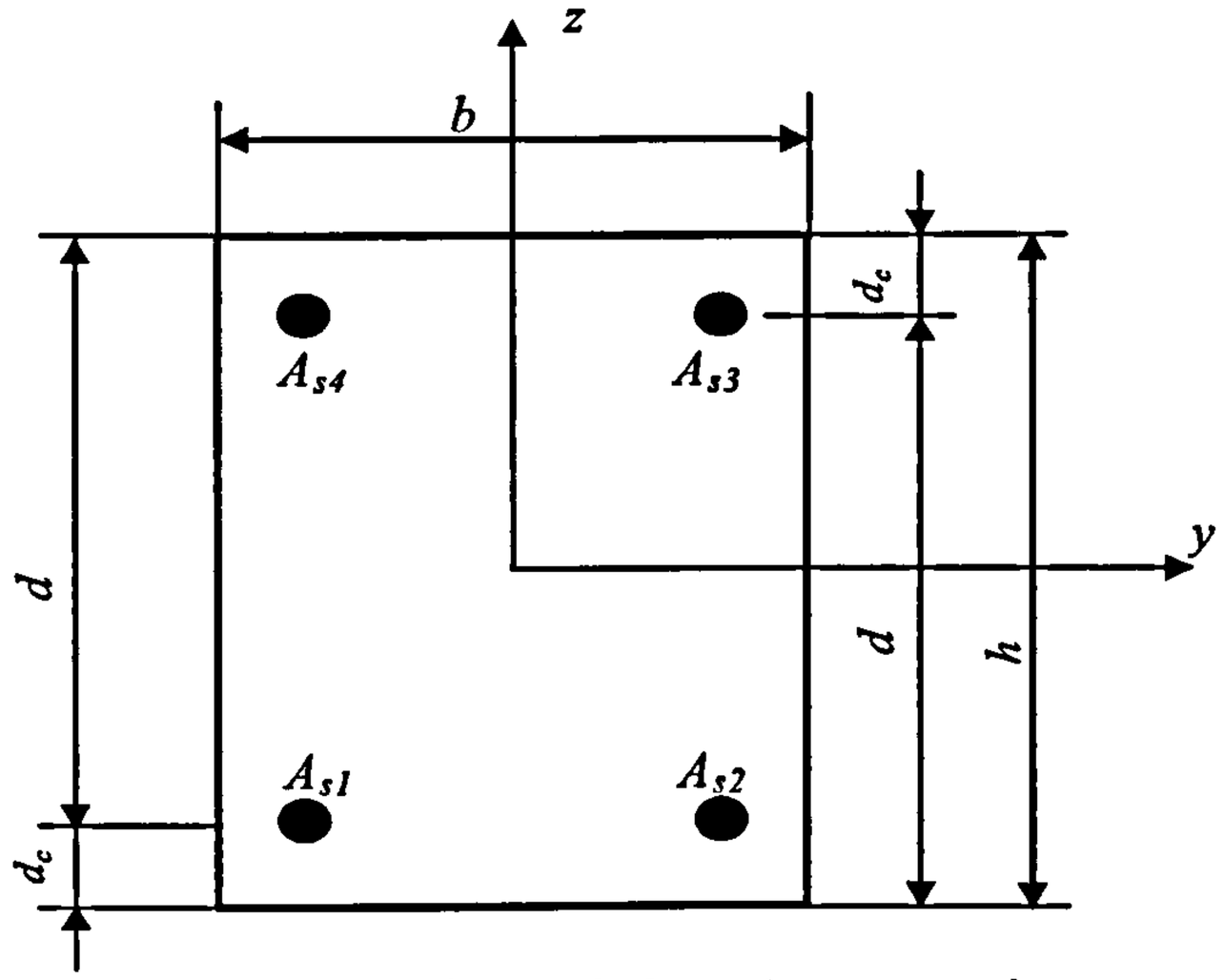

Figure 7.4 Idealised reinforced cross section

It is further assumed that the cross section remains plane after deformation, thus the strain distribution over the cross section is given by

$$\varepsilon(y,z) = \varepsilon_c + \kappa_y z - \kappa_z y \tag{7.2}$$

where ε_c is axial strain corresponding to the centre of the cross section, while κ_y and κ_z are curvatures corresponding to principal axis y and z respectively.

Stress distribution over the cross section is calculated from the stress-strain curve for compression of concrete in bending, with the additional assumption that concrete takes no stress in tension. Thus assuming that the tension zone is cracked, the compression zone of the cross section is identified as shown in Figure 7.5(a) (shaded area). The neutral axis position is found by making equation (7.2) equal to zero. This gives z a function of y.

The bending moments about the principal axis y is given as

$$M_y = \int_{\Omega_c} \sigma(y,z) z \, dA = \int_{\Omega_c} \sigma(y,z) z \, dy \, dz \tag{7.3}$$

while the moment about the principal axis z is given as

$$M_z = -\int_{\Omega_c} \sigma(y,z) y \, dA = -\int_{\Omega_c} \sigma(y,z) y \, dy \, dz \tag{7.4}$$

In a similar way the axial force is given by

$$F_c = \int_{\Omega_c} \sigma(y,z) \, dA = \int_{\Omega_c} \sigma(y,z) dy \, dz \tag{7.5}$$

Both stress distribution and the shape of the compression zone make the above integrals difficult to obtain in a closed form. Thus Gaussian integration is adopted instead. For this purpose the compression zone is first divided into quadrilaterals and each quadrilateral is mapped onto a square as shown in Figure 7.5

$$y = y(\xi,\eta); \qquad z = z(\xi,\eta) \quad \text{and} \quad \sigma = \sigma(\xi,\eta) \tag{7.6}$$

Thus the integration is done in the ξ–η coordinate system as

$$M_y = \int_{\Omega_c} \sigma(\xi,\eta) z(\xi,\eta) \det\mathbf{J} d\xi \, d\eta \tag{7.7}$$

$$M_z = -\int_{\Omega_c} \sigma(\xi,\eta) y(\xi,\eta) \det\mathbf{J} d\xi \, d\eta \tag{7.8}$$

$$F_c = \int_{\Omega_c} \sigma(\xi,\eta) \det\mathbf{J} d\xi \, d\eta \tag{7.9}$$

where **J** is the Jacobian matrix

$$\mathbf{J} = \begin{bmatrix} \frac{\partial y}{d\xi} & \frac{\partial y}{d\eta} \\ \frac{\partial z}{d\xi} & \frac{\partial z}{d\eta} \end{bmatrix} \tag{7.10}$$

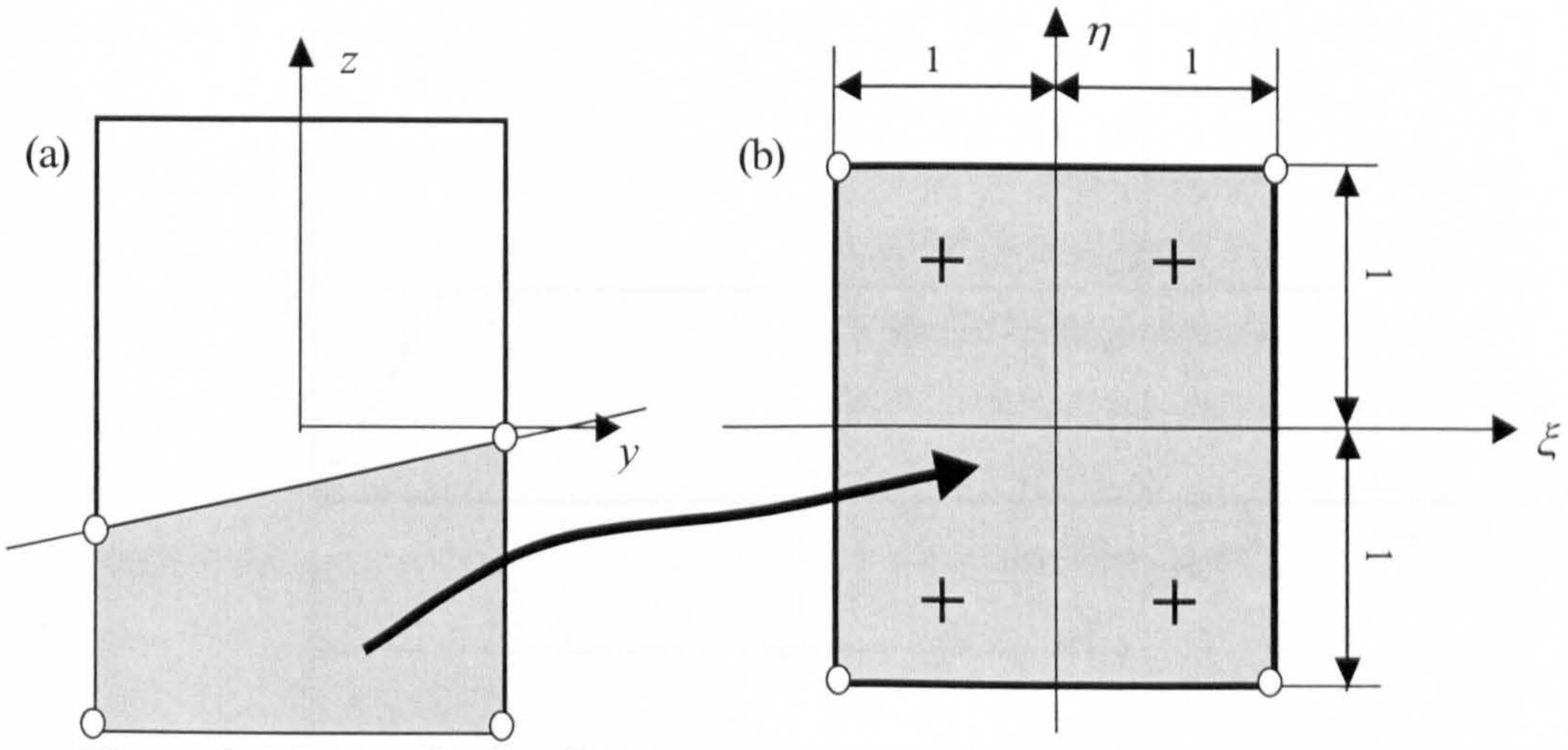

Figure 7.5 Stress distribution: a) Compression zone b) Mapped compression zone

Four integration points are used, transforming the above integrals into a summation over Gaussian points

$$M_y = \sum_{I=1}^{4} \sigma(\xi_i, \eta_i) z(\xi_i, \eta_i) w_i \det \mathbf{J}_i \tag{7.11}$$

$$M_z = -\sum_{I=1}^{4} \sigma(\xi_i, \eta_i) y(\xi_i, \eta_i) w_i \det \mathbf{J}_i \tag{7.12}$$

$$F_c = \sum_{I=1}^{4} \sigma(\xi_i, \eta_i) w_i \det \mathbf{J}_i \tag{7.13}$$

where w_i are weights for Gaussian integration given by

$$w_i = 1, \quad i = 1,2,3,4 \tag{7.14}$$

while (ξ_i, η_i) are coordinates of Gaussian points

$$(\xi_i, \eta_i) = (\pm 1/\sqrt{3}, \pm 1/\sqrt{3}), \quad i = 1,2,3,4 \tag{7.15}$$

The contribution of the steel to the bending moments and the axial force is calculated from the total strain, ε_t for each of steel bars. The total strain is calculated by substituting coordinates of each of the steel bars into equation (7.2). Stress in each of the bars is thus obtained from strain using the stress-strain curve for steel. The bilinear stress-strain curve is conveniently assumed as given in Figure 7.6

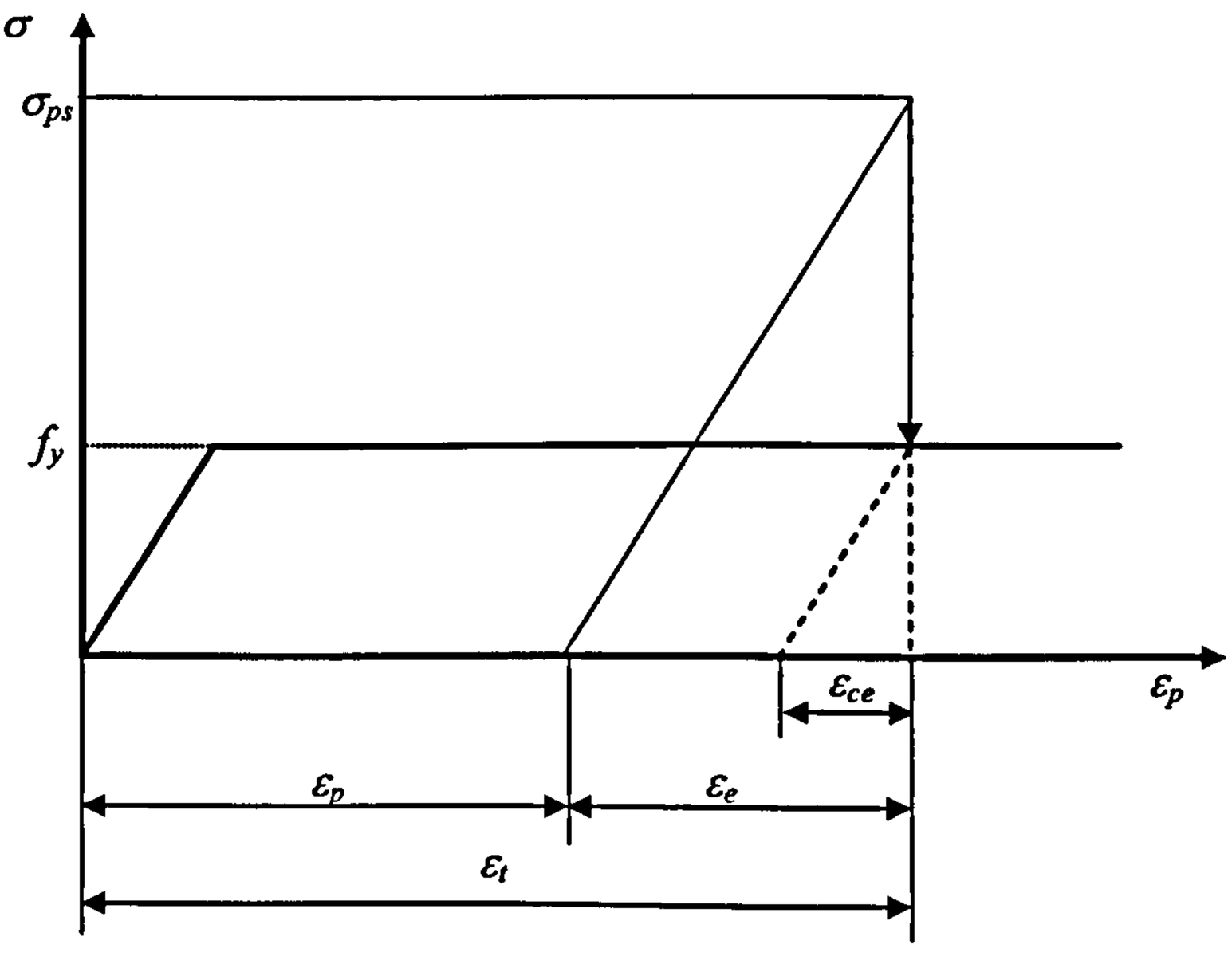

Figure 7.6 Bilinear stress-strain curve for steel bars

Plastic strain is stored as a state variable. Thus the elastic strain ε_e is obtained by subtracting the plastic strain ε_p from the total strain ε_t

$$\varepsilon_e = \varepsilon_t - \varepsilon_p \tag{7.16}$$

The elastic stress predictor is then obtained by multiplying the elastic strain by the modulus of elasticity of steel

$$\sigma_e = \varepsilon_e E_{st} \tag{7.17}$$

If this stress predictor violates the yield criterion the correction of plastic strain is performed resulting in corrected plastic strain

$$\varepsilon_{cp} = \varepsilon_t - \frac{f_y}{E_{st}} \tag{7.18}$$

7.4 Numerical results

The above described finite element and integration procedures have been implemented into a combined finite-discrete element code. Using this code the beams presented by Alca et al. [2] have been analysed. The details of the experiments can be found elsewhere [2]. However a summary of the experimental results is given below.

The experimental programme set up by Alca et.al.[2] included twelve high strength concrete reinforced beams being subjected to two point loading as shown in Figure 7.7. In this work only four beams were used, namely SL1, SH1, LL1 and LH1. The properties of these beams are summarised in Table 7.1.

Table 7.1 Beam geometry

Beam	Φ (mm)	b (mm)	d (mm)	h (mm)	L (mm)
SL1	16	150	230	282	3740
SH1	16	150	230	302	3740
LL1	35.7	335	515	630	8380
LH1	35.7	335	515	630	8380

Two letters and a number designate each beam. The first letter S or L refers to the small or large beam. The second letter L or H refers to low or high strength concrete. Alca et.al. [2] tested two beams of each type to failure (letter 1 or 2).
The material properties for the first set of beams are given in Table 7.2.

Table 7.2 Beam material properties

Beam	f_c' (MPa)	f_y (MPa)	ρ %
SL1	51.1	410	2.32
LL1	54.2	409	2.32
SH1	90.1	410	4.64
LH1	90.3	406	4.64

where f_c' is concrete cylinder strength, f_y is steel yield strength and ρ is reinforcement ratio.

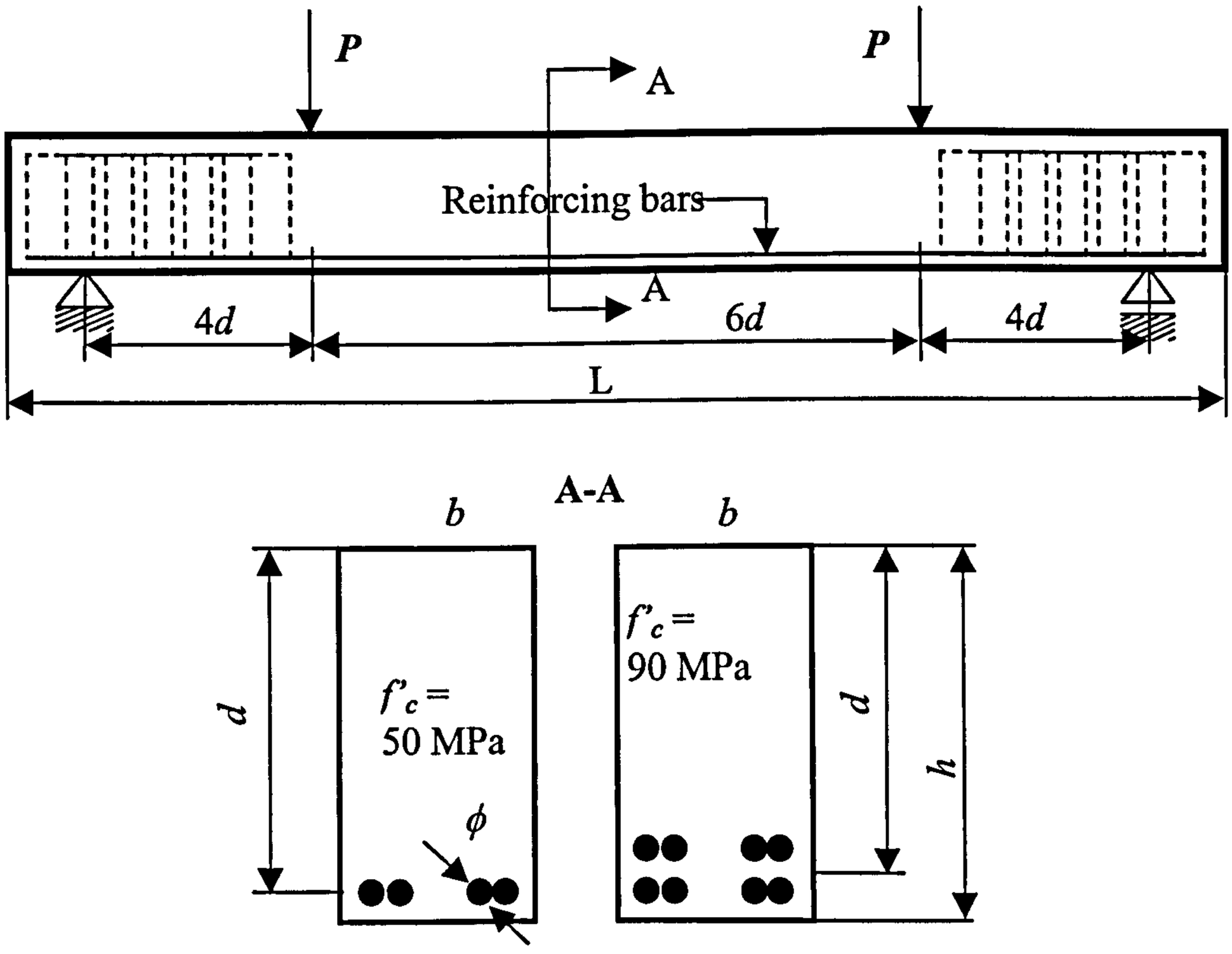

Figure 7.7 Loading arrangements, cross section and reinforcing bars for experimental beams

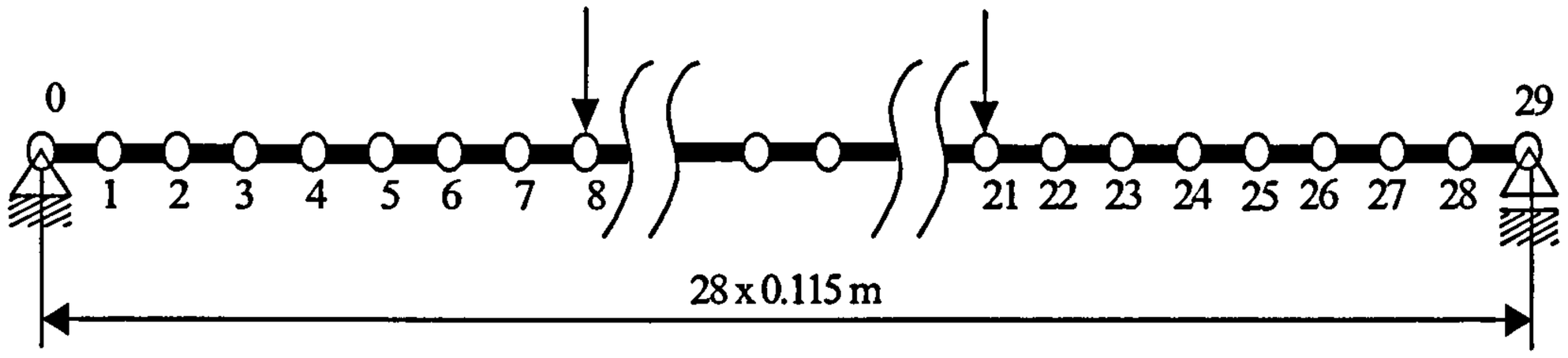

Figure 7.8 Finite element discretization of small beams

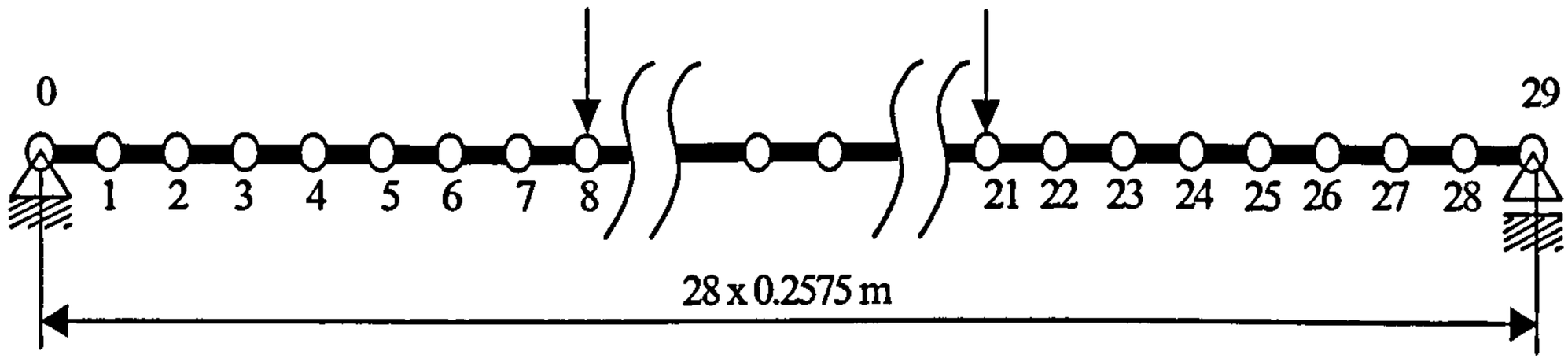

Figure 7.9 Finite element discretization of large beams

7.5 Combined finite element discrete element analysis

The above beams have been modelled using the combined finite/discrete element code. The beams, as in the experiments, are loaded by two concentrated loads. However, the beams are modelled from support to support and the overhang beyond the supports is ignored. The finite element discretization for small beams is shown in Figure 7.8. The finite element discretization for large beams is shown in Figure 7.9.

For all beams the following approximation for the stress-strain curve for concrete is adopted (obtained by curve fitting the experimental stress-strain curves, see Figure 7.10)

$$\sigma(\varepsilon) = E\varepsilon - \frac{E^2}{4f'_c}\varepsilon^2 \tag{7.19}$$

where f'_c is the concrete strength in bending.

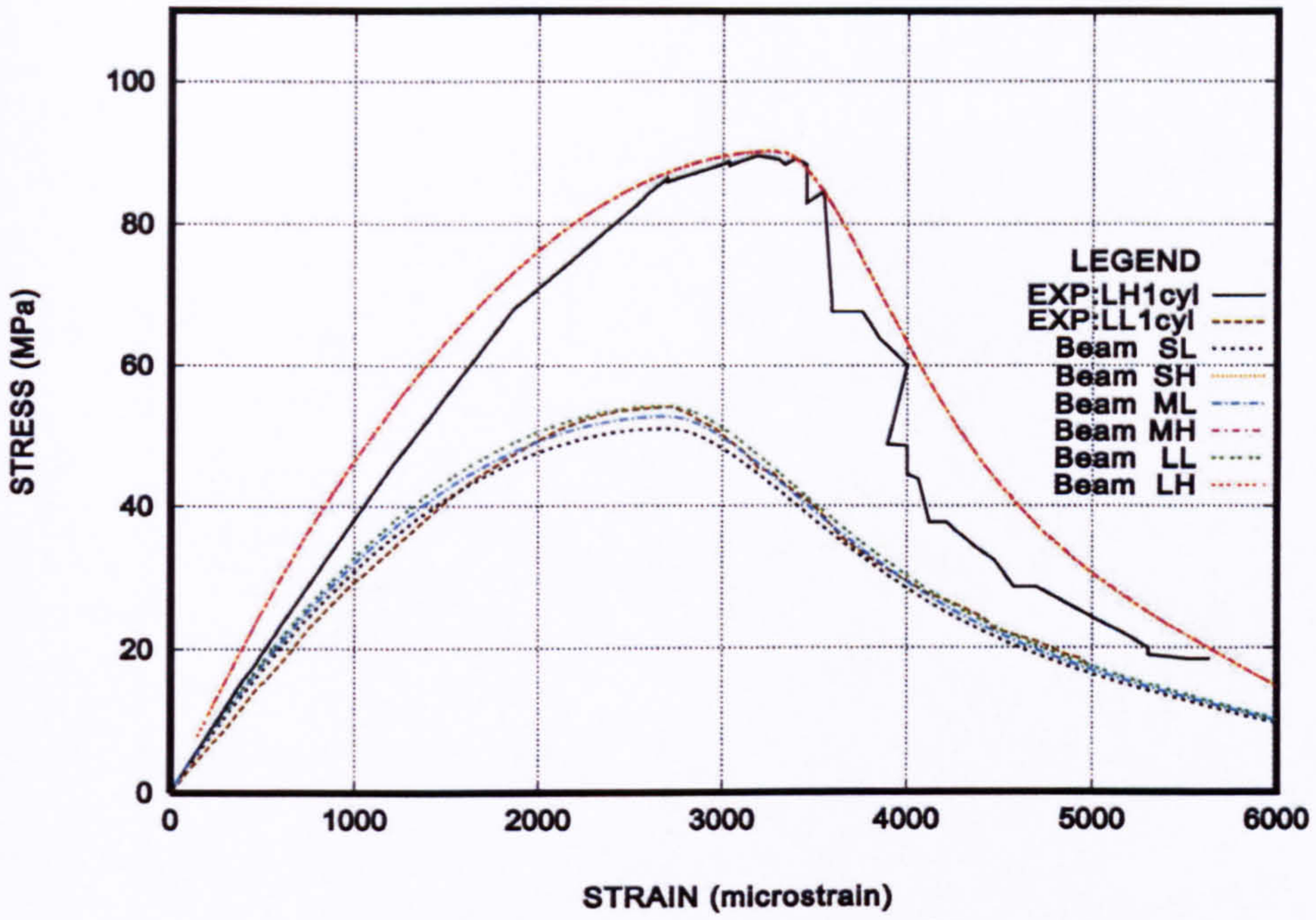

Figure 7.10 Adopted stress-strain curves for concrete

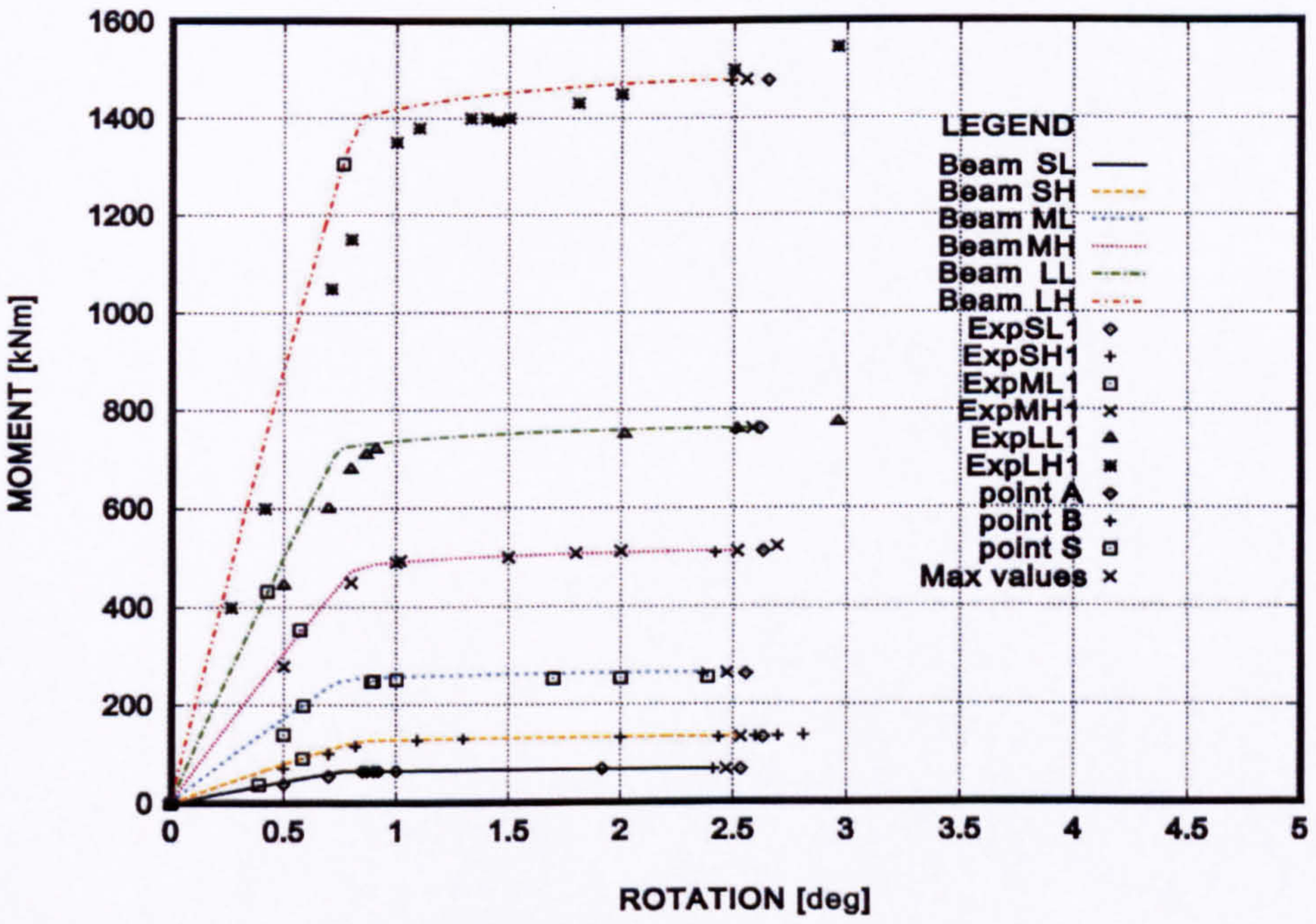

Figure 7.11 Moment rotation curves

For lower strength beams it is calculated using average concrete cylinder strength of beams, yielding

$$f_c^{'} = 0.85(51.1 + 54.2 + 52.7)/3 = 44.77\,\text{MPa} \tag{7.20}$$

where the factor 0.85 allows for the difference between the bending strength and the cylinder crushing strength. For higher strength beams concrete strength in bending is calculated from average concrete cylinder strength of beams, yielding.

$$f_c^{'} = 0.85(90.1 + 90.3 + 90.3)/3 = 76.70\,\text{MPa} \tag{7.21}$$

The above approximations of the stress-strain curves are in good agreement with stress-strain curves estimated from experimental measurements [1] using Smith and Orangun method [4], as shown in Figure 7.10.

The results of the above described combined finite-discrete element analysis for small and large beams for both lower and higher strength concrete are compared to experimental results from Alca et.al [2], Figure 7.11. For both experimental and numerical results the bending moment at midspan versus total angle change is shown. For all beams the total angle change in both experimental and numerical results is measured over a length of 3.7*d*.

In both cases good agreement can be seen between the two sets of results. This applies to both bending moments and ultimate rotations. The numbers for ultimate rotations are summarised in Table 7.3 In this table ω is the mechanical reinforcement ratio given by

$$\omega = \frac{A_s f_y}{f_c^{'} bd} \tag{7.22}$$

where A_s = the area of steel reinforcement, b = beam width , d = beam effective depth, while $f_c^{'}$ is concrete cylinder strength and f_y = steel yield strength.

It is evident from this table that the numerical model employed reproduces the experimental results by Alca et.al [2], i.e. both experimental and numerical results shown indicate no significant size effect on the rotational capacity of the beam .

Table 7.3 Comparison of ultimate rotations

Beam	Experimental			Numerical	
	ω	θ_u (rad)	$\theta_u \omega / 3.7$	θ_u (rad)	$\theta_u \omega / 3.7$
SL1	0.186	0.0448	0.00225	0.04606	0.00232
SL2	0.186	0.0604	0.00304	0.05370	0.00273
SH1	0.211	0.0518	0.00295	0.04656	0.00266
LL1	0.183	0.0517	0.00256	0.05510	0.00272
LH1	0.219	0.0517	0.00297	0.0495	0.00293

7.6 Conclusions

It is worth mentioning that the proposed algorithmic solutions for the combined finite-discrete element analysis of reinforced concrete structures also include failure and collapse. This is due to implicit inclusion of elements breaking apart followed by contact impact solutions resolving progressive collapse, which are both standard features of the combined finite-discrete element method. The finite element presented here is relatively simple and inexpensive in terms of CPU time, thus enabling the same finite element mesh to be used for both finite element analysis and contact interaction [3]. The results obtained agree well with analytical results for linear behaviour. In addition combined finite-discrete analysis of non-linear behaviour and failure reproduces the experimental results of Alca et.al [2]. The proposed numerical integration over the reinforced cross section incorporates both bending and axial force and is suitable for both beams and columns. However, the proposed model does not take into account the influence of shear reinforcement and/or links.

Hence, it is can be concluded that the proposed model gives accurate approximation of the rotational capacity provided that the influence of links and/or shear reinforcement does not significantly influence concrete properties in compression zone.

7.7 References

1. W.G.Corley, "Rotational capacity of Reinforced Concrete Beams", *Jour. Of the Structural Division, Proc. ASCE pp 4939-4941* (1966)

2. N.Alca, D.B.A.Scott, J.G.MacGregor, "Effect of Size on Flexural Behaviour of High Strength Concrete Beams" *ACI Structural Journal* **94(1)** *pp 59-67 (*1997).
3. A.Munjiza, K.R.F.Andrews, J.R. White, "Discretized Contact Solution for combined finite-discrete Method", *5th ACME Conf. London UK* pp 96-100, (1997).
4. R.G.Smith, C.O.Orangun, "Evaluation of the Stress-Strain Curve of Concrete in Flexure Using the Method of Least Squares", *ACI Journal* **66(7)** *pp 553-559 (*1969)

Chapter 8

Validation of the finite/discrete element using R.C. dynamic loading experiments

8.1 Introduction

The collapse of the flats at Ronan Point[1] in the U.K., built using the Larsen-Nielson construction system, was caused by a gas explosion resulting in the progressive collapse of the South East corner of the block. This incident prompted engineers to recognise the phenomena of progressive collapse and initiate its inclusion into the design codes. More recent examples of progressive collapse include the Alfred P Murrah building in Oklahoma City. Here a vehicle bomb destroyed three key supporting columns to induce progressive collapse. The recent destruction of the WTC towers in New York is also an example of a progressive collapse on a much larger scale. The combined effects of the plane impact and the high temperatures resulting from the burning aviation fuel acutely damaged the structure's ability to support itself below the point of impact. Thus the weight of the upper floors induced a progressive collapse [2]. The structural components from the upper floors impacted with structural component from the lower floors. In all these examples the inertia effects resulting from the fracture and collapse of the structural components combined with contact impact played a significant role in the progressive collapse.

These and similar such events have added to the need to develop accurate computational tools to analyse the failure modes of structures under hazardous loads. Such analysis is an invaluable tool during the design stage. It can help to prevent a progressive collapse all together. However in the event of failure and collapse such analysis would be useful in the planning of safety corridors, evacuation procedures and systems.

It could also be used to position vital equipment and data in those areas of the building which are not likely to suffer great damage. The survivability and safety considerations of the collapse on the building in question together with adjacent buildings could also be evaluated for use in insurance appraisals.

It is worth noting that any comprehensive failure simulation needs to address the elastic and elasto-plastic behaviour of structural components including failure, fracture, fragmentation, transient motion, contact impact, collapse, energy dissipation mechanisms and the state of rest. To this end a recently developed state of the art combined finite–discrete element method (FEM/DEM) offers a capability to attend to all of these.

An element has been presented and successfully tested for the case of a reinforced concrete beam, which is subjected to static loading conditions. The aim of the research here presented in this chapter is to further assess the accuracy provided by the use of this simple element when used under the milieu of dynamic loading. This is done using a computer code based on the combined finite/discrete element method.

A discrete element system comprises of any number of separate and distinct solids interacting with each other in a defined space. Each of these bodies occupies only one single point in that space at any particular point in time. In such a system contact interaction and contact detection are important factors in the interacting behaviour of each of the bodies. In the case of 2D contact interaction is understood by integrating the governing equations and solving for translation and rotation about the centre of mass. For 3D discrete element systems the task is complicated by the finite rotations about the centre of mass of the discrete element. The algorithm used for contact detection and contact interaction has been described chapter 6 [4,5,6,7,8].

8.2 Finite element analysis

The element adopted is shown in Figure 1. For the purposes of 3D analysis the element has six degrees of freedom and is defined by end nodes *i* and *j*. Each node has three rotational as well as three translational degress of freedom. The rotational degrees of freedom are eliminated through static condensation.

In order to eliminate much of the complexity of calculation without any sacrifice in terms of accuracy, it is convienient to ensure that the static condensation does not involve any matrix inversion. It should be noted that where one of the element nodes is rotated, the bending moment on the other element node is kept at zero.

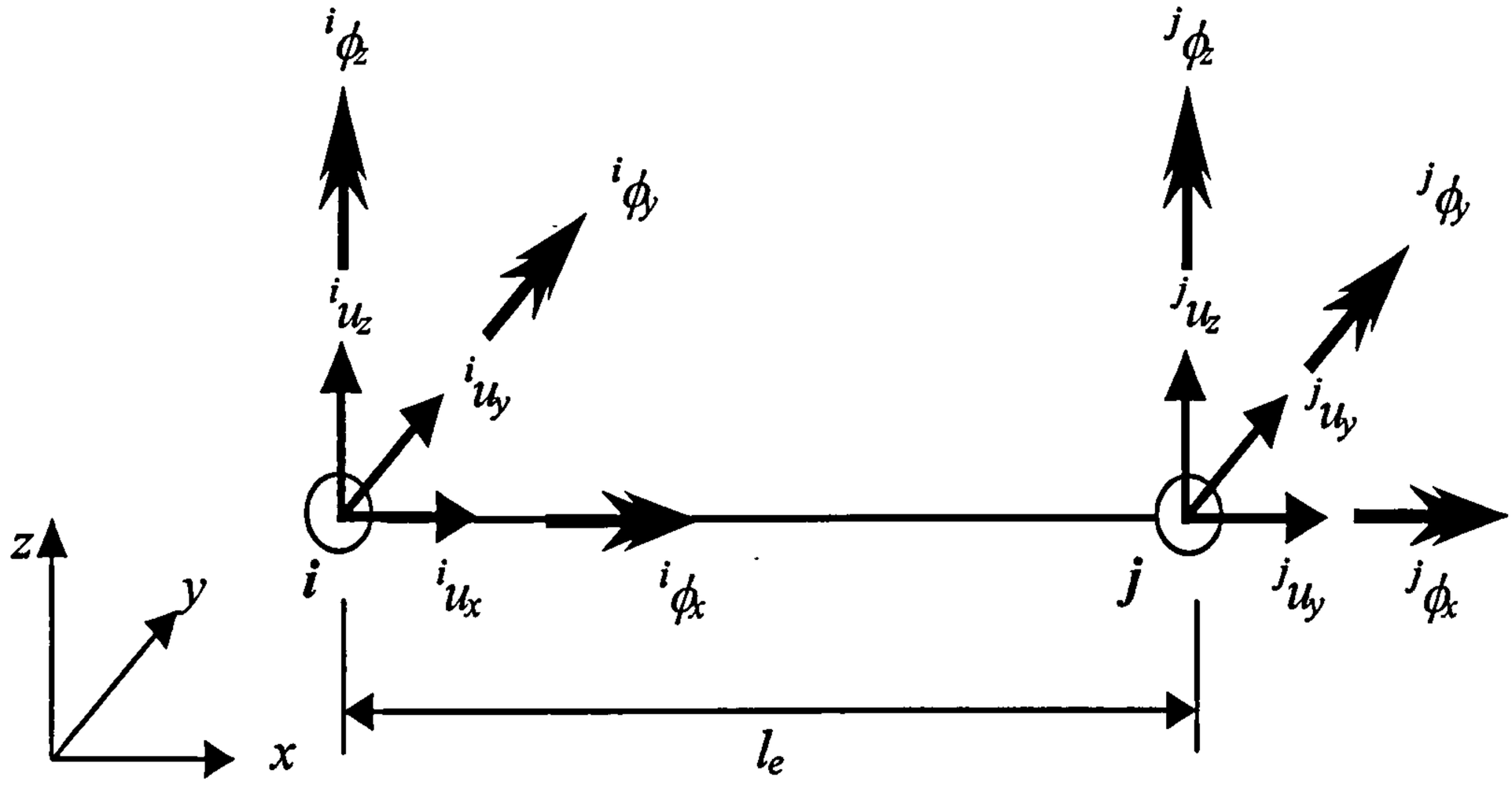

Figure 8.1 Finite element with degrees of freedom

This eliminates the use of matrix inversion when applying static condensation. Hence the equation of motion is represented by

$$\mathbf{f(t)} = \hat{\mathbf{K}}\mathbf{u} + \hat{\mathbf{M}}\ddot{\mathbf{u}} + \mathbf{C}\dot{\mathbf{u}} \tag{8.1}$$

where $\hat{\mathbf{K}}$ is the condensed stiffness matrix, $\mathbf{K}$ is the stiffness matrix, $\hat{\mathbf{M}}$ is the lumped mass matrix and $\mathbf{C}$ is the damping matrix. These are fully expressed as

$$\mathbf{f(t)} = \begin{bmatrix} f \\ \vdots \\ M \\ \vdots \end{bmatrix} \quad \mathbf{u} = \begin{bmatrix} u \\ \vdots \\ \theta \\ \vdots \end{bmatrix} \quad \hat{\mathbf{M}} = \begin{bmatrix} m_1 & 0 & 0 & 0 \\ 0 & m_2 & 0 & 0 \\ 0 & 0 & m_3 & 0 \\ 0 & 0 & 0 & m_4 \end{bmatrix} \quad \mathbf{K} = \begin{bmatrix} \mathbf{K}_{tt} & \vdots & \mathbf{K}_{u\theta} \\ \cdots & \vdots & \cdots \\ \mathbf{K}_{\theta u} & \vdots & \mathbf{K}_{\theta\theta} \end{bmatrix} \tag{8.2}$$

where, u and θ represent the translational and rotational degrees of freedom respectively. $\mathbf{K}_{\theta\theta}$ is a diagonal matrix. The damping matrix can be taken as zero or the damping coefficients can be calculated by standard methods.

8.3 SFIT Experiments on impacting concrete beam

Experiments carried out at the Institute of Structural Engineering of the Swiss Federal Institute of Technology [9,10,11,12] (Zurich) are used for the purposes of comparison and validation. These experiments tested a total of twenty-four beams. The beams were hinged at one end whilst the other end was raised and then released to drop upon a shock absorber. This action was noted as a cost effective way of simulating impact loading upon the beam [13]. The force-displacement properties of the shock absorber were investigated using a truss with a concrete end mass. This truss was raised and released in the same way as the beams prior to landing on the shock absorber. The effect of varying several parameters were studied including beam mass, length, reinforcement, shock absorber type, the number of drops and the beam cross section.

Only one of the beams (beam B1) is modelled in this work as this is in line with the stated aim of the chapter. The numerical simulation will first concentrate on investigating the force displacement properties of the shock absorber. The results are then used to accurately predict the reactive force provided by the shock absorber upon landing of the beam. The beam is discretised and loaded in a similar way to the truss. The strain-time relationship in the reinforcement and the deflection of the beam is computed at different points along its length. A deflection profile is also enumerated. The results are then compared to the experimental results in order to verify the effectiveness of the element when used in dynamic situations.

Beam B1 is chosen for the numerical simulation. The properties of this beam are described in Table 1.1. Type IIIa naturhart reinforcing steel is used [14, 15].

Table 1.1 Beam Properties

$(d*b)$m	Length (m)	Mass (kg/m)	Upper Rein.	Lower Rein.	EI (kNm^2)	f_{cu} (N/mm^2)	f_{cw} (kg/mm^2)	f_{sy} (N/mm^2)
0.3 x 0.4	8.15	300	3ϕ10	3ϕ16	32998	30	35.3 (at 5 days)	550

where d = depth of the beam, b = breadth of the beam, E = Youngs modulus, I = second moment of inertia, f_{cu} = concrete strength, f_{cw} = concrete cube strength and f_{sy} = reinforcement yield strength.

The experiment set up is shown in Figure 8.2.

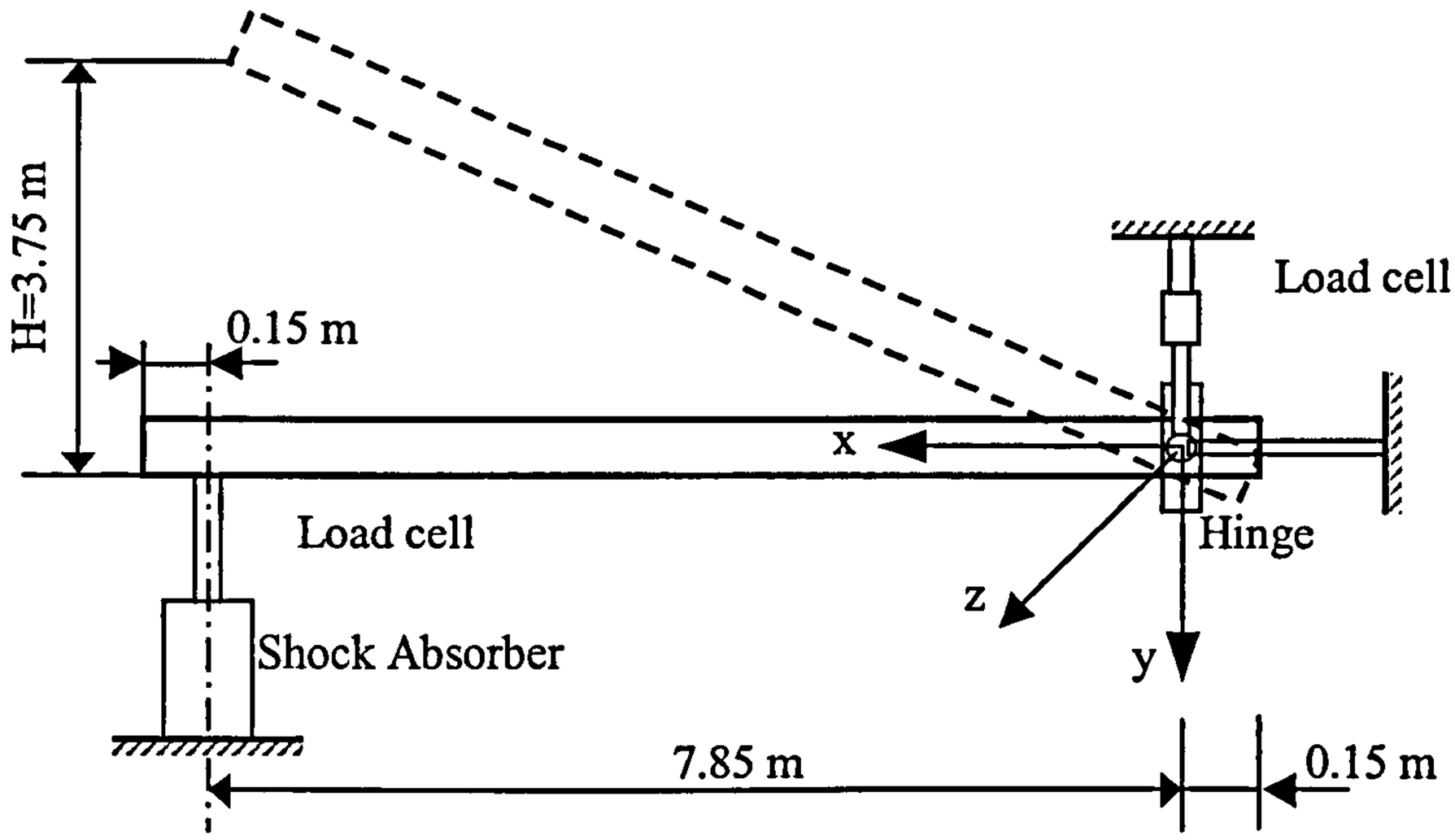

Figure 8.2 Experimental set Up for beam B1

The beam is raised by means of an overhead crane and then dropped from a height of 3.75 m onto a shock absorber. Only one single drop takes place. The authors state that this way of simulating impact loading has the advantage of low cost and mechanical simplicity.

A ringfederpuffer (Spring) type shock absorber was used in the case of this particular beam. This shock absorber can endure a maximum force of the order of 3000 kN. A small plate of mass 57 kg was placed at the base of the shock absorber. The impact force of the beam was measured using three force transducers, numbered 17 to 19, positioned underneath the plate. The system is illustrated in Figure 8.3.

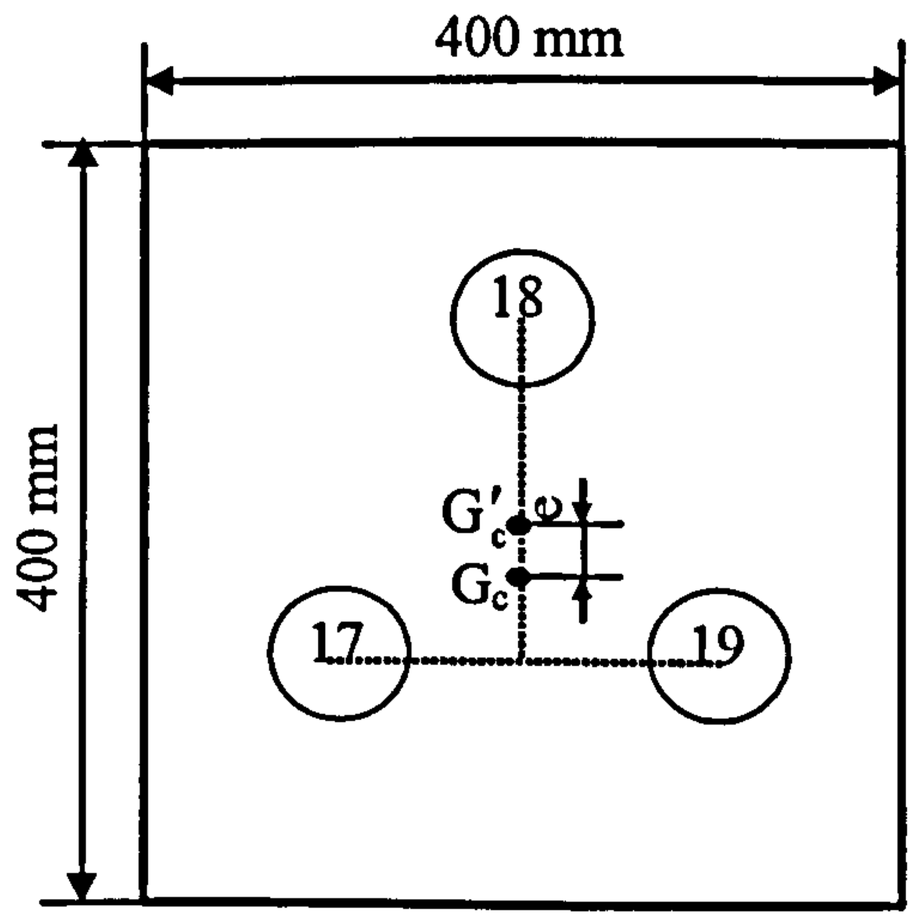

Figure 8.3 Landing plate covering three force transducers

The properties of this shock absorber were investigated using a truss with a concrete block positioned at its end, as shown in Figure 8.4. The mass of the block and the truss were 997 kg and 342 kg respectively. The drops heights used were limited up to 0.75 m.

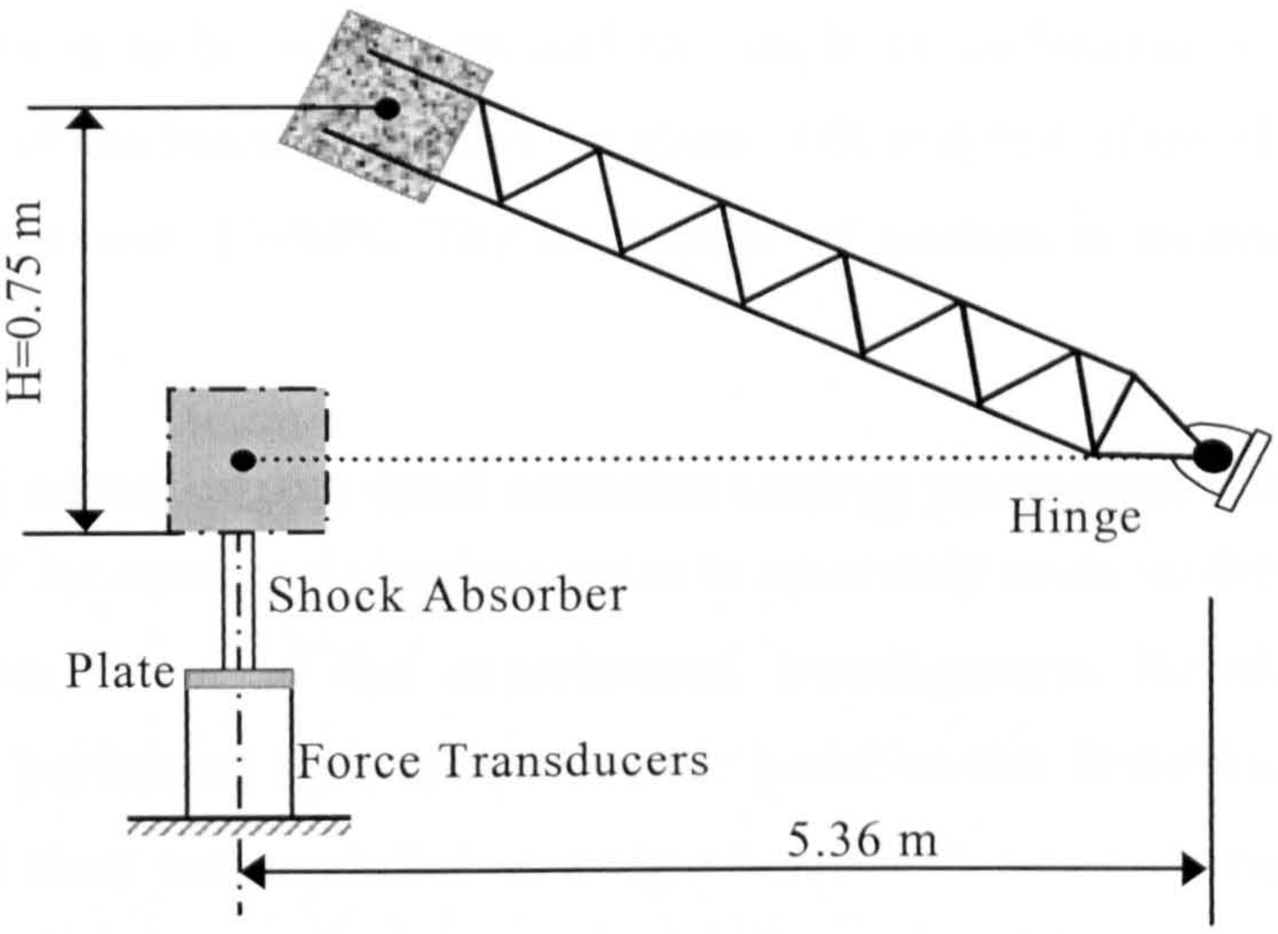

Figure 8.4 Experimental set up to test shock absorber properties

Difficulties were noted in positioning the shock absorber at the gravity centre of the plate, G_c. The impact point of the beam was also difficult to position at the gravity centre. Hence an effective centre of gravity, G'_c, with eccentricity, e, of 29 mm from G_c, was adopted. For these reasons each of the transducers did not register the same force at the time of impact. Transducer number 18 registered 50% of the impact force, while numbers 17 and 19 registered 22% and 28% respectively. One further reason for this, which was cited by the authors, was the difference in distance of each transducer from the effective centre of gravity. The relationship between force, displacement and time for the shock absorber was obtained.

Once beam B1 had landed on the shock absorber bending was induced almost instantaneously and vibration ensued. After the vibration passes the maximum plastic deflection is measured as 590 mm and the ultimate bending moment is found to be 90 kNm. Cameras using high-speed exposures were employed to photograph the beam at the rate of 1000 exposures per second. This is used to plot the deflection of the beam and the deflection at certain points along the beam as a function of time. Maximum deflection is reached at a time of 0.164 seconds after release and occurs approximately 4m from the hinge. The impact reaction at the support was found to be 860 kN and the reaction at the joint was found to be ± 88 kN. This impact reaction was found to have a linear relation with the drop height to the order of $H^{3/5}$. A similar linear relation, also of

the order of $H^{3/5}$, was found to exist between the impact reaction and the mass. The peak accelerations were found to be higher for those points along the beam, which were closer to the impact location. Minor shear cracking was observed in beam B1 with the crack-width measured to be 1/100 mm and the angle of inclination to be 85°. The energy dissipation of the beam is found to be about 70% and that of the shock absorber was found to be between 15-30%. The total angle of rotation is measured as 0.422 radians.

8.4 Numerical simulation and results using program Y-code

The first task of the numerical simulation was to accurately simulate the properties of the shock absorber found in the experimental investigations. Simulation of the impacting truss is performed by a computer code based on the finite/discrete element method. The steel truss was modelled as a rigid beam with seven elements. The end element was given greater mass, thus representing the mass of the concrete block. The length of the truss is 5.36 metres.

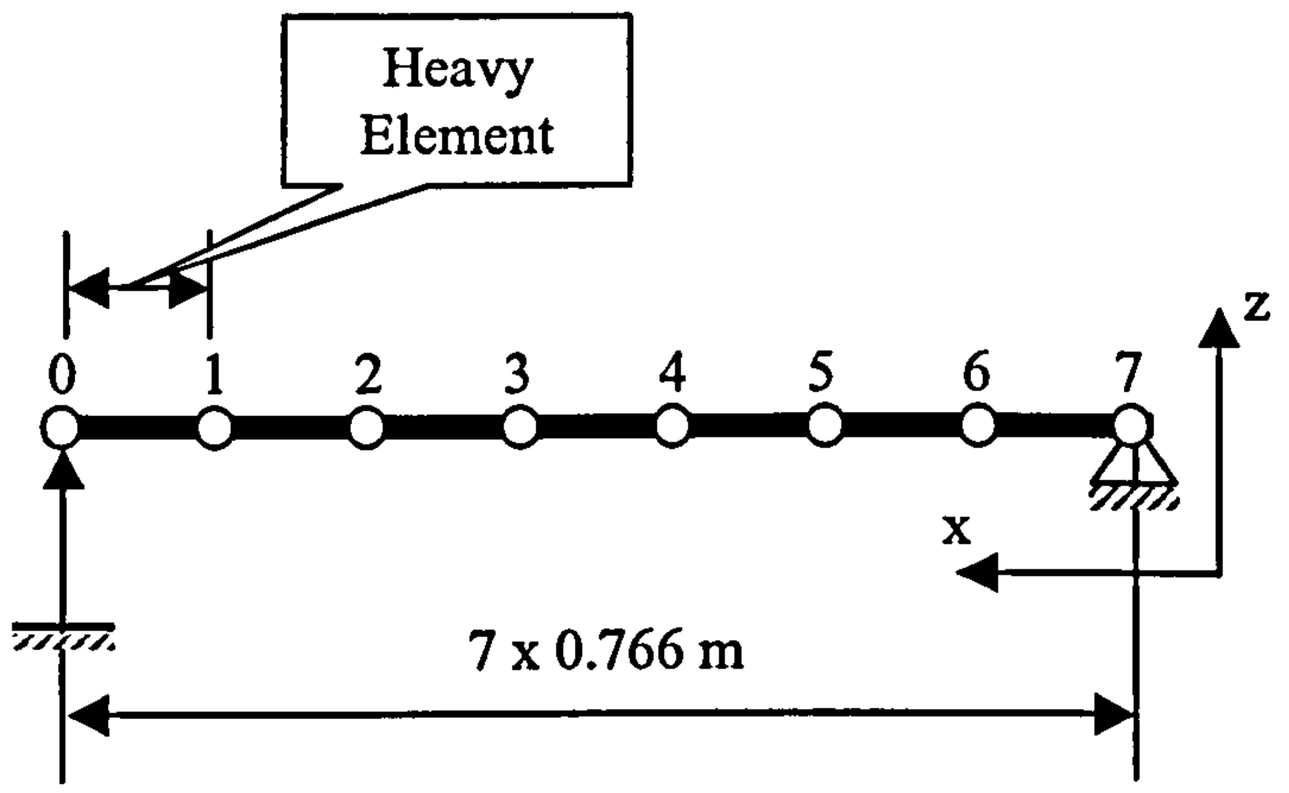

Figure 8.5 Discretized truss

A velocity field is applied along the truss with maximum velocity at node 0 and zero velocity at the hinge. Drop heights of 0.30, 0.65 and 0.75 m were simulated. The velocity formulation for the nodes along the truss is now derived. The potential energy, E_p for the complete length is given by

$$E_p = \int_0^L \frac{h}{L} \cdot x\rho g \, dx = \frac{1}{2} ghL\rho \tag{8.3}$$

The kinetic energy for the whole beam length is determined as

$$E_k = \int_0^L \frac{1}{2} \cdot \frac{v^2}{L^2} x^2 \rho \, dx = \frac{1}{6} v^2 L\rho \tag{8.4}$$

Thus by equating the kinetic and potential energies the formulation for velocity arrived at is as equation (8.5)

$$v = \sqrt{3gH} \tag{8.5}$$

Hence the maximum velocity is calculated for the truss at a drop height of 0.75 m is calculated as follows

$$v = \sqrt{3 \times 9.81 \times 0.75} = 4.698\ m/s^2 \tag{8.6}$$

The rotational velocity, ω is now easily derived as

$$\omega = \frac{v}{L} = \frac{1}{5.36}\sqrt{3gH} = 0.876 rad/s \tag{8.7}$$

The results for the force-time, displacement-time and force displacement properties for the shock absorber are compared in Figure 8.6 to Figure 8.8. Figure 8.6 shows the force-time relationship of the shock absorber obtained for drop heights of 300 mm, 650 mm and 750mm. The experimental result for a drop height of 650 mm is also shown on the plot. A good agreement between both experimental and numerical plots is seen.

The displacement-time relationships for the same drop heights, of 300mm, 650mm and 750 mm are plotted in Figure 8.7. Here good agreement is also found between numerical and experimental results plotted for the drop height of 650 mm. Larger displacements are seen to occur as the drop height increases. Figure 8.8 shows the force displacement relationship of the shock absorber. In this case the drop heights of 300, 650 and 750 mm were also investigated. Here the result for the drop height of 750 mm is compared with the experimental result. The comparison shows good agreement between the two.

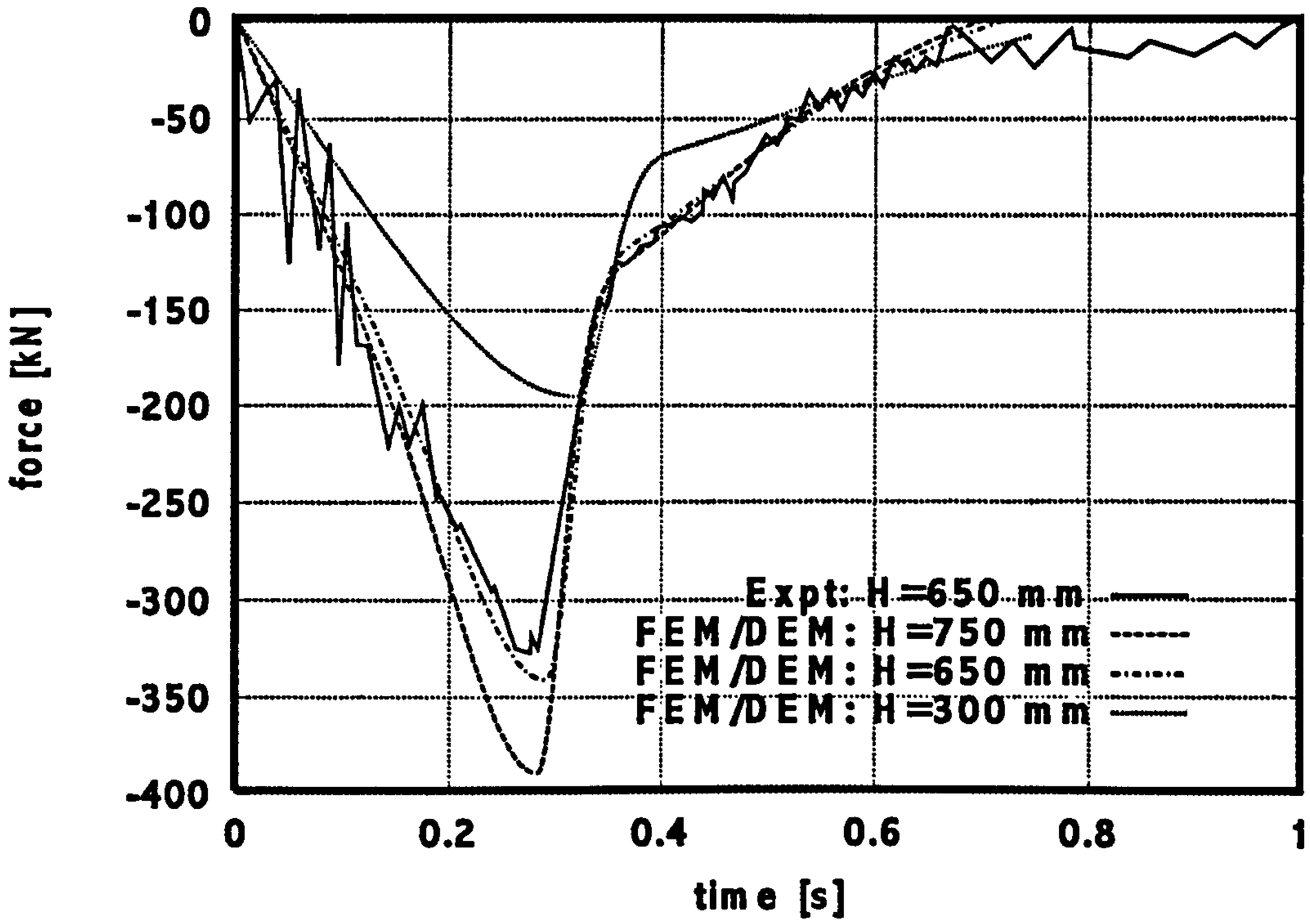

Figure 8.6 Force-time relationship of the shock absorber for various drop heights

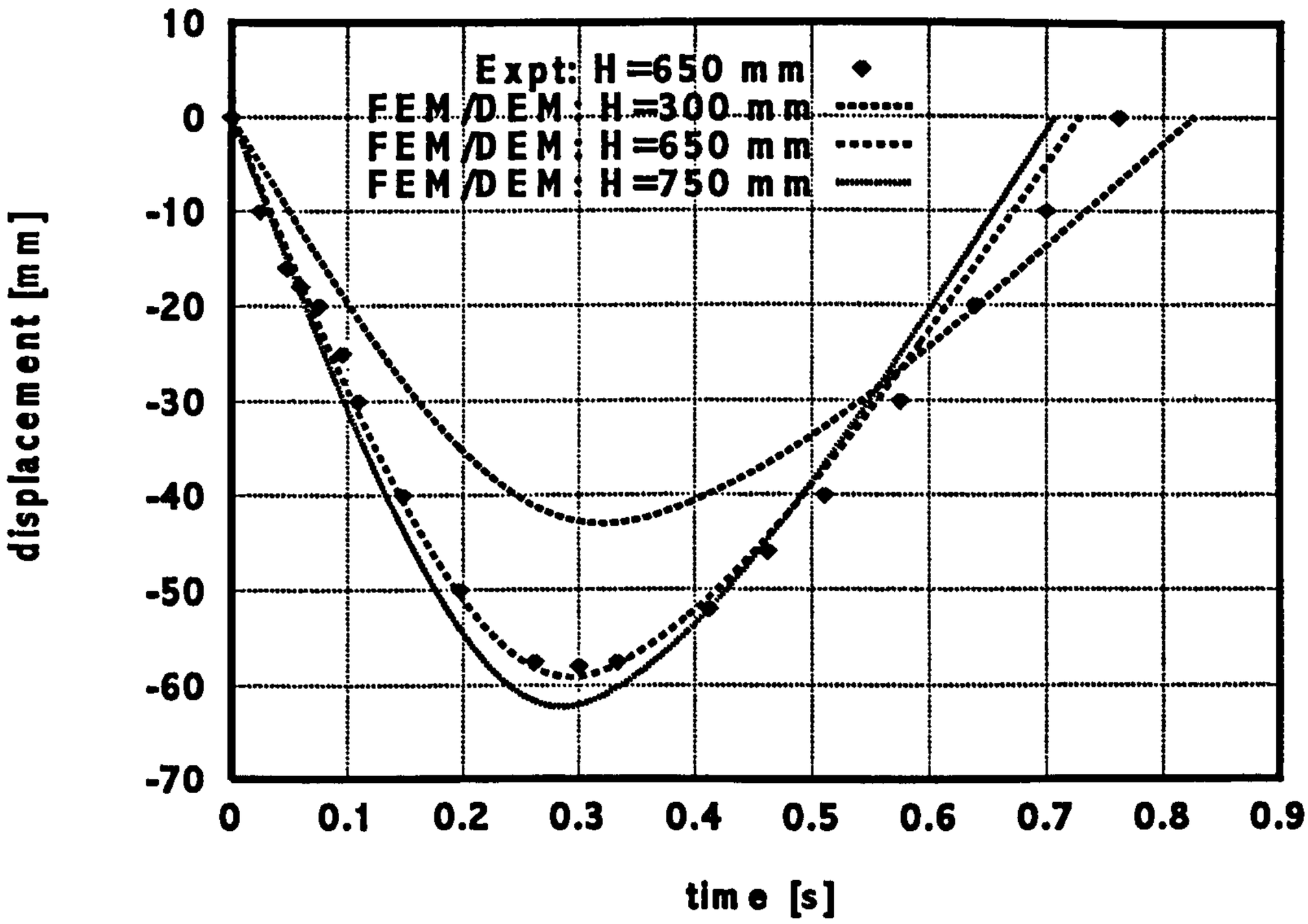

Figure 8.7 Displacement-time relationship of the shock absorber for various drop heights

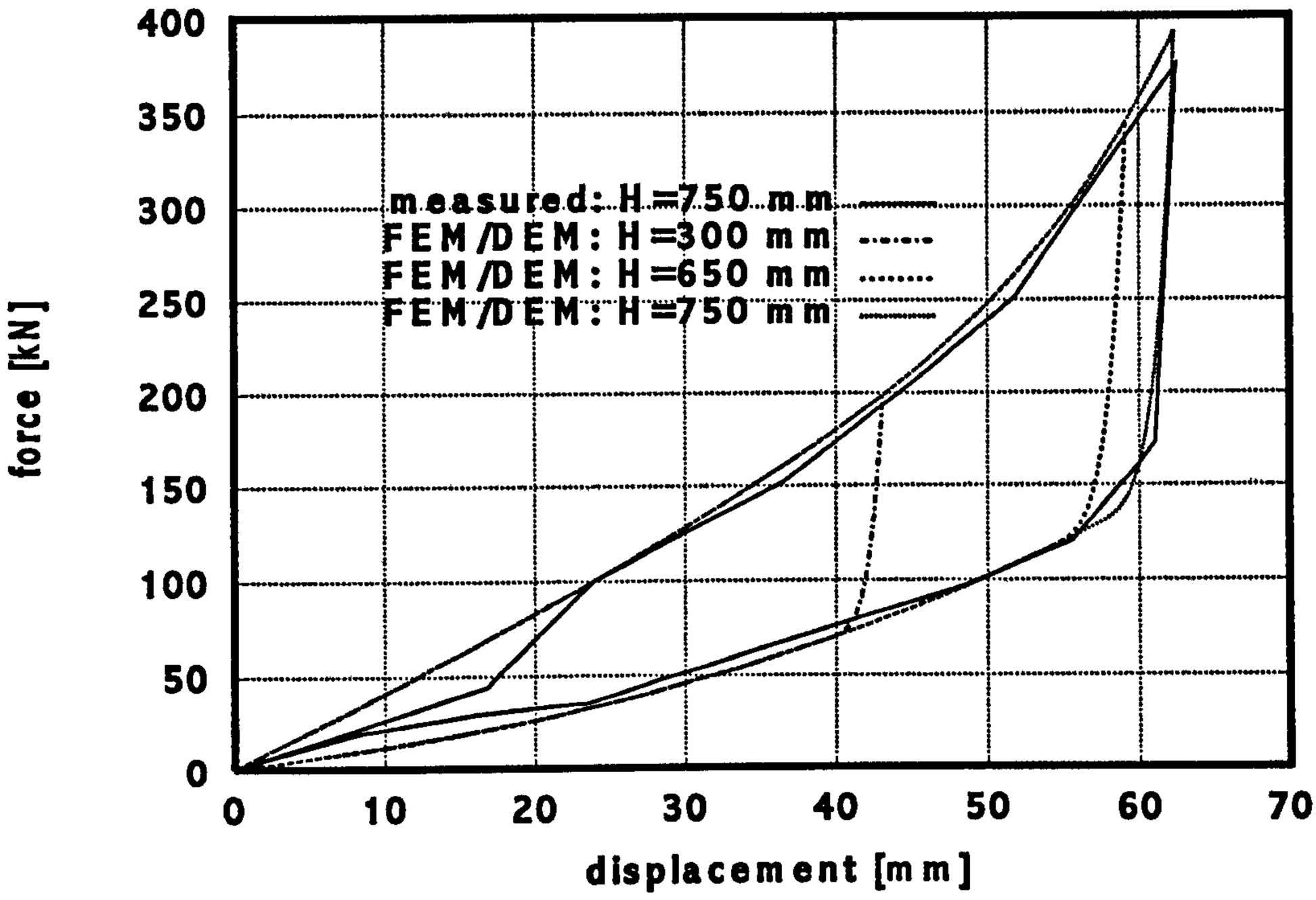

Figure 8.8 Force-displacement relationship of the shock absorber for various drop heights

The same computer code is then used to model the beam impact. The beam is discretized into 57 nodes and 55 elements as shown in Figure 8.9.

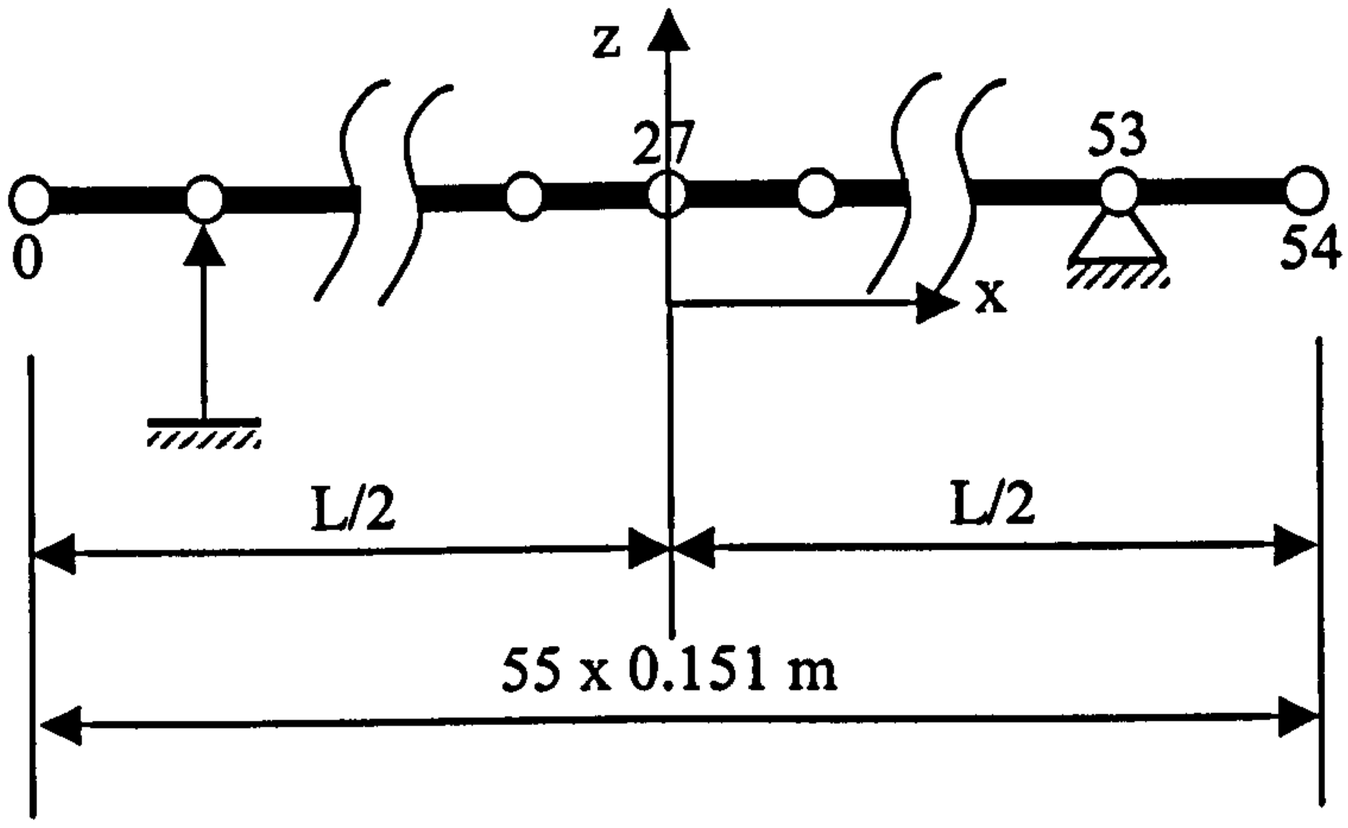

Figure 8.9 Discretized beam B1 with boundary conditions

The mass of each node is taken to extend across half the element on either side as illustrated in Figure 8.10.

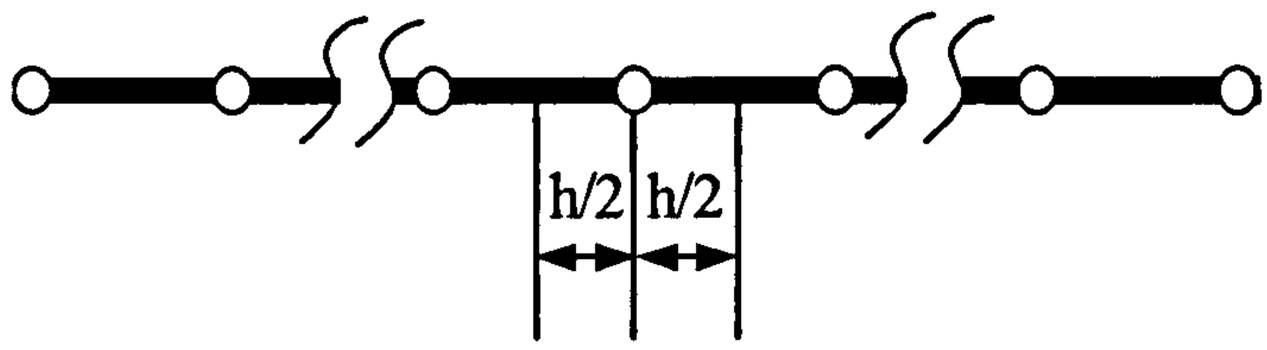

Figure 8.10 Nodal mass

The mass of the can be found from the following expression

$$m = \sum_{elements} \rho b d \frac{h}{2} \tag{8.8}$$

The dropping action performed in the experiment is modelled by applying a velocity field along the beam. This is illustrated in Figure 8.11. The maximum velocity is applied at the free end and this decreases along the nodes with zero velocity at the hinge. The impact between the beam and shock absorber is modelled through the contact of the beam and shock absorber nodes. A reactive force is also applied at this location in order to simulate the properties of the shock absorber.

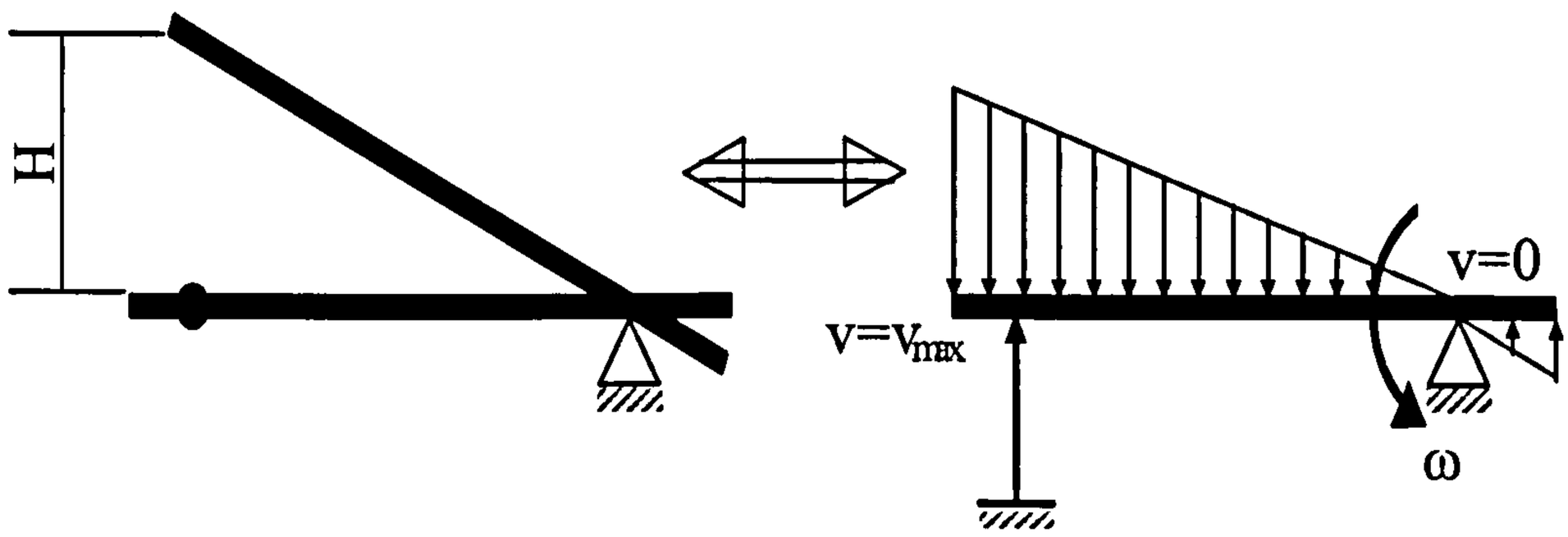

Figure 8.11 Initial conditions for beam B1

The beam is assumed to fall as a rigid body and as such the moments due to beams self weight, are so small that the elastic energy in the beam is neglected. This assumption is validated by the following mathematical analysis.

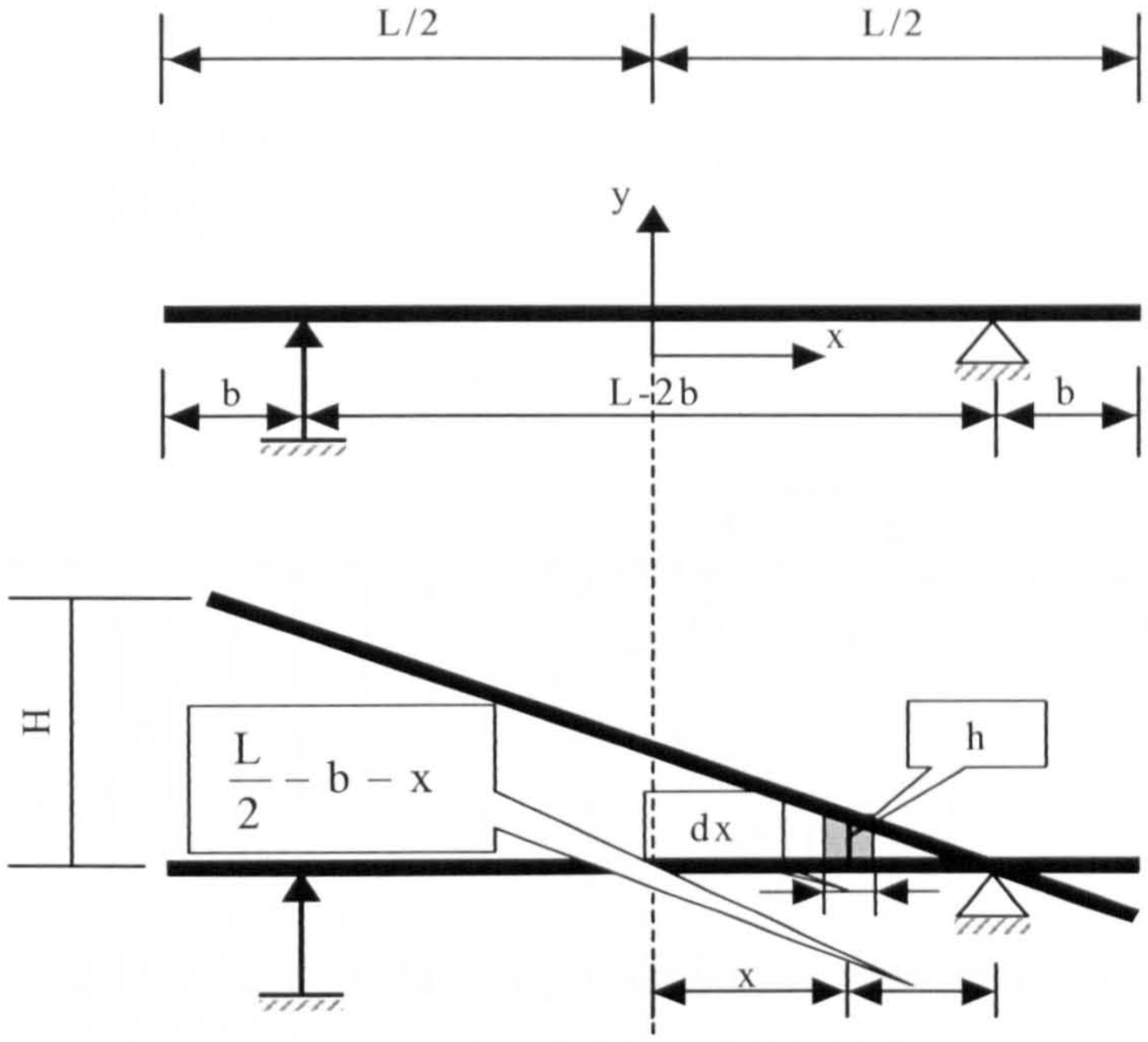

Figure 8.12 Beam B1 at initial drop height

The potential energy, E_p for the complete beam length, shown in Figure 8.12, is given by

$$E_p = \int_{-L/2}^{L/2} \rho g h \, dx \tag{8.9}$$

where ρ is the mass per unit length of the beam. The height of the beam, h at a distance x from the centre line is given by

$$h = \frac{H}{L-2b}\left(\frac{L}{2} - b - x\right) \tag{8.10}$$

Substituting equation (8.10) into equation (8.9) gives

$$E_p = \frac{H\rho g}{L-2b}\int_{-L/2}^{L/2}\left(\frac{L}{2} - b - x\right)dx \tag{8.11}$$

This can be further simplified to

$$E_p = \frac{H\rho g}{L-2b}\left[\frac{L^2}{2} - bL\right] \tag{8.12}$$

where ρ is the mass per unit length calculated as follows

$$\rho = A_s \rho_c = 0.4 \times 0.3 \times 2400 = 288 \text{ kg/m length} \tag{8.13}$$

where A_s is the cross sectional area and ρ_c is the concrete density

By substituting the values the value of the potential energy is obtained

$$E_p = \frac{3.75 \times \rho \times 9.81}{8.15 - 2 \times 0.15}\left[\frac{8.15^2}{2} - 0.15 \times 8.15\right] = 43173.81\text{Nm} \tag{8.14}$$

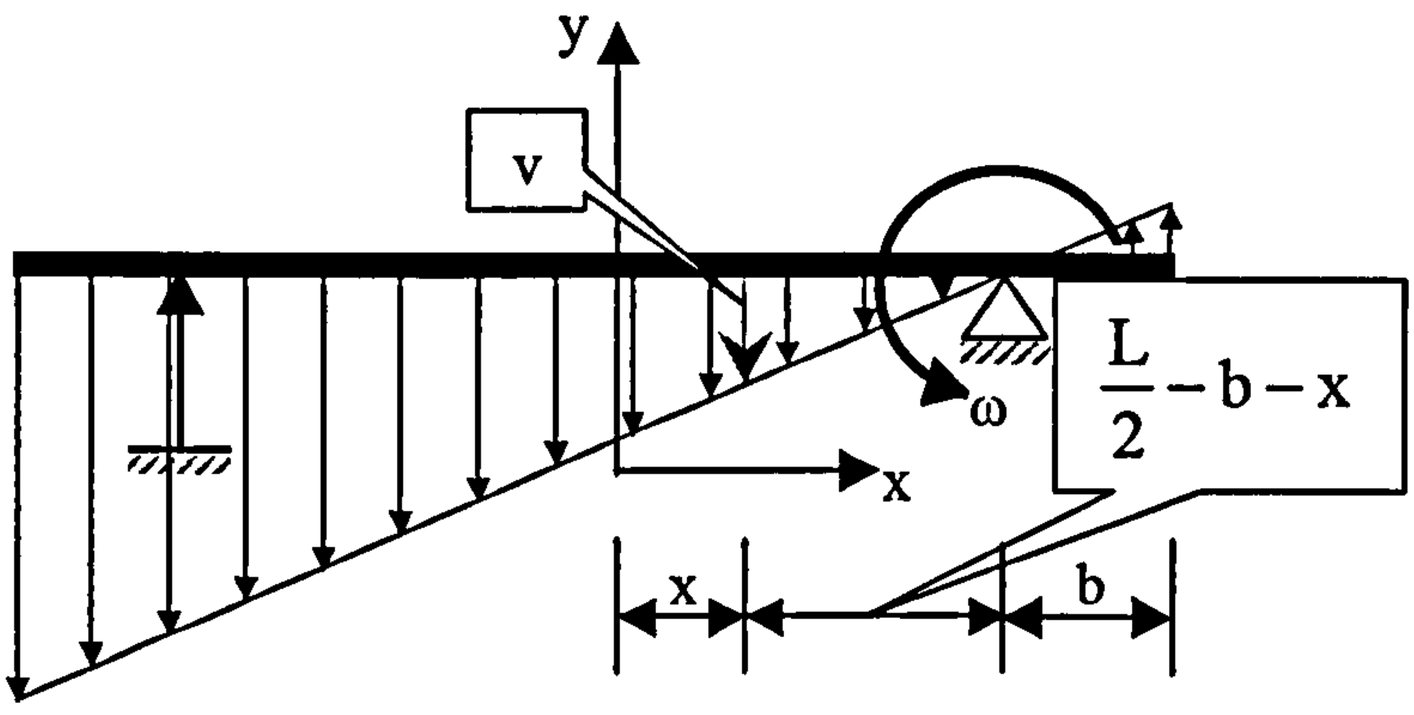

Figure 8.13 Velocity field along beam B1 just prior to landing

The kinetic energy for the whole beam length just prior to landing is determined as

$$E_k = \int_{-L/2}^{L/2} \frac{1}{2}\rho\omega^2 \tag{8.15}$$

The velocity v at distance x from the centre line of the beam is given by

$$v = \omega\left(\frac{L}{2} - x - b\right) \tag{8.16}$$

Hence upon substituting equation (8.16) into equation (8.15) the kinetic energy can be found from

$$E_k = \int_{-L/2}^{L/2} \frac{1}{2}\rho\omega^2\left(\frac{L}{2} - x - b\right)^2 \tag{8.17}$$

This simplifies to

$$E_k = \rho\omega^2\left[\frac{L^3}{3} + b^2 L\right] \tag{8.18}$$

Equating the kinetic and potential energy gives the angular velocity as

$$\omega = \sqrt{\frac{3gH}{L^2 + 3b^2}} = 1.288\,rad/s \tag{8.19}$$

where $L = 8.15$ m and $b = 0.15$ m.

The angular acceleration, ε, is found by taking moments about the supports. The forces are illustrated in Figure 8.14.

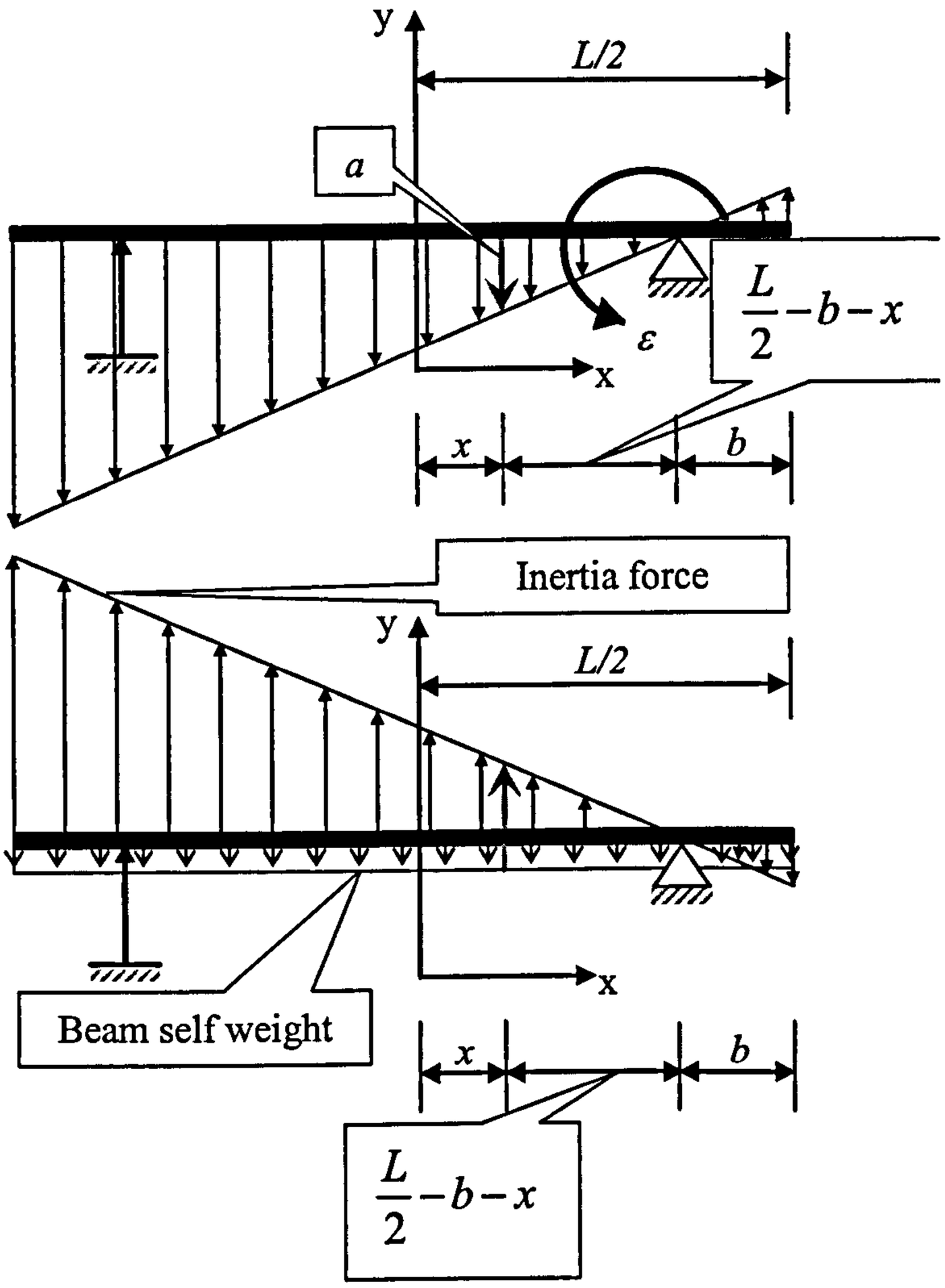

Figure 8.14 Force fields along beam B1

The acceleration at a point x from the centre line is given by

$$a = \varepsilon\left(\frac{L}{2} - x - b\right) \tag{8.20}$$

The self weight, W is given as

$$W = \rho g \tag{8.21}$$

and the inertia forces, F_I are given by

$$F_I = \rho \varepsilon x \tag{8.22}$$

Assuming anticlockwise to be positive the resultant moment equation is

$$\int_{-L/2}^{L/2}\left(\rho g\left(\frac{L}{2}-b-x\right)-\rho\varepsilon\left(\frac{L}{2}-b-x\right)\left(\frac{L}{2}-b-x\right)\right)dx=0 \tag{8.23}$$

This equation is further simplified to

$$\int_{-L/2}^{L/2}\left(g\left(\frac{L}{2}-b-x\right)-\varepsilon\left(\frac{L^2}{4}-bL-Lx+2bx+b^2+x^2\right)\right)dx=0 \tag{8.24}$$

Equation (8.25) reduces to

$$\left[g\left(\frac{Lx}{2}-bx-\frac{x^2}{2}\right)-\varepsilon\left(\frac{L^2x}{4}-bLx-\frac{Lx^2}{2}+\frac{2bx^2}{2}+b^2x+\frac{x^3}{3}\right)\right]_{\frac{-L}{2}}^{\frac{L}{2}}=0 \tag{8.25}$$

This simplifies as

$$g\left(\frac{L^2}{2}-bL\right)-\varepsilon\left(\frac{L^3}{3}-b^2L-\frac{5bL^2}{4}\right)=0 \tag{8.26}$$

By rearranging equation (8.26) for ε

$$\varepsilon=\frac{6(L^2-2bL)}{(4L^3+12b^2L-15bL^2)} \tag{8.27}$$

and substituting in the values the angular acceleration, ε, is found

$$\varepsilon=\frac{6(8.15^2-2\times8.15\times0.15)}{(4\times8.15^3+12\times0.15^2\times8.15-15\times0.15\times8.15^2)}=0.19 \tag{8.28}$$

The reactive force at the support resulting from the combination of the inertia forces and the self-weight is calculated as follows

The inertia force function is integrated over the length of the beam

$$\int_{-L/2}^{L/2} f_i\,dx-R_{f_i}=0 \tag{8.29}$$

Therefore this reduces to

$$R_{f_i}=\frac{1}{2}\rho\varepsilon(L-b)(L-b) \tag{8.30}$$

By substituting the values the reactive force due to the inertia forces is found as

$$R_{f_i} = \frac{1}{2} \times \rho \times 0.19(8.15 - 0.15)^2 = 231.944\,\mathrm{N} \tag{8.31}$$

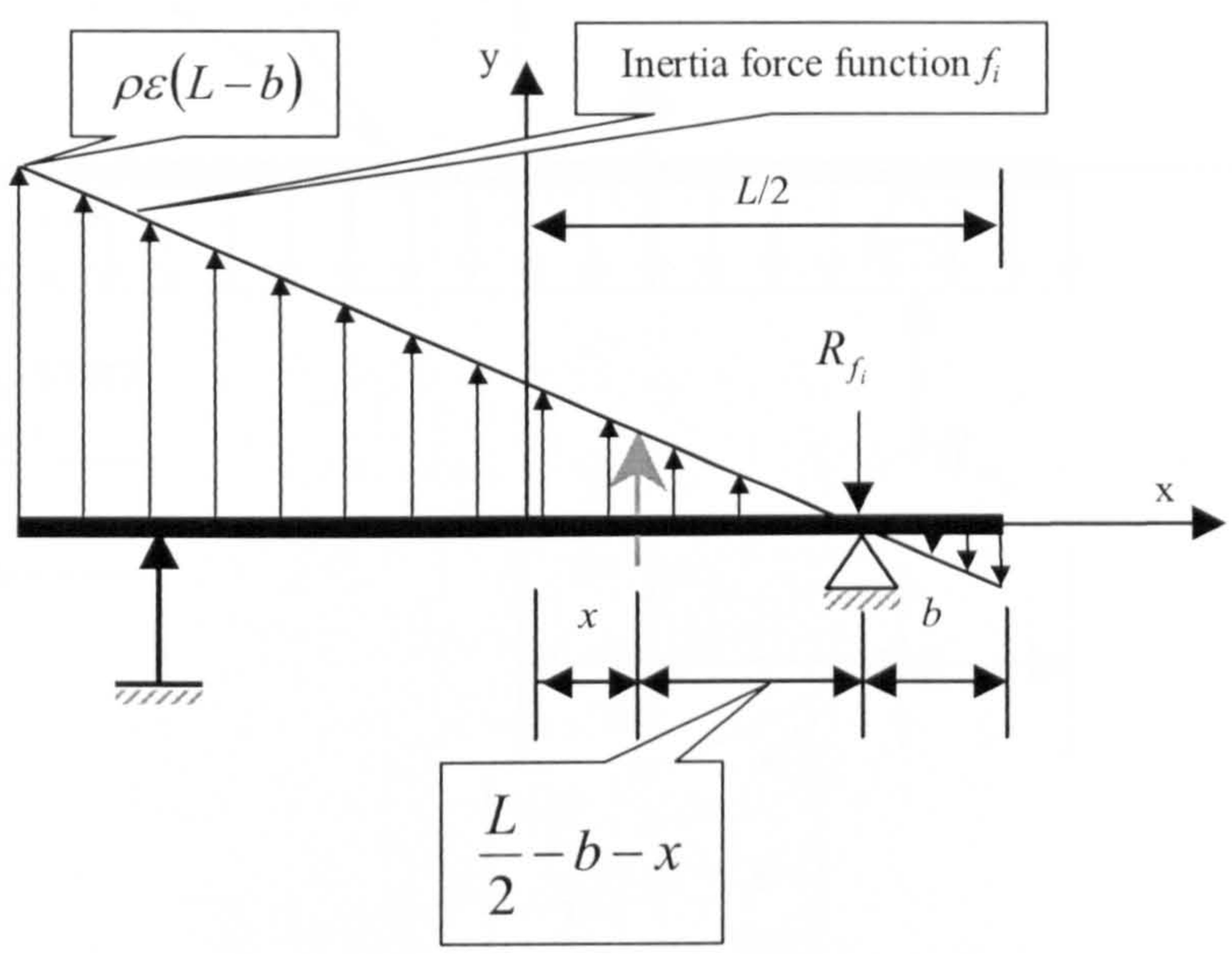

Figure 8.15 Force fields along beam B1

The self weight function is integrated over the length of the beam to find the reactive force acting due to the self weight of the beam

$$\int_{-L/2}^{L/2} \rho g dx - R_{w_s} = 0 \tag{8.32}$$

Rearanging to give the reactive force and integrating gives

$$R_{w_s} = \rho g L \tag{8.33}$$

Upon substituting the values this reduces to

$$R_{w_s} = \rho \times 9.81 \times 8.15 = 23026.032\,\mathrm{N} \tag{8.34}$$

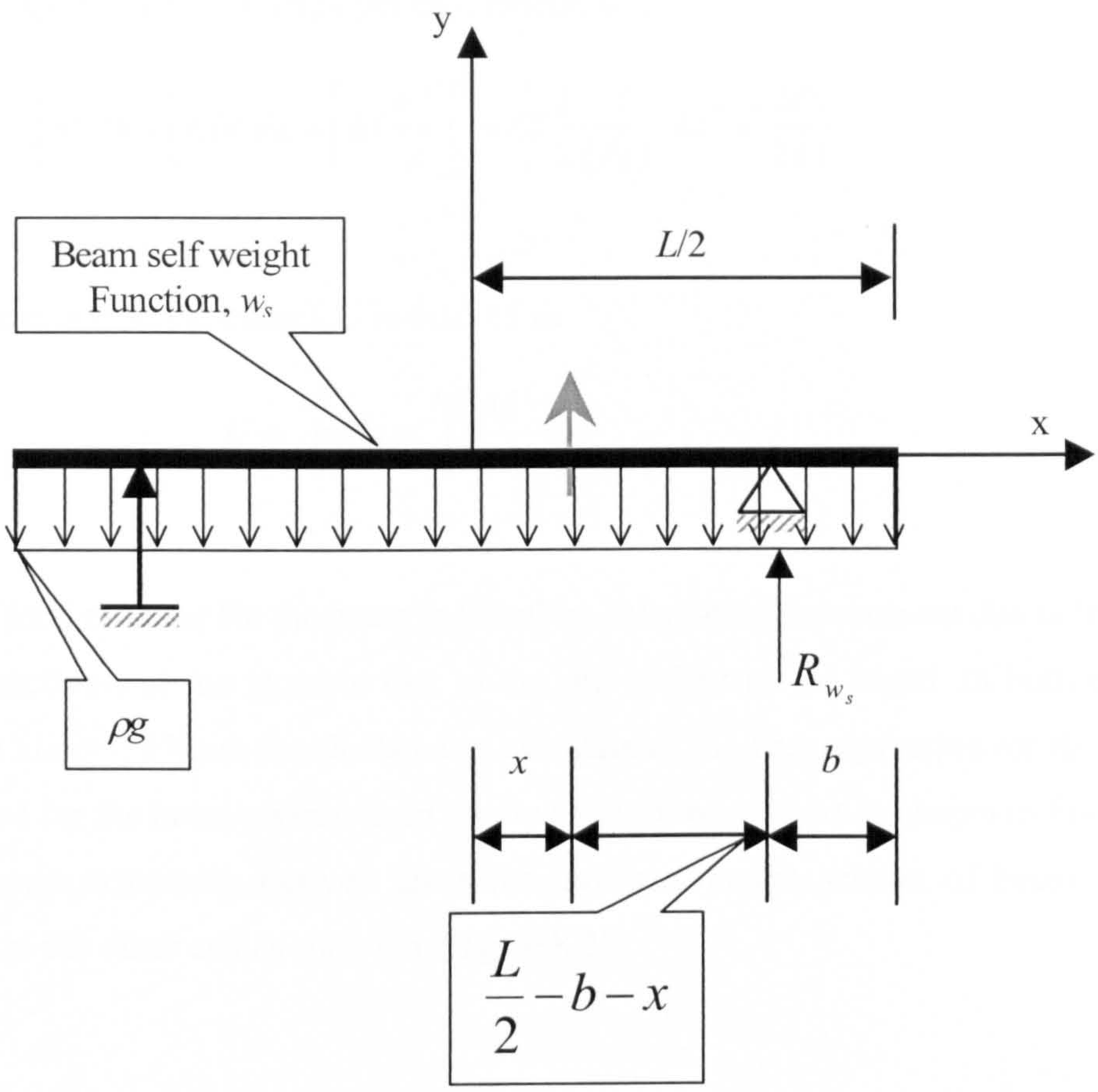

Figure 8.16 Force fields along beam B1

The moment - curvature (M-κ) relation is given by and is illustrated in Figure 8.17

$$M = EI\kappa \tag{8.35}$$

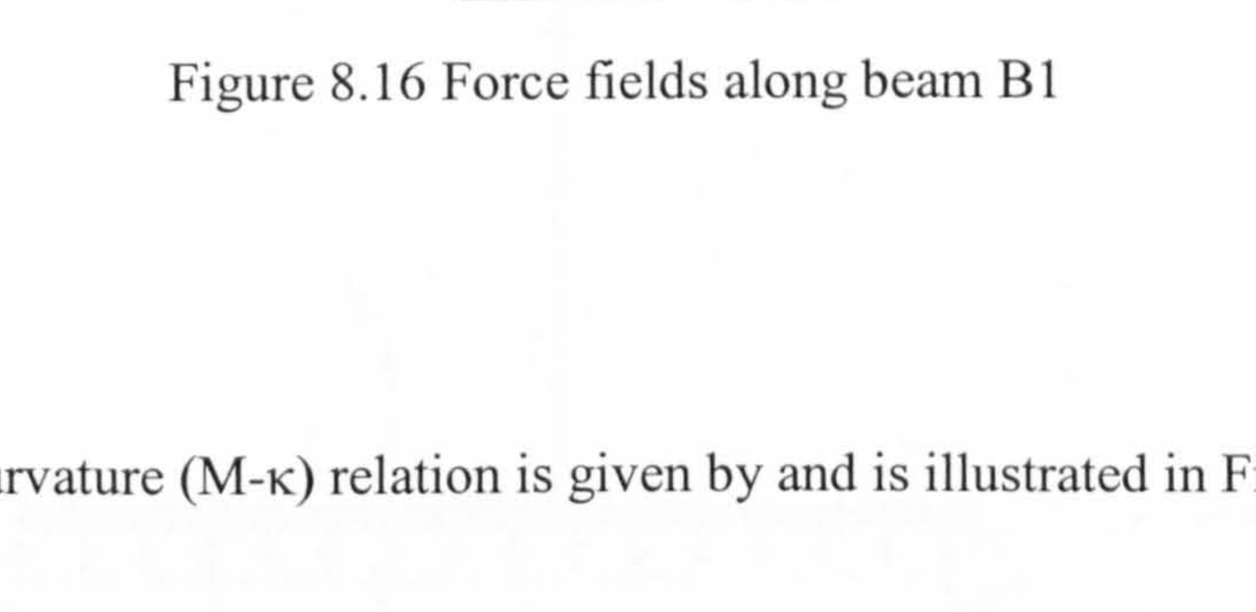

Figure 8.17 Moment – curvature relationship

Thus the specific strain energy per unit length, u is

$$u = \int_0^{\kappa} M \, d\kappa = \int_0^{\kappa} EI\kappa \, d\kappa = \left[EI\frac{\kappa^2}{2} \right]_0^{\kappa} = EI\frac{1}{2}\frac{1}{(EI)^2}M^2 = \frac{M^2}{2EI} \tag{8.36}$$

Thus the elastic strain energy,U is derived as

$$U = \int_{-L/2}^{L/2} u \, dx = \int_{-L/2}^{L/2} \frac{M^2}{2EI} dx \tag{8.37}$$

The total moment for the beam is found by calculating the moment due to the inertia force function and the moment due to the self weight of the beam. In both cases the moment along the beam is calculated in two stages. The first expression for the moment is derived for the beam section from the free end to the support as shown in Figure 8.24. The second expression derived gives the moment for the section of beam from the support to the other end as shown in Figure 8.25.

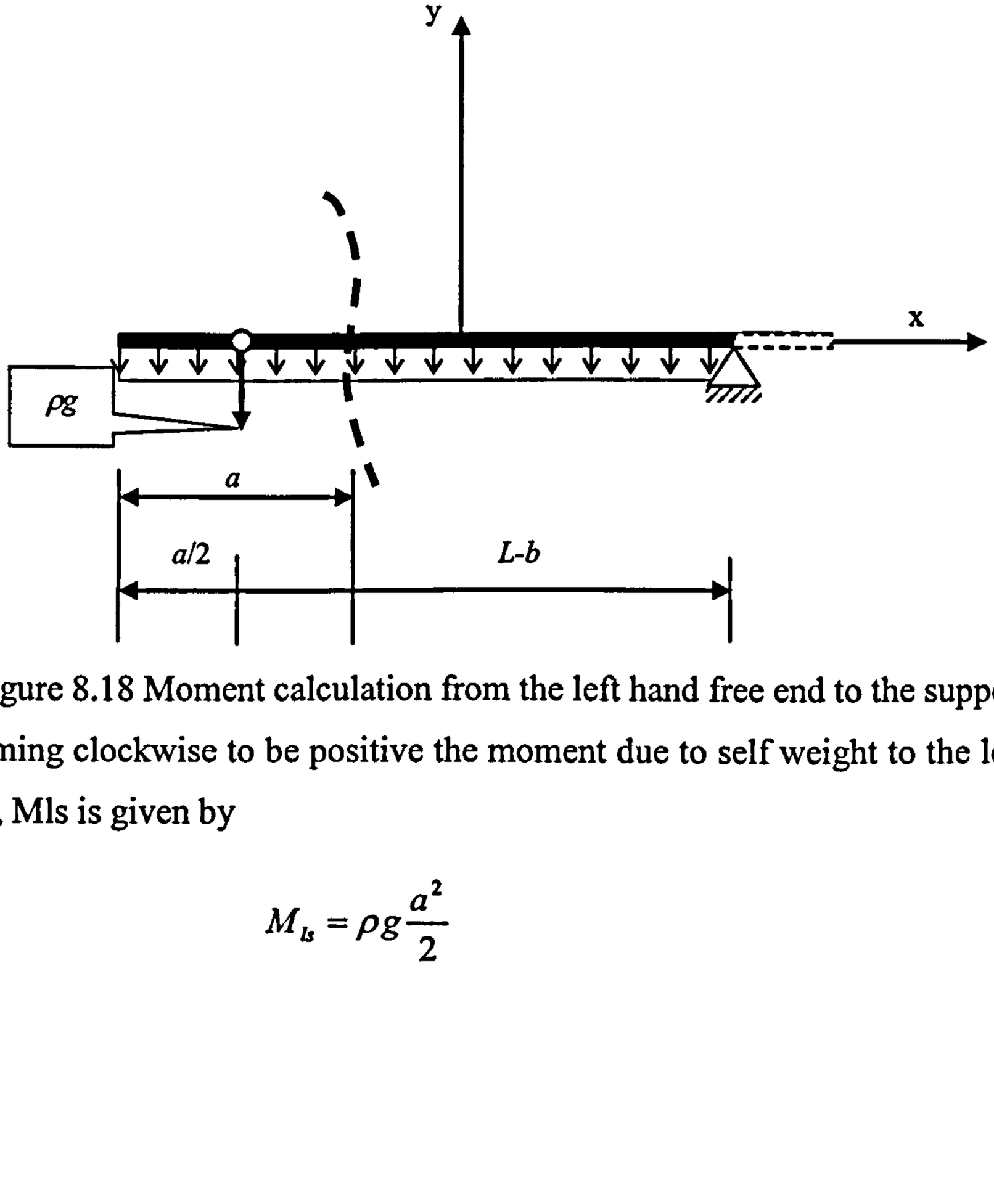

Figure 8.18 Moment calculation from the left hand free end to the support

Assuming clockwise to be positive the moment due to self weight to the left side of the beam, Mls is given by

$$M_{ls} = \rho g \frac{a^2}{2} \tag{8.38}$$

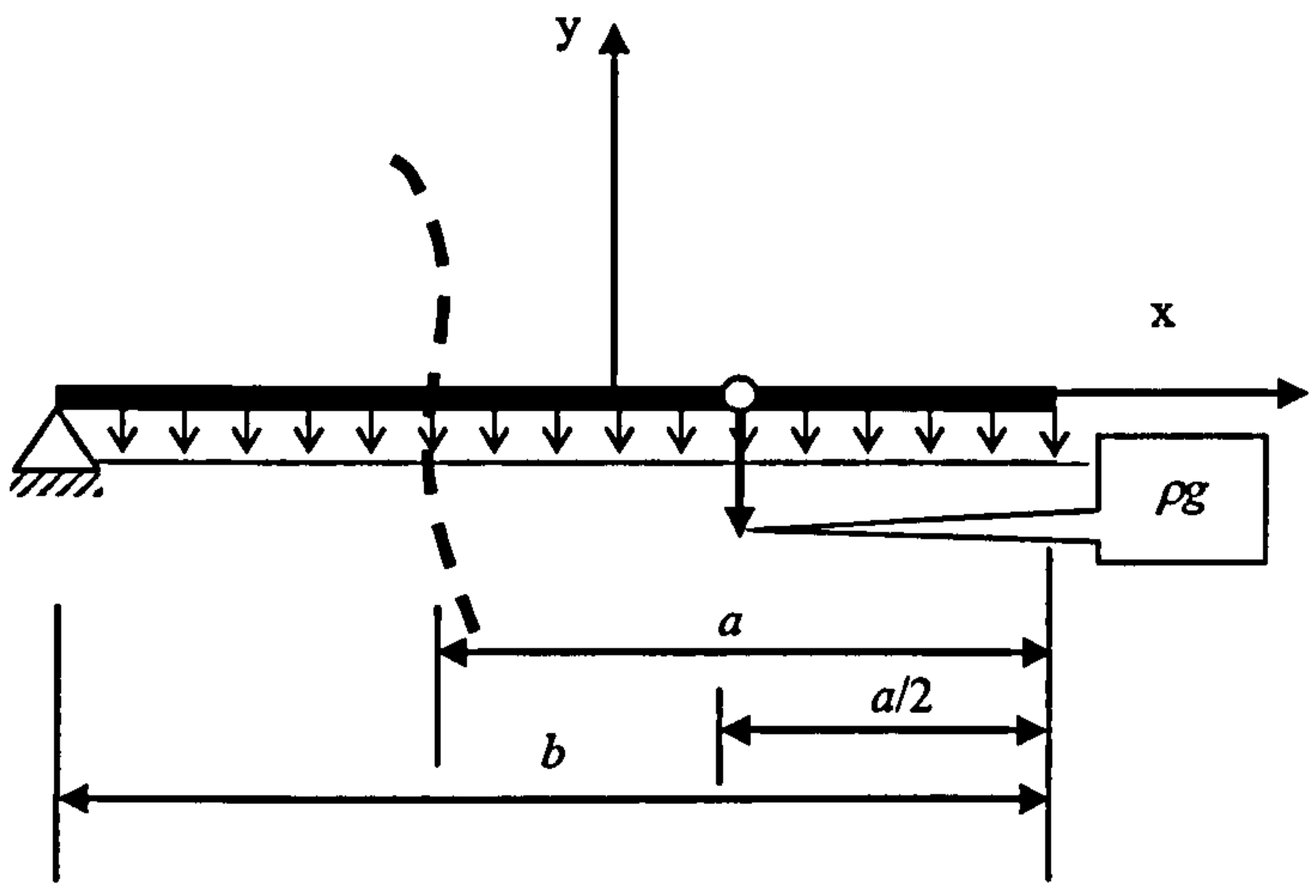

Figure 8.19 Moment calculation from the right hand free end to the support

The moment to the right side of the beam due to self weight, Mrs is also given by equation (8.38). The bending moment diagram is shown in Figure 8.20.

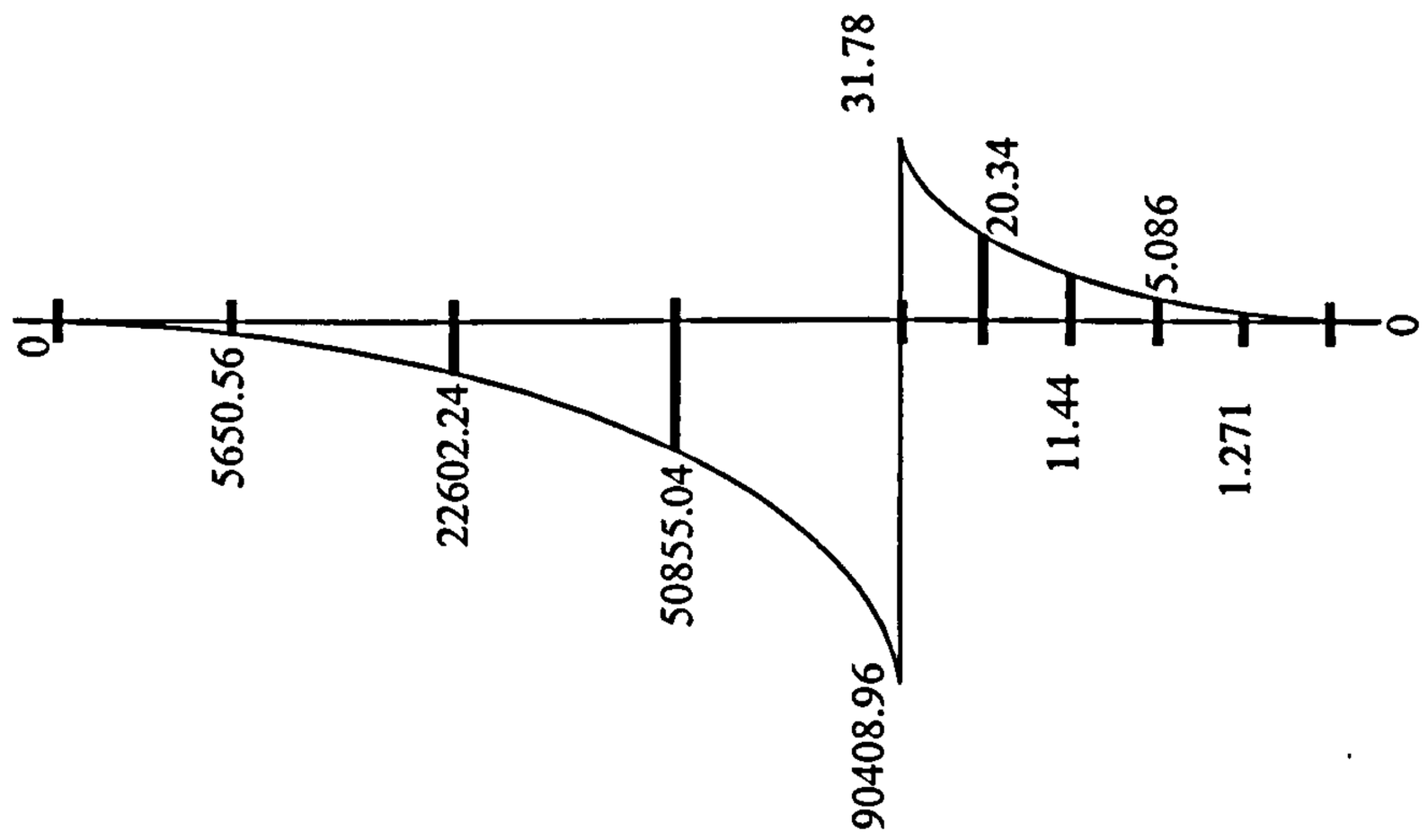

Figure 8.20 Bending moment diagram due to self weight of the beam

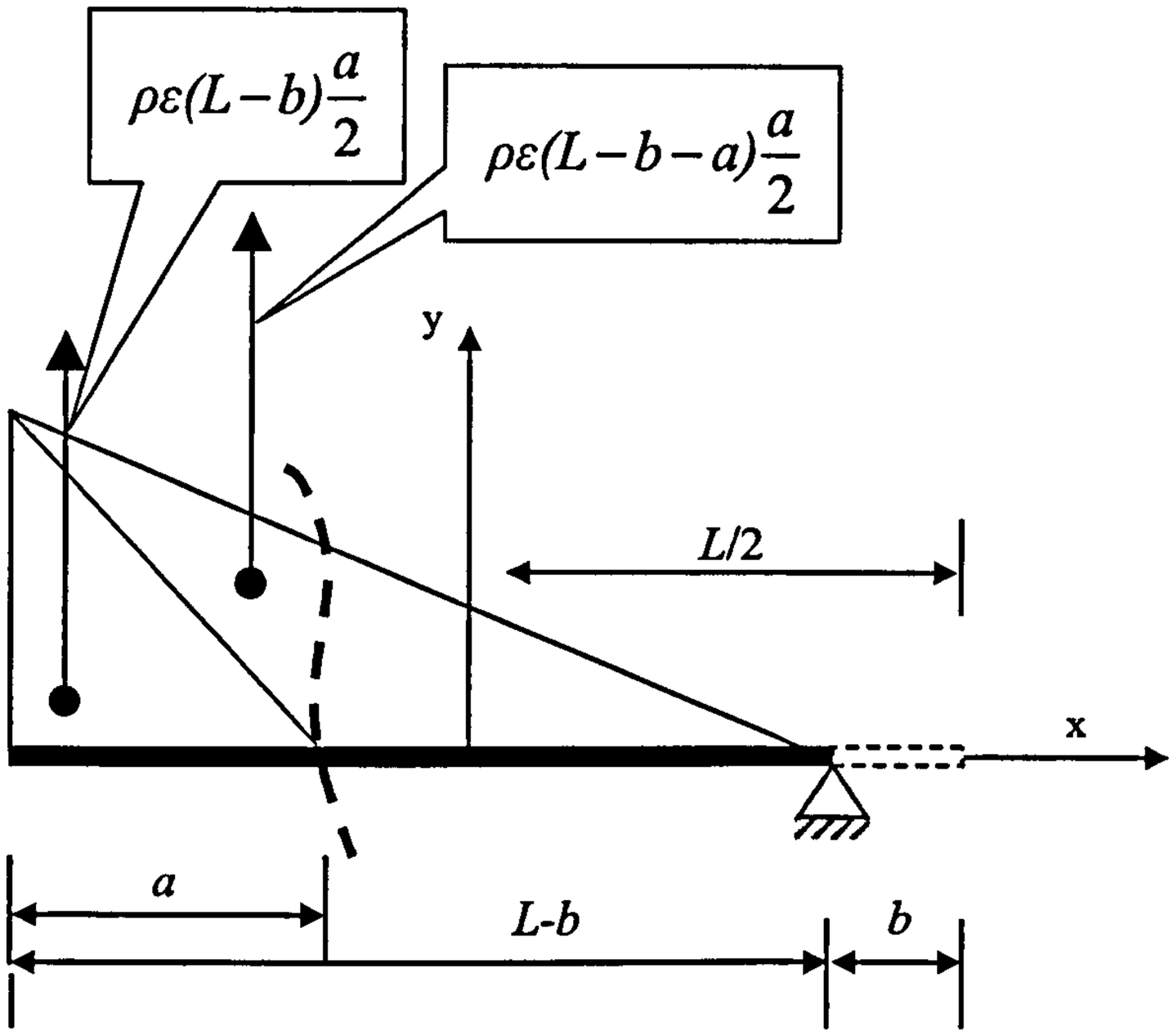

Figure 8.21 Bending moment diagram due to inertia forces applied to the left side of the beam

The moment, M_{ri} due to the applied inertia forces for the right hand side of the beam is given by

$$M_{li} = \frac{a^3}{3}\rho\varepsilon(L-b) + \frac{a^2}{6}\rho\varepsilon(L-b-a) \tag{8.39}$$

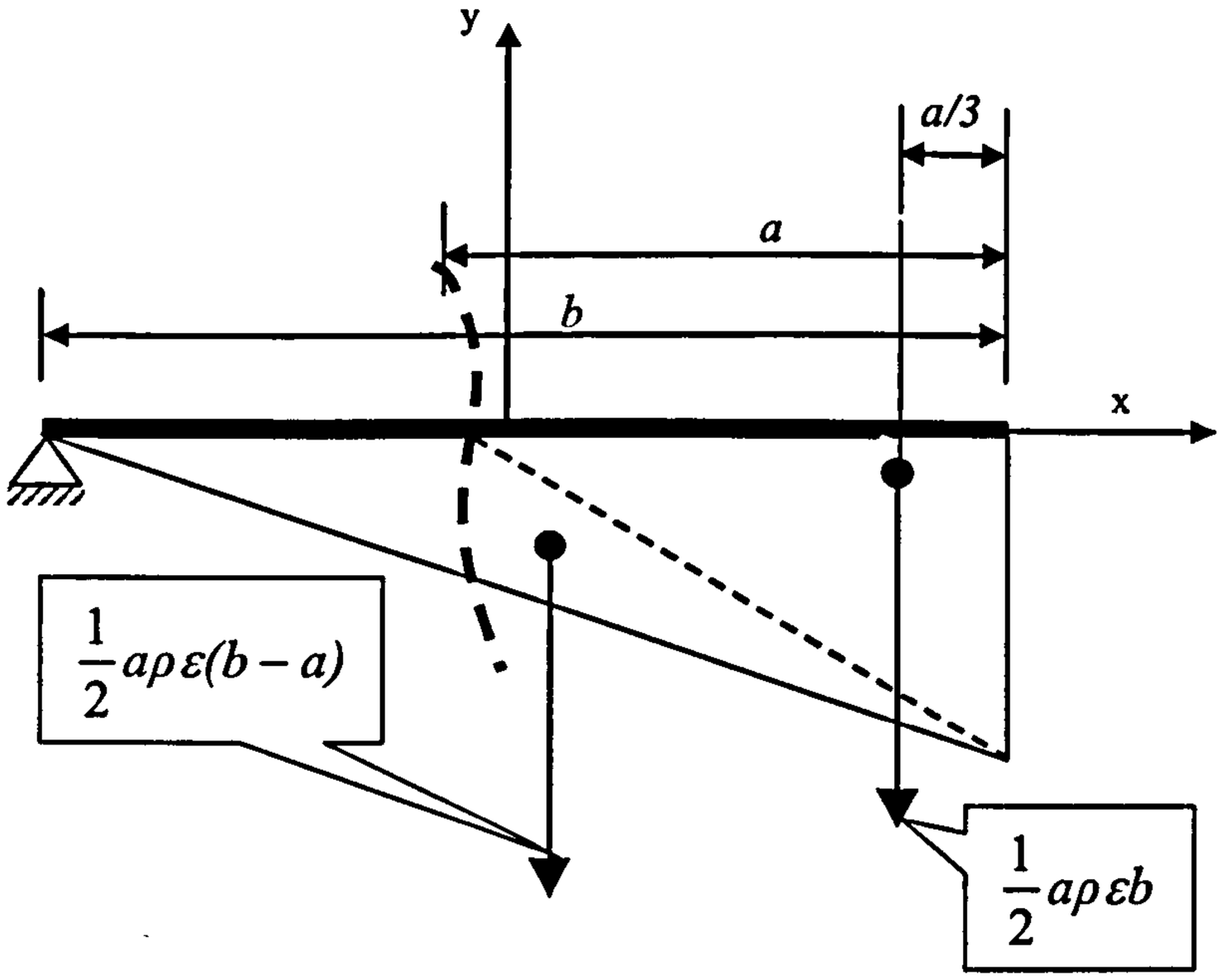

Figure 8.22 Bending moment diagram due to inertia forces applied to the right side of the beam

The moment, M_{ri} due to the applied inertia forces for the right hand side of the beam is given by

$$M_{ri} = \frac{1}{3}\rho\varepsilon b a^2 + \frac{1}{6}\rho\varepsilon(b-a)a^2 \tag{8.40}$$

Hence the bending moment diagram for the beam under inertia loading is

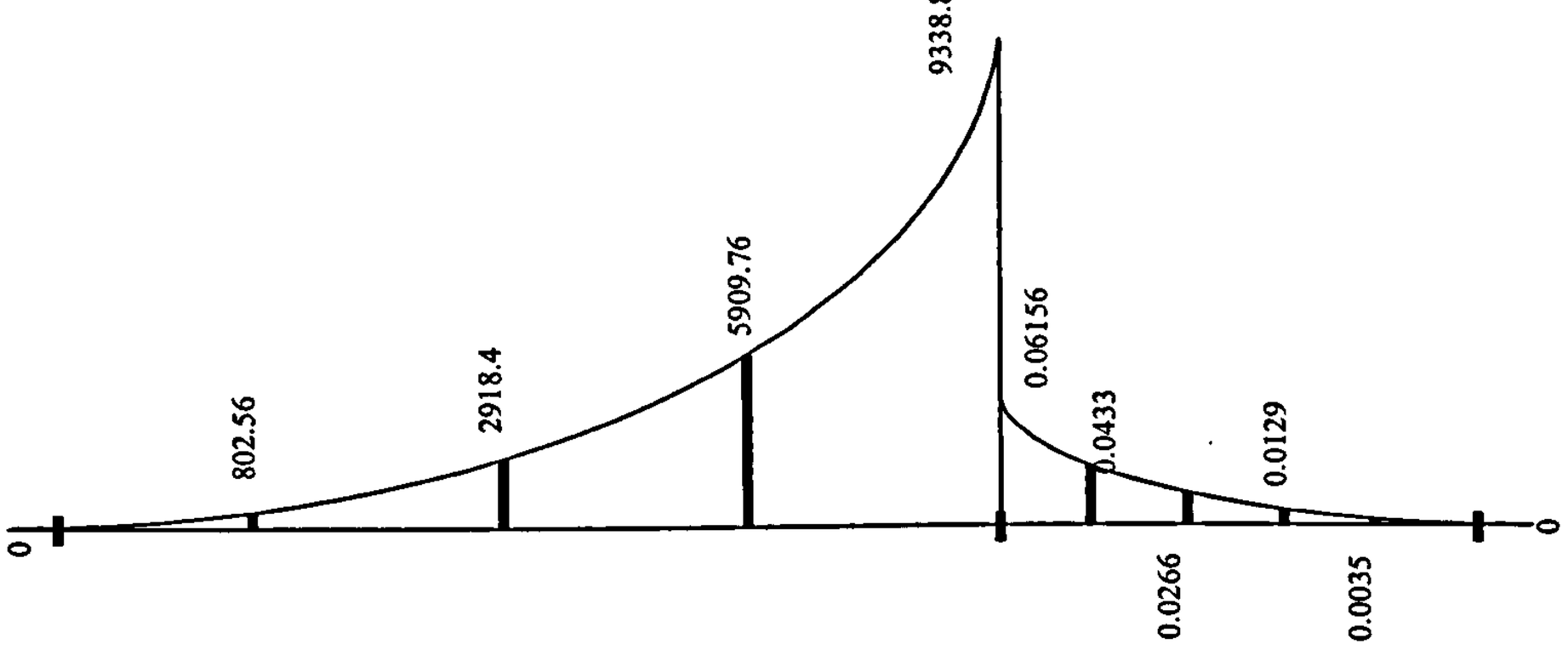

Figure 8.23 Bending Moment Diagram for Beam under Inertia Loads

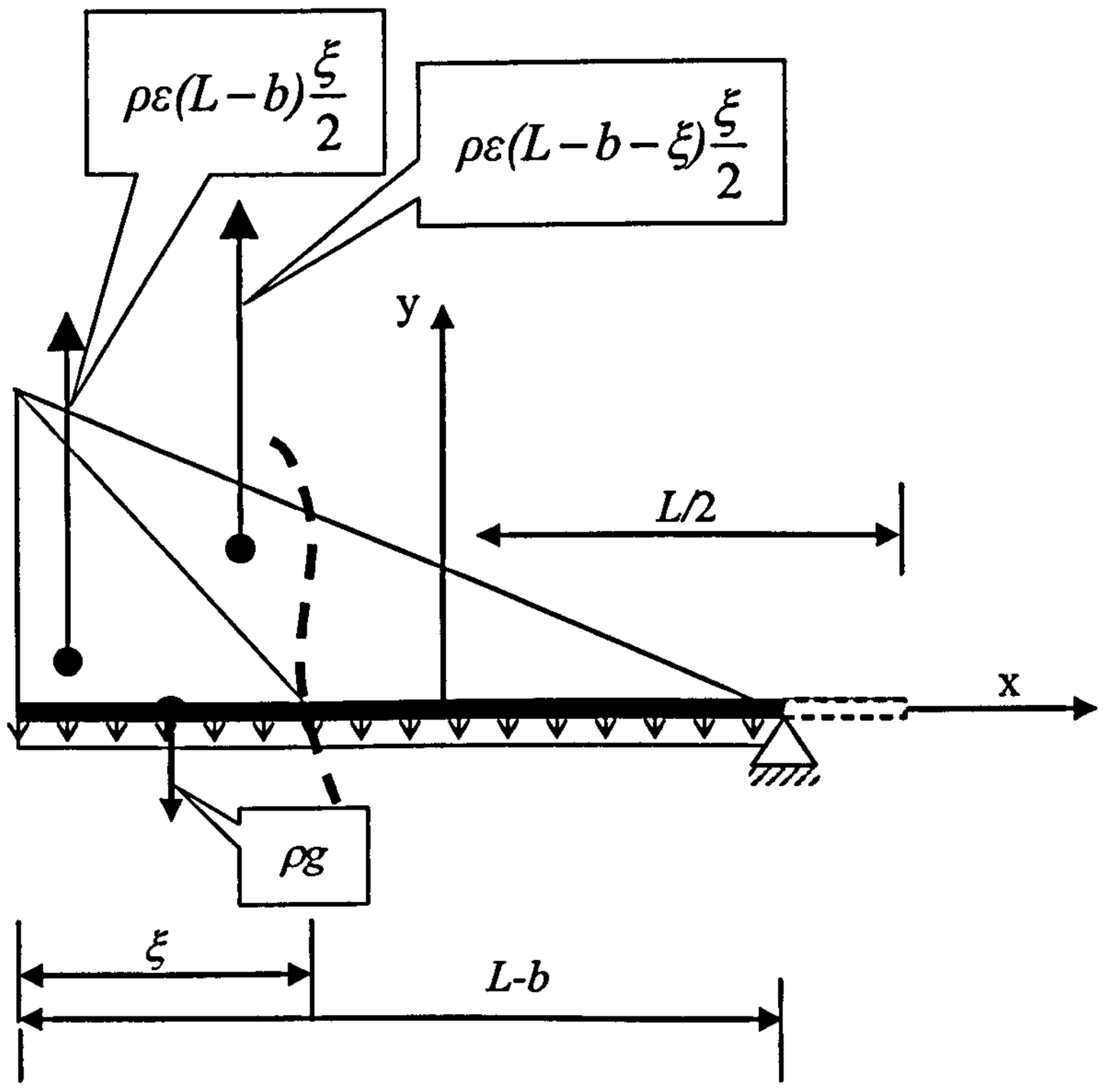

Figure 8.24 Force fields along beam B1

Assuming the following coordinate system from the left of the beam

$$\xi = \frac{L}{2} + x \tag{8.41}$$

The combined moment of the self weight and the inertia force is expressed as

$$M_1 = \frac{1}{3}\xi\rho\varepsilon(L-b) + \frac{1}{2}\xi\rho\varepsilon(L-b-\xi)\frac{\xi}{3} - \frac{\rho g\xi^2}{2} \tag{8.42}$$

This simplifies to

$$M_1 = \frac{1}{3}\rho\varepsilon\xi^2(L-b) + \frac{1}{6}\rho\varepsilon\xi^2(L-b-\xi) - \frac{1}{2}\rho g\xi^2 \tag{8.43}$$

Upon substituting the values (8.43) becomes

$$M_1 = \frac{1}{3}\times 288\times 0.19\times 8\times \xi^2 + \frac{1}{6}\times 288\times \xi(8-\xi) - \frac{1}{2}\times 288\times 9.81\times \xi^2 \tag{8.44}$$

Thus

$$M_1 = 145.92\xi^2 + 384\xi^2 - 48\xi^2 - 1412.64\xi^2 \tag{8.45}$$

Equation (8.45) simplifies to

$$M_1 = -1316.72\xi^2 + 384\xi^2 \tag{8.46}$$

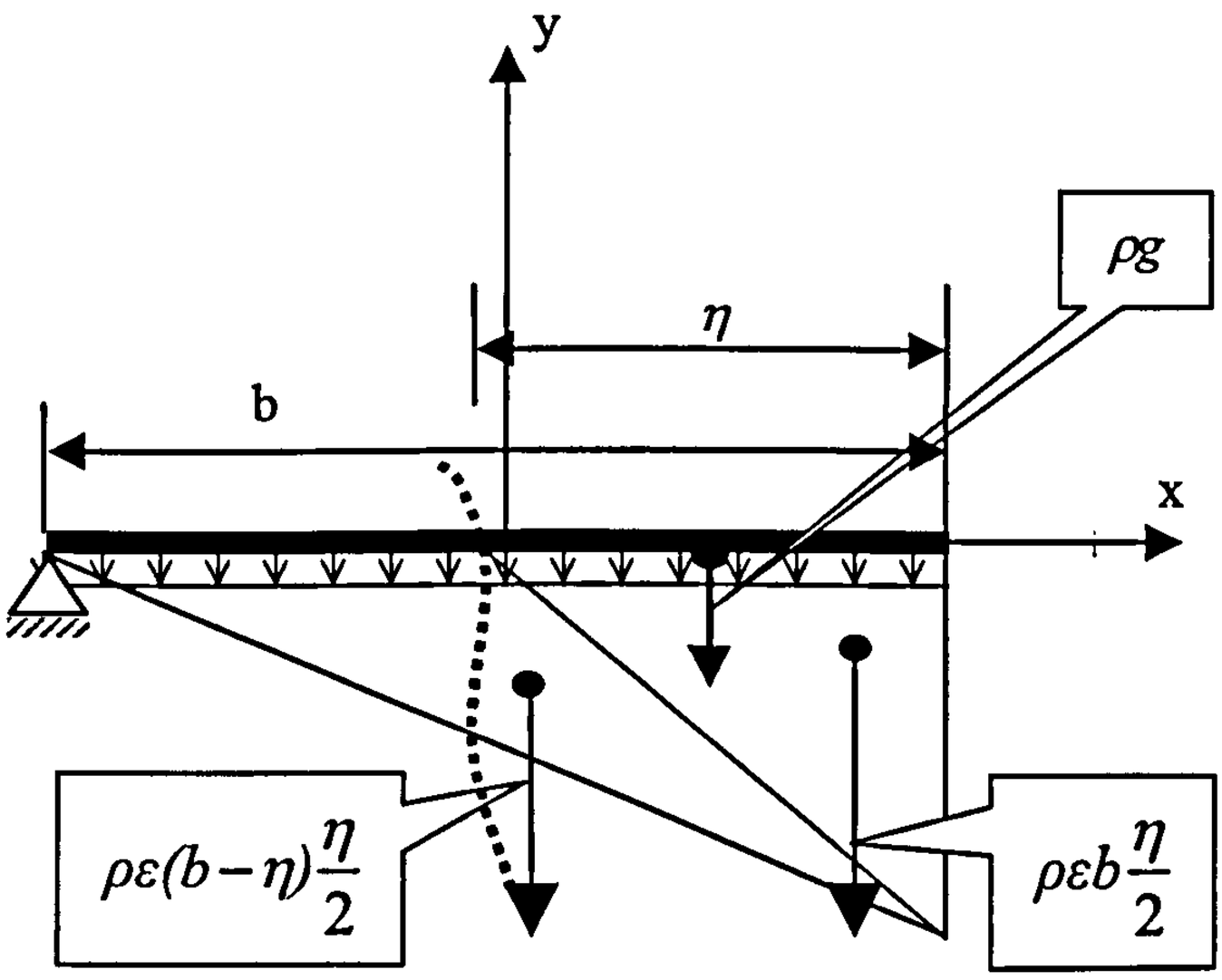

Figure 8.25 Force fields along beam B1

By using the following coordinate system the moments to the right of the support are evaluated

$$\eta = x - \frac{L}{2} \tag{8.47}$$

The moments due to the self weight and the inertia forces to the right of the support, M_r is given by

$$M_r = \frac{1}{2}\eta\rho\varepsilon b\frac{2}{3}\eta + \frac{1}{2}\eta\rho\varepsilon(b-\eta)\frac{\eta}{3} + \frac{1}{2}\rho g\eta^2 \tag{8.48}$$

which simplifies to

$$M_r = \frac{1}{3}\rho\varepsilon b\eta^2 + \frac{1}{6}\rho\varepsilon\eta^2(b-\eta) + \frac{1}{2}\rho g\eta^2 \tag{8.49}$$

Upon substituting the values equation (8.49) becomes

$$M_r = \frac{1}{3}\times 288\times 0.19\times 0.15\times\eta^2 + \frac{1}{6}\times 288\times 0.19\times\eta^2(0.15-\eta) + \frac{1}{2}\times 288\times 9.81\times\eta^2$$

which simplifies as

$$M_r = 2.736\eta^2 + 1.368\eta^2 - 9.12\eta^3 + 1412.64\eta^2 \tag{8.50}$$

Therefore the combined moment is expressed as

$$M_r = 1416.74\eta^2 - 9.12\eta^3 \tag{8.51}$$

Hence by applying equation (8.37) the strain energy is found from

$$U = \frac{1}{2EI}\int_0^{\varepsilon} M_l^{\,2} + \frac{1}{2EI}\int_0^{\eta} M_r^{\,2} \tag{8.52}$$

Thus

$$\frac{1}{2EI}\int_0^{\varepsilon} M_l^{\,2} = \frac{1}{2EI}\int_0^{\varepsilon} 1734489\xi^4 + 1011456\xi^3 + 147456\xi^2 \tag{8.53}$$

Hence

$$\frac{1}{2EI}\int_0^{\varepsilon} M_l^{\,2} = \left[346899\xi^5 + 252864\xi^4 + 49152\xi^3\right]_0^8 \tag{8.54}$$

Equation (8.54) is computed as

$$\frac{1}{2EI}\int_0^{\varepsilon} M_l^{\,2} = \frac{1.243e10}{2EI} \tag{8.55}$$

The second half of equation (8.52) is resolved as

$$\frac{1}{2EI}\int_0^{\eta} M_r^{\,2} = \frac{1}{2EI}\int_0^{0.15} 2007889\eta^5 - 25846.08\eta^6 + 83.17\eta^7 \tag{8.56}$$

Hence

$$\frac{1}{2EI}\int_0^{\eta} M_r^{\,2} = \frac{1}{2EI}\left[401577.8\eta^5 - 4307.68\eta^6 + 11.88\eta^7\right]_0^{0.15} \tag{8.57}$$

Equation (8.57) is calculated as

$$\frac{1}{2EI}\int_0^{\eta} M_r^{\,2} = \frac{30.44}{2EI} \tag{8.58}$$

The second moment of Inertia, I is found from

$$I = \frac{bh^3}{12} = \frac{0.4 \times 0.3^3}{12} = 0.0009\,\mathrm{m}^4 \tag{8.59}$$

The value of E is taken as $2.5\text{x}10^9$. Hence the equation for strain energy becomes

$$U = \frac{1.243e10}{2EI} + \frac{30.44}{2EI} = \frac{2.48}{I} = \frac{2.48}{0.0009} = 2755.55\,\mathrm{Nm} \tag{8.60}$$

Since the strain energy is considerably less than the potential energy our initial assumption that the beam falls as a rigid beam is valid.

The reinforcement is placed at the four corners of the cross section. The area of the three compression reinforcement bars was calculated and split into two halves, one half placed in each bottom corner. A similar approach was adopted for the tensile reinforcement (Figure 8.26). The cover, d_c, to the reinforcement was taken to be 0.02m.

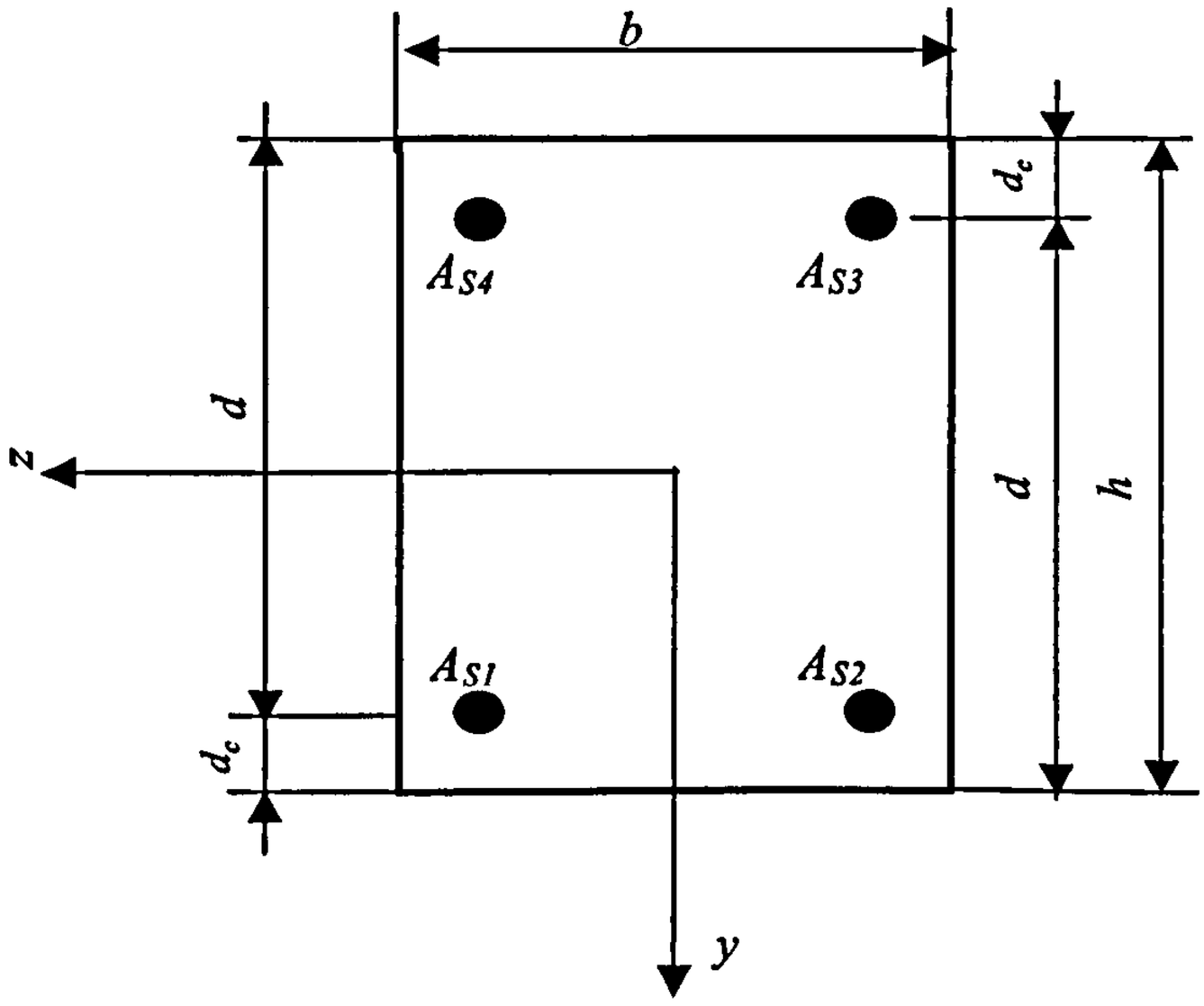

Figure 8.26 Reinforcement modelling for beam B1

The net deflection of the beam is calculated by subtracting the deflection due to rigid body motion from the total deflection as shown in Figure 8.27.

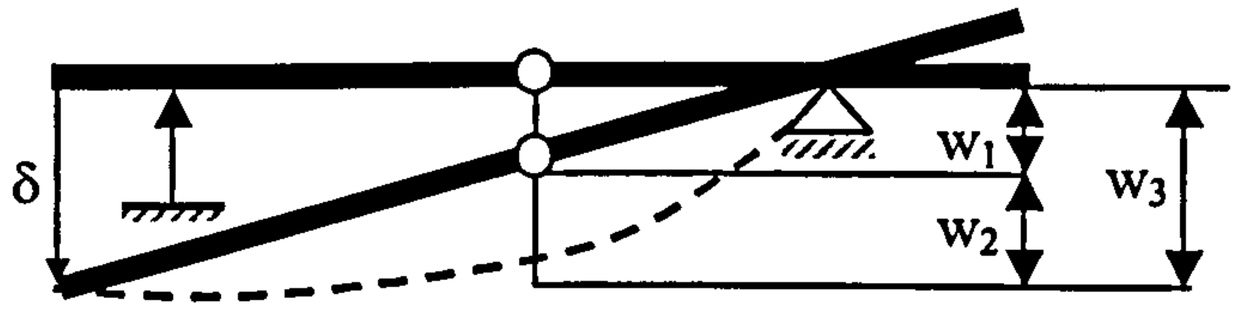

Figure 8.27 Net deflection of the beam

Hence for any node along the beam the nodal deflection, w_2 is calculated by subtracting the rigid body deflection, w_1 from the total deflection, w_3.

$$w_2 = w_3 - w_1 \tag{8.61}$$

The rigid body deflection is found from

$$\frac{\delta}{w_1} = \frac{x_h}{x_h - x_n} \tag{8.62}$$

where the suffix h and the suffix n stand for the hinge and nodal x coordinate respectively.

The results from the fem/dem model for the deflection-time relationship and the deflected form of the beam are shown in Figure 8.28 to Figure 8.30. The deflection at points 2.5, 4.0 and 5.0 m from the beam is enumerated and compared with those of the experiment. This is shown in Figure 8.28. Greater deflection is seen to result as the time increases. The value of the deflection is also higher for points farther along the beam. For all three x values along the beam excellent agreement is seen to exist between the two sets of results.

The deflected form of the beam is shown in Figure 8.29. The deflected form of the beam is shown in at various time steps after the beam had hit the shock absorber. At each time step the plastic hinge is seen to travel along the beam as the deflection increases with time. This is shown by the dotted line on the plot and is confirmed by experimental observations made at the Swiss Institute of Technology.

This output is reproduced at time 0.022s, 0.059s and 0.164s and compared as shown in Figure 8.30. Experimental results for the same time periods are plotted on the same curve. The results are seen to concur favourably.

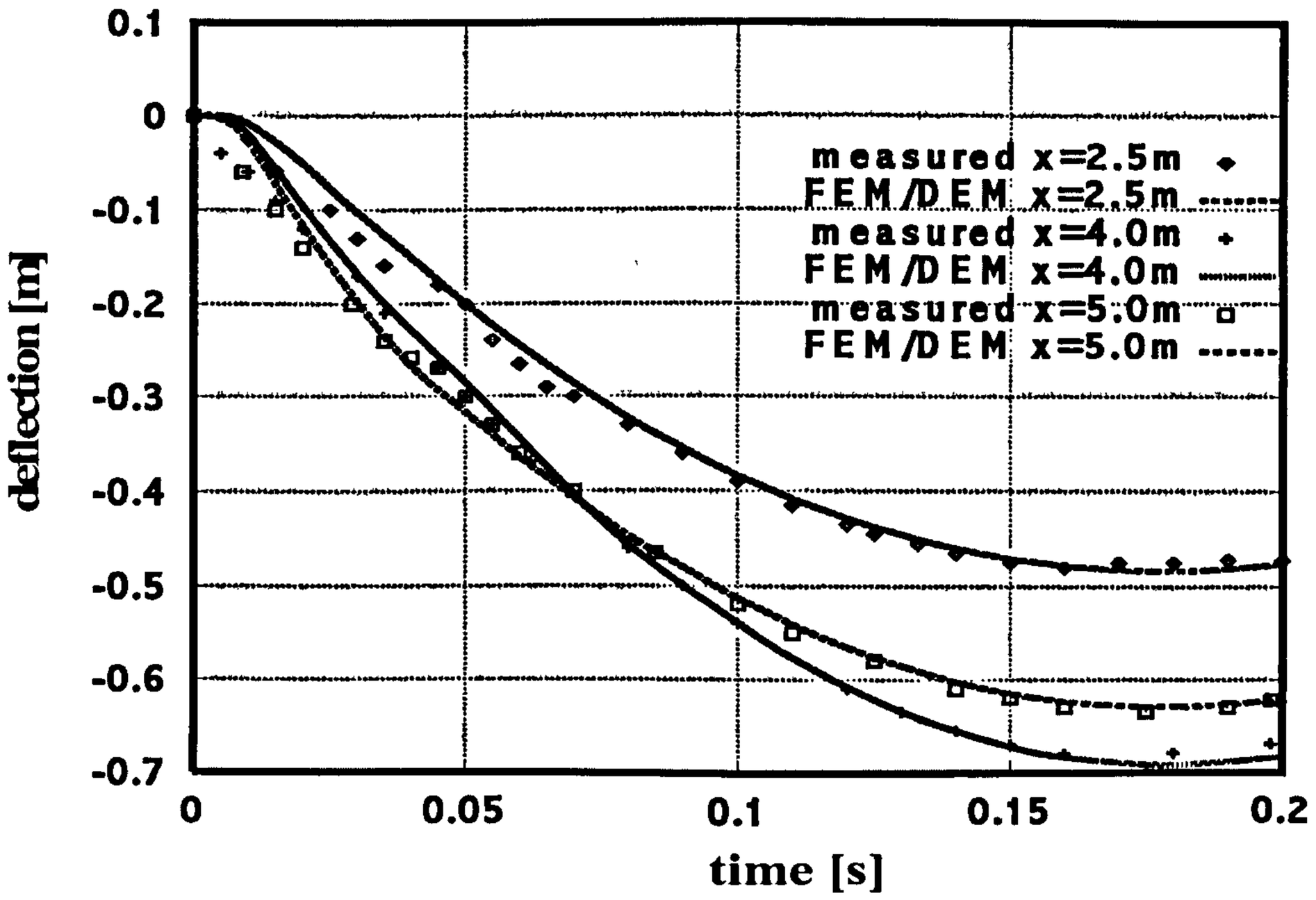

Figure 8.28 Deflection-Time relation at various points from the hinge

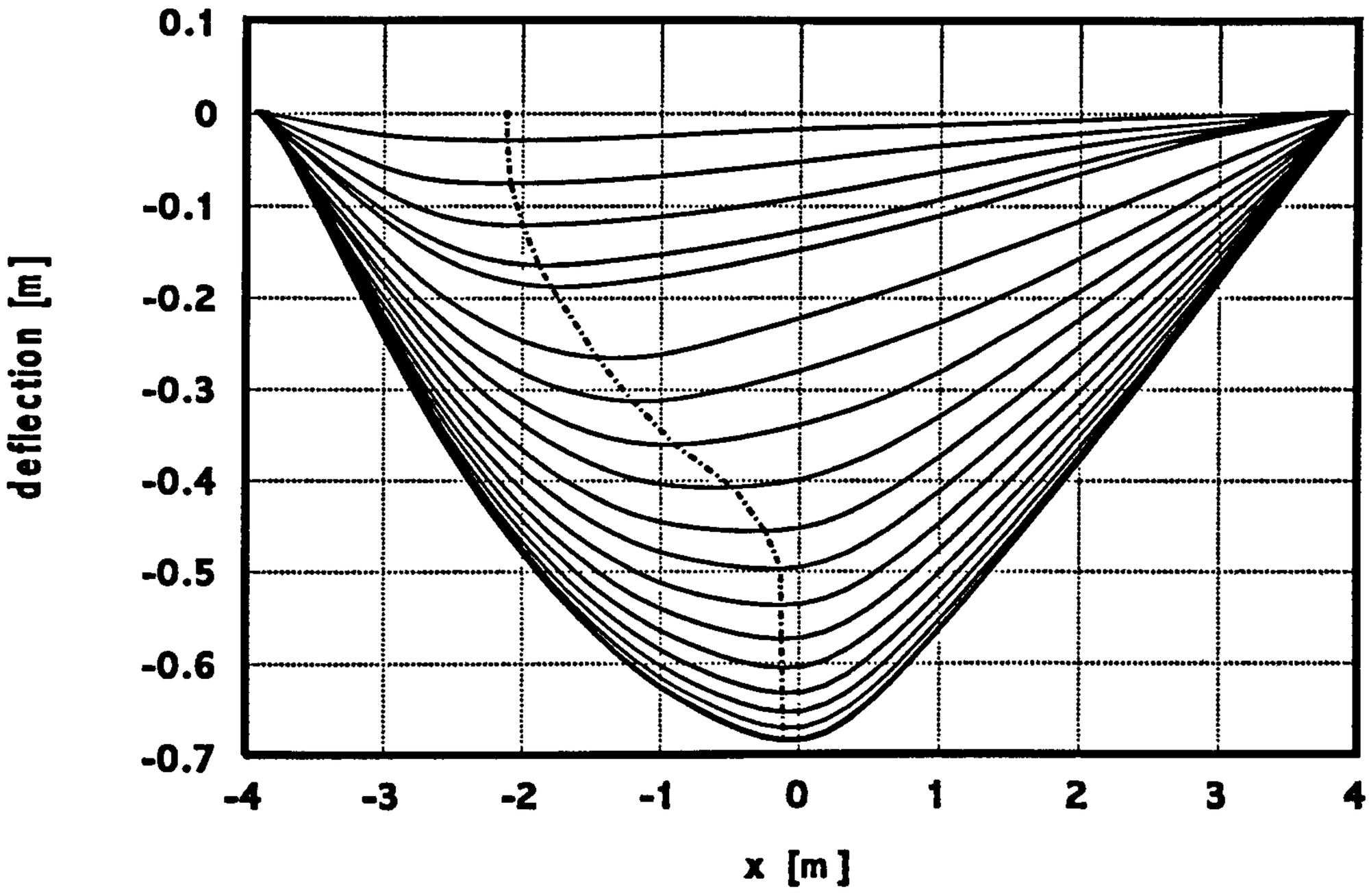

Figure 8.29 Deflected Form of beam B1

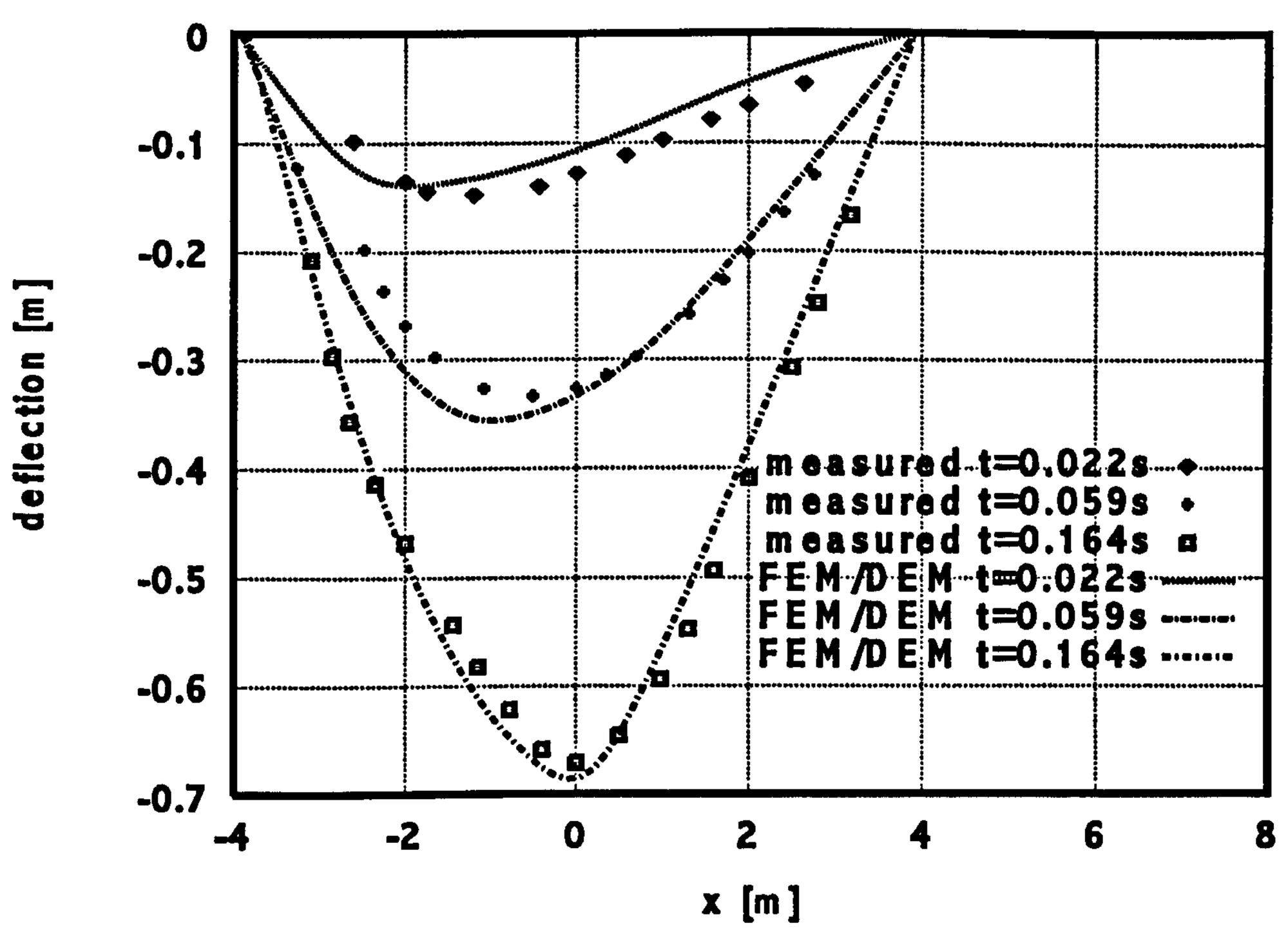

Figure 8.30 Deflected form of beam B1 at various times

8.5 Conclusions

A simple element has been tested in combination with dynamic loading conditions. The FEM/DEM simulation first concentrated on accurately reproducing the properties of the shock absorber. These properties were then applied in the FEM/DEM analysis to simulate the beam impact. Lumped mass approach is used for the dynamic analysis, as is a regular grid over beam length, thus adopting the standard approach for transient dynamic problems. The benefit derived by using regular grid spacing is the greater efficiency obtained during contact detection and contact interaction procedures.

The results obtained from the analysis show good agreement with the experimental measurements. Figure 8.29 also validates the conclusion of the authors of the Swiss Institute's report that the plastic hinge moves along the beam as the deflection increases with time. This is shown by the dotted line.

It has been shown that the simple element is highly effective when used in combination with dynamic loading conditions. Static condensation can be performed without matrix inversion; thus the CPU processing time is kept to the minimum.

It is worth noting that the procedures described in this work are not aimed at thick beams and are limited therefore to thin beams. As the numerical experiments demonstrate, large displacements are by default taken into account, as is the standard approach with FEM/DEM. However this excludes finite strains.

The most important novelty of the solutions presented in this section is that they are found to fit very well within the contact interaction and contact detection concepts of the combined finite-discrete element method, thus enabling robust solutions for structural failure and collapse simulations involving hundreds, even millions of interacting particles [3]. In addition a novel integration procedure for nonlinear behaviour of both steel and concrete has been introduced. The element proposed enable the use of state of the art contact detection solutions including NBS type algorithms together with discretised contact interaction concepts without interfering with either CPU or RAM efficiency or robustness of the above. It is in this context that the importance of the solutions described in this chapter presents itself.

8.6 References

1. Sir A. Pugsley et.all, "Report of the Inquiry into the Collapse of Flats at Ronan Point, Canning Town", *HMSO* (1968)

2. FEMA report 403, "World Trade Center Building Performance Study:Data Collection, Preliminary Observations & Recommendations" May (2002)
3. A. Munjiza "Computational Challenge of Large Scale Discontinua" *Keynote Address, Third International Conference on Discrete Element Methods, Sante Fe* September (2002)
4. A. Munjiza, D.R.J. Owen, N. Bicanic, "A combined finite-discrete element method in transient dynamics of fracturing solids", *Int. J Engineering Computations, 12, pp 145-174* (1995)
5. A.Munjiza, K.R.F.Andrews, "NBS contact detection algorithm for bodies of similar size", *Int. J. Num. Methods Eng* , **43** (1998)
6. A. Munjiza, D.R.J. Owen, A.J.L Crook, "Energy and Momentum Preserving Contact Algorithm for General 2D and 3D Contact Problems", *Proc 4th Int. Conf Computational Plasticity- Fundementals and Applications, Barcelona pp 829-841* 3 –6 April (1995)
7. A.Munjiza, K.R.F.Andrews, J.R. White, "Discretized Contact Solution for combined finite-discrete Method", *5th ACME Conf. London UK* pp96-100, (1997).
8. A.Munjiza, K.R.F.Andrews, "Penalty function method for in combined finite-discrete element systems comprising large number of separate bodies", *Int. J. Num. Methods Eng.*, **49**, *pp1377-1396*, (2000)
9. Ammann, W., Bachmann, H., Muhlematter, M., "Versuche an Stahlbeton und Spannbetonbalken unter stossartiger Beanspruchung Teil 2- Konzeption und Durchfuhrung der Balkenversuch, Zusammenfassung der Versuchresultate" *Birkhauser Verlag Institure fur Baustatik und Konstruction, Zurich,* (1982)
10. Ammann, W., Bachmann, H., Muhlematter, M., "Versuche an Stahlbeton und Spannbetonbalken unter stossartiger Beanspruchung Teil 3- P1, P2 und B1 bis B8" *Birkhauser Verlag Institure fur Baustatik und Konstruction, Zurich,*(1982)
11. Ammann, W., Bachmann, H., Muhlematter, M., "Versuche an Stahlbeton und Spannbetonbalken unter stossartiger Beanspruchung Teil 4- B9 bis B21" *Birkhauser Verlag Institure fur Baustatik und Konstruction, Zurich,*(1982)
12. Ammann, W., Bachmann, H., Muhlematter, M., "Versuche an Stahlbeton und Spannbetonbalken unter stossartiger Beanspruchung Teil 5- Verhalten von zweifeldrigen Stahlbetonbalken bei Ausfall einer Unterstutzung" *Birkhauser Verlag Institure fur Baustatik und Konstruction, Zurich,* (1982)

13. Ammann, W., Bachmann, H., Muhlematter, M., "Experiments and Numerical Investigation of Reinforced and Prestressed Concrete Beams for Shock Loading" *Transaction of the 6th International conference on Structural mechanics in reactor Technology, Paris,* (1981)
14. SIA-162 Norm Ausgabe, M., "Betonbauten" *Schweizerischer Ingenieur und Architekten, Zurich,* (1989)
15. SIA-162/1 Norm Ausgabe, M., "Betonbauten Materialprufung" *Schweizerischer Ingenieur und Architekten, Zurich,* (1989)

Chapter 9

Global analysis of Murrah building using FEM/DEM method of analysis

9.1 Introduction

The Alfred P Murrah building was subjected to an explosion resulting from a vehicle bomb at 9:02 am on Wednesday, April 19th 1995. A lorry parked approximately 3.05 m in front of the North side of the structure was said to have contained the bomb. As a result the building suffered severe structural failure. Structural damage was also found to be evident in buildings situated up to 2.6 km from ground zero. The consequent 167 deaths that followed were attributed mostly to falling structural debris. This incident prompted the US government to review security at all eight thousand Federal buildings.

The Federal Emergency Management Agency (FEMA) [1] was charged with the forensic investigation of the Murrah building's structural failure. They in turn commissioned a Building Performance Assessment Team (BPAT), which recruited engineers from the US Army Corps of Engineers, The American Society of Civil Engineers, The General Services Administration and the National Institute of Standards and Technology. Their investigation was to centre on the possible collapse mechanism of the structure and strategies for blast mitigation [2].

The data collection concentrated on interviews with the consulting engineer. Samples of concrete and reinforcement were taken and analysed at the Construction Research Laboratories in Illinois. A recorded tape provided evidence of the duration of the collapse which was found to be three seconds [3]. Soil test boring data was also taken revealing the pavement to be 45.72 cm (18 in). The soil was found to be a combination of layers of sand and sandstone.

Figure 9.1 View of the Murrah building [1]

9.2 Structural layout the Alfred P. Murrah building

The Murrah building comprised of a nine storey section either side of which was a single storey building as shown in Figure 9.2. Figure 9.2 also shows a multi level underground car park in front of the south face of the Murrah building. The structure was erected using a tower crane.

The full force of the bomb was taken by a nine storey section of the structure. This structure was an ordinary moment frame rising nine floors supported by columns as shown by Figure 9.4 [4]. The north face was covered with one inch thick bronze insulated glass cladding. At each floor level a further quarter inch bronze tempered glass had been placed. The cladding curved inwards for the first two floors. The distance between the cladding and the exterior wall was 1.5 m (5 ft).

Circular vertical tubes were constructed at each corner of the building as part of the structure's ventilation system.

The floor spacing was 3.96 m except for the ninth floor, which was 4.27 m. The roof consisted of a monofilament membrane supported by a one inch thick vent board. Concrete roof pedestals existed for use with window washing mechanisms.

The east and west floors consisted of vertical board formed spandrels in between three 7.63 cm (3in) concrete infill walls. These infill walls were made of granite stone with steel studs and drywall backing. The infill walls were also covered with the glass cladding.

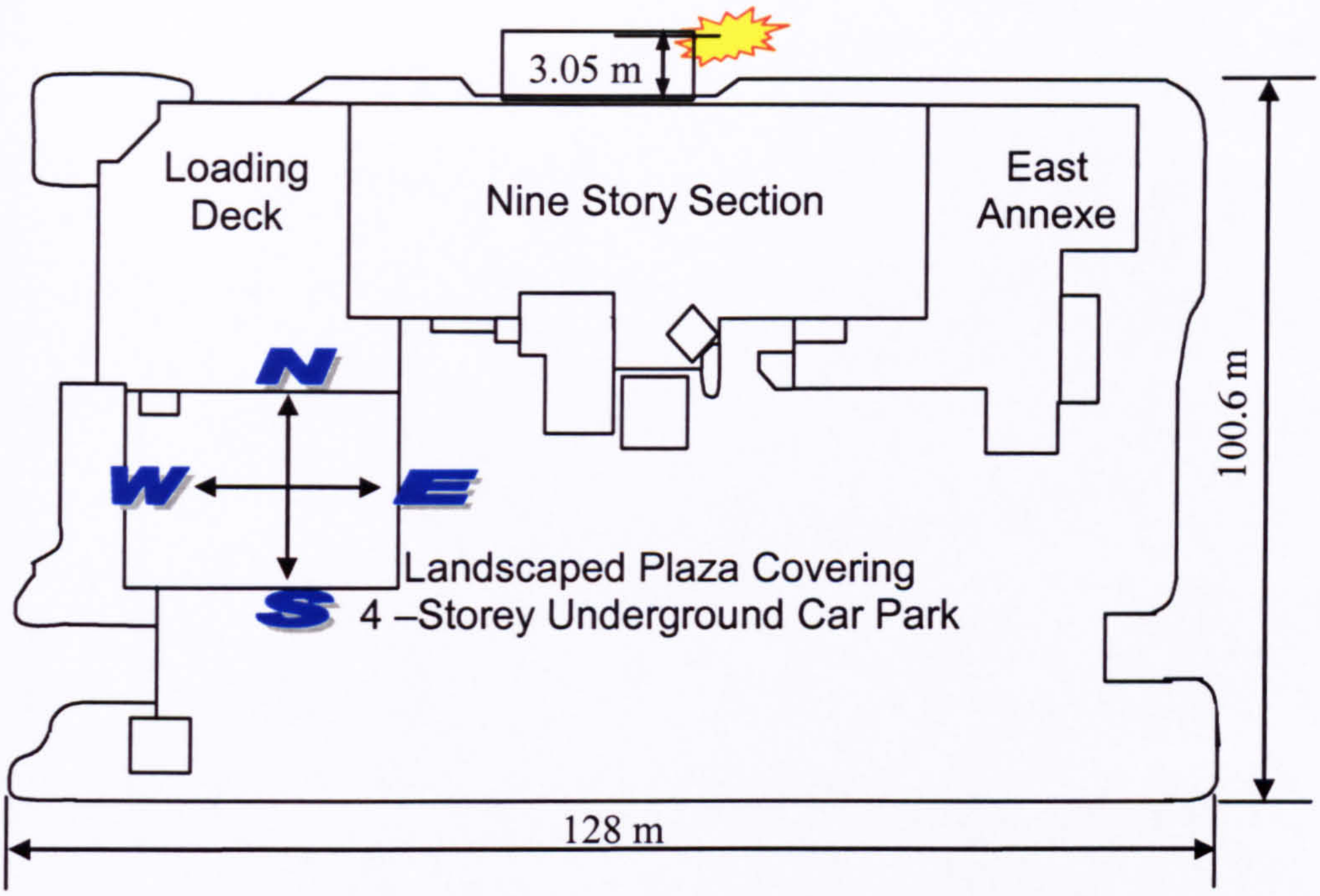

Figure 9.2 Plan of the Murrah building

Exposed precast concrete spandrels with in between glass cladding were to found on the southside face. Board formed core walls and shear walls were exposed on the southside.

Each floor is divided into ten bays spanning east to west and two bays spanning north to south. At the third floor a transfer girder of cross section 1.52 by 6.91m supported intermediate columns from the upper floors. Columns spanning the first two floors in turn supported this transfer girder.

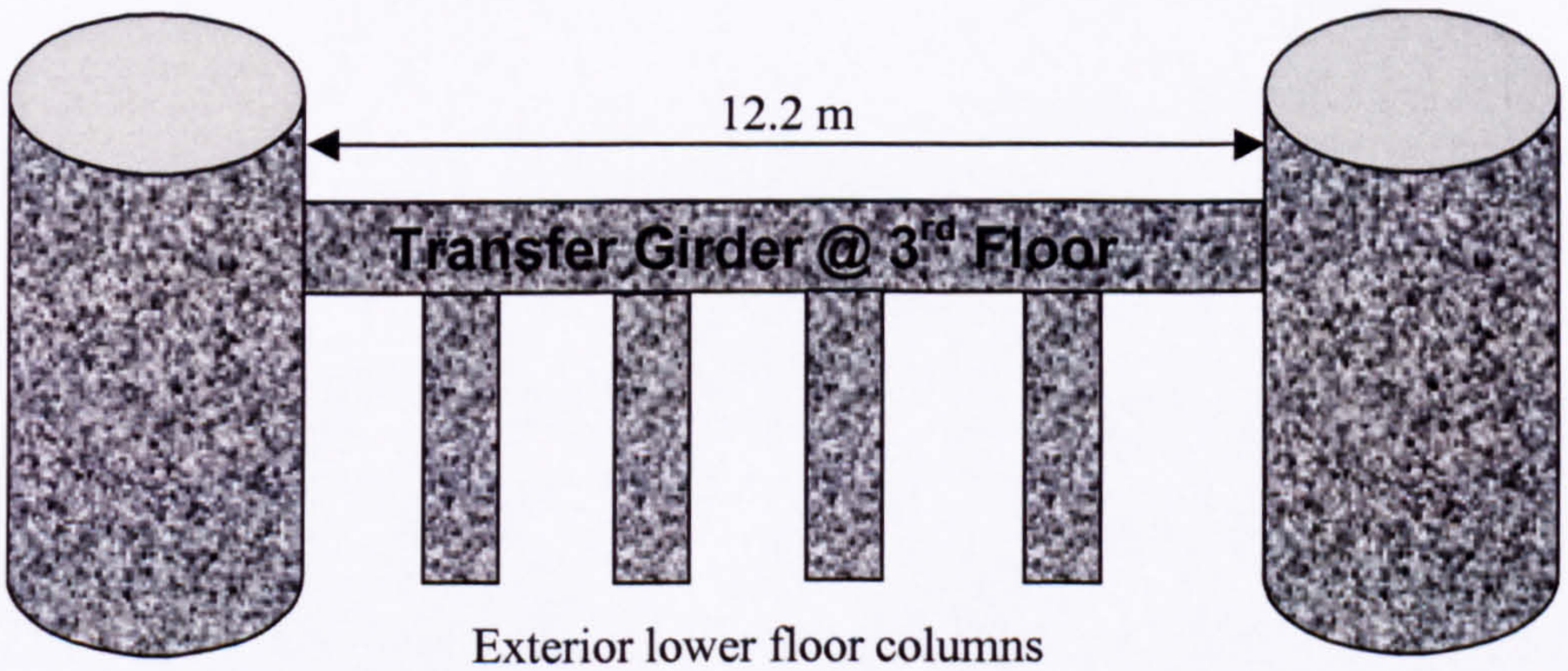

Figure 9.3 Section through the Murrah building

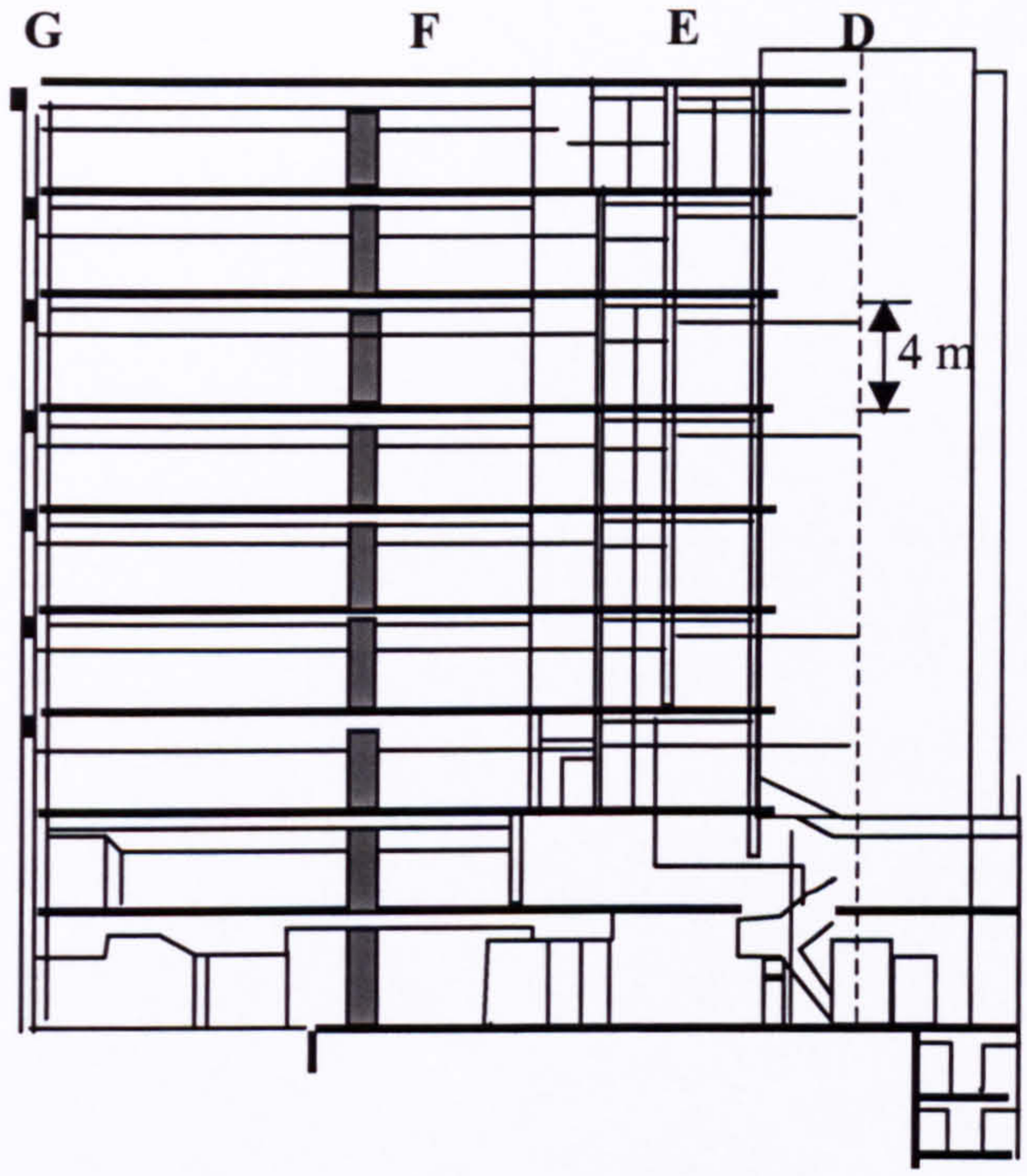

Figure 9.4 Sectional elevation the Murrah building

9.3 Structural damage to the Alfred P Murrah building

The explosion occurred 3.05 m away from the northside of building close to column G20 [5, 6]. The failure line is marked on the floor plan as shown in Figure 9.5.

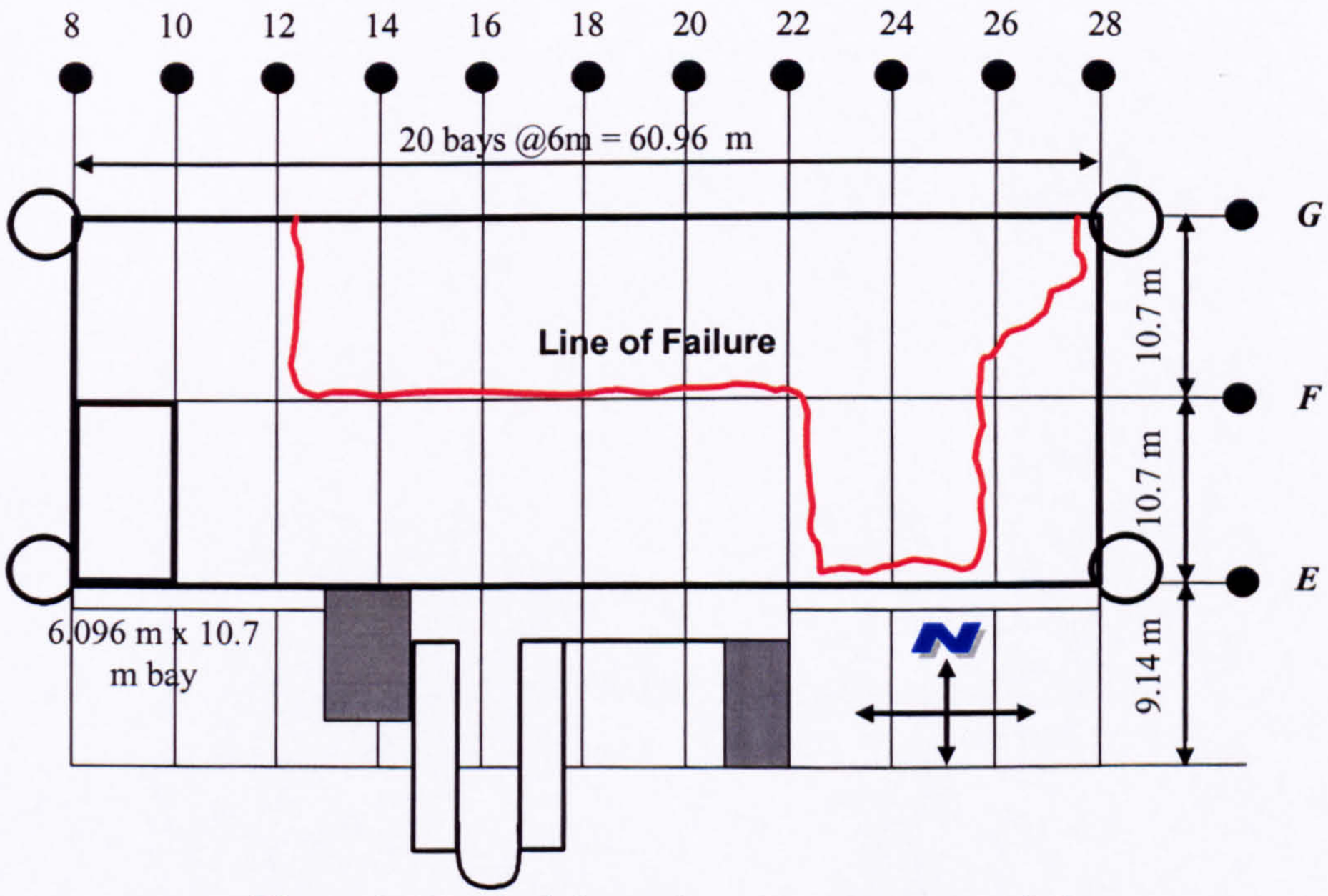

Figure 9.5 Typical floor plan of the Murrah building

The extent of the damage and progressive collapse is illustrated in Figure 9.6 to Figure 9.11.

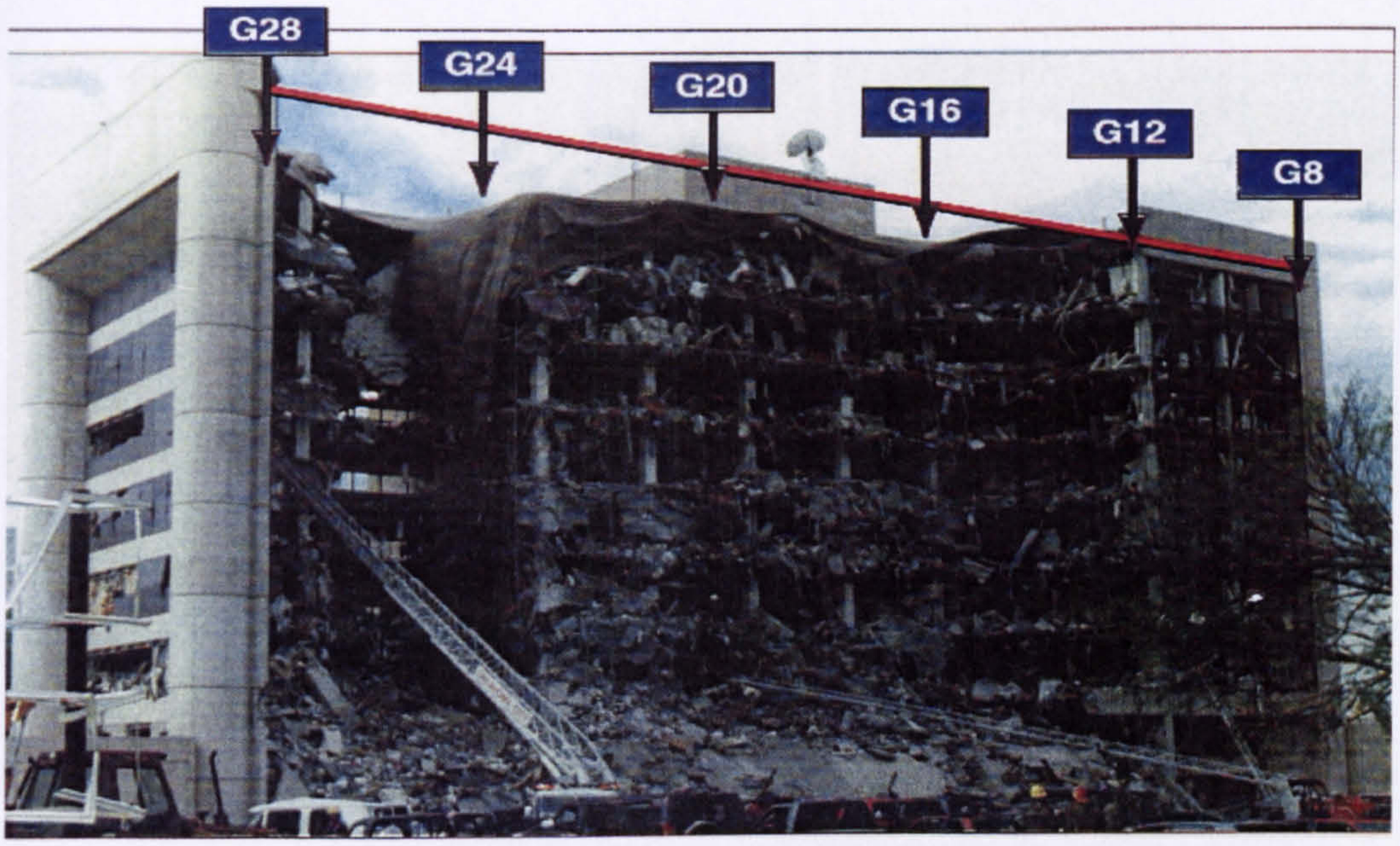

Figure 9.6 Damage to the North side of the Murrah building

Columns G16, G20 and G24 collapsed resulting in the progressive failure of all the floors above. Eight out of the ten bays in the above floors failed. The failure line extended 10.67 m into the building between grid line G12 and G22. The failure of F24 resulted in the failure of a further two bays on the second and third floors extending 21.3 m between G22 and G26. Between column lines 8 and 12 the transfer girders, mullions, columns and spandrels remained undamaged. The glass cladding was completely destroyed. Figure 9.7 shows the destruction at the G column line.

Figure 9.7 G Column line [5]

Figure 9.8 and Figure 9.9 shows the results of the progressive failure. As the upper floor failed the resulting mass falls on to the floor below. This induces failure on that level. The inertia created by the falling mass then induces destruction of the floors below.

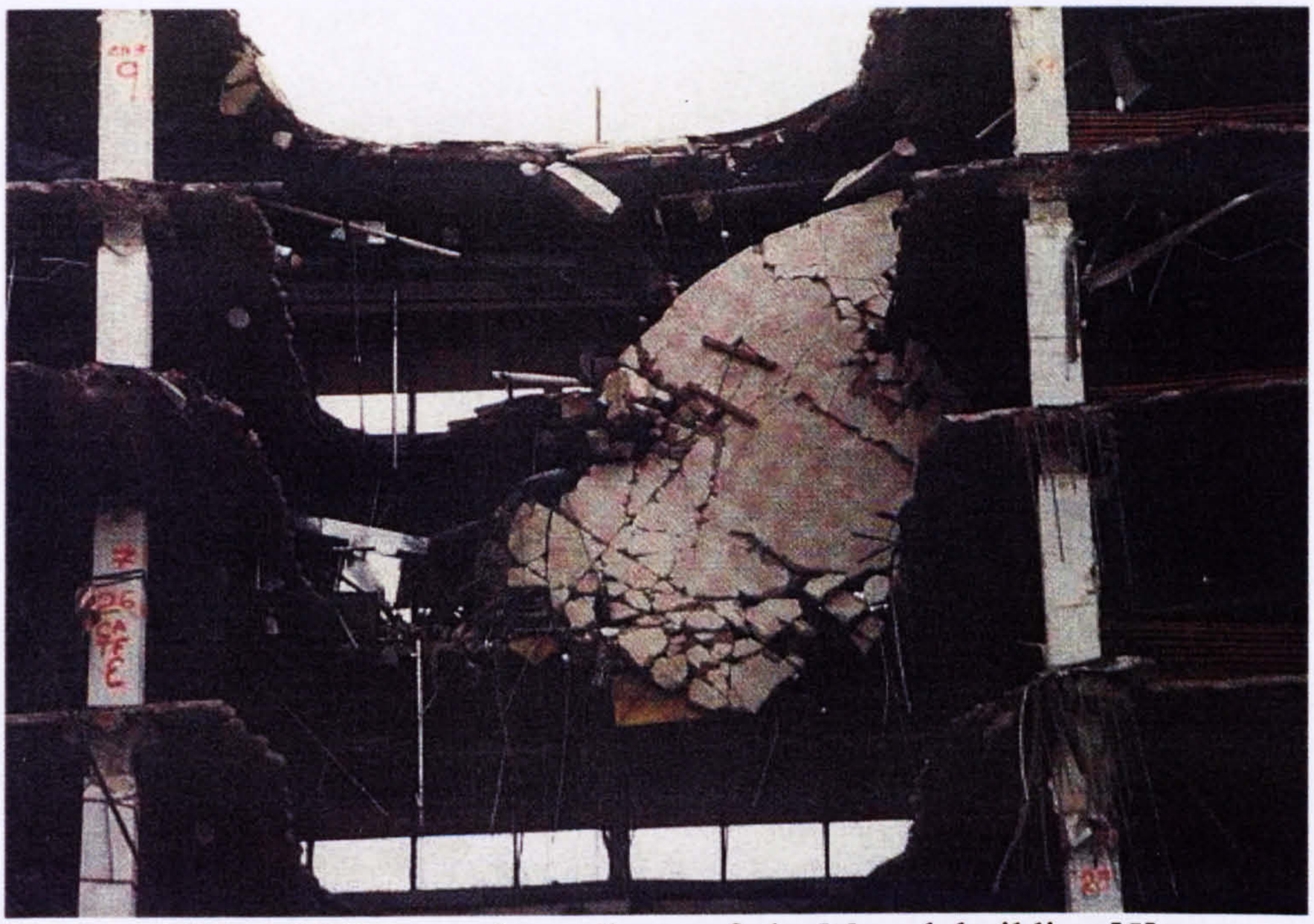

Figure 9.8 Progressive collapse of the Murrah building [5]

Figure 9.9 Progressive collapse [5]

The failure of G16 and G24 was thought to be as a result of the inward rotation of the transfer girder between the second and third floor. Column F24 failed since unlike nearby columns it was not provided with additional lateral bracing from the lift core and stairway. Column F14 failed in shear.

The girder failed at the midspan where an intermediate column had been supported. The bottom reinforcement had been pulled out thus pulling out the connecting shear ties. The floor slab behind the girder had been pulled down by the failing columns. The relative good condition of the transfer beam showed that load transfer did not occur (Figure 9.10).

Figure 9.10 Remains of the transfer girder [5]

Most of the failures were brittle and occurred mostly at the connections. This resulted in the progressive collapse of the higher floors as illustrated in Figure 9.7. Only where the full force of the explosion was not felt, some ductility was observed. The collapse was deemed to have occurred in three seconds as a result of subsequent forensic investigations.

The south face did not endure the full force of the blast and in comparison suffered insignificant damage to the doorframes, glass cladding and mullions. Much of the buildings lateral stiffness was concentrated in the form of shear/core walls along column line E (referred to as the core section of the building) on the south face of the building. The investigating team concluded this to be a major reason why this side did not suffer as much damage as the north face.

Figure 9.11 South side of the Murrah building [1]

The core section and to a lesser extent the circular shafts provided the lateral restraint and the team also concluded that no meaningful lateral or torsional displacement occurred as a part of the global response during collapse.

Of the end walls the east end wall endured most damage. All the granite infill panels failed in flexure and some were dislodged. The west wall endured a similar flexural failure pattern to its infill walls but most remained in place.

The interior ceiling, ductwork and floor panels failed. Columns along lines G and F failed either entirely or partially. Masonary partition walls in the core area also failed in particular on the first three floors.

9.4 Structural plans for the floors of the A P Murrah building

The ground floor level will be assumed as fixed at the base with columns rising to the first floor. The first floor is idealised by the beam slab arrangement shown in Figure 9.12 [7]. The letters B and S denote the beams and slabs respectively. The columns on the line F′ extend from the ground floor upwards to beneath the first floor.

Figure 9.13 and Figure 9.14 show the plans for the second and third floors respectively.

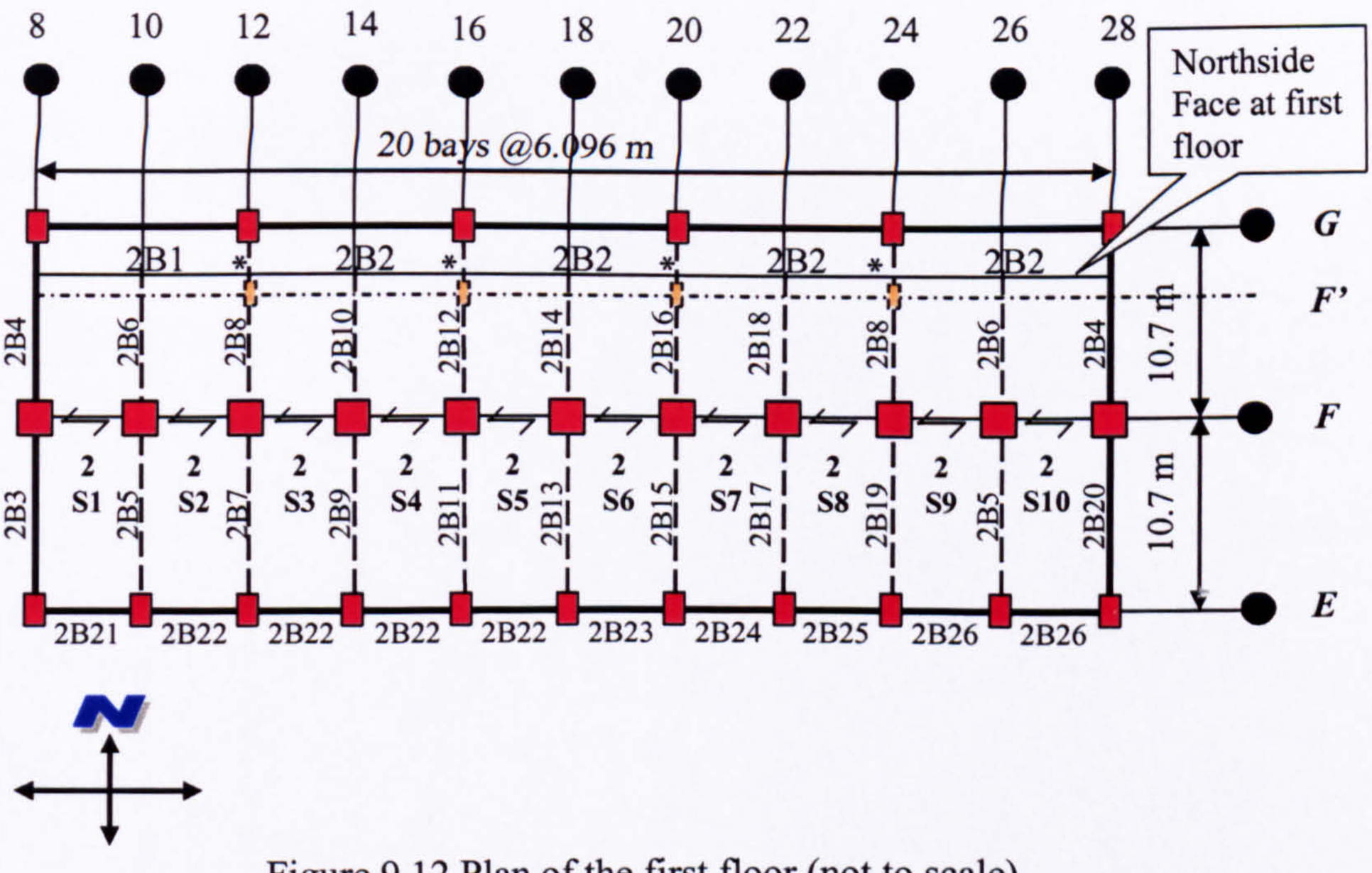

Figure 9.12 Plan of the first floor (not to scale)

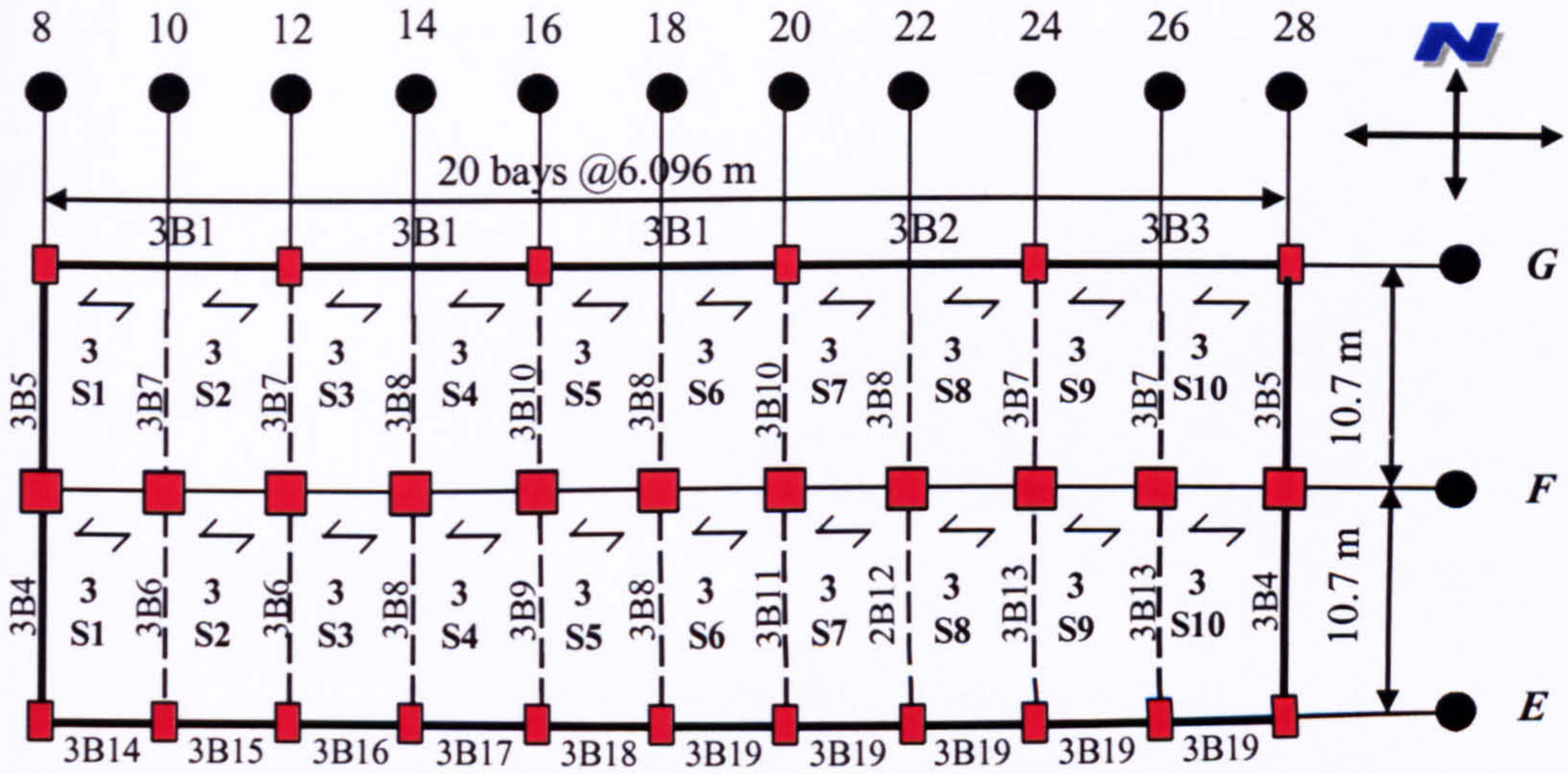

Figure 9.13 Plan of the second floor (not to scale)

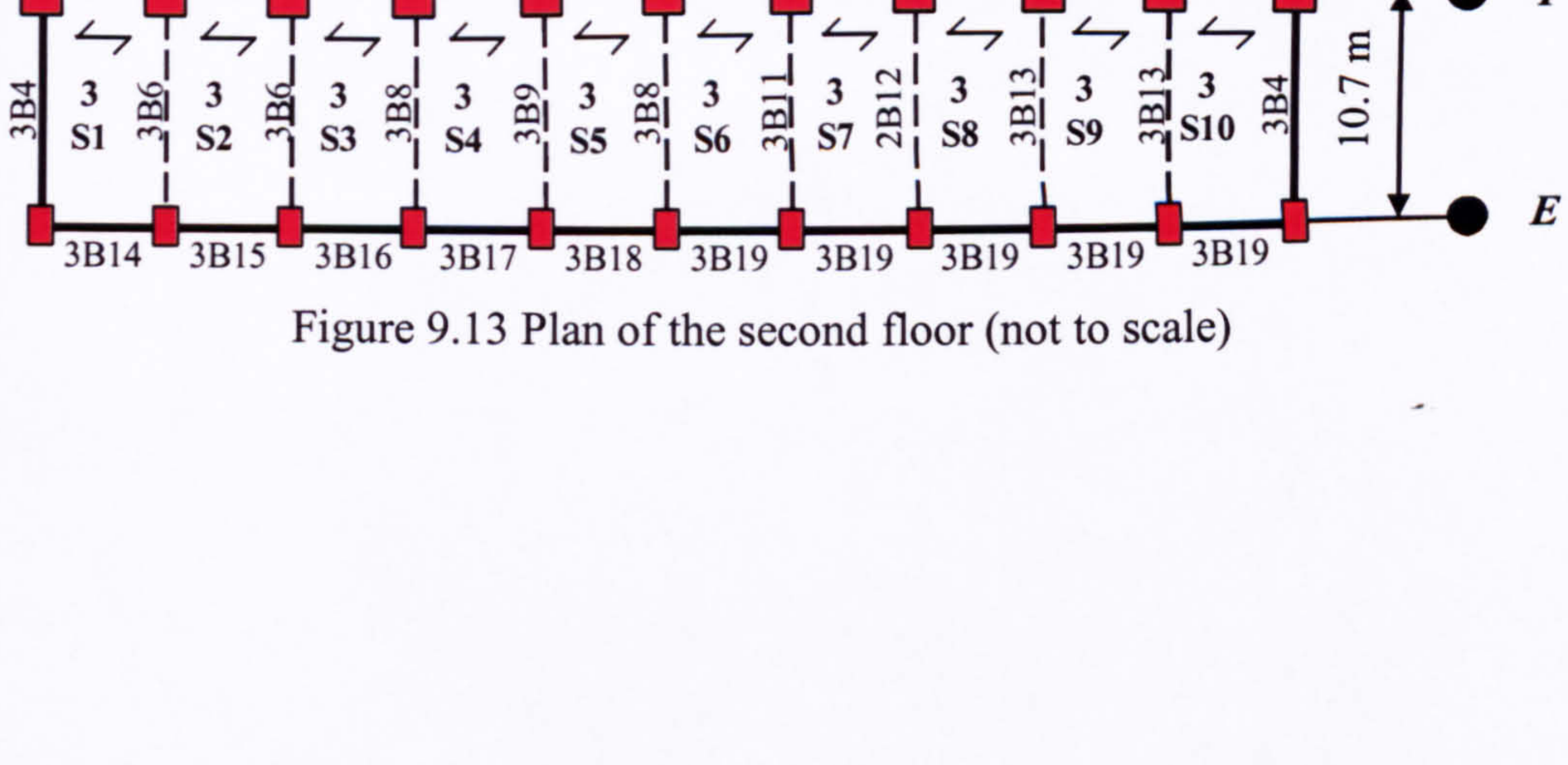

Figure 9.14 Plan of the third floor (not to scale)

Figure 9.15 shows the roof plan. This beam and slab detailing shown is used for the fourth through to ninth floors.

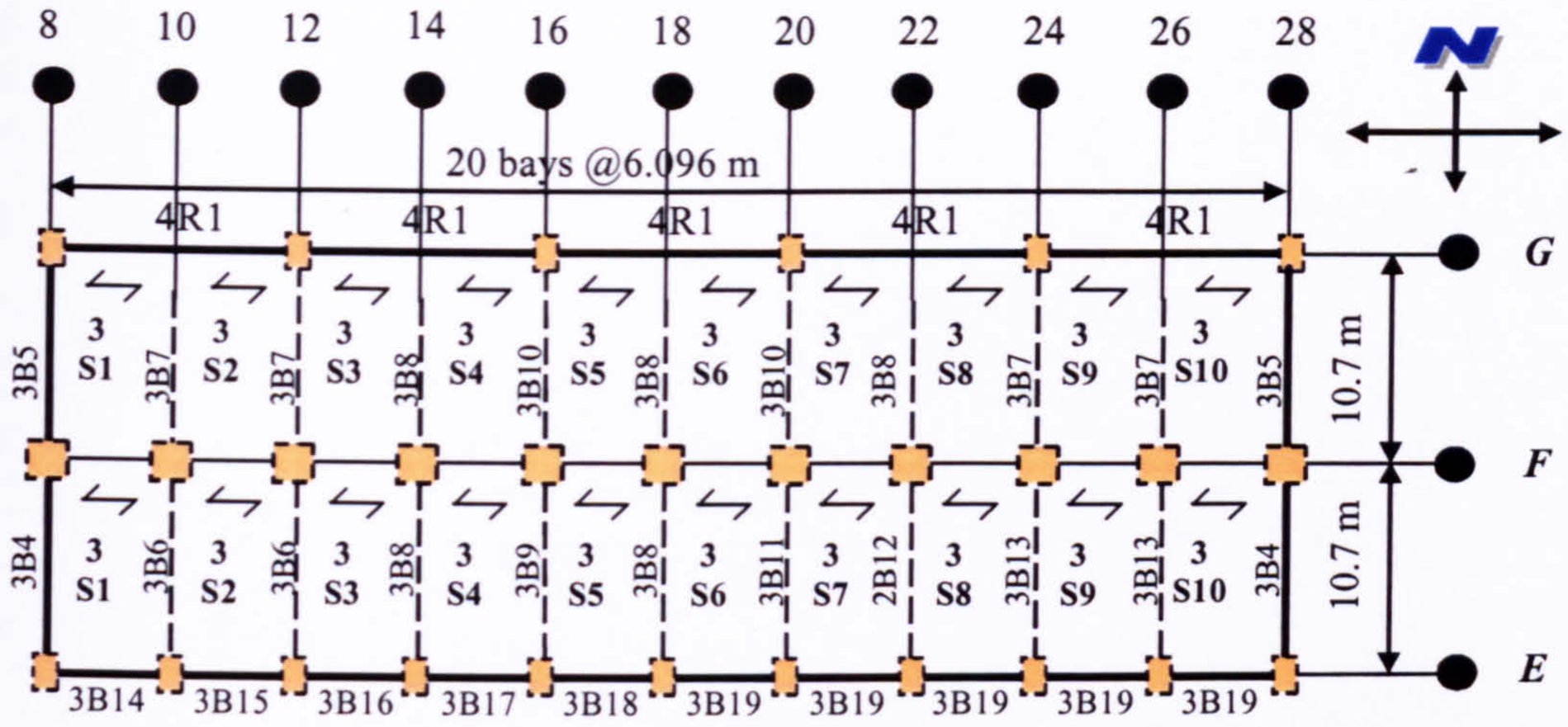

Figure 9.15 Plan of the roof (not to scale)

9.5 Material properties and reinforcement detailing

The concrete eight day compressive strength was 27.5 MPa and the yield strength of the reinforcing bars were 413.7 MPa [5]. The density of the concrete samples tested at CRL ranged from 2346.8 – 2396.5 kg/m^3 (146.4 to 149.5 lb/ft^3) [1]. The properties of the reinforcement samples tested are summarised in Table 9.1.

Table 9.1 Properties of the Reinforcement Samples [1]

Parameter / BarSize	**#8**	**#5**
Design Yield Stress	413.7 MPa	413.7 MPa
Measured Yield Stress	495.061 MPa	449.554 MPa
Yield Load	252.2 kN	89.9 kN
Ultimate Load	377.64 kN	148.1 kN
Ultimate Stress	737.765 kN	737.765 kN
Elongation	9.8 %	11.1 %
Modulus of Elasticity	196507.5 MPa	196507.5 MPa

These parameters were compiled on the basis of the following conversion factors

1 lb/ft^3 = 16.03 kg/m^3

1lb/ft^2 = 0.006895 MPa

1 lb = 4.448 N

The reinforcement used for the columns and their detailing is described and illustrated below in Figure 9.16. The column heights are taken as 3.96 m for floors up to floor 9. The ninth floor columns are taken as 4.27 m .

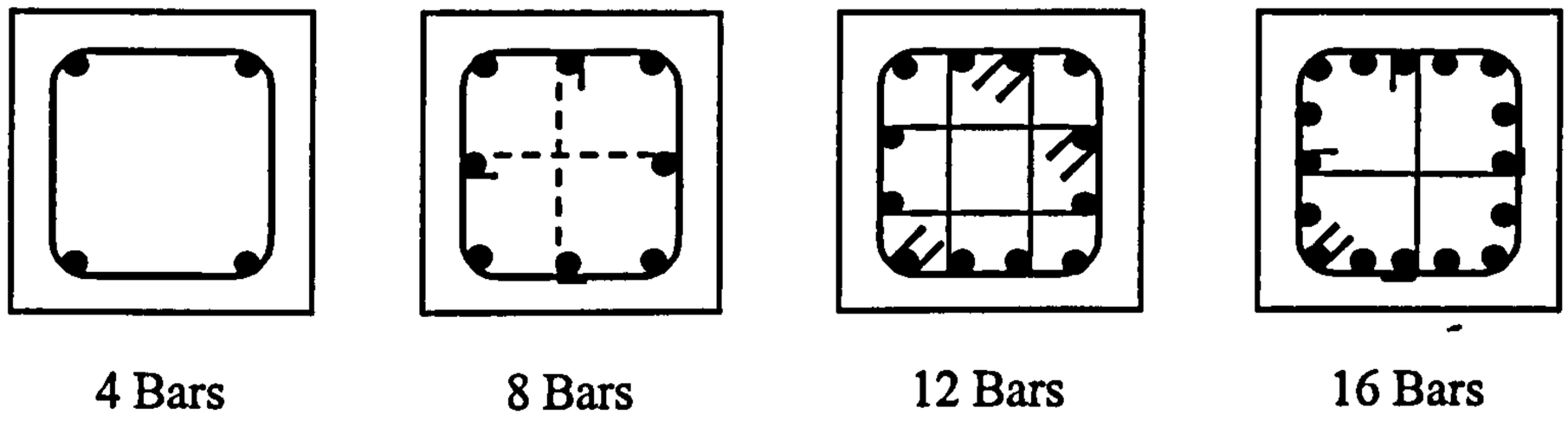

Figure 9.16 Reinforcement detailing for the columns

9.6 Numerical simulation of blast loading

The Alfred P Murrah building is modelled as a rectangular structure of ten floors. As Figure 9.11 shows the south side of the structure remained relatively intact after the blast loading. This part of the structure consisted of the core structure of the building including the lift shafts and stairwells. These acted as shear walls providing the principal lateral bracing against the explosion loading. The circular concrete air ducts at the four corners of the structure added to the structures overall stiffness. In order to accurately model the structures response behaviour to blast loading, the corner column nodes were fixed. In addition the nodes on the ground floor and the nodes representing the south face were also fixed.

The original structure had a seven foot square hole at each floor level. This was omitted from the model as its influence upon the overall structural behaviour is limited.

The material properties used in the modelling are described in Table 9.2.

Table 9.2 Input values for material properties

Property	Magnitude of property
Max Concrete Strain	0.0035
Concrete Elastic Modulus	25.0e+09 N/m^2
Strength of Concrete	540.2e+06 N/m^2
Density of Concrete	2.4e+03 kN/m^2
Steel Elastic Modulus	210.0e+09 N/m^2
Steel Yield Stress	560.0e+06 N/m^2

The size of element used and the reinforcement is described in Table 9.3.

Table 9.3 Element geometry and reinforcement used in the model

Structural Element	b (m)	h (m)	d_c (m)	A_0 (m^2)	A_1 (m^2)	A_2 (m^2)	A_3 (m^2)
East/West outer wall	6.1e-01	8.9e-01	5e-02	9.82e-04	9.82e-04	1.29e-03	1.29e-03
North/South outer wall	5.7e-01	1.27e00	9.0e-02	2.01e-03	2.01e-03	1.206e-03	1.206e-03
Transfer Girder	6.91e-01	1.52e00	1.0e-01	4.0125e-03	4.0125e-03	6.036e-03	6.036e-03
G column	5.1e-01	9.1e-01	5e-02	3.027e-03	3.027e-03	3.027e-03	3.027e-03
F' column	3.1e-01	3.2e00	2.2e-01	3.83e-03	3.83e-03	3.83e-03	3.83e-03
F column	6.1e-01	6.1e-01	4e-02	2.52e-03	2.52e-03	2.52e-03	2.52e-03
E column	4.1e-01	9.1e-01	5e-02	2.77e-03	2.77e-03	2.77e-03	2.77e-03

The blast pressure is applied along the local axis of the cross section of the element, a_1 and a_2. These loads are over a specified time period using three factors, which modify the load according to the point in time. For example if the applied load is 500 N/m^2 a time t_1, then f_1 would equal one. The values of f_2 and f_3 would be a fraction of one according to how the load decreased over time period t_1 to t_2.

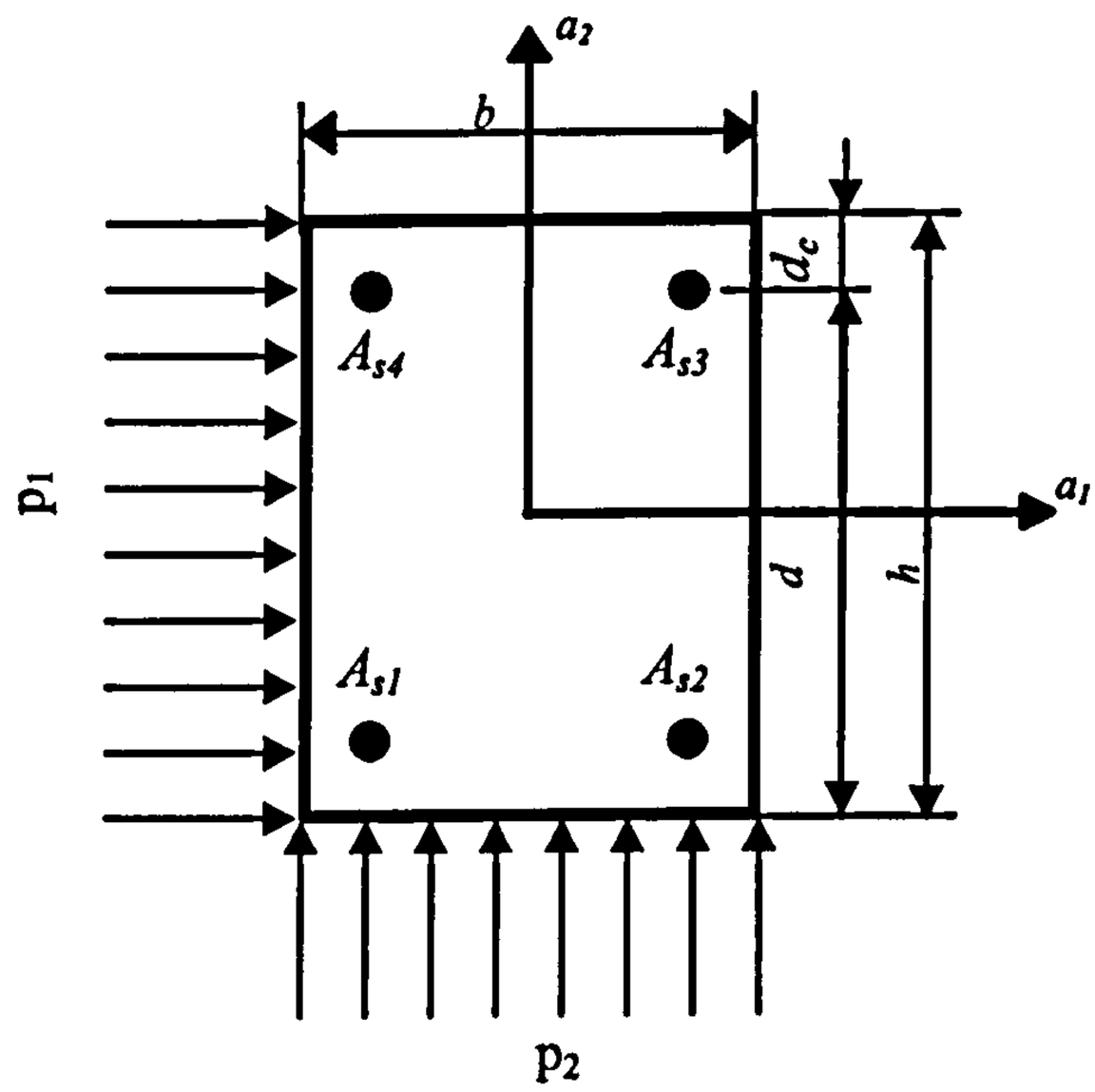

Figure 9.17 Blast pressure loading

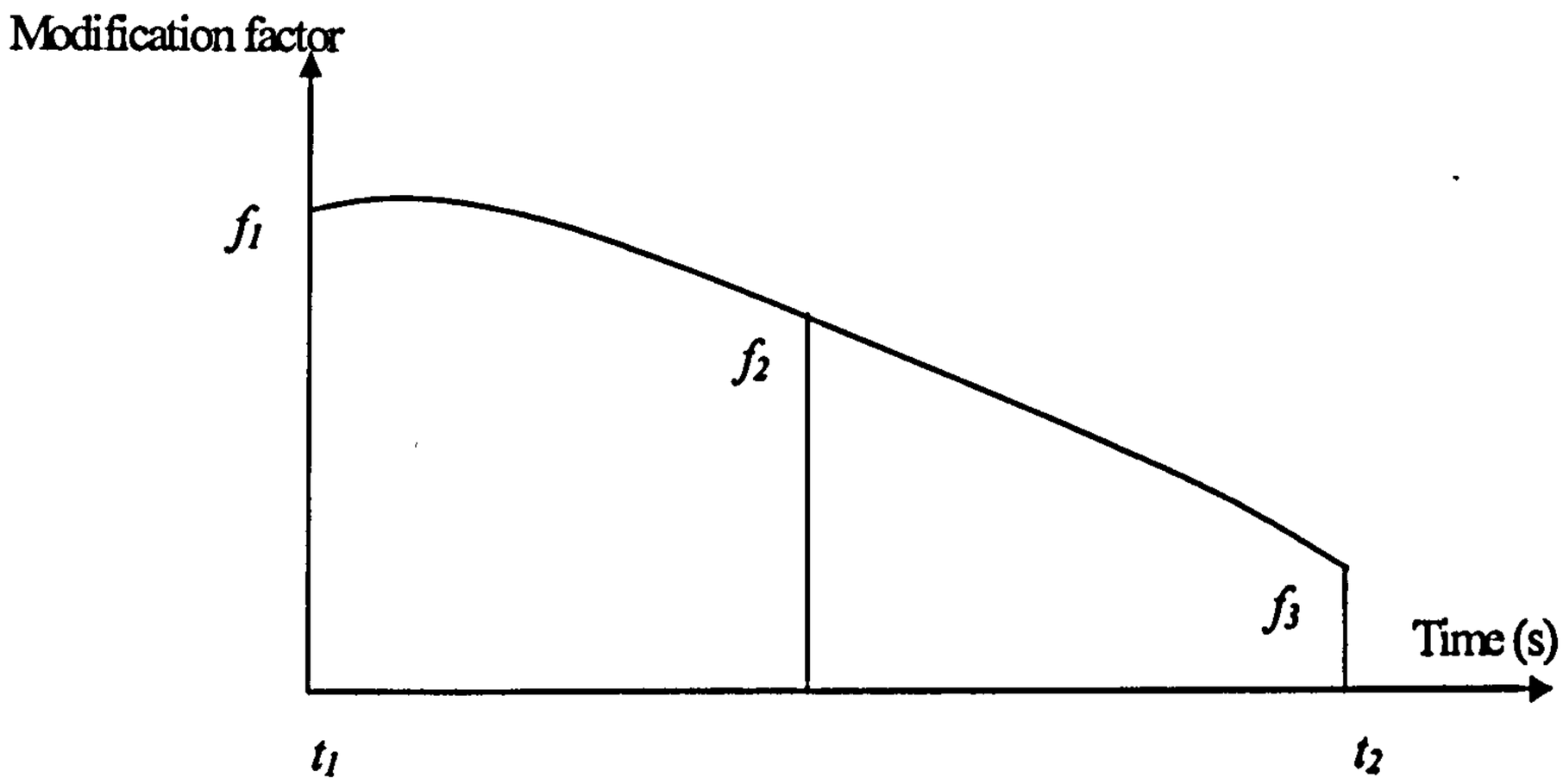

Figure 9.18 Load modification factors

Two blast load scenarios were modelled and are described below. Failure of the models occurs at the nodes.

LOAD CASE 1

In this case the load is applied across all of the floors at all levels and along the G line columns. The various blast pressure profiles are shown in Figure 9.19 to 9.20. The duration of this simulation is 12 ms. Stages of the failure simulation are shown in Figure 9.21 to Figure 9.29.

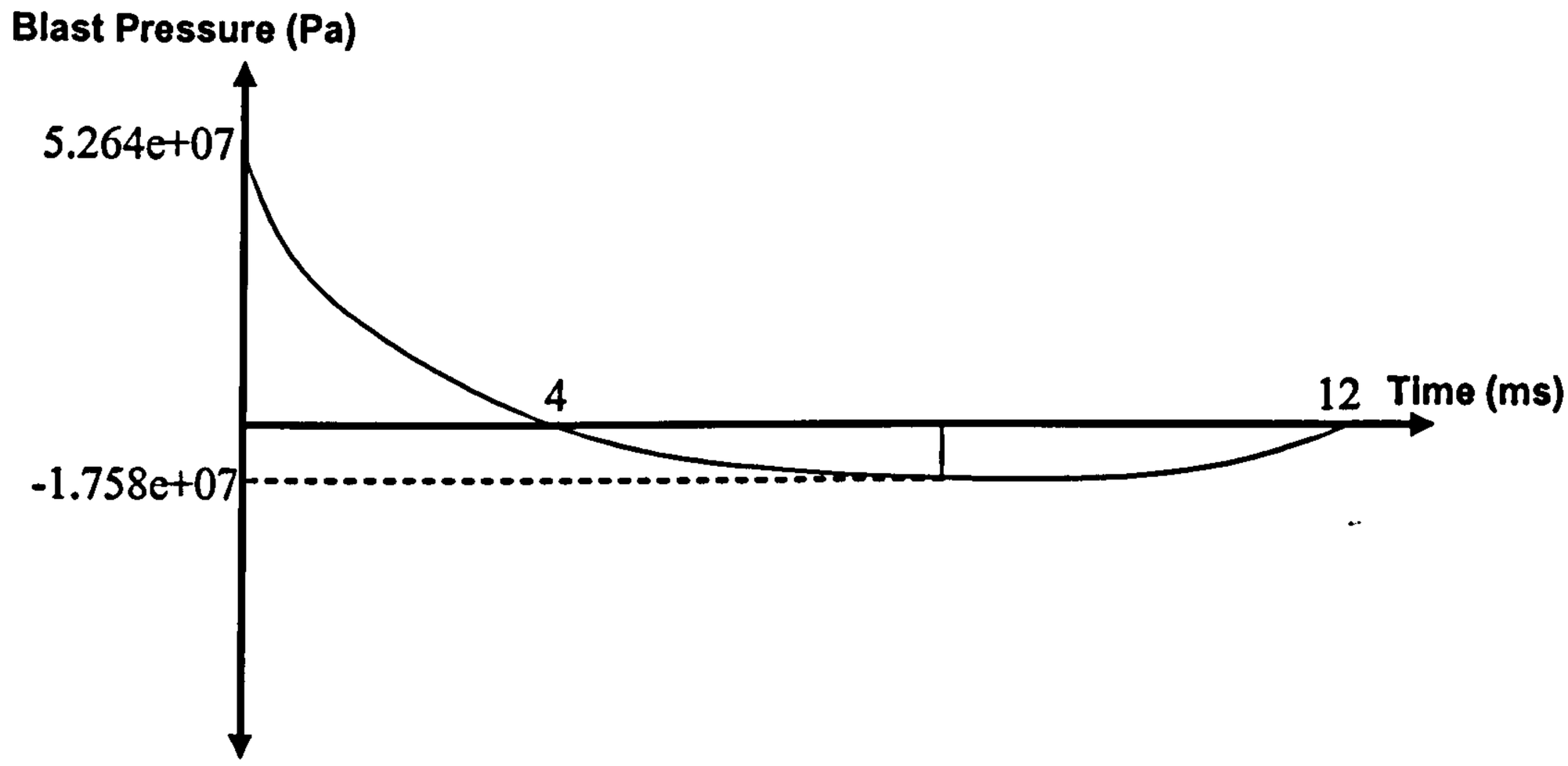

Figure 9.19 Blast pressure loading for slabs

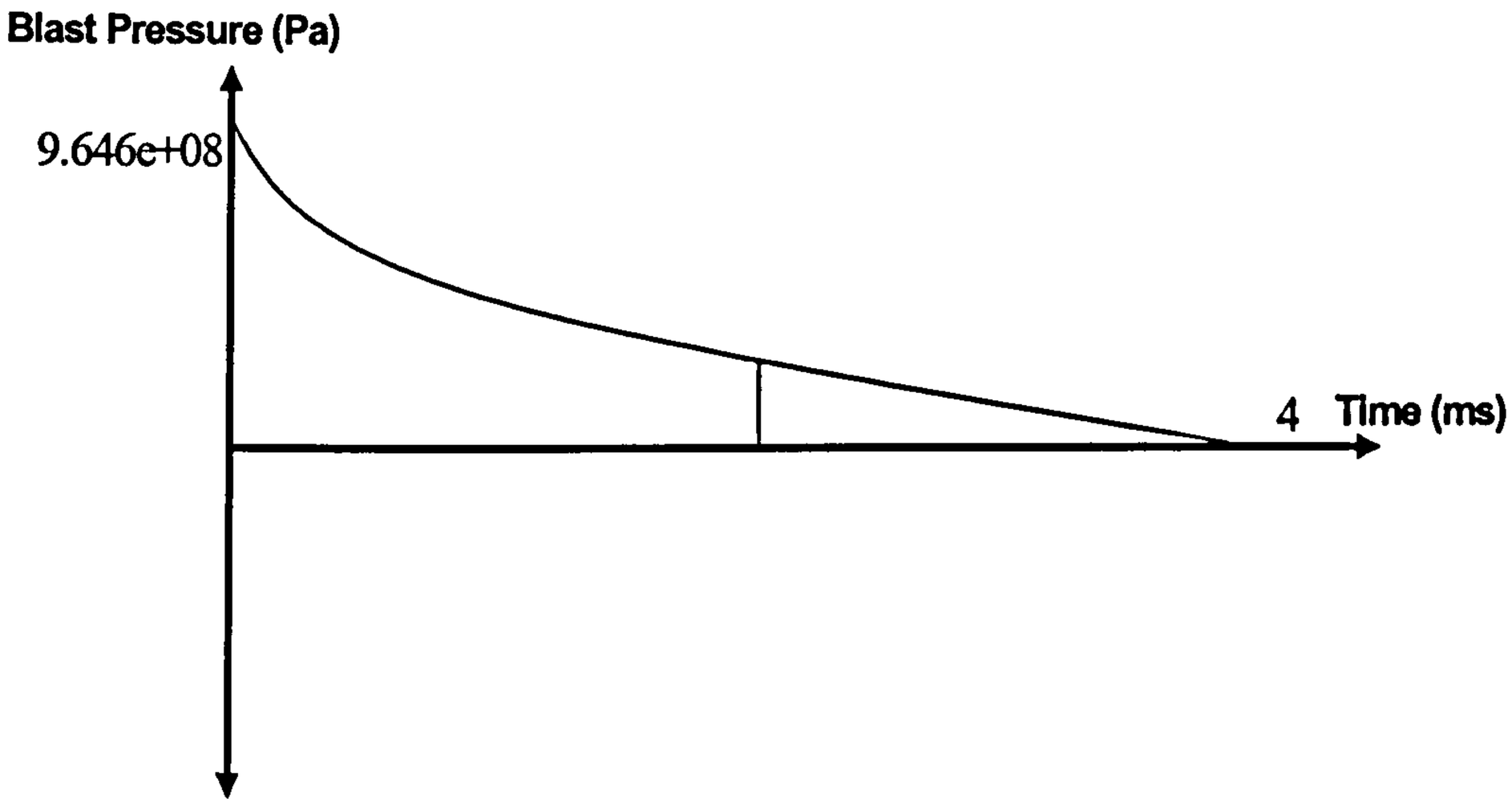

Figure 9.20 Blast pressure load for columns

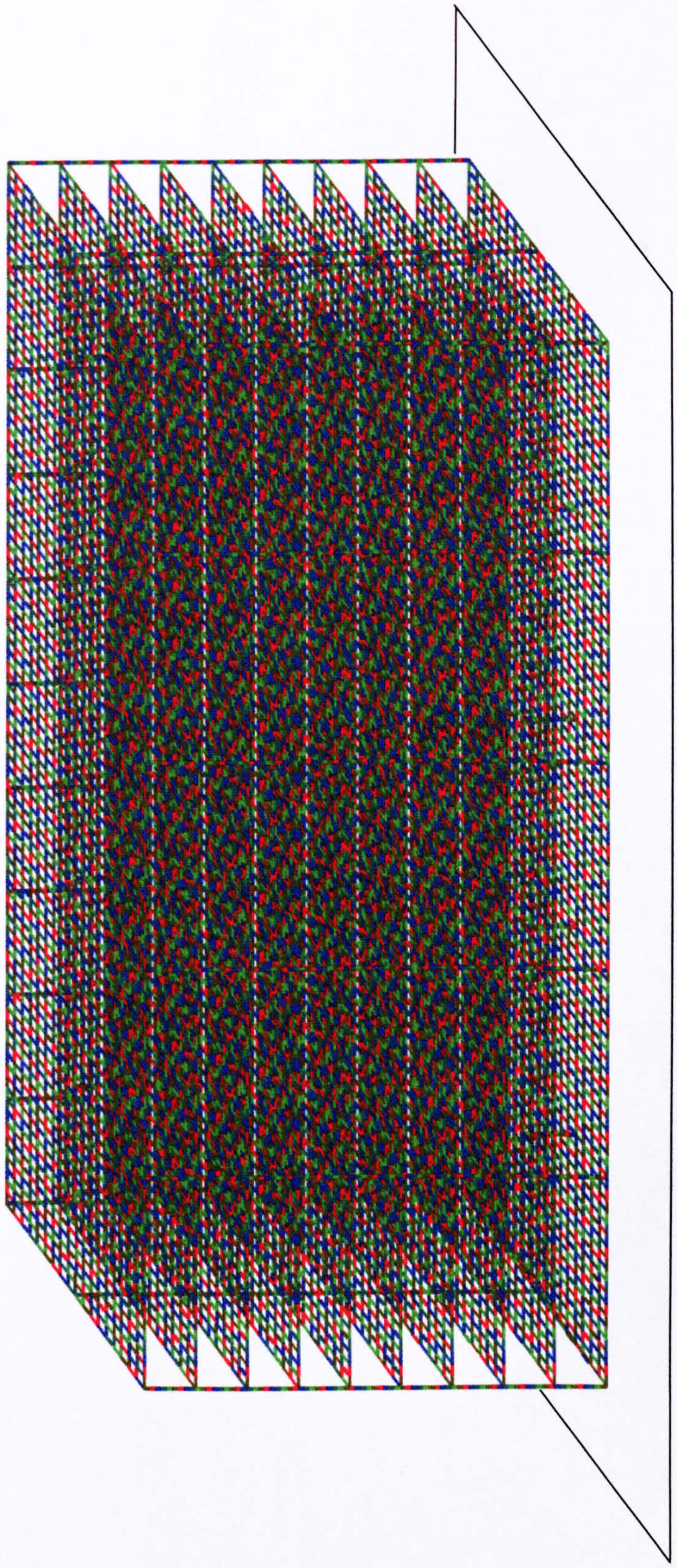

t = 0.0 s. The structure before blast load application

Figure 9.21 Murrah building collapse sequence t = 0.0 s

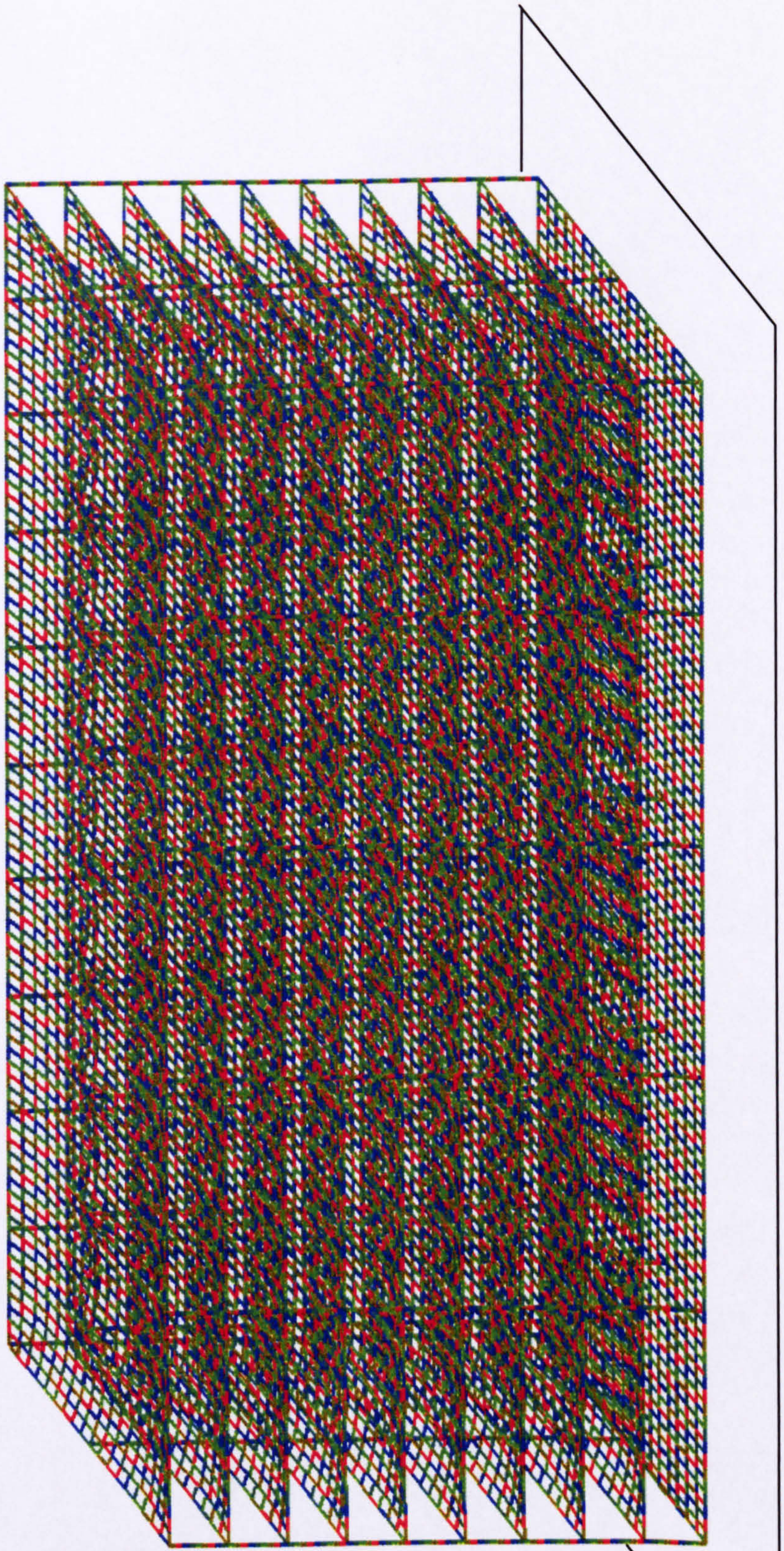

t = 0.3 s. At this time the structure has begun to deform at the floor levels.

Figure 9.22 Murrah building collapse sequence t = 0.3 s

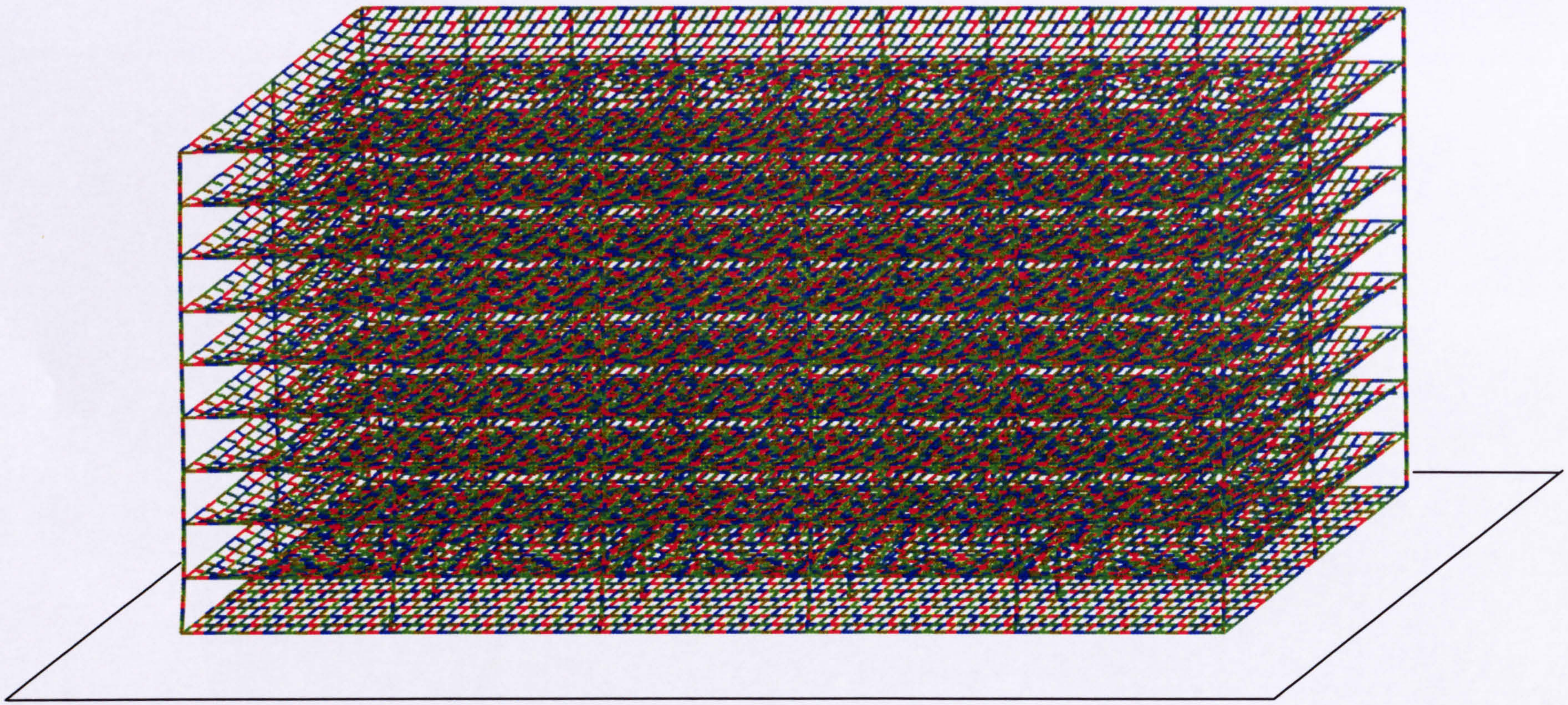

t = 0.45 s. The structure is seen to further deform at the floor levels with some elements detaching at the right rear (South face) circular vent shaft.

Figure 9.23 Murrah building collapse sequence t = 0.45 s

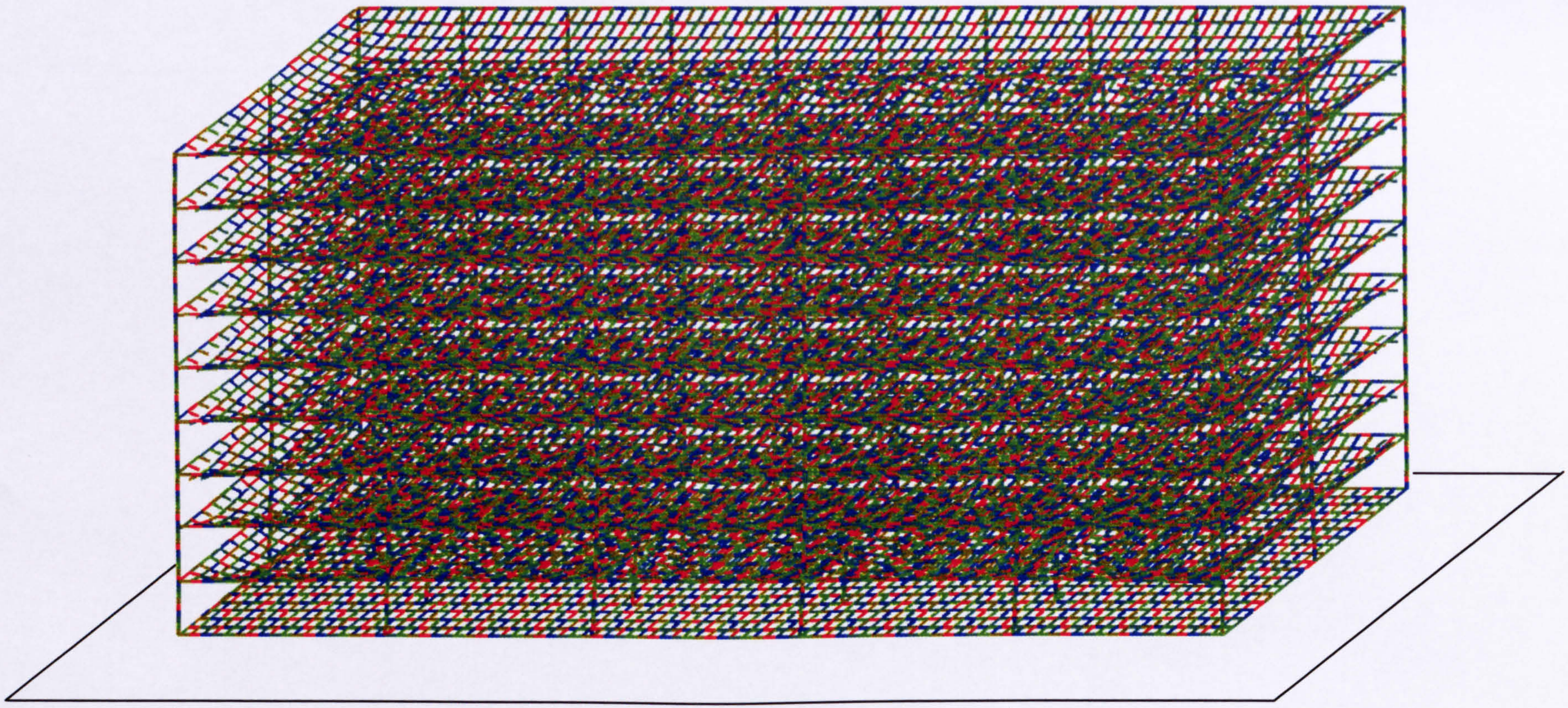

t = 0.55 s. Further element detachment is seen on the South facing left side circular vent shaft.

Figure 9.24 Murrah building collapse sequence t = 0.55 s

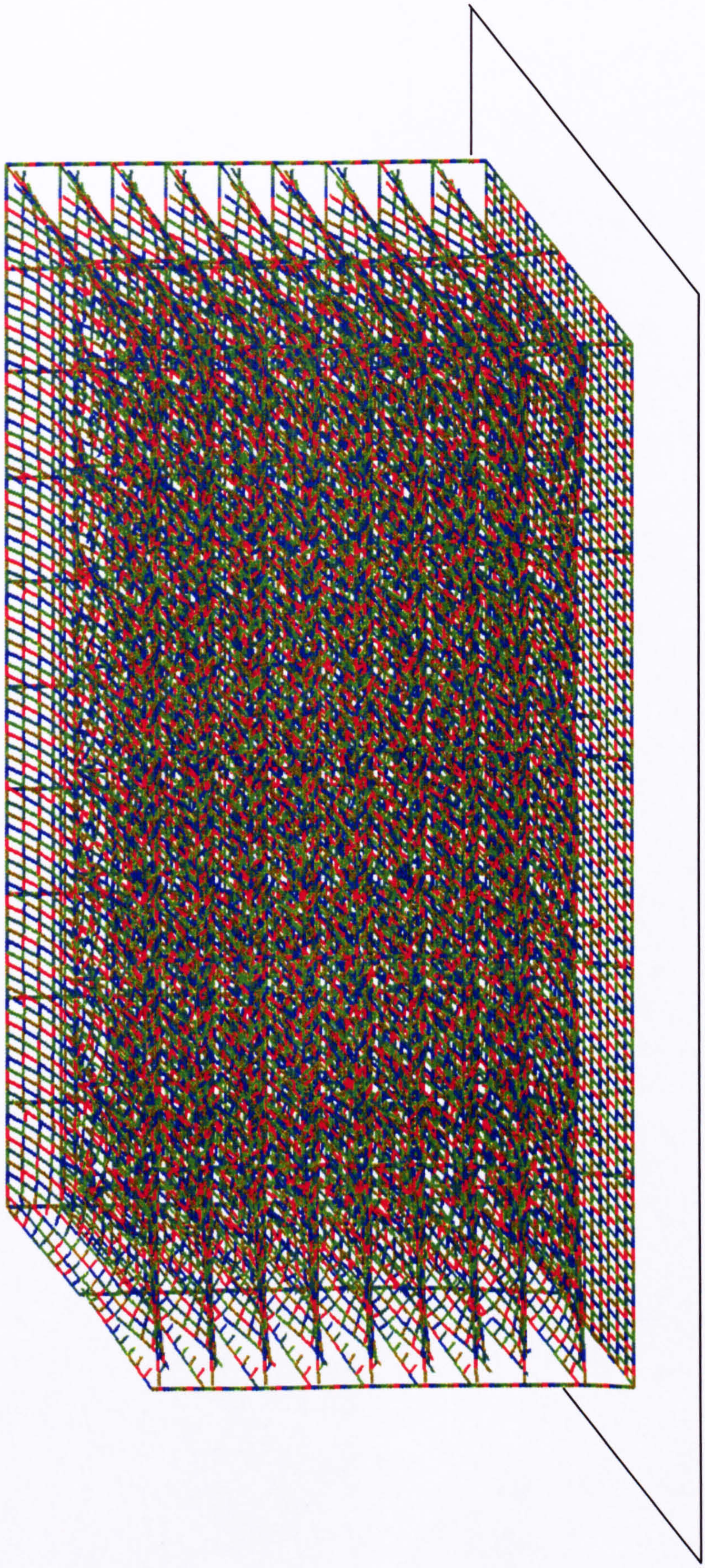

t = 0.65 s. At this time the breakage at all floor levels is severe.

Figure 9.25 Murrah building collapse sequence t = 0.65 s

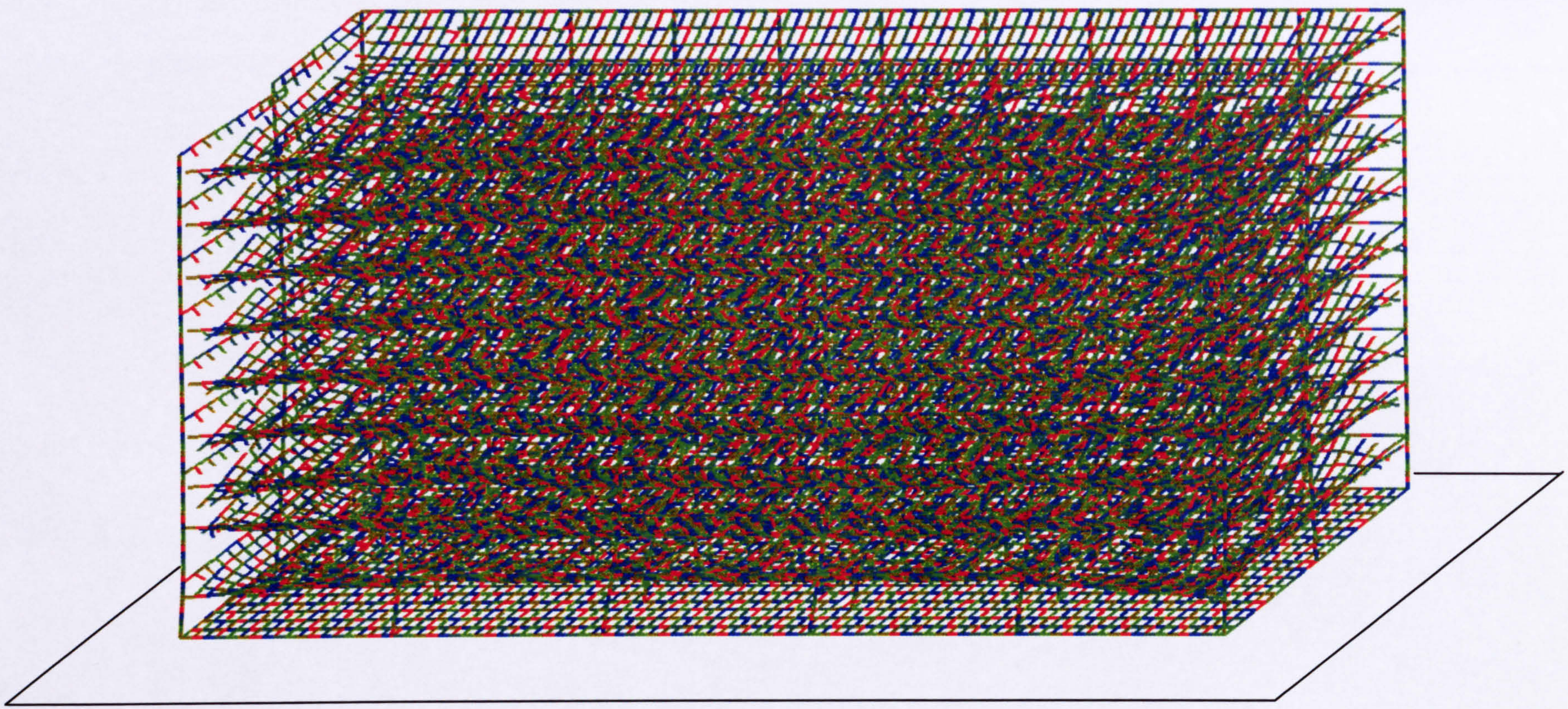

t = 0.8 s. Further breakage occurs with the floors and columns showing major deflection. The east side face is now showing breakage at the roof level.

Figure 9.26 Murrah building collapse sequence t = 0.8 s

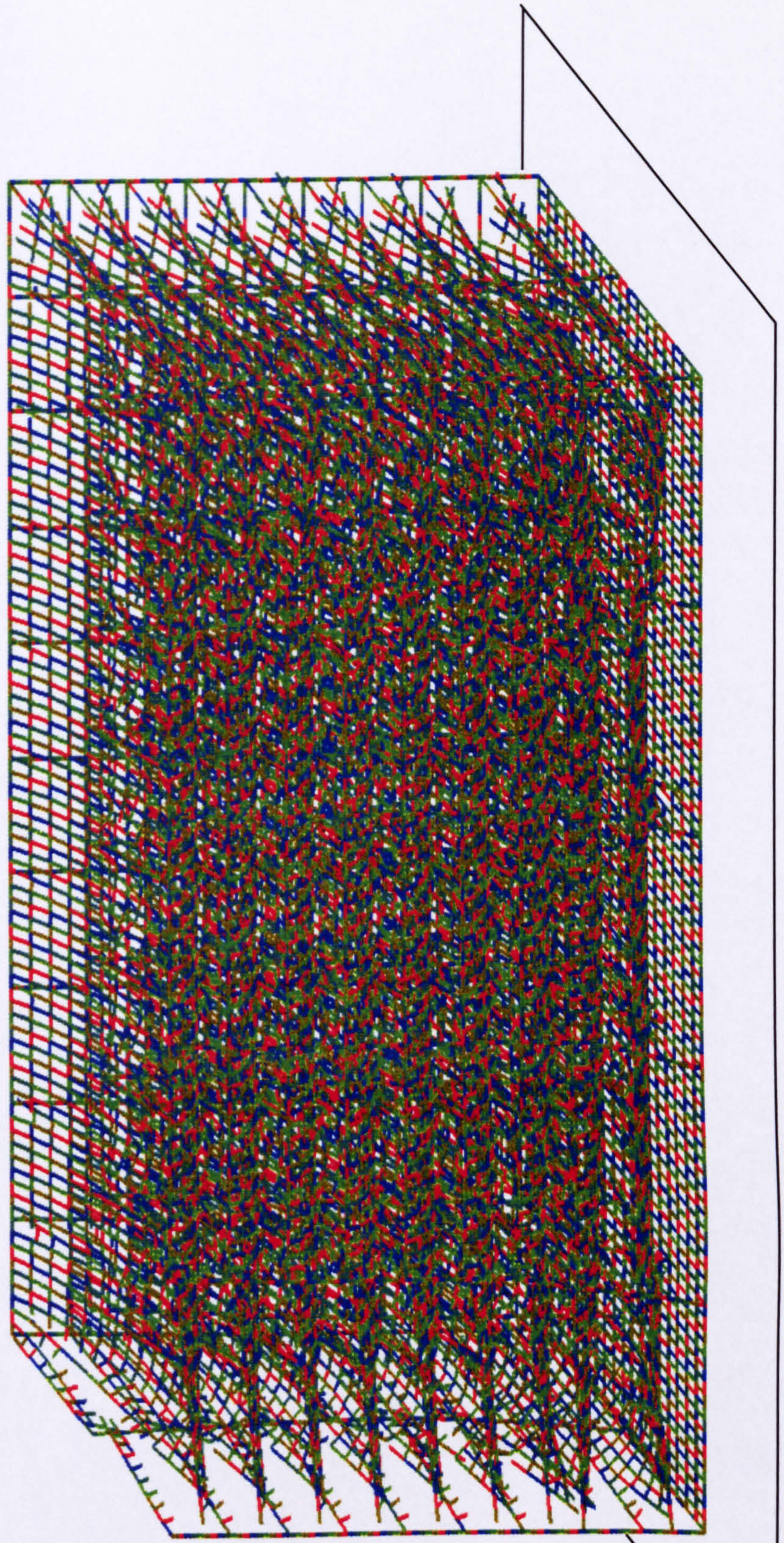

t = 0.95 s. More pronounced failure is beginning to occur.

Figure 9.27 Murrah building collapse sequence t = 0.95 s

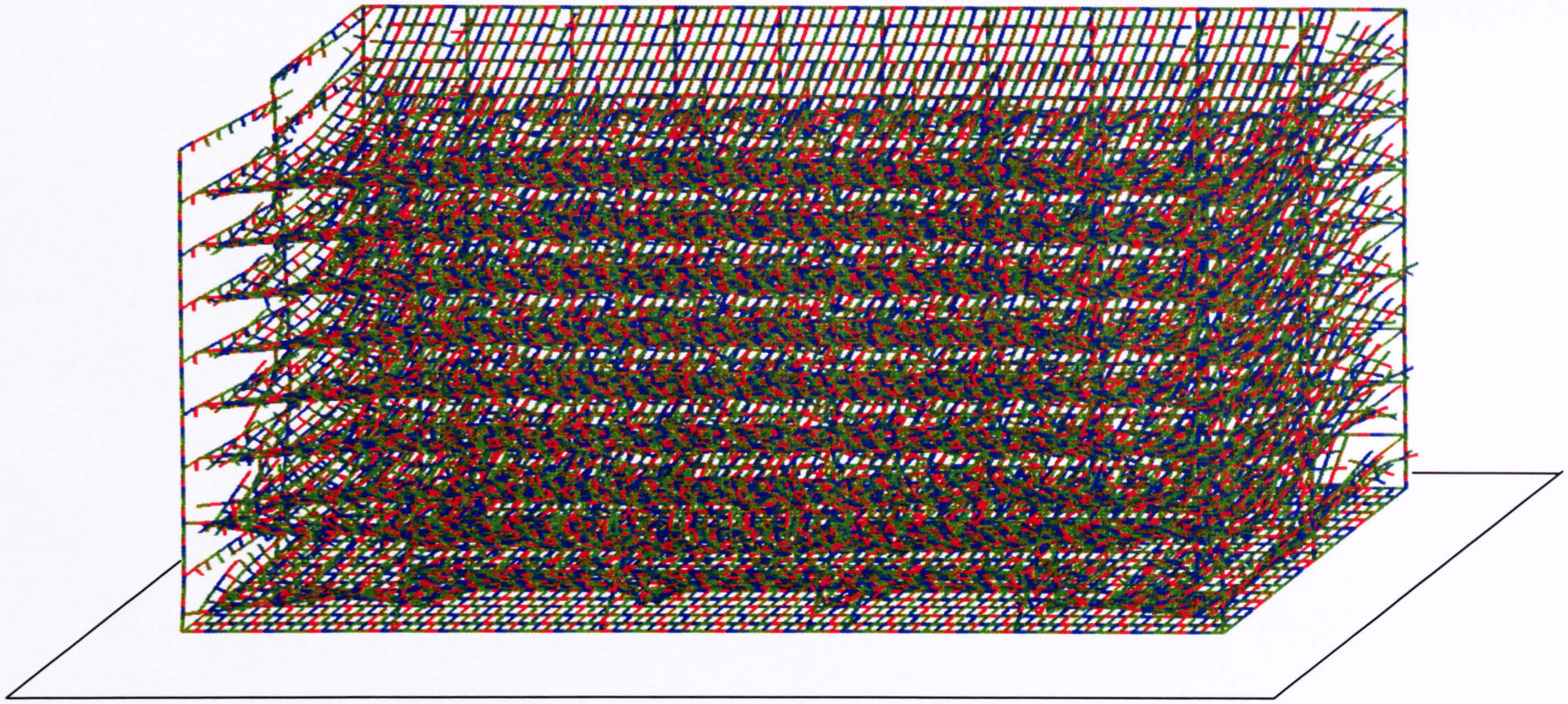

t = 1.1 s. All the floors and columns are collapsing.
Figure 9.28 Murrah building collapse sequence t = 1.1 s

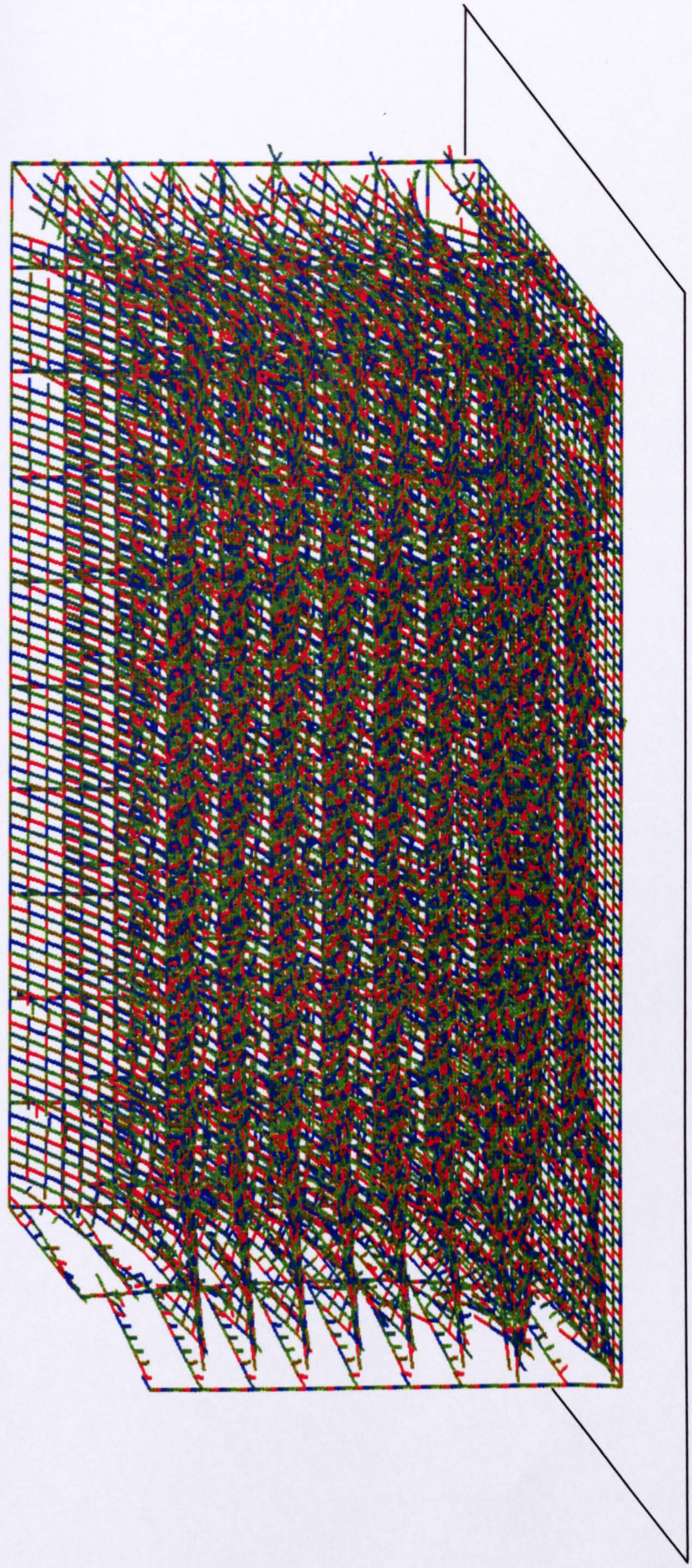

t =1.35 s. Progressive failure has been shown to be induced.

Figure 9.29 Murrah building collapse sequence t = 1.35 s

LOAD CASE 2

The load is applied across the floor area marked by the yellow area shown in Figure 9.30. The columns were not loaded. The blast load time function is shown in Figure 9.31. The duration of this simulation is 12 milliseconds. Stages of the failure simulation are shown in Figures 9.32 to Figure 9.41.

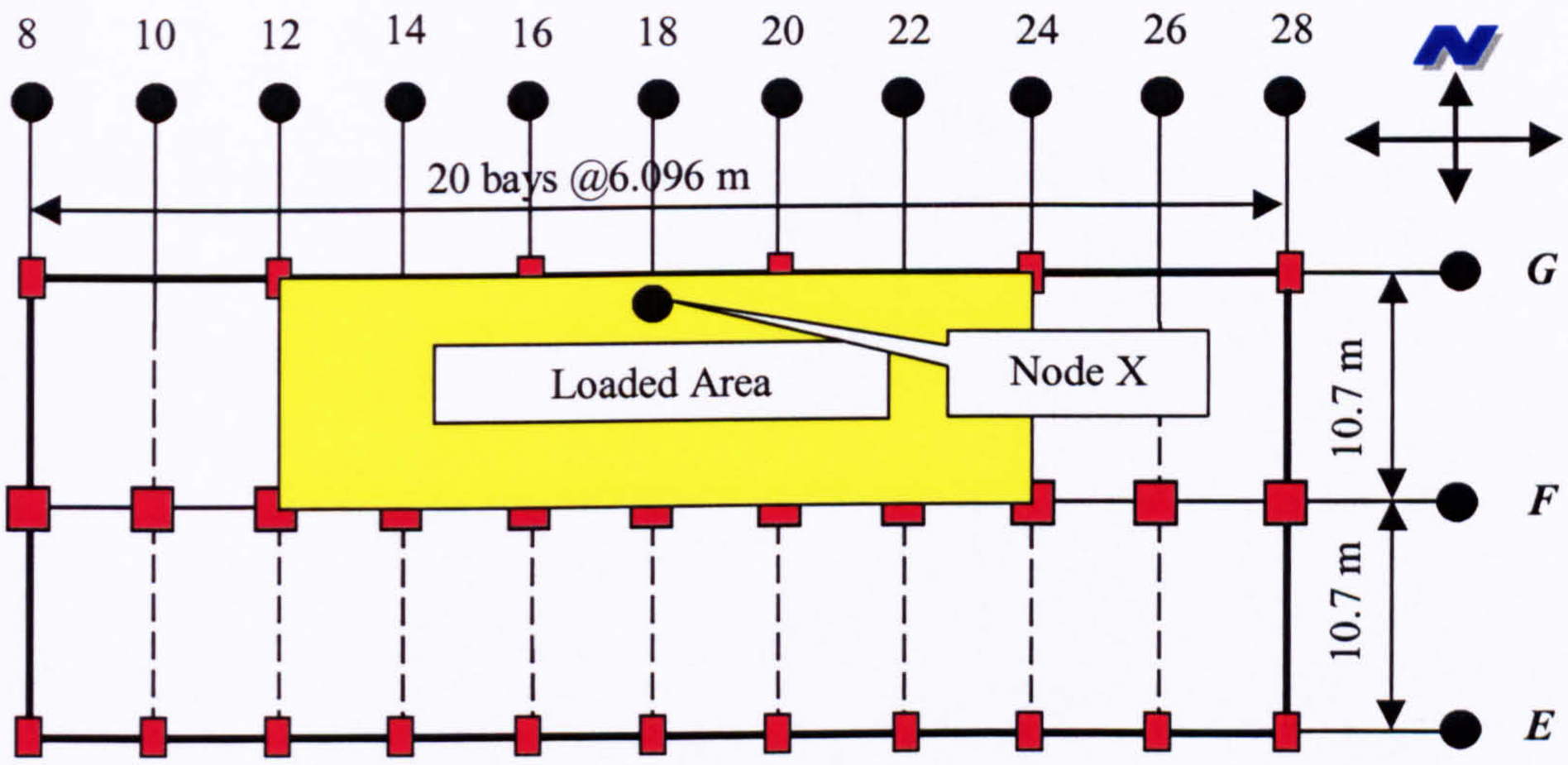

Figure 9.30 Loaded area

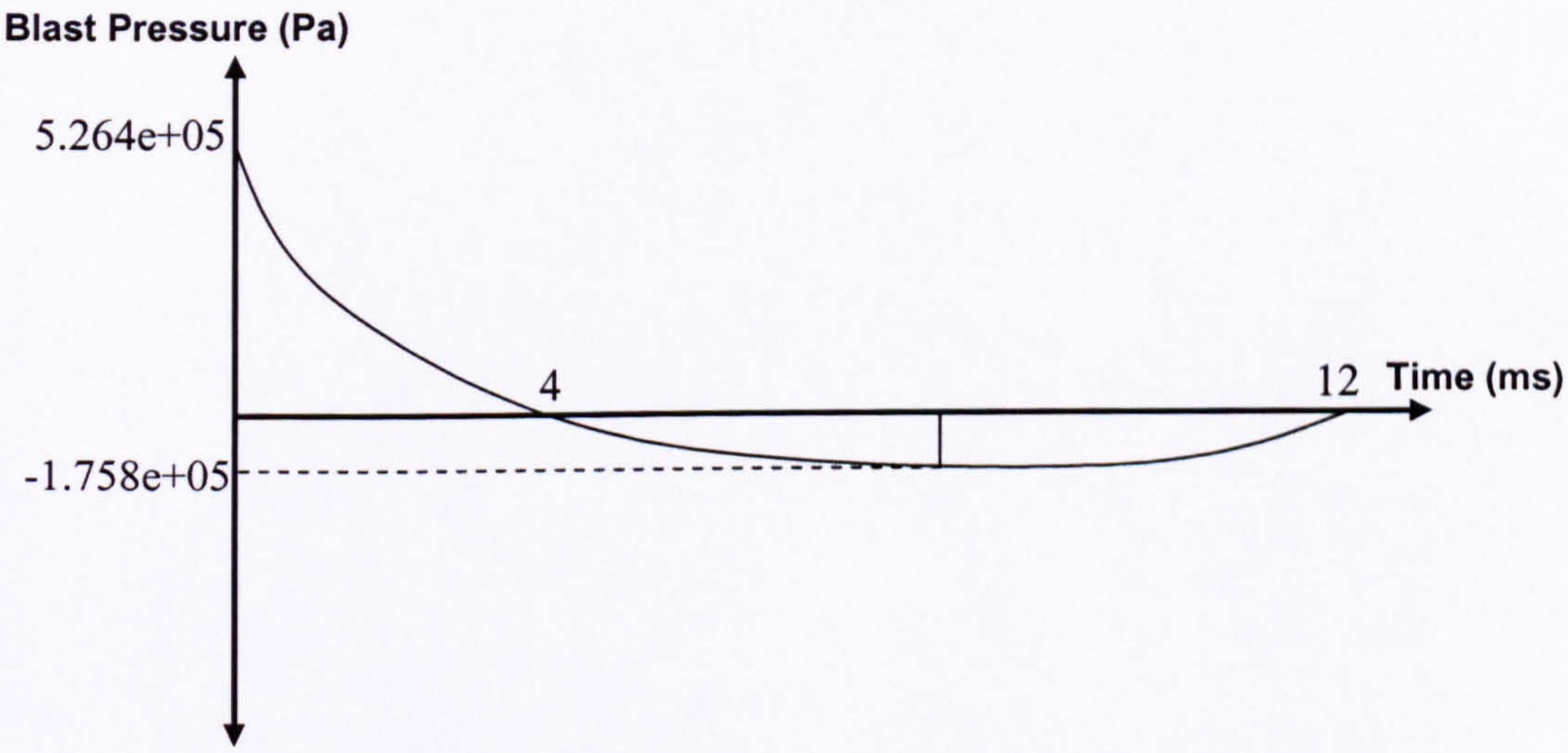

Figure 9.31 Blast pressure profile for elements in the loaded area

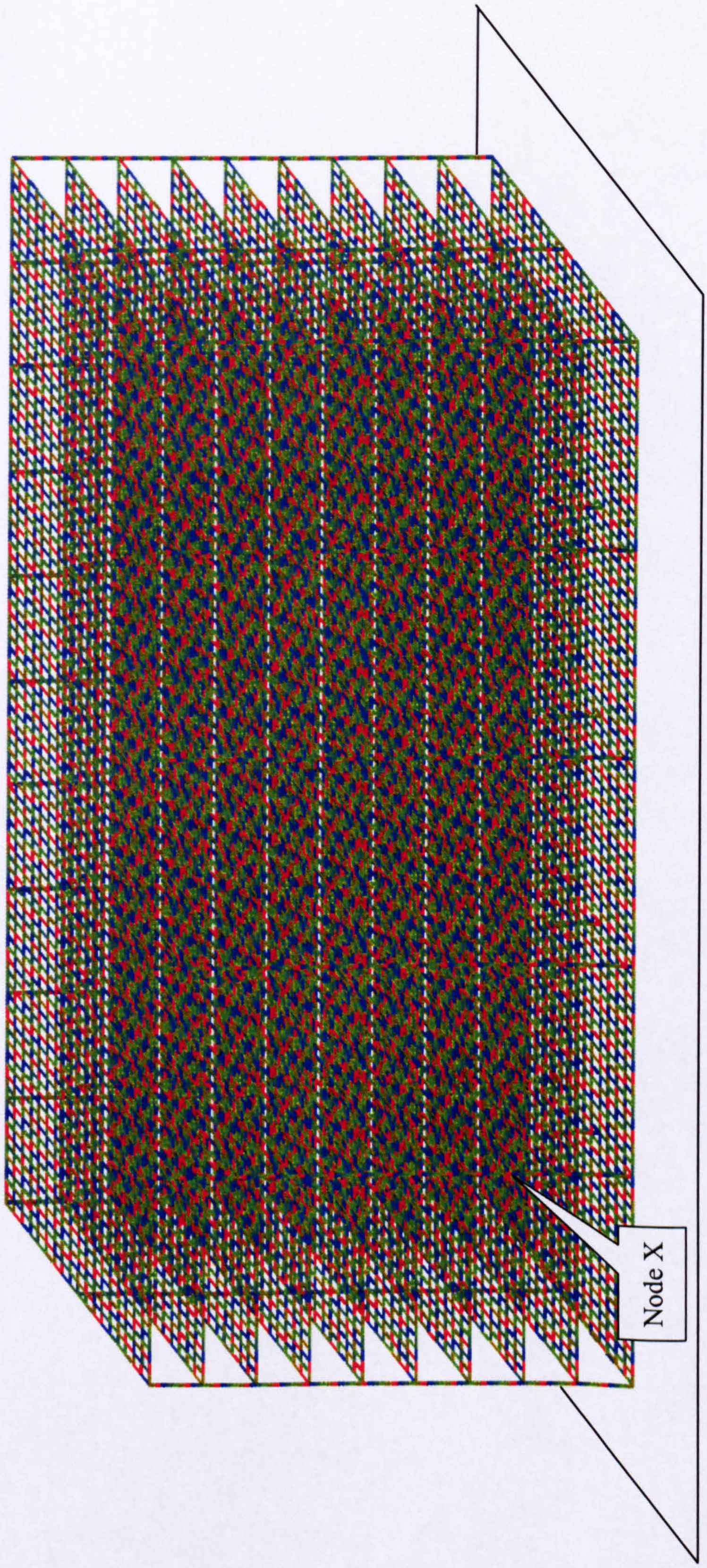

t = 0.0 s. The structure before blast load application

Figure 9.32 Murrah building collapse sequence t = 0.0 s

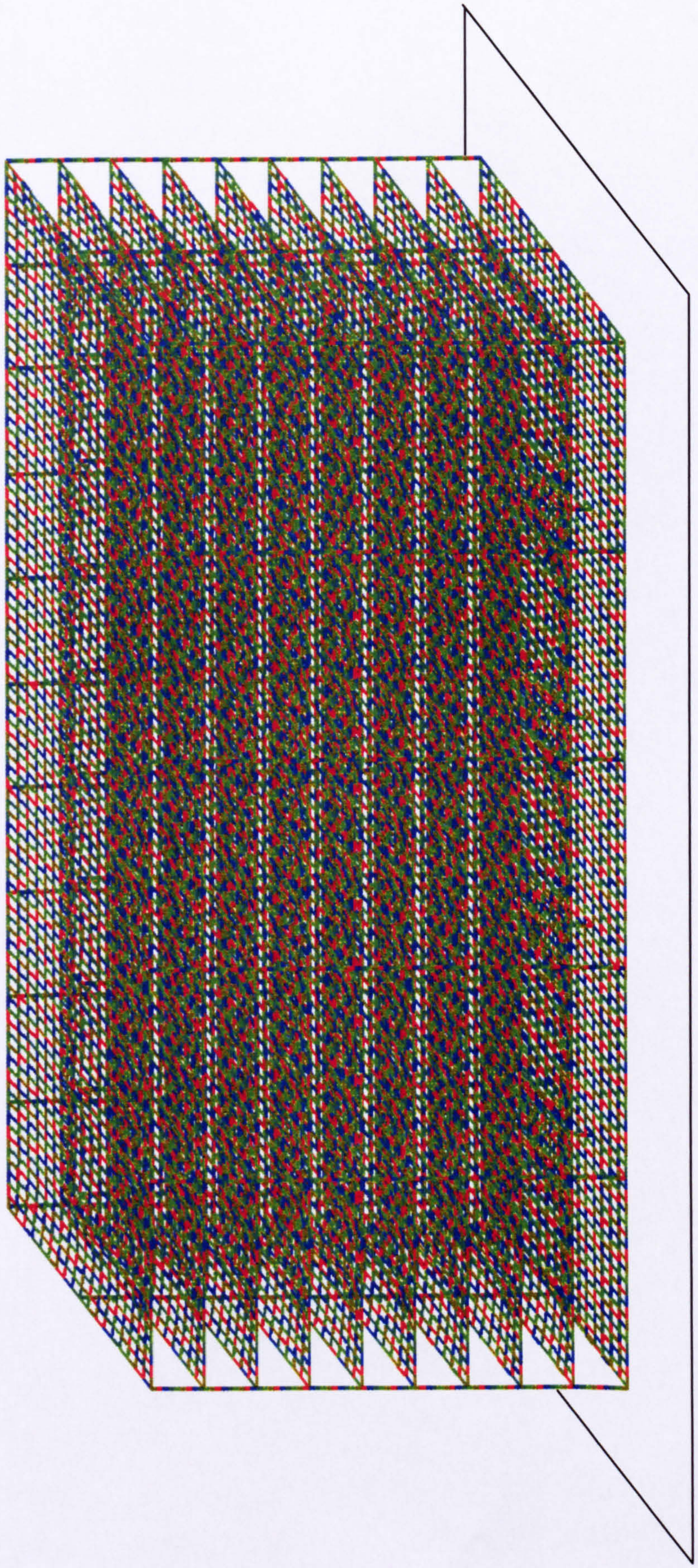

t = 0.225 s. The lower floors are begin to deflect

Figure 9.33 Murrah building collapse sequence t = 0.225 s

t = 0.3 s. Deflection starts to occur at all floor levels.
Figure 9.34 Murrah building collapse sequence t = 0.3 s

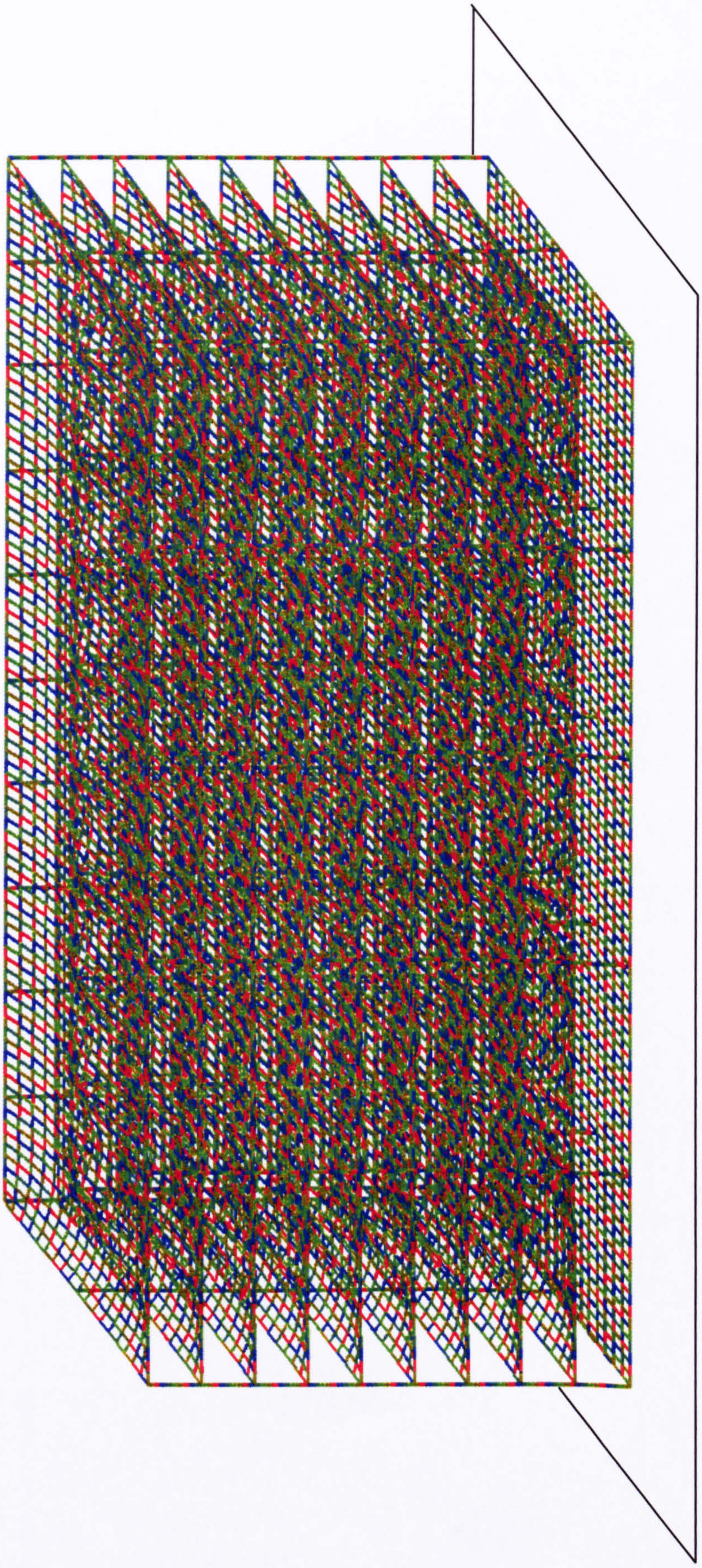

t = 0.45 s. The deflected form is has become more pronounced.

Figure 9.35 Murrah building collapse sequence t = 0.45 s

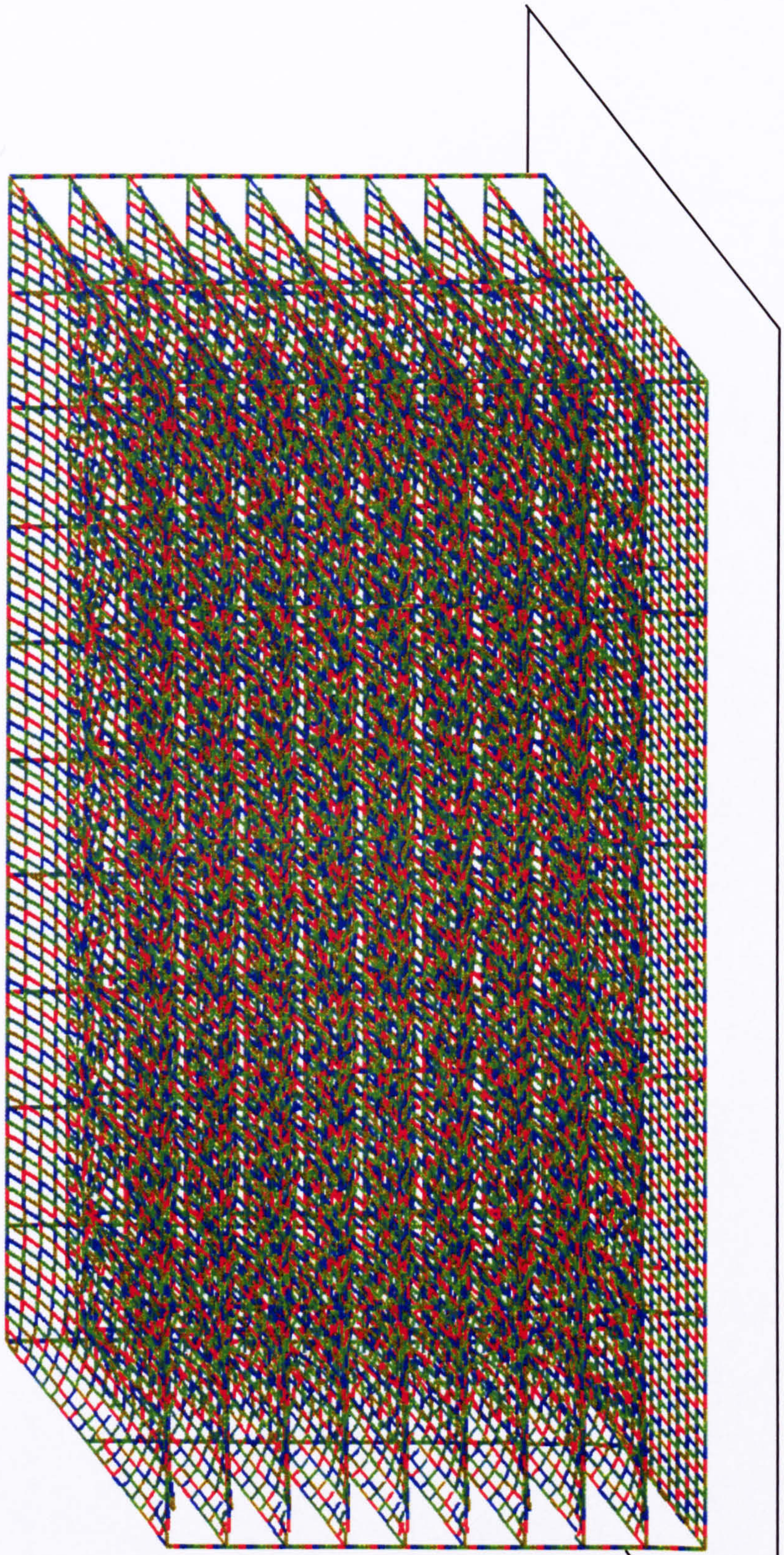

t = 0.525 s. Failure at the front left hand corner (North side) between the column vent and the floor levels begins to occur.

Figure 9.36 Murrah building collapse seauence t = 0.525 s

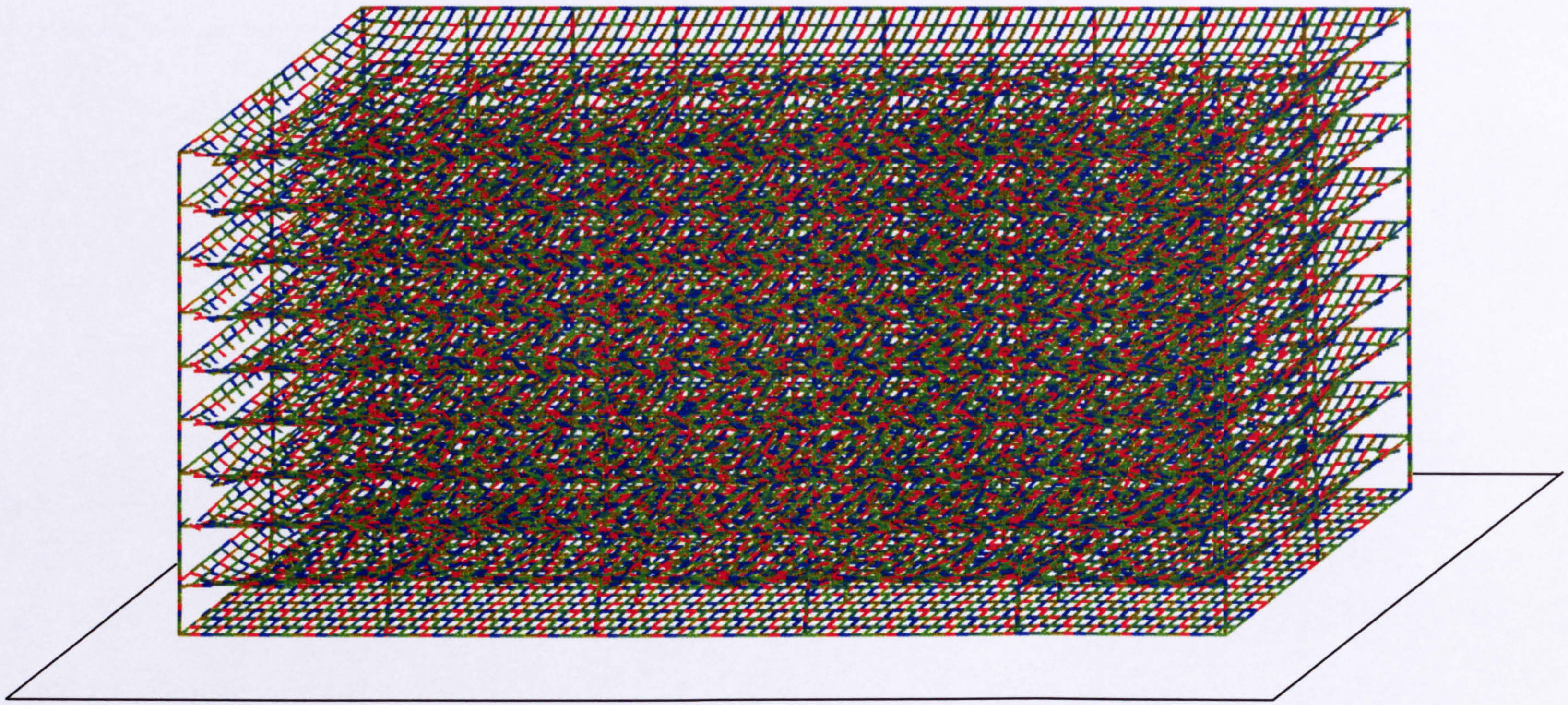

t = 0.6 s. Failure increases to wards the rear of the building.
Figure 9.37 Murrah building collapse sequence t = 0.6 s

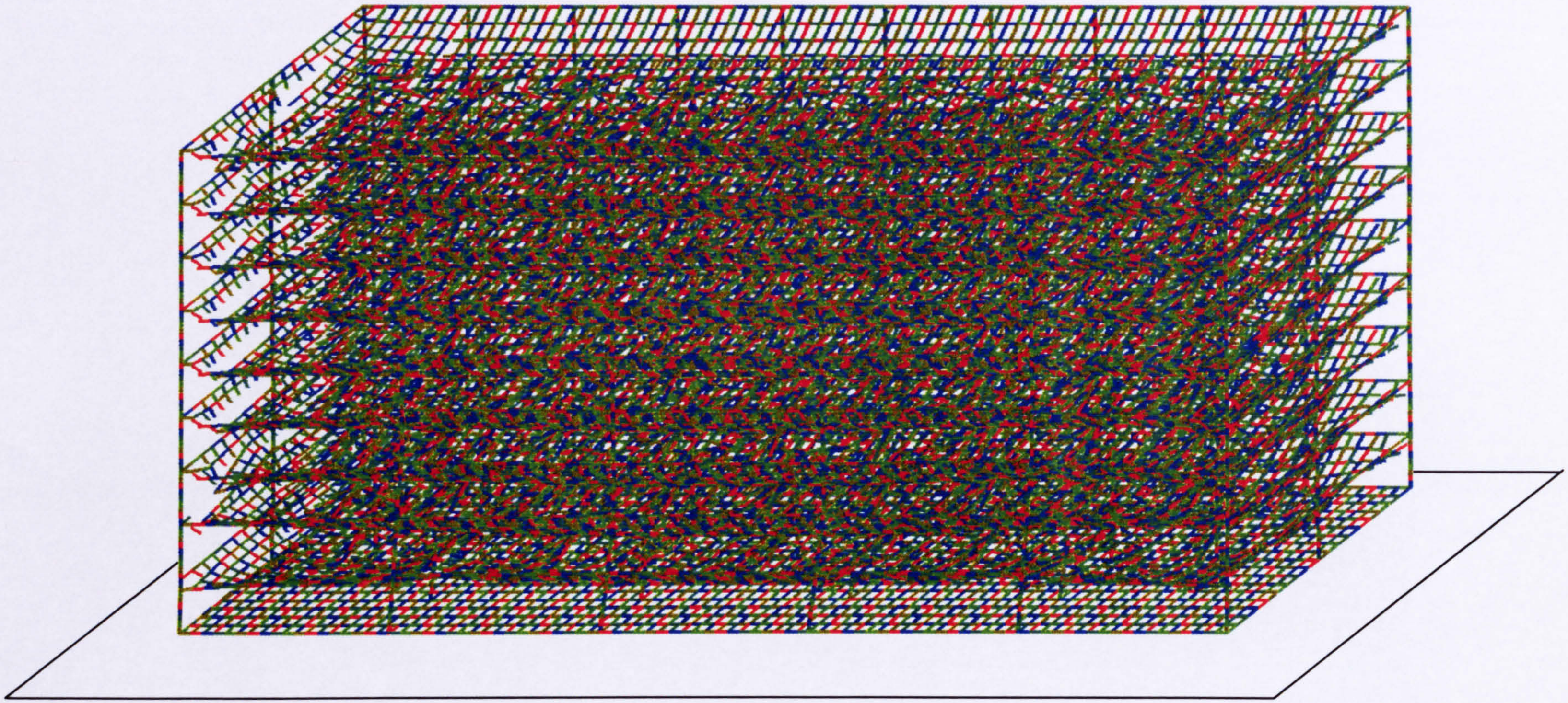

t = 0.675 s. Further breakage is seen to occur inducing the start of a progressive collapse.

Figure 9.38 Murrah building collapse sequence t = 0.675 s

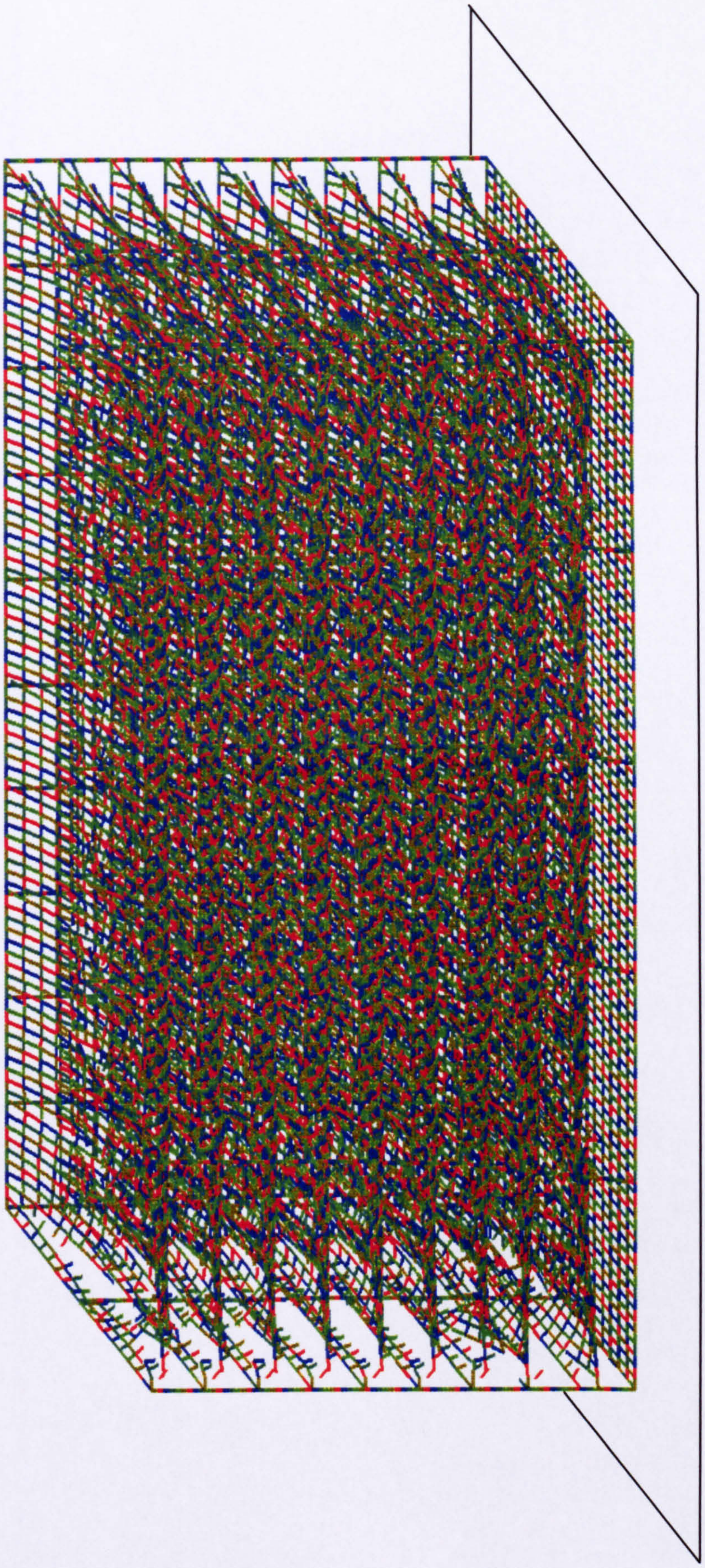

t = 0.75 s. All floors are seen collapsing.

Figure 9.39 Murrah building collapse sequence t = 0.75 s

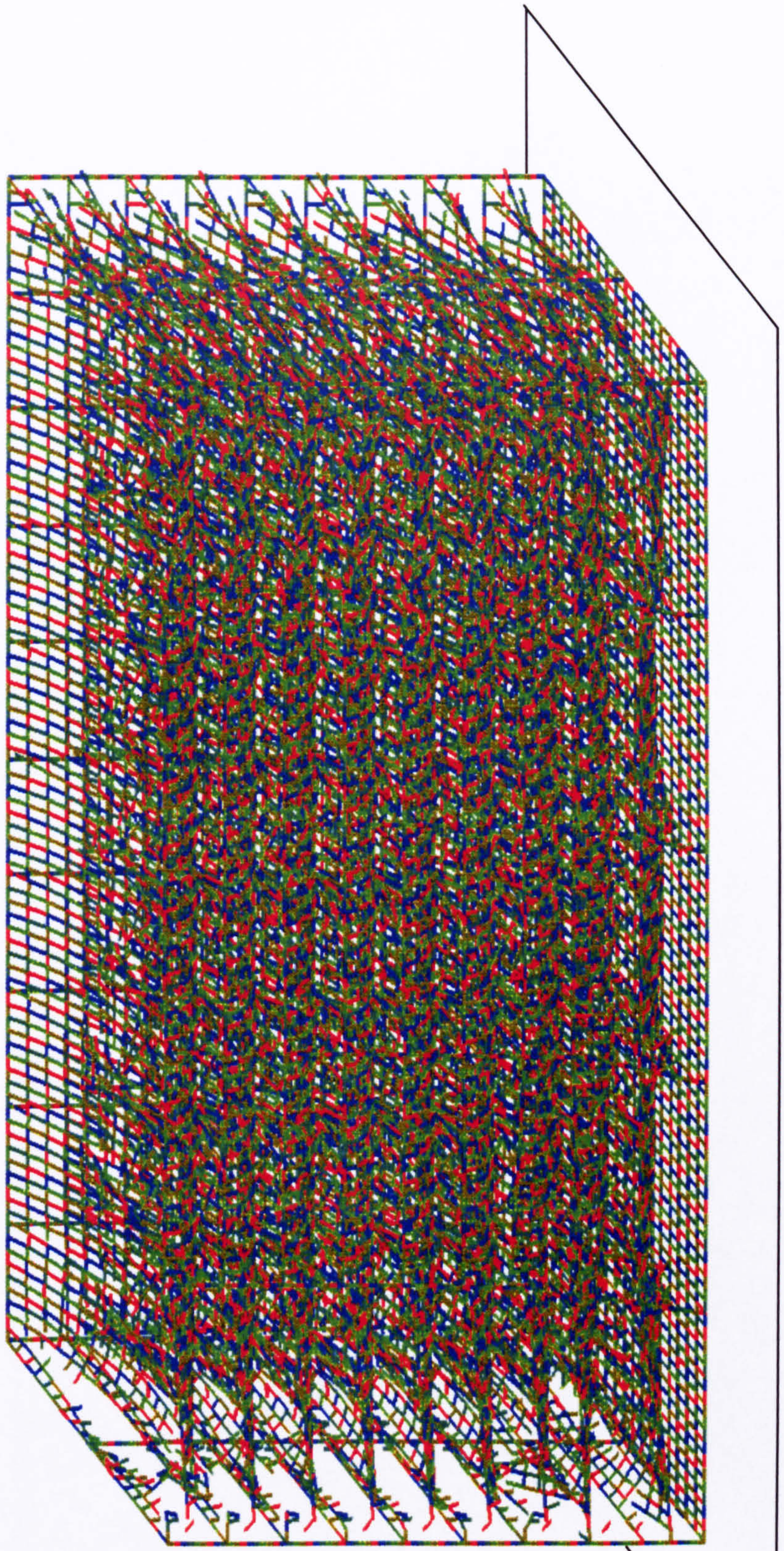

t = 0.825 s. The columns on the front left North side has completely disconnected

Figure 9.40 Murrah building collapse sequence t = 0.825 s

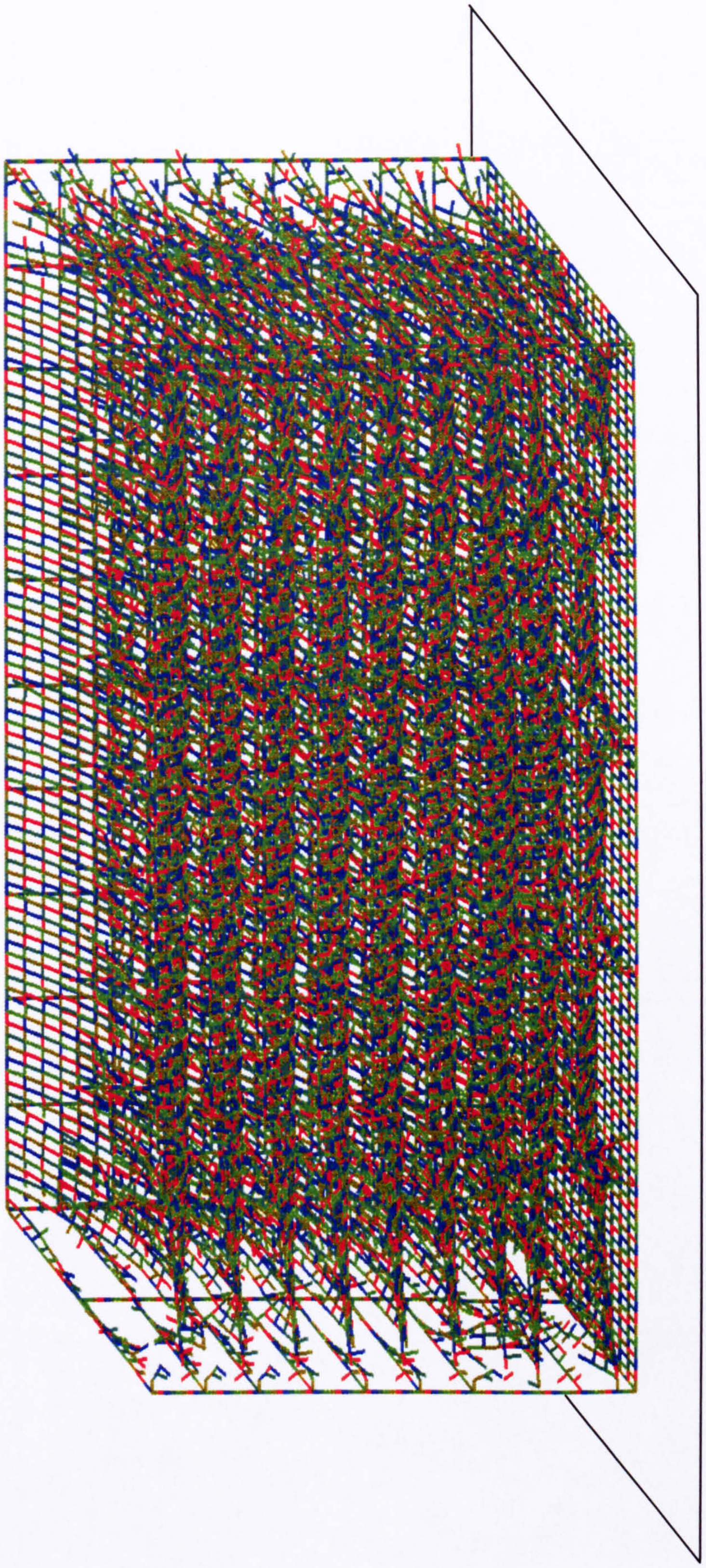

t = 0.9375s. Progressive collapse has occurred.

Figure 9.41 Murrah building collapse sequence t = 0.9375 s

The variation of velocity with time of node X positioned on the second floor is shown in the Figure 9.42. The velocity is initially small during the elastic stage. At approximately 1.4 milliseconds the nodal velocity changes indicating it has impacted with another node. The velocity at this stage has increased approximately two fold. Hence the kinetic energy will have increased four fold. Thus in order to avoid structural collapse through progressive failure this energy needs to be dissipated in some way.

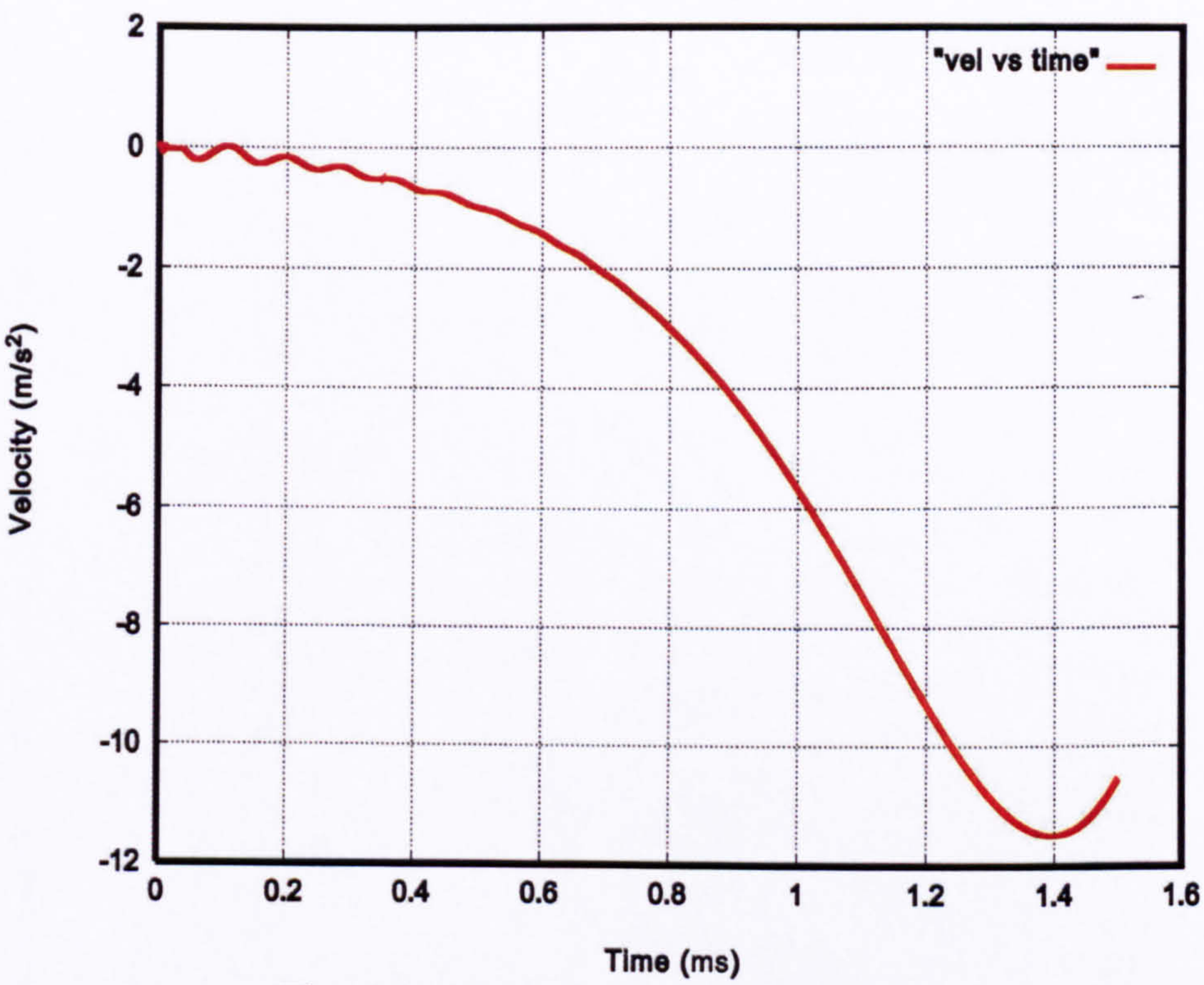

Figure 9.42 Velocity vs time for node X

9.7 Conclusions

An element, which has been successfully tested for both dynamic and static simulations has been applied to the numerical simulation of a full scale structure subjected to blast loading. By adopting a simplified approach the potential of the FEM/DEM modelling procedure is demonstrated, thus showing that this technology presents enormous opportunities, unforeseen benefits and potential breakthroughs for engineering modelling.

The results obtained present a good representation of the failure of the structure. These results were realised by incorporating membrane effects, strain stiffening, realistic stress strain curves for concrete and dynamically localised finite strains especially in the reinforcement.

In load case one the approximate failure line is illustrated in Figure 9.43. The structure has failed completely on the North face, leaving the south face standing. The west side at the roof level is also seen to have failed. The rest of the west face shoes damage but has not completely failed. The East face also shows damage but again remains standing. A similar failure scenario is seen in the second load case. However the East and West faces are seen to endure less damage than in the first loading case. The results compare well with the damage sustained by the actual structure. The actual structure was also seen to show minimal damage to the south face, whilst the East and West faces were also seen to remain standing with damage to cladding and infill panels. However in the actual structure some of the floor bays remained in place, where as the floor areas were seen to fail completely in the numerical model.

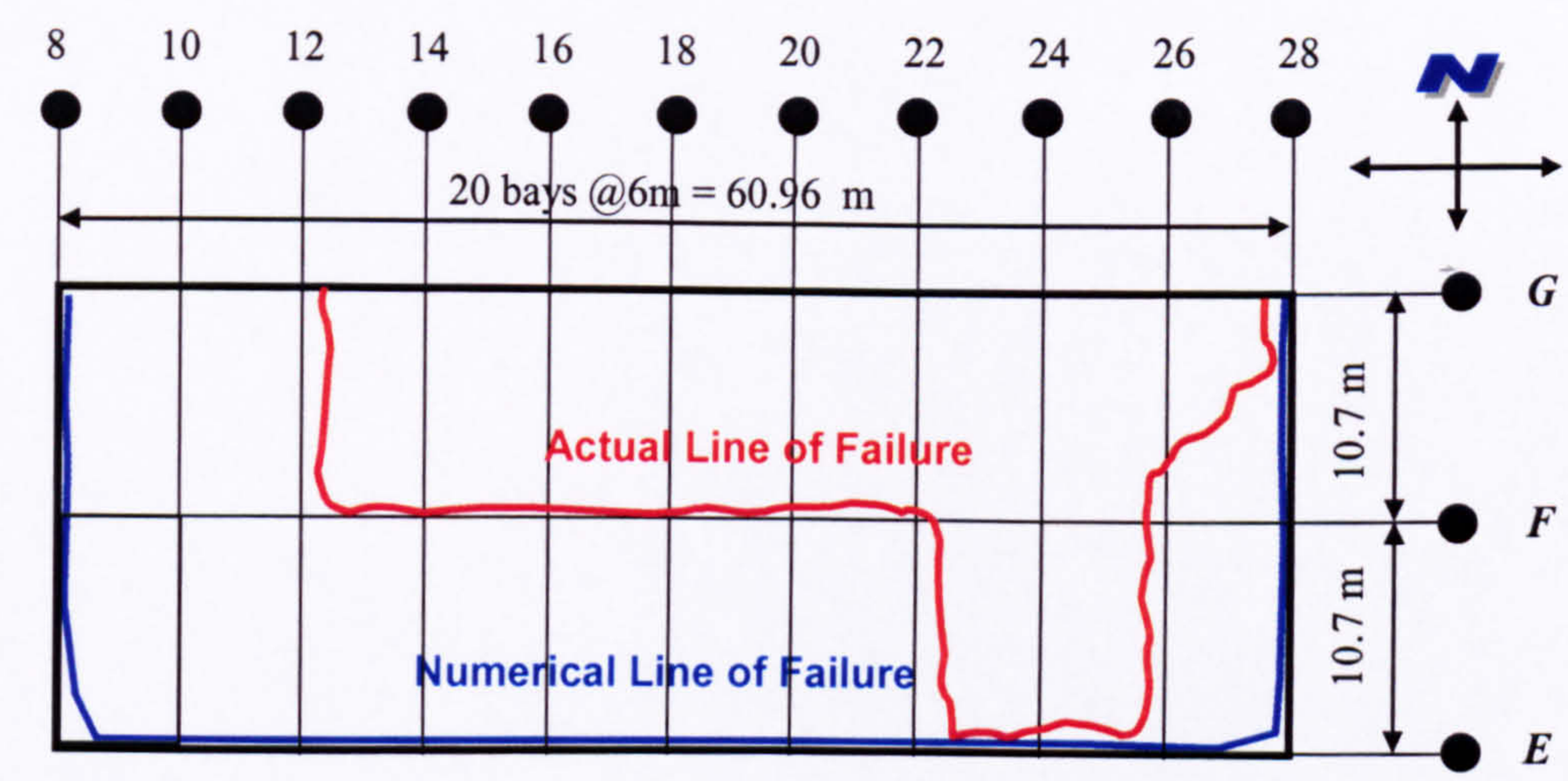

Figure 9.43 Actual and obtained failure lines

The results could be improved with greater knowledge of the magnitude and sequence of the loading, which is unknown. Alternatively further accuracy could be achieved by incorporating the coupling effects of the fluid structure interaction into the numerical simulation of the blast loading. Slab elements incorporating membrane effects could also be developed to provide greater flexibility in the modelling procedure.

This simulation indicates that a radical rethinking may be needed in the context of structural design. This is particularly true for tall buildings. Buildings cannot be made more resistant to effects of blast loading, simply by increasing the reinforcement or even employing stronger materials. The only approach is to come up with different structural concepts, perhaps incorporating new lightweight materials. Hence a new challenge presents itself in terms of structural concepts, structural systems and structural materials.

There are two obvious approaches to designing a structure to resist blast loading. The first is to avoid building such tall structures. The second is to offer complete shielding from any hazardous loading. However both of these solutions are not practical.

Thus new and different concepts in building design, structural materials, structural concepts etc are necessary to increase the robustness of structures. Methods such as the use of various types of glass, use of damage controlled structures [8] and novel cladding systems [9,10,11] are steps in this direction. Use of differing reinforcement patterns [12,13] and structural geometries [14,15,16] already described also provides positive research to this end.

9.8 References

1. WG Corley *et al.*, "The Oklahoma City Bombing, Improving Building Performance through Multi-Hazard mitigation" *FEMA Bull 277, ASCE Press* (1996)
2. WG Corley *et al.*, "Effects of Structural Integrity on Damage from the Oklahoma City, USA Bombing", *Forensic Engineering, Thomas Telford, London* (2001)
3. WG Corley *et al.*, "Using Forensic Engineering Techniques To Obtain data from the Oklahoma City Bombing", *Proc 1st Forensic Engineering Congress, Reston Va., ASCE Press* (1997)
4. W G Corley *et al.*, "Blast Loading and Response of the Murrah Building" *Jour. Perf. Constr. Fac., 12 No3 pp 100-112, ASCE Press* (1995)
5. E Hinmann, "Lessons from the Oklahoma City Bombing-Defensive Design Techniques", *ASCE Press* (1997)
6. E E Hinman, "Explosion and Collapse: Disaster in Milliseconds", *Fire Engineering* (Oct 1995)

7. Kirkpatrick Engineering Company (KEC)- Engineering Drawings of the Oklahoma Building received by the Author (2001)
8. JJ Connor *et al.*, "Damage Controlled Structures I: Preliminary Design Methodology for Seismically Active Regions", *Jour Struct. Eng. 123 No 4 pp 423-431* (1997)
9. WF Anderson *et al.*, "The Resistance of SIFCON to High Velocity Impact", *Structures Under Shock and Impact II, Computational Mechanics Publications, pp 89-98* (1992)
10. V Shustov, "Energy Absorbing Technique: Challenge of Proportioning", *Structures under Shock and Impact III, Computational Mechanics Publications, pp 479-485* (1994)
11. V Shustov, "Shock Evader", *Structures under Shock and Impact III, Computational Mechanics Publications, pp 485-494* (1994)
12. GJ Ha, "Response of Reinforced HSC Beam Column Joints under Load Reversals", *Mag Conc. Res. 44 No 160, pp 175-184* (1992)
13. M Moretti *et al.*, "On the Behaviour and Ductility of RC Coupling Beams of Shear Walls", *ACI Structural Jour. 93 No 6, pp 711-720* (1996)
14. T Schmitt, "Shock Wave Propagation in a Re-entrant Corner" *Jour Physics and Fluids 24(9)* (1981)
15. JE Slater *et al.*, "Development of Computational Methods and Conduct of Experimental Tests for Blast Loading Analysis" *Structures under Shock and Impact III, Computational Mechanics Publications, pp 383-392* (1994)
16. M Barakat *et al.*, "New Architectural Forms to Reduce the Effects of Blast Waves and Fragments on Structures", *Structures under Shock and Impact V Computational Mechanics Publications, pp 53-61* (1998)

Chapter 10

Conclusions and Future Recommendations

Research has been carried out on applying the combined finite-discrete element method to reinforced concrete elements. Using novel numerical solutions, the method is applied to concrete elements subject to monotonic static and dynamic impact loads. The purpose of the main method was to evaluate and assess the failure and collapse of first the reinforced concrete elements and then to carry out a global finite-discrete element analysis upon a chosen constructed facility.

It is therefore necessary to test the accuracy of this new element and validate it under both static and dynamic loading conditions. The experimental work carried out at the University of Alberta and the Swiss Federal Institute of Technology were adopted to test the analytical solutions obtained from program Y-code developed for the analysis.

It was also necessary to find a selected explosion facility such that the damage scenario can be compared with that, which is produced by the results obtained from the combined finite-discrete element technique given in this thesis. For this purpose the Alfred P Murrah building was chosen for the global analysis.

Chapter 1 gives an explosion damage review for selected explosion facilities. The researcher is then led to Chapter 2 in which a comprehensive treatment is given on blast load phenomena and preliminary assessment of concrete elements subject to blast loads using existing or established codified design methods.

In order to carry out the analytical model test analysis it was imperative to include Chapter 3, which covers material response and structural strength criteria. This work is largely simulated later on in the finite-discrete element analysis.

Chapter 4 is entirely devoted to the rotational capacity of RC beams, since this analysis is the hub of the finite-discrete element technique. The chapter covers comprehensively the behaviour of concrete in particular the rotational capacity and moment curvature effect. In this chapter strain localisation is investigated and a simple constitutive law is proposed. The results showed that no strain localisations occurred in the beams tested and the concrete is likely to fail prior to any significant strain softening in the compression zone. Since this concept is supported by the ACI code, no further investigation was carried out on the size effect upon rotational capacity. The results advocated a bi-linear moment curvature law. This was used in the combined FEM/DEM code to numerically assess the structural response to blast loading. Here wider implications of this research are indicated since all limit state design codes depend on inelastic rotational capacity of the hinging regions in RC members.

The effects of varying the reinforcement, strain rates and axial loading were also investigated. The results showed the concrete to fail in a similar manner developing huge shear stresses at the point of failure as confirmed by the bi-linear moment curvature law. It was interesting to note that the ductility of concrete was seen to reduce with increasing axial loading. The effect of reducing the area of reinforcement used was to reduce the ductility. Increasing the curvature rate in all three cases of reinforcement also had the effect of reducing the ductility of concrete.

The research that has been carried out has shown the finite-discrete element technology to be a powerful tool with enormous potential. In Chapter 5 and Chapter 6 the reader is introduced to the subject and is also made aware of the contact detection algorithms used with this method. The reader/researcher is now fully versed in the numerical and analytical methodology behind the research.

The next stage of the work is to carry out validation procedures for both the static and dynamic loading cases. These are elaborated upon in Chapters 7 and 8 respectively. It is worth mentioning that the proposed algorithmic solutions for the combined finite-discrete element analysis of reinforced concrete structures also include failure and collapse. This is due to implicit inclusion of elements breaking apart followed by contact impact solutions resolving progressive collapse, which are both standard features of the combined finite-element method. The finite element presented here is relatively simple and inexpensive in terms of CPU time, thus enabling the same finite element mesh to be used for both finite element analysis and contact interaction.

The comprehensive numerical results produced indicate that they are in good agreement with the experimental results. The most important novelty of the solutions presented in this research is that they are found to fit very well within the contact detection concepts of the combined finite-element method, thus enabling robust solutions for hundreds, even millions of interacting particles. In addition a novel integration procedure for non-linear behaviour of both steel and concrete has been introduced.

In both static and dynamic loading conditions, the numerical results obtained are in full agreement with the experimental work, thus paving the way for the finite-discrete element analysis to be placed as one of the most powerful three dimensional methods. The developed numerical techniques are now applied to the global analysis of the Alfred P Murrah building. The designers have provided a complete set of design drawings and relevant data, which were consulted in the adoption of the mesh sequence. With slight modifications of the corner details, the entire building was modelled and the damage scenario was found to be similar. The failure modes are indicated and are clearly established.

Since it has been shown to be a very powerful method with reduced CPU times, more and more applications in engineering sciences including rock mechanics, thermal problems and gas container problems can make use of its potential. Future researchers can take into account some improvements to the finite element method, some of which are suggested below

- The influence of size effects on the FEM/DEM analysis of reinforced and prestressed concrete structures under impact/blast load effects.
- The concrete failure model incorporated in the FEM/DEM analysis is no doubt effective for simple blast effects. However two, three, four and five parameter failure models can also be incorporated with and without temperature effects
- The research can be broadened for use in simulating three dimensional concrete failures or cracking with and without concrete aggregate interlocking effects.

- The code can further be modified to incorporate the effects of penetration, perforation, scabbing and spalling, all of which can result from explosion damage. Subroutines developed can be checked with well known empirical formulae such as those from NDRC, Bechtel, IRS, ACE, modified Kar, modified CEA/EDF and CKW-BRL.
- The reinforcement yield and bond slip and concrete-steel bond linkage behaviour can be analysed by incorporating the reinforcement into the body of the element or made to coincide with the nodes of the discretised mesh.
- Explosions result in fires. Thus the FEM/DEM technology can be applied to the production of 3D simulations under fire conditions.

A number of other areas can be identified for this powerful tool such as the design of underground chambers, soil structure interaction, offshore structures, aircraft and naval structures, which are beyond the scope of this research.

In the current research, all results are fully collaborated and corroborated with experimental results.

A comprehensive list of references and bibliography is provided for those wishing to study and research this topic further.

The papers published thus far from this thesis are here listed

- *"Analysis of structural failure using the combined finite-discrete element method" Advances in Fracture and Damage Mechanics Conference Milan, Italy 2001*
- *"FEM/DEM modelling of RC beams under Impact" SUSI VII conference Montreal, Canada May 2002*
- *"A Computationally Efficient Beam Element for FEM/DEM Simulations for Structural Failure and Collapse" Third International Conference on Discrete Element Methods, Santa Fe, USA September 2002*
- *"Experimental validation of combined FEM/DEM simulation of RC beams under impact induced failure" ICADD-5 conference Wuhan, China October 2002*

- *"Discontinuous analysis approach to full scale simulation of structures subject to blast loads" ICADD-5 conference Trondhiem, Norway October 2003*
- *"The combined finite discrete element method for structural failure and collapse" International Journal of Fracture Mechanics (accepted for journal publication September 2003)*
- *"Dynamic Modelling of a RC beam impact using the combined finite discrete element method" Computational Mechanics Journal April 2003 Springer Verlag*

T Bangash

Appendix I
Statement by the candidate

For technical reasons, the candidate has agreed with the advice given by his supervisor not to include the computer program together with the subroutines developed by the candidate in this thesis. They are available with the candidate.

T Bangash

Appendix II
Bibliography

Blast load phenomena and codified methods for the design of structural elements

- J M Biggs, "Introduction to Structural Dynamics", *McGraw Hill Book Company*,(1964)
- MYH Bangash, "Prototype Building Structures: Analysis and Design", *Thomas Telford* (1999)
- ASCE, "Design of Structures to Resist Nuclear Weapons Effects", *ASCE Reports and manuals Practice No 42* (1985)
- GC Mays and PD Smith, "Blast Effects on Buildings", *Thomas Telford* (1995)
- H L Brode, "Numerical Solution of Spherical Blast Waves", *Jour. Appl. Physics*, (June 1955)
- C K Wiehle *et al.*, "Dynamic Analysis of Reinforced Concrete Floor Systems", *Stanford Research Institute for US Defence Civil Preparedness Agency,AD768-206* (1973)
- JG Kirkwood *et al.* "Theory of Propagation of Shock Waves from Explosive Sources in Air and Water", *OSRD 4814* (1944)
- N M Newmark, "An Engineering Approach to Blast Resistant Design", *ASCE No 2786* (1956)
- E Vlasov, "Principles of Explosion Dynamics", *Mockba* (1965)
- E Cohen *et al.*, "Design of Blast Construction for Atomic Explosions", *Jour. ACI 26 No 7 pp589-695* (1955)
- BS8110:1985 The Structural Use of Concrete
- ACI: Building Code *pp 318*-83 (1983)
- C N Kingery, "Airblast parameters versus Distance for Hemispherical TNT Surface Bursts", Report No 1344 Aberdeen Proving Ground Maryland USA (1966)
- J Henrych, " The dynamics of Explosion and its use" *Elsevier* Amsterdam (1979)
- W J H Rankine, "Philosophical Transactions of the Royal Society", *160 277* (1870)

- H W Liepmanwt al, "Elements of Gas Dynamics", *Wiley* New York (1957)
- B Hopkinson, "*British Ordinance Board Minutes 13565*" (1915)
- C Cranz, "Lehrbruch der Ballistik", *Springer Verlag*, Berlin (1926)
- R G Sachs, "The Dependence of Blast on Ambient Pressure and Temperature", *BRL Report 466*, Aberdeen Proving Ground Maryland USA (1944)
- C L Elliot *et al.*, "The protection of buildings against terrorism and disorder", *Proceedings of the Institution of Civil Engineers, Structures and Buildings No 94 pp 287-97* (August 1992)
- C L Elliot, "The defence of buildings against terrorism and disorder- a design philosophy for the construction of ordinary buildings and installations to resist terrorism and disorder" *MPhil Thesis, Cranfield Institute of Technology* (1990)
- S Glasstone *et al.*, "The effects of Nuclear Weapons" *United Stated Departments of Defence and Energy (Third Edition)* (1977)
- Military Applications of Blast Simulation Symposia Proceedings No6 Cahors France 1979, No 7 Medicine Hat Canada 1981, No8 Spiez Switzerland 1983, No9 Oxford UK 1985, No 10 Bad Reicheenhall, Germany 1987, No11 Alberquerque USA 1989, No 12 Perpignn France 1991, No 13 The Hague, Netherlands (1993)

Material response to explosive loads and structural strength enhancement criteria

- Bangash, MYH., "Manual of Numerical Methods in Concrete" *Thomas Telford,* (2002)
- M Boutros *et al.*, "Testing and Analysis on Elastic Pinned Beams under Impulsive Loading", *Structures Under Shock and Impact V, Computational Mechanics Publications pp 191-199* (1998)
- A Miyamoto, "Integrated Analytical Procedures for Concrete Slabs under Impact Loads", *Jour Struct. Eng. 120 No 6 pp 1685-1702* (1994)
- AJ Pretlove *et al.*, "Dynamic Effects in Progressive failure of Structures", *Int. J. Impact Eng, 11 No 4 pp 539-546* (1991)
- V Shustov, "Energy Absorbing Technique: Challenge of Proportioning", *Structures under Shock & Impact III, Computational Mechanics Publications pp479-485* , (1994)

- XY Su *et al.*, "Inertia sensitive Impact Energy absorbing structures part I & II", *Int J. Impact Eng., 16 No 4 pp 651-.689* (1995)
- WQ Shen *et al.*, "Dynamic Response of a Mass Grillage under Mass Impact", *Int J. Impact Eng. 13 No 4 pp 555-565* (1993)
- X Yuliang, "Shear Ductility of Reinforced Concrete Beams of Normal and High Strength Concrete" *ACI Structural Jour. 91 No 2 pp 140-195* (1994)
- R Park, "What do we Know about confinement of Concrete Columns" *ACI Structural Jour.* (1990)
- P Sorousian, "Bond of deformed Bars to Concrete: Effects of Confinement and Strength", *ACI Materials Jour. 88 No 3 pp 227-232* (1991)
- M Shams, "State of the Art Concrete Filled Steel Tubular Columns", *ACI Structural Jour. 94 No 5 pp 558-571* (1995)
- RE McConnel, "Force Deformation Equations for Initially Curved Laterally Loaded Beam Columns", *Jour Eng. Mech. 118 No 7 pp 1287-1302* (1992)
- M Boutros *et al.*, "Testing and Analysis of Elastic-Plastic Beams under Impulsive Loading", *Structures under Shock and Impact V Computational mechanics Publications pp 191-199* (1998)
- JM Dewey *et al.*, "E-Blast-an Emergency Blast Expert System", *Structures under Shock and Impact V Computational mechanics Publications pp 320-329* (1998)
- P Rericha, "A Test for the Rate Effect on Concrete Fracture Energy", *Structures under Shock and Impact V Computational mechanics Publications pp 461-469* (1998)
- K Jitsu, "Effects of Strain Rate on Concrete Strength subjected to Impact Load-Dynamic Compressive strength test by Split Hopkinson Pressure Bar Method", *Structures under Shock and Impact V Computational mechanics Publications pp 470-479* (1998)
- D Grady, "Scaling Issues in Dynamic fragmentation", *Structures under Shock and Impact V Computational mechanics Publications pp 525-538* (1998)
- N Geebeken *et al.*, "On the Concrete Material Response to Explosive Loading-Numerical Simulations", *Structures under Shock and Impact V Computational mechanics Publications pp 773-782* (1998)

- N Duranovic, "Impulsive Loading on RC Slabs – Modelling Considerations", *Structures under Shock and Impact V Computational mechanics Publications pp 817-826* (1998)
- S Oden *et al.*, "Prediction of Impact Force by Impact Response Method", *Int. Jour Impact Eng. 11 No 2 pp 149-158,* (1991)
- MA Macaulay, "Introduction to Impact Engineering", *Chapman and Hall 1987*
- CA Brebbia *et al.* (Ed), "Shock and Impact on Structures", *Computational Mechanics Publications* (1994)
- AJ Watson *et al.*, "The Response of Civ Eng Structures to Impulsive Loads", *Structures under Shock and Impact III, Computational Mechanics Publications pp 3-10* (1994)
- R Eytan, "Practical Methods for Increasing the Blast Resistance of Existing Buildings" *Structures under Shock and Impact III, Computational Mechanics Publications pp 29-36* (1994)
- B Hobbs, "Vulnerability Assessment of Large Structures Subjected to Dynamic Loading" *Structures under Shock and Impact III, Computational Mechanics Publications pp 449-458* (1994)
- T Krauthammer *et al.*, "Fracture and High Loading Rate Effects on Concrete Response", *Structures Under Shock and Impact II, Computational Mechanics Publications pp 223-234* (1992)
- HL Riad *et al.*, "Dynamic Response of Concrete Structures under Direct Impact", *Structures Under Shock and Impact II, Computational Mechanics Publications pp 235-246* (1992)
- KV Hϕiseth, "Response of RC Structures Exposed to Transient Loadings", *Structures Under Shock and Impact II, Computational Mechanics Publications pp 247-258* (1992)
- HM Shanaa, "Modified Analysis of RC Structures under Localised and Distributed Impulsive Loads", *Structures Under Shock and Impact II, Computational Mechanics Publications pp 333-344* (1992)
- R Eytan, "Response of Real Structures to Blast Loading – the Israeli Experience", *Structures Under Shock and Impact II, Computational Mechanics Publications pp 483-496* (1992)

- R Forsen, "Damage of RC Slabs due to a Combination of Blast and Fragment Loading" ,*Structures Under Shock and Impact II, Computational Mechanics Publications pp 509-520* (1992)
- AJM Sloane, "Structural Design for Hazardous Loads", *Paper 4 pp32-40 Proc. Structural Designs for Hazardous Loads E & FN Spon Brighton* (1991)
- N Duranovic *et al.*, "Integrating Simplified Test Results to assess the Effect to Dynamic Loading on RC Slabs and Beams", *Paper 18 pp 171-182 Proc. Structural Designs for Hazardous Loads E & FN Spon Brighton* (1991)
- SJ Pritchard *et al.*, "Hard Impact Testing of Confined Concrete Cylinders", *Structures Under Shock and Impact V, Computational Mechanics Publications pp 493-502* (1998)
- N Gebbeken, "On the Concrete Material Response to Explosive Loading-Numerical Simulation", *Structures Under Shock and Impact V, Computational Mechanics Publications pp 773-781* (1998)
- P Rericha, "A Test for the Rate Effect on Concrete fracture Energy", *Structures Under Shock and Impact V, Computational Mechanics Publications pp 461-470* (1998)
- M Boutros *et al.*, "Testing and Analysis on Elastic Pinned Beams under Impulsive Loading", *Structures Under Shock and Impact V, Computational Mechanics Publications pp 191-199* (1998)
- PS Symonds *et al.*, "Impulsive Loading of Fully Clamped Beams with Finite Plastic Deflections and Strain Rate Sensitivity", *Int Jour of Mech Science 14 pp 49-69* (1982)
- R Hill, "The Mathematical Theory of Plasticity", *Oxford at the Clarendon Press* (1956)
- Ammann, W., Bachmann, H., Muhlematter, M.,"Stress-Strain Behaviour of Non-Prestressed and Prestressed Reinforcing Steel at High Strain rates" *Proc. BAM Concrete Structures under Impact and Impulsive Loading, Berlin,* (1982)
- HL Brode, "Numerical Solution of Spherical Blast Waves" , *Jour Appl Physics No 6* (1955)
- CN Kingery, "Air Blast Parameters vs Design for Hemispherical Surface TNT Bursts" , *BRE report No 1344 Aberdeen Proving Ground Maryland USA* (1966)
- MYH Bangash, "Impact and Explosions", *Blackwell* (1993)

- R.B Phillips, "REN 558",*Library Archives of the Institution of Civil Engineers*, (1945)

Discrete element technology

- Y.T.Feng, K.Han, D.R.J.Owen, "A Spatial Digital Tree Based Contact Detection Algorithm" *Proc. 4th Int. Conf. Discontinuous Deformation Analysis ,University of Glasgow, pp 427-439* 6th–8th June (2001).
- C Chang *et al.*, "Discrete element analysis for active and passive pressure distribution on retaining wall", *Computers and geotechnics, **16** No 4 pp 291-310* (1994)
- A Anandrajah, "Discrete element method for simulating behaviour of a cohesive soil", *ASCE journal of geotechnical engineering, **120** No 94 pp 1593-1613* (1994)
- N Barton, "Physical and discrete element models for excavation and failure in jointed rock", *Norwegian Geotechnical Institute publication, No 194* (1994)
- B Dverstorp, "Analysing flow and transport in fractured rock using the discrete fracture network concept", *Royal Institute of Technology Stockholm,,* **TRITA-VBI-151** *pp 1593-1613* (1994)
- JS Kim *et al.*, "Analysis of soil nailed earth slope by discrete element method", *Computers and geotechnics, **20*** **No 1** *pp 1-14* (1997)
- J Viera De Lamos, "Discrete element analysis of dam foundations", *Lisboa Laboratario Nacional de Engenharia Civil,* **817** (1999)
- BK Cook *et al.*, "Discrete element methods numerical modelling of discontinua", *Proceedings of the 3rd International conference Sante Fe USA,ASCE* (Sept.2002)
- A Munjiza, "Discrete elements in transient dynamics of fractured media", *PhD thesis*, University College Swansea, (1992)

Discrete element methods and contact detection

- J. Lemos, R. D. Hart, and P. A. Cundall, "A generalised distinct element Program for modelling jointed rock mass", *in O. Stephenson (ed.), Fundamentals of Rock Joints, Centek Publishers* (1985)

- J. R. Williams, G. Hocking and G. G. W. Mustoe, 'The Theoretical Basis of disc elements', *NUMETA '85 Numerical Methods in Engineering, Theory and Applications, Balkema Rotterdam,* (1985)
- J. R. Williams and G. Mustoe, *Proc 2nd U.S. Conference on Discrete Element Methods, MIT MA* (1993)
- J. R. Williams and G. Mustoe, *Proc 1st U.S. Conference on Discrete Element Methods, Golden, Colorado* (1989)
- S. Gen Hua and R. E. Goodman, 'Discontinuous deformation Analysis- a new method for computing stress, strain and sliding of block systems', *Key Questions in Mechanics, Balkema Rotterdam, pp 381-393* (1988)
- M. Oldenburg and L. Nilsson, "The Position Code Algorithm for Contact Searching", *Int Jour Numer Meth Engng* **37** *pp 359-386* (1994)
- J. Bonnet and J. Peraire, "An Alternative digital Tree (ADT) Algorithm for 3D Geometric Searching and Intersection Problems", *Int Jour Number Meth Engng* **31** *pp 1-17* (1991)
- R. O'Connor , J. Gill and J. R. Williams, "A Linear Complexity contact Detection Algorithm for Multi Body Simulations", *Proc 2nd U.S. Conference on Discrete Element Methods,* MIT MA (1993)
- D.S. Preeece and S. L. Burchell, "Variation of Element Packing Angle and it's influence on Computer Simulations of Blast Induced Rock Motion", *Proc 2nd U.S. Conference on Discrete Element Methods,* MIT MA (1993)
- B. Mirtich, "Impulse-based Dynamic simulation of Rigid Body Systems", *PhD Thesis,* Berkely, California, (1998)
- Munjiza, D.R.J. Owen, N. Bicanic, "A combined finite-discrete element method in transient dynamics of fracturing solids", *Int. J Engineering Computations,* **12,** *pp 145-174* (1995)
- A.Munjiza, K.R.F.Andrews, "NBS contact detection algorithm for bodies of similar size", *Int. J. Num. Methods Eng* , **43** (1998)
- A.Munjiza, D.R.J. Owen, A.J.L.Crook, "Energy and Momentum Preserving Contact Algorithm for General 2D and 3D Contact Problems", *Proc 4th Int. Conf*

Computational Plasticity- Fundamentals and Applications, Barcelona pp 829-841 3 –6 April (1995)

- A.Munjiza, K.R.F.Andrews, "Penalty function method for in combined finite-discrete element systems comprising large number of separate bodies', *Int. J. Num. Methods Eng.*, **49**, *pp 1377-1396*, (2000)
- A.Hillerborg, "Fracture Mechanics Concepts applied to Moment Capacity and Rotational Capacity of Reinforced Concrete Beams" *Engineering Fracture Mechanics, 35(1/2/3) pp 233-240* (1990)
- ACI Committee 318 "Building Code Requirements for Reinforced Concrete and Commentary", *ACI 318-890/ACI318R-89,ACI Detroit pp 4939-4941* (1989).
- A.Hillerborg, "Fracture Mechanics Concepts applied to Moment Capacity and Rotational Capacity of Reinforced Concrete Beams" *Proc. of the Inter. Conf. On Fracture of Concrete and Rock, July 4-6* (1988)
- J.Williams, E.Perkins, "Cgrid- Neighbour search for Many Body Simulation" *Proc. 4th Int. Conf. Discontinuous Deformation Analysis ,University of Glasgow, pp 427-439* 6th–8th June (2001).
- Gen-Hua Shi, "Three Dimensional Discontinuous Deformation Analysis " *Proc. 4th Int. Conf. Discontinuous Deformation Analysis ,University of Glasgow, pp 1-23* 6th–8th June (2001).

Oklahoma

- G. Corley, "Dissecting the Collapses", *Civil Engineering Magazine 72 No5, ASCE., pp 36-45,* (May 2002)
- Construction News "Oklahoma Blast Forces Unsettling Design Questions" (1-5-1995)
- Times international Index *Westminster Research Library, London Volumes from* (1961-1997)
- TL Holzer *et al.* "Interpretation of Seismographs of April 19 1995 Oklahoma City Bombing" *US Geological Survey Menlo Pk CA.* 1995
- HS Norville *et al.* "Glass Related Injuries in the Oklahoma City Bombing" Jour. Perf. Constr. Fac. 13 No 3 pp 100-112 ASCE Press (1995)
- ENR News "Weighing future safety of Federal Buildings" *McGraw-Hill Companies* (May 8 1995)

- M Ettouney *et al.* "Blast resistant design of Commercial Buildings" *Practice Periodical on Structural Design and Construction 1 No1 ASCE Feb* (1996)
- A Longinow *et al.* "Protecting Vehicles against Vehicle Bomb Attacks" *Practice Periodical on Structural Design and Construction 1 No1 ASCE Feb* (1996)
- J O'Connell "Supporting a Fractured Building" *Fire Engineering Nov* (1995)
- M G Brown "The Work of a Task Force: Dismantling a Dying Building" *Fire Engineering Nov* (1995)
- T Carrl "USAR Task Force Logistics" *Fire Engineering (*Nov 1995)
- R Massa"Vulnerability of Buildings to Bombs: Additional Thoughts After Oklahoma City" *Fire Engineering Nov* (1995)
- D J Hammond "Engineering the Collapse: Making the Structure Safe" *Fire Engineering (*Nov 1995)